Lecture Notes in Electrical Engineering 337

Zhidong Deng
Hongbo Li
Editors

Proceedings of the 2015 Chinese Intelligent Automation Conference

Intelligent Automation

Springer

Lecture Notes in Electrical Engineering

Volume 337

About this Series

"Lecture Notes in Electrical Engineering (LNEE)" is a book series which reports the latest research and developments in Electrical Engineering, namely:

- Communication, Networks, and Information Theory
- Computer Engineering
- Signal, Image, Speech and Information Processing
- Circuits and Systems
- Bioengineering

LNEE publishes authored monographs and contributed volumes which present cutting edge research information as well as new perspectives on classical fields, while maintaining Springer's high standards of academic excellence. Also considered for publication are lecture materials, proceedings, and other related materials of exceptionally high quality and interest. The subject matter should be original and timely, reporting the latest research and developments in all areas of electrical engineering.

The audience for the books in LNEE consists of advanced level students, researchers, and industry professionals working at the forefront of their fields. Much like Springer's other Lecture Notes series, LNEE will be distributed through Springer's print and electronic publishing channels.

More information about this series at http://www.springer.com/series/7818

Zhidong Deng · Hongbo Li
Editors

Proceedings of the 2015 Chinese Intelligent Automation Conference

Intelligent Automation

Springer

Editors
Zhidong Deng
Tsinghua University
Beijing
China

Hongbo Li
Department of Computer Science
and Technology
Tsinghua University
Beijing
China

ISSN 1876-1100 ISSN 1876-1119 (electronic)
Lecture Notes in Electrical Engineering
ISBN 978-3-662-46462-5 ISBN 978-3-662-46463-2 (eBook)
DOI 10.1007/978-3-662-46463-2

Library of Congress Control Number: 2015932968

Springer Heidelberg New York Dordrecht London

Printed on acid-free paper

Springer-Verlag GmbH Berlin Heidelberg is part of Springer Science+Business Media (www.springer.com)

Contents

Chapter 1
Variable Thrust Angle Constant Thrust Collision Avoidance Maneuver

Yongqiang Qi and Yong Ma

Abstract In this paper, variable thrust angle (VTA) constant thrust collision avoidance maneuver is studied. For in-plane motion, robust controllers satisfying the requirements can be designed by solving this optimization problem. For out-plane motion, a new algorithm of constant thrust fitting is proposed through impulse compensation and fuel consumption under theoretical continuous thrust and the actual constant thrust is calculated. Finally, illustrative example is provided to show the effectiveness of the proposed control design method.

Keywords Collision avoidance maneuver · Constant thrust · Variable thrust angle · Linear matrix inequality · Robust controller

1.1 Introduction

During the last few decades, the problem of collision avoidance maneuver has been extensively studied and many results have been reported [1–3]. In addition, the variable thrust angle (VTA) constant thrust maneuver, until recent years, has been the least studied [4, 5]. In our previous studies [6], constant thrust control for collision avoidance maneuver was studied based on C-W equations and analytical solutions. However, the traditional open-loop control method used in our previous studies is not applicable although they are often utilized during the long-distance navigation process. To overcome this problem, robust closed-loop variable thrust angle control laws for constant collision avoidance maneuver to enhance orbital control accuracy is proposed in this paper. It is found that the fuel consumption of constant thrust is less than that of the theoretical continuous using the method proposed in this paper.

Y. Qi (✉) · Y. Ma
College of Sciences, China University of Mining and Technology (CUMT), Xvzhou, China
e-mail: qiyongqiang3@163.com

Z. Deng and H. Li (eds.), *Proceedings of the 2015 Chinese Intelligent Automation Conference*, Lecture Notes in Electrical Engineering 337,
DOI 10.1007/978-3-662-46463-2_1

The purpose of this paper is to study VTA constant thrust collision avoidance maneuver; in other words, to design robust closed-loop variable thrust angle control laws for in-plane motion. For in-plane motion, robust control laws for constant thrust variable thrust angle, which satisfy the requirements can be designed by solving the convex optimization problem. Then, for out-plane motion, a new algorithm of constant thrust fitting is proposed using the impulse compensation method. Finally, optimal fuel consumption can be obtained by comparing the theoretical continuous thrust and the actual constant thrust, and then the actual working times of the thrusters can be computed using time series analysis method. An illustrative example is provided to show the effectiveness of the proposed control design method.

1.2 The Robust Variable Thrust Angle Control Laws for In-Plane Motion

The relative motion coordinate system can be established as follows: first, the target spacecraft is assumed as a rigid body and in a circular orbit, and the relative motion can be described by Clohessy-Wiltshire equations. Then, the centroid of the target spacecraft O_T is selected as the origin of coordinate; the x-axis is opposite to the target spacecraft motion, the y-axis is from the center of the earth to the target spacecraft, and the z-axis is determined by the right-handed rule. Then the collision avoidance process can be divided into in-plane motion and out-plane motion based on the relative motion dynamic model as follows, with the relative motion dynamic model of the in-plane motion:

$$\begin{cases} \ddot{x} - 2\omega\dot{y} = \frac{F_x + \eta_x}{m} \\ \ddot{y} + 2\omega\dot{x} - 3\omega^2 y = \frac{F_y + \eta_y}{m} \end{cases} \tag{1.1}$$

where ω represents the angular velocity of the target spacecraft. F_x, F_y represent the vacuum thrust of the chaser and η_x, η_y represent the sum of the perturbation and nonlinear factors in the x-axis and in the y-axis, respectively. m represents the mass of the chaser at the beginning of the collision avoidance maneuver. Suppose there are six thrusters installed on the chaser as shown in Fig. 1.1.

Suppose the actual constant thrusts of the chaser are F_x, F_y, F_z, the maximum thrusts are $\widehat{F}_x, \widehat{F}_y, \widehat{F}_z$, and the theoretical continuous thrusts are F_x^*, F_y^*, F_z^*. The range of the thrust angle in the x-axis θ_x is defined as shown in Fig. 1.2.

The goal of the collision avoidance maneuver is to design a proper controller for the chaser, such that the chaser can be asymptotically maneuvered to the target position. Define the state error vector $x_e(t) = x(t) - x_t(t)$, and its state equation can be obtained as

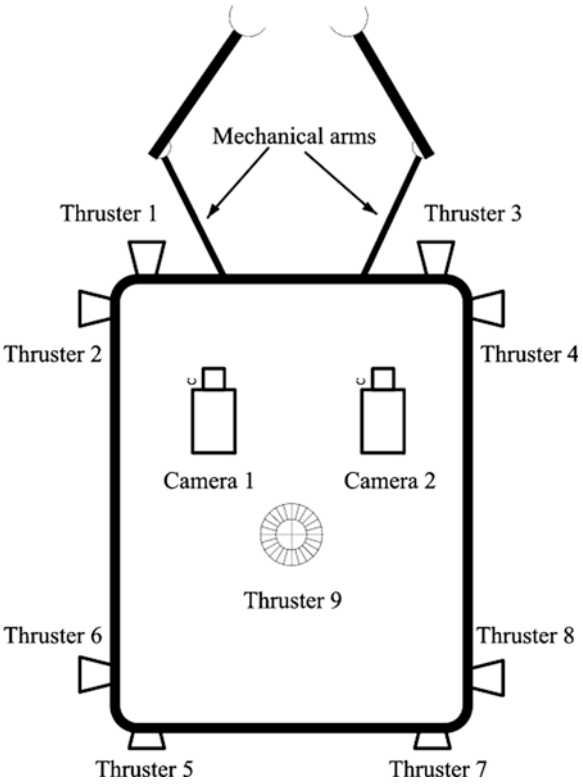

Fig. 1.1 The thrusters of the chaser

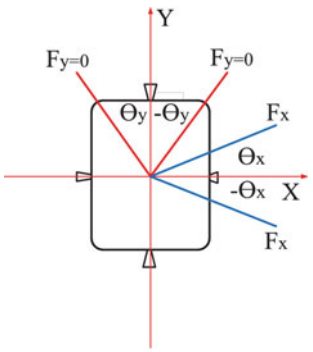

Fig. 1.2 Variable thrust angle thrusters

$$\begin{cases} \dot{x}_e(t) = (A_1 + \Delta A)x_e(t) + (B_1 + \Delta B)u(t) \\ u(t) = Kx_e(t) \end{cases} \tag{1.2}$$

Lyapunov function is defined as follows:

$$V = x_e^T(t)Px_e(t) \tag{1.3}$$

where P is a positive definite symmetric matrix. According to the system stability theory, the necessary and sufficient conditions for robust stability of the system are (1.2) as follow:

$$A^T P + PA < 0 \tag{1.4}$$

Then a multiobjective controller design strategy is proposed by translating a multiobjective controller design problem into a convex optimization problem, and the control input constraints can be met simultaneously. Assuming the initial conditions satisfy the following inequality, where ρ is a given positive constant.

$$x^T(0)Px(0) < \rho \tag{1.5}$$

Theorem 1.1 *If there exist a corresponding dimension of the matrix L, a symmetric positive definite matrix X and two parameters $\varepsilon_1 > 0, \varepsilon_2 > 0$, then the sufficient condition for robust stability exists in a state feedback controller K which can meet the following conditions simultaneously.*

$$\begin{pmatrix} \Sigma & X & L \\ X & -\varepsilon_1 & 0 \\ L^T & 0 & -\varepsilon_2 \end{pmatrix} < 0, \qquad \begin{pmatrix} \rho I & x^T(0) \\ x(0) & X \end{pmatrix} < 0, \tag{1.6}$$

where $\Sigma = XA_0^T + A_0X + L^TB_0 + B_0L + \varepsilon_1\alpha^2 I + \varepsilon_2\beta^2 I$, then the theoretical state feedback controller K can be calculated as follows:

$$K = LX^{-1} = \begin{pmatrix} K_{11} & K_{12} & K_{13} & K_{14} \\ K_{21} & K_{22} & K_{23} & K_{24} \end{pmatrix} \tag{1.7}$$

Then the following results can be obtained.

$$\begin{cases} \dfrac{L_x}{N_x}\hat{F}_x \cos\theta_x + \dfrac{L_y}{N_y}\hat{F}_y \sin\theta_y = k_{11}x_e(t) + k_{12}y_e(t) + k_{13}\Delta V_x + k_{14}\Delta V_y \\ \dfrac{L_x}{N_x}\hat{F}_x \sin\theta_x + \dfrac{L_y}{N_y}\hat{F}_y \cos\theta_y = k_{21}x_e(t) + k_{22}y_e(t) + k_{23}\Delta V_x + k_{24}\Delta V_y \end{cases} \tag{1.8}$$

Then the thrust angle control laws θ_x, θ_y which satisfy the robust stability of the in-plane motion can be obtained from Eq. (1.8).

1.3 Constant Thrust Control Laws for the Out-Plane Motion

The relative motion dynamic model of the out-plane motion is

$$\ddot{z} + \omega^2 z = \frac{F_z + \eta_z}{m} \tag{1.9}$$

For the out-plane motion, a new algorithm of constant thrust fitting is proposed by using the impulse compensation method as follows. Suppose the thrusters in the z-axis can provide different sizes of constant thrust to meet different thrust requirements.

Case I: if the theoretical working time of z-axis thruster in the ith thrust arc $t_z^* = 0$, then the actual constant thrust of the chaser in the z-axis is $F_z = F_z^* = 0$.

Case II: if the working time of z-axis in the ith thrust arc $\Delta T < t_z^* < T_i = M_i \Delta T$, then the constant thrust fitting should be discussed in several subcategories.

Case III: if the theoretical working time of z-axis thruster in the ith thrust arc $t_z^* = \Delta T < T_i$ and t_z^* can be any one of M_i shortest switching time interval in the ith thrust arc. Without loss of generality, suppose that t_z^* is the first shortest switching time interval and the impulse error in the z-axis in the ith thrust arc ΔI_{zi} can be calculated as follows:

Step 1: Choose the size of the constant thrust in Case I. There are $N_z + 1$ thrust levels can be selected and the level of the constant thrust in Case I can be calculated as follows:

$$L_z = \left[\frac{N_z \int_{T_i}^{T_i + \Delta T} \left| F_z^*(t) \right| \mathrm{d}t}{\hat{F}_z \Delta T} \right] \tag{1.10}$$

Step 2: Calculate the impulse error.

$$\Delta I_{zi} = \mathrm{sgn}(F_z^*(t)) \left| \int_{T_i}^{T_{i_l} + \Delta T} \left| F_x^*(t) \right| \mathrm{d}t - \frac{L_z \hat{F}_z \Delta T}{N_z} \right| \tag{1.11}$$

Step 3: Determine the value of the impulse compensation threshold. Suppose that the value of the impulse compensation threshold is a positive constant $\gamma > 0$.

(1) if the impulse error ΔI_{zi} satisfies the following condition:

$$\left| \int_{T_i}^{T_{i_l} + \Delta T} \left| F_x^*(t) \right| \mathrm{d}t - \frac{\hat{F}_z \Delta T}{N_z} \left[\frac{N_z \int_{T_i}^{T_i + \Delta T} \left| F_z^*(t) \right|}{\hat{F}_z \Delta T} \right] \right| \leq \gamma \tag{1.12}$$

the actual constant thrust of the chaser in the z-axis can be calculated as follows:

$$F_z = \mathrm{sgn}(F_z^*(t))\frac{\hat{F}_z\Delta T}{N_z}\left[\frac{N_z\int_{T_i}^{T+\Delta T_i}\left|\hat{F}_z^*(t)\right|\mathrm{d}t}{\hat{F}_z\Delta T}\right] \tag{1.13}$$

then the chaser will not carry out impulse compensation.

(2) if the impulse error ΔI_{zi} satisfies the following condition:

$$\gamma < \left|\int_{T_i}^{T_{i_i}+\Delta T}\left|F_x^*(t)\right|\mathrm{d}t - \frac{\hat{F}_z\Delta T}{N_z}\left[\frac{N_z\int_{T_i}^{T_i+\Delta T}\left|F_z^*(t)\right|}{\hat{F}_z\Delta T}\right]\right| \le \hat{F}_z\Delta T \tag{1.14}$$

then the chaser should carry out impulse compensation and the size of the constant thrust impulse compensation of the chaser in the z-axis can be calculated as follows:

$$\Delta\tilde{I}_{xi} = F_5\Delta T = \frac{\hat{F}_z\Delta T}{N_z}, (F_z^*(t) < 0), \qquad \Delta\tilde{I}_{xi} = F_6\Delta T = -\frac{\hat{F}_z\Delta T}{N_z}, (F_z^*(t) > 0) \tag{1.15}$$

1.4 Simulation Example

The height of target spacecraft is assumed to be 356 km in a circular orbit, then the mean angular velocity is $\omega = 0.0654 \times 10^{-3}$ rad/s and the uncertainty parameters is assumed as $\Delta\omega = \pm 1 \times 10^{-3}$ rad/s. The initial mass of the chaser is assumed to be 200 kg at the beginning of collision avoidance maneuver. The size of thrusts is assumed to be ±1,000 N in three axes and the shortest switching time is $\Delta T = 1$ s. The initial position and velocity of the chaser are assumed to be (1000, −300, and 200 m) and (−10, 3, and −2 m/s). Suppose the thrusters in three axes can provide 10 different sizes of constant thrust. Suppose the value of the impulse compensation threshold is a positive constant $\gamma = 300$ Ns.

Figure 1.3 shows the change in x, y, and z and the theoretical thrust F_x, F_y, F_z during collision avoidance maneuver.

The results in Fig. 1.4 show the change of V_x, V_y, V_z and the thrust angles θ_x, θ_y during collision avoidance maneuver.

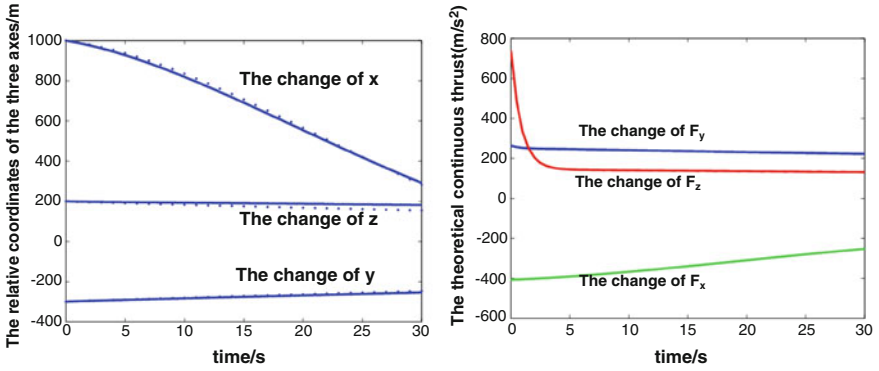

Fig. 1.3 The change in position and thrust

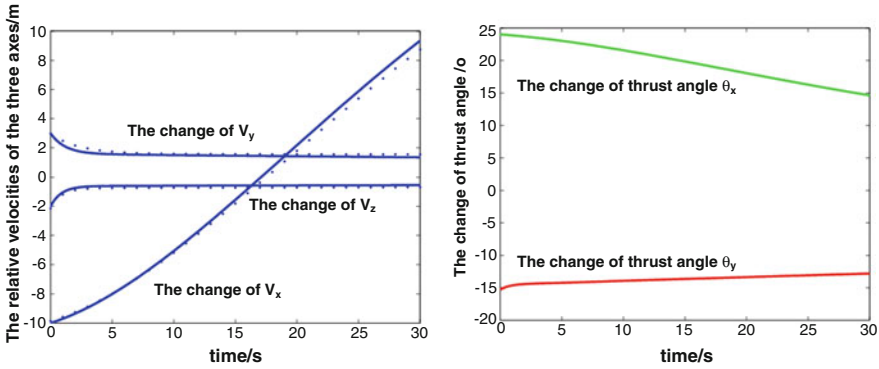

Fig. 1.4 The change in velocity and the thrust angles

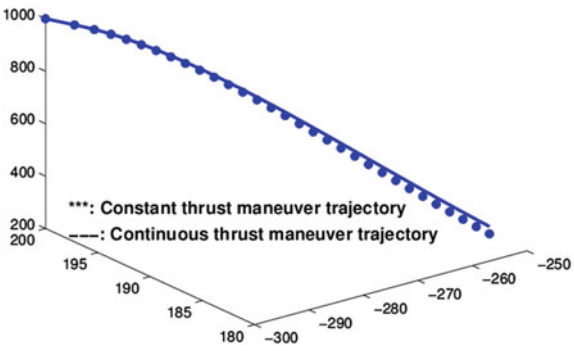

Fig. 1.5 The trajectory of the chaser during collision avoidance

The result in Fig. 1.5 shows the trajectory of chaser during active collision avoidance maneuver. It can be seen that with the switch control, the chaser can get to the 30 target positions smoothly.

Acknowledgments This work was supported by the NSFC 61304088 and 2013QNA37.

References

1. Patera RP, Peterson GE (2003) Space vehicle maneuver method to lower collision risk to an acceptable level. J Guid Control Dyn 26:233–237
2. Slater GL, Byram SM, Williams TW (2006) Collision avoidance for satellites in formation flight. J Guid Control Dyn 29:1140–1146
3. Patera RP (2007) Space vehicle conflict-avoidance analysis. J Guid Control Dyn 30:492–498
4. Schouwenaars T, How JP, Feron E (2004) Decentralized cooperative trajectory planning of multiple aircraft with hard safety guarantees. AIAA paper
5. Richards A, Schouwenaars T, How J et al (2002) Spacecraft trajectory planning with avoidance constraints using mixedinteger linear programming. J Guid Control Dyn 25(4):755–764
6. Qi YQ, Jia YM (2011) Active collision avoidance maneuver under constant thrust. Adv Space Res 48(2):349–361

Chapter 2
Robust Control for Constant Thrust Rendezvous

Yongqiang Qi and Minghui Ou

Abstract In this paper, a robust orbit design approach under constant thrust is proposed based on the relative motion dynamic model. First, the design problem is cast into a convex optimization problem by introducing a Lyapunov function subject to linear matrix inequalities. Next, the robust controllers satisfying the requirements can be designed by solving this optimization problem. At last, the proposed method has the advantage of saving fuel is proved and the actual constant thrust switch control laws are obtained through the isochronous interpolation method, an illustrative example is provided to show the effectiveness of the proposed control design method.

Keywords Rendezvous · Constant thrust · Linear matrix inequality · Robust controller

2.1 Introduction

New challenges arise from the International Space Station (ISS) and the numerous formation flight projects [1, 2]. The close range rendezvous phase is usually divided into two subphases: a preparatory phase leading to the final approach corridor and a final approach phase leading to the mating conditions. The objectives of the close range rendezvous phase are the reduction of the range to the target and the achievement of conditions allowing the acquisition of the final approach corridor [3]. This means that at the end of this phase the chaser is, concerning position, velocity, attitude, and angular rates, ready to start the final approach on the proper approach axis within the constraints of the safety corridor [4, 5].

The rendezvous problem has been extensively studied as an optimal control problem [3, 6]. Both impulsive thrust and the continuous thrust assumptions have

Y. Qi (✉) · M. Ou
College of Sciences, China University of Mining and Technology, Beijing, China
e-mail: qiyongqiang3@163.com

Z. Deng and H. Li (eds.), *Proceedings of the 2015 Chinese Intelligent Automation Conference*, Lecture Notes in Electrical Engineering 337,
DOI 10.1007/978-3-662-46463-2_2

been exploited through the Pontryagin's maximum principle, respectively. In actual practice, maneuver during rendezvous and docking operations cannot normally be considered as continuous thrust or impulsive maneuver. In our previous study, constant thrust fuel-optimal control for spacecraft rendezvous was studied according to the C-W equations and the analytical solutions. But the traditional open-loop control method used in our previous studies is not applicable while they are often utilized during the long-distance navigation process. To overcome this problem, a robust closed-loop control law for constant thrust rendezvous to enhance the orbital control accuracy is proposed in this paper. And the fuel consumption of constant thrust is less than that of the continuous thrust by using the method proposed in this paper.

2.2 Multiobjective Robust Controller Design

The relative motion coordinate system can be established as follows: first, the target spacecraft is assumed as a rigid body and in a circular orbit, and the relative motion can be described by Clohessy-Wiltshire equations. Then, the centroid of the target spacecraft O_T is selected as the origin of coordinate, the x-axis is opposite to the target spacecraft motion, the y-axis is from the center of the earth to the target spacecraft, and the z-axis is determined by the right-handed rule.

$$\begin{cases} \ddot{x} - 2\omega\dot{y} = \frac{F_x + \eta_x}{m} \\ \ddot{y} + 2\omega\dot{x} - 3\omega^2 y = \frac{F_y + \eta_y}{m} \\ \ddot{z} + \omega^2 z = \frac{F_z + \eta_z}{m} \end{cases} \tag{2.1}$$

where ω represents the angular velocity. F_x, F_y, F_z represent the vacuum thrust of the chaser, η_x, η_y, η_z represent the sum of the perturbation and nonlinear factors in the three axes, respectively. m represents the mass of the chaser at the beginning of the rendezvous. Suppose that the maximum thrusts are $\widehat{F}_x, \widehat{F}_y, \widehat{F}_z$ and the theoretical thrusts are F_x^*, F_y^*, F_z^*. The range of the thrust angle in the x-axis θ_x is defined as shown in Fig. 2.1.

The goal of the rendezvous maneuver is to design a proper controller for the chaser, such that the chaser can be asymptotically maneuvered to the target position. Define the state error vector $x_e(t) = x(t) - x_t(t)$, and its state equation can be obtained as

$$\begin{cases} \dot{x}_e(t) = (A_1 + \Delta A)x_e(t) + (B_1 + \Delta B)u(t) \\ u(t) = Kx_e(t) \end{cases} \tag{2.2}$$

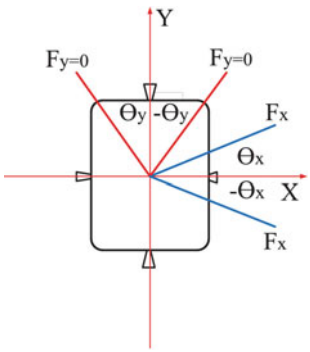

Fig. 2.1 Variable thrust angle thrusters

Lyapunov function is defined as follows:

$$V = x_e^T(t)Px_e(t) \tag{2.3}$$

where P is a positive definite symmetric matrix. According to the system stability theory, the necessary and sufficient conditions for robust stability of the system (2.3) are as follow:

$$A^TP + PA < 0 \tag{2.4}$$

Then a multiobjective controller design strategy is proposed by translating a multiobjective controller design problem into a convex optimization problem. And the control input constraints can be met simultaneously. Assuming the initial conditions satisfy the following inequality, where ρ is a given positive constant.

$$x^T(0)Px(0) < \rho \tag{2.5}$$

Theorem 2.1 *If there exist a corresponding dimension of the matrix L, a symmetric positive definite matrix X, and two parameters* $\varepsilon_1 > 0, \varepsilon_2 > 0$*, then the sufficient condition for robust stability is there exist a state feedback controller K which can meet the following conditions simultaneously.*

$$\begin{pmatrix} \Sigma & X & L \\ X & -\varepsilon_1 & 0 \\ L^T & 0 & -\varepsilon_2 \end{pmatrix} < 0, \quad \begin{pmatrix} \rho I & x^T(0) \\ x(0) & X \end{pmatrix} < 0, \tag{2.6}$$

where $\Sigma = XA_0^T + A_0X + L^TB_0 + B_0L + \varepsilon_1\alpha^2I + \varepsilon_2\beta^2I$*, then the theoretical state feedback controller K can be calculated as follows*:

$$K = LX^{-1} = \begin{pmatrix} K_{11} & K_{12} & K_{13} & K_{14} \\ K_{21} & K_{22} & K_{23} & K_{24} \end{pmatrix} \tag{2.7}$$

Then the following results can be obtained.

$$\begin{cases} \dfrac{L_x}{N_x}\hat{F}_x \cos\theta_x + \dfrac{L_y}{N_y}\hat{F}_y \sin\theta_y = k_{11}x_e(t) + k_{12}y_e(t) + k_{13}\Delta V_x + k_{14}\Delta V_y \\ \dfrac{L_x}{N_x}\hat{F}_x \sin\theta_x + \dfrac{L_y}{N_y}\hat{F}_y \cos\theta_y = k_{21}x_e(t) + k_{22}y_e(t) + k_{23}\Delta V_x + k_{24}\Delta V_y \end{cases} \tag{2.8}$$

Then the thrust angle control lows θ_x, θ_y which satisfy the robust stability of the in plane motion can be obtained from Eq. (2.8).

2.3 Compare Fuel Consumption and Calculate the Control Law

Constant thrust fitting is proposed by using the impulse compensation method as follow. Suppose that the thrusters in the z-axis can provide different sizes of constant thrust to meet different thrust requirements. If the theoretical working time of z-axis thruster in the ith thrust arc $t_z^* = \Delta T < T_i$ and t_z^* can be any one of M_i shortest switching time interval in the ith thrust arc. Without loss of generality, suppose that t_z^* is the first shortest switching time interval and the impulse error in the z-axis in the ith thrust arc ΔI_{zi} can be calculated as follows:

There are $N_z + 1$ thrust levels that can be selected and the level of the constant thrust can be calculated as follows:

$$L_z = \left[\frac{N_z \int_{T_i}^{T_i+\Delta T} \left|F_z^*(t)\right| \mathrm{d}t}{\hat{F}_z \Delta T} \right] \tag{2.9}$$

Calculate the impulse error.

$$\Delta I_{zi} = \mathrm{sgn}(F_z^*(t)) \left| \int_{T_i}^{T_{i_l}+\Delta T} \left|F_x^*(t)\right| \mathrm{d}t - \frac{L_z \hat{F}_z \Delta T}{N_z} \right| \tag{2.10}$$

Determine the value of the impulse compensation threshold. Suppose that the value of the impulse compensation threshold is a positive constant $\gamma > 0$, if the impulse error ΔI_{zi} satisfies the following condition,

$$\left| \int_{T_i}^{T_{i_i}+\Delta T} \left|F_x^*(t)\right| \mathrm{d}t - \frac{\hat{F}_z \Delta T}{N_z} \left[\frac{N_z \int_{T_i}^{T_i+\Delta T} \left|F_z^*(t)\right|}{\hat{F}_z \Delta T} \right] \right| \leq \gamma \tag{2.11}$$

the actual constant thrust of the chaser in the z-axis can be calculated as follows:

$$F_z = \mathrm{sgn}(F_z^*(t)) \frac{\hat{F}_z \Delta T}{N_z} \left[\frac{N_z \int_{T_i}^{T+\Delta T_i} \left|\hat{F}_z^*(t)\right| \mathrm{d}t}{\hat{F}_z \Delta T} \right] \tag{2.12}$$

then the chaser will not carry out impulse compensation. The fuel savings in the x-axis in the ith thrust arc can be calculated as follows:

$$\Delta P_{zi} = \sum_{j=0}^{M_1} \int_{T_i+j\Delta T}^{T_i+(j+1)\Delta T} \left\{ \frac{p_0 N_z \left|F_z^*(t)\right|}{\hat{F}_z} - \mathrm{sgn}(F_z^*(t)) p_0 \left[\frac{N_z \int_{T_i+j\Delta T}^{T+(j+1)\Delta T} \left|\hat{F}_z^*(t)\right| \mathrm{d}t}{\hat{F}_z \Delta T} \right] \right\} \mathrm{d}t \tag{2.13}$$

Then the total number of the accelerating time intervals and the decelerating time intervals is $M_1 - m_1$ and the number of zero-thrust time intervals is $M_1 - M_1 + m_1$. The position of the three types of time intervals is decided by the curve of the theoretical continuous thrust.

At last, the switch control laws for the rendezvous maneuver can be given in three axes. For convenience, let us take the time intervals in the ith thrust arc in the x-axis for example:

$$S_{zi} = \left\{ \left(T_i + j\Delta T, \mathrm{sgn}(F_z^*(t)) \frac{\hat{F}_z \Delta T}{N_z} \left[\frac{N_z \int_{T_i+j\Delta T}^{T+(j+1)\Delta T} \left|\hat{F}_z^*(t)\right| \mathrm{d}t}{\hat{F}_z \Delta T} \right] \right) \right\} \tag{2.14}$$

2.4 Simulation Example

The height of target spacecraft is assumed to be 356 km in a circular orbit, then the mean angular velocity is $\omega = 0.0654 \times 10^{-3}$ rad/s and the uncertainty parameters is assumed as $\Delta\omega = \pm 1 \times 10^{-3}$ rad/s. The initial mass of the chaser is assumed to be 300 kg at the beginning of rendezvouse maneuver. The size of thrusts are assumed to be ±3,000 N in three axes and the shortest switching time is $\Delta T = 1$ s. The initial position and velocity of the chaser are assumed to be (2000, 100, −500 m) and (−20, 10, 5 m/s). Suppose that the thrusters in three axes can provide

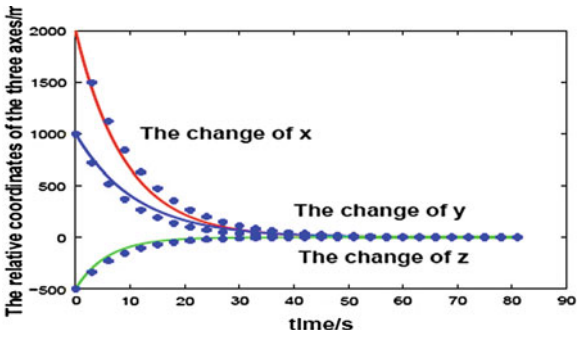

Fig. 2.2 The change of position during rendezvous maneuver

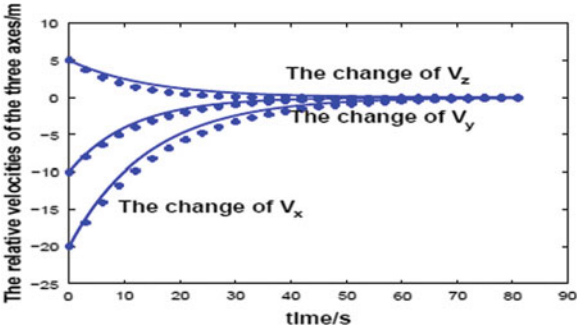

Fig. 2.3 The change of velocity during rendezvous maneuver

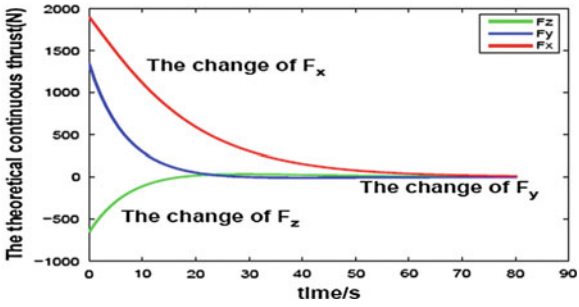

Fig. 2.4 The change of thrust during rendezvous maneuver

10 different sizes of constant thrust. Suppose that the value of the impulse compensation threshold is a positive constant $\gamma = 300$ Ns.

Figure 2.2 shows the change of x, y, and z during rendezvous maneuver.

The results in Fig. 2.3 show the change of $V_{x,}V_{y}, V_{z}$ during rendezvous maneuver.

The results in Fig. 2.4 show the change of $F_{x}, F_{y,}F_{z}$ during rendezvouse maneuver.

The results in Fig. 2.5 show the change of F_z during rendezvous maneuver.

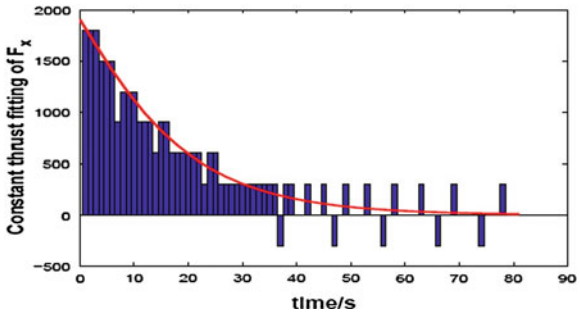

Fig. 2.5 The constant thrust fitting of F_x during rendezvous maneuver

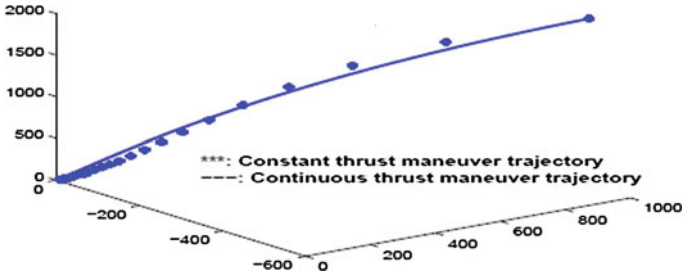

Fig. 2.6 The trajectory of the chaser during rendezvouse maneuver

The result in Fig. 2.6 shows the trajectory of chaser during rendezvous maneuver. It shows that with the switch control control, the chaser can get to the 27 target positions smoothly. The solid lines represent the curves caused by theoretical thrust and the dotted lines represent the curves caused by constant thrust.

The fuel savings in the x-axis in the ith thrust arc can be calculated as follows:

$$\Delta P_{zi} = \sum_{i=1}^{27} \sum_{j=1}^{3} \int_{T_i}^{T_i+j} \left\{ \frac{\left|F_z^*(t)\right|}{30} - 10\mathrm{sgn}(F_z^*(t)) \left[\frac{N_z \int_{T_i}^{T+j} \left|\hat{F}_z^*(t)\right| \mathrm{dt}}{300} \right] \right\} \mathrm{dt} = 19.9158\mathrm{g} \tag{2.15}$$

At last, the switch control laws for the ith thrust arc in the z-axis for example:

$$S_{zi} = \{1{,}000\ \mathrm{m}; -10\ \mathrm{m/s}; (1\ \mathrm{s}, 1{,}800\ \mathrm{N}); \ldots (77\ \mathrm{s}, -300\ \mathrm{N}); \ldots\} \tag{2.16}$$

Acknowledgments This work was supported by the NSFC 61304088 and 2013QNA37.

References

1. Patera RP, Peterson GE (2003) Space vehicle maneuver method to lower collision risk to an acceptable level. J Guid Control Dyn 26:233–237
2. Slater GL, Byram SM, Williams TW (2006) Rendezvouse for satellites in formation flight. J Guid Control Dyn 29:1140–1146
3. Richards A, Schouwenaars T, How J et al (2002) Spacecraft trajectory planning with avoidance constraints using mixed integer linear programming. J Guid Control Dyn 25(4):755–764
4. Patera RP (2007) Space vehicle conflict-avoidance analysis. J Guid Control Dyn 30:492–498
5. Schouwenaars T, How JP, Feron E (2004) Decentralized cooperative trajectory planning of multiple aircraft with hard safety guarantees. In: AIAA paper
6. Qi YQ, Jia YM (2012) Constant Thrust fuel-optimal control for spacecraft rendezvous. Adv Space Res 49(7):1140–1150

Chapter 3
Dissipativity Analysis and Synthesis of Singular Systems via Delta Operator Method

Chun-ming Qi, Xin-zhuang Dong and Lin Liu

Abstract This paper investigates the problems of dissipativity analysis and synthesis for singular systems through delta operator method. First, a sufficient condition is obtained such that a singular delta operator system is admissible and strictly dissipative. Then the existence condition and explicit expression of a state feedback strictly dissipative controller are presented. A numerical example is also provided to demonstrate the effectiveness of the theoretical results.

Keywords Singular delta operator systems · Admissibility · Strict dissipativity · State feedback · Linear matrix inequality

3.1 Introduction

During the past decades, much attention has been paid to singular systems as they can describe many practical systems such as economic systems, electrical networks, highly interconnected large-scale systems, etc. [1]. Many achievements have been made in singular system theory in recent years [1–5, 8–10, 15]. Dissipativity theory is an important part in control theory which has made a positive effect on studying stability and other properties of control systems [12, 13]. There have been some valuable results on dissipativity analysis and dissipative control for singular systems [2, 8, 9]. For example, a necessary and sufficient condition was obtained to ensure an uncertain singular discrete system admissible and strict dissipative [2]. The existence condition and explicit expression of a state feedback strictly dissipative controller were also given in [2]. The results of robust dissipativity analysis and some design method of a robust dissipative controller were presented for singular continuous systems with affine uncertainty in [8, 9], respectively.

C. Qi · X. Dong (✉) · L. Liu
College of Automation Engineering, Qingdao University, Qingdao 266071, China
e-mail: xzdong@hotmail.com

Z. Deng and H. Li (eds.), *Proceedings of the 2015 Chinese Intelligent Automation Conference*, Lecture Notes in Electrical Engineering 337,
DOI 10.1007/978-3-662-46463-2_3

In control theory, most research results adopt the standard shift operator in the study of discrete systems. But there exists a problem that the dynamic response of a discrete system does not converge smoothly to its continuous counterpart when the sampling period tends to zero [11], which is called the numerical ill-condition. In order to avoid the above problem, a delta operator method was proposed in [6]. It was shown that the delta operator requires smaller word length when implementing fixed-point digital control processors than the shift operator does [7]. The delta operator method is also significantly less sensitive than the shift operator method at high sampling rates [14]. Furthermore, the delta operator model can provide a theoretically unified formulation of normal continuous and discrete systems. Most recently, the delta operator method has been introduced to study singular systems and some valuable results have been derived. Dong [3] and Dong et al. [4] studied the problem of admissibility analysis for singular systems via delta operator method. Dong et al. [4] and Mao et al. [10] considered the problem of admissible control for singular delta operator systems. But until now there is no result on dissipativity analysis and control for singular delta operator systems.

In this paper, we consider the problems of dissipativity analysis and synthesis for singular delta operator systems. A sufficient condition is obtained such that a singular delta operator system is admissible and strictly dissipative. Based on the above result, the existence condition and explicit expression of a state feedback strictly dissipative controller are presented. A numerical example is also provided to demonstrate the effectiveness of the theoretical results.

Throughout this paper, the following notations are adopted: δ is the delta operator defined by $\delta x(t) = \dot{x}(t)$ when $h = 0$ and $\delta x(t) = h^{-1}(x(t+h) - x(t))$ when $h \neq 0$, where h is the sampling period. Matrix $P > 0$ (or $P < 0$, respectively) means that P is symmetric and positive definite (or negative definite, respectively). $D_{\text{int}}(a, r)$ is the interior of the region in the complex plane with the center at $(a, 0)$ and the radius r. $\lambda(A, B) = \{z | \det(zA - B) = 0\}$.

3.2 Preliminaries

Consider the following singular delta operator system:

$$\begin{aligned} E\delta x(t_k) &= Ax(t_k) + B_1 w(t_k) \\ z(t_k) &= Cx(t_k) + D_1 w(t_k) \end{aligned} \tag{3.1}$$

where $x(t_k) \in R^n$ is the state, $w(t_k) \in R^p$ is the disturbance input, $z(t_k) \in R^q$ is the controlled output, t_k means the time $t = kh$, and $h > 0$ is the sampling period. $E \in R^{n \times n}$ and $\text{rank}(E) = r < n$, A, B_1, C, D_1 are known real matrices with appropriate dimensions.

Consider the following system:

$$E\delta x(t_k) = Ax(t_k) \tag{3.2}$$

Definition 3.1 [3] The system (3.2) is said to be regular if $\det(\eta E - A)$ is not identically zero. The system (3.2) is said to be causal if $^{\circ}(\det(\eta E - A)) = \text{rank}(E)$. The system (3.2) is said to be stable if $\lambda(E, A) \subset D_{\text{int}}(-1/h, 1/h)$. The system (3.2) is said to be admissible if it is regular, causal, and stable.

Lemma 3.1 [3] *The system (3.2) is admissible if and only if there exist matrices $P > 0$ and F satisfying $hA^TPA + A^TPE + E^TPA + FG^TA + A^TGF^T < 0$, where G is any matrix of full column rank and satisfies $E^TG = 0$.*

The energy supply function of the system (3.1) is defined by $E(w, z, T) = <z, Qz>_T + 2<z, Sw>_T + <w, Rw>_T$, where T is a nonnegative integer; Q, S, and R are known real matrices with Q and R symmetric. $<u, v>_T$ is defined as $<u, v>_T = \sum_{k=0}^{T} u(t_k)^T v(t_k)$.

Definition 3.2 [2] The system (3.1) is said to be strictly (Q, S, R) dissipative if for some scalar $\alpha > 0$ and under zero initial state $x(0) = 0$, the following inequality holds

$$E(w, z, T) \geq \alpha <w, w>_T, \quad \forall T \geq 0 \tag{3.3}$$

In order to include H_∞ performance (where $Q = -I, S = 0, R = \gamma^2 I$) and passivity (where $Q = 0, S = I, R = 0$) as special cases of the above strict (Q, S, R) dissipativity, we make the following assumption:

Assumption 3.1 $Q \leq 0$.

3.3 Dissipativity Analysis

The purpose of this section is to present some conditions for the system (3.1) to be admissible (when $w(t_k) = 0$) and strictly dissipative (when $w(t_k) \neq 0$). The dissipativity analysis result is given in the following theorem:

Theorem 3.1 *Let the matrices Q, S, and R be given with Q and R symmetric and Assumption 3.1 holds. Then the system (3.1) is admissible and strictly (Q, S, R) dissipative if there exist matrices $P > 0$ and F satisfying*

$$\begin{bmatrix} \Sigma_{11} & \Sigma_{21}^T & C^TQ_1^T \\ \Sigma_{21} & \Sigma_{22} & D_1^TQ_1^T \\ Q_1C & Q_1D_1 & -I \end{bmatrix} < 0 \tag{3.4}$$

where Q_1 is any matrix satisfying $Q_1^T Q_1 = -Q$, G is any matrix of full column rank and satisfies $E^T G = 0$, $\Sigma_{11} = hA^T PA + A^T PE + E^T PA + FG^T A + A^T GF^T$, $\Sigma_{21} = hB_1^T PA + B_1^T PE + B_1^T GF^T - S^T C$, $\Sigma_{22} = hB_1^T PB_1 - D_1^T S - S^T D_1 - R$.

Proof Assume that the inequality (3.4) holds. From (3.4) it is easy to obtain

$$hA^T PA + A^T PE + E^T PA + FG^T A + A^T GF^T < 0 \tag{3.5}$$

Then from Lemma 3.1 we have that the system (3.1) is admissible.
From $E^T G = 0$ we have

$$0 = 2\delta x(t_k)^T E^T GF^T x(t_k) = \begin{bmatrix} x(t_k)^T & w(t_k)^T \end{bmatrix} \Omega_1 \begin{bmatrix} x(t_k) \\ w(t_k) \end{bmatrix}$$

where

$$\Omega_1 = \begin{bmatrix} A^T GF^T + FG^T A & FG^T B_1 \\ B_1^T GF^T & 0 \end{bmatrix}$$

Let $V(x(t_k)) = (x(t_k))^T E^T PEx(t_k)$ and then we can derive $V(x(t_k)) \geq 0$ for any $k \geq 0$ from $P > 0$. Then we have

$$\begin{aligned} J &= \delta V(x(t_k)) - z(t_k)^T Qz(t_k) - 2z(t_k)^T Sw(t_k) - w(t_k)^T Rw(t_k) \\ &= (E\delta x(t_k))^T PEx(t_k) + x(t_k)^T E^T PE\delta x(t_k) + h(E\delta x(t_k))^T PE\delta x(t_k) \\ &\quad - z(t_k)^T Qz(t_k) - 2z(t_k)^T Sw(t_k) - w(t_k)^T Rw(t_k) \\ &= \begin{bmatrix} x(t_k)^T & w(t_k)^T \end{bmatrix} \Omega_2 \begin{bmatrix} x(t_k) \\ w(t_k) \end{bmatrix} \\ &= \begin{bmatrix} x(t_k)^T & w(t_k)^T \end{bmatrix} (\Omega_1 + \Omega_2) \begin{bmatrix} x(t_k) \\ w(t_k) \end{bmatrix} \end{aligned}$$

where

$$\Omega_2 = \begin{bmatrix} E^T PA + A^T PE + hA^T PA - C^T QC & E^T PB_1 + hA^T PB_1 - C^T S - C^T QD_1 \\ B_1^T PE + hB_1^T PA - S^T C - D_1^T QC & \Sigma_{22} - D_1^T QD_1 \end{bmatrix}$$

When (3.4) holds, from Schur complement we have that (3.4) is equivalent to $\Omega_1 + \Omega_2 < 0$ which means $J < 0$. In this case, a sufficiently small scalar $\alpha > 0$ can always be found such that $J + \alpha w(t_k)^T w(t_k) \leq 0$. Sum the above inequality up from 0 to T, and notice that $h > 0, x(0) = 0$, $V(x(t_T)) \geq 0$, we can obtain

$$h^{-1} V(x(t_T)) - E(w, z, T) + \alpha < w, w >_T \leq 0$$

Therefore from the above inequality and Definition 3.2 we have that the system (3.1) is strictly (Q, S, R) dissipative. This completes the proof.

3.4 Dissipative Control

Consider the following singular delta operator system with control input

$$\begin{aligned} E\delta x(t_k) &= Ax(t_k) + B_1 w(t_k) + B_2 u(t_k) \\ z(t_k) &= Cx(t_k) + D_1 w(t_k) + D_2 u(t_k) \end{aligned} \tag{3.6}$$

where $u(t_k) \in R^m$ is the control input, B_2, D_2 are known real matrices with appropriate dimensions, the other notations are the same as those in (3.1).

The purpose of this section is to design a state feedback controller

$$u(t_k) = Kx(t_k) \tag{3.7}$$

for the system (3.6), such that the resulting closed-loop system

$$\begin{aligned} E\delta x(t_k) &= A_c x(t_k) + B_1 w(t_k) \\ z(t_k) &= C_c x(t_k) + D_1 w(t_k) \end{aligned} \tag{3.8}$$

is admissible and strictly (Q, S, R) dissipative, and in this case the controller (3.7) is said to be a strictly dissipative controller for the system (3.6), where K is the controller gain matrix to be designed and $A_c = A + B_2 K, C_c = C + D_2 K$.

The dissipativity synthesis result is given in the following theorem.

Theorem 3.2 *Let the matrices Q, S, and R be given with Q and R symmetric and Assumption* 3.1 *hold. Then there exists a state feedback strictly dissipative controller* (3.7) *for the system* (3.6) *if there exist matrices* $P > 0, F$ *and a scalar* $\varepsilon \geq 0$ *satisfying*

$$\begin{bmatrix} \Sigma_{11} - W^T Z^{-1} W & \Sigma_{21}^T & C^T Q_1^T \\ \Sigma_{21} & \Sigma_{22} & D_1^T Q_1^T \\ Q_1 C & Q_1 D_1 & -I \end{bmatrix} < 0 \tag{3.9}$$

where $Q_1, G, \Sigma_{11}, \Sigma_{21}, \Sigma_{22}$ *are the same as those in Theorem* 3.1, *and* $M = \Sigma_{22} - D_1^T Q D_1, N = hB_1^T PB_2 - S^T D_2 - D_2^T Q D_1, L = \Sigma_{21} - D_1^T QC, Z = hB_2^T PB_2 - D_2^T Q D_2 - N^T M^{-1} N + \varepsilon I > 0$, $W = hB_2^T PA + B_2^T PE - B_2^T GF^T - D_2^T QC - N^T M^{-1} L$. *In this case, the gain matrix K of the controller* (3.7) *can be designed as*

$$K = -Z^{-1} W \tag{3.10}$$

Proof Assume that the inequality (3.9) holds. From Theorem 3.1, we have that system (3.8) is admissible and strictly (Q, S, R) dissipative, if there exist matrices $P > 0$ and F satisfying the following inequality:

$$\begin{bmatrix} \Pi_{11} & \Pi_{21}^T & C_c^T Q_1^T \\ \Pi_{21} & \Sigma_{22} & D_1^T Q_1^T \\ Q_1 C_c & Q_1 D_1 & -I \end{bmatrix} < 0 \tag{3.11}$$

where Π_{11}, Π_{21} are obtained from Σ_{11}, Σ_{21} by replacing the matrices A, C with A_c, C_c, respectively.

From Schur complement, the inequality (3.11) is equivalent to

$$\begin{bmatrix} \Pi_{11} & \Pi_{21}^T \\ \Pi_{21} & \Sigma_{22} \end{bmatrix} - \begin{bmatrix} C_c^T \\ D_1^T \end{bmatrix} Q \begin{bmatrix} C_c & D_1 \end{bmatrix} < 0 \tag{3.12}$$

Again by Schur complement, we know that (3.12) is equivalent to $M < 0$ and

$$H = \Pi_{11} - C_c^T Q C_c - (\Pi_{21}^T - C_c^T Q D_1) M^{-1} (\Pi_{21} - D_1^T Q C_c) < 0 \tag{3.13}$$

The inequality (3.13) is also the same as

$$H = H_1 + W^T K + K^T W + K^T (Z - \varepsilon I) K < 0 \tag{3.14}$$

where $H_1 = \Sigma_{11} - C^T Q C - L^T M^{-1} L$.

Similarly, from Schur complement, we can obtain that the inequality (3.9) is equivalent to $H_1 - W^T Z^{-1} W < 0$, which together with $\varepsilon \geq 0$ and (3.10) gives

$$\begin{aligned} H &\leq H_1 + W^T K + K^T W + K^T Z K \\ &= H_1 - W^T Z^{-1} W + (K^T + W^T Z^{-1}) Z (K + Z^{-1} W) = H_1 - W^T Z^{-1} W < 0 \end{aligned}$$

Then the inequality (3.14) (i.e. (3.11)) holds. Thus from Theorem 3.1 we have that the closed-loop system (3.8) is admissible and strictly (Q, S, R) dissipative and the controller (3.7) is indeed a strictly dissipative controller of the system (3.6). This completes the proof.

3.5 Example

Consider the system (3.6) with the following parameter matrices

$$E = \begin{bmatrix} 1 & 0 \\ 2 & 0 \end{bmatrix}, A = \begin{bmatrix} -1 & 0 \\ 1 & 7 \end{bmatrix}, B_1 = \begin{bmatrix} -0.4 \\ 1 \end{bmatrix}, B_2 = \begin{bmatrix} -2 \\ -1 \end{bmatrix}$$

$$C = [-2 \quad 1], D_1 = 1, D_2 = -6, h = 0.1$$

Let $Q = -1, S = 0.4, R = 2$ and $G = [-2 \quad 1]^T$. First we solve the inequality (3.4) and cannot find a feasible solution. Thus from Theorem 3.1 we know that the above system is not admissible and strictly dissipative. Next we want to design a state feedback strictly dissipative controller for the above system. Select

$$P = \begin{bmatrix} 1 & -0.01 \\ -0.01 & 0.02 \end{bmatrix}, F = \begin{bmatrix} 0.1 \\ -1 \end{bmatrix}, \varepsilon = 0$$

and then we can obtain that the inequality (3.9) indeed holds from

$$\begin{bmatrix} -5.839 & 0.8871 & 0.5614 & -2 \\ 2.8871 & -1.5647 & -1.1832 & 1 \\ 0.5614 & -1.1832 & -2.7812 & 1 \\ -2 & 1 & 1 & -1 \end{bmatrix} < 0$$

Then by Theorem 3.2, there exists a strictly dissipative controller (3.7) for the system (3.1) and it can be designed as $u(t_k) = [-0.2816 \quad 0.1763]x(t_k)$.

3.6 Conclusion

In this paper, the problems of dissipativity analysis and synthesis have been considered for singular systems via delta operator method. A sufficient condition about dissipativity analysis has been presented for singular delta operator systems. Based on the above result, the existence condition and design method of a state feedback strictly dissipative controller have also been derived. An example is also provided to illustrate the effectiveness of the obtained results.

Acknowledgments This work is supported by National Natural Science Foundation of China under Grant 61104001.

References

1. Dai L (1989) Singular control systems. Springer-Verlag, Berlin
2. Dong X (2007) Robust strictly dissipative control for discrete singular system. IET Control Theory Appl 1(4):1060–1067
3. Dong X (2014) Admissibility analysis of linear singular systems via a delta operator method. Int J Syst Sci 45(11):2366–2375
4. Dong X, Tian W, Mao Q et al (2013) Robust admissibility analysis and synthesis of uncertain singular systems via delta operator approach. In: 10th IEEE international conference on control & automation, Hangzhou, China, pp 1059–1064

5. Duan G, Yu H, Wu A et al (2012) Analysis and design of descriptor linear systems. Science Press, Beijing
6. Goodwin GC, Lozano Leal R, Mayne DQ, Middleton RH (1986) Rapproachement between continuous and discrete model reference adaptive control. Automatica 22(2):199–207
7. Li G, Gevers M (1993) Comparative study of finite wordlength effects in shift and delta operator parameterizations. IEEE Trans Autom Control 38(5):803–807
8. Liu L, Dong X, Wang W (2011) Robust strict dissipativeness analysis for affinely uncertain singular systems. In: 2011 IEEE 5th international conference on cybernetics and intelligent systems, Qingdao, China, pp 81–86
9. Liu L, Dong X, Wang W (2011) State feedback robust dissipative control for singular systems with affine uncertainty. In: 2011 IEEE 5th international conference on cybernetics and intelligent systems, Qingdao, China, pp 99–104
10. Mao Q, Dong X, Tian W (2012) Admissibility conditions for linear singular delta operator systems: analysis and synthesis. In: Proceedings of the 10th world congress on intelligent control and automation. Beijing, China, pp 1870–1875
11. Middleton R, Goodwin GC (1986) Improved finite word length characteristics in digital control using delta operators. IEEE Trans Autom Control 31(11):1015–1021
12. Willems JC (1972) Dissipative dynamical systems—part 1: general theory. Arch Ration Mech Anal 45(5):321–351
13. Willems JC (1972) Dissipative dynamical systems—part 2: linear systems with quadratic supply rates. Arch Ration Mech Anal 45(5):352–393
14. Wu J, Li G, Istepanian RH, Chu J (2000) Shift and delta operator realisation for digital controllers with finite word length consideration. IEEE Proc Control Theory Appl 147(6): 664–672
15. Xu S, Lam J (2006) Robust control and filtering of singular systems. Springer, Berlin

Chapter 4
Intelligent Welding Robot Path Planning

Xue Wu Wang, Ying Pan Shi, Rui Yu and Xing Sheng Gu

Abstract Spot welding robots are now widely used in manufacturing industry, and usually many welding joints have to be traversed in welding process. The path planning for welding robot is based on engineering experiments where teaching and playback were applied in most cases. It usually takes the engineer much time to obtain desired welding path, and sometimes, it is difficult to find an optimal path for spot welding robot especially when the number of welding joints is huge. Hence, welding robot path planning has become one key technology in this field. Intelligent optimization algorithm is beneficial for realizing effective welding robot path planning. To this end, particle swarm optimization (PSO) algorithm was improved first. Then, the improved PSO algorithm was applied for path planning of welding robot, and the simulation results show the effectiveness of the method.

Keywords Welding robot · Path planning · Particle swarm optimization · Genetic algorithm

4.1 Introduction

Welding is an important part in industrial manufacturing, and welding robots are widely used in automotive, aerospace, machinery, and processing industries. With the extensive application of welding robots, more and more researches on welding robot technology have been conducted. Spot welding robot path planning is beneficial to welding process, especially when many welding joints existed. A reasonable welding path for welding robot can shorten the overall time, improve production efficiency, and reduce production costs. Otherwise, it would be time consuming when the welding path is not reasonable. The development of intelligent

X.W. Wang (✉) · Y.P. Shi · R. Yu · X.S. Gu
School of Information Science and Engineering, East China University of Science and Technology, Shanghai 200237, China
e-mail: wangxuew@ecust.edu.cn

Z. Deng and H. Li (eds.), *Proceedings of the 2015 Chinese Intelligent Automation Conference*, Lecture Notes in Electrical Engineering 337,
DOI 10.1007/978-3-662-46463-2_4

algorithm provides effective methods for solving path planning of welding robot problem. Currently, GA and PSO algorithms are effective methods used to solve the problem of robot path planning [1, 2].

The particle swarm optimization (PSO) algorithm is simple to implement and has less parameters [3]; hence, it has been widely used for solving both continuous optimization and discrete optimization problems in recent years, such as drilling sequence optimization for PCB circuit boards and traveling salesman problem (TSP) [1, 4]. Genetic algorithm (GA) was presented in the early 1960 by John Holland in the University of Michigan. It is a heuristic searching algorithm that mimics the process of natural selection. As a global optimization algorithm, GA simulates natural genetic selection in biological evolution and natural selection probability [5]. The idea of GA originated from Darwin's evolution theory and Mendelian inheritance, which simulates the mechanisms of biological evolution to construct an algorithm's iterative process. It is already used in solving the multiple welding joints optimization problems [2, 6]. In this paper, hybrid PSO is presented in Sect. 4.2 first. Then, improved PSO algorithms are presented to solve welding robot path planning problem in Sect. 4.3. At last, the conclusion is given in Sect. 4.4.

4.2 Hybrid Particle Swarm Optimization

4.2.1 GA-PSO

The diversity of particles in PSO can be improved after GA was combined due to its mutation characteristic, then the global search capability of PSO will be improved too. In Ref. [7], GA was used to initialize the particles in PSO to solve the design of a diesel engine combustion chamber, and the simulation results showed its effectiveness. However, GA is easy to fall into local optimum for large dimensional problem. The selection and crossover operations in GA were improved to ensure the diversity of particles, and a good result was obtained for the global optimization of multimodal functions [8]. In Ref. [9], the iteration of particles is updated based on probability operation of GA to realize discrete PSO application. In Ref. [10], a hybrid GA-PSO based on clustering algorithm was proposed to optimize the scheduling problem in the computer industry. Based on the above researches, a double global optimum GA-PSO algorithm is proposed to solve welding robot path planning problem in this paper.

In the particle iteration, each particle is updated based on the personal best (*pbest)* and global best particle (*gbest*). Then the ultimate solution converges to optimal or suboptimal because the particles are always updated based on *pbest* and *gbest*. But when the *pbest* and *gbest* fell into local optimal solution, the particle cannot jump out of the local optimal solutions either.

Double global optimum GA-PSO algorithm has two global optimal solutions: one is the best particle of PSO (*gbest*) and the other is from GA (*GAbest*). GA is

used to search another global optimal solution, which is used for particle update. Hence, the update of particles will be influenced by three parameters: *pbest*, *gbest*, and *GAbest*. It will increase the diversity of particles and enhance the ability to find the optimal solution because *gbest* and *GAbest* are not relevant.

The Eqs. (4.1) and (4.2) is the particle update equation for improved GA-PSO. Compared with the basic PSO, *GAbest* from GA is added in the Eq. (4.1). Thus, the particles are always updated according to the *gbest,* and *GAbest.* Mutation operator in GA will help the algorithm obtain global optimal solution, because it can help particle jump out of local optimal solution greatly.

$$\begin{aligned} v_i(t+1) = wv_i(t) + c_1 r_1(p_i(t) - x_i(t)) \\ + c_2 r_2(p_g(t) - x_i(t)) \end{aligned} \tag{4.1}$$

$$x_i(t+1) = x_i(t) + v_i(t+1) \tag{4.2}$$

4.2.2 Partition PSO

The basic discrete PSO has a good ability to find optimal solution for small-scale problems. But usually there are a lot of welding joints in the welding task, and it is hard to get the optimal solution using basic discrete PSO. Hence, the partition-PSO will be used to solve large-scale welding joints path planning problem here.

For *N*-dimensional welding path optimization problem, the number of the possible solutions is $(N-1)!/2$, when $N = 20$, there will be more than 10^{16} possible solutions. For larger scale, the number will grow explosively. If the *N*-dimensional problem is divided into several small-scale problems, which are described as $n_1, n_2, \ldots n_k$, the number of the possible solutions will be $\frac{(n_1-1)!}{2} + \frac{(n_2-1)!}{2} + \cdots + \frac{(n_k-1)!}{2}$, the search space will be reduced greatly. Hence, partitioning is an effective way for large welding joints path planning problem.

Partitioning principle for particles is based on the distance between different particles. Particle $X_i = (x_{i1}, x_{i2}, \ldots x_{iD})$ will be divided into k zones as $X_i = ([x_{i1_1}, x_{i1_2}, \ldots], [x_{i2_1}, x_{i2_2}, \ldots], \ldots, [x_{ik_1}, x_{ik_2}, \ldots])$ according to the partition principle. The first step of partition is to find the boundary points, and define k reference points from the boundary points. In order to ensure that the welding joint can get a reasonable allocation, these k reference points should be defined as decentralized as possible. Based on the above operation, all the elements in particle i can be divided into k zones. Then, PSO algorithm is used to obtain optimal welding joints sequence for different zones separately. In order to ensure the global optimal, the distance between adjacent areas in the zones should be shortest; it means that the last element in a zone and the first element in the next zone should be the nearest. Figure 4.1 is the schematic of partition-PSO algorithm.

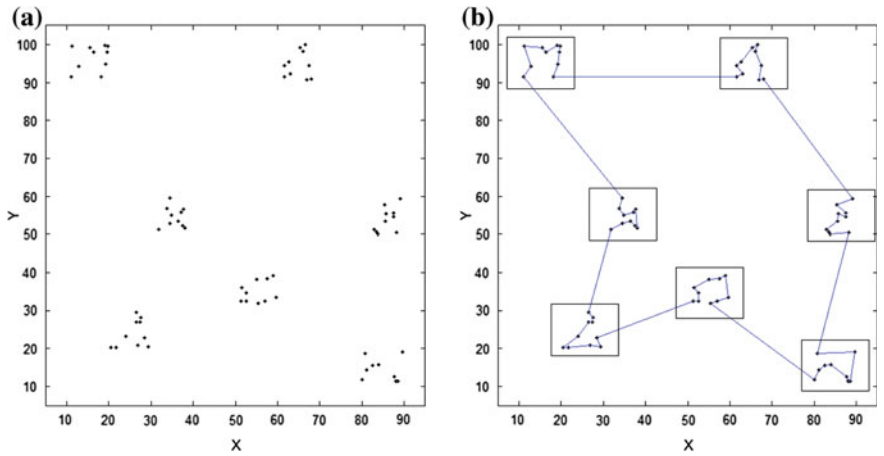

Fig. 4.1 Schematic of partition-PSO algorithm, **a** welding joints distribution, **b** result of partition-PSO algorithm

4.3 Welding Path Optimization

4.3.1 Definition of Welding Robot Path Planning

Welding joints sequence planning is an important issue of welding robot production, and how to find an optimal path to go through all the welding joints is the most concern. In general, there are many solutions for welding joints sequence planning, and one optimal path will be selected based on certain criteria. Hence, welding robot path planning problem can be described as obtaining a reasonable welding joints sequence for welding robot under some criteria. The criteria may be the shortest path, the least time consuming, the minimum welding deformation, or the minimum energy consumption, and so on. Therefore, the robot path planning is a constrained optimization problem. In this paper, the shortest path is used as the criterion to optimize the welding path for verifying the effectiveness of the optimization algorithms.

Considering a welding joints welding task $C = (c_1, c_2, \ldots c_N)$, the distance between two welding joints can be described as $d(c_i, c_j) \geq 0$, where $c_i, c_j \in C (1 \leq i, j \leq N)$, c_i stands for a welding joint. The task in this paper is to find the best welding joints sequence $\pi = \{c_1, c_2, \ldots c_N, \}$ to make sure the total path length of the welding robot is minimal.

$$f(\pi) = \sum_{i=1}^{N-1} d(c_i, c_{i+1}) + d(c_N, c_1) \tag{4.3}$$

where $f(\pi)$ denotes the distance when the welding path is π.

4.3.2 2D Welding Path Planning

Above algorithms are used for a two-dimensional path planning problem where 40 welding joints exist. Figure 4.2a shows the comparison of the convergence curves of GA, PSO, partition-PSO, and GA-PSO. It can be seen that the curve based on GA-PSO converges much faster than any other algorithm. Figure 4.2b is the path planning result of GA-SPO algorithm. The optimization results and convergence speeds of various algorithms are given in the Table 4.1. The search capability of basic PSO is better than basic GA in both best solution and convergence speed. The 40 welding joints are not a large-scale optimization problem; hence, basic PSO has a good effect, and the result of PSO is very close to the true optimal solution. Because the partition PSO is a local optimum algorithm designed to solve the large-scale problems, the result of partition PSO is worse than the basic PSO. GA-PSO combines the advantages of GA and PSO, so it converges faster than the basic PSO.

4.3.3 3D Welding Path Planning

Figure 4.3a is a car door with 115 welding joints, and Fig. 4.3b is the 3D coordinates of the welding joints. Figure 4.3c is the convergence curve comparison of

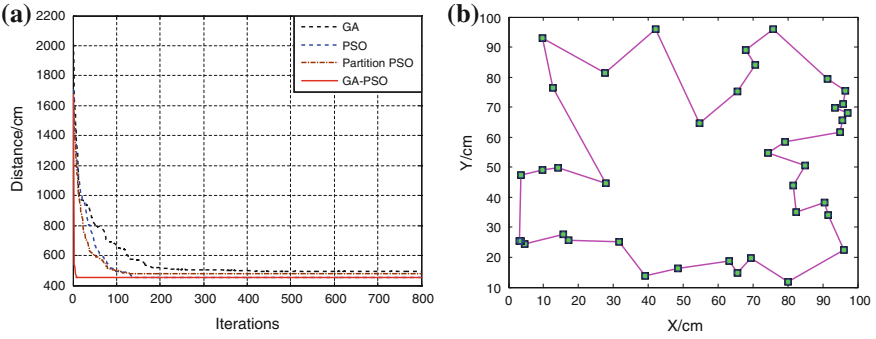

Fig. 4.2 Simulation results display, **a** comparison of convergence curves, **b** path planning result of GA-PSO

Table 4.1 Path planning results of four algorithms

	Optimal solution (cm)	Convergence speed
GA	494.5505	500
PSO	451.0650	140
Partition PSO	477.6789	120
GA-PSO	450.9147	20

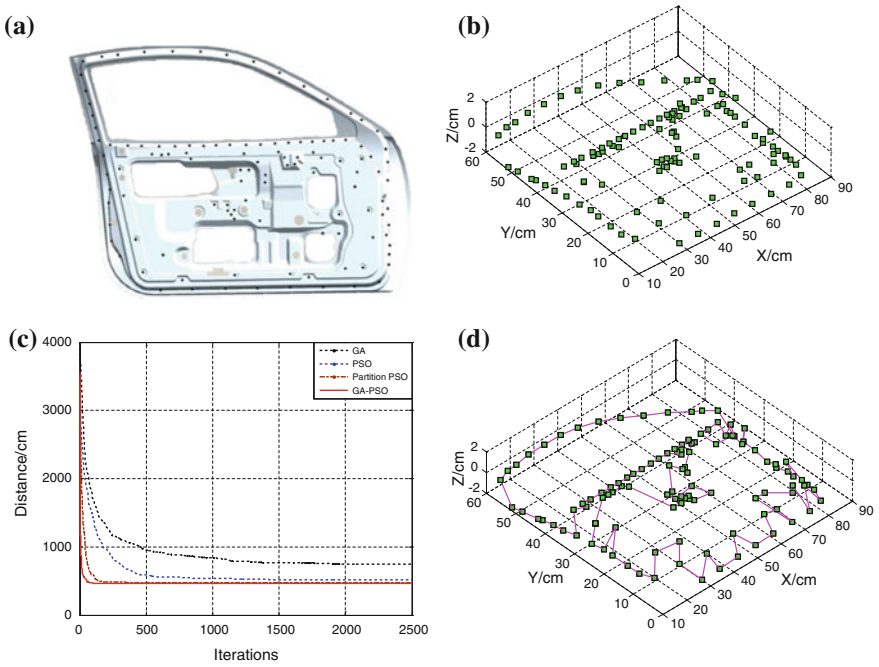

Fig. 4.3 Simulation results display, **a** welding joints of a door, **b** 3D coordinates of the welding joints, **c** comparison of convergence rate curves, **d** path planning result of GA-PSO

GA, PSO, partition PSO, and GA-PSO. Figure 4.3d shows the path optimized based on GA-PSO. Table 4.2 shows the comparison of path planning results, and GA-PSO is better than other three algorithms. 115 welding joints is a large-scale path planning problem, the shortcoming of prematurity of GA is completely revealed. The optimal solution of GA is the worst among all the algorithms, and the convergence speed is the slowest as well. PSO is also easy to fall into local optimum when it comes to more welding joints, but it is still better than GA. Partition PSO shows its advantage when there are many welding joints, all the welding joints are divided into four zones to search optimal path in this case, which increase its optimization capability greatly. GA-PSO remains its good characteristic, the diversity of particles are greatly increased after the optimal solution of GA was used

Table 4.2 Path planning results of four algorithms

	Optimal solution (cm)	Convergence speed
GA	744.1097	2,000
PSO	512.4208	1,400
Partition PSO	479.8333	220
GA-PSO	467.0721	50

as another global optimal position. Hence, its global search capability is greatly improved, and the best result was obtained based on GA-PSO.

4.3.4 Performance Comparison

Although GA and PSO are global convergence intelligent algorithms, both of them have the drawback of prematurity, which means they are easy to fall into local optimum, especially in a large search space. They can be used to solve small-scale path planning in a welding task. Partition PSO divides large search space into several small ones, and simplifies the complexity problem. However, when the partition is established, the exchange of two zones is limited to the two connection points, and points inside of each zone are separated. Hence, the partition PSO is a local convergence intelligent algorithm, the advantage of partition PSO can be shown in more welding joints path planning. The GA-PSO proposed in this article is a combination of GA and PSO, the diversity of particles is greatly increased, and the global search capability is improved as well. It is suitable for both small welding joints case and more welding joints case. Besides, after effective mutation operator was applied in the partition PSO algorithm to make the algorithm jump out of local optimal solutions, the better optimization results were obtained [11].

4.4 Conclusion

For improving traditional path planning effects, intelligent algorithms are used to realize effective path planning. Besides GA and PSO, the partition PSO and GA-PSO are proposed and compared. Simulation results show that when the number of welding joints increases to a certain level, partition PSO shows advantage over basic PSO. However, for the path planning of few welding joints, the superiority is not reflected. The hybrid GA-PSO proposed in this paper combines the advantages of both GA and PSO, and the diversity of particles in PSO is greatly increased. Hence, the global search capability of PSO has been greatly enhanced. Simulation results show that the result of GA-PSO is the best among all the algorithms, and it is not affected by the number of welding joints. In future research work, other criteria, such as the least time consuming, the minimum deformation, and the minimum energy consumption will be considered in path optimization.

Acknowledgments The authors appreciate the support of Shanghai Natural Science Foundation (14ZR1409900), Key Program for the Fundamental Research of Shanghai Committee of Science and Technology (12JC1403400), and National Major Scientific Instruments Equipment Development Project (2012YQ15000105).

References

1. Adam A, Abidin AFZ, Ibrahim Z et al (2010) A particle swarm optimization approach to robotic drill route optimization. In: 2010 fourth Asia international conference on mathematical/analytical modelling and computer simulation, pp 60–64
2. Kim KY, Kim DW, Nnaji BO (2002) Robot arc welding task sequencing using genetic algorithms. IIE Trans 34(10):865–880
3. Eberhart RC, Shi Y (2001) Particle swarm optimization: developments, applications and resources. In: Proceedings of the 2001 congress on evolutionary computation, vol 1, pp 81–86
4. Huilian FAN (2010) Discrete particle swarm optimization for TSP based on neighborhood. J Comput Inform Syst 6(10):3407–3414
5. Holland JH (1992) Genetic algorithms. Sci Am 267(1):66–72
6. Lim SS, Kim JS, Park JH (2013) Multi-objective genetic algorithm for high-density robotic workcell. In: 2013 44th international symposium on robotics (ISR), pp 1–3
7. Jeong S, Hasegawa S, Shimoyama K et al (2009) Development and investigation of efficient GA/PSO-hybrid algorithm applicable to real-world design optimization. IEEE Comput Intell Mag 4(3):36–44
8. Kao YT, Zahara E (2008) A hybrid genetic algorithm and particle swarm optimization for multimodal functions. Appl Soft Comput 8(2):849–857
9. Huang HC (2012) FPGA-based hybrid GA-PSO algorithm and its application to global path planning for mobile robots. Przeglad Elektrotechniczny 88(7B):281–284
10. Kuo RJ, Lin LM (2010) Application of a hybrid of genetic algorithm and particle swarm optimization algorithm for order clustering. Decis Support Syst 49(4):451–462
11. Wang XW, Shi YP, Gu XS, Ding DY (2014) Partition mutation PSO for welding robot path optimization. The proceedings of 2014 international conference on robotic welding, intelligence and automation (RWIA'2014), Shanghai, P. R. China, pp 100–108, 10.25–10.27

Chapter 5
The Design and Implementation of a Somatosensory Tactile Actuator and the Dynamic Calibration System for Its Output Frequencies

Hui Wang, Bowei Li, Aiguo Song and Quanjun Song

Abstract In this study, based on the characteristics of magnetic steel, we developed a somatosensory tactile actuator which could generate constant low-frequency vibration stimulation. Moreover, based on the relationship between input stresses and output voltages of polyvinylidene fluoride (PVDF) membrane working as a piezoelectric film sensor, a dynamic calibration system for stimulator's output frequencies was designed later. We could get the actual excitation frequency of actuator based on spectral analysis of the output voltage of PVDF membrane. And so the output frequency of controller could be collected according to the frequency calibration curves ultimately. Experimental results showed that the errors between the expected output frequencies of controller and the actual measured frequencies of the actuator were quite small. The calibration table was given according to the fitting curve in the end. It can be looked forward that the developed actuator would lay a good hardware foundation for carrying out BCI experimental study based on steady-state somatosensory evoked potentials (SSSEPs) next.

Keywords Stimulation · Tactile vibration · Polyvinylidene fluoride · Piezoelectric film sensor · Dynamic calibration

5.1 Introduction

Neuroscience research has found that when the body is subject to a periodic external stimulation of constant frequency, the brain will produce continuous response of neural electrophysiological signals of the same frequency with the external stimulus

H. Wang (✉) · B. Li · A. Song
School of Instrument Science and Engineering, Southeast University, Nanjing 210096, China
e-mail: wanghui@iim.cas.cn

H. Wang · Q. Song
Institute of Intelligent Machines, Hefei Institutes of Physical Science, Chinese Academy of Sciences, Hefei 230031, China

Z. Deng and H. Li (eds.), *Proceedings of the 2015 Chinese Intelligent Automation Conference*, Lecture Notes in Electrical Engineering 337,
DOI 10.1007/978-3-662-46463-2_5

or with its harmonics. The strength of that response can be indicated by the obtained voltage signal measured on the scalp or the surface of the skin, and that is called steady-state evoked potential (SSEP). SSEP is generated from the primary/secondary sensory cortex of brain areas corresponding to specific patterns of the stimulation, and steady-state somatosensory evoked potentials (SSSEP) can be observed in somatosensory cortex after steady-state vibration stimulation [1–3].

In the study of somatosensory evoked potentials (SEP), current pulses are commonly used to stimulate cutaneous nerves of fingers and toes or the sensory fibers in the hybrid neural limb stem to achieve the purpose of somatosensory stimulation. Commonly, that electrical stimulation has high requirements for performance parameters of equipment; moreover, the devices are complicated, expensive, and with poor flexibility, so that electrical stimulation has limitations in application. In addition, there are certain traumas and dangers to subjects (if applied electrical stimulation is too strong, the subjects could produce cramps). By contrast, applying certain vibratory stimulation can equally be applicable to SEP studies, and that is noninvasive or low-invasive, easy to be controlled and has higher safety factor, so a large number of subjects accept it. Therefore, somatosensory stimulus technology based on the vibration tactile has been widely approved and accepted. SSSEP is a recently developing brain–computer interface (BCI) paradigm where the brain response to tactile stimulation of a specific frequency is used [4]. The SSSEP amplitude modulation caused by selective attention to the outside vibration excitation of constant frequency is increasingly becoming hot at home and abroad in the field of BCI technology [5–8].

This study developed a portable, flexible, and noninvasive "magnet-style" somatosensory tactile actuator with high-performance price ratio, which can produce haptic vibration stimulation of adjustable low frequency that people can feel precisely. Effective implementation of the somatosensory tactile stimulus would provide prior basis for SSSEP researches or clinical applications. The project will help to develop new ways of human–computer exchange in order to achieve the control of external devices, and it also has great actual significance on the combination of BCI technology and neural engineering.

5.2 Design Principle of Somatosensory Tactile Actuator

The stimulus system utilizes the characteristics of magnetic steel that "the same polarity brings repulsion and the different polarity brings attraction" to produce the desired vibration. The whole apparatus includes one square magnetic steel, one circular magnetic steel, a stepper motor, one shaft housing, one sleeve, a knock-out pin, and a soleplate. When the stepper motor turns around at a certain rotate speed, the magnetic steel fixed to the output shaft of the motor which can rotate with it and the magnetic steel placed in the sleeve which can move up and down have alternating effects of attraction and exclusion based on the characteristics of magnetic steel. So the knock-out pin is driven up and down, and then the mechanical

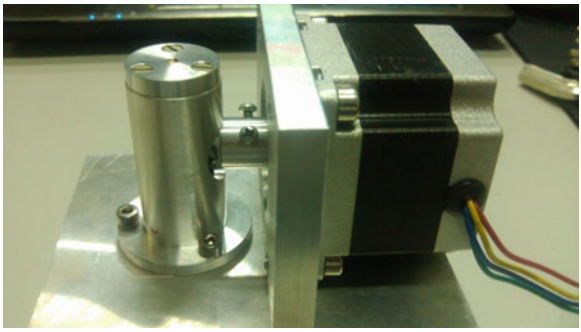

Fig. 5.1 The whole physical map of the somatosensory tactile actuator

vibratory stimulation of constant frequency is produced. It should be mentioned out that, the output shaft of the motor and the square magnetic steel are connected by the shaft housing.

The knock-out pin is one part of the device that can generate vibration, and it transmits the vibration to the tested finger through the top of the knock-out pin. The designed circular magnetic steel is connected firmly to the knock-out pin. Copper is used as the work material for the knock-out pin in order to prevent other substances from affecting the magnetism and the magnetic force-direction, and there is a M3 screw thread near the bottom of the knock-out pin so that the circular magnetic steel can be easily set and fixed with the knock-out pin through a screw cap. The upper part of the knock-out pin is smooth, so it can reduce friction between the knock-out pin and the cover of sleeve during the vibration; therefore, it can not only prevent jamming but also reduce vibration noise.

To prevent the permeable material from influencing the work, the main part of the system is aluminum. The whole mechanical system is placed on one aluminum base plate, to ensure stability when the motor is rotating. The other aluminum plate is also fixed on the aluminum base plate vertically so that the output shaft of the stepper motor embed in the sleeve will not hit the wall of the sleeve. Below the aluminum base plate, there is glued plastic foam, which can significantly reduce the noise produced during the system operation. Figure 5.1 is the whole mechanical physical map.

The host computer sends commands through a wireless transmitting module; after the wireless receiving module connected to slave computer receives the command sent by the host computer, it produces pulse signal of certain frequency according to the command, and the motor driving module drives the motor to rotate in accordance with the set frequency. Then the square magnetic steel fixed to the output shaft of the motor which can rotate with it and the circular magnetic steel placed in the sleeve which can move up and down have alternating effects of attraction and exclusion based on the characteristics of magnetic steel. Those effects result in the knock-out pin up and down, producing mechanical vibration stimulation of constant frequency.

Figure 5.2 is the control system flowchart. Upper computer software of the system realizes the function of port configuration, connection, and disconnection

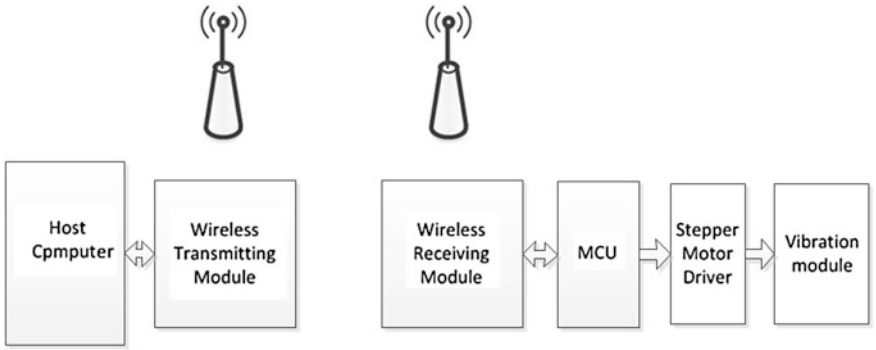

Fig. 5.2 The flowchart of control system

with the wireless signal transmitter, the frequency settings of the actuator, startup and shutdown of actuator, and so on. Specifically, PC software comprises the serial communication procedures, after the algorithm design of frequency calculation, it can establish a stable and reliable connection with the launch pad and send the stimulus frequency data that the operator set which is precise to the launch pad, then the launch pad sends the data out. The wireless communication procedures enable the lower computer to receive PC command accurately, and the lower computer comprises drive programs of actuator to ensure the accurate control of the actuator. After the wireless single chip microcomputer receives the data from the launch pad, it generates the pulse signal of certain frequency according to the received command, then the stepper motor driver controls speed based on the pulse frequency, and so the square magnetic steel fixed to the output shaft of the motor rotates with it.

5.3 Calibration of a Somatosensory Tactile Actuator Based on PVDF Sensor

Polyvinylidene fluoride (PVDF) is a kind of organic polymer material, composed of many CH_2=CF_2 (monomer partial fluorine ethylene). So far, PVDF material is found to be the high polymer material with the highest piezoelectric properties and it is the new type of flexible organic sensitive material.

Figure 5.3 shows the piezoelectric properties of microunit of PVDF. When the piezoelectric thin film is under stresses, the relationship between output charges and external forces is as follows:

$$q_i = d_{ij}\sigma_j \tag{5.1}$$

where, q_i stands for the output charges of the film per unit area, σ_j stands for the confined stresses of the film per unit area, and d_{ij} stands for the piezoelectric strain constant.

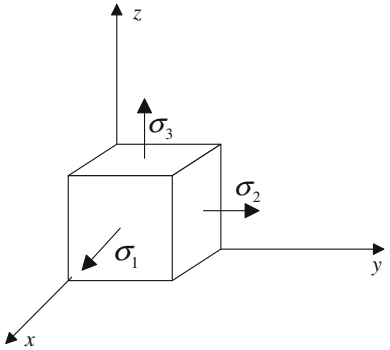

Fig. 5.3 The piezoelectric properties of microunit of PVDF

As a new type of piezoelectric macromolecule polymer material, PVDF has many advantages [9, 10] such as: high piezoelectric voltage constant, light weight, low density, good flexibility, wide frequency response, low acoustic impedance, high sensitivity, good stability, ease of processing, and installation. When it is processed into thin film and is used as a sensor, the effect of vibration response to the system is very small; therefore, the PVDF sensors have been widely used in the field of vibration control and structural modal test of beam [11, 12]. The basic principle of measurement based on PVDF piezoelectric film is: When the PVDF film is put some stresses on, PVDF microunit can produce induction charge caused by extrusion, and when the applied stress changes periodically, the measured charges produced by PVDF piezoelectric film will also be periodical.

The frequency calibration experiment based on PVDF film was carried out on the tactile actuator. We glued the PVDF film onto the top of the knock-out pin. When the knock-out pin began to start vibration up and down with certain frequency, it exerted force on the PVDF film, the PVDF film would produce a periodic charge signal. Then through the charge amplifier, this charge signal was changed into voltage signal, and then was conditioning amplified. After the acquisition by PC, based on the Fourier transform of the collected data, we could obtain actual operating tactile actuator excitation frequency which was the maximum amplitude of the frequency domain. In this way, mechanical vibration signal could be converted into frequency signal through the PVDF film.

In the calibration experiment, a 10-mm wide and 30-mm long PVDF film was used. Two metal electrodes were completely covered on the surface of piezoelectric PVDF films, using 2 mm × 6 mm of copper as the pins. The physical diagram of calibration system is shown in Fig. 5.4.

The host computer changed the output frequency of controller which ranged from 0 to 25 Hz. We did four operations, two of which were forward and another two of which were backward, and so a series of calibration points were got. After fitting these calibration points, a frequency calibration curve of somatosensory tactile actuator frequency calibration curve could be obtained.

Figure 5.5 showed the characteristic curves of the frequencies controlled by the tactile actuator tested both in forward and backward operations.

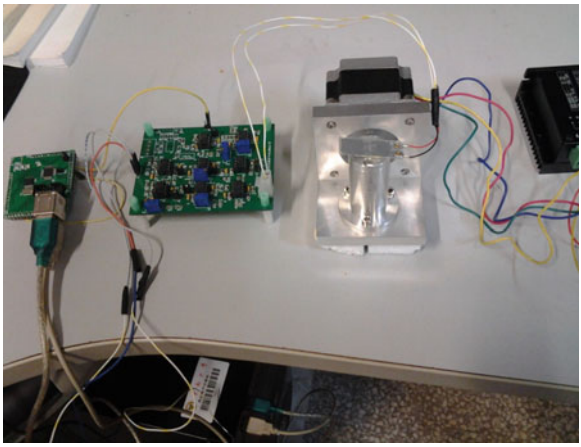

Fig. 5.4 The physical diagram of calibration system

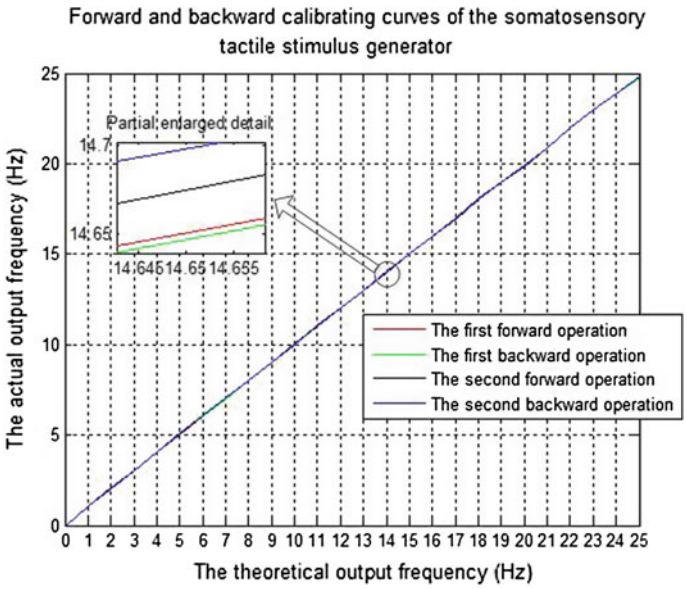

Fig. 5.5 Forward and backward stroke curve ranging from 0 to 25 Hz

Based on the least square principle, we got the equation of fitting curve:

$$y = 0.9935x + 0.0748 \tag{5.2}$$

where, x stands for the actual measured frequencies of the actuator, and y stands for the expected output frequencies of controller.

The calculation formula for nonlinear error is:

$$\delta_L = \frac{\Delta L_{\max}}{U_{\mathrm{FS}}} \times 100\,\% \tag{5.3}$$

where, δ_L stands for nonlinear error, U_{FS} stands for full scale, and $\Delta L_{\max}$ stands for the maximum deviation of ideal curve and the actual curve.

The calculation formula for repeatability error is:

$$\delta_R = \frac{\Delta R}{U_{\mathrm{FS}}} \times 100\,\% \tag{5.4}$$

where, δ_R stands for repeatability error, U_{FS} stands for full scale, and ΔR stands for the max deviation between the co-rotating stroke curves.

Based on the above formulae, we could figure out that the nonlinear error is 0.61 % and the repeatability error is 0.26 %.

In this system, the uncertainties of nonlinear error and repeatability error are independent of each other, so we can get the synthetic standard uncertainty for the calibration system:

$$u_c = \sqrt{u_1^2 + u_2^2} \tag{5.5}$$

where, u_1 stands for the uncertainties of nonlinear error and u_2 stands for the uncertainties of repeatability error.

The precision of actuator can be assessed according to the comprehensive error, the calculating formula is:

$$\sigma = \sqrt{\delta_L^2 + \delta_R^2} \tag{5.6}$$

Its value is equal to the total uncertainty of the system. Based on the above formula, we can get the synthetic standard uncertainty of this measurement is 0.66 %.

The frequency calibration table for the somatosensory tactile actuator was given in Table 5.1 according to the fitting curve. In the table, "OF" stands for the expected output frequencies of controller and "MF" stands for the actual measured frequencies of the actuator.

Table 5.1 Frequency calibration table for the somatosensory tactile actuator

OF/Hz	1	2	3	4	5	6	7	8	9
MF/Hz	0.931	1.938	2.944	3.951	4.957	5.964	6.971	7.977	8.984
OF/Hz	10	11	12	13	14	15	16	17	18
MF/Hz	9.990	10.997	12.003	13.010	14.016	15.023	16.029	17.036	18.043
OF/Hz	19	20	21	22	23	24	25	–	–
MF/Hz	19.049	20.056	21.062	22.069	23.075	24.082	25.088	–	–

5.4 Conclusion

In the background of the development of a somatosensory tactile actuator which could produce some constant low-frequency vibration, combining with the calibration of output frequency parameters in demand, we put forward a design scheme of automatic test system for stimulator's output frequency dynamic calibration based on PVDF membrane, and gave the detailed design of the calibration system. According to the relationship between the output voltages and the input stresses of the PVDF film, dynamic mechanical vibration signals were transformed into electrical signals using the PVDF film. We intended to obtain actual operating frequency of the stimulator according to frequency spectrum of output voltage after FFT transform, and finally correct the output frequency of controller according to the frequency calibration curve. Experimental results showed that the errors between the expected output frequencies of controller and the actual measured frequencies of the actuator were quite small, and we gave the calibration table according to the fitting curve in the end. The actuator developed in this research would lay a good hardware foundation for carrying out BCI experimental study based on SSSEPs next.

Acknowledgments The authors would like to thank the financial support of the National Natural Science Foundation of China (Grant no. 61104206) and the Natural Science Foundation of Anhui Province (Grant no. 1208085QF121). We are very grateful to the unknown referees for their valuable remarks.

References

1. Zhang D (2010) Studies on multimodal selective attention based on steady-state evoked potentials. Tsinghua University, Beijing
2. Nam Y, Cichocki A, Choi S (2013) Common spatial patterns for steady state somatosensory evoked potentials. In: Proceedings of IEEE EMBS conference, Osaka, Japan
3. Ahn S, Jun SC (2012) Feasibility of hybrid BCI using ERD- and SSSEP-BCI. International conference on control, automation and systems, Jeju Island, Korea
4. Nam Y, Koo B, Choi S (2014) Spatial patterns of SSSEP under the selective attention to tactile stimuli in each hand. In: 2014 International winter workshop on brain–computer interface (BCI), Jeongsun-kun
5. Müller-Putz GR, Scherer R, Pfurtscheller G (2006) Steady-state somatosensory evoked potentials: suitable brain signals for brain computer interfaces? IEEE Trans Neural Syst Rehabil Eng 14:30–37
6. Zhang D, Wang Y, Maye A, Engel AK, Gao X, Hong B et al (2007) A brain-computer interface based on multi-modal attention. In: Proceedings of the 3rd international IEEE EMBS conference on neural engineering
7. Voisin JI, Rodrigues E, Hétu S et al (2011) Modulation of the response to a somatosensory stimulation of the hand during the observation of manual actions. Exp Brain Res 208:11–19
8. van der Waal M, Severens M, Geuze J, Desain P (2012) Introducing the tactile speller: an ERP-based brain-computer interface for communication. J Neural Eng 9(045002):1–11

9. Xu HX (1999) Developments of PVDF piezoelectric films. J Jiangsu Univ Sci Technol (Nat Sci) 20(5):88–91
10. Liu XZ, Ye SG, Gong SF, Zhang WY (1999) Study of characteristics copolymer ultrasound transducer. ACTA Acustica 20(4):429–437
11. Wang BT (1998) The PVDF-based wave number domain sensing. Techniques for active sound radiation control from a simply supported beam. J Acoust Soc Am 103(4):1904–1915
12. Lee CK, Moon FC (1990) Modal sensors/actuator. J Appl Mech 57:434–441

Chapter 6
A Visual Feedback Control Framework Oriented to Lung Branching Pattern Formation Simulation

Hui Xu, Mingzhu Sun, Jianda Han and Xin Zhao

Abstract Mathematical modeling based on reaction-diffusion partial differential equations, is a well-known way to study the mechanism of lung branching pattern formation. However, model parameter identification is one of the key problems in the research, which is both labor-intensive and of low efficiency. To work out this problem, a visual feedback control framework is proposed in this paper. The framework based on automatic control theory is built, by means of pattern feature feedback, to identify model parameters. The results suggest that this framework is effective and feasible.

Keywords Visual feedback control framework · Lung branching pattern formation · Model parameter identification · Pattern feature extraction

H. Xu · M. Sun (✉) · X. Zhao
Institute of Robotics and Automatic Information System,
Nankai University, Tianjin 300071, China
e-mail: sunmz@nankai.edu.cn

H. Xu
e-mail: xhui_yolanda@163.com

X. Zhao
e-mail: zhaoxin@nankai.edu.cn

H. Xu · M. Sun · X. Zhao
Tianjin Key Laboratory of Intelligent Robotics, Nankai University,
Tianjin 300071, China

H. Xu · M. Sun · J. Han
State Key Laboratory of Robotics, Shenyang Institute of Automation,
Chinese Academy of Sciences, Shenyang 110016, China
e-mail: jdhan@sia.cn

Z. Deng and H. Li (eds.), *Proceedings of the 2015 Chinese Intelligent Automation Conference*, Lecture Notes in Electrical Engineering 337,
DOI 10.1007/978-3-662-46463-2_6

6.1 Introduction

In humans and most other vertebrates, the lung is known as the essential respiratory organ. Scientists from stem cell biology, molecular biology, biochemistry, theoretical modeling, and other disciplines have attempted to understand the mechanisms of lung pattern formation for years [1–3]. Yet it is still a long-standing work.

A well-established paradigm in the theoretical study of lung branching pattern formation is mathematical modeling based on reaction-diffusion theory proposed by Turing [4]. Following the work of Turing, Gierer and Meinhardt put forward an Activator-Inhibitor model [5], which has also been utilized for many other biological processes [6–9]. In order to investigate the mechanism of lung development in the modeling study, a suitable model with applicable parameters need to be chosen, which is capable of reproducing key characteristics of lung [10, 11]. Because different model parameter values lead to different simulation patterns, the determination of model parameters becomes quite important after the model is selected. However, such a model comprises many parameters, and most parameter values need to be estimated from a wide range. Hence, model parameter identification is a critical problem in the modeling study of lung pattern formation.

In biological research, researchers manually select the simulation approximate to the actual biological pattern by trying large quantities of parameter combinations [10–14]. In this way, the problem of model parameter identification is settled. However, several obvious disadvantages of this manual selection method, such as labor-intensive, low-efficiency, and lack of quantitative evaluation criteria can be seen.

Oriented to simulation of lung branching pattern formation based on reaction-diffusion partial differential equations, we provide a visual feedback control framework in this paper. Instead of manual work, this framework can automatically search out the simulation result that conforms to the target pattern and realize model parameter identification.

6.2 Visual Feedback Control Framework

The visual feedback control framework, as shown in Fig. 6.1, consists of three modules: visual simulation module, pattern feature extraction module, and model parameter identification module. The visual simulation module is equivalent to the actuator in this feedback control system, in which we present and output the numerical simulations of the lung branching model as images based on visualization; the pattern feature extraction module is equivalent to the sensor, in which we extract and quantify the features of lung pattern simulation to compare with the reference input; the model parameter identification module is equivalent to the controller to realize model parameter correcting.

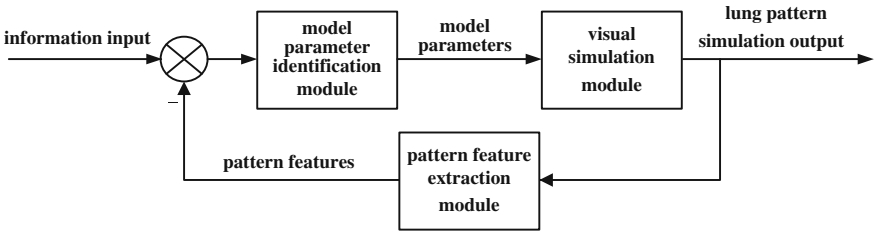

Fig. 6.1 Visual feedback control framework

The operating procedures of this framework are listed in detail as follows:

Step 1: Input the information about the target pattern and initialize the model parameters.

Step 2: Numerically solve reaction-diffusion partial differential equations in the mathematical model with the parameter values, and represent the solutions by a two-dimensional image as the simulated lung pattern output.

Step 3: Extract and quantitatively describe features of the simulated pattern by a series of image processing, then take the features as a feedback.

Step 4: Adjust the model parameters by utilizing the pattern feature deviation between the target pattern and the simulation. If the deviation drops to zero or this framework reaches its maximum running time limit, then this framework would stop running and output the simulation result with the corresponding model parameters. Otherwise go to Step 2.

6.3 Methods of Visual Feedback Control Framework

6.3.1 Visual Simulation Module

In this framework, we use a reaction-diffusion model postulating 4 variables and 14 parameters [11]. The model is defined as:

$$\begin{aligned}
\frac{\partial A}{\partial t} &= \frac{cA^2S}{H} - \mu A + \rho_A Y + D_A \nabla^2 A \\
\frac{\partial H}{\partial t} &= cA^2S - vH + \rho_H Y + D_H \nabla^2 H \\
\frac{\partial S}{\partial t} &= c_0 - \gamma S - \varepsilon YS + D_S \nabla^2 S \\
\frac{\partial Y}{\partial t} &= dA - eY + \frac{Y^2}{1 + fY^2}
\end{aligned} \tag{6.1}$$

where A, H, and S, are respectively, the activator BMP-4, the inhibitor MGP, and the substrate chemical ALK1-TGF-β complex, and Y is a marker variable of cell differentiation ($Y = 1$ means the cell is differentiated).

In this model, it is assumed that differentiated cells Y produce the activator A at rate ρ_A and the inhibitor H at rate ρ_H, with taking up substrate S at rate ε. The activator A is in a process degraded at rate μ and diffusing at rate D_A requiring S and inhibited by H. Similarly, the inhibitor H is also produced by A, degraded at rate v, and diffuses at rate D_H. Substrate S, is supplied at rate c_0, degrades at rate γ, and diffuses at rate D_S. Lastly, Y also can degrade at rate e and increase in the presence of A.

Here, we set model parameters d, ρ_H and ε in the equations above, the adjustable parameters need to be identified according to the lung branching pattern features selected to quantitatively characterize. More detail on the selection of the identified parameters will be reported in the following section (see Sect. 6.3.2).

Initial conditions of model are given by setting $A = 0.001$, $H = 0.01$, $S = 1$, $Y = 0$, uniformly distributed in space. The constant parameter values used are: $c = 0.002$, $\mu = 0.16$, $\rho_A = 0.03$, $D_A = 0.02$, $v = 0.04$, $D_H = 0.3$, $c_0 = 0.02$, $\gamma = 0.02$, $D_S = 0.06$, $e = 0.1$, $f = 10$.

We perform numerical simulation of model on a 200 × 200 grid, with no-flux boundary conditions, using two-step Runge-Kutta methods. We directly save the solution of the variable Y as the two-dimensional simulation of lung branching pattern. The simulation is stopped and outputted when the growth of lung branching pattern reaches a certain degree. In order to improve the simulation efficiency, we present a parallel computing technique based on Graphics Processing Unit (GPU) and Compute Unified Device Architecture (CUDA) programming.

6.3.2 Pattern Feature Extraction Module

In this paper, based on the growth characteristics, the lung branching pattern is roughly divided into four categories: alternating side branching pattern, zygomorphic side branching pattern, tip branching pattern, and hybrid branching pattern (see Fig. 6.2). Alternating side branching pattern and zygomorphic side branching pattern are formed by monopodial branching in which lateral branches grow on both sides from a long straight main stem, and secondary lateral branches grow out in the same way taking lateral branches as main stem, and so on. The distinction between the two patterns is the symmetry of the side branching growth. Tip branching pattern and hybrid branching pattern are formed by dichotomous branching in which the main stem bifurcates into two equally sized branches from its apex, and likewise, each branch can split into two daughter branches. Hybrid branching pattern can be considered as a kind of tip branching pattern with side branching growing out. In view of this, for hybrid branching pattern, we further distinguish whether side branches grow on either or both the main stem and dichotomous branches. Figure 6.2d shows the simulation picture of hybrid branching pattern with side branches growing on both main stem and dichotomous branches.

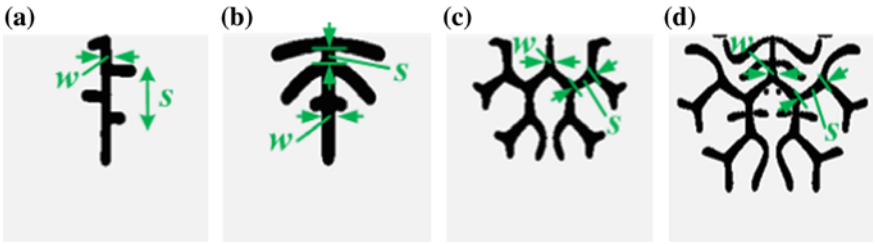

Fig. 6.2 Four different lung branching patterns with labeling corresponding extracted features: **a** alternating side branching pattern; **b** zygomorphic side branching pattern; **c** tip branching pattern; **d** hybrid branching pattern

Besides pattern category information, we use the width of main stem and the spacing between two adjacent branches as the extracted pattern features, by considering the growth morphology of lung branching pattern and biological concerns on the study of lung development. These extracted pattern features are used to describe lung branching pattern. Various branching patterns may have different definitions of the spacing between two adjacent branches with different measure methods (see Fig. 6.2). In Fig. 6.2, w and s are given as the width of main stem and the spacing between two adjacent branches. In addition, further analysis indicates that the change in the values of parameters d, ρ_H and ε in the model influences a change in the pattern features and pattern category information. Thus, d, ρ_H and ε are chosen to be the identified parameters.

To sum up, pattern feature extraction, as shown in Fig. 6.3, proceeds along two stages: pattern discrimination and feature extraction. We set an unknown branching pattern as the input object of pattern feature extraction. In the first stage, we judge whether the unknown pattern is formed by monopodial branching or dichotomous branching. If its branch growth is entirely monopodial, we further confirm whether the pattern belongs to alternating side branching pattern or zygomorphic side branching pattern based on the symmetry of the side branching growth. If its branch growth is dichotomous, then we judge whether the pattern has side branches or not. If so, the pattern belongs to hybrid branching pattern, and we should further identify which kind of hybrid branching the pattern belongs to by determining the growth of these side branches. Otherwise, the pattern belongs to tip branching pattern. In the second stage, by knowing the category of the pattern, we extract and quantify the corresponding features by a series of image processing methods such as skeleton extraction and pixel scan.

6.3.3 Model Parameter Identification Module

In this framework, we optimize model parameters by using differential evolution (DE) algorithm, which is an efficient heuristic approach for global optimization in high-dimensional space based on a stochastic and parallel direct search method [15].

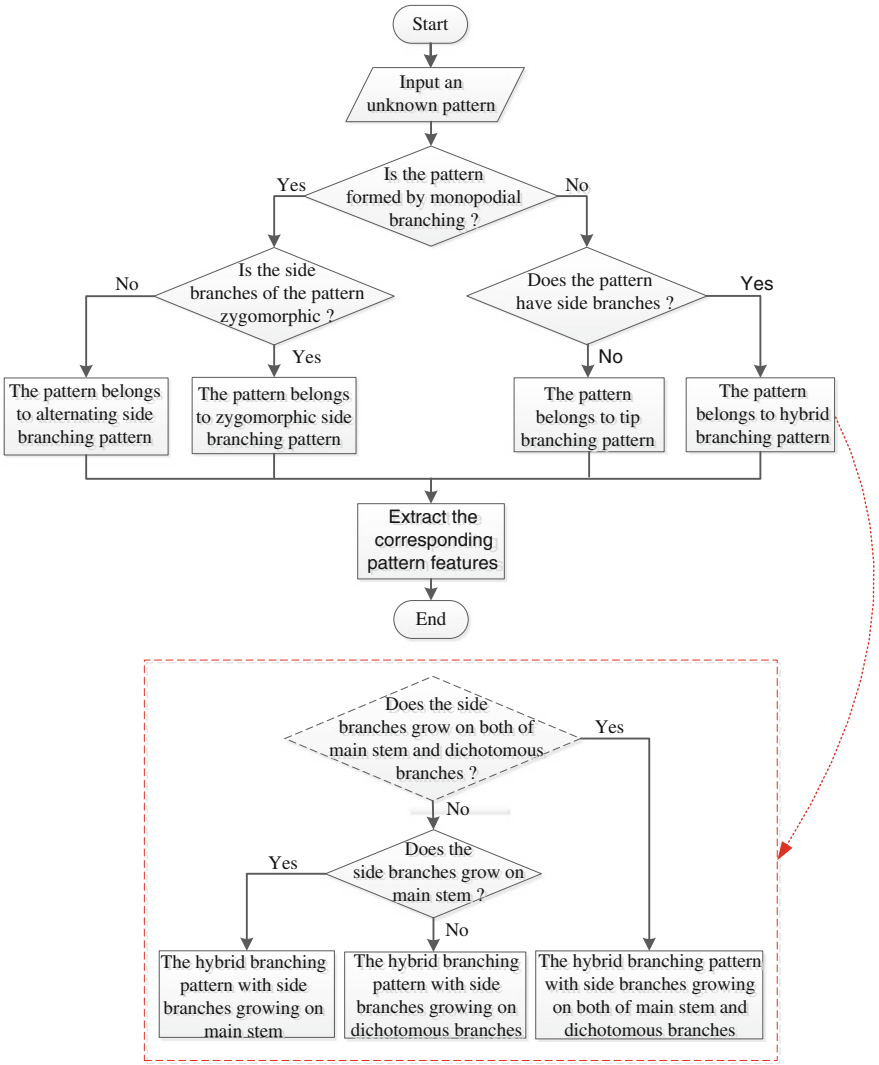

Fig. 6.3 The flowchart of pattern feature extraction

We define the cost function as:

$$F = \delta_{x,y} + \sum_{i}^{n} u_i (a_i - \bar{a}_i)^2 \tag{6.2}$$

where the Kronecker delta is $\delta_{x,y} = \{0, x = y; \infty, x \neq y\}$, with x and y representing the current simulation and the target pattern, n is given as the number of the

quantitatively described pattern features, and a_i is the ith quantitatively described feature value of the current simulation, with $\bar{a}_i$ and u_i, respectively, corresponding to the standard feature value and the feature weight value.

The initial extent of the adjustable parameters is: $d \in [0.0050, 0.0200]$, $\rho_H \in [0.000005, 0.000150]$, $\varepsilon \in [0.030, 1.200]$.

6.4 Results

6.4.1 Simulation of Lung Branching Pattern Set as the Target Pattern

We set different categories of simulation patterns as the target pattern to test this framework. The feature information about each target pattern with the known model parameters, is extracted as the reference input of the visual feedback control framework. Four examples are presented in this section, respectively, for setting alternating side branching pattern, zygomorphic side branching pattern, tip branching pattern, and hybrid branching pattern as the target pattern. These target patterns are shown in the first row of Fig. 6.4, while the corresponding result patterns, obtained through framework processing, are shown in the second row of Fig. 6.4. Their pattern feature information and model parameter values are reported in Table 6.1.

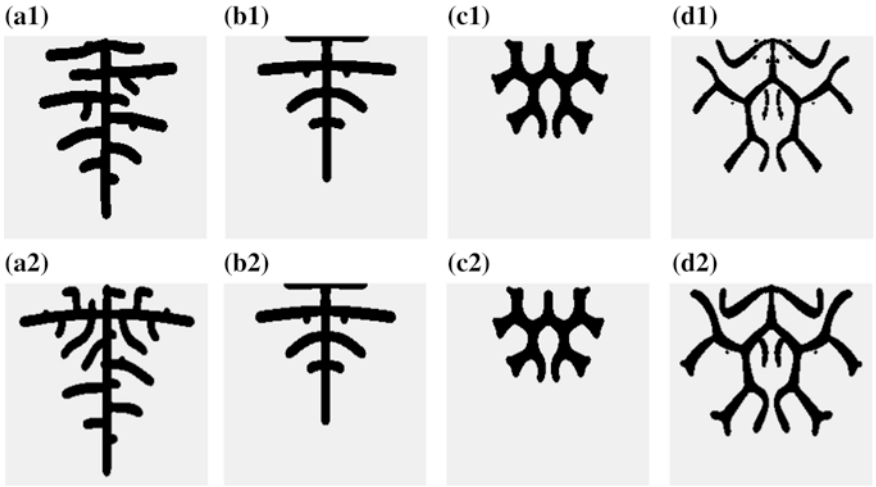

Fig. 6.4 The target patterns and the corresponding result patterns of the framework, in the case of different categories of simulation patterns set as the target pattern. The *first row* shows the target patterns, while the *second row* shows the corresponding result patterns

Table 6.1 The feature information and model parameter values of target patterns and corresponding result patterns obtained through framework processing, in the case of different categories of simulation patterns as the target pattern

		Feature information		Model parameter values		
		w	s	d	ρ_H	ε
Alternating side branching pattern	Target pattern	10	27	0.00800	0.000100	0.030
	Result pattern	10	27	0.00630	0.000085	0.051
Zygomorphic side branching pattern	Target pattern	10	27	0.00800	0.000100	0.060
	Result pattern	10	27	0.00820	0.000085	0.061
Tip branching pattern	Target pattern	10	15	0.01500	0.000100	1.700
	Result pattern	10	15	0.01550	0.000085	1.790
Hybrid branching pattern	Target pattern	6	26	0.00400	0.000020	1.000
	Result pattern	8	26	0.00634	0.000037	0.652

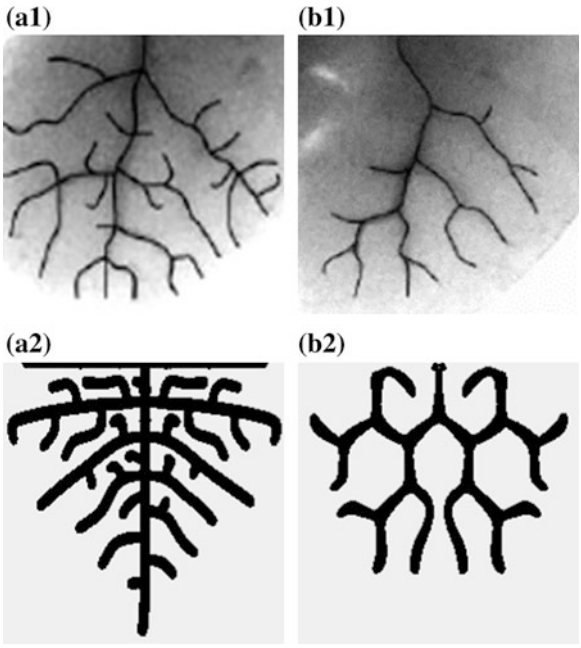

Fig. 6.5 The target patterns and the corresponding result patterns of the framework, in the case of actual lung branching patterns, are set as the target pattern. The *first row* shows the target patterns, while the *second row* shows the corresponding result patterns

In the example of alternating side branching pattern as the target pattern, with their shared pattern category and feature information, the result pattern is similar to the target pattern from the point of view of the growth morphology, and the difference between their model parameter values is tiny (see Fig. 6.4a1, a2, and Table 6.1, rows 3 and 4). In the examples of zygomorphic side branching pattern and tip branching pattern as the target patterns, besides their corresponding target patterns and result patterns have pattern category and feature information in common, both result patterns are almost the same as their suitable target patterns, and there is little difference between the model parameters of their target patterns and result patterns (see Fig. 6.4b1, b2, c1, c2, and Table 6.1, rows 5, 6, 7, and 8). For instance, in hybrid branching pattern as the target pattern, the result pattern and target pattern belong to one branching pattern category, while there is still a feature distinction between the target pattern and the result pattern; however, the result pattern is very close to the target pattern; furthermore, both model parameter values are near (see Fig. 6.4d1, d2, and Table 6.1, rows 9 and 10).

6.4.2 Actual Lung Branching Pattern Set as the Target Pattern

In order to test this framework further, different categories of actual lung branching patterns are chosen as the target pattern. Two examples are presented as follow, in which both the target patterns are acquired from the literature [11]. The first example sets the actual lung pattern that belongs to alternating side branching pattern as the target pattern in this framework (see Fig. 6.5a1), while the second example sets the actual lung pattern that belongs to tip branching pattern as the target pattern (see Fig. 6.5b1). The corresponding result patterns are obtained through visual feedback control framework processing (see Fig. 6.5a2, b2). The two examples demonstrate that the proposed framework can find the simulation pattern approximate to the actual lung pattern.

6.5 Conclusion and Future Work

With the basic principle of feedback control system, the visual feedback control framework is proposed to solve the problem of model parameter identification in the modeling study of lung. The results of this framework show that the method presented in this paper is reasonably feasible and practically significant. Compared with the manual model parameter selection in biological research, this framework greatly reduces the staff workload, standardizes the selection criteria, and improves the overall efficiency. Furthermore, we believe that the design principle of the visual feedback control framework is not limited to the study of lung development as it can be easily generalized to other types of biological pattern formation.

In our ongoing work, we are improving and refining our algorithms of the proposed framework. We also plan to extend our framework to three-dimensional simulation of lung pattern formation. We will increase the number of the adjustable model parameters and the extracted features of lung branching pattern, which may lead to form some new growth patterns of the lung. These studies may make our framework more closely integrated with biological research and contribute to better understanding of the biophysical mechanisms of lung pattern formation.

Acknowledgments This research is supported by Tianjin Research Program of Application Foundation and Advanced Technology (14JCQNJC04700), National Natural Science Foundation of China (NSFC: 61105107, 61327802, 61273341), the Research Fund for Doctoral Program of Higher Education of China (Grant No. 2011003111032), and the State Key Laboratory of Robotics (2013-O03).

References

1. Cardoso WV (1995) Transcription factors and pattern formation in the developing lung. Am J Physiol Lung Cell Mol Physiol 13(4):L429
2. Warburton D, El-Hashash A, Carraro G, Tiozzo C, Sala F, Rogers O, Jesudason E (2010) Chapter three-lung organogenesis. Curr Top Dev Biol 90:73–158
3. Warburton D, Schwarz M, Tefft D, Flores-Delgado G, Anderson KD, Cardoso WV (2000) The molecular basis of lung morphogenesis. Mech Dev 92(1):55–81
4. Turing AM (1952) The chemical basis of morphogenesis. Philos Trans R Soc Lond B Biol Sci 237(641):37–72
5. Gierer A, Meinhardt H (1972) A theory of biological pattern formation. Kybernetik 12(1):30–39
6. Bard JB (1981) A model for generating aspects of zebra and other mammalian coat patterns. J Theor Biol 93(2):363–385
7. Garfinkel A, Tintut Y, Petrasek D, Boström K, Demer LL (2004) Pattern formation by vascular mesenchymal cells. Proc Natl Acad Sci USA 101(25):9247–9250
8. Meinhardt H, Klinger M (1987) A model for pattern formation on the shells of molluscs. J Theoret Biol 126(1):63–69
9. Nijhout HF (1980) Pattern formation on lepidopteran wings: determination of an eyespot. Dev Biol 80(2):267–274
10. Guo Y, Chen TH, Zeng X, Warburton D, Boström KI, Ho CM, Garfinkel A (2014) Branching patterns emerge in a mathematical model of the dynamics of lung development. J Physiol 592 (2):313–324
11. Yao Y, Nowak S, Yochelis A, Garfinkel A, Boström KI (2007) Matrix GLA protein, an inhibitory morphogen in pulmonary vascular development. J Biol Chem 282(41):30131–30142
12. Kondo S (2009) How animals get their skin patterns: fish pigment pattern as a live Turing wave. In: Systems biology, Springer, Japan, pp 37–46
13. Maini P, Paintera K, Chau HP (1997) Spatial pattern formation in chemical and biological systems. J Chem Soc Faraday Trans 93(20):3601–3610
14. Vanag VK, Epstein IR (2009) Pattern formation mechanisms in reaction-diffusion systems. Int J Dev Biol 53(5):673
15. Storn R, Price K (1997) Differential evolution-a simple and efficient heuristic for global optimization over continuous spaces. J Global Optim 11(4):341–359

Chapter 7
Path Following and Obstacle Avoidance Control Based on Different Fuzzy Grains

Yifei Kong, Chaoyi Chen, Yuequan Yang and Zhiqiang Cao

Abstract This paper presented a hierarchical fuzzy path following control scheme based on different fuzzy grain size in a class of unknown environment with static obstacles. By employing fine-grained fuzzy division and design of fuzzy rule table for the rotation angle and speed of a robot, a more accurate path following control was achieved, while more effective fuzzy obstacle avoidance was realized with coarse-grained fuzzy division strategy. The proposed controller was a two-leveled architecture in which the higher level was the decision-making of the sub-task switching of path following or obstacle avoidance, while the lower level was motion control of path following and fuzzy obstacle avoidance. Finally, the simulation experiments were carried out to demonstrate the feasibility and effectiveness of the proposed scheme.

Keywords Robot · Fuzzy control · Path following · Obstacle avoidance

7.1 Introduction

With the continuous development of intelligent robotics research, mobile robot control problem attracts increasing attention, and has become a hotspot in this area. Based on kinematic model with pole method, a path tracking control method [1] was proposed by making the path following error below an adjustable threshold limit to achieve more precise path following control. With backstepping method, an

Y. Kong · C. Chen · Y. Yang (✉)
College of Information Engineering, Yangzhou University,
Yangzhou 225009, China
e-mail: yang@yzu.edu.cn

Z. Cao (✉)
State Key Laboratory of Management and Control for Complex Systems,
Institute of Automation Chinese Academy of Sciences, Beijing 100190, China
e-mail: zqcao@compsys.ia.ac.cn

Z. Deng and H. Li (eds.), *Proceedings of the 2015 Chinese Intelligent Automation Conference*, Lecture Notes in Electrical Engineering 337,
DOI 10.1007/978-3-662-46463-2_7

underwater robots tracking control [2] was provided in the presence of disturbances to overcome the problem of defining the initial conditions. As for the problem of multi-wheeled robot path following, using linearization method to achieve the robot kinematics model, a lateral position tracking control scheme and longitudinal path following with using classical correction [3] are given. A nonlinear feedback control scheme [4] was proposed with a hydrodynamic parameter identification scheme based on the integral form of a closed-loop control.

Fuzzy control is a method to imitate the way humans think, through the establishment of mathematical models and rule bases. Fuzzy control was applied to many robot jobs combined with a variety of algorithms [5, 6] in complex and unknown environment. Using genetic algorithms to optimize the width and central value of the parameter membership function, an offline self-optimization scheme [7] was obtained. For the security and path match issue of robot soccer, a fuzzy control method [8] was combined to improve the accuracy of path planning to modify potential field function, the angle of potential field force, and timely adjustment potential field repulsion. For local minima problems in artificial potential field method, the repulsion gain coefficient [9] was given to describe the importance of obstacles around the robot. Based on the adjacent angle between the robot and the fellowship, three types of fuzzy controllers [10] were employed to achieve local coordination between robots. An adaptive fuzzy neural network [11] was employed to realize the real-time online adjustment of the pre-aiming direction of the mobile robot based on output perturbation angle.

For expected path following circumference type path, this paper presents a hierarchical fuzzy control program based on different fuzzy grain sizes. The upper level focuses on the behavior decision, while the lower level completes a fuzzy control of action. By employing fine grain fuzzy division for rotation angle and speed of a robot, a more accurate desired path following can be achieved. Considering the urgency requirement of obstacle avoidance, an effective obstacle avoidance strategy with coarse-grained fuzzy division is proposed.

7.2 Problem Description

Located in the global coordinate system XOY, suppose that the pose coordinates of a robot R at the t_n time is $(x(t_n), y(t_n), \psi(t_n))$, $\vec{v}$ is speed with forward direction of the robot R, and ψ is the angle between $\vec{v}$ and X ax. At the same time, assume the first i discrete points of the expected following path is $P_d(i) = [x_i, y_i, \zeta_i]^T$, where ζ_i is the angle between the desired direction of movement (i.e., tangential direction t the point $P_d(i)$), $i = 1, 2...n$, n is the number of discrete points. So, the expected following path can be expressed as a sequence of discrete points

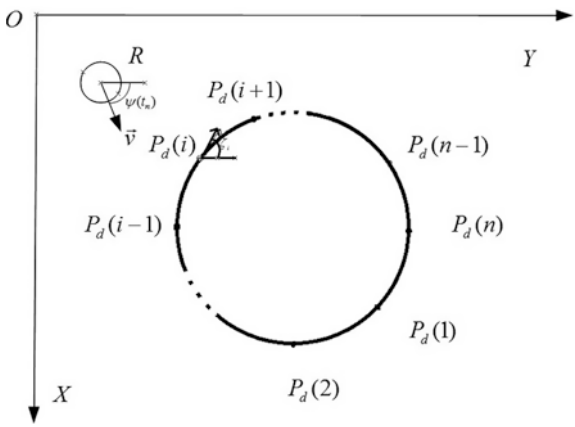

Fig. 7.1 Relationship between robot R and the expected following path

$\{P_d(1), P_d(2)\ldots P_d(n)\}$. And assuming the sensor detection range of the robot is [0, D], D is the maximum detection distance of sensors. To achieve the control of expected path following, the relationship between robot R and the expected following path of the circumference is shown in Fig. 7.1.

Assume that the discrete-time kinematic model of the robot R is

$$\begin{cases} x(t_{n+1}) = x(t_n) + Tv(t_n)\cos\psi(t_n) \\ y(t_{n+1}) = y(t_n) + Tv(t_n)\sin\psi(t_n) \\ \psi(t_{n+1}) = \psi(t_n) + \Delta\psi(t_n) \end{cases} \tag{7.1}$$

where T is the sampling period, v represents the linear velocity, $\Delta\psi$ represents the deflection angle. $\Delta\psi$ is defined as $\Delta\varphi$ when the robot was on the expected following path, and $\Delta\psi$ is defined as $\Delta\theta$ when avoiding an obstacle.

7.3 Fuzzy Control Scheme

As different accuracies are required for different behaviors during the path following movement of the robot, two different fuzzy grain sizes are designed to make fuzzy partition and fuzzy rules. To achieve more accurate path following when the robot moves onto the expected path, fine grain size strategy is employed in the fuzzy partition and the design of the fuzzy rules. But when there is obstacle avoidance in some instances, the primary task of robot is to avoid round static obstacles effectively; with relatively lower requirement of accuracy, fuzzy coarse-grained scheme is utilized. In this paper, two-level hierarchical fuzzy control scheme is proposed.

7.3.1 Fine Grains with Fuzzy Path Following

Here, the first discussion is on fine-grained control strategy in the scenario that robot R moves from outside of the desired path to a nearest discrete point $P_d(i)$. Assume the distance between the robot R and a discrete point $P_d(i)$ is d at t_n, the angle between the direction of robot R and the tangential direction at $P_d(i)$ is φ, and the direction of movement of robot R at $P_d(i)$ is tangential direction of $P_d(i)$. Moreover, $\Delta\varphi$ is defined as the deflection angle at t_n when R arrives at $P_d(i)$ smoothly and finally to follow the desired direction shown in Fig. 7.2.

Now fine-grained fuzzy partition and fuzzy rules design of d and φ to achieve the control value of v and $\Delta\varphi$. Assume the robot R moves to a discrete point $P_d(i)$ with its desired speed direction. Suppose the basic domain of d is $[0, \overline{D}]$, using fuzzy set VN, QN, N, QF, and VF. The basic domain of φ is $[0°, 180°]$, with the fuzzy set VS, S, N, B, and VB. In this paper, the basic domain of speed v for the robot R is [0, 0.3], and the basic domain of deflection $\Delta\varphi$ is $[0°, 90°]$, with the fuzzy set VS, S, N, B, and VB. The membership functions of d, φ, v, $\Delta\varphi$ are shown in Fig. 7.3, respectively.

According to d and φ, to design the fuzzy rule table to control the speed v and the deflection angle $\Delta\varphi$ of the robot R, shown in Tables 7.1 and 7.2. Using Mamdani inference method and height defuzzification method, the solution of defuzzification of the speed v and the deflection angle $\Delta\varphi$ are as follows:

$$v = \sum_{k,i} [u_{\varphi}^{k}(x) \wedge u_{d}^{i}(y) u_{v}] / \sum_{k,i} [u_{\varphi}^{k}(x) \wedge u_{d}^{i}(y)] \tag{7.2}$$

$$\Delta\varphi = \sum_{k,i} [u_{\varphi}^{k}(x) \wedge u_{d}^{i}(y)] u_{\Delta\varphi} / \sum_{k,i} [u_{\varphi}^{k}(x) \wedge u_{d}^{i}(y)] \tag{7.3}$$

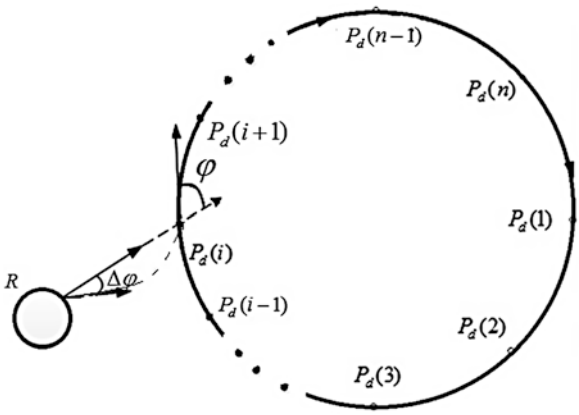

Fig. 7.2 The angle of φ and $\Delta\varphi$

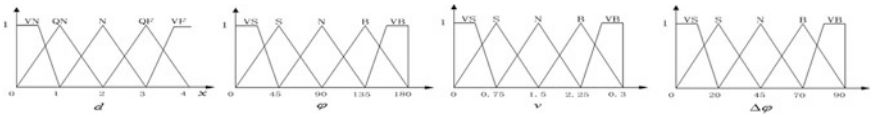

Fig. 7.3 The membership functions of d, φ, v, and $\Delta\varphi$

Table 7.1 The fuzzy rule of speed v

d / φ	VN	QN	N	QF	VF
VS	S	S	N	B	VB
S	S	S	N	N	B
N	VS	S	S	N	N
B	VS	VS	S	S	N
VB	VB	VS	VS	S	N

Table 7.2 The fuzzy rule of deflection $\Delta\varphi$

d / φ	VN	QN	N	QF	VF
VS	VS	VS	VS	VS	VS
S	S	N	S	S	S
N	VS	N	N	S	S
B	N	B	B	N	N
VB	B	VB	B	B	N

where $u_{\varphi}^{k}(x)$ is the membership degree of φ, $u_{d}^{i}(y)$ is the membership degree of d, u_v is a membership function corresponding to the peak value of v, and $u_{\Delta\varphi}$ is a membership function corresponding to the peak value of $\Delta\varphi$. The range set of k is {VS, S, N, B, VB}, the set of i is {VN, QN, N, QF, VF}.

Here to observe fine-grained control performance with $d = 1.2$ and $\varphi = 100°$, where the fuzzy rules are triggered as follows. When d is QN and φ is N, v is S and $\Delta\varphi$ is N. When d is QN and φ is B, v is VS and the $\Delta\varphi$ is B. When d is N and φ is N, v is S and $\Delta\varphi$ is B. When d is N and φ is B, v is S and $\Delta\varphi$ is B. Its Mamdani inference processes are shown from Figs. 7.4, 7.5, 7.6 and 7.7.

According to the Mamdani reasoning, four fuzzy rules have been triggered in d and φ after taking small are 0.77, 0.23, 0.2, and 0.2. Peak values of memberships of v are 0.75, 0.4, 0.75, and 0.75. The value of φ membership function corresponding peaks are 45, 70, 45, and 70. According to formulas (7.2) and (7.3), the speed of robot R is 0.7 and $\Delta\varphi$ is 52°.

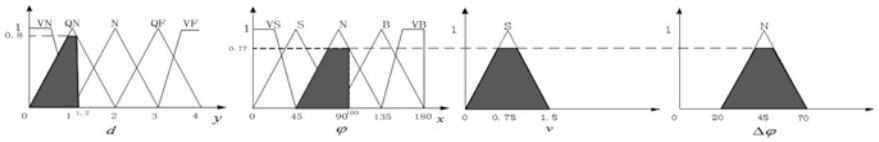

Fig. 7.4 The first trigger fuzzy rules corresponding membership

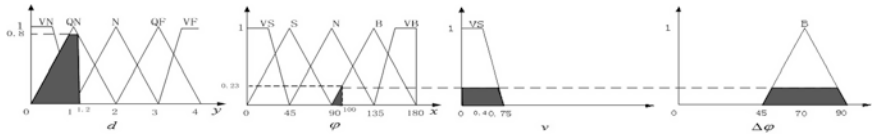

Fig. 7.5 The second trigger fuzzy rules corresponding membership

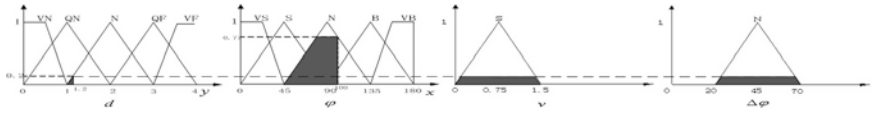

Fig. 7.6 The third trigger fuzzy rules corresponding membership

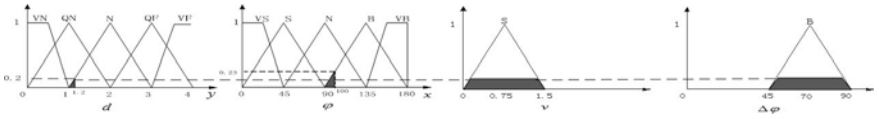

Fig. 7.7 The fourth trigger fuzzy rules corresponding membership

7.3.2 Fuzzy Obstacle Avoidance Control of Coarse Grains Size

Here only consider the case of circular obstacles. Using the method of [12], the centroid and radius of a static circular obstacle *Obs* can easily be computed. Assume the angle θ is positive when the movement direction of robot R is at the right of the line between the centroid and the obstacle *Obs*. Otherwise, the θ is negative. The distance between robot R and obstacle *Obs* is taken as s. And define the output angle $\Delta\theta$ positive in clockwise direction, while $\Delta\theta$ is negative in counterclockwise. Robot R is first required to be capable of feasible and effective avoidance in the process of global path following. The basic idea of obstacle avoidance is that robot R turns right with angle $\Delta\theta$ when the centroid of *Obs* is detected on the left side of movement direction of robot R, and conversely, robot R turns left with the angle $\Delta\theta$, shown in Fig. 7.8. The dashed line in Fig. 7.8 is the unfeasible region for the robot with its angle β. If $|\theta| < \beta/2$ at t_n, the movement of

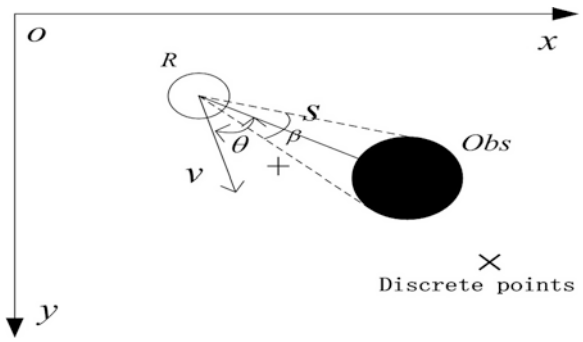

Fig. 7.8 The obstacle avoidance mode of robot R

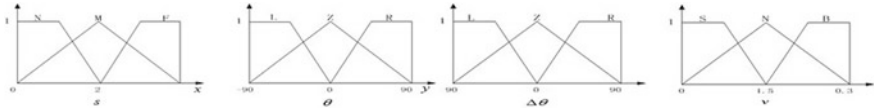

Fig. 7.9 Membership functions of s, θ, $\Delta\theta$ and v, respectively

robot R is within unfeasible region. Therefore, design appropriate $\Delta\theta$ fuzzy rule so that robot R moves outside the unfeasible region at t_{n+1}, that is, $|\theta + \Delta\theta| > \frac{\beta}{2}$.

At the same time, R moves in the direction away from the center of the obstacle when the centroid of the obstacle is at the inside of at a path circular trajectory. In this paper, assume the basic domain of s is [0, D], using fuzzy set N, M, and F. The basic domain of θ is $[-90°, 90°]$ with fuzzy set L, Z, and R. The basic domain of $\Delta\theta$ is $[-90°, 90°]$ with fuzzy set L, Z, and R. The basic domain of v is [0, $V_{\max}$] with fuzzy set S, N, and B. The membership functions of s, θ, $\Delta\theta$, and v are shown in Fig. 7.9. Here, two nested fuzzy controllers are designed to realize the coarse grained obstacle avoidance control. The upper layer is to determine output deflection angle $\Delta\theta$ according to the value of s and θ, while the second one is to obtain the speed control of R through s and $\Delta\theta$.

The fuzzy rule tables of the deflection angle $\Delta\theta$ and the speed v are shown in Tables 7.3 and 7.4, respectively.

Similarly, according to reasoning and height defuzzification method, by Mamdani inference, $\Delta\theta$ and v can be obtained as follows:

$$\Delta\theta = \sum_{m,n} [u_\theta^m(x) \wedge u_s^n(y)] u_{\Delta\theta} / \sum_{m,n} [u_\theta^m(x) \wedge u_s^n(y)] \tag{7.4}$$

$$v = \sum_{m,n} [u_{\Delta\theta}^m(x) \wedge u_s^n(y)] u_v / \sum_{m,n} [u_{\Delta\theta}^m(x) \wedge u_s^n(y)] \tag{7.5}$$

Table 7.3 Fuzzy rules of deflection angle $\Delta\theta$

θ / s	L	Z	R
N	L	R	L
M	Z	R	Z
F	Z	R	Z

Table 7.4 Fuzzy rules of speed v

θ / s	L	Z	R
N	S	S	S
M	N	S	N
F	B	N	B

where $u_{\theta}^{m}(x)$ is the membership of θ, $u_{s}^{n}(y)$ is the membership of s, $u_{\Delta\theta}^{m}(x)$ is the membership of $\Delta\theta$, $u_{\Delta\theta}$ is the peak of membership function of $\Delta\theta$, and u_{v} is the peak of membership function of v. The ranges of m is {L, Z, R}, the ranges of n is {N, M, F}.

7.4 Simulations

In this paper, we use a robot simulation platform All-user based on VC++ to design two fuzzy controllers, respectively, to achieve the circumference type desired path following and obstacle avoidance. Assume the radius of robot R is 0.2, and its maximum speed is 0.3.

Experiment 1: Expected path following is the dual semicircle path set, which includes the first clockwise and the second counterclockwise one with the center (16, 16) and (32, 16), respectively, and the radius 6, shown in Fig. 7.10. As the starting position of robot R is (2.7, 22.1), there are *Obs4*, *Obs5*, and *Obs6* obstacles on the desired path. When the obstacle *Obs4* was detected, the robot turned right

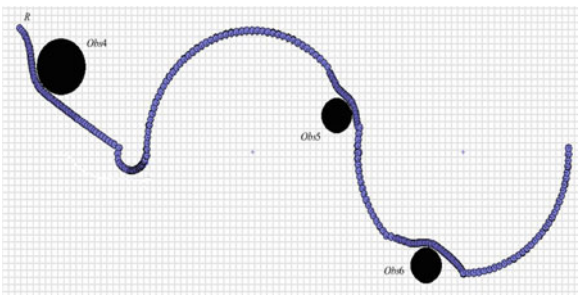

Fig. 7.10 Path following control in dual semi-circumference path with obstacles

and moved 69 steps to avoid *Obs4* effectively. When the distance between robot and corresponding discrete points was 4, robot *R* turned right and moved 40 steps to reach the desired path accurately and then path following continued. When *Obs5* was detected, robot *R* turned left, then moved 36 steps while it turned left and moved 49 steps to avoid *Obs6*.

7.5 Conclusions

This paper proposed a hierarchical fuzzy path following control scheme with different fuzzy partition granularity. By employing fine-grain fuzzy division for the rotation angle and speed of a robot, more accurate path following control was achieved; and obstacle avoidance was realized with coarse grain fuzzy division strategy. The high level was the behavioral decision-making, to determine the robot to follow the desired path or obstacle avoidance, the lower level can achieve fuzzy desired path following and obstacle avoidance, which was based on different grain sizes.

Acknowldgments This work is partially supported by the National Natural Science Foundation of China under Grants 61175111 and 61273352.

References

1. Aicardi M, Cassalino G, Aguiar A, Encarnacao P, Pacsoal A (2001) A planer path following controller for underactuated marine vehicles. In: IEEE mediterranean conference on control and automation, pp 456-465
2. Do KD, Pan J (2003) State and output-feedback robust path-following controllers for actuated ships using Serret-Frenet. Ocean Eng 31(5–6):587–613
3. Liu Z, Ding Y, Jiang Y (2011) Following control of four-wheeled mobile robot. J Cent South Univ (Sci Technol) 42(5):1348–1353 (in Chinese)
4. Yan Z, Chi D, Zhou J, Zhao Z (2012) NGPC-based path following control of UUV. J Huazhong Univ Sic Technol (Nat Sci Ed) 40(5):122–124 (in Chinese)
5. Vadakkepat P, Miin OC, Peng X, Lee TH (2004) Fuzzy behavior based control of mobile robots. IEEE Trans Fuzzy Syst 12(4):559–564
6. Cai C, Yang C (2007) A fuzzy-based collision avoidance approach for multi-robot systems. IEEE Int Conf Robot Bio 3:451–459
7. Wang J, Xiao L (2009) Collision prevention planning of a multi-robot system based on the fuzzy control. Ind Control Appl 28(1):451–459 (in Chinese)
8. Su W, Meng R, Chong C (2010) A study on soccer robot path planning with fuzzy artificial potential field. Int Conf Comput Control Ind Eng 1:386–390
9. Cui GQ, Wang Z, Li CS, Ren K (2011) Fuzzy controller for path planning research of mobile robot. IEEE Int Conf Syst Sci Eng Des Manuf Inf 2:319–322

10. Yuan Y, Jiao J, Cao Z, Zhou C (2011) Fuzzy control coordination based hunting of multiple of multiple autonomous robots. J Huazhong Univ Sci Technol (Nat Sci Ed) 39(II):328–331 (in Chinese)
11. Qian X, Song A (2012) Path planning for mobile robot based on adaptive fuzzy neural network. J SE Univ (Nat Sci Ed) 42(4):637–642 (in Chinese)
12. Yang Y, Han F, Cao Z, Tan M, Jin L (2013) Laser sensor based dynamic fitting strategy for obstacle avoidance control and simulation. J Syst Simul 25(4):704–708 (in Chinese)

Chapter 8
Artificial Immune System Used in Rotating Machinery Fault Diagnosis

Linhui Zhao, Lihua Zhou, Yaping Dai and Zhongjian Dai

Abstract The concept and application of artificial immune system (AIS) is summarized together with the introduction of common Fault Diagnosis in Rotation Machinery. By analysis, the current status of artificial immune system which used in rotation machinery, comments for the achievements and challenge questions are given out in this paper. Furthermore, the expectation and prospect about AIS used in fault diagnosis are discussed also in conclusion.

Keywords Artificial immune system · Fault diagnosis · Rotation machinery

Rotating machinery is essential equipment of the petrochemical, metallurgy, electric power, aerospace and other industries; once a failure occurs, it will cause huge economic losses and security problems [1]. Fault diagnosis is an important means of modern automated production to increase system reliability and safety [2], in the last decades of development, the field has achieved fruitful results [3–5]. Common rotating machinery fault diagnosis method includes:

(1) Diagnosis methods based on probability and statistics time series: Literature [6] analyzes the probability of a dimensionless parameter characteristic distribution in the time domain and selects distinct characteristic parameters used for fault diagnosis of rotating machinery.
(2) Signal processing method based on wavelet transform and fractal geometry: Literature [7] proposed a multiscale slope characteristic extraction method based on multiresolution wavelet analysis.
(3) Intelligent diagnosis method based on artificial neural network: Literature [8] using a neural network, using large datasets of 606 different scenarios for training and testing system, solves the rotating machinery mechanical failure classification problem.

L. Zhao · L. Zhou · Y. Dai (✉) · Z. Dai
School of Automation, Beijing Institute of Technology, No. 5, Zhongguancun South Street, Haidian District, Beijing 100081, China
e-mail: daiyaping@bit.edu.cn

Z. Deng and H. Li (eds.), *Proceedings of the 2015 Chinese Intelligent Automation Conference*, Lecture Notes in Electrical Engineering 337,
DOI 10.1007/978-3-662-46463-2_8

In addition to the above-mentioned intelligent methods, there are fault diagnosis method based on fuzzy logic inference, fault diagnosis method based on fuzzy neural network, pattern recognition method based on Bayesian decision rule, fault diagnosis approach based on expert system and intelligent fusion fault diagnosis methods [9]. However, these methods have varying degrees of drawbacks, such as: rule-based approach requires a lot of prior knowledge, but prior knowledge is very difficult to obtain [10]; the difficulties of signal processing based method is it needs to collect samples of the actual fault, for the cases that the experimental study and site circumstances are very different, it will affect the reliability of diagnosis [11]; due to the model structure and physical meaning are not clear, neural networks based method need enough training data to learn failure mode; when new failures occur, it needs to retrain the entire network [12] and so on.

AIS is a biological immune system simulation, with a powerful information processing capability, it is an computing paradigm inspired by biological theory, draws on some features, principles, and models of the immune system for judgment and decision-making of complex problems [13]. Over the past decade researchers have proposed artificial immune network model, artificial immune system application framework model, the general immune algorithm, negative selection algorithm, clonal selection algorithm, and immune learning algorithm. Compared with the other methods of rotating machinery fault diagnosis, AIS has advantages of providing noise tolerance, unsupervised learning, self-organization, articulate knowledge, forgetting forget seldom-used knowledge, content accessible memory, etc. Therefore, AIS method overcomes some shortcomings in common rotating machinery fault diagnosis methods, and does not require extensive prior knowledge, does not need a complete list of abnormal samples, can be keep learning online, and establish multilayers diagnosis mechanism. Obviously, AIS method provides us more new ideas for rotating machinery fault diagnosis.

This paper first gives a brief introduction about rotating machinery fault, then analyzes a variety of artificial immune algorithms applied in the rotating machinery fault diagnosis, provides an overview of the research status, and summarizes the research results appear stages; in the last, this paper discusses the development direction of artificial immune system in rotating machinery fault diagnosis.

8.1 Introduction of Rotating Machinery Fault

Rotating machinery is one of the most critical parts of all kinds of mechanical equipment, motor is still the most important kind of rotating machinery [14]. Misuse and dynamic loads being the main reasons for the wear of the motor [15]. Induction motor failure can be divided into stator fault which is caused by short circuit or open circuit of the phase windings, rotor/end ring fault, gap irregular, and bearing and gear failure [16–19].

With the development of the structure of the rotating machinery, the requirement of diagnostic accuracy for concurrent fault is increasing, such as rolling bearings,

gearboxes, and compressors [20]. Early detection and accurate diagnosis of motor failure is the key to obtain safe and reliable operation in the motor drive system, early fault detection and diagnosis can quickly repair the motor and shorten the motor drive system downtime [21]. Accurate diagnosis of rolling bearing failure is often directly affect the accuracy, reliability, and host life [22]. With the rapid development of Prognostics and Health Management Technology (PHM), a variety of diagnostic and predictive techniques have been developed for complex dynamic systems, designed to improve the reliability and safety of the system [23]. In recent years, the study of online motor fault diagnosis is heating up, for the online fault diagnosis plays a crucial role in providing fault tolerance for drive system in the critical field [24].

8.2 Research Status of AIS in Rotating Machinery Fault Diagnosis

At present, the main algorithms and models of AIS are negative selection algorithm (NSA), clonal selection algorithm, and immune network model. Among them, the negative selection algorithm has the unique characteristics that it does not require a lot of priori knowledge, and it can use a small amount of normal samples to detect unlimited abnormal samples, so it has become the core technology in AIS [25].

8.2.1 Negative Selection Algorithm

Biological immune system has a very complex defense mechanism; it can detect foreign substances and produce antibodies to attack antigens. This capability is mainly implemented by two types of lymphocytes: B cells and T cells. T cells must pass through a negative selection procedure carried out in the thymus; only those that do not match the self-proteins are released, to prevent immune system from attacking our body, this process is the use of negative selection mechanism.

Literature [26] designs T module and B module, builds the immune system framework, T module uses real-valued vector negative selection algorithm to generate an abnormal detector, B module responses to the actual state of the system to form the alarm module, and feedback them to T module. This reference uses fixed radius detectors and the number of detectors increased exponentially with the size of the normal space [27]; in the fault space, the coverage and the overlap of detectors are difficult to equalize, limiting the application of such negative algorithm.

Literature [28] based on variable radius detector and immune memory cells, the center and radius variation is stored to memory cells, when a new detector is generated, its position is dynamically adjusted so that the coverage is improved. This document uses variable radius detectors, effectively reducing the overlap between the detectors.

Literature [22] uses real-valued matching negative selection algorithm to produce typical fault samples, as the input of radial basis function neural network for rolling bearings' fault diagnosis.

NSA does not require a lot of prior knowledge; it is able to distinguish abnormal state and normal state based on a small amount of normal samples, solving the engineering problem of hard to get a complete list of exceptions. When the new failure occurs, NSA does not require retraining to detect the new failure, it only needs increasing the detectors or redistribution. NSA also has a memory function, for those failures occurred before, NSA can diagnose them through memory detectors very quickly. But the NSA is not able to identify the fault types, the initial generation of detectors consumes a large quantity of time. And it is also need to be further improved in the other aspects, such as sample represent and detector represent.

8.2.2 Clonal Selection Algorithm

Clonal selection algorithm (CSA) is inspired by genetic programming and immune theory. It has continuing learning and memory function, and has been successfully applied to engineering problems such as character recognition, multi-objective optimization and traveling salesman problem. Literature [23] used the expression to describe antibody, use the clone selection algorithm to design classifier, its effectiveness has been verified on a different speed rotating machinery. Literature [24] uses clonal selection algorithm and genetic algorithm to optimize the structure of RBF neural network and the selection probability based on density and fitness improves the convergence performance of neural network.

CSA has good optimization and memory ability; it can find the approximate optimal solution in the global scope, but also to keep multiple local optima. Compared with the genetic algorithm, CSA has no "crossover" part, so the convergence rate is faster. However, affinity, proliferation copy operator and mutation operator of CSA lacks a unified paradigm.

8.2.3 Artificial Immune Network

Jerne proposed the immune network hypothesis in 1974, creating a unique type of network theory, after that a variety of different types of artificial immune network (AIN) appeared, successfully applied to fault diagnosis. In Literature [15], initial individuals are formed by the B cells network which is generated by the original data, clone individuals are generated by clone and mutation, and B cells are formed by the initial individuals and clone individuals. B cells produce inhibition when antibodies recognize each other, so it avoids using antibody's unlimited growth by immune network theory and reduce data redundancy. Literature [29] proposed an

immune network model based on improved fault diagnosis algorithm. It can adaptively adjust the rule of pruning and threshold of antibody's affinity according to the matching relationship between the group of antibodies and the group of antigens, and overcomes the shortcomings of the AiNet network does not recognize the new failure.

AIN researches how systems maintain immune stable in a dynamic environment, mutual restraint relations among antibody groups and among antibody–antigen groups. AIN avoids infinite antibody population growth, reduces data redundancy to ensure proper diagnosis and diagnostic time, maintenance homeostasis in fault diagnosis system. So far, AIN has developed various theories, but relative to the natural immune system, immune network mechanism is not perfect; reasonable selection of pruning threshold, affinity thresholds, and other parameters need to be further studied.

8.3 Research Achievements of AIS in RMFD

AIS in RMFD is in the development stage, aiming at the slowly varying, intermittent, composite, and other characteristics of rotating mechanical failure, experts and scholars at home and abroad made various of improvements in artificial immune system, and made a series of valuable achievements. Research achievements in the existing stage focused on the following aspects.

8.3.1 Dimensionless Indexes as the Detector Sample to Improve Diagnostic Results

In the RMFD using vibration signal, the time domain vibration waveform is the simplest and most direct form of expression. In the time domain, the dimensionless index is sensitive to failure, but vulnerable to variation load, speed, and other conditions. Dimensionless index is not sensitive to disturbance, but it is difficult to search for the relationship among fault characteristics [30]. Literature [18] build dimensionless immune detectors offline, each detector diagnostic results is transformed into a distribution of confidence, solving the overlap phenomenon in the dimensionless parameter ranges, in order to achieve the goal of online fault diagnosis.

8.3.2 Negative Selection Detect Faults Species

Basic NSA can only distinguish abnormal state from the normal state, but cannot really identify the fault types, so it cannot meet the requirements of the actual

project. Aiming at this problem, some scholars have developed a variety of negative selection algorithms which can recognize the fault types. Literature [31] trains multiple detectors; each detector corresponds to a particular fault, so the fault types can be obtained according to the activated detector. Literature [32] divides the fault diagnosis procedure into two layers, the first layer only conducts fault detection, and the second layer decided the fault types.

8.3.3 CSA Optimize the Detector

The initial detector of negative selection algorithm is randomly generated, which is often inefficient, therefore negative selection is often combined with CSA, using the optimization characteristics of CSA to improve the coverage of the detector, reducing the number of detectors. For example, literature [33] uses CSA to online updates detectors, effectively improve the coverage of abnormal space while maintaining a low number of detectors.

8.3.4 CSA for Parameter Optimization in Other Fault Diagnosis Methods

CSA has advantages of good global search ability and fast convergence speed, it is often used to optimize parameters. SVM has become one of the most popular classification methods in software calculation, however, SVM classification accuracy depends on the kernel and the penalty parameter. Literature [34] uses a three-phase motor current, builds feature vectors based on Park's vector method, and then uses AIS to regulate SVM's kernel and penalty parameter, use SVM classification to recognize broken rotor bar and stator short-circuit fault. Literature [15] uses artificial immune system to define a data clustering algorithm, selects the RBF center number and location of the hidden layer neural network adaptively.

8.4 Development Direction of AIS in RMFD

AIS provides new ideas, new methods for RMFD; however, it needs to fit engineering needs in practical application of rotating machinery fault diagnosis. Rotating machinery fault diagnosis applied in AIS also has the following problems which are worth studying.

8.4.1 Issue of NSA to Balance Real-Time Performance and Coverage

In the negative selection algorithm, normal mode and abnormal mode of rotating machine are detected by detectors, whose detection accuracy depends on the coverage of non-self-space; the higher the coverage ratio, the higher the accuracy. But the greater the number of detectors, real-time performance becomes worse too. So, how to overcome the contradictions between real-time performance and coverage is a topic worthy of further study.

8.4.2 The Initial Detector Efficiency of the NSA Needs to Be Improved

After the initial negative selection of the detector selected, fault diagnosis can be carried through a process of negative selection. Because the initial detection is randomly generated, the more the number of detectors, the negative selection process is longer. How to develop more efficient rules of initial detector is one of the challenging issues of negative selection algorithm.

8.4.3 Immune Algorithm and Immune Principle Need Further Development

Although various immune algorithms and models in fault diagnosis of rotating machinery applications get some good results, but they are still somewhat rough for the construction of AIS, a lot of complex mechanisms of the biological immune system have not been described and applied in the AIS, which will affect the effectiveness improvement of artificial immune algorithm, as principle studies, it is also the basic problem.

8.4.4 Immune Algorithm Complementary with Other Algorithms

Although CSA has been applied in optimization and conjunction with SVM and neural networks intelligent method, but theoretical system, experimental validation and other aspects of combining artificial immune algorithm with other algorithms have great and expandable study space. In the actual operating environment, there will be some complex, vague, intermittent nature, and other mechanical fault of

rotating machinery. AIS can be combined with a fuzzy system, dimming the fixed parameters of artificial immune systems, such as the radius of the detector, the number of clones, and improving the capability of artificial immune system response to fault diagnosis, so we can achieve the correct diagnosis of rotating machinery composite failure and intermittent faults.

8.5 Summary and Conclusion

In this paper, the application of artificial immune system in rotating machinery fault diagnosis is reviewed. It introduces the present research situation of negative selection algorithm, clone selection algorithm, and artificial immune network in the rotating machinery fault diagnosis. Furthermore, the classifications of the existing research results are also introduced.

In general, the application of artificial immune system in rotating machinery fault diagnosis is still in the stage of development, focusing on the negative selection algorithm, clone selection algorithm and artificial immune network, so we think we should conduct in-depth research in the following areas: (1) The mechanism of the natural immune system combined with the actual production should be fully studied to develop more effective fault diagnosis algorithm; (2) Mathematical theory of artificial immune algorithm analysis also needs further research. If a kind of general-purpose computing paradigm is proposed, it will be more convenient for rotating machinery fault diagnosis; (3) For using negative selection algorithm to specific fault diagnosis of rotating machinery efficiency, a kind of method that can improve the efficiency of initial detector generation rule should be further researched; (4) Considering artificial immune system combined with fuzzy system, fixed parameters of the radius of the detector and cloning individual numbers in the artificial immune system can be blurred to improve the human immune system's ability of dealing with uncertainty problems in fault diagnosis and achieve the correct diagnosis of rotating machinery composite fault and Intermittent fault.

Based on the above analysis, artificial immune method will get more extensive application in fault diagnosis of rotating machinery.

Acknowledgments This work was financially supported by the Importation and Development of High-Caliber Talents Project of Beijing Municipal Institutions (CIT&TCD201404081).

References

1. Wei D, Zhan SL, Xiao WW (2007) Application of image recognition based on artificial immune in rotating machinery fault diagnosis. In: 1st international conference on bioinformatics and biomedical engineering, pp 1047–1052
2. Zhou DH, Hu YY (2009) Fault diagnosis techniques for dynamic systems. Acta Autom Sinica 35(6):748–758 (in Chinese)

3. Lemos A, Caminhas W, Gomide F (2013) Adaptive fault detection and diagnosis using an evolving fuzzy classifier. Inf Sci 220:64–85
4. Ghate VN, Dudul SV (2011) Cascade neural-network-based fault classifier for three-phase induction motor. IEEE Trans Ind Electron 58(5):1555–1563
5. Zhou DH, Shi JT, He X (2014) Review of intermittent fault diagnosis techniques for dynamic systems. Acta Autom Sinica 40(2):161–171 (in Chinese)
6. Chang J, Li T, Li P (2010) The selection of time domain characteristic parameters of rotating machinery fault diagnosis. In: 2010 international conference on logistics systems and intelligent management. IEEE, vol 1, pp 619–623
7. Li P, Kong F, He Q et al (2013) Multiscale slope feature extraction for rotating machinery fault diagnosis using wavelet analysis. Measurement 46(1):497–505
8. Lima AA, Prego MT, Netto SL et al (2013) On fault classification in rotating machines using fourier domain features and neural networks. In: IEEE fourth latin american symposium on circuits and systems (LASCAS), IEEE, 2013, pp 1–4
9. Zhang QH (2004) Fault diagnosis technology research based on artificial immune system. South China University of Technology, Guangzhou (in Chinese)
10. Wei D, Zhan SL (2009) A recognition method of vibration parameter image based on improved immune negative selection algorithm for rotating machinery. J Harbin Inst Technol 16(1):5–10
11. Duan F, Lei M, Li J et al (2007) A motor fault diagnosis method based on immune mechanism. In: Workshop on intelligent information technology application, IEEE, pp 157–160
12. Hou SL, Li YH, Li MK, Wei XK (2007) Sensor fault diagnosis for aircraft engine based on artificial immune networks. J Propul Technol 28(1):86–91 (in Chinese)
13. Abbass HA, Newton CS, Sarker R (2002) Data Mining: A Heuristic Approach. IGI Global, Hershey, PA, pp 1–310. doi:10.4018/978-1-93070-825-9
14. Immovilli F, Bellini A, Rubini R et al (2010) Diagnosis of bearing faults in induction machines by vibration or current signals: a critical comparison. IEEE Trans Ind Appl 46 (4):1350–1359
15. Wen X, Wei S, Liu H et al (2008) Application research of immune neural network on motor fault diagnosis. In: International workshop on education technology and training and 2008 international workshop on geoscience and remote sensing ETT and GRS. IEEE, (1), 618–621
16. Zhang P, Du Y, Habetler TG et al (2011) A survey of condition monitoring and protection methods for medium-voltage induction motors. IEEE Trans Ind Appl 47(1):34–46
17. Chilengue Z, Dente JA, Branco PJ (2011) An artificial immune system approach for fault detection in the stator and rotor circuits of induction machines. Electr Power Syst Res 81 (1):158–169
18. Sun G, Qin A, Zhang Q et al (2013) A compound fault integrated diagnosis method for rotating machinery base on dimensionless immune detector. In: 25th Chinese control and decision conference (CCDC). IEEE, 2013, pp 4390–4394
19. Zhang CL, Yue X, Li S et al (2011) Fault diagnosis of rotating machinery base on wavelet packet energy moment and HMM. Key Eng Mater 455:558–564
20. Zhang QH, Hu Q, Sun G et al (2013) Concurrent fault diagnosis for rotating machinery based on vibration sensors. Int J Distrib Sens Netw 2013:1–10
21. Tian Y (2009) On diagnosis prototype system for motor faults based on immune model. In: International conference on business intelligence and financial engineering, 2009. BIFE'09. IEEE, pp 126–129
22. Ma X, Wei X, An F et al (2010) Bearing fault diagnosis based on negative selection algorithm of feature extraction and neural network. In: Control and decision conference (CCDC), Chinese. IEEE, 2010, pp 3938–3941
23. Tang P, Gan Z, Chow TWS (2011) Clonal selection programming for rotational machine fault classification and diagnosis. In: Prognostics and system health management conference (PHM-Shenzhen). IEEE, 2011, pp 1–6
24. Wen X, Brown DJ (2010) Online motor fault diagnosis using hybrid intelligence techniques. In: IEEE symposium on industrial electronics & applications (ISIEA). IEEE, 2010, pp 355–360

25. Jin ZZ, Liao MH, Xiao G (2013) Survey of negative selection algorithms. J Commun 34 (1):159–170 (in Chinese)
26. Liu Y, Shang YS, Wang YP (2011) Fault diagnosis method based on immune model and its application. Comput Eng 37(16):5–7 (in Chinese)
27. Govender P, Kyereahene, Mensah DA (2010). Fault diagnosis based on the artificial immune algorithm and negative selection. In: 2010 IEEE 17th international conference on industrial engineering and engineering management (IE&EM). IEEE, pp 418–423
28. Gui LY, Shi WQ, Jian Z (2012) Fault diagnosis of induction motor based on artificial immune system. In: International conference on industrial control and electronics engineering (ICICEE)
29. Zheng YH, Li RH (2010) Improved fault diagnosis algorithm based on immune network model. Control Decis 25(6):847–851 (in Chinese)
30. Cen J, Zhang QH, Xu BG et al (2009) Fault diagnosis model of rotating machinery based on artificial immunity and its application. In: International workshop on intelligent systems and applications. ISA 2009. IEEE, 2009, pp 1–4
31. Alizadeh E, Meskin N, Benammar M et al (2013) Fault detection and isolation of the wind turbine based on the real-valued negative selection algorithm. In: 2013 7th IEEE GCC conference and exhibition (GCC). IEEE, pp 11–16
32. Gao XZ, Wang X, Zenger K et al (2012) Negative selection algorithm-based motor fault diagnosis. In: Practical applications of intelligent systems. Springer, Berlin, Heidelberg, pp 173–183
33. Wang C, Zhao Y (2008) A new fault detection method based on artificial immune systems. Asia-Pac J Chem Eng 3(6):706–711
34. Aydin I, Karakose M, Akin E (2010) Generation of classification rules using artificial immune system for fault diagnosis. In: 2010 IEEE international conference on systems man and cybernetics (SMC), IEEE, pp 343–349

Chapter 9
The Application of a Parameter Adaptive Iterative Learning Control on Three-Axis Angular Vibration Turntable

Ruoxuan Luan and Zhen Chen

Abstract Angular vibration turntable is an important device in the performance test of inertial device. First, the mathematical model of the three-axis angular vibration turntable is established in this paper; second, the iterative learning control algorithm based on the mathematical model is designed; and considering the situations of parameter uncertainty and parameter time-varying, in order to improve the precision during the period of tracking periodic anticipant input, the method of parameter adaptive is introduced based on the traditional PID iterative learning control; third, the convergence analysis of the adaptive parameter iterative learning control algorithm is carried out; finally, the experiments are carried out on the three-axis angular vibration turntable in order to verify the control algorithm proposed in this paper. The results of the experiments show that the parameter adaptive iterative learning control, compared to traditional PID control, can improve the precision of the system during tracking the periodic input, and the design is of benefit to reducing the periodic disturbance too.

Keywords Three-axis angular vibration turntable · Iterative learning control · Parameter adaptive · System disturbance · Robustness

9.1 Introduction

With the rapid development of science and technology, the requirements on the maneuverability of aircraft and weapons in the aviation, spaceflight field are increasingly higher. Accordingly, the requirements on the frequency response bandwidth of inertial navigation devices are even higher [1]. As the test device for the inertial components, the angular vibration turntable requests higher performance

R. Luan (✉) · Z. Chen
5th South Street, Zhongguancun, Haidian District, Beijing 100081, China
e-mail: bit_lrx@163.com

Z. Deng and H. Li (eds.), *Proceedings of the 2015 Chinese Intelligent Automation Conference*, Lecture Notes in Electrical Engineering 337,
DOI 10.1007/978-3-662-46463-2_9

index than the device under test. Therefore, it also faces the challenge of moving in the direction of high frequency response and high acceleration [2].

The traditional PID control algorithm has a history of over 50 years and is still the most widely used industrial control algorithm [3]. But the PID controller has simple structure, when the controlled object is of higher order, parameter time-varying and nonlinear; it is unable to provide favorable control performance. With the development of the control theory, a variety of new control methods arise in recent years, including iterative learning control, adaptive control, intelligent control system, variable structure control, and so on. Iterative learning control (ILC) is a control theory that could completely track the desired trajectory, it is essentially a feed forward control, which belongs to a branch of intelligent control [4]. When the turntable is in vibration mode, it is given a periodic signal so that it has certain periodic tracking error. When the controlled object contains uncertain parameters or time-varying parameters, there is a big defect [5, 6]. Therefore, parameters adaptive iterative learning control (AILC) is introduced in this paper.

9.2 Mathematical Models of the System

Modeling of turntable is mainly modeling of dc motor.

We can get the system transfer function from Fig. 9.1

$$\Omega(s) = \frac{1/K_e}{T_m T_e s^2 + T_m s + 1} U_a(s) - \frac{R_a/K_t K_e}{T_m T_e s^2 + T_m s + 1} T_L(s) \tag{9.1}$$

where K_e is the potential coefficient, K_t is the torque coefficient, thus $E = K_e\omega$, $T_e = K_t I_a$; the mechanical and electrical time constant is $T_m = JR_a/K_t K_e$, the electrical time constant is $T_e = L/R_a$; $\Omega(s)$ is the Laplace transform of the angular velocity ω, $U_a(s)$ is the Laplace transform of the input voltage U_a, $T_L(s)$ is the Laplace transform for motor disturbance torque T_L.

In the practical control process, the motor inductance is often ignored, and then the Eq. (9.1) can be simplified as the following form:

$$\Omega(s) = \frac{1/K_e}{T_m s + 1} U_a(s) - \frac{T_m/J}{T_m s + 1} T_L(s) \tag{9.2}$$

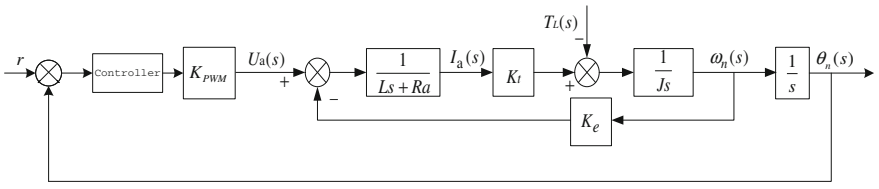

Fig. 9.1 Dynamic structure of the dc motor

The output voltage is proportional to the amount of input control, that is $u = K_u U_a$. Laplace inverse transformation is made for the Eq. (9.2):

$$T_m \dot{\omega} + \omega = \frac{1}{K_u K_e} u - \frac{T_m}{J} T_L \tag{9.3}$$

In this paper, T_L is simplified as viscous friction T_f, thus $T_L = T_f = \sigma\omega$, where $\sigma > 0$ is the viscous friction coefficient. Substituting Eq. (9.3) into (9.2), we can get:

$$\dot{\omega} = \frac{1}{K_u K_t T_m} u - (\frac{\sigma}{J} + \frac{1}{T_m})\omega \tag{9.4}$$

9.3 The Design of Parameter Adaptive Iterative Learning Control Law

The form of the parameter adaptive iterative learning control law proposed in this paper is as follows:

$$u_{k+1}(t) = u_k(t) + K_P e_{k+1}(t) + K_D \dot{e}_{k+1}(t) \tag{9.5}$$

where K_P is the proportional parameter, K_D is the differential parameter, $e_k(t)$ is the tracking error of the kth cycles. Without loss of generality, considering the nonlinear system:

$$\begin{cases} \dot{x}(t) = g(t,x) + Bu(t) \\ y = Cx \end{cases} \tag{9.6}$$

where $x = [\,\omega \quad \theta\,]^T$, the output equation is $y = \theta$.

Make the following assumptions about the system described by Eq. (9.6) [7]: the nonlinear function $g(t,x)$ satisfies the global *Lipschitz* condition, so there exists a *Lipschitz* constant $M > 0$, which makes $\|g(t,x_1) - g(t,x_2)\| \le M\|x_1 - x_2\|$.

Theorem 9.1 *If the system described by Eqs.* (9.5) *and* (9.6) *satisfies the following conditions: (1)* $\|I - K_D CB\| < 1$, *(2)* $x_k(0) = x_0$, $(k = 0, 1, 2\cdots)$, *then the output error sequences* $\{\Delta y_k(t)\}$ *and the control input error sequences* $\{\Delta u_k(t)\}$ *converge to zero, where* $\Delta y_k(t) = y_d - y_k$, $\Delta u_k(t) = u_d - u_k$, *thus:* $\lim_{k\to\infty}(y_d - y_k) = 0$, $\lim_{k\to\infty}(u_d - u_k) = 0$.

Proof let $f_1(t,x) = g(t,x_d) - g_1(t,x_d - x)$, $\Delta x_k(t) = x_d - x_k$, $\forall x \in R^n$, it can be obtained:

$$\begin{cases} \Delta\dot{x}_k = g_1(t, x_d) + B\Delta u_k \\ \Delta y_k = C\Delta x_k \\ \Delta u_{k+1} = \Delta u_k - K_P\Delta y_k - K_D\Delta\dot{y}_k \end{cases} \tag{9.7}$$

Then it can be obtained from Eq. (9.7):

$$\Delta u_{k+1} = (I - K_D CB)\Delta u_k - K_P C\Delta x_k - K_D C g_1(t, \Delta x_k) \tag{9.8}$$

So we have:

$$\begin{aligned} \|\Delta u_{k+1}\| =& \|(I - K_D CB)\Delta u_k - K_P C\Delta x_k - K_D C g_1(t, \Delta x_k)\| \\ \le& \|(I - K_D CB)\Delta u_k\| + \|K_P C\Delta x_k\| + \|K_D C g_1(t, \Delta x_k)\| \\ \le& \|I - K_D CB\|\|\Delta u_k\| + (\|K_P C\| + M\|K_D C\|)\|\Delta x_k\| \\ \le& \|I - K_D CB\|[\|I - K_D CB\|\|\Delta u_{k-1}\| + \eta_{k-1}] + \eta_k \\ \le& \|I - K_D CB\|^{k+1}\|\Delta u_0\| + \sum_{i=0}^{k}\|I - K_D CB\|^{k-i}\eta_i \end{aligned} \tag{9.9}$$

where $\eta_i = (\|K_P C\| + M\|K_D C\|)\|\Delta x_i\|$, $i = 0, 1, \ldots, k$.

It can be seen from Eq. (9.9): under the condition of $\|I - K_D CB\| < 1$, when $k \to \infty$, there is $\|\Delta u_{k+1}\| \to 0$. And $\|\Delta y_{k+1}\| \to 0$ can be proved with similar method. So, if only K_D is chosen appropriately that makes $\|I - K_D CB\| < 1$, there is $\lim_{k\to\infty}(y_d - y_k) = 0$ and $\lim_{k\to\infty}(u_d - u_k) = 0$.

The parameter adaptive adjusting method is designed as follows:

$$K_P = \begin{cases} K_{P0}, & k = 1 \\ \dfrac{K_{P0}e_i(k)}{e_i(k) + e_k(t)}, & k > 1 \end{cases}, \quad K_D = \begin{cases} K_{D0}, & k = 1 \\ \dfrac{K_{D0}e_i(k)}{e_i(k) + e_k(t)}, & k > 1 \end{cases}. \tag{9.10}$$

where $e_i(k)$ is the cumulative error of the kth cycles, K_{P0} is the initial value of proportional parameter, K_{D0} is the initial value of differential parameter, which can be chosen according to the actual situation.

9.4 Experimental Results and Analysis

In order to verify the effectiveness of the AILC control algorithm proposed in this paper, the experiments are carried out on a three-axis angular vibration turntable.

9.4.1 Experiment 1

Considering the two cases of AILC and ILC: (1) in the case of AILC, the parameters are chosen as $K_{P0} = 0.5$, $K_{D0} = 0.001$; (2) in the case of ILC, in order to facilitate comparison, the parameters are chosen as $K_P = K_{P0} = 0.5$, $K_D = K_{D0} = 0.001$.

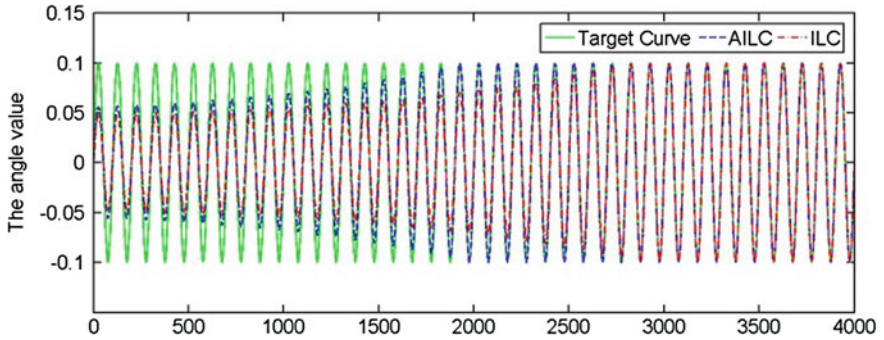

Fig. 9.2 The tracking curve

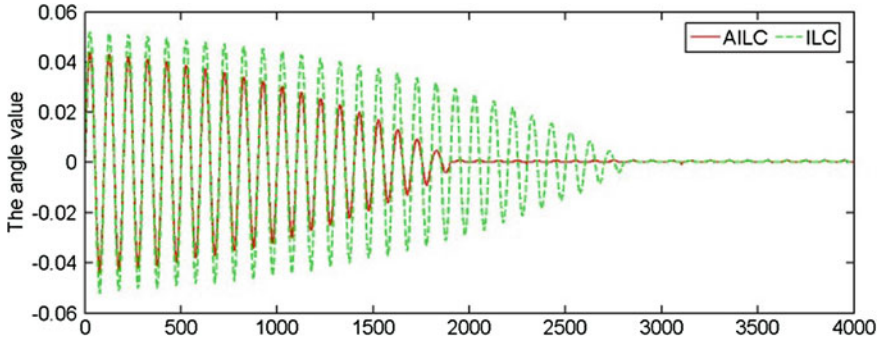

Fig. 9.3 The error curve

Let the three-axis angular vibration turntable do sinusoidal vibration with an amplitude of 0.1° and frequency of 10 Hz. The experimental result curves of the two cases are as follows (the ordinate shows the angle value whose unit is (°), the abscissa shows time and the sampling frequency of the data is 100 Hz):

It can be seen from Figs. 9.2 and 9.3, AILC can make the three-axis angular vibration turntable track the target curve faster. In the case of AILC, the turntable needs 1.9 s to track the target curve while ILC needs 2.8 s. The convergence speed of the system is greatly improved through parameter adaptive adjusting. When the system is stable, the steady-state error of AILC is 0.0002° while ILC is 0.0003°. Therefore, under the control of AILC control algorithm proposed in this paper, the three-axis angular vibration turntable has better tracking performance and strong robustness to the uncertain disturbance (Table 9.1).

Table 9.1 The three groups of parameter values

	K_{P0}	K_{D0}
Parameter 1	0.5	0.001
Parameter 2	0.55	0.001
Parameter 3	0.5	0.002

9.4.2 Experiment 2

Choose different parameter values, and compare the experimental results.

The curves of the experimental results are as follows:

As shown in Figs. 9.4, 9.5, and 9.6, the convergence time (s) and steady-state maximum error (°) of different parameters are shown in Table 9.2:

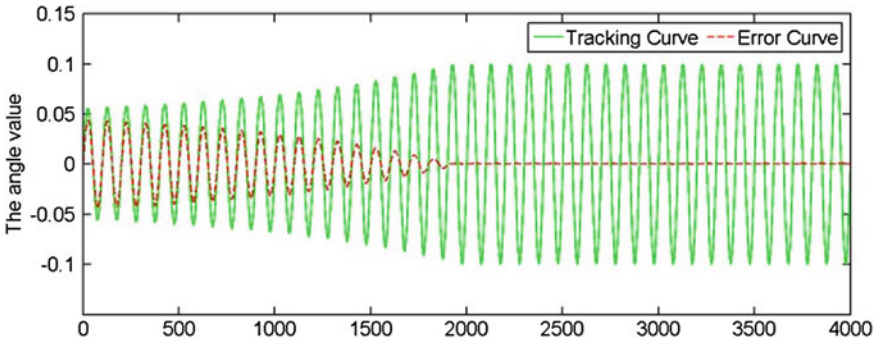

Fig. 9.4 Parameter 1

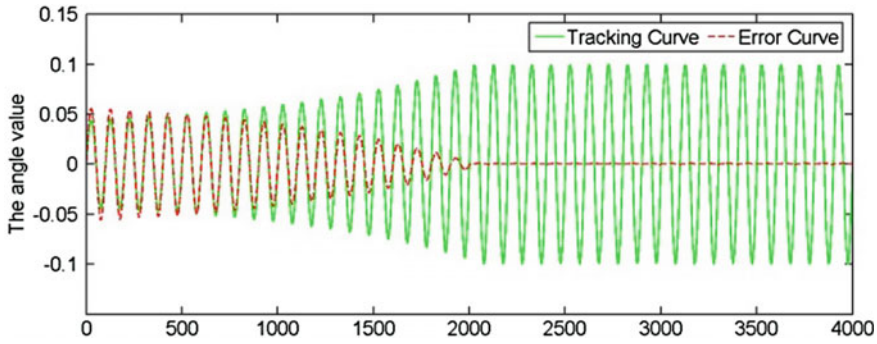

Fig. 9.5 Parameter 2

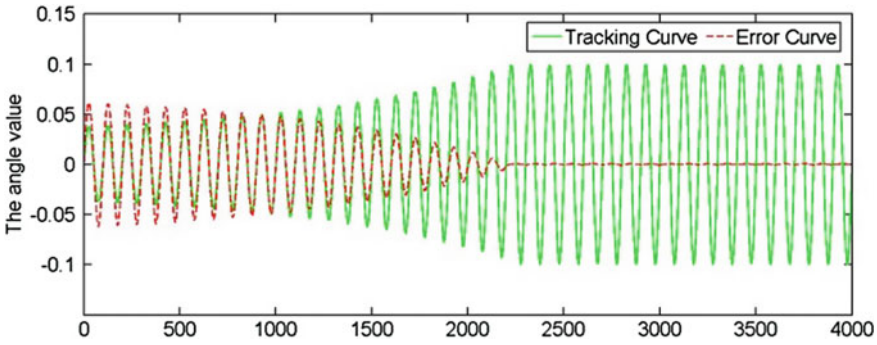

Fig. 9.6 Parameter 3

Table 9.2 Convergence time and Steady-state error

	Convergence time	Steady-state error
Parameter 1	1.9	0.0002
Parameter 2	2.0	0.0003
Parameter 3	2.2	0.0005

It can be seen from Experiment 2, AILC can achieve better control effect by adjusting the values of K_{P0} and K_{D0}. And the control effects of the three groups of parameter values are all better than that of ILC.

In summary, the parameter adaptive iterative learning control law proposed in this paper has better control effect and stronger robustness, compared with parameter fixed iterative learning control law.

9.5 Conclusions

In this paper, a parameter adaptive iterative learning control algorithm is proposed and experiments are carried out on a three-axis angular vibration turntable to verify the effectiveness of the control algorithm.

The results of the experiments indicate that the parameter adaptive iterative learning control law proposed in this paper improves the tracking performance of the three-axis angular vibration turntable obviously, compared with the parameter fixed iterative learning control law. The turntable can track the target signal faster and has a stronger robustness to the uncertain disturbance. It can be seen that the parameter adaptive iterative learning control can be used in angular vibration turntable control. Since the convergence time of the system is relatively long, the parameter adaptive iterative learning control can be combined with other control methods in the practical application in the future, in order to make the system have faster convergence time without sacrificing the accuracy.

References

1. Gao W, Fang X, Liu F (2012) Analysis on the influence of three-axis turntable nonorthogonal error on gyro calibration of SINS. In: 2012 international conference mechatronics and automation (ICMA)
2. Ren S, Li W (2010) Research on sequential test of Gyro's error model coefficients. In: International conference on intelligent system design and engineering application
3. Qi J, Ren S, Wang C (2006) Angular velocity test plan design for identifying the error model coefficients of Gyro using three-axis turntable. J Astronaut 27(3):565–570
4. Fu KS (1970) Learning control systems—review and outlook. IEEE Trans Autom Control 15:210–221
5. De Roover D, Bosgra OH, Steinbuch M (2000) Internal-model-based design of repetitive and iterative learning controllers for linear multivariable systems. Int J Control 73:914–929
6. Lu Z, Xu F, Zhang J (2010) Disturbance attenuation in test turntable dynamic unbalance of iterative learning control. Syst Control Aerosp Astronaut, 902–906, Harbin, 8–10 June 2010
7. Tang S, Li J-M (2012) AILC for nonlinearly parameterized systems with unknown distributed time-varying delays and unknown control direction. Chinese Control Conference (CCC), 2960–2965, Hefei, 25–27 July 2012

Chapter 10
Position Control of Interior Permanent Synchronous Motor Based on Improved Shakeless Fuzzy Controller

Mingling Shao, Haisheng Yu, Zihan Wang, Hongchao Xie and Shuai Zhao

Abstract The intelligent control method and maximum torque per ampere (MTPA) principle are used to develop the modeling and position control of interior permanent magnet synchronous motor (IPMSM) in this paper. As the conventional fuzzy controller adopts fixed output scaling factor and it has the problem of output shaking, the steady-state accuracy of conventional fuzzy controller is not high. In order to improve the dynamic response characteristics for a high-precision position servo system of IPMSM, a new scheme based on single neuron control online adjusting the output scaling factor of shakeless fuzzy controller is proposed. Then the improved shakeless fuzzy controller is applied to the IPMSM servo system as a position controller, which can realize accurate position control. The simulation results show that the proposed scheme exhibits good position control and load torque disturbances attenuation performances.

Keywords Permanent magnet synchronous motor · Maximum torque per ampere · Fuzzy controller · Single neuron control

10.1 Introduction

Recently, interior permanent magnet synchronous motor (IPMSM) drives play a vitally important role in motion-control applications [1]. This is mainly due to their compact size, high efficiency, high power density, large torque to inertia ratio, and low rotor losses [2]. It has been known that IPMSM is a multivariable and strong coupled nonlinear system [3]. In recent years, many intelligent control techniques, such as fuzzy control [4], neural networks control, and other control methods have been developed and applied to the position control of servo motor drives to obtain

M. Shao · H. Yu (✉) · Z. Wang · H. Xie · S. Zhao
College of Automation Engineering, Qingdao University, No. 308, NingXia Road, Qingdao 266071, People's Republic of China
e-mail: yu.hs@163.com

Z. Deng and H. Li (eds.), *Proceedings of the 2015 Chinese Intelligent Automation Conference*, Lecture Notes in Electrical Engineering 337,
DOI 10.1007/978-3-662-46463-2_10

high operating performance. The fuzzy logic and neural networks are capable of approximating any continuous nonlinear functions to arbitrary accuracy [5]. Aiming at the parameters of the shakeless fuzzy controller, the single neuron control is introduced to adjust the output scaling factor online. Then, in order to verify the performance of the proposed algorithm controller, the IPMSM position servo system using the improved shakeless fuzzy controller in MTPA is simulated. The simulations show that the proposed algorithm controller has faster position response and better anti-interference ability.

The remainder of the paper is organized as follows. In Sect. 10.2, the model of IPMSM drive is described. The control principle and positions design are described in Sect. 10.3. Then the stability of the system is analyzed in Sect. 10.4. In Sect. 10.5, the simulation results are given. Finally, some conclusions are presented.

10.2 Model of IPMSM Drive

The system model of the IPMSM model can be described in a synchronously rotating $d-q$ reference frame as [6]

$$\begin{cases} L_d \dfrac{\mathrm{d}i_d}{\mathrm{d}t} = -R_s i_d + n_p \omega L_q i_q + u_d \\ L_q \dfrac{\mathrm{d}i_q}{\mathrm{d}t} = -R_s i_q - n_p \omega L_d i_d - n_p \omega \Phi + u_q \\ J \dfrac{\mathrm{d}\omega}{\mathrm{d}t} = \tau - \tau_L = n_p \left[\left(L_d - L_q \right) i_d i_q + \Phi i_q \right] - \tau_L \\ \dfrac{\mathrm{d}\theta}{\mathrm{d}t} = \omega \end{cases} \tag{10.1}$$

where Φ is the rotor flux linking the stator, n_p is the number of pole pairs, J is the moment of inertia, R_s is the stator resistance, L_d and L_q are d—axes and q—axes stator inductances, respectively, ω and θ are mechanical angular speed and position of rotor, τ and τ_L are electromagnetic and load torque respectively.

10.3 Control Principle of the IPMSM Servo System

The simulation model is built according to the structure shown in Fig. 10.1. Here, MTPA control strategy is adopted and it is a kind of torque optimization control strategy. PI algorithms are applied to the two current-loops and speed-loop, respectively. However, the general shakeless fuzzy controller adopting fixed parameters is difficult to adapt to the control performance of the system. Therefore,

with the purpose to solve this problem, on the basis of shakeless fuzzy controller, the method using single neuron control adjusting the output scaling factor online is proposed. Further, the new controller is adopted as the position controller.

10.3.1 Position-Loop Controller Design

A improved shakeless fuzzy controller based on single neuron control to adjust the output scaling factor is designed in this section.

The output of shakeless fuzzy controller can be described as follows: [7]

$$\omega^*(k) = f(e(k), \Delta e(k)) \cdot K_u \cdot e(k) + \frac{1}{T_i} \int_{kT}^{(k+1)T} e(k) \mathrm{d}\tau \tag{10.2}$$

$$K_u = K_{u0} + K_{uc} \tag{10.3}$$

where $e(k) = \theta^*(k) - \theta(k)$ is defined as the position error of IPMSM servo system, $\theta^*(k)$ is the reference position, $\theta(k)$ is the actual position. And K_e and K_{ec} are the input scaling factors, K_u is the whole output scaling factor, K_{u0} is the output scaling factor of fuzzy controller, K_{uc} the output of single neuron control, T_i is the integral time constant, $f(e(k), \Delta e(k))$ is the output of fuzzy logic inference system in fuzzy controller [8].

When $e(k)$ is almost equal to zero, $f(e(k), \Delta e(k)) \cdot K_u \cdot e(k)$ is also tending to zero, avoiding steady-state shaking problem. The K_u is adjusted by the output of single neuron control. The adjustment of weight coefficient for single neuron control is realized by the Hebb learning rule [8].

10.3.2 Speed-Loop Controller Design

The electromagnetic torque τ^* is obtained through the PI controller using speed error. Speed-loop controller C_1 is

$$\tau^* = K_{p1} \Delta\omega + \mathrm{K}_{i1} \int_0^t \Delta\omega \mathrm{d}t \tag{10.4}$$

where $\Delta\omega = \omega^* - \omega$, K_{p1} and K_{i1} are proportional and integral coefficients.

To get maximum torque output, the maximum torque per ampere (MTPA) principle is used in IPMSM position servo system [9]. Define $i_s = \sqrt{i_d^2 + i_q^2}$, $i_d = -i_s \sin\beta$, $i_q = i_s \cos\beta$, under this situation, Eq. (10.1) can be reconstructed as

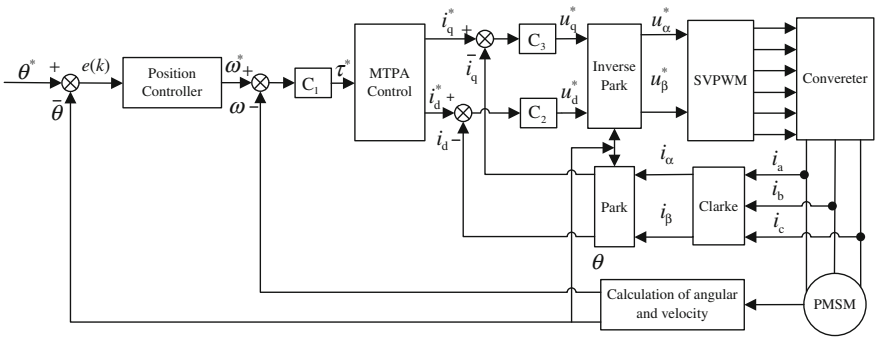

Fig. 10.1 System configuration of field-oriented control IPMSM servo drive

$$\tau = n_p\left[\Phi i_s \cos\beta - \frac{1}{2}\left(L_d - L_q\right) i_s^2 \sin(2\beta)\right] \tag{10.5}$$

to satisfy the MTPA principle, the following conditions need to be satisfied $\frac{\mathrm{d}\tau}{\mathrm{d}\beta} = 0$, $\frac{\mathrm{d}^2\tau}{\mathrm{d}\beta^2} < 0$, adopting the MTPA principle, we have $\tau = \tau^*$, $i_q = i_q^*$ and $i_d = i_d^*$, we can obtain

$$i_d^*\left(i_d^* - \frac{\Phi}{L_d - L_q}\right)^3 = \left[\frac{\tau^*}{n_p\left(L_d - L_q\right)}\right]^2, i_q^* = \sqrt{\frac{\Phi i_d^* + \left(L_d - L_q\right)\left(i_d^*\right)^2}{L_d - L_q}} \tag{10.6}$$

10.3.3 d—Axes and q—Axes Current-Loop Design

The d—axes current-loop controller C_2 is

$$u_d^* = K_{p2}\Delta i_d + K_{i2}\int_0^t \Delta i_d \mathrm{d}t \tag{10.7}$$

where $\Delta i_d = i_d^* - i_d$, K_{p2} and K_{i2} are proportional and integral coefficients.

The q—axes current-loop controller C_3 is

$$u_q^* = K_{p3}\Delta i_q + K_{i3}\int_0^t \Delta i_q \mathrm{d}t \tag{10.8}$$

where $\Delta i_q = i_q^* - i_q$, K_{p3} and K_{i3} are proportional and integral coefficients.

10.4 Stability Analysis of Position Servo Control System

Lyapunov stability theorem is used to analyze the stability of position system.

The discrete Lyapunov function is selected as $V(k) = \frac{1}{2}e^2(k) > 0$, where $e(k)$ is the defined position error of IPMSM servo system. The Lyapunov's convergence criterion must be satisfied such that $V(k)\Delta V(k) < 0$, where $\Delta V(k) = V(k) - V(k-1)$ is the change in the Lyapunov function.

The stability condition is satisfied when $\Delta V(k) < 0$. The $\Delta V(k)$ is given by

$$\Delta V(k) = \frac{1}{2}\left[e^2(k) - e^2(k-1)\right] \tag{10.9}$$

fuzzy equation for the IPMSM position control is calculated by

$$W^*(k) = W^*(k-1) \circ E(k-1) \circ \mathrm{R} \tag{10.10}$$

where "$\circ$" is synthetic operator, $W^*(k)$ and $E(k)$ are fuzzy variables of $\omega^*(k)$ and $e(k)$, respectively. By using (10.2) and (10.10), we can obtain

$$\begin{aligned}\omega^*(k) &= D_\Delta\{[W^*(k) \wedge E(k)] \circ R\} \\ &= f(e(k), \Delta e(k)) \cdot K_u \cdot e(k) + \frac{1}{T_i}\int_{kT}^{(k+1)T} e(k)\mathrm{d}\tau\end{aligned} \tag{10.11}$$

hence, the position error $e(k)$ is stated as

$$e(k) = \frac{\left[D_\Delta\{[W^*(k) \wedge E(k)] \circ R\} - \frac{1}{T_i}\int_{kT}^{(k+1)T} e(k)\mathrm{d}\tau\right]}{f(e(k), \Delta e(k)) \cdot K_u} \tag{10.12}$$

where D_Δ is the solution of fuzzy operator.

The solution of fuzzy operator D_Δ is choose as

$$D_\Delta\{[W^*(k) \wedge E(k)] \circ R\} = f(e(k), \Delta e(k)) \cdot K_u \cdot \frac{1}{4}e(k-1) + \frac{1}{T_i}\int_{kT}^{(k+1)T} e(k)\mathrm{d}\tau$$

under such a condition, $e(k)$ can be rewritten as the following equation

$$e(k) = -\frac{1}{4}e(k-1) \tag{10.13}$$

the term $\Delta V(k)$ can be expressed as $\Delta V(k) = -\frac{15}{32}e^2(k-1) < 0$, so $V(k)$ is positive definite, $\Delta V(k)$ is negative definite.

Applying Lyapunov stability theorem, the IPMSM position system is stable.

10.5 Simulation Results

To test the performance of improved shakeless fuzzy controller, simulations of IPMSM system have been performed by using MATLAB/Simulink. The parameters are given: $R_s = 2.875\,\Omega$, $L_d = 0.0045\,\text{H}$, $L_q = 0.0085\,\text{H}$, $\Phi = 0.175\,\text{Wb}$, $J = 0.025\,\text{kg m}^2$, $n_p = 4$. In Figs. 10.2, 10.3 and 10.4, at $t = 0\,\text{s}$, the rotor given position is 16 rad, the given load torque is 1 N m, and at $t = 0.6\,\text{s}$, the load torque is 2 N m.

The position response curve based on the improved shakeless fuzzy controller and based on the shakeless fuzzy controller is given in Fig. 10.2. From Fig. 10.2, it can be seen that IPMSM based on the improved shakeless fuzzy controller has advantages of faster response time than that based on the shakeless fuzzy controller. Figures 10.3 and 10.4 illustrate the speed response curve, stator current response

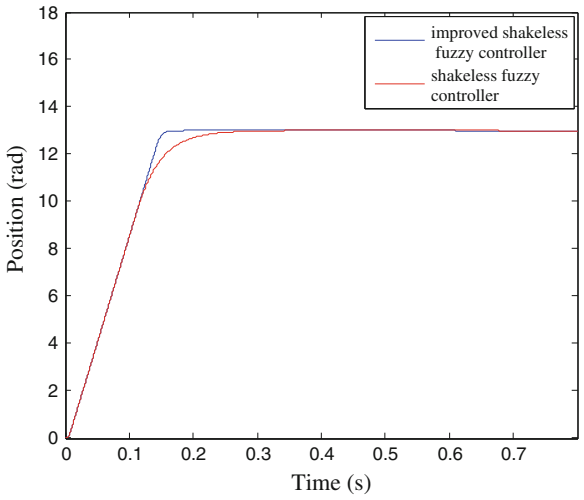

Fig. 10.2 Position curve

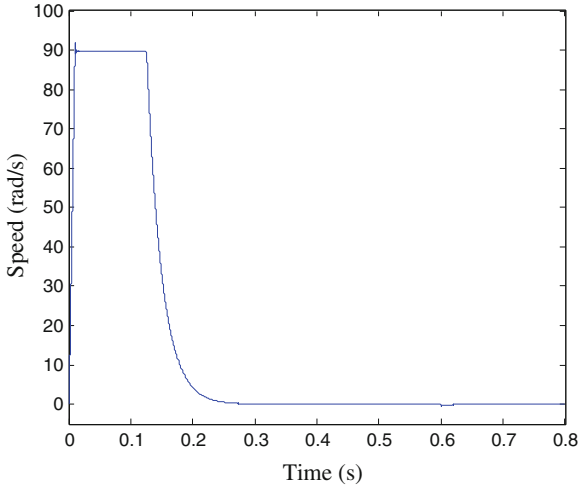

Fig. 10.3 Speed curve

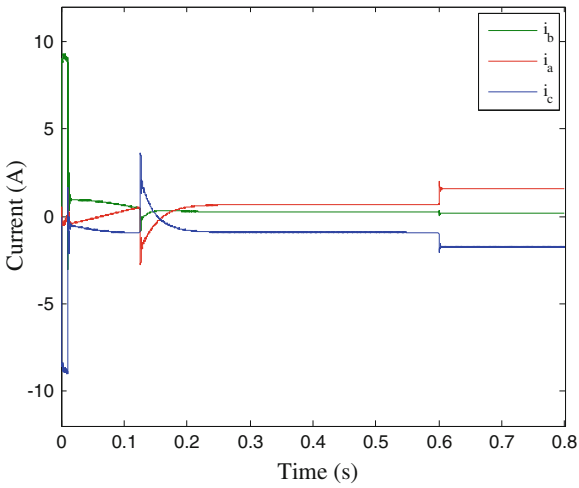

Fig. 10.4 Stator current curve

curve, and based on the improved shakeless fuzzy controller, respectively. Obviously, when load torque mutations, speed of the motor is almost not influenced by external disturbances.

10.6 Conclusions

In this paper, IPMSM position control system is a complex system that has the characteristics of nonlinearity, strong coupling, and multivariable. The conventional shaklelss fuzzy controller cannot adapt to the continuous change of process as its fixed parameters. To improve the performance of the IPMSM system, the improved shakeless fuzzy controller based on the single neuron control is designed. Then IPMSM position system using the proposed controller in MTPA controller is simulated by MATLAB/Simulink. The simulation results show that the proposed algorithm ensures a high degree of position precision and a high degree of dynamic response characteristics than the conventional fuzzy controller.

Acknowledgments This work is supported by the Natural Science Foundation of China (61174131, 61104076), the Science and Technology Project of College and University in Shandong Province (J11LG04).

References

1. EI-Sousy FFM (2013) Intelligent optimal recurrent wavelet Elman neural network control system for permanent-magnet synchronous motor servo drive. IEEE Trans Ind Inform 9 (4):1986–2003
2. Chaoui H, Sicard P (2012) Adaptive fuzzy logic control of permanent magnet synchronous machines with nonlinear friction. IEEE Trans Ind Electron 59(2):1123–1133

3. Liu GH, Chen LL, Zhao WX et al (2013) Internal model control of permanent magnet synchronous motor using support vector machine generalized inverse. IEEE Trans Ind Inform 9 (2):890–898
4. Duan XG, Deng H, Li HX (2013) A saturation-based tuning method for fuzzy PID controller. IEEE Trans Ind Electron 60(11):5177–5185
5. Gadoue SM, Giaouris D, Finch JW (2010) Mras sensorless vector control of an induction motor using new sliding-mode and fuzzy-logic adaptation mechanisms. IEEE Trans Energy Convers 25(2):394–402
6. Yu HS, Yu JP, Liu XD et al (2012) Port-Hamiltonian system modelling and position tracking control of PMSM based on maximum output power principle. ICIC Exp Lett 6(2):437–442
7. Liu GR (2012) Multivariable system adaptive fuzzy/neural network control. Science Press, Beijing
8. Liu JK (2004) Advanced PID control MATLAB simulation. Electronic Industry Press, Beijing
9. Yu HS, Wang HL, Zhao KY (2006) Maximum torque per ampere control of PMSM based on port-controlled hamiltonian theory. Proc CSEE 26(8):82–87 (in Chinese)

Chapter 11
Modeling and Stability Analysis for Networked Hierarchical Control of Islanded Microgrid

Lizhen Wu, Xusheng Yang, Hu Zhou and Xiaohong Hao

Abstract The microgrids (MGs) are key elements for integrating distributed energy resources as well as distributed energy-storage systems. In this paper, a network-based hierarchical control scheme is proposed for the enhancement of frequency, voltage quality in MGs. The primary control includes the droop method and the virtual impedance loops, in order to share active and reactive power. The secondary control restores the frequency and amplitude deviations produced by the primary control. And the tertiary control regulates the power flow between the grid and the Microgrid. Also, a distributed networked control system is used in order to implement a distributed secondary control (DSC) thus avoiding the use of a microGrid central control (MGCC). The frequency and voltage of the MGs not only ensures reactive proposed approach, but also able to restore power sharing. The modeling and stability analyses of the hierarchical control system are derived. Real-time simulation results from hierarchical-controlled MGs are provided to show the feasibility of the proposed approach.

Keywords Distributed generation (DG) · Network-based hierarchical control · Microgrids (MGs) · Distributed secondary control (DSC)

11.1 Introduction

Recently, microgrids have been emerging as a framework for testing future smart grid issues in small scale. MGs are local grids that comprise different technologies such as power electronics converters; distributed generations, energy-storage

L. Wu · X. Yang · X. Hao (✉)
College of Electrical and Information Engineering of Lanzhou University of Technology, Lanzhou 730050, Gansu, China
e-mail: wulzh@lut.cn

H. Zhou
Gansu Electric Power Corporation, Lanzhou 730030, China

Z. Deng and H. Li (eds.), *Proceedings of the 2015 Chinese Intelligent Automation Conference*, Lecture Notes in Electrical Engineering 337,
DOI 10.1007/978-3-662-46463-2_11

systems, and telecommunications which can operate connected to the traditional centralized grid, but also could operate autonomously in islanded mode [1].

However, apart from these obvious benefits of MGs, their introduction into the traditional distribution network raises many new challenges; with one of the most important being the frequency and voltage participation in islanded operation mode. Control strategies have an important role to provide global stability in MGs. This problem has been investigated in recent years. In order to enhance the reliability and performances of the droop-controlled voltage source inverters (VSIs), virtual impedance control algorithms have developed providing the inverters with hot-swap operation, harmonic power sharing, and robustness for large-line power impedance variations [2–4]. Droop control is a kind of cooperative control that allows parallel connection of VSIs sharing active and reactive powers. It can be seen as a primary power control of a synchronous machine. However, droop control still has several drawbacks such as poor harmonic current sharing and high dependence on the power line impedances. In order to improve these drawbacks, a hierarchical control concept from the traditional power system has been introduced for MGs in [5–7]. The first level of this hierarchy is primary control which is strictly local and deals with the inner voltage and current control loops and droop control of the individual DGs, in order to adjust the frequency and amplitude according to active and reactive power of the units. Secondary control is conceived to compensate frequency and voltage deviations produced inside the MG by the virtual inertias and output virtual impedances of primary control. Tertiary control is responsible for global optimization of the MG and managing power flow between MGs and the distribution network of the main grid [7]. In all of these literatures, a central secondary control (CSC) has been used in order to manage the MG. The centralized control strategy has an inherent drawback of the single point of failure, i.e., all DGs measure signals of interest and send them to a common single MG central controller (MGCC), an MGCC failure terminates the secondary control action for all units [8].

In this paper, a networked hierarchical control for multiple parallel VSI system was developed. A new approach of distributed secondary control (DSC) strategy is proposed to implement it in a distributed way along the local control with communication systems. This kind of distributed control strategies are also named as networked control systems (NCS). A simple networked control scheme based on the industrial network for the DSC of MGs is presented. This way, every DG has its own local secondary control which can produce appropriate control signal for the primary control level by using the measurements of other DGs in each sample time.

This paper is organized as follows: Sect. 11.2 provides a networked hierarchical control structure for the MGs. The DSC of islanded MGs and its modeling and small-signal stability analysis are presented in Sect. 11.3. Section 11.4 provides simulation results of an islanded MG evaluating the proposed algorithm for DSC. Section 11.5 concludes this paper and outlines future research directions.

11.2 Networked Hierarchical Control Structure of MGs

MGs for standalone and grid-connected applications have been considered in the past as separate approaches. Nevertheless, nowadays, it is necessary to conceive flexible MGs that are able to operate in both grid-connected and islanded modes. Thus, the study of topologies, architectures, planning, and configurations of MGs are necessary [9]. This paper deals with the hierarchical control of MGs consisting of the same three control levels as presented in large power systems. Such a kind of system is supposed to operate over large synchronous machines with high inertias and inductive networks. However, in power electronic-based MGs, there are no inertias and the nature of the networks is mainly resistive. Consequently, there are important differences between both systems that we have to take into account when designing their control schemes. This three-level hierarchical control is organized as follows. The primary control deals with the inner control of the DG units, adding virtual inertias and controlling their output impedances. The secondary control is conceived to restore the frequency and amplitude deviations produced inside the MG by the virtual inertias and output virtual impedances. The tertiary control regulates the power flow between the grid and the MG at the point of common coupling (PCC). In this paper, we use networked control system (NCS) for MGs. From the NCS perspective, DSC requires that every DG obtains the global average of the parameters of interest, i.e., frequency, voltage, and active and/or reactive power, in order to derive the local control signals. The provision of global averages is the task of underlying communication infrastructure. Several communication technologies have been introduced for NCSs, both wired and wireless [10]. Figure 11.1 illustrates the architecture of networked hierarchical control for islanded MG.

As shown, secondary control is locally embedded in each DG unit, similar to primary control; however, the local secondary control requires an underlying communication network to operate properly. In turn, the local secondary controllers operate on these parameters, regulating the frequency and voltage of the system and sharing power between the units.

11.3 Distributed Secondary Control of Islanded MGs

Conventional CSC is only responsible for restoring frequency and voltage inside the whole MG using common measurements of the system. However, DSC using the proposed communication algorithm is able to not only control frequency and voltage but also share power between units in the MG.

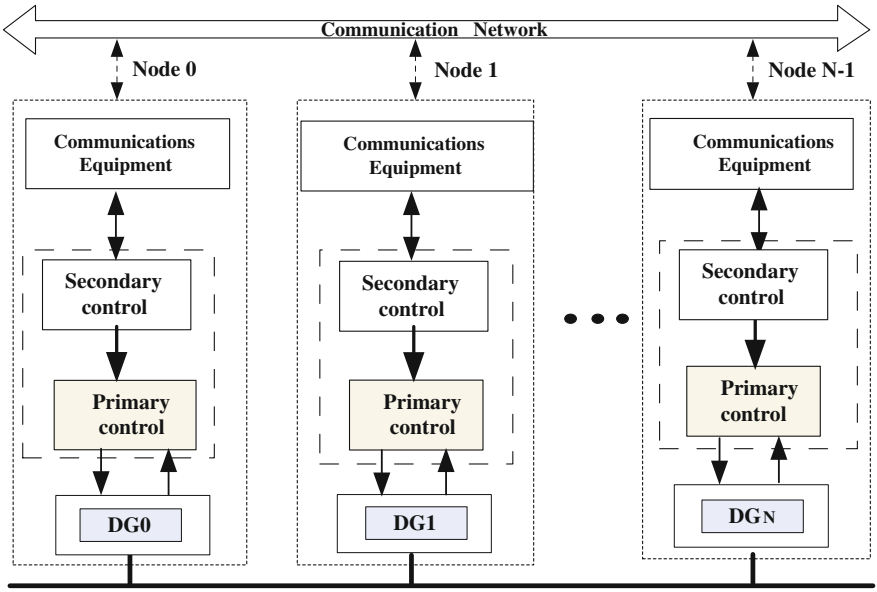

Fig. 11.1 The architecture of networked hierarchical control for islanded MGs

11.3.1 Frequency/Voltage Control and Power Sharing

In the distributed strategy, each DG has its own local secondary control to regulate the frequency. In this sense, each unit measures its frequency at each sampling instant, averaging the received information from other units and then sending its average $\bar{f}_{\mathrm{MG}}$ to the other units through the communication network. The averaged data are compared with the nominal frequency of f^*_{MG} and sent to the secondary controller of DGi to restore the frequency as follows:

$$\delta f_s = k_{\mathrm{pf}}(f^*_{\mathrm{MG}} - \bar{f}_{\mathrm{MG}}) + k_{\mathrm{if}} \int (f^*_{\mathrm{MG}} - \bar{f}_{\mathrm{MG}})\mathrm{d}t \tag{11.1}$$

where k_{pf} and k_{if} are the control parameters of the PI compensator of unit i, and δf_s is the secondary control signal sent to the primary control level in order to remove the frequency deviations.

Similar approach can be used as in the distributed frequency control one, in which each inverter will measure the voltage error, and tries to compensate the voltage deviation caused by the Q-V droop. In this secondary voltage control strategy, after calculating the average value of voltage $\bar{E}_{\mathrm{MG}}$ that is based on the information exchanged over the communication network, every local secondary controller measures the voltage error and compares it with the voltage reference E^*_{MG}. In the next step, the local secondary controller sends control signal δEs to the

primary level of control as a set point to compensate for the voltage deviation. The voltage restoration control loop of DG_i can be expressed as follows:

$$\delta E_s = k_{\mathrm{pE}}(E^*_{\mathrm{MG}} - \bar{E}_{\mathrm{MG}}) + k_{\mathrm{iE}} \int (E^*_{\mathrm{MG}} - \bar{E}_{\mathrm{MG}})\mathrm{d}t \tag{11.2}$$

With k_{pE} and k_{iE} are the PI controller parameters of the voltage secondary control. In a low R/X MG, reactive power is difficult to be precisely shared between units using Q-V droop control, since voltage is not common in the whole system as opposed to frequency. A solution is to implement a distributed average power sharing in the secondary loop, where the averaging is performed through the communication network. The averaging power process is done in each DG, so that finally, as the information is common, all of them will have the same reference. Therefore, the reactive power sharing can be expressed as

$$\delta Q_s = k_{\mathrm{pQ}}(Q_i - \bar{Q}_{\mathrm{MG}}) + k_{\mathrm{iQ}} \int (Q_i - \bar{Q}_{\mathrm{MG}})\mathrm{d}t \tag{11.3}$$

where k_{pQ} and k_{iQ} are the PI controller parameters, Q_i is the locally calculated reactive power (which can be active power in the case of high-resistive-line MGs), $\bar{Q}_{\mathrm{MG}}$ is the average power obtained through the communication network, and δQ_s is the control signal produced by the secondary control in each sample instant and afterward sent to the primary loop.

11.3.2 Modeling and Small-Signal Stability Analysis

Figure 11.2 shows the equivalent circuit of n inverters connected to an AC bus. It is assumed that the output impedance of the inverters is mainly inductive ($\theta = 90°$). In order to analyze the stability of the system and to adjust the parameters of DSC, a small-signal model has been developed. In this situation, the active power and reactive power injected into the bus by every inverter are expressed as the following equations [11]:

$$P_i = \frac{E_i V \sin \phi_i}{X_i}; \quad Q_i = \frac{E_i V \cos \phi_i - V^2}{X_i} \tag{11.4}$$

where E_i and V are the amplitudes of the ith inverter output voltage and the common bus voltage, ϕ_i is the power angle of the inverter, and X_i is the magnitude of the output reactance for the ith inverter. From the above equations, it can be seen that if the phase difference between E_i and V is small enough, the active power is strongly influenced by power angle ϕ_i, and the reactive power flow depends on the voltage amplitude difference. Consequently, the frequency and the amplitude of the inverter output voltage can be expressed by the droops control method as [11].

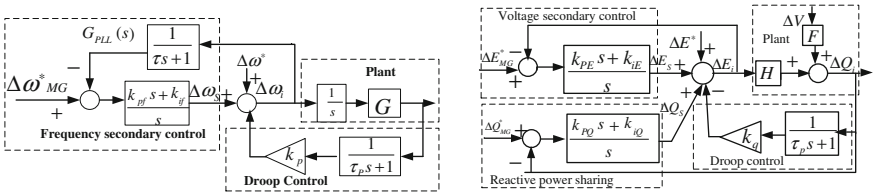

Fig. 11.2 Small-signal representation of frequency\voltage control\reactive power sharing

$$\begin{cases} \omega_i = \omega^* - k_p P_i \\ E_i = E^* - k_q Q_i \end{cases} \tag{11.5}$$

where $\omega^*$and $E^*$are the output voltage frequency and amplitude references, and *kp* and *kq* are the droop frequency and amplitude coefficients. As aforementioned, the outputs of secondary control obtained through (11.1–11.3) are added to the droops to shift the droop lines in order to restore the frequency and voltage of the system and to share the power between the units. Therefore, (11.5) are updated as,

$$\begin{cases} \omega_i = \omega^* - k_p p_i + \delta\omega_s \\ E_i = E^* - k_q Q_i + \delta E_s + \delta Q_s \end{cases} \tag{11.6}$$

So a small-signal model is obtained by linearizing (11.4–11.6) at operating points P_{ie}, Q_{ie}, E_{ie}, *Ve*, and ϕ_{ie} as follows:

$$\begin{cases} \Delta\omega_i(s) = \Delta\omega^*(s) - k_p \Delta p_i(s) + \Delta\omega_s(s) \\ \Delta E_i(S) = \Delta E^*(s) - k_q \Delta Q_i(s) + \Delta E_s(S) + \Delta Q_s(s) \end{cases} \tag{11.7}$$

$$\Delta\phi_i = \int \Delta\omega_i \mathrm{d}t \tag{11.8}$$

$$\Delta p_i(s) = G\Delta\phi_i(s) \tag{11.9}$$

$$\Delta Q_i(s) = H\Delta E_i(s) + F\Delta V(s) \tag{11.10}$$

where

$$G = \frac{E_{\text{ie}} V_e \cos\phi_{\text{ie}}}{X_i}, \quad H = \frac{2E_{\text{ie}} - V_e \cos\phi_{\text{ie}}}{X_i}, \quad F = -\frac{E_{\text{ie}} \cos\phi_{\text{ie}}}{X_i} \tag{11.11}$$

Figure 11.2 show the small-signal representation of frequency and voltage control and reactive power sharing control model. The dynamics of the system around the operating point may be expressed in state-space form as follows:

$$\dot{x}(t) = Ax(t) \tag{11.12}$$

The frequency control model, $x = [x_1, x_2, x_3, x_4]^T$ and A is

$$A = \begin{bmatrix} -\frac{1}{\tau_p} & 0 & 0 & G \\ -\frac{k_p}{\tau_p} & -\frac{1+k_{pf}}{\tau} & 1 & 0 \\ 0 & -\frac{k_{if}}{\tau} & 0 & 0 \\ -\frac{k_p}{\tau_p} & -\frac{k_{pf}}{\tau} & 1 & 0 \end{bmatrix} \tag{11.13}$$

To realize the droop functions, it is necessary to employ low-pass filters (LPFs) in order to calculate the active and reactive power from the instantaneous power. The state variables x_1, x_2, x_3, and x_4 are assigned to the output of LPF, PLL, PI controller, and the integral term of the power angle, respectively.

For voltage control, $x = [x_1, x_2]^T$ and A is

$$A = \begin{bmatrix} \frac{1 + k_{pE} + k_q H}{\tau_p(1 + k_{pE})} & \frac{H}{1 + k_{pE}} \\ \frac{k_q k_i E}{\tau_p(1 + k_{pE})} & -\frac{k_i E}{1 + k_{pE}} \end{bmatrix} \tag{11.14}$$

where x_1 and x_2 are chosen as the state variable of LPF and PI controller. Note that in the related analysis, the communication delay and packet losses were assumed to be negligible.

11.4 Simulation Results

For the calculation of plant parameters (G, H, and F), we can choose $E_{\text{ie}} = 1$ per unit, $Ve = 1$ per unit, and $\phi_{\text{ie}} = 0$. Moreover, we assume $X_i = 0.001$ per unit. Other needed parameters can be found in reference [12].

Figure 11.3 shows the trajectory of the low-frequency eigenvalues of both the frequency and voltage models as a function of the secondary control parameters. From the figure we can see that as the proportional terms of PI controllers are increased, the eigenvalues of the system move toward an unstable region, making the system more oscillatory and eventually leading to instability. However, the integral term parameter has no significant effect on the dynamics of the system. Similar analysis can be performed for the other parameters of the presented model.

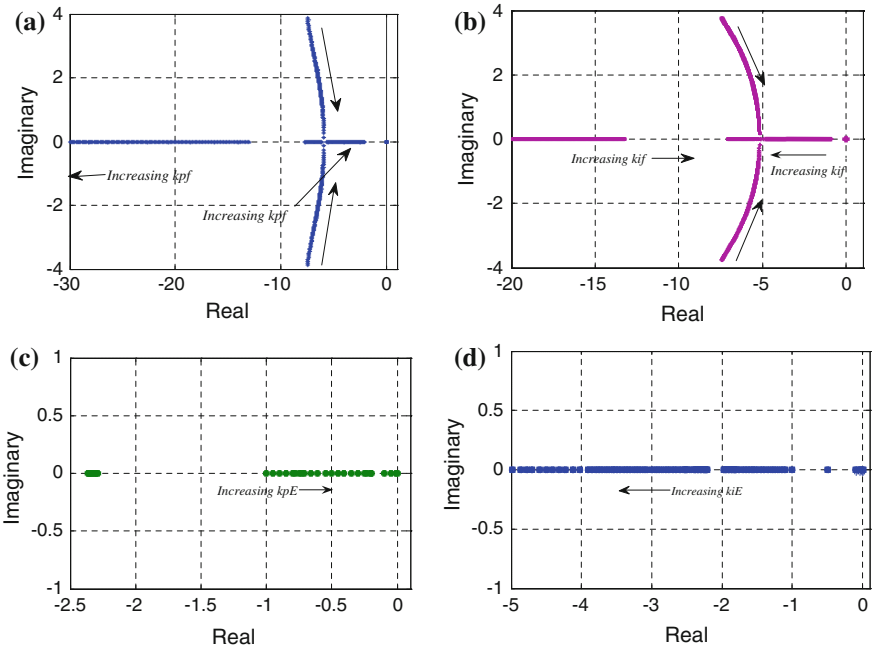

Fig. 11.3 Trace of eigenvalues as a function of secondary control parameters. **a** Frequency control of increasing k_{pf}. **b** Frequency control of increasing k_{if}. **c** Voltage control of increasing k_{pE}. **d** Voltage control of increasing k_{iE}

11.5 Conclusions

In this paper, the evaluation of the hierarchical control is presented and discussed. A new approach of distributed secondary control based on network for islanded MGs has been proposed. The primary control includes the droop method and the virtual impedance loops, in order to share active and reactive power. The secondary control restores the frequency and amplitude deviations produced by the primary control. The modeling, controller design, and stability analysis for the microgrids consist of a number of voltage source inverters (VSIs) operating in parallel are derived. Simulation results show the good performance of the MG system using the proposed DSC method. Finally, an impact analysis of communications in frequency and active power control in hierarchic multi-MG structures, considering both packet delays and losses is the next work to be done.

Acknowledgments This work was supported by the National Natural Science Foundation of China (No. 51467009), Science and Technology Foundation of STATE GRID Corporation of China, The project of Lanzhou science and technology plan (2014-1-162).

References

1. Katiraei F, Iravani MR, Lehn PW (2005) Microgrid autonomous operation during and subsequent to islanding process. IEEE Trans Power Delivery 20:248–257
2. Green TC, Prodanovic M (2007) Control of inverter-based micro-grids. Electr Power Syst Res 77(9):1204–1213
3. Delghavi MB, Yazdani A (2011) An adaptive feedforward compensation for stability enhancement in droop-controlled inverter-based microgrids. IEEE Trans Power Delivery 26 (3):1764–1773
4. Vasquez J, Guerrero JM, Savaghebi M (2013) Modeling, analysis, and design of stationary reference frame droop controlled parallel three-phase voltage source inverters. IEEE Trans Industr Electron 60(4):1271–1280
5. Mohamed YARI, Radwan AA (2011) Hierarchical control system for robust microgrid operation and seamless mode transfer in active distribution systems. IEEE Trans Smart Grid 2:352–362
6. Guerrero JM, Vasquez JC, Matas J, Castilla LM (2011) Hierarchical control of droop-controlled AC and DC microgrids—a general approach towards standardization. IEEE Trans Industr Electron 51(8):158–172
7. Bidram A, Davoudi A (2012) Hierarchical structure of microgrids control system. IEEE Trans Smart Grid 3(4):1963–1976
8. Vasquez J, Guerrero JM, Teodorescu R (2013) Modeling, analysis, and design of stationary reference frame droop controlled parallel three-phase voltage source inverters. IEEE Trans Industr. Electron 60(4):1271–1280
9. Bidram A, Davoudi A, Lewis FL, Qu Z (2013) Secondary control of microgrids based on distributed cooperative control of multi-agent systems. IET Gener Transm Distrib 7(8):822–831
10. Zhang Y, Ma H (2012) Theoretical and experimental investigation of networked control for parallel operation of inverters. IEEE Trans Industr Electron 59(4):1961–1970
11. Guerrero JM, Garcia de Vicuna L, Miret J (2005) Output impedance design of parallel-connected UPS inverters with wire-less load-sharing control. IEEE Trans Industr Electron 52 (4):1126–1135
12. Sao CK, Lehn PW (2005) Autonomous load sharing of voltage source converters. IEEE Trans Power Delivery 20(2):1009–1016

Chapter 12
Variable Thrust Angle Constant Thrust Rendezvous

Yongqiang Qi and Ding Lv

Abstract In this paper, variable thrust angle (VTA) constant thrust rendezvous is studied. In particular, the rendezvous process is divided into in-plane motion and out-plane motion based on the relative motion dynamic model. For the in-plane motion, the calculation of thrust angle control lows is cast into a convex optimization problem by introducing a Lyapunov function subject to linear matrix inequalities. For the out-plane motion, a new algorithm of constant thrust fitting is proposed through the impulse compensation. The illustrative example is provided to show the effectiveness of the proposed control design method.

Keywords Rendezvous · Constant thrust · Variable thrust angle · Robust controller

12.1 Introduction

The problem of rendezvous has been studied and many results have been reported. For example, the optimal impulsive control method for rendezvous is studied in [1]; adaptive control theory is applied to the rendezvous problem in [2]; an annealing algorithm method for rendezvous orbital control is proposed in [3]; maneuvers during rendezvous operations cannot normally be considered as continuous thrust maneuver or impulsive maneuver [4–6]. In addition, the variable thrust angle (VTA) constant thrust maneuver, until recent years, has been the least studied.

The purpose of this paper is to study VTA constant thrust rendezvous, in other words, to design robust closed-loop VTA control laws for the in-plane motion, and to calculate and compare the fuel consumption under the theoretical continuous thrust and the actual constant thrust. First of all, for in-plane motion, the robust control laws for constant thrust VTA satisfying the requirements can be designed by

Y. Qi (✉) · D. Lv
College of Sciences, China University of Mining and Technology (CUMT), Xvzhou, China
e-mail: qiyongqiang3@163.com

Z. Deng and H. Li (eds.), *Proceedings of the 2015 Chinese Intelligent Automation Conference*, Lecture Notes in Electrical Engineering 337,
DOI 10.1007/978-3-662-46463-2_12

solving the convex optimization problem. Then, for out-plane motion, a new algorithm of constant thrust fitting is proposed by using the impulse compensation method. Finally, the optimal fuel consumption can be obtained by comparing the theoretical thrust and the actual constant thrust, and then the actual working times of the thrusters can be computed using time series analysis method. An illustrative example shows the effectiveness of the proposed control design method.

12.2 The Robust Variable Thrust Angle Control Laws for In-plane Motion

The relative motion coordinate system can be established as follows: first, the target spacecraft is assumed as a rigid body and in a circular orbit, and the relative motion can be described by Clohessy-Wiltshire equations. Then, the centroid of the target spacecraft O_T is selected as the origin of coordinate, the x-axis is opposite to the target spacecraft motion, the y-axis is from the center of the earth to the target spacecraft, the z-axis is determined by the right-handed rule. Then the collision avoidance process can be divided into in-plane motion and out-plane motion based on the relative motion dynamic model as follows, where the relative motion dynamic model of the in-plane motion is:

$$\begin{cases} \ddot{x} - 2\omega\dot{y} = \frac{F_x + \eta_x}{m} \\ \ddot{y} + 2\omega\dot{x} - 3\omega^2 y = \frac{F_y + \eta_y}{m} \end{cases} \tag{12.1}$$

where ω represents the angular velocity of the target spacecraft. F_x, F_y represent the vacuum thrust of the chaser and η_x, η_y represent the sum of the perturbation and nonlinear factors in the x-axis and in the y-axis, respectively. m represents the mass of the chaser at the beginning of the collision avoidance maneuver.

Suppose the actual constant thrusts of the chaser are F_x, F_y, F_z, the maximum thrusts are $\widehat{F}_x, \widehat{F}_y, \widehat{F}_z$, and the theoretical continuous thrusts are F_x^*, F_y^*, F_z^*.The range of the thrust angle in the x-axis θ_x is defined as shown in Figs. 12.1.

The goal of the collision avoidance maneuver is to design a proper controller for the chaser, such that the chaser can be asymptotically maneuvered to the target position. Define the state error vector $x_e(t) = x(t) - x_t(t)$, and its state equation can be obtained as

$$\begin{cases} \dot{x}_e(t) = (A_1 + \Delta A)x_e(t) + (B_1 + \Delta B)u(t) \\ u(t) = Kx_e(t) \end{cases} \tag{12.2}$$

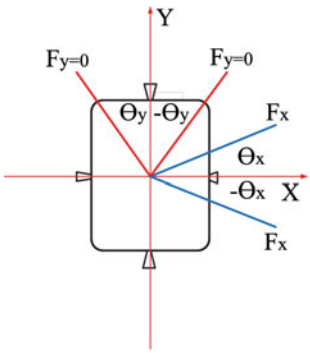

Fig. 12.1 Variable thrust angle thrusters

Lyapunov function is defined as follows:

$$V = x_e^T(t)Px_e(t) \tag{12.3}$$

where P is a positive definite symmetric matrix. According to the system stability theory, the necessary and sufficient conditions for robust stability of the system (12.2) are as follow:

$$A^T P + PA < 0 \tag{12.4}$$

Then a multi-objective controller design strategy is proposed by translating a multi-objective controller design problem into a convex optimization problem. And the control input constraints can be met simultaneously. Assuming the initial conditions satisfy the following inequality, where ρ is a given positive constant.

$$x^T(0)Px(0) < \rho \tag{12.5}$$

Theorem 12.1 *If there exist a corresponding dimension of the matrix L, a symmetric positive definite matrix X and two parameters* $\varepsilon_1 > 0, \varepsilon_2 > 0$, *then for sufficient condition for robust stability there exist a state feedback controller K which can meet the following conditions simultaneously*:

$$\begin{pmatrix} \Sigma & X & L \\ X & -\varepsilon_1 & 0 \\ L^T & 0 & -\varepsilon_2 \end{pmatrix} < 0, \qquad \begin{pmatrix} \rho I & x^T(0) \\ x(0) & X \end{pmatrix} < 0, \tag{12.6}$$

where $\Sigma = XA_0^T + A_0X + L^TB_0 + B_0L + \varepsilon_1\alpha^2 I + \varepsilon_2\beta^2 I$, *then the theoretical state feedback controller K can be calculated as follows*:

$$K = LX^{-1} = \begin{pmatrix} K_{11} & K_{12} & K_{13} & K_{14} \\ K_{21} & K_{22} & K_{23} & K_{24} \end{pmatrix} \tag{12.7}$$

Then the following results can be obtained:

$$\begin{cases} \dfrac{L_x}{N_x}\hat{F}_x \cos\theta_x + \dfrac{L_y}{N_y}\hat{F}_y \sin\theta_y = k_{11}x_e(t) + k_{12}y_e(t) + k_{13}\Delta V_x + k_{14}\Delta V_y \\ \dfrac{L_x}{N_x}\hat{F}_x \sin\theta_x + \dfrac{L_y}{N_y}\hat{F}_y \cos\theta_y = k_{21}x_e(t) + k_{22}y_e(t) + k_{23}\Delta V_x + k_{24}\Delta V_y \end{cases} \tag{12.8}$$

Then the thrust angle control lows θ_x, θ_y which satisfy the robust stability of the in plane motion can be obtained from Eq. (12.8).

12.3 Compare Fuel Consumption for the Out-plane and Calculate the Control Law

The relative motion dynamic model of the out-plane motion:

$$\ddot{z} + \omega^2 z = \frac{F_z + \eta_z}{m} \tag{12.9}$$

For the out-plane motion, a new algorithm of constant thrust fitting is proposed using the impulse compensation method as follows. Suppose the thrusters in the z-axis can provide different sizes of constant thrust to meet different thrust requirements.

Constant thrust fitting is proposed by using the impulse compensation method as follows. Suppose the thrusters in the z-axis can provide different sizes of constant thrust to meet different thrust requirements. If the theoretical working time of z-axis thruster in the ith thrust arc $t_z^* = \Delta T < T_i$ and t_z^* can be any one of M_i shortest switching time interval in the ith thrust arc. Without loss of generality, suppose t_z^* is the first shortest switching time interval and the impulse error in the z-axis in the ith thrust arc ΔI_{zi} can be calculated as follows:

There are $N_z + 1$ thrust levels that can be selected and the level of the constant thrust can be calculated as follows:

$$L_z = \left[\frac{N_z \int_{T_i}^{T_i + \Delta T} \left| F_z^*(t) \right| \mathrm{d}t}{\hat{F}_z \Delta T} \right] \tag{12.10}$$

Calculate the impulse error.

$$\Delta I_{zi} = \operatorname{sgn}\left(F_z^*(t)\right)\left|\int_{T_i}^{T_{ii}+\Delta T}\left|F_x^*(t)\right|\mathrm{dt} - \frac{L_z\hat{F}_z\Delta T}{N_z}\right| \tag{12.11}$$

Determine the value of the impulse compensation threshold. Suppose the value of the impulse compensation threshold is a positive constant $\gamma > 0$, if the impulse error ΔI_{zi} satisfies the following condition:

$$\left|\int_{T_i}^{T_{ii}+\Delta T}\left|F_x^*(t)\right|dt - \frac{\hat{F}_z\Delta T}{N_z}\left[\frac{N_z\int_{T_i}^{T_i+\Delta T}\left|F_z^*(t)\right|}{\hat{F}_z\Delta T}\right]\right| \le \gamma \tag{12.12}$$

the actual constant thrust of the chaser in the z-axis can be calculated as follows:

$$F_z = \operatorname{sgn}(F_z^*(t))\frac{\hat{F}_z\Delta T}{N_z}\left[\frac{N_z\int_{T_i}^{T+\Delta T_i}\left|\hat{F}_z^*(t)\right|dt}{\hat{F}_z\Delta T}\right] \tag{12.13}$$

then the chaser will not carry out impulse compensation. Suppose

$$\left[\left|\int_{T_i}^{T_i+M_1\Delta T}\frac{F_z^*(t)N_z}{\hat{F}_z\Delta T}\mathrm{dt} - \int_{\mathrm{T_1}+(\mathrm{m_1}+1)\Delta\mathrm{T}}^{\mathrm{T_i}+\mathrm{M_1}\Delta\mathrm{T}}\{\frac{\operatorname{sgn}(\mathrm{F_z^*(t)})}{\Delta\mathrm{T}}\left[\frac{\mathrm{N_z}\int_{\mathrm{T_i}+\mathrm{j}\Delta\mathrm{T}}^{\mathrm{T_i}+(\mathrm{j}+1)\Delta\mathrm{T}}\left|\mathrm{F_z^*(t)dt}\right|}{\hat{\mathrm{F}}_\mathrm{z}\Delta\mathrm{T}}\right]\}\mathrm{dt}\right|\right] = m_2 \tag{12.14}$$

Furthermore, if the impulse error ΔI_{zi} satisfies the following condition:

$$\left[\left|\int_{T_i}^{T_i+M_1\Delta T}F_z^*(t)\mathrm{dt} - \int_{\mathrm{T_1}+(\mathrm{m_1}+1)\Delta\mathrm{T}}^{\mathrm{T_i}+\mathrm{M_1}\Delta\mathrm{T}}\{\operatorname{sgn}(\mathrm{F_z^*(t)})\frac{\hat{\mathrm{F}}_\mathrm{z}}{\mathrm{N_z}}\left[\frac{\mathrm{N_z}\int_{\mathrm{T_i}+\mathrm{j}\Delta\mathrm{T}}^{\mathrm{T_i}+(\mathrm{j}+1)\Delta\mathrm{T}}\left|\mathrm{F_z^*(t)dt}\right|}{\hat{\mathrm{F}}_\mathrm{z}\Delta\mathrm{T}}\right]\}\mathrm{dt}\right|\right] < \gamma \tag{12.15}$$

if the impulse error ΔI_{zi} satisfies the following condition:

$$\left[\left|\int_{T_i}^{T_i+M_1\Delta T}F_z^*(t)\mathrm{dt} - \int_{\mathrm{T_1}+(\mathrm{m_1}+1)\Delta\mathrm{T}}^{\mathrm{T_i}+\mathrm{M_1}\Delta\mathrm{T}}\{\operatorname{sgn}(\mathrm{F_z^*(t)})\frac{\hat{\mathrm{F}}_\mathrm{z}}{\mathrm{N_z}}\left[\frac{\mathrm{N_z}\int_{\mathrm{T_i}+\mathrm{j}\Delta\mathrm{T}}^{\mathrm{T_i}+(\mathrm{j}+1)\Delta\mathrm{T}}\left|\mathrm{F_z^*(t)dt}\right|}{\hat{\mathrm{F}}_\mathrm{z}\Delta\mathrm{T}}\right]\}\mathrm{dt}\right|\right] > \gamma \tag{12.16}$$

then the chaser should carry out impulse compensation and the size of the constant thrust impulse compensation in the z-axis can be calculated as follows:

$$\begin{aligned}\Delta I_{zi} &= F_5 m_2 \Delta T = \frac{m_2 \hat{F}_z \Delta T}{N_z}, (F_z^*(t) < 0) \\ \Delta I_{zi} &= F_6 m_2 \Delta T = -\frac{m_2 \hat{F}_z \Delta T}{N_z}, (F_z^*(t) > 0)\end{aligned} \tag{12.17}$$

the actual constant thrust of the chaser in the x-axis can be calculated as follows. The fuel savings in the x-axis in the ith thrust arc can be calculated as follows:

$$\Delta P_{zi} = \sum_{j=0}^{M_1} \int_{T_i+j\Delta T}^{T_i+(j+1)\Delta T} \left\{ \frac{p_0 N_z \left| F_z^*(t) \right|}{\hat{F}_z} - \mathrm{sgn}(F_z^*(t)) p_0 \left[\frac{N_z \int_{T_i+j\Delta T}^{T+(j+1)\Delta T} \left| \hat{F}_z^*(t) \right| dt}{\hat{F}_z \Delta T} \right] \right\} dt \tag{12.18}$$

Finally, the switch control laws for the rendezvous maneuver can be given in three axes. For convenience, let us take the time intervals in the ith thrust arc in the x-axis for example:

$$S_{zi} = \left\{ \left(T_i + j\Delta T, \mathrm{sgn}(F_z^*(t)) \frac{\hat{F}_z \Delta T}{N_z} \left[\frac{N_z \int_{T_i+j\Delta T}^{T+(j+1)\Delta T} \left| \hat{F}_z^*(t) \right| dt}{\hat{F}_z \Delta T} \right] \right) \right\} \tag{12.19}$$

12.4 Simulation Example

The height of target spacecraft is assumed to be 356 km in a circular orbit, then the mean angular velocity is $\omega = 0.0654 \times 10^{-3}$rad/s and the uncertainty parameters is assumed as $\Delta\omega = \pm 1 \times 10^{-3}$rad/s. The initial mass of the chaser is assumed to be 180 kg at the beginning of rendezvous maneuver. The size of thrusts are assumed to be $\pm$1,200 N in three axes and the shortest switching time is $\Delta T = 1$s The initial position and velocity of the chaser are assumed to be (1000, 500, −200 m) and (−10; −5; 2 m/s).

Figure 12.2 shows the change in x, y, z and V_x, V_y, V_z during rendezvous maneuver.

The results in Fig. 12.3 show the change in F_x, F_y, F_z during rendezvous maneuver.

The result in Fig. 12.4 shows the trajectory of chaser and the change of the thrust angles during rendezvous maneuver. It shows that with the switch control control, the chaser can get to the 20 target positions smoothly.

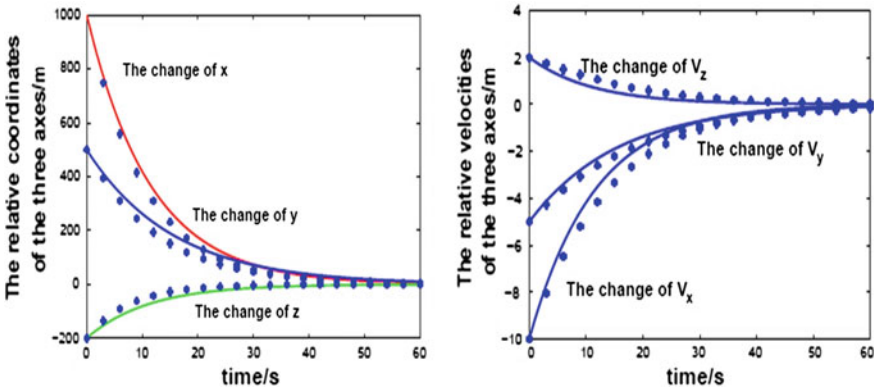

Fig. 12.2 The change of position and velocity during rendezvous maneuver

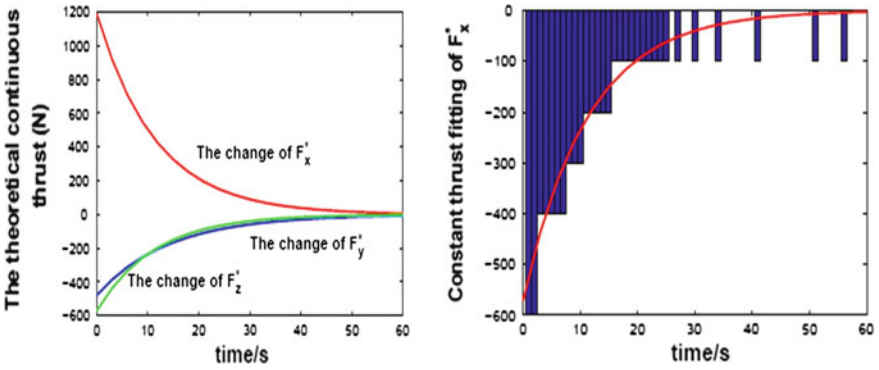

Fig. 12.3 The change of thrust during rendezvous maneuver

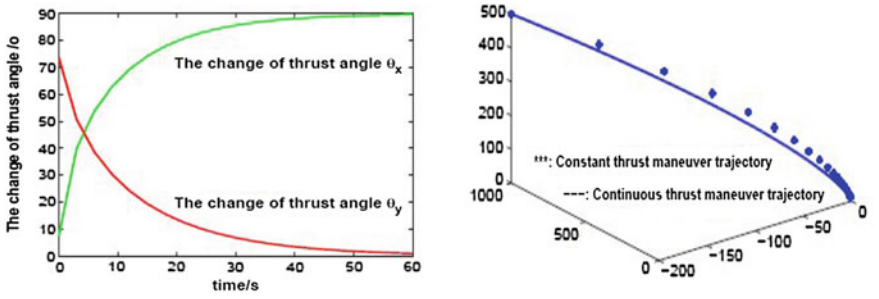

Fig. 12.4 The change in the trajectory of the chaser and thrust angles

The switch control laws can be given according to the sizes and the directions of the thrust of the chaser. Taking the switch control law in the z-axis as an example:

$$S_{zi} = \{(\Delta T, -600); \ldots; (27\Delta T, -100); \ldots; (30\Delta T, 0)\} \tag{12.20}$$

Acknowledgments This work was supported by the NSFC 61304088 and 2013QNA37.

References

1. Jezewski DJ, Donaldson JD (1979) An analytical approach to optimal rendezvous using Clohessy-Wiltshire equations. J Astronaut Sci 27(3):293–310
2. Slater GL, Byram SM, Williams TW (2006) Rendezvous for satellites in formation flight. J Guidance Control Dyn 29:1140–1146
3. Ebrahimi B, Bahrami M, Roshanian J (2008) Optimal sliding-mode guidance with terminal velocity constraint for fixed-interval propulsive maneuvers. Acta Astronaut 60(10):556–562
4. Schouwenaars T, How JP, Feron E (2004) Decentralized cooperative trajectory planning of multiple aircraft with hard safety guarantees. In: AIAA paper, 2004
5. Richards A, Schouwenaars T, How J et al (2002) Spacecraft trajectory planning with avoidance constraints using mixed integer linear programming. J Guidance Control Dyn 25(4):755–764
6. Qi YQ, Jia YM (2012) Constant thrust fuel-optimal control for spacecraft rendezvous. Adv Space Res 49(7):1140–1150

Chapter 13
Robust Control Method Applied in Constant Thrust Rendezvous Under Thrust Failure

Yongqiang Qi

Abstract A robust constant thrust rendezvous approach under thrust failure is proposed based on the relative motion dynamic model. A new algorithm of constant thrust fitting is proposed through the impulse compensation and the fuel consumption under the theoretical continuous thrust and the actual constant thrust is calculated and compared. At last, the proposed method has the advantage of saving fuel is proven and the constant thrust switch control laws are obtained through the isochronous interpolation method; an illustrative example is provided to show the effectiveness of the proposed control design method.

Keywords Rendezvous · Constant thrust · Robust controller

13.1 Introduction

Spacecraft rendezvous has been studied during the last few decades. Rendezvous based on both impulsive thrust and the continuous thrust assumptions have been extensively researched [1–5]. Although there have been many results in this field, the rendezvous orbital control problem has not been fully investigated and still remains challenging. Zhang proposed a robust adaptive integrated translation and rotation finite-time control of a rigid spacecraft with actuator misalignment and unknown mass property [2]. Ebrahimi studied the optimal sliding-mode guidance with terminal velocity constraint for fixed-interval propulsive maneuvers [3]. Hall proposed minimum-time orbital phasing maneuvers [4]. In actual practice, however, the thrusts of the spacecraft can be constant thrusts; therefore, maneuver during rendezvous and docking operations cannot normally be considered as a continuous thrust maneuver or impulsive maneuver.

Y. Qi (✉)
College of Sciences, China University of Mining and Technology (CUMT), Xvzhou, China
e-mail: qiyongqiang3@163.com

Z. Deng and H. Li (eds.), *Proceedings of the 2015 Chinese Intelligent Automation Conference*, Lecture Notes in Electrical Engineering 337,
DOI 10.1007/978-3-662-46463-2_13

In our previous study [6], a constant thrust spacecraft rendezvous was studied according to the *C-W* equations and the analytical solutions. But the traditional open-loop control method used in our previous studies are not applicable, while they are often utilized during the long-distance navigation process. To overcome this problem, a robust closed-loop control laws for constant thrust rendezvous to enhance the orbital control accuracy is proposed in this paper. And the fuel consumption of constant thrust is less than that of the continuous thrust by using the method proposed in this paper.

13.2 The Calculation of the Theoretical Continuous Thrust

The relative motion coordinate system can be established as follows: First, the target spacecraft is assumed as a rigid body and in a circular orbit, and the relative motion can be described by Clohessy-Wiltshire equations. Then, the centroid of the target spacecraft O_T is selected as the origin of coordinate, the x-axis is opposite to the target spacecraft motion, the y-axis is from the center of the earth to the target spacecraft, and the z-axis is determined by the right-handed rule. In this paper, thrust failure in the y-axis as follows,

$$\begin{cases} \ddot{x} - 2\omega\dot{y} = \frac{F_x+\eta_x}{m} \\ \ddot{y} + 2\omega\dot{x} - 3\omega^2 y = \frac{\eta_y}{m} \\ \ddot{z} + \omega^2 z = \frac{F_z+\eta_z}{m} \end{cases} \tag{13.1}$$

where ω represents the angular velocity. F_x, F_z represent the vacuum thrust of the chaser, η_x, η_y, η_z represent the sum of the perturbation and nonlinear factors in the three axes, respectively. m represents the mass of the chaser at the beginning of the rendezvouse. Suppose that the maximum thrusts are $\widehat{F}_x, \widehat{F}_z$ and the theoretical thrusts are F_x^*, F_y^*, F_z^*. The goal of the rendezvouse maneuver is to design a proper controller for the chaser, such that the chaser can be asymptotically maneuvered to the target position. Define the state error vector $x_e(t) = x(t) - x_t(t)$, and its state equation can be obtained as

$$\begin{cases} \dot{x}_e(t) = (A_1 + \Delta A)x_e(t) + (B_1 + \Delta B)u(t) \\ u(t) = Kx_e(t) \end{cases} \tag{13.2}$$

Lyapunov function is defined as follows:

$$V = x_e^T(t)Px_e(t) \tag{13.3}$$

where P is a positive definite symmetric matrix. According to the system stability theory, the necessary and sufficient conditions for robust stability of the system (13.3) as follows:

$$A^T P + PA < 0 \tag{13.4}$$

Then a multiobjective controller design strategy is proposed by translating a multiobjective controller design problem into a convex optimization problem. And the control input constraints can be met simultaneously. Assuming the initial conditions satisfy the following inequality, where ρ is a given positive constant.

$$x^T(0)Px(0) < \rho \tag{13.5}$$

Theorem 13.1 *If there exist a corresponding dimension of the matrix L, a symmetric positive definite matrix X and two parameters* $\varepsilon_1 > 0, \varepsilon_2 > 0$*, then the sufficient condition for robust stability is there exist a state feedback controller K which can meet the following conditions simultaneously.*

$$\begin{pmatrix} \Sigma & X & L \\ X & -\varepsilon_1 & 0 \\ L^T & 0 & -\varepsilon_2 \end{pmatrix} < 0, \quad \begin{pmatrix} \rho I & x^T(0) \\ x(0) & X \end{pmatrix} < 0, \tag{13.6}$$

where $\Sigma = XA_0^T + A_0X + L^TB_0 + B_0L + \varepsilon_1\alpha^2 I + \varepsilon_2\beta^2 I$*, then the theoretical state feedback controller K can be calculated as follows:*

$$K = LX^{-1} = \begin{pmatrix} K_{11} & K_{12} & K_{13} & K_{14} \\ K_{21} & K_{22} & K_{23} & K_{24} \end{pmatrix} \tag{13.7}$$

Then the following results can be obtained.

$$\begin{cases} \dfrac{L_x}{N_x}\hat{F}_x \cos\theta_x = k_{11}x_e(t) + k_{12}y_e(t) + k_{13}\Delta V_x + k_{14}\Delta V_y \\ \dfrac{L_x}{N_x}\hat{F}_x \sin\theta_x = k_{21}x_e(t) + k_{22}y_e(t) + k_{23}\Delta V_x + k_{24}\Delta V_y \end{cases} \tag{13.8}$$

Then the thrust angle control lows θ_x, θ_y *which satisfy the robust stability of the in-plane motion can be obtained from Eq.* (13.9).

13.3 Compare Fuel Consumption for the Out-plane and Calculate the Control Law

According to the layout of chaser's thrusters as shown in Fig. 13.1, the actual constant thrust and the theoretical thrust satisfy the following conditions:

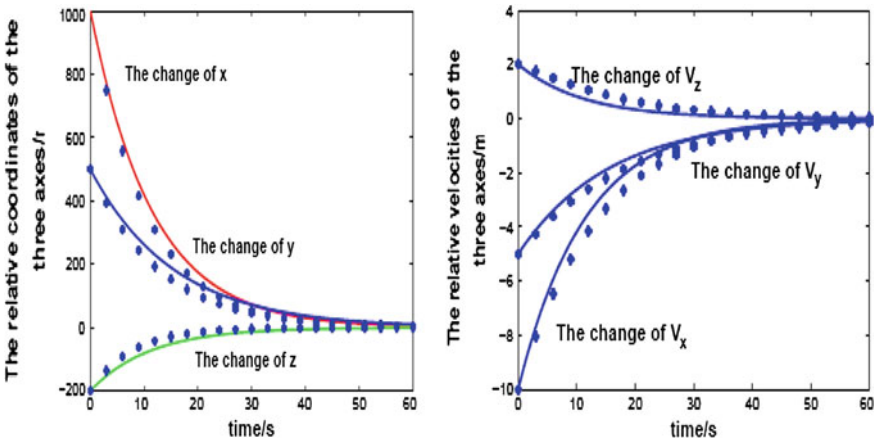

Fig. 13.1 The change of position and velocity during rendezvouse maneuver

$$\begin{cases} F_x = F_1 + F_3, (F_x > 0); F_x = F_5 + F_7, (F_x < 0) \\ F_z = F_9, (F_z < 0); F_z = F_{10}, (F_z < 0) \end{cases} \tag{13.9}$$

The relative motion dynamic model of the out-plane motion:

$$\ddot{z} + \omega^2 z = \frac{F_z + \eta_z}{m} \tag{13.10}$$

For the out-plane motion, a new algorithm of constant thrust fitting is proposed by using the impulse compensation method as follows. Suppose that the thrusters in the z-axis can provide different sizes of constant thrust to meet different thrust requirements.

Constant thrust fitting is proposed by using the impulse compensation method as follows. Suppose that the thrusters in the z-axis can provide different sizes of constant thrust to meet different thrust requirements. If the theoretical working time of z-axis thruster in the ith thrust arc $t_z^* = \Delta T < T_i$ and t_z^* can be any one of M_i shortest switching time interval in the ith thrust arc. Without loss of generality, suppose that t_z^* is the first shortest switching time interval and the impulse error in the z-axis in the ith thrust arc ΔI_{zi} can be calculated as follows:

The chaser's thrusters in the x-axis can supply high, middle, and low thrust levels to be selected as follows, and the level of the constant thrust in case I can be calculated as follows:

$$\frac{j\hat{F}_x}{3}, j = 0, 1, 2, 3\ , \quad j = \left[\frac{3 \int_{T_i}^{T_i + \Delta T} \left| F_z^*(t) \right| \mathrm{d}t}{\hat{F}_z \Delta T} \right] \tag{13.11}$$

Calculate the impulse error.

$$\Delta I_{zi} = \operatorname{sgn}(F_z^*(t)) \left| \int_{T_i}^{T_{i_i}+\Delta T} \left| F_x^*(t) \right| \mathrm{d}t - \frac{j\hat{F}_z \Delta T}{3} \right| \tag{13.12}$$

Determine the value of the impulse compensation threshold. Suppose that the value of the impulse compensation threshold is a positive constant $\gamma > 0$, if the impulse error ΔI_{zi} satisfies the following condition,

$$\left| \int_{T_i}^{T_{i_i}+\Delta T} \left| F_x^*(t) \right| \mathrm{d}t - \frac{\hat{F}_z \Delta T}{3} \left[\frac{3 \int_{T_i}^{T_i+\Delta T} \left| F_z^*(t) \right| \mathrm{d}t}{\hat{F}_z \Delta T} \right] \right| \leq \gamma \tag{13.13}$$

the actual constant thrust of the chaser in the z-axis can be calculated as follows:

$$F_z = \operatorname{sgn}(F_z^*(t)) \frac{\hat{F}_z \Delta T}{3} \left[\frac{3 \int_{T_i}^{T+\Delta T_i} \left| \hat{F}_z^*(t) \right| \mathrm{d}t}{\hat{F}_z \Delta T} \right] \tag{13.14}$$

then the chaser will not carry out impulse compensation. Suppose that

$$\left[\left| \int_{T_i}^{T_i+M_1\Delta T} \frac{F_z^*(t) N_z}{\hat{F}_z \Delta T} \mathrm{d}t - \int_{T_1+(m_1+1)\Delta T}^{T_i+M_1\Delta T} \left\{ \frac{\operatorname{sgn}(F_z^*(t))}{\Delta T} \left[\frac{3 \int_{T_i+j\Delta T}^{T_i+(j+1)\Delta T} \left| F_z^*(t) \mathrm{d}t \right|}{\hat{F}_z \Delta T} \right] \right\} \mathrm{d}t \right| \right] = m_2 \tag{13.15}$$

Furthermore, if the impulse error ΔI_{zi} satisfies the following condition,

$$\left[\left| \int_{T_i}^{T_i+M_1\Delta T} F_z^*(t) \mathrm{d}t - \int_{T_1+(m_1+1)\Delta T}^{T_i+M_1\Delta T} \left\{ \operatorname{sgn}(F_z^*(t)) \frac{\hat{F}_z}{3} \left[\frac{3 \int_{T_i+j\Delta T}^{T_i+(j+1)\Delta T} \left| F_z^*(t) \mathrm{d}t \right|}{\hat{F}_z \Delta T} \right] \right\} \mathrm{d}t \right| \right] < \gamma \tag{13.16}$$

if the impulse error ΔI_{zi} satisfies the following condition,

$$\left[\left| \int_{T_i}^{T_i+M_1\Delta T} F_z^*(t) \mathrm{d}t - \int_{T_1+(m_1+1)\Delta T}^{T_i+M_1\Delta T} \left\{ \operatorname{sgn}(F_z^*(t)) \frac{\hat{F}_z}{3} \left[\frac{3 \int_{T_i+j\Delta T}^{T_i+(j+1)\Delta T} \left| F_z^*(t) \mathrm{d}t \right|}{\hat{F}_z \Delta T} \right] \right\} \mathrm{d}t \right| \right] > \gamma \tag{13.17}$$

then the chaser should carry out impulse compensation and the size of the constant thrust impulse compensation in the z-axis can be calculated as follows:

$$\begin{aligned}\Delta I_{zi} &= F_5 m_2 \Delta T = \frac{m_2 \hat{F}_z \Delta T}{3}, (F_z^*(t) < 0) \\ \Delta I_{zi} &= F_6 m_2 \Delta T = -\frac{m_2 \hat{F}_z \Delta T}{3}, (F_z^*(t) > 0)\end{aligned} \tag{13.18}$$

the actual constant thrust of the chaser in the x-axis can be calculated as follows. The fuel savings in the x-axis in the ith thrust arc can be calculated as follows:

$$\Delta P_{zi} = \sum_{j=0}^{M_1} \int_{T_i+j\Delta T}^{T_i+(j+1)\Delta T} \left\{ \frac{3p_0 |F_z^*(t)|}{\hat{F}_z} - \mathrm{sgn}(F_z^*(t)) p_0 \left[\frac{3 \int_{T_i+j\Delta T}^{T+(j+1)\Delta T} |\hat{F}_z^*(t)| \mathrm{d}t}{\hat{F}_z \Delta T} \right] \right\} \mathrm{d}t \tag{13.19}$$

At last, the switch control laws for the rendezvous maneuver can be given in three axes. For convenience, let us take the time intervals in the ith thrust arc in the x-axis for example:

$$S_{zi} = \left\{ \left(T_i + j\Delta T, \mathrm{sgn}(F_z^*(t)) \frac{\hat{F}_z \Delta T}{3} \left[\frac{3 \int_{T_i+j\Delta T}^{T+(j+1)\Delta T} |\hat{F}_z^*(t)| \mathrm{d}t}{\hat{F}_z} \right] \right) \right\} \tag{13.20}$$

13.4 Simulation Example

The height of target spacecraft is assumed to be 356 km in a circular orbit, then the mean angular velocity is $\omega = 0.0654 \times 10^{-3}$ rad/s and the uncertainty parameters is assumed as $\Delta\omega = \pm 1 \times 10^{-3}$ rad/s. The initial mass of the chaser is assumed to be 180 kg at the beginning of rendezvouse maneuver. The size of thrusts are assumed to be ± 1200 N in three axes and the shortest switching time is $\Delta T = 3$ s. The initial position and velocity of the chaser are assumed to be (1000, 500, −200 m) and (−10; −5; 2 m/s).

Figure 13.1 show the change of x, y, z, and V_x, V_y, V_z during rendezvouse maneuver.

The results in Fig. 13.2 show the change of F_x, F_z during rendezvouse maneuver.

The result in Fig. 13.3 shows the trajectory of chaser during rendezvous maneuver. It can be seen that with the switch control, the chaser can get to the 20 target positions smoothly.

The switch control laws can be given according to the sizes and the directions of the thrust of the chaser. Taking the switch control law in the z-axis as an example:

$$S_{zi} = \{(\Delta T, 1200); \ldots; (29\Delta T, 0); \ldots; (30\Delta T, 600)\} \tag{13.21}$$

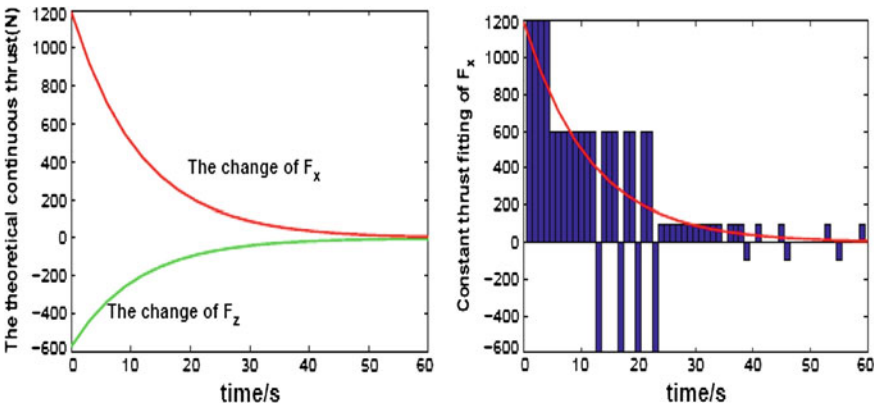

Fig. 13.2 The change of thrust during rendezvouse maneuver

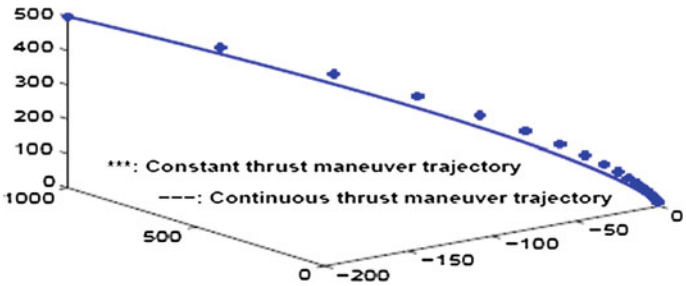

Fig. 13.3 The change of the trajectory of the chaser

Acknowledgments This work was supported by the NSFC 61304088 and 2013QNA37.

References

1. Chiou JC, Hwang MC, Wuf SD, Yang JY (1997) Robust attitude control of spacecraft using sliding mode control and productive networks. Int J Syst Sci 28:435–446
2. Duan Z, Zhang J, Zhang C (2006) Robust H2 and H1 filtering for uncertain linear systems. Automatica 42:1919–1926
3. Ebrahimi B, Bahrami M, Roshanian J (2008) Optimal sliding-mode guidance with terminal velocity constraint for fixed-interval propulsive maneuvers. Acta Astronautica 60:556–562
4. Fehse W (2003) Automated rendezvous and docking of spacecraft. Cambridge University Press, Cambridge
5. Richards A, Schouwenaars T, How J et al (2002) Spacecraft trajectory planning with avoidance constraints using mixed integer linear programming. J Guidance Control Dyn 25(4):755–764
6. Qi YQ, Jia YM (2012) Constant thrust fuel-optimal control for spacecraft rendezvous. Adv Space Res 49(7):1140–1150

Chapter 14
Stabilization of Underactuated Surface Vessel Based on Backstepping Control Method

Chuang Zhang and Chen Guo

Abstract To address the problem of stabilization of underactuated surface vessels with parameter uncertainties and external disturbances, a stabilization control based on backstepping control method is designed, First, the conditions can make the system globally stable and prove the correctness of existing conditions using diffeomorphism transformation. Then the original stabilization problem can be changed into an equal new one, and backstepping method is used to construct the controller of the stabilization function. The controller has global asymptotic stability. Eventually, simulations of the stabilization control for the underactuated surface vessel with disturbances or without disturbances are performed. Results validate the effectiveness of the proposed method.

Keywords Underactuated surface vessels · Stabilization control · Backstepping · Global asymptotic stabilization

14.1 Introduction

Control of underactuated systems has been one of the active research areas because of its intrinsic nonlinear nature and practical applications [1]. As a typical example of underactuated systems, control of an underactuated ship has attracted much attention recently. The main difficulty with control of underactuated ships is that they are not actuated in the sway axis. This configuration is by far the most common among surface ships. Furthermore, unlike underactuated systems with non-integrable constraints, the surface vessels under consideration are a class of underactuated systems with non-integrable dynamics and are not transformed into a driftness system [2]. Nevertheless, the stabilization controller for underactuated surface vessel is more difficult owing to the conclusion of general non-integrity

C. Zhang (✉) · C. Guo
Navigation College, Dalian Maritime University, Linghai Road, Dalian, Liaoning, China
e-mail: zhchuangdmu@163.com

Z. Deng and H. Li (eds.), *Proceedings of the 2015 Chinese Intelligent Automation Conference*, Lecture Notes in Electrical Engineering 337,
DOI 10.1007/978-3-662-46463-2_14

system that cannot be applied to the underactuated system directly [3]. On the condition of parameter identification of ship's model being not accurate, to achieve stabilization control has important practical significance to underactuated surface vessel.

This paper proposes the stabilization controller based on backstepping for underactuated surface vessel. Diffeomorphism transformation is implemented in order to construct a new system. Additionally, the stabilization controller is designed according to backstepping for the system, and thereby ensure that the system is global asymptotic stabilization.

14.2 System Model

The underactuated surface vessel can be described by the following model [4].

$$\begin{cases} \dot{x} = u\cos(\psi) - v\sin(\psi) \\ \dot{y} = u\sin(\psi) + v\cos(\psi) \\ \dot{\psi} = r \\ m_{11}\dot{u} = m_{22}vr - d_{11}u + \tau_u \\ m_{22}\dot{v} = -m_{11}ur - d_{22}v \\ m_{33}\dot{r} = (m_{11} - m_{22})uv - d_{33}r + \tau_r \end{cases} \tag{14.1}$$

where (x, y) represents inertial position and ψ is course in geodetic coordinate system, u, v, r describe surge, sway, and yaw rate of ship motion in the body fixed coordinate frame. d_{11}, d_{22}, d_{33}, m_{11}, m_{22}, m_{33} denote the hydrodynamic damping and ship inertia including added mass in surge, sway, and yaw. The available controls are the surge force τ_u and the yaw control moment τ_r. However, we do not have available control in the sway direction, thus the problem of controlling the ship in three degrees of freedom is an underactuated control problem.

Alternation of control input is defined as

$$\begin{cases} \tau_u = \dfrac{m_{22}}{m_{11}}vr - \dfrac{d_{11}}{m_{11}}u + \dfrac{1}{m_{11}}\tau_1 \\ \tau_r = \dfrac{m_{11} - m_{22}}{m_{33}}uv - \dfrac{d_{33}}{m_{33}}r + \dfrac{1}{m_{33}}\tau_3 \end{cases} \tag{14.2}$$

Assume A and B are given as follows: $A = m_{11}/m_{22}$, $B = d_{22}/m_{22}$. Then by (14.1) and (14.2), we obtain

$$\begin{cases} \dot{u} = \tau_u \\ \dot{v} = -Auv - Bv \\ \dot{r} = \tau_r \end{cases} \tag{14.3}$$

According to coordinate transformation $Z_2 = z_2 + v/b$. Then (z_1, Z_2) can be transformed as

$$\begin{cases} \dot{z}_1 = u + Z_2 r - \dfrac{v}{B} r \\ \dot{Z}_2 = -\dfrac{A}{B} u r - z_1 r \end{cases} \tag{14.4}$$

Then τ_α is selected as $B/A(z_1 + \alpha) - r(Z_2 - v/B) - \tau_u A/B$, Virtual control input α is adhibited, then

$$\begin{cases} \dot{z}_1 = -\frac{B}{A} z_1 - \frac{B}{A}\alpha + Z_2 r - \frac{v}{B} r \\ Z_2 = \alpha r \\ \dot{z}_3 = r \\ \dot{v} = -Bv + B(z_1 + \alpha) r \\ \dot{\alpha} = \tau_\alpha \\ \dot{r} = \tau_r \end{cases} \tag{14.5}$$

The same original system as the new system can prove stable after the diffeomorphism transform.

$$\begin{cases} f_1(t, x_1) + G(t, x) x_2 = \begin{bmatrix} -\frac{B}{A} z_1 - \frac{B}{A}\alpha - Z_2 r - \frac{v}{B} r \\ -Bv + B(z_1 + \alpha) r \end{bmatrix} \\ f_2(t, x_2, u) = \begin{bmatrix} \alpha r & r & \tau_\alpha & \tau_r \end{bmatrix}^T \end{cases} \tag{14.6}$$

Theorem *For given two cascaded subsystems* Σ_1 *and* Σ_2, *the conditions of global asymptotic stabilization are as follows* [5]:

1. $f_1(t, x_1)$ *is global asymptotic stabilization.*
2. $G(t, x)$ *satisfy the following condition:*

$$\|G(t, x)\|_2 \leq \theta_1 \|x_2\|_2 + \theta_2(\|x_2\|_2)\|x_1\|_2 \tag{14.7}$$

3. *The existence of a control law u in order to make* Σ_2 *stabilization.*

Proof System can be rewritten as

$$\dot{x}_1 = f_1(t, x_1) = \begin{bmatrix} -B & 0 \\ 0 & -\frac{B}{A} \end{bmatrix} x_1 = A x_1 \tag{14.8}$$

As subsystem x_1 is linear time invariant system and the matrix is nonsingular, $A + A^T$ is negative. $f_1(t, x_1)$ is global asymptotic stabilization. From Eq. (14.6), $G(t, x)$ can be chosen as

$$\begin{aligned} G(t,x) &= G_1(t,x_1) + G_2(t,x) \\ &= \begin{bmatrix} 0 & 0 & 0 & -\frac{v}{B} \\ 0 & 0 & 0 & Bz_1 \end{bmatrix} + \begin{bmatrix} r & 0 & -\frac{B}{A} & 0 \\ 0 & 0 & Br & 0 \end{bmatrix} \end{aligned} \tag{14.9}$$

where $\|G_1(t,x_1)\|_2 \le \max(B, 1/B)\sqrt{z_1^2 + v^2} = \max(B, 1/B)\|x_1\|_2 = \theta_1\|x_1\|_2$

Thus $\|G(t,x)\|_2 \le \|G_1(t,x_1)\|_2 + \|G_2(t,x)\|_2$ meet condition 2 in Theorem.

The control law u must be designed in order to make subsystem Σ_2 stable. Suppose α and r are virtual control input, from Eq. (14.6), it can be chosen as

$$\begin{cases} y_1 = Z_2 & y_2 = \alpha & y_3 = z_3 \\ u_1 = r & \dot{r} = \tau_r & u_2 = \tau_\alpha \end{cases} \tag{14.10}$$

In order to realize the desired exponential convergence to zero in Z_3, feedback control input $u_1 = -k_3 Z_3$ of linear should be chosen. As discussed earlier, the feedback control law u_2 should be designed on the basis of backstepping.

A nonnegative control Lyapunov function is chosen to analyze the stability of system, this function is formed as

$$V_1(y_1) = \frac{1}{2} y_1^2 \tag{14.11}$$

y_2 is virtual control input of y_1. In this paper, we assume that $y_2 = k_1 y_1 / k_3 y_3$. The derivative of V_1 along the trajectory of system is

$$\dot{V}_1(y_1) = y_1 \dot{y}_1 = -k_3 y_1 y_2 y_3 = -k_1 y_1^2, \quad k_1 \ge 0 \tag{14.12}$$

If you want to meet the system y_2 is stable. Define a new variable ζ_1, meanwhile $\zeta_1 = y_2 - \Psi_1(y_1, y_3)$ is Deviation between y_2 and virtual control input $\Psi_1(y_1, y_3)$. The Lyapunov function can be chosen as

$$V_2(y_1, y_2) = \frac{1}{2}\zeta_1^2 + V_1(y_1) \tag{14.13}$$

Then, it follows that

$$\begin{aligned} \dot{V}_2(y_1, y_2) &= \zeta_1 \dot{\zeta}_1 + \dot{V}_1(y_1) \\ &= -k_1 y_1^2 + \zeta_1 (u_2 + k_1(\zeta_1 + \Psi_1(y_1, y_3)) - k_1 y_1 / y_3 - k_3 y_1 y_3) \end{aligned} \tag{14.14}$$

To prove the stability, control law should be defined as

$$\dot{V}_2(y_1, y_2) = -k_1 y_1^2 - k_2 \zeta_1^2 \leq 0, \quad k_2 \geq 0 \tag{14.15}$$

Therefore, we can write y_1 and ζ approaches 0 when t approach ∞.

If you want to meet the first order linear system which is stable, then define a new variable ζ_2, meanwhile $\zeta_2 = u_1 - \Psi_2(y_3)$ is deviation between u_1 and virtual control input $\Psi_2(y_3)$. The Lyapunov function can be chosen as

$$V_3(r) = \frac{1}{2}\zeta_2^2 + V_2(y_1, y_2) \tag{14.16}$$

Then, it follows that

$$\dot{V}_3(r) = \zeta_2 \dot{\zeta}_2 + \dot{V}_2 = \zeta_2(\tau_r + k_3 r) - k_1 y_1^2 - k_2 \zeta_1^2 \tag{14.17}$$

For a control law τ_r, where

$$\tau_r = -k_3 r - k_4 \zeta_2 = -k_3 r - k_4(r + k_3 y_3) \tag{14.18}$$

Therefore, we can write $\dot{V}_3(r) < 0$, which completes the proof.

14.3 Simulation Results

To evaluate performance of proposed method, the computer simulation has been used. Consider an underactuated surface vessel with model parameters as $m_{11} = 200$ kg, $m_{22} = 250$ kg, $m_{33} = 80$ kg m^2, $d_{11} = 70$ kg s^{-1}, $d_{22} = 100$ kg s^{-1} and $d_{33} = 50$ kg m^2 s^{-1}. Choice of initial condition for the vessel system: $[x_0, y_0, \Psi_0, u_0, v_0, r_0]^{\mathrm{T}} = [5\text{ m}, 5\text{ m}, \pi/4\text{ rad}, 0\text{ m/s}, 0\text{ m/s}, 0.5\text{ rad/s}]^{\mathrm{T}}$.

14.3.1 Simulation Results in No Flow Conditions

The control parameters are taken as $k_1 = 0.8$, $k_2 = 1$, $k_3 = 0.4$, $k_4 = 1.55$ and the simulation time is set to 50 s.

Figure 14.1 displays the course of ship trajectory tracking under the proposed backstepping law. It is clearly seen that the ship follows the reference trajectory with high accuracy. Figure 14.2 shows the response of yaw angle and angular velocity of the surface vessel. System state average index of underactuated surface vessel can be converged to zero by controller designed by backstepping method, and better convergence curve. Figure 14.3 shows intermediate variables can be

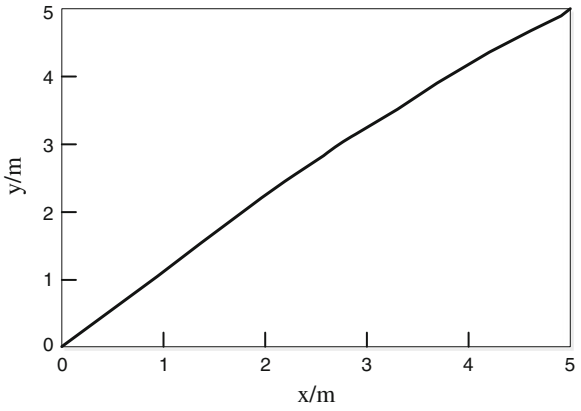

Fig. 14.1 Trajectory tracking of underactuated surface vessel

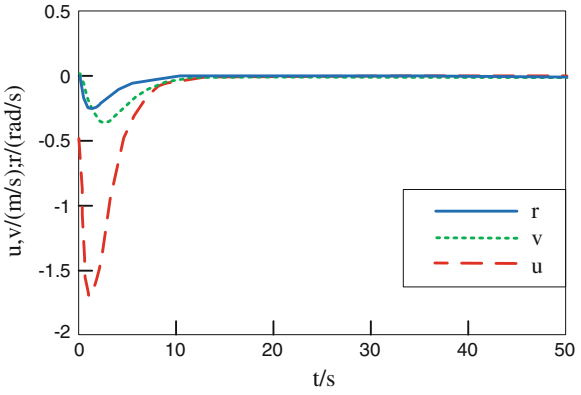

Fig. 14.2 Response of yaw angle and angular velocity

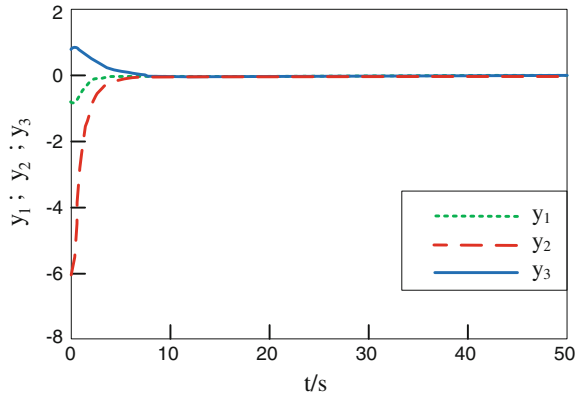

Fig. 14.3 Curve of intermediate variable

converged within 15 s and controller is stabilized to the origin. Curve convergence rate of y_3 is smaller than y_1 and y_2 due to controller is designed, but time of convergence is longer.

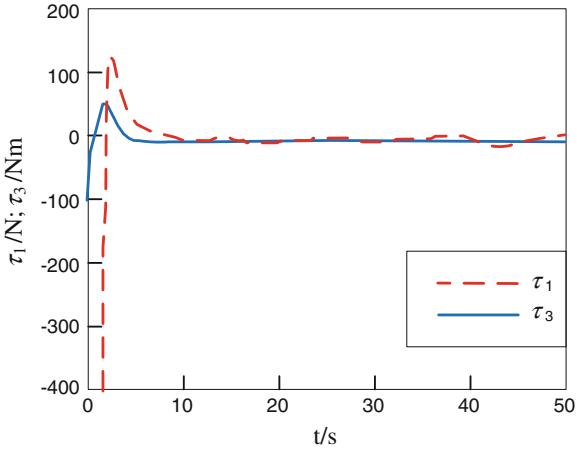

Fig. 14.4 Curve of forces applied to the vessel

14.3.2 Simulation Results in Flow Conditions

The disturbance torque is caused by the flow of the external wind and wave as [6].

The control parameters are taken as $k_1 = 0.8$, $k_2 = 1$, $k_3 = 0.4$, $k_4 = 1.55$ and the simulation time is set at 50 s.

Figure 14.4 displays the forces applied to the vessel. If stabilized at the origin, it should provide negative thrust and torque because the initial position is positive. When underactuated surface vessel is disturbed, the control force and torque vibrates in the vicinity of the equilibrium point. Figure 14.5 shows the longitudinal velocity and rate of heading. Figure 14.6 shows the strong robustness and stability in the vicinity of the origin for the underactuated surface ship in the presence of disturbances, nevertheless ship trajectory tracking is unideal. Figure 14.7 shows the

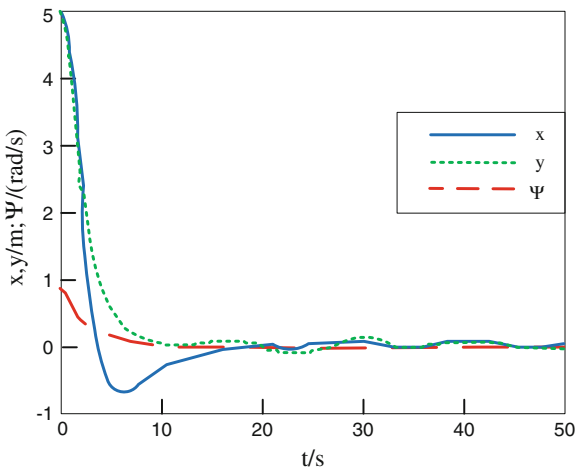

Fig. 14.5 Curve of location variable

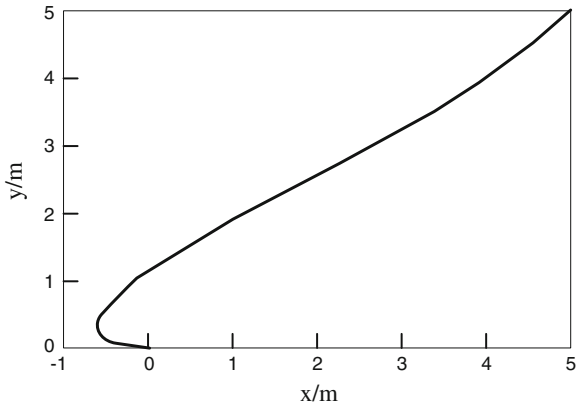

Fig. 14.6 Trajectory tracking of underactuated surface vessel

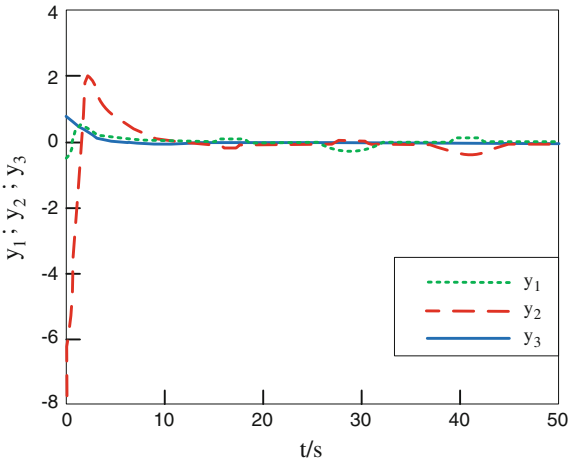

Fig. 14.7 Curve of intermediate variable

anti-jamming ability of y_3 is poor, furthermore, the amplitude of vibration is slightly larger than the other variables. Because the disturbances are positive, y_3 vibrates in the vicinity of 0.08.

14.4 Conclusion

In this paper, we proposed the new approach to stabilization of underactuated surface vessel based on backstepping control. Robustness and high performance can be achieved with the proposed scheme. Simulation results are included to demonstrate that the maneuvering motion of underactuated surface vessel is stabilized to the origin of the suggested approach, and is applied to engineering systems of underactuated vessel.

Acknowledgments This work was supported by the National Nature Science Foundation of China (No. 61374114) and supported by the Fundamental Research Funds for the Central Universities (DMU No. 3132014321).

References

1. Ghommam J, Mnif F, Derbel N (2010) Global stabilisation and tracking control of underactuated surface vessels. IET Control Theor Appl 4(1):71–88
2. Do KD, Pan J (2006). Global robust adaptive path following of underactuated ships. Automatica 42(10):1713–1722
3. Yongping PAN, Daoping HUANG, Zonghai SUN (2011) Backstepping adaptive fuzzy control for track-keeping of underactuated surface vessels. Control Theor Appl 28(7):907–914
4. Tang XH, Lu JA, Zhang WW (2007) The FPS of chaotic system using backstepping design. China Dyn Control 0705:216
5. Wang W, Yi J, Zhao D et al (2004) Design of a stable sliding-mode controller for a class of second-order underactuated systems. IEE Proc Control Theor Appl 151(6):683–690
6. Yu R, Zhu Q, Xia G, Liu Z (2011). Sliding mode tracking control of an underactuated surface vessel. IET Control Theor Appl 6(3):461–466

Chapter 15
BMI Optimization Based on Improved Path-Following Method in Control

Jian Chen and Chong Lin

Abstract This paper deals with the optimization of the bilinear matrix inequality problems by using an improved path-following method. First, the existing path-following method is depicted in detail, including its implementation and limit. Then, based on a new linearization method, an improved path-following method is given. In order to enhance the ability of global optimization, a wide range of perturbation steps is added. Both methods are implemented on static output feedback control problems. Finally, a numerical example is presented to show that the convergence and optimization ability of the improved path-following method are better than the existing one.

Keywords Bilinear matrix inequalities · Control problem · Path-following method · Convergence

15.1 Introduction

The bilinear matrix inequality (BMI) problems are not convex optimization problems due to the bilinear terms in the constraint [1] and, therefore, can have multiple local solutions. BMI problems are proved to be NP-hard [2]. In recent years, considerable research effort has been devoted to the development of algorithms to solve BMI problems. Branch and bound method [3, 4] is a global optimization algorithm for solving BMIs, which is an implicit enumeration. Based on some branching rules and bounding approaches, the local minima is decided in order to obtain the global minimum. But the combination explosion problem is common in

J. Chen · C. Lin (✉)
The Institute of Complexity Science, Qingdao University, Qingdao 266071, China
e-mail: linchong_2004@hotmail.com

J. Chen
The College of Science, Qingdao Technological University, Qingdao 266555, China
e-mail: janec@163.com

Z. Deng and H. Li (eds.), *Proceedings of the 2015 Chinese Intelligent Automation Conference*, Lecture Notes in Electrical Engineering 337,
DOI 10.1007/978-3-662-46463-2_15

solving high-order BMI problems. Another simple global optimization algorithm is random search method [5]. In this method, the probability to find a solution as well as the number of random trials can be evaluated. The drawback is that the probability that the algorithm fails is not equal to zero for a finite number of iterations and the computation complex is still high. The rank minimization approach [1], also a global optimization method, is based on the semidefinite programming relaxation approach to indefinite quadratic programming. But the convergence rate is slow and sometimes it cannot find the global optimum. As global methods have so many difficulties, most of the algorithms formed in the literature that claim the applicability to control-related problems of practical size are local search algorithms. Most of the existing local approaches are computationally fast but, depending on the initial condition, may not converge to the global optimum. The simplest local approach makes use of the fact that by fixing some of the variables, the BMI problem becomes convex in the remaining variables, and vice versa, and iterates between them [6–9]. This method is not guaranteed to converge to a local solution. Another local approach is the so-called over-bounding method [10], which splits two variables in BMI terms into different LMI ones, and the nonpositive quadratic terms are successively replaced by their upper bounds. Over-bounding method can reduce the conservatism arising from seeking a common LMI solution in the past results. But sometimes it has the defect of low convergence rate. Path-following method (PFM) was proposed in [11]. As a step-by-step method, implying linearization approach at its key step, it has shown a significant advantage [12–14]. However, the linearization method of this method leads to nonconvergence when the perturbation is too wide, or the rate of convergence is very slow when the perturbation is too small.

The main purpose of this paper is to provide an improvement on the path-following method. The result is based on a new linearization method. By solving the problem of static output feedback control, the detailed steps of the method is presented. A numerical example is given to show the effectiveness of our method.

This paper is organized as follows. Section 15.2 describes the existing path-following method steps and the improved path-following method in detail. Section 15.3 applies this algorithm to the numerical examples, and compares results with the existing path-following method. Finally, Sect. 15.4 conclude the work with some comments.

15.2 Problem Formulation and Path-Following Method

15.2.1 Problem Formulation

Consider the problem of static output feedback (SOF) design for the linear following time-invariant dynamical system:

$$\begin{cases} \dot{x} = Ax + Bu \\ y = Cx, \end{cases} \tag{15.1}$$

The SOF stabilization problem is to find a SOF controller $u = Fy$, such that the closed-loop system given by

$$\dot{x} = (A + BFC)x \tag{15.2}$$

is stable. As is known, the closed-loop system (15.2) is stable if and only if there exists a $P = P^T > 0$ such that

$$P(A + BFC) + (A + BFC)^T P < 0 \tag{15.3}$$

As mentioned in [8], if

$$P(A + BFC) + (A + BFC)^T P - \alpha P < 0 \tag{15.4}$$

holds for some negative number α, the closed-loop system matrix $A + BFC$ has its eigenvalues on the strict left-hand side of the line α in the complex s-plane. If $\alpha \leq 0$ satisfying (15.4) can be found, the SOF stabilization problem is solved. So, the SOF optimization problem in control is

$$\begin{aligned} OP1 \quad & \min \alpha \\ \text{subject to} \quad & P(A + BFC) + (A + BFC)^T - \alpha P < 0. \end{aligned}$$

15.2.2 PFM

In order to solve optimization problem OP1, the PFM developed in [11] can be adopted. The method consists of three steps.

Step1: *Initialization step*. At initial, this step is to search suboptimal values of F_0, P_0, and α_0 by computing OP1 as follows.

(1) Select an initial value M such that $A + BM$ is Hurwitz;
(2) Solve the optimization problem OP2 with respect to P.

$$\begin{aligned} OP2 \quad & \min \alpha \\ \text{subject to} \quad & P(A + BM) + (A + BM)^T P - \alpha P < 0 \end{aligned}$$

(3) For fixed P, solve OP1 with respect to α and F.

If $\alpha \leq 0$, F is the stabilising SOF gain, stop. Else, set $k = 1$, $i = 1$, and let $\alpha_0 = \alpha$, $F_0 = F$, $Ac = A + BF_0C$.

Step 2: *Perturbation step*. The BMI (15.4) is then linearized around (F_k, P_k, α_k) by means of perturbations ΔF, ΔP and $\Delta\alpha$. Set $\beta = \beta_0$. The LMI problem to be solved in this step is

$$\begin{aligned} OP3 \quad & \min \alpha \\ \text{subject to} \quad & P_k + \Delta P > 0 \\ & \begin{pmatrix} \beta P_k & \Delta P \\ \Delta P & \beta P_k \end{pmatrix} > 0 \\ & (P_k + \Delta P)A_c + A_c^T(P_k + \Delta P) + P_k B\Delta FC + (B\Delta FC)^T P_k < \alpha P_k \end{aligned}$$

Step 3: *Update step*. Let $F_k = F_k + \Delta F, P_k = P_k + \Delta P, \alpha_k = \alpha_k + \Delta\alpha$. For fixed F_k, compute new P_k by solving OP1, and then compute new F_k and α_k by solving OP1. Let $Ac = A + BF_kC$.

If $\alpha \leq 0$, stop. Else if the relative improvement in α is larger than a preset value, let $k = k + 1$, go to Step 2.

15.3 Main Result

In this section, the new linearization method and IPFM is given as follows.

Write $\Delta F = F - F_k$, $\Delta P = P - P_k$ and $A_c = A + BF_kC$, where F_k and P_k are fixed matrices. The left side of inequality (15.3) is expanded around (F_k, P_k) as follows:

$$\begin{aligned} & P(A + BFC) + (A + BFC)^T P \\ & = P_k(A_c + B\Delta FC) + (A_c + B\Delta FC)^T P_k + \Delta P A_c + A_c^T \Delta P \\ & \quad + \Delta P B\Delta FC + (B\Delta FC)^T \Delta P \\ & \quad \leq P_k(A_c + B\Delta FC) + (A_c + B\Delta FC)^T P_k + \Delta P A_c + A_c^T \Delta P \\ & \quad + \frac{1}{2}(\Delta P + B\Delta FC)^T(\Delta P + B\Delta FC) \\ & = b(\Delta F, \Delta P). \end{aligned}$$

Then, by applying Schur complement, $b(\Delta F, \Delta P) < 0$ is equivalent to the following LMI condition:

$$\begin{pmatrix} (P_k + \Delta P)A_c + A_c^T(P_k + \Delta P) + P_k B\Delta FC + (B\Delta FC)^T P_k & * \\ B\Delta FC + \Delta P & -2I \end{pmatrix} < 0 \quad (15.5)$$

The algorithm for improved path-following method consists of five steps.

Step 1: *Initialization step.* This step is the same as the initialization step in PFM.
Step 2: *Small range of perturbation step.* The BMI (15.4) is then linearized around (F_k, P_k, α_k) by means of perturbations ΔF, ΔP and $\Delta\alpha$. Set $\beta = \beta_0$. The LMI problem to be solved in this step is

$$
\begin{aligned}
OP4 \quad & \min \alpha \\
\text{subject to} \quad & P_k + \Delta P > 0 \\
& \begin{pmatrix} \beta P_k & \Delta P \\ \Delta P & \beta P_k \end{pmatrix} > 0 \\
& \begin{pmatrix} (P_k + \Delta P)A_c + A_c^T(P_k + \Delta P) + P_k B\Delta FC + (B\Delta FC)^T P_k - \alpha P_k & * \\ B\Delta FC + \Delta P & -2I \end{pmatrix} < 0
\end{aligned}
$$

Step 3: *Update step*. Let $F_k = F_k + \Delta F, P_k = P_k + \Delta P, \alpha_k = \alpha_k + \Delta\alpha$. For fixed F_k, compute new P_k by solving OP1, and then compute new F_k and α_k by solving OP1. Let $A_c = A + BF_kC$.
If $\alpha \leq 0$, stop. Else if $|\alpha_k - \alpha_{k-1}| < \varepsilon_1$, a prescribed tolerance, set $j = 1$, let $\beta = \beta \times 2Z$, $F_0 = F_k, P_0 = P_k, \alpha_0 = \alpha_k$; Else let $k = k + 1$ go to Step 2.
Step 4: *Wide range of perturbation step.* Solve $OP4$ with replacement of k by j.
Step 5: *Update step*. Let $F_j = F_j + \Delta F, P_j = P_j + \Delta P, \alpha_j = \alpha_j + \Delta\alpha$. For fixed F_j, compute new P_j by solving OP1, and then compute new F_j and α_j by solving OP1.
Let $A_c = A + BF_jC$.
If $\alpha \leq 0$, stop. Else, if the difference $\alpha_j - \alpha_{j-1} < -\varepsilon_2$, let $F_0 = F_j, P_0 = P_j$, $\alpha_0 = \alpha_j$, $i = i + 1$, set $k = 1$, go to step 2; Else, if the difference $\alpha_j - \alpha_{j-1} > -\varepsilon_2$, and $j < 3$, let $j = j + 1$ and $\beta = \beta \times 2$, and then go to step 4; Else, if the difference $\alpha_j - \alpha_{j-1} > -\varepsilon_2$, and $j \geq 3$, stop. The system may not be stable via output feedback.

15.4 Numerical Example

An example concerning the SOF control problem is given in this section.

Example 15.1 Consider the SOF stabilization problem of system (15.1) with the following parameter matrices [6]:

$$A = \begin{pmatrix} -4 & -2 & -8 & 5 & -1 & -8 & 4 \\ -9 & -7 & -6 & -3 & -2 & 2 & 6 \\ -7 & -3 & 7 & 5 & 2 & 10 & -1 \\ -6 & -3 & 8 & 1 & 2 & 3 & -7 \\ 0 & -5 & 6 & -3 & -4 & 6 & 1 \\ 2 & 8 & -4 & 6 & -9 & -2 & -4 \\ 5 & 8 & 3 & 1 & 9 & -6 & 3 \end{pmatrix},$$

$$B = \begin{pmatrix} -3.9 & 2 & 0.1 & -2.5 & -1 & 2.5 & -1 \\ 0.5 & 0.5 & -1 & -0.5 & 1 & 2 & -0.05 \end{pmatrix}^T,$$

$$C = \begin{pmatrix} 3 & 6 & -5 & -2 & -1 & -7 & 5 \\ -1 & -4 & -7 & -1 & -6 & -5 & -3 \end{pmatrix}.$$

In this example, two different initialization methods are used in the first step, which aims to test whether IPFM is sensitive to the initial value. The first initialization method is shown in our algorithms, which is very simple, but the initial value is not good enough. The second one in [6] is to optimize the initial value by iteration. It is more complex but a better initial value can be obtained.

Using the initialization method in our algorithms, we obtain the initial value

$$F_{01} = \begin{pmatrix} 0.4890 & 0.1910 \\ 0.4440 & 1.4200 \end{pmatrix}$$

and $\alpha_{01} = 49.8330$. After four iterations of small range of perturbation and three iterations of large range of perturbation of IPFM, a SOF gain is found as

$$F = \begin{pmatrix} 0.5663 & 3.5617 \\ -0.0314 & 1.3763 \end{pmatrix},$$

$\alpha = -1.7580$, and the eigenvalues of the closed-loop system are $-20.9826 \pm j25.8332$, $-0.9704 \pm j12.6477$, $-0.9618 \pm j0.0784$ and -5.0692. But the existing path-following method (PFM) cannot find a stabilizing solution.

Using the initialization step in [6], the initial value is obtained

$$F_{02} = \begin{pmatrix} -0.8871 & 4.9310 \\ -0.6576 & 0.9867 \end{pmatrix}$$

and $\alpha_{02} = 0.00079717$. After two iterations of small range of perturbation and 0 iterations of large range of perturbation, a SOF gain F is found as

Table 15.1 The comparison of convergence between IPFM and PFM (Example 1)

Method	Initial value	$\beta = 0.2$	$\beta = 0.5$
IPFM	$\alpha_{01} = 49.8330$ $F_{01} = \begin{pmatrix} 0.4890 & 0.1910 \\ 0.4440 & 1.4200 \end{pmatrix}$	$\alpha = -1.7580$ $F = \begin{pmatrix} 0.5663 & 3.5617 \\ -0.0314 & 1.3763 \end{pmatrix}$	$\alpha = -0.0479$ $F = \begin{pmatrix} 21.7030 & 57.3726 \\ 23.0029 & 60.7208 \end{pmatrix}$
PFM		$\alpha = 10.1310$ $F = \begin{pmatrix} 5.5164 & -0.3290 \\ -0.3591 & 5.5478 \end{pmatrix}$	$\alpha = 51.0277$ $F = 1.0e+006^{*} \begin{pmatrix} 5.7511 & -2.3282 \\ 3.2026 & -1.2965 \end{pmatrix}$

$$F = \begin{pmatrix} -0.8664 & 4.7886 \\ -0.6107 & 0.8197 \end{pmatrix},$$

$\alpha = -1.0250$, and the eigenvalues of the closed-loop system are $-6.6636 \pm j35.4503$, $-0.8788 \pm j12.6648$, -0.5967 and $-4.8248 \pm j6.2698$. In this case, the PFM can also find a solution as

$$F = \begin{pmatrix} -0.7647 & 4.5271 \\ -0.5021 & 0.6122 \end{pmatrix},$$

and $\alpha = -2.7612$.

Table 15.1 shows the comparison of convergence between IPFM and PFM. Let $\beta = 0.2$, both of them are convergent; when the value increases to 0.5, IPFM is still convergent, but PFM will not converge.

The results indicate that IPFM is able to quickly obtain the stable SOF gain under the two initial value. However, PFM can solve the SOF problem under the initial value F_{02} and cannot solve it under the initial value F_{01}. It shows IPFM is not sensitive to the initial values. This is owing to the newly wide range of perturbation step introduced, IPFM has the ability to escape from local optimum.

15.5 Conclusion

In this paper, we have given the improved path-following method. Compared with the existing path-following method, our method is to linearize the BMIs by use of a new linearization approach, which improved convergence to a great extent. Then, by means of adding a wide range of perturbation step, IPFM is able to escape from local optimum. A numerical example is presented to show that the convergence and optimization ability of IPFM are better than PFM.

Acknowledgments This work was supported in part by the National Natural Science Foundation of China (61174033, 61473160) and in part by the Natural Science Foundation of Shandong Province, China (ZR2011FM006).

References

1. Ibaraki S, Tomizuka M (2001) Rank minimization approach for solving BMI problems with random search. In: Proceedings of the American control conference, Arlington, VA, pp 1870–1875
2. Blondel VD, Tsitsiklis JNT (1997) NP-hardness of some linear control design problems, SIAM J Control Signals Syst 35(21):18–27
3. Fukuda M, Kojima M (2001) Branch-and-cut algorithms for the bilinear matrix inequality eigenvalue problem. Comput Optim Appl 19(19):79–105
4. Kawanishi M, Shibata Y (2007) BMI global optimization using parallel branch and bound method with a novel branching method. In: Proceeding of the 2007 American control conference, New York City, USA, pp 1664–1669, 11–13 July 2007
5. Toscano R (2006) A simple method to find a robust output feedback controller by random search approach. ISA Trans 45(1):35–44
6. He Y, Wang QG (2006) An improved ILMI method for static output feedback control with application to multivariable PID control. IEEE Trans Autom Control 51(10):1678–1683
7. Shu Z, Lam J (2008) An augmented system approach to static output-feedback stabilization with H_∞ performance for continuous-time plants. Int J Robust Nonlinear Control 19(7):768–785
8. Cao YY, Lam J, Sun YX (1998) Static output feedback stabilization: an ILMI approach. Automatica 34:1641–1645
9. Xu T, Yang X, Zuo W, Hao L (2010) Fuzzy static output feedback control based on iterative linear matrix inequality. J Jilin Univ (Eng Technol Ed) 40(3):795–799 (in Chinese)
10. Shimomura T, Fujii T (2005) Multiobjective control via successive over-bounding of quadratic terms. Int J Robust Nonlinear Control 15:363–381
11. Hassibi A, How JP, Boyd SP (1999) A path-following method for solving BMI problems in control. In: Proceedings of the American control conference, Evanston, IL, pp 1385–1389
12. Ostertag E (2008) An improved path-following method for mixed $H2/H_\infty$ controller design. IEEE Trans Autom Control 53(8):1967–1971
13. Ostertag E (2008) Continuous-and discrete-time path-following design of mixed *H2/H∞* state-feedback controllers. In: Proceeding of the 17th World Congress: the international federation of automatic control, Seoul, Korea, pp. 3988–3993, 6–11 July 2008
14. Ostertag E (2012) Path-following *H2/H∞* design of dynamic output-feedback controllers via LMI's. In: 51st IEEE conference on decision and control, Maui, Havaii, USA, pp 644–649, Dec 2012

Chapter 16
H-Infinity Quantized Feedback Control for Networked Control Systems with Periodic Scheduling Protocol

Chuan Zhou, Hui Lu and Ronghao Wang

Abstract A novel simultaneous design scheme of H-infinity quantized feedback controller and periodic scheduling protocol for a class of networked control systems (NCSs) with bit rate constraints and time delay is proposed in this paper. A mid-tread uniform quantizers is used and the quantization error is treated as a model uncertainty by utilizing sector-bounded method. Next NCSs is modeled as a discrete-time switched system with parameter uncertainties. The procedures for H-infinity controller design under the static periodic scheduling protocol are given to maintain the asymptotic stability and robust performance of the closed-loop NCSs. Finally a simulation example is given to illustrate effectiveness of the proposed method.

Keywords Networked control systems · Periodic scheduling

16.1 Introduction

Networked control systems (NCSs) have attracted increasing attention in the recent years. However, the introduction of the networked communication channel in control system brings many challenges for the analysis and design of NCSs, such as network-induced delay, packet dropout quantization effect, etc. Consequently, the resource scheduling of networked systems with limited bandwidth have been extensively investigated by many researchers. We refer the reader to [1–3] for the case of nodes scheduling, and [4, 5] for the case of sampling period scheduling.

C. Zhou (✉) · H. Lu
School of Automation, Nanjing University of Science and Technology,
Nanjing 210094, China
e-mail: njust_zc@126.com

R. Wang
College of Defense Engineering, PLA University of Science and Technology,
Nanjing 210007, China

Z. Deng and H. Li (eds.), *Proceedings of the 2015 Chinese Intelligent Automation Conference*, Lecture Notes in Electrical Engineering 337,
DOI 10.1007/978-3-662-46463-2_16

The quantized control is considered as an alternative that has significance on the achievable performance of the networked systems because of networked digital communication channel. In the quantized control systems, the logarithmic static quantizer and the time-variant quantizer have been extensively studied. Nicola investigates design problem of design quantized state-feedback controllers and quantized state estimator, hybrid output-feedback controllers for networked systems by logarithmic quantizers [6]. In [7], the state-feedback and the output-feedback control problem are considered for NCSs involving in signal quantization. In [8], the problems of analysis and synthesis for quantized feedback networked control systems with two time-variant quantizers are addressed, considering the effect of nonideal network environment. The H_∞ controller is designed by using Riccati equation that the systems maintain the asymptotic stability and have good robust performance in [9]. For NCSs with bandwidth-limited, the more control signals need to be scheduled, the few bits are assigned to each signal which leads to the reduction of the quantization precision and vice versa. However, to the authors' best knowledge, taking both scheduling and quantized control into consideration simultaneously have not received enough attention. Therefore, the problem on co-design of the quantized scheduling strategy and feedback control is the motivation of this paper.

16.2 Problem Description

The structure of networked control system is shown in Fig. 16.1, and the plant to be controlled is described by the linear time-invariant system model:

$$\begin{cases} \dot{x}(t) = A_p x(t) + B_p \hat{u}(t) + H_p w(t) \\ y(t) = Cx(t) \end{cases} \tag{16.1}$$

where $x(t) \in R^n$, $\hat{u}(t) \in R^m$ and $y(t) \in R^l$ are the state, control input and controlled output. $w(t) \in R^d$ is disturbance input and $w(t) \in L_2[0, \infty)$. A_p, B_p, H_p and C are constant matrices of appropriate dimensions.

Assumption 16.1 The sensors are time-driven with sampling period h, and controllers and actuators are event driven.

Assumption 16.2 $\tau_k = \tau_k^{sc} + \tau_k^{ca}$ is constant, and $0 < \tau_k < h$.

Assumption 16.3 At each sampling period, at most R bits can be sent through the network with a limited bandwidth.

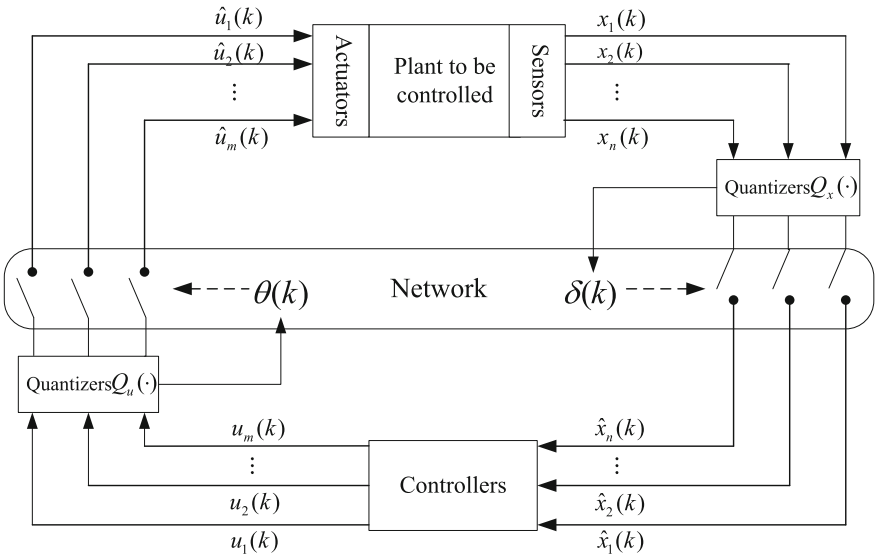

Fig. 16.1 The structure of networked control system

Therefore the discrete time representation of system (16.1) is as follows:

$$\begin{cases} x(k+1) = Ax(k) + B_0\hat{u}(k) + B_1\hat{u}(k-1) + Hw(k) \\ y(k) = Cx(k) \end{cases} \tag{16.2}$$

where $A = e^{A_p h}$, $B_0 = \int_0^{h-\tau_k} e^{A_p t} B_p \mathrm{d}t$, $B_1 = \int_{h-\tau_k}^{h} e^{A_p t} B_p \mathrm{d}t$, $H = \int_0^h e^{A_p t} H_p \mathrm{d}t$.

Considering Assumption 3, the mid-tread uniform quantizers $Q_x(\cdot)$ and $Q_u(\cdot)$ used in this paper are as follows:

$$Q(v) = \begin{cases} L, & \text{if} \quad v > L \\ -L, & \text{if} \quad v < -L \\ \lfloor v/d + 1/2 \rfloor \times d, & \text{otherwise} \end{cases} \tag{16.3}$$

$Q(v)$ uniquely associates to a real scalar $v \in \mathrm{R}$, and a nearest neighbor in the set of reconstruction levels:

$$\left\{ n \cdot d,\ n = 0, \pm 1, \pm 2, \ldots, \pm(2^{p-1} - 1) \right\}$$

where $d = L/(2^{p-1} - 1)$ represents the sensitivity and L represents the quantization range of the quantizer, and $p \in N$ is the number of bits used to reconstruct the quantization precision.

By utilizing the sector bound method to deal with quantization error as follows: $Q_{xi}(x_i(k)) = (1 + \Delta_{xi})x_i(k)$, $Q_{uj}(u_j(k)) = (1 + \Delta_{uj})u_j(k)$, $|\Delta_{xi}| \leq 1$ and $|\Delta_{uj}| \leq 1$.

Considering Assumption 3, introduce the quantization precision vector $P(k) = [p_1(k), p_2(k), \ldots, p_n(k), p_{n+1}(k), \ldots, p_{n+m}(k)]^T \in R^{n+m}$ where $p_i(k)(i = 1, 2, \ldots, n)$ denotes the number of bits sent through network that the ith state variable can obtain. $p_{n+j}(k)(j = 1, 2, \ldots, m)$ describes the number of bits sent through network that the jth control input can obtain. The condition $\sum_{l=1}^{n+m} p_l(k) \leq R$ must be satisfied by Assumption 3.

The scheduling vector $\delta(k) = [\delta_1(k), \delta_2(k), \ldots, \delta_n(k)]^T$ is introduced, and $\delta_i(k) = 1$ when $p_i(k) \neq 0(i = 1, 2, \ldots, n)$, which implies the ith state variable can be transmitted through network after being quantized. $\delta_i(k) = 0$ when $p_i(k) = 0$, which implies the ith state variable can not be transmitted through network due to limited bandwidth and be maintained the last value by used zero-order holders, then we have

$$\hat{x}_i(k) = \begin{cases} Q_{xi}(x_i(k)), & \text{if } \delta_i(k) = 1 \\ \hat{x}_i(k-1), & \text{if } \delta_i(k) = 0 \end{cases} \qquad i = 1, 2, \ldots, n \tag{16.4}$$

Let the diagonal matrix $\Lambda(k) = \text{diag}\{\delta_1(k), \delta_2(k), \ldots, \delta_n(k)\}$, and is recorded as Λ. Then the controller input is described as follows:

$$\hat{x}(k) = \Lambda Q_x(x(k)) + (I - \Lambda)\hat{x}(k-1) \tag{16.5}$$

Similarly, the scheduling vector $\theta(k)$ ($\theta(k) = [\theta_1(k), \theta_2(k), \ldots, \theta_m(k)]^T$) is introduced. $\theta_j(k) = 1$ when $p_{n+j}(k) \neq 0(j = 1, 2, \ldots, m)$, which implies the jth controller output can be transmitted through network after being quantized. $\theta_j(k) = 0$ when $p_{n+j}(k) = 0$, which implies the jth controller output cannot be transmitted through network and be maintained the last value by used zero-order holders. Such that

$$\hat{u}_j(k) = \begin{cases} Q_{uj}\big(u_j(k)\big), & \text{if } \theta_j(k) = 1 \\ \hat{u}_j(k-1), & \text{if } \theta_j(k) = 0 \end{cases} \quad j = 1, 2, \ldots, m \tag{16.6}$$

Let the diagonal matrix $\Pi(k) = \text{diag}\{\theta_1(k), \theta_2(k), \ldots, \theta_m(k)\}$, and is recorded as Π. Then the controlled plant input is described as follows:

$$\hat{u}(k) = \Pi Q_u(u(k)) + (I - \Pi)\hat{u}(k-1) \tag{16.7}$$

From (16.2), (16.4)–(16.7), generalized discrete time model of NCSs is as follows:

$$\begin{cases} x(k+1) = Ax(k) + B_0\hat{u}(k) + B_1\hat{u}(k-1) + Hw(k) \\ y(k) = Cx(k) \\ \hat{x}(k) = \Lambda Q_x(x(k)) + (I-\Lambda)\hat{x}(k-1) \\ \hat{u}(k) = \prod Q_u(u(k)) + (I-\prod)\hat{u}(k-1) \\ Q_x(x(k)) = (I+\Delta_x)x(k) \\ Q_u(u(k)) = (I+\Delta_u)u(k) \end{cases} \tag{16.8}$$

16.3 Quantized Scheduling Strategy and H_∞ Feedback Control

Definition 16.1 [10] (*Periodic Quantization Sequence*) A periodic quantization sequence s^{T-1} of period T, width N and maximal precision M is an infinite sequence $(s_0, s_1, \ldots, s_{T-1}, \ldots)$ of elements of $\{0, 1, \ldots, M\}^N$ verifying $s_{k+iT} = s_k$, $\forall i \in \{0, 1, \ldots, T-1\}$. A periodic quantization sequence is fully characterized by the sequence $s^{T-1} = (s_0, s_1, \ldots, s_{T-1})$.

The state-feedback controllers are of the following form

$$u(k) = K_i\hat{x}(k) \qquad i \in \{0, 1, \ldots, T-1\} \tag{16.9}$$

where $\hat{x}(k) \in R^n$ and $u(k) \in R^m$ are controller input and output, the state gain K_i corresponding to $P_i(k)$ will be designed. The discrete-time periodic switched system model is described as follows:

$$\begin{cases} x(k+1) = Ax(k) + B_0\hat{u}(k) + B_1\hat{u}(k-1) + Hw(k) \\ y(k) = Cx(k) \\ \hat{x}(k) = \Lambda_i Q_x(x(k)) + (I-\Lambda_i)\hat{x}(k-1) \\ \hat{u}(k) = \Pi_i Q_u(u(k)) + (I-\Pi_i)\hat{u}(k-1) \\ Q_x(x(k)) = (I+\Delta_x)x(k) \\ Q_u(u(k)) = (I+\Delta_u)u(k) \\ u(k) = K_i\hat{x}(k) \end{cases} \tag{16.10}$$

Define the augmented vector $z(k) = \begin{bmatrix} x^T(k) & \hat{x}^T(k-1) & \hat{u}^T(k-1) \end{bmatrix}^T$, we can obtain the following closed-loop NCSs model:

$$\begin{cases} z(k+1) = \Phi_i z(k) + \bar{H}w(k) \\ y(k) = \bar{C}x(k) \end{cases} \qquad i \in \{0, 1, \ldots T-1\}. \tag{16.11}$$

$$\Phi_i = \begin{bmatrix} A + B_0\Pi_i(I+\Delta_u)K_i\Lambda_i(I+\Delta_x) & B_0\Pi_i(I+\Delta_u)K_i(I-\Lambda_i) & B_0(I-\Pi_i)+B_1 \\ \Lambda_i(I+\Delta_x) & I-\Lambda_i & 0 \\ (I+\Delta_u)K_i\Lambda_i(I+\Delta_x) & \Pi_i(I+\Delta_u)K_i(I-\Lambda_i) & I-\Pi_i \end{bmatrix}$$
$$= G_i + \bar{B}\Pi_i(I+\Delta_u)K_i(\Lambda_i(I+\Delta_x)I_1 + (I-\Lambda_i)I_2) + I_2^T\Lambda_i(I+\Delta_x)I_1$$

$$\bar{H} = \begin{bmatrix} H \\ 0 \\ 0 \end{bmatrix},\ \bar{C} = [\,C \quad 0 \quad 0\,],\ G_i = \begin{bmatrix} A & 0 & B_0(I-\Pi_i)+B_1 \\ 0 & I-\Lambda_i & 0 \\ 0 & 0 & I-\Pi_i \end{bmatrix},$$
$$\bar{B} = \begin{bmatrix} B_0 \\ 0 \\ I \end{bmatrix},\ I_1 = [\,I \quad 0 \quad 0\,],\ I_2 = [\,0 \quad I \quad 0\,]$$

Definition 16.2 *Let* $\gamma > 0$ be given, the system (16.10) is stable with $H\infty$ performance level γ if there exists a feedback control law $u(k) = K_i\hat{x}(k)$ which need to satisfy the following conditions: (1) The closed-loop system is asymptotical stable without external disturbance. (2) Under the zero-initial condition, the controlled output $y(k)$ satisfies $\|y(k)\|_2 < \gamma\|w(k)\|_2$.

Theorem 16.1 *Based on the above static periodic quantized scheduling strategy and the state-feedback controller* (16.9)*, the closed-loop system* (16.10) *is asymptotically stable with* H_∞ *performance lever* γ*, if there exist a group of symmetrical positive definite matrices* P_i $(i = 0, 1, \ldots, T-1)$*, such that the following LMIs hold*:

$$\begin{bmatrix} P_i & 0 \\ 0 & \gamma^2 I \end{bmatrix} > \begin{bmatrix} \Phi_i & \bar{H} \\ \bar{C} & 0 \end{bmatrix}^T \begin{bmatrix} P_{i+1} & 0 \\ 0 & I \end{bmatrix} \begin{bmatrix} \Phi_i & \bar{H} \\ \bar{C} & 0 \end{bmatrix} \tag{16.12}$$

proof Select the Lyapunov function as $V(z(k)) = z^T(k)P_iz(k)$.

The difference of the Lyapunov functional is given by

$$\begin{aligned} \Delta V(z(k)) &= z^T(k+1)P_{i+1}z(k+1) - z^T(k)P_iz(k) \\ &= z^T(k)\Phi_i^TP_{i+1}\Phi_iz(k) - z^T(k)P_iz(k) \\ &= z^T(k)(\Phi_i^TP_{i+1}\Phi_i - P_i)z(k) \end{aligned}$$

Then

$$\begin{bmatrix} \Phi_i^TP_{i+1}\Phi_i - P_i + \bar{C}^T\bar{C} & \Phi_i^TP_{i+1}\bar{H} \\ \left(\Phi_i^TP_{i+1}\bar{H}\right)^T & \bar{H}^TP_i\bar{H} - \gamma^2 I \end{bmatrix} < 0 \tag{16.13}$$

Since $V(z(\infty)) \geq 0$ and $V(z(0)) = 0$ under the zero-initial condition, then $J < 0$ from (16.13), that is $\|y(k)\|_2 < \gamma \|w(k)\|_2$. Therefore, the closed-loop system (16.10) satisfies H_∞ performance level γ.

Theorem 16.2 *Based on the static periodic quantized scheduling strategy and state-feedback controller* (16.9), *the closed-loop system* (16.10) *is asymptotically stable with* H_∞ *performance lever* γ, *if there exist a group of symmetrical positive definite matrices* X_i, *the state-feedback gain matrices* K_i, *and two sets of scalars* $\alpha_i > 0, \beta_i > 0 (i = 0, 1, \ldots, T-1)$ *such that the following LMIs hold*

$$\begin{bmatrix} -X_i & 0 & (G_i X_i + I_2^T \Lambda_i I_1 X_i)^T & (\bar{C} X_i)^T & 0 & 0 & 0 & 0 & X_i \\ * & -\gamma^2 I & \bar{H}^T & 0 & 0 & 0 & 0 & 0 & 0 \\ * & * & -X_{i+1} + a_i \bar{B} \Pi_i \Pi_i^T \bar{B}^T & 0 & 0 & 0 & \bar{B} \Pi_i K_i \Lambda_i + I_2^T \Lambda_i & \bar{B} \Pi_i K_i L_i & 0 \\ * & * & * & -I & 0 & 0 & 0 & 0 & 0 \\ * & * & * & * & -a_i I & 0 & K_i \Lambda_i & K_i L_i & 0 \\ * & * & * & * & * & -\beta_i I & 0 & \beta_i I_1 & 0 \\ * & * & * & * & * & * & -\beta_i I & 0 & 0 \\ * & * & * & * & * & * & * & -I & 0 \\ * & * & * & * & * & * & * & * & -I \end{bmatrix} < 0 \tag{16.14}$$

where $L_i = [\Lambda_i \quad I - \Lambda_i \quad 0]$ and "*" denote the entries of matrices implied by symmetry.

16.4 Simulation Example

Considering model of the plant to be controlled in the NCS as follows:

$$\dot{x}(t) = \begin{bmatrix} 0 & 2 \\ -2 & -3 \end{bmatrix} x(t) + \begin{bmatrix} -1 & 0 \\ 0 & 1 \end{bmatrix} u(t) + \begin{bmatrix} -0.1 & -0.1 \\ -0.1 & -0.1 \end{bmatrix} w(t)$$

$$y(t) = \begin{bmatrix} 1 & 0 \\ 0 & 1 \end{bmatrix} x(t)$$

In the example, the sampling period $h = 0.02\,\text{s}$ and time delay $\tau_k = 0.004\,\text{s}$,

By giving $\gamma = 2.6$ and solving the LMIs (16.14) in Theorem 16.2, we obtain the controller gain

$$K_1 = \begin{bmatrix} -0.2178 & 0 \\ 0 & -2.869 \end{bmatrix}, K_2 = \begin{bmatrix} -0.2639 & 0 \\ 0 & -0.1986 \end{bmatrix}.$$

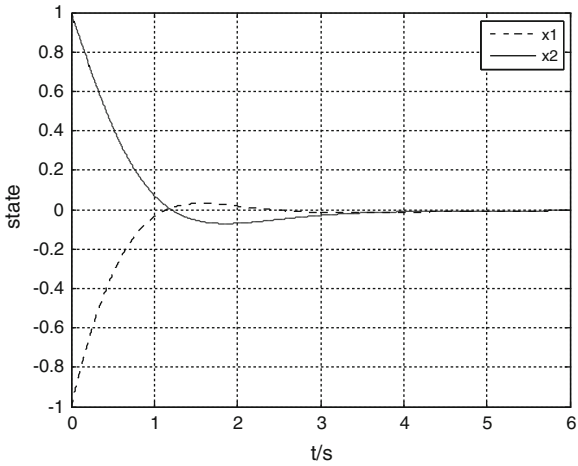

Fig. 16.2 The state response of the NCS

Simulation results are shown in Fig. 16.2. The simulation results show that NCS is asymptotic stable and has good robust performance, which demonstrates the effectiveness of the proposed scheme.

16.5 Conclusions

In this paper, robust quantized control problem for a class of NCSs with bandwidth constraints and time delay is investigated, and a novel simultaneous design scheme of static period scheduling strategy and H_∞ quantized feedback controller is proposed to maintain asymptotical stability of the closed-loop systems. However, the NCSs may have the conservative performance by using the static scheduling strategy, the future work is to investigate a dynamic scheduling strategy to reduce conservative of the systems.

Acknowledgments This research is supported by Graduate Student Innovative Program 2014 in Nanjing University of Science and Technology, China.

References

1. Dacic DB, Nesic D (2007) Quadratic stabilization of linear networked control systems via simultaneous protocol and controller design Automatica 43(7):1145–1155
2. Maurice WP, Heemels H, Teel AR et al (2010) Networked control systems with communication constraints: tradeoffs between transmission intervals, delays and performance. IEEE Trans Autom Control 55(8):1781–1796

3. Song H, Yu L, Zhang WA (2008) Stabilisation of networked control systems with communication constraints and multiple distributed transmission delays. Control Theory Appl 3(10):1307–1316
4. Izák M, Görges D, Liu S (2010) Stabilization of systems with variable and uncertain sampling period and time delay. Nonlinear Anal Hybrid Syst 4:291–305
5. Wang YL, Yang GHH (2008) controller design for networked control systems via active-varying sampling period method. Acta Autom Sinica 34(7):814–818
6. Elia N (2001) Mitter S.K. Stabilization of linear systems with limited information. IEEE Trans Autom Control 46(9):1384–1400
7. Niu YG, Jia TG, Wang X et al (2009) Output-feedback control design for NCSs subject to quantization and dropout. Inf Sci 179:3804–3801
8. Tian EG, Yue D, Peng C (2008) Quantized output feedback control for networked control systems. Inf Sci 178:2734–2749
9. Peng C, Tian YC (2007) Networked H-infinity control of linear systems with state quantization. Inf Sci 177:5763–5774
10. Gaid MEMB, Cela A (2010) Trading quantization precision for update rates for systems with limited communication in the uplink channel. Automatica 46(7):1210–1214

Chapter 17
Wind Speed Estimation and Station-Keeping Control for Stratospheric Airships with Extended Kalman Filter

Shaoping Shen, Ling Liu, Bomin Huang, Xianwu Lin, Weiyao Lan and Huiyu Jin

Abstract Wind speed estimation and station-keeping control for stratospheric airship are studied. A mathematical model of the stratospheric airship flying against the wind is derived. Then using the position information of the airship, an extended Kalman filter (EKF) is designed to estimate the speeds of the airship and the wind. Numerical simulations show the filter is effective and robust so that it can be used in not only wind speed estimation but also station-keeping control of the stratospheric airship.

Keywords Stratospheric airship · Wind speed estimation · Extended Kalman filter · Robustness · Station-Keeping control

17.1 Introduction

The stratosphere airship is an important floated platform which works in about 20 km altitude for a long time with a lot of payload. It can play a role similar to man-made satellite in the fields of communications relay, remote sensing to the ground, and air traffic control. Compared with the satellite, the stratosphere airship which can move in a broader range, without the limitation of the orbit, is helpful to observe more accurately, and has advantages in energy conservation and environmental protection [1–4]. At present many countries, such as the US, Russia, Germany, Britain, Japan, Korea, Israel, and China, are stepping up the research of the stratosphere airship [5–9].

S. Shen (✉) · L. Liu · B. Huang · X. Lin · W. Lan · H. Jin (✉)
Department of Automation, Xiamen University, Xiamen 361005, People's Republic of China
e-mail: shen_shaoping@163.com

H. Jin
e-mail: jinhy@xmu.edu.cn

Z. Deng and H. Li (eds.), *Proceedings of the 2015 Chinese Intelligent Automation Conference*, Lecture Notes in Electrical Engineering 337,
DOI 10.1007/978-3-662-46463-2_17

Wind speed estimation is an important problem of the stratosphere airship. Due to the earth's rotation, there is a strong west wind in mid-latitude stratosphere while the wind speed changes along with the height, the latitude and longitude, and the season. To work in a fixed-point, the airship must overcome the influence of the wind based on solar energy, which requires to measure wind speed near the airship in real time and accurately. Because the stratosphere airship moves slowly, the widely used air anemometer's error is too large to meet the need of theoretical analysis and actual control of the airship. So, it is necessary to investigate a new method to measure of estimate the stratosphere wind speed.

In this paper, the real-time stratosphere wind speed is estimated based on the position information of the airship. As the airship always flies against the wind to reside in a fixed-point, its movement can be simplified to one-dimensional motion of the center of mass. This paper established the one-dimensional motion model of the stratosphere airship, in which the wind speed is a random input while the position of the airship which can be measured by GPS or ground station is the output. Then an extended Kalman filter (EKF), which is used to estimate the current wind speed and speed of the airship is designed. The effectiveness and robustness of the EKF method are validated by numerical simulation.

The structure of this paper is as follows. The airship one-dimensional motion model is established in the second section. In the third section, the current airspeed and wind speed are estimated by EKF. The effectiveness and parameter variation robustness of EKF are proved by numerical simulation in the fourth section. The fifth section presents the application of wind speed estimation in station-keeping control for stratospheric airship.

17.2 The One-Dimensional Motion Model of the Stratosphere Airship

Consider the problem to keep a stratosphere airship which uses the hard airbag structure at a fixed-point in a horizontal plane. Suppose the yawing moment is balanced by the lateral moment produced by the wing propulsion system and the vertical tail so that the airship's head is always against the wind, while the thrust T balances with the wind resistance R and the additional inertia forces R_a. In this case, the model of the airship can be simplified to the one-dimensional motion and the force analysis is shown in Fig. 17.1.

Let m be the mass of airship, x and v_g be the airship displacement and the airship speed respectively. According to Newton's second law, the kinematics equations are

$$\begin{aligned} \frac{\mathrm{d}x}{\mathrm{d}t} &= v_g, \\ m\frac{\mathrm{d}v_g}{\mathrm{d}t} &= T - R - R_a. \end{aligned} \tag{17.1}$$

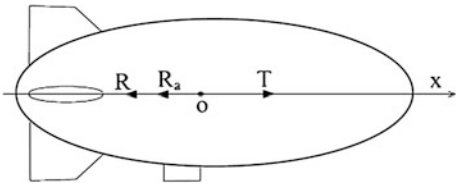

Fig. 17.1 Force analysis of the airship

The resistance and the added mass inertia force are expressed as

$$\begin{aligned} R &= \frac{1}{2}\rho C_x S(v_g + v_w)^2, \\ R_a &= m_0(\dot{v}_g + \dot{v}_w), \end{aligned} \tag{17.2}$$

where v_w, ρ, C_x and S are the wind speed, air density, aerodynamic coefficient, and the airship's reference area. Let m_0 be the add mass which can be calculated as

$$m_0 = k\rho V. \tag{17.3}$$

Let V be the airship volume and k be the inertia factor.

Suppose the stratosphere wind field is composed of constant wind V_a and gust $\omega(t)$. The expression of wind speed is to add these two together [10]

$$v_w(t) = v_a + \omega(t). \tag{17.4}$$

Suppose $\omega(t)$ is a color noise produced by a zero mean white noise source $\eta(t) \sim N(0, Q)$ through the shaping filter [11]

$$\dot{\omega}(t) = \frac{1}{L_H}\omega(t) + \sqrt{\frac{2}{L_H}}\sigma_H \eta(t), \tag{17.5}$$

in which L_H is the longitudinal integral scale of lever wind, σ_H^2 is the variance of wind speed.

Substituting (17.2), (17.3) and (17.4) into (17.1), we have

$$(m + m_0)\frac{\mathrm{d}v_g}{\mathrm{d}t} = T - \frac{1}{2}\rho C_x S(v_g + v_a + \omega(t))^2 - m_0(\dot{v}_a + \dot{\omega}(t)). \tag{17.6}$$

And with (17.5), we get

$$\begin{aligned}\dot{v}_g = &\frac{T}{m+m_0} - \frac{\rho C_x S}{2(m+m_0)}(v_g + v_a + \omega(t))^2 \\ &+ \frac{m_0}{(m+m_0)L_H}\omega(t) - \sqrt{\frac{2}{L_H}}\frac{\sigma_H m_0}{(m+m_0)}\eta(t).\end{aligned} \tag{17.7}$$

Let the state variables be

$$x = (\,x_1 \quad x_2 \quad x_3 \quad x_4\,)' = (\,x \quad v_g \quad v_a \quad \omega(t)\,)',$$

and

$$\begin{aligned}f_2(x) = &\frac{T}{m+m_0} - \frac{\rho C_x S}{2(m+m_0)}(x_2 + x_3 + x_4)^2 \\ &+ \frac{m_0}{(m+m_0)L_H}x_4,\end{aligned} \tag{17.8}$$

$$\mathbf{L} = \left(0 \quad \sqrt{\tfrac{2}{L_H}}\tfrac{\sigma_H m_0}{(m+m_0)} \quad 0 \quad \sqrt{\tfrac{2}{L_H}}\sigma_H\right), \tag{17.9}$$

$$\mathbf{f}(\mathbf{x}) = \left(x_2\ f_2(x) \quad 0 \quad \frac{1}{L_H}x_4\right)', \tag{17.10}$$

Based on the formulas (17.1), (17.5) and (17.7), the system-state equation can be obtained as

$$\dot{\boldsymbol{x}} = \boldsymbol{f}(\boldsymbol{x}) + \boldsymbol{L}\eta(t) \tag{17.11}$$

On the other hand, the airship position can be measured by GPS or ground station, and the output equation of the system is

$$y = x_1 + d(t), \tag{17.12}$$

where $d(t) \sim N(0, R)$ is the measurement error.

17.3 Wind Speed Estimation Based on EKF

17.3.1 Algorithm of EKF

EKF is an effective filter method for nonlinear system [11, 12]. Consider the nonlinear system

$$\begin{aligned} \dot{\mathbf{x}} &= \mathbf{f}(\mathbf{x}) + \mathbf{L}\eta(t), \\ y(t) &= h(x(t)) + d(t), \end{aligned} \tag{17.13}$$

where $\eta(t)$ and $d(t)$ are the system model noise and measurement noise. Discretizing the system (17.13) and assuming the sampling period is Δt, we get

$$\begin{aligned} \boldsymbol{x_k} &= \boldsymbol{\Phi}(\hat{\boldsymbol{x}}_{\boldsymbol{k-1}})\boldsymbol{x_{k-1}} + \boldsymbol{U_{k-1}} + \boldsymbol{v_{k-1}} \\ y_k &= \boldsymbol{H_k}\boldsymbol{x_k} + d_k \end{aligned} \tag{17.14}$$

where

$$\begin{aligned} \boldsymbol{\Phi}(\hat{\boldsymbol{x}}_{\boldsymbol{k-1}}) &= \boldsymbol{I} + \frac{\partial \boldsymbol{f}}{\partial \boldsymbol{x}}\boldsymbol{\Delta t} \\ \boldsymbol{H_k} &= \frac{\partial h}{\partial \boldsymbol{x}'}|_{x=\hat{\boldsymbol{x}}_{\boldsymbol{k-1}}} \\ \boldsymbol{U_{k-1}} &= \left[\boldsymbol{f}(\hat{\boldsymbol{x}}_{\boldsymbol{k-1}}) - \frac{\partial \boldsymbol{f}}{\partial \boldsymbol{x}'}\boldsymbol{\Delta t}\Big|_{x=\hat{\boldsymbol{x}}_{\boldsymbol{k-1}}} \hat{\boldsymbol{x}}_{\boldsymbol{k-1}}\right]\Delta t \end{aligned} \tag{17.15}$$

In formula (17.14), $v_{\mathrm{k}-1}$ and d_k not only contain the model noise and measurement noise, but also an approximation discrete error. The EKF algorithm includes prediction equations and filtering equations [11], the rediction equations are

$$\begin{aligned} \hat{\boldsymbol{x}}_{\boldsymbol{k/k-1}} &= \hat{\boldsymbol{x}}_{\boldsymbol{k-1}} + \boldsymbol{f}(\hat{\boldsymbol{x}}_{\boldsymbol{k-1}})\boldsymbol{\Delta t} \\ y_{k/k-1} &= \boldsymbol{H_k}\hat{\boldsymbol{x}}_{\boldsymbol{k/k-1}} \\ \boldsymbol{P_{k/k-1}} &= \boldsymbol{\Phi}(\hat{x}_{\boldsymbol{k-1}})\boldsymbol{P_{k-1}}\boldsymbol{\Phi}(\hat{\boldsymbol{x}}_{\boldsymbol{k-1}})' + Q_{k-1}\boldsymbol{\Delta t} \end{aligned} \tag{17.16}$$

while the filtering equations are

$$\begin{aligned} \boldsymbol{x_k} &= \hat{\boldsymbol{x}}_{\boldsymbol{k/k-1}} + \boldsymbol{K_k}\left(\boldsymbol{y_k} - \hat{\boldsymbol{y}}_{\boldsymbol{k/k-1}}\right) \\ \boldsymbol{K_k} &= \boldsymbol{P_{k/k-1}}\boldsymbol{H_k'}\left(\boldsymbol{H_k}\boldsymbol{P_{k/k-1}}\boldsymbol{H_k'} - \boldsymbol{R_k}\right)^{-1} \\ \boldsymbol{P_k} &= (\boldsymbol{I} - \boldsymbol{K_k}\boldsymbol{H_k})\boldsymbol{P_{k/k-1}} \end{aligned} \tag{17.17}$$

where, $\hat{\boldsymbol{x}}_{\boldsymbol{k}}$ is the estimation of $\boldsymbol{x_k}$ and

$$\begin{aligned} \mathrm{Cov}[\mathbf{v_k}, \boldsymbol{v_j}] &= \boldsymbol{Q_k}\delta_{kj} \\ \mathrm{Cov}[d_k, d_j] &= \boldsymbol{R_k}\delta_{kj} \end{aligned} \tag{17.18}$$

with the initial values

$$\begin{aligned} \boldsymbol{x_0} &= E\boldsymbol{x}_0 \\ \boldsymbol{P}_0 &= \mathrm{Var}\,\boldsymbol{x}_0 \end{aligned} \tag{17.19}$$

the state $\boldsymbol{x}$ can be estimated through the extended filter equations.

17.3.2 The Wind Speed Estimation by EKF

Plugging (17.10) into (17.15), we have

$$\vec{\Phi}(\boldsymbol{x_{k-1}}) = \begin{pmatrix} \boldsymbol{1} & \boldsymbol{\Delta t} & \boldsymbol{0} & \boldsymbol{0} \\ \boldsymbol{0} & \boldsymbol{1+\Phi_1\Delta t} & \boldsymbol{\Phi_2\Delta t} & \boldsymbol{\Phi_3\Delta t} \\ \boldsymbol{0} & \boldsymbol{0} & \boldsymbol{1} & \boldsymbol{0} \\ \boldsymbol{0} & \boldsymbol{0} & \boldsymbol{0} & \boldsymbol{1-\frac{1}{L_H}} \end{pmatrix} \tag{17.20}$$

in which

$$\begin{aligned} \Phi_1 &= -\frac{\rho C_x S}{(m+m_0)}(x_2+x_3+x_4) \\ \Phi_2 &= -\frac{\rho C_x S}{(m+m_0)}(x_2+x_3+x_4) \\ \Phi_3 &= -\frac{\rho C_x S}{(m+m_0)}(x_2+x_3+x_4) + \frac{m_0}{(m+m_0)L_H} \end{aligned} \tag{17.21}$$

Comparing (17.12) with (17.14), we obtain

$$\boldsymbol{H_k} = \begin{pmatrix} 1 & 0 & 0 & 0 \end{pmatrix}' \tag{17.22}$$

And $\boldsymbol{Q_k}$ and $\boldsymbol{R_k}$ can be calculated based on (17.9) and (17.18) according to the literature [12]

$$\begin{cases} \boldsymbol{Q_k \approx LL'Q\Delta t} \\ \begin{pmatrix} 0 & 0 & 0 & 0 \\ 0 & \frac{2}{L_H}\frac{\sigma_H^2 m_0^2}{(m+m_0)^2}Q\Delta t & 0 & -\frac{2}{L_H}\frac{\sigma_H^2 m_0}{(m+m_0)^2}Q\Delta t \\ 0 & 0 & 0 & 0 \\ 0 & -\frac{2}{L_H}\frac{\sigma_H^2 m_0}{(m+m_0)^2}Q\Delta t & 0 & \frac{2}{L_H}\sigma_H^2 Q\Delta t \end{pmatrix} \\ \boldsymbol{R_k = \frac{R}{\Delta t}} \end{cases} \tag{17.23}$$

Finally, substitute (17.9), (17.21), (17.22) and (17.23) into (17.16) and (17.17), and then carry out iterative operation under the initial condition.

17.4 Numerical Simulations of Wind Speed Estimation

The numerical simulation is adopted to prove the effectiveness of EKF in this section. First, the accuracy of the method is proved by supposing that the model parameters are known accurately. Then the situation of the error model parameters verifies the robustness of this method.

17.4.1 The Situation of Accurate Model Parameters

The model parameters are taken as Table 17.1. The initial condition is $\boldsymbol{x}_0 = [0, 0, 5, 0]^T$, $\boldsymbol{P}_0 = \text{diag}([1 \quad 1 \quad 1 \quad 1])$. The actual values of airship displacement, velocity, and wind speed can be calculated by the airship movement model and the wind speed model, which are shown in Figs. 17.2 and 17.3, while their estimation values can be obtained through the EKF algorithm. The deviation between the estimations and the actual values is shown in Fig. 17.4. As can be seen, the error is almost zero after 50 s, which shows that the EKF filter is effective.

Table 17.1 Parameter identification

Parameter value	Parameter value
m 2.300×10^4(kg)	C_x 5.500×10^2
m_0 6.200×10^3(kg)	v_a 1.000×10 (m/s)
S 8.100×10^3(m^2)	σ_H 4.119×10^{-1}
T 9.000×10^3(N)	L_H 3.000×10^3(kg)
Δt 1.000×10^{-1}(s)	ρ 8.800×10^{-3}
Q 1.000	R 1.0×10

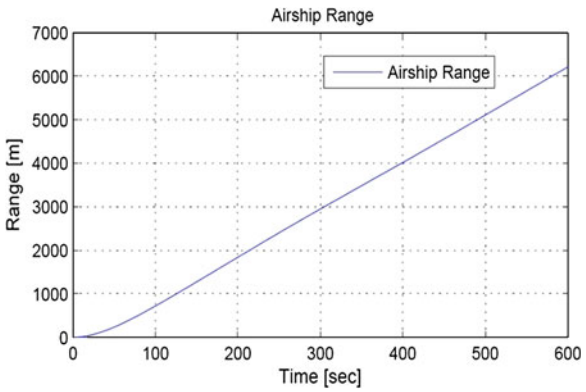

Fig. 17.2 The displacement of airship

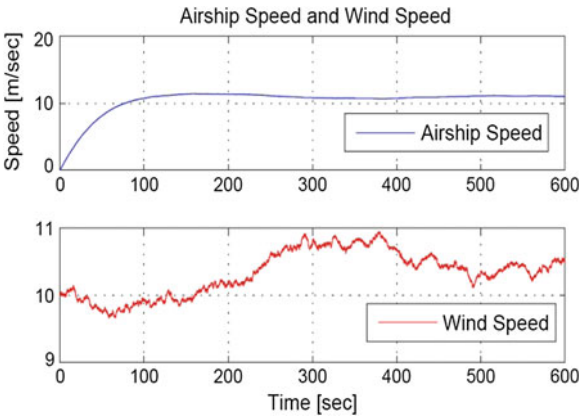

Fig. 17.3 The airship speed and the wind speed

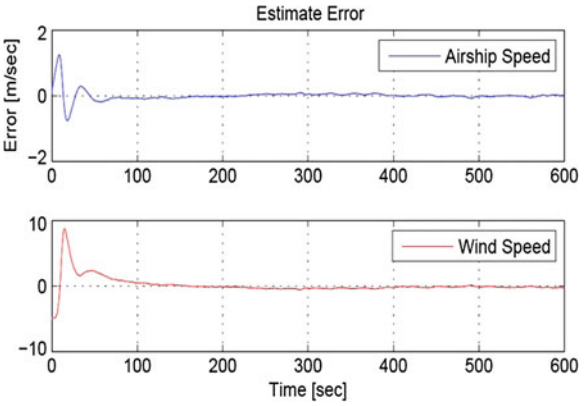

Fig. 17.4 The estimation error of EKF

17.4.2 The Error of Model Parameters

First, consider that the structural parameters of the airship error exists. The other airship parameters are accurate except the add mass. Its true value is $m_0 = 3.000 \times 10^3(\text{kg})$. The estimation errors of the airship speed and wind speed are shown in Fig. 17.5, which indicates that EKF is robust to the add mass error.

Second, assume that the wind speed model parameters, such as the wind speed variance and the wind speed longitudinal integration scale, are not accurate. Their true values are $\sigma_H = 8.000 \times 10^{-1}, L_H = 6.000 \times 10^2$. The estimation errors of the airship speed and wind speed are shown in Fig. 17.6, which shows that the measurement method of EKF is robust to these two parameters.

Finally, consider the aerodynamic parameter C_x exists error and its real value is $C_x = 6.500 \times 10^{-3}$. The measurement errors of the wind speed and the airship speed are shown in Fig. 17.7. From the figure, the airship speed can be still

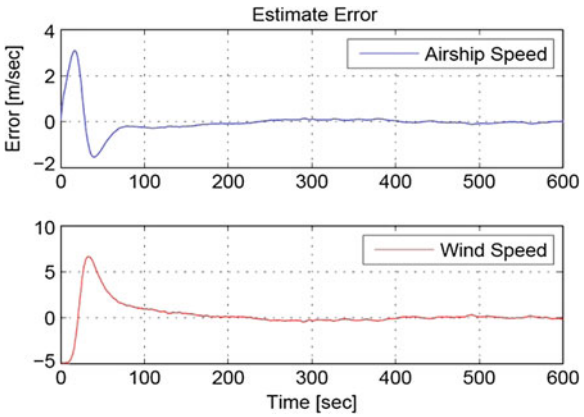

Fig. 17.5 $m_0 = 3.000 \times 10^3(\text{kg})$ estimation error

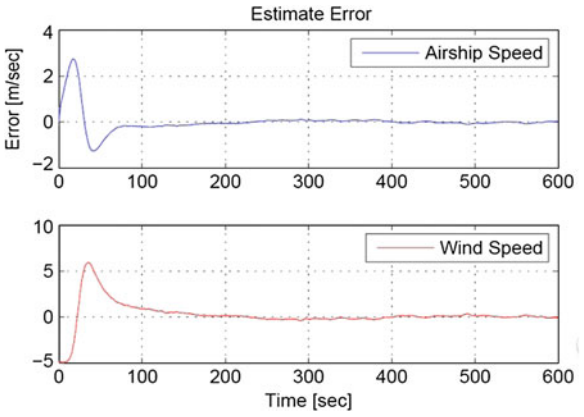

Fig. 17.6 $\sigma_H = 8.000 \times 10^{-1}, L_H = 6.000 \times 10^2$ estimation error

estimated accurately by the filter, but there exists error to estimate the wind speed. It indicates that the EKF is sensitive to the aerodynamic parameter error. To measure the wind speed accurately, we need more in-depth study of the aerodynamics to calculate C_x precisely.

17.5 The Station-Keeping Control with Wind Speed Estimation

The method of wind speed estimation based on EKF is applied to the station-keeping control for stratospheric airship in this section. Assume that the airship is located at -2 km at initial moment and is expected to be controlled and

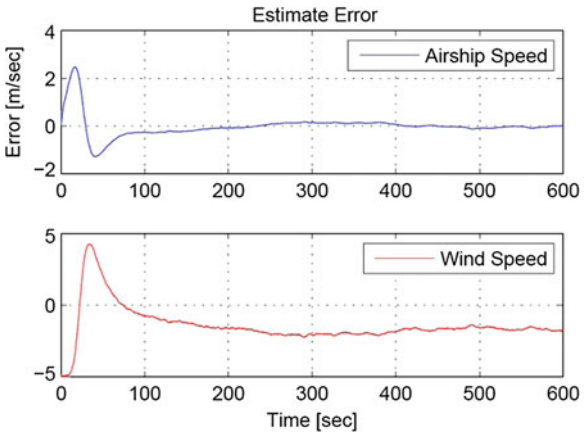

Fig. 17.7 $C_x = 6.500 \times 10^{-3}$ estimation error

resided near the origin. In this case, a saturated PD wind speed controller is adopted

$$T = K_p(r - \hat{x}_1) + K_d\hat{x}_2 + \hat{R} + \hat{R}_a \tag{17.24}$$

in which K_p is the proportionality factor, K_d is the differential coefficient, r is the target position.

A saturated unit

$$T = \begin{pmatrix} 0 & M \le 0 \\ M & 0 \le M \le 9000 \\ 9000 & M \ge 9000 \end{pmatrix}$$

is following the PID controller. Let

$$\begin{aligned} \hat{R} &= \frac{1}{2}\rho C_x S(\hat{x}_2 + \hat{x}_3 + \hat{x}_4)^2, \\ \hat{R}_a &= m_0(\dot{\hat{x}}_2 + \dot{\hat{x}}_4), \end{aligned} \tag{17.25}$$

where $\hat{x}_1, \hat{x}_2, \hat{x}_3, \hat{x}_4$ are the outputs of the filter. $\dot{\hat{x}}_2$ and $\dot{\hat{x}}_4$ are obtained from $\hat{x}_2$ and $\hat{x}_4$ through the finite difference. The control structure of the whole closed-loop simulation system is shown in Fig. 17.8.

Let $K_p = 300$, $K_d = 20{,}000$ and other accurate model parameters are known. A numerical simulation is employed to the station-keeping control.

The displacement of airship and the controller output are shown in Fig. 17.9. Figure 17.10 is the magnification of displacement when the airship arrives at the origin. The red curve represents the actual displacement while the green curve represents the filter estimated value. It can be seen that the error is almost zero.

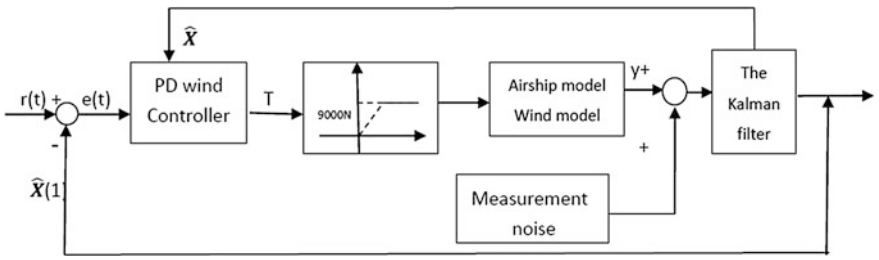

Fig. 17.8 Closed-loop simulation system of the airship station-keeping control

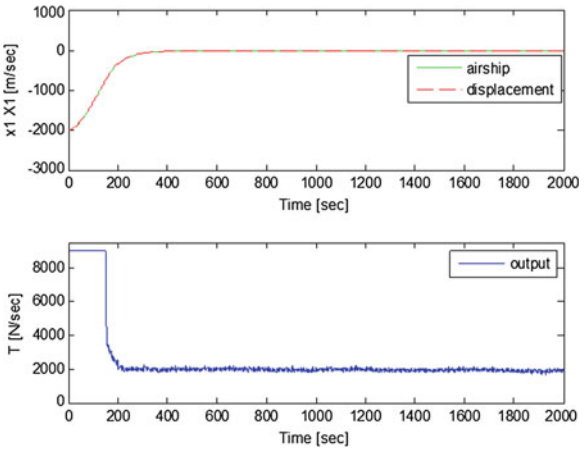

Fig. 17.9 The airship displacement and the controller output (The controller with wind speed estimation)

There is a small deviation between the actual value and the estimated value. Besides, the airship can be controlled and resided near the origin by using PD controller with the estimated wind speed. The deviation between the airship displacement and origin is within 5 m. The controller is a simple saturated PD controller without adding the estimated wind speed as follows:

$$T = K_p(r - \hat{x}_1) + K_d\hat{x}_2 \tag{17.26}$$

K_p, K_d are known. The airship displacement and the controller output shown in Fig. 17.11. Figure 17.12 is a partial amplification of the airship displacement near the origin. As can be seen from the figure, the deviation between the airship position and the origin is within 10–15 m, which is significantly greater than the control results of the PD controller with wind speed estimation. Therefore, it is necessary to estimate the wind speed and apply it to the station-keeping control of stratospheric airship.

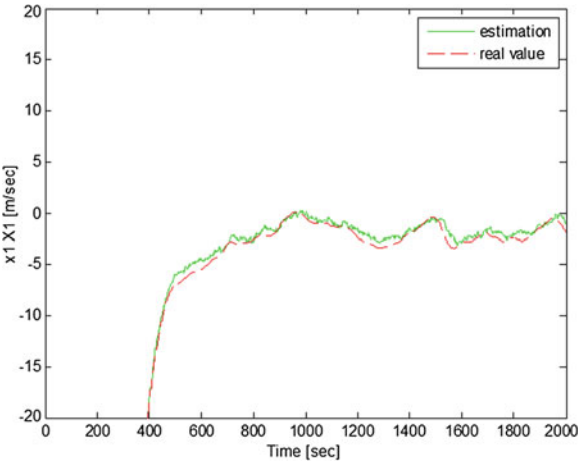

Fig. 17.10 The enlarge of the real and estimated displacement (The controller with wind speed estimation)

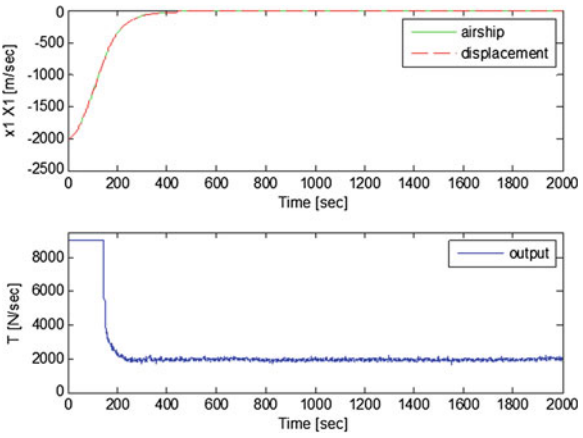

Fig. 17.11 The airship displacement and the controller output (The controller without wind speed estimation)

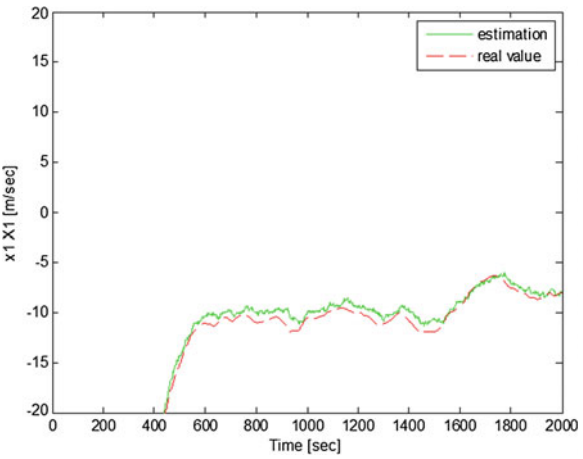

Fig. 17.12 The enlarge of the real and estimated displacement (The controller without wind speed estimation)

17.6 Conclusion

This paper proposes to estimate the stratospheric wind speed and the airship speed with the position information of the airship. The EKF is designed based on the one-dimensional motion model of the airship. Numerical simulations show that EKF is accurate in estimating wind speed, has robustness against some model parameters' uncertainty, and can be used in the station-keeping control of the airship. These results provide a foundation for further studies of wind speed estimation and station-keeping control of stratospheric airship.

References

1. Li Z, Wu L, Zhang J (2012) Review of dynamics and control of stratospheric airships. Mech Prog 42(4):482–493 (in Chinese)
2. Fan C (2005) A new develop mobile communication—the research of stratospheric communications. Mod Electron Technol 210(19):1–3 (in Chinese)
3. Khoury GA, Gillett JD (1999) Airship technology. Cambridge University Press, London
4. Toshitaka T, Takashi A (2001) Effects of meteorological condition the operation of a stratospheric platform. In: The 3 rd Stratospheric Platform System Workshop, Tokyo, Japan
5. Nayler A (2003) Airship activity and development world-wide. AIAA 2003–6727
6. Sano M, Komatsu K, Kimura J et al (2003) Airship shaped balloon test flights to the stratosphere. AIAA 2003–6798
7. Harada K, Eguchi K, Sano M et al (2003) Experimental study of thermal modeling for stratospheric platform airships. AIAA 2003–6833
8. Lin X, Hong L, Lan W (2013) One dimensional trajectory optimization for stratospheric airship with varying thruster efficiency. In: 10th IEEE International Conference on. IEEE, pp 378–383
9. Hong L, Lin X, Lan W (2014) Mode switch sequence analysis on one-dimensional trajectory optimization of stratospheric airships. Control Int Syst 42(2):151–158
10. Nichita C, Luca D, Dakyo B et al (2002) Large band simulation of the wind speed for real time wind turbine simulators. IEEE Trans Energy Convers 17(4):523–529
11. Xu M, Ding S (2003) Flight Dynamics. Science Press. Beijing, China, pp 14–26 (in Chinese)
12. Qin Y, Zhang H, Wang S (2012) Kalman filter and the principle of integrated navigation (the second edition). Northwestern Polytechnic University Press, Xi'an (in Chinese)

Chapter 18
Integral Sliding Mode Control for Vehicle-Mounted Gyro-Stabilized Platform Based on Extended State Observer

Haoze Sun, Tianqing Chang, Junwei Chen, Lei Zhang and Kuifeng Su

Abstract For the problems of system performance degradation caused by nonlinearity such as friction and parameter varieties to a system, an integral sliding mode controller for vehicle-mounted gyro-stabilized platform based on extended state observer (ESO) was proposed. An error integral compensation term was introduced in the sliding surface base on the state variables in order to reduce the steady-state error and break through the restrictions that the derivative of the tracking signal must be known. The ESO was introduced to estimate and compensate the inner and outer disturbances of the system. This helps to reduce the required value of switching gain for the sliding mode control method,which can reduce the chattering phenomenon of system. The simulation and experiment result shows that the method can restrain the influences caused by the diversified nonlinearity, and can improve the system performance effectively.

Keywords Steady sighting system · Nonlinearity disturbance · Integral sliding mode control · Extended state observer

18.1 Introduction

In vehicle-mounted environment, the carrier vibration in the azimuth and elevation direction induces the line of sight (LOS) shaking, which influences the precise of target tracking. Therefore, the LOS stabilized technology must be used to keep the

H. Sun (✉) · T. Chang · J. Chen · L. Zhang · K. Su
Department of Control Engineering, Academy of Armored Force Engineering, PLA No 21, Dujiakan, Fengtai, Beijing, China
e-mail: 22587286@qq.com

Z. Deng and H. Li (eds.), *Proceedings of the 2015 Chinese Intelligent Automation Conference*, Lecture Notes in Electrical Engineering 337,
DOI 10.1007/978-3-662-46463-2_18

LOS stabilization in the inertial space. Currently, the vehicle-mounted LOS stabilization mainly adopts the gyro-stabilized platform structure, which uses gyro as sensitive elements of the space rate-sensitive to measure platform-axis angular motion and drive the torque motor to offset the disturbance torque. It guarantees the stability of LOS in inertial space and realizes the accurate tracking of the input signal [1].

Vehicle-mounted gyro-stabilized platform is a complex system within the essence of nonlinear characteristics. Some factors, such as friction, imbalance torque, parameters drift, etc., have a serious impact on system performance. At the same time, with the developing requirement of stable precision, anti-interference ability and others to a system, the classic PID control algorithm is more and more difficult to meet the requirements. In recent years, scholars have carried out extensive research on this problem and proposed many control methods, such as H_α control, equivalent compound control, intelligent control, etc. [2–4]. These methods have achieved certain results in theory. However, a majority of these algorithms are too complex and difficult to be realized in practice. By combining the sliding mode controller (SMC) and ESO with respective advantages, an integral sliding mode controller (ISMC) based on ESO was proposed in this paper. An error integral compensation term was introduced in the sliding surface based on the state variables in order to reduce the steady-state error and break through the restrictions that the derivative of the tracking signal must be known. The ESO was introduced to estimate and compensate the inner and outer disturbances of the system, which helps to reduce the SMC chattering phenomenon of system. Finally, the simulation and experiment results show that the method is effective and feasible.

18.2 The Mathematical Model of Stabilized Platform

This equipment is mainly composed of a two degree of freedom flexible gyroscope, DC torque motor, PWM power amplifier, bearing solver, 1/2 belt transmission mechanism, platform frame, and upper mirror. The system control loop is made up of azimuth and elevation servo systems, which have the same structure and work independently when ignoring the influence of the shaft coupling. To pitch servo system, for example, all the devices can be considered as linear and proportional except the compensator and DC motor. Then the model of pitching control loop can be described as Fig. 18.1.

In Fig. 18.1, K is the gain of pre amplifiers, sensors, amplification, and demodulator. R_a is the total resistance of the armature circuit. $G_C(s)$ is stabilization loop controller. M_d is disturbance torque. J_M is the moment of inertia. K_m and C_e denote torque coefficient and electromotive force coefficient, respectively. $\theta_r(t)$ and $\theta(t)$ denote the input and output signal of system, respectively.

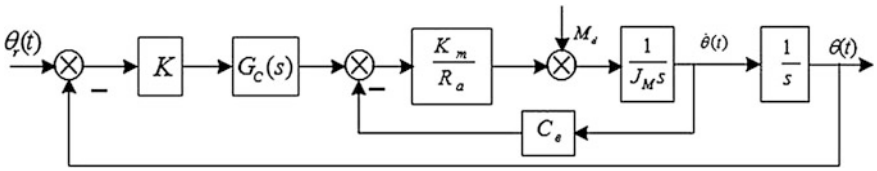

Fig. 18.1 Model of pitching control loop

In vehicle-mounted environment, stable platform is usually influenced by many nonlinear disturbance torques, including friction, mass unbalance torque, etc. The friction torque, which is one of the mainly disturbance factors and has the obvious nonlinear characteristic, can reflect the influence of disturbance torques on system performance adequately. Therefore, the Stribeck friction model is added to the simulink model. The friction model can be described as

$$M_f(\dot{\theta}) = [M_c + (M_s - M_c) \cdot \mathrm{e}^{-\alpha|\dot{\theta}|}]\mathrm{sgn}\left(\dot{\theta}\right) + K_v \cdot |\dot{\theta}| \tag{18.1}$$

where M_s and M_c denote the maximum static friction torque and the coulomb friction torques, $\dot{\theta}(t)$ denotes the rotation angular velocity, K_v denotes the viscous friction coefficient.

Taking the friction model into system model, considering the influence of system disturbance factors such as parameter perturbation, external load disturbance factors, etc., and assuming $\theta(t)$ and $\dot{\theta}(t)$ as state variables, then the system state equations can be defined as

$$\begin{cases} \dot{x}_1 = x_2 \\ \dot{x}_2 = (a + \Delta a)x_2 + (b + \Delta b)u + cM_f + U_T \\ y = x_1 \end{cases} \tag{18.2}$$

where a equals $-\frac{C_e K_m}{J_m R_a}$, b equals $\frac{KK_m}{J_m R_a}$, c equals $\frac{1}{J}$, Δa and Δb denote variation of system parameters, M_f denotes friction torque, U_T denotes nonideal current and other uncertainties. Assuming d equals $\Delta a\dot{\theta} + \Delta bu + cM_f + U_T$, then the system state equations can be described as

$$\begin{cases} \dot{x}_1 = x_2 \\ \dot{x}_2 = f(X,t) + bu(t) + d(t) \\ y = x_1 \end{cases} \tag{18.3}$$

18.3 ISMC Controller Design Based on Extended State Observer

18.3.1 Integral Sliding Surface Design Based on the State Variable

Traditional sliding mode controller usually uses switching surface based on error term, which not only need to know the expectation output of system, but also need to know its derivatives of each order. If one of the derivatives signals does not exist, the designed controller will be noneffective. In order to eliminate the derivatives items of output in the controller, the tracking error item was introduced into switching function, the error term was replaced by state variable [5]. For system (18.3), the integral sliding surface based on state variable can be designed as

$$\sigma(X,t) = \lambda x_1 + x_2 + k\int_0^t e\mathrm{d}\tau \tag{18.4}$$

where λ, k are constants. For (18.4), the derivative can be obtained:

$$\dot{\sigma}(X,t) = \lambda x_2 + \dot{x}_2 + k(x_1 - y_d) \tag{18.5}$$

Assuming the disturbance of system (18.3) is bounded and meets the equation $|d(t)| \leq D$. While the switching gains $k_1 > D$, the controller can be designed as

$$u(t) = -\frac{1}{b}[f(X,t) + \lambda x_2 + k(x_1 - y_d) + k_1 \mathrm{sgn}(\sigma(X,t))] \tag{18.6}$$

Taking $\dot{\sigma}(X,t) = 0$ into Eq. (18.5) and considering (18.3):

$$\dot{V}_d = -|\sigma|(k_1 - d(t)) \tag{18.7}$$

According to the assumption $k_1 > D \geq d(t)$, while $\sigma(X,t) \neq 0$, the Lyapunov stabilization equation $\dot{V}_d < 0$ can be met. So the sliding mode control system is asymptotically stable, namely the existence and accessibility of sliding mode can be met. Meanwhile, the controller did not include the derivative term of the output which break through the restrictions that the derivative of the tracking signal must be known.

18.3.2 Chatter Weakened Based on Extended State Observer

When the bound of system disturbances was known, the integral sliding mode control strategy (18.6) can achieve good control effect. However, the disturbance factors of stabilized platform are numerous and difficult to confirm the variation

range of the system disturbances. If we design the controller according to the worst condition, the switch gain need to be big enough to eliminate the effects of disturbances, which is easy to cause high-frequency chattering on the switching surface [6]. ESO is a kind of observer with superior performance. According to the input and output data of controlled object, the disturbances could be estimated and compensated by ESO in real time. ESO can be divided into linear and nonlinear. To facilitate the adjustment of the parameters, this paper adopts linear extended state observer form. Based on integral sliding mode control strategy (18.6), using ESO to estimate and compensate the total disturbances of the system, the sliding model chattering of system could be weakened effectively.

For system (18.3), the linear ESO could be designed as

$$\begin{cases} \dot{\tilde{x}}_1 = \tilde{x}_2 + l_1(x_1 - \tilde{x}_1) \\ \dot{\tilde{x}}_2 = \tilde{x}_3 + l_2(x_1 - \tilde{x}_1) + bu \\ \dot{\tilde{x}}_3 = l_3(x_1 - \tilde{x}_1) \end{cases} \tag{18.8}$$

The estimate of variable is achieved by $\dot{\tilde{x}}_1$, $\dot{\tilde{x}}_2$ while $\dot{\tilde{x}}_3$ estimate the total disturbance. $L = [l_1, l_2, l_3]^T$ denotes the gain matrix, which determines the accuracy of the observer. According to the bandwidth parametric method in literature [7], the characteristic polynomial of observer (18.8) can be expressed as

$$\lambda(s) = s^3 + l_1 s^2 + l_2 s^2 + l_3 = (s + \omega_0)^3 \tag{18.9}$$

Therefore, ω_0 is the only parameter which need to be set in ESO. Generally, with the increasing of ω_0, the observer is getting more accurate, while the observation noise will also increase. So ω_0 should compromise between control performance and noise resistance.

Then, the integral sliding mode control strategy compensating by ESO can be designed as

$$u(t)^* = -\frac{1}{b}[f(X,t) + \lambda x_2 + k^*(x_1 - y_d) + k_1 \mathrm{sgn}(\sigma(X,t)) + \dot{\tilde{x}}_3] \tag{18.10}$$

where $\dot{\tilde{x}}_3$ means the estimated value of disturbance $d(t)$. Assuming $d(t) - \dot{\tilde{x}}_3$ is bounded and meet the condition: $\left|d(t) - \dot{\tilde{x}}_3\right| \le D^*$, when $k_1^* > D^*$, it can be proved that the sliding mode control system is asymptotically stable.

Meanwhile, comparing the switching surface of (18.6) and (18.10):

$$\dot{\sigma} = -k_1 \mathrm{sgn}(\sigma) + d(t) \tag{18.11}$$

$$\dot{\sigma} = -k_1^* \mathrm{sgn}(\sigma) + (d(t) - \dot{\tilde{x}}_3) \tag{18.12}$$

Obviously, the disturbance of system changes to $d(t) - \dot{\tilde{x}}_3$ after compensating by ESO, the upper bound D^* of $d(t) - \dot{\tilde{x}}_3$ is much smaller than D of $d(t)$. Therefore, under the premise of not sacrificing the robustness of system, the switching gain of (18.10) could be smaller, which weaken the sliding mode chattering significantly.

18.4 Simulation and Experimental Result Analysis

18.4.1 Numerical Simulation Analysis

According to Fig. 18.1, the system simulation model was established in Matlab/Simulink simulation environment. The input signal was assumed as $\omega_d = 20 \sin t(\text{m rad/s})$ and the variation of rotational inertia J_m was assumed as 10 %. PID controller, ISMC, and integral sliding mode controller based on extended state observer observing compensation (ISMC + ESO) were used for system simulation.

Here, the friction torque and its observed value by ESO are shown in Figs. 18.2 and 18.3, respectively. Comparing these two figures, the results show that ESO has good tracking ability, also can track and estimate the disturbance accurately in real time.

Figures 18.4, 18.5 and 18.6 display the position tracking, velocity tracking, and controlling output by three methods, respectively. From Fig. 18.4, PID control strategy cannot restrain the influence of nonlinear interference factors, because position tracking curve exists "flat top" phenomenon and speed tracking curve exists "dead zone" phenomenon. ISMC has certain control effect for nonlinear disturbance factors, the position tracking is high-precision. However, due to the big switching gain, there is chattering phenomenon in the speed tracking and controlling output curve, which is shown obviously in Fig. 18.6b. As is shown in

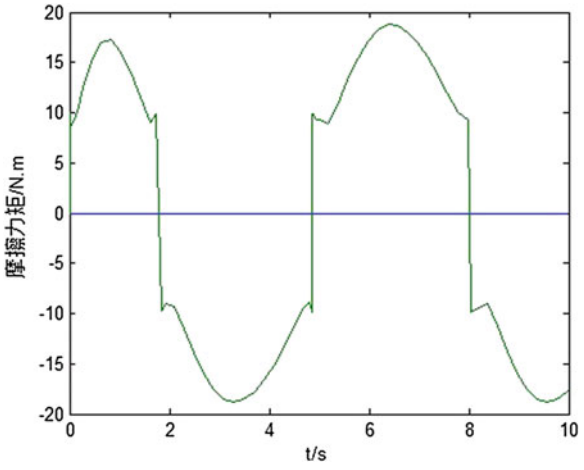

Fig. 18.2 Friction moment

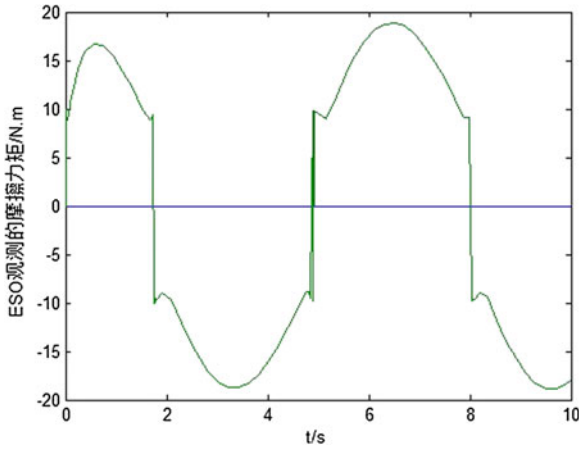

Fig. 18.3 Friction moment observed by ESO

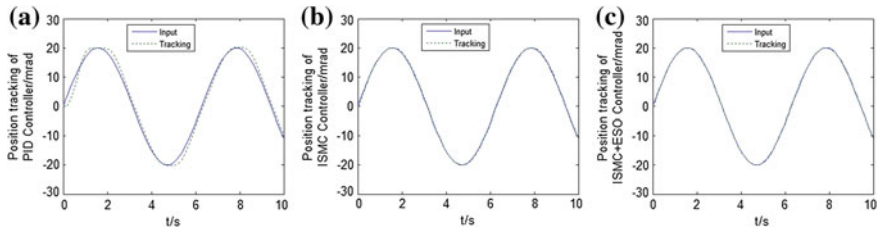

Fig. 18.4 Curve of velocity tracking. **a** PID controller. **b** ISMC controller. **c** ISMC + ESO controller

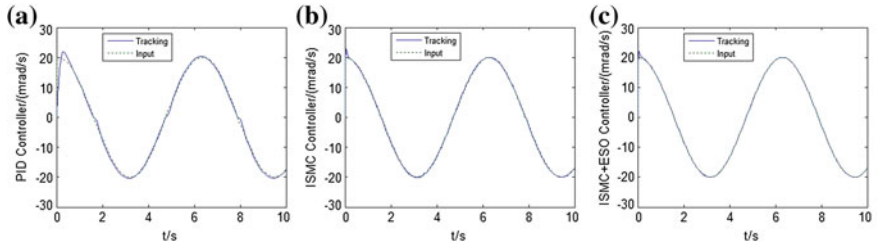

Fig. 18.5 Curve of position tracking. **a** PID controller. **b** ISMC controller. **c** ISMC + ESO controller

Fig. 18.6, after compensating by ESO, with smaller switching gain, position tracking and velocity tracking can achieve higher accuracy while controlling output changes smooth. This indicates that the chattering existed in ISMC was restrained effectively.

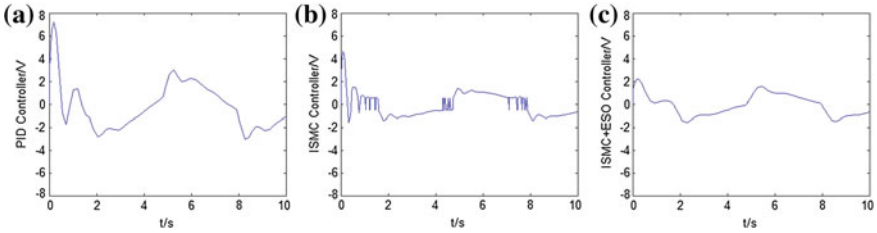

Fig. 18.6 Curve of controller output. **a** PID controller. **b** ISMC controller. **c** ISMC + ESO controller

18.4.2 Platform Experimental Analysis Test

The experimental mechanism adopts digital control scheme. A DSP-TMS320F28335 was used as the main control chip to realize the control algorithm and parameter adjustment. Considering the carrier disturbance is nonlinear perturbation whose amplitude and frequency are less than 10° and 1 Hz [8], respectively, we drive the swing table to do sine motion with amplitude of 10° and frequency of 1 Hz. For examining the transient and steady state, PID and ISMC + ESO controller strategy are tested with both tracking and stabilization experiments.

Figure 18.7 shows the speed tracking curves for two controllers due to sine input. It shows that the tracking curve of PID controller exists obviously crawl and distortion phenomenon due to the influence of nonlinear disturbance factors, while the ISMC-ESO controller can restrain the influence of nonlinear disturbance factors

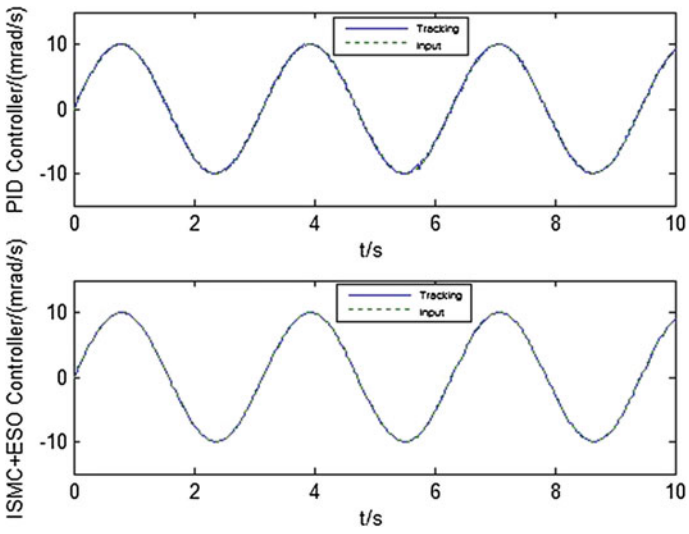

Fig. 18.7 Sine tracing curve

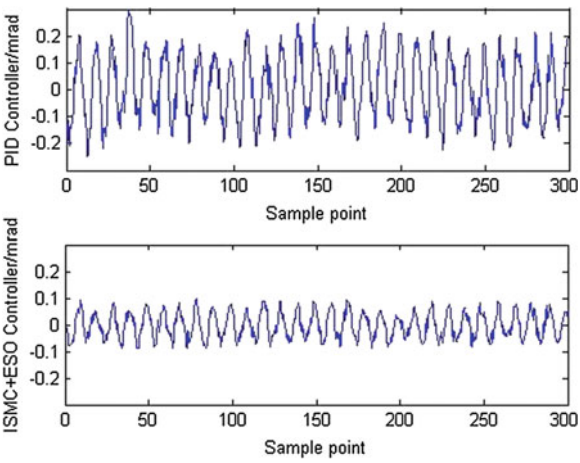

Fig. 18.8 LOS stabilization error

and keep a high tracking accuracy. Figure 18.8 displays the stabilization precision while aiming at a static target. From this figure, we can see that the using of ISMC-ESO controller can significantly improve the stability accuracy of the system. The maximum stable error is 0.1 mil and can meet the design requirements.

18.5 Conclusions

For problems of system performance degradation caused by nonlinearity such as friction and parameter varieties to a system, an integral sliding mode controller for armored vehicles steady sighting system based on ESO was proposed to replace the PID controller. The controller combines the advantages of integral sliding mode control and extended state observer, and has the characteristics of simple structure, easy realization and strong robustness, etc. The simulation and experiment result show that ESO could compensate the system disturbance accurately and restrain the slide model chattering effectively; the ISMC-ESO controller can restrain the non-linear disturbance caused by carrier and significantly improve the stability accuracy.

References

1. Jing-fu ZHU (2003) Modern tank fire control system. National Defense Industry Press, Beijing (in Chinese)
2. Marathe R, Moorty JARK, Sule' VR (2002) H_α control low for line-of-sight stabilization for mobile land vehicle. Opt Eng (41):2935–2944
3. Li R , Jilkov VP (2002) Survey of maneuvering target tracking. part I: Dynamic models. IEEE Trans. Aerosp Electron Syst (4):1333–1364

4. Jing-qing HAN (1998) Auto-disturbances-rejection controller and it's application. Control Decis 1:20–23 (in Chinese)
5. Guan C (2005) Sliding mode adaptive control of non linear system and application to electro-hydraulic control system. College of Electrical Engineering Zhejiang University, Hangzhou (in Chinese)
6. Kim BK, Chung WK, Ohba K (2009) Design and performance tuning of sliding-mode controller for high-speed and high-accuracy positioning systems in disturbance observer framework. IEEE Trans Ind Electron 10:3798–3809
7. Gao Z (2003) Scaling and bandwidth-parameterization based controller turning. In: Proceedings of American control conference, pp 4989–4996
8. Qiu X, Dou L, Shan D et al (2010) Design of active disturbance rejection controller for electro-optical tracking servo system. Opt Precis Eng 1:220–226 (in Chinese)

Chapter 19
Robust H_∞ Fuzzy Dynamic Output Feedback Control of Nonlinear NCS and Its Application

Qingfeng Wang and Hongbo Wang

Abstract The problem of time delay induced by communication channel in nonlinear networked control system (NCS) is studied. The nonlinear plant is modeled by a T-S fuzzy model and the time delays are modeled by a finite state Markov process with partially known transition probability matrix. The controller's member functions and premise variables can be different with those of the plant. The membership functions are approximated as polynomial functions and incorporated into the design of a fuzzy output feedback controller which can be computed in terms of a sum of square inequalities. Using the software NS2 to simulate real networked performance, we designed and implemented a real-time simulation platform for NCS. A truck–trailer experiment was carried out on the platform and the simulations have demonstrated the effectiveness of the proposed approach.

Keywords Networked control system · Fuzzy control · Transmission delay · Markov process · Transition probability matrix

19.1 Introduction

Markov chain has been proven to be very effective in modeling delays in NCS. The transition probability matrix is assumed completely known and the overall system becomes a Markov jump system in [1]. But in practical it is very costly or impossible to obtain a completely known transition probability matrix. In [2, 3], the unknown transition probabilities are modeled as polytope uncertainties and show that their approach is less conservative. However, none of the aforementioned approaches consider NCSs where the Markov chain models the network-induced delays between the system components.

Q. Wang (✉) · H. Wang
College of Electronics Science and Engineering, Jilin University,
Qianjin Street 2699, Changchun 130012, China
e-mail: wangqf@jlu.edu.cn

Z. Deng and H. Li (eds.), *Proceedings of the 2015 Chinese Intelligent Automation Conference*, Lecture Notes in Electrical Engineering 337,
DOI 10.1007/978-3-662-46463-2_19

It is well known that the dynamic of nonlinear systems can be represented with T-S fuzzy model. The controller gains can be common regardless of local linear systems if the premise variables in T-S fuzzy plant and controller are asynchronous [4]. However, the recent research of controller design such as [5, 6] did not include membership functions. The major disadvantage of disregarding them is that the obtained controller is valid for any membership functions, leading to severe conservatism. So it is significant to investigate ways to incorporate membership functions in the controller design.

19.2 Networked Control System Description

The nonlinear plant is to be controlled and described by the T-S fuzzy model

$$\text{IF} \quad \theta_1(x(k)) \text{ is } J_1^g \text{ AND } \cdots \text{ AND } \theta_p(x(k)) \text{ is } J_p^g,$$
$$\text{THEN} \begin{cases} x(k+1) = \left[A_g + \Delta A_g(k)\right]x(k) + \left[B_{1g} + \Delta B_{1g}(k)\right]\omega(k) + \left[B_{2g} + \Delta B_{2g}(k)\right]u(k) \\ z(k) = \left[C_{1g} + \Delta C_{1g}(k)\right]x(k) + \left[D_{1g} + \Delta D_{1g}(k)\right]\omega(k) + \left[D_{2g} + \Delta D_{2g}(k)\right]u(k) \\ y(k) = C_{2g}x(k) \end{cases} \tag{19.1}$$

where g denotes the gth fuzzy inference rule, $g = 1, \ldots, r$; $\theta_1(x(k)), \ldots, \theta_p(x(k))$ are the premise variables, p is the number of premise variables, and $J_1^g, \ldots, J_p^g$ are the fuzzy terms, $x \in R^{n_x}$, $u \in R^{n_u}$, $z \in R^{n_z}$, $y \in R^{n_y}$, $\omega \in R^{n_\omega}$ are the state, input, controlled output, measured output, and disturbance, respectively. The matrices $\Delta A_g(k)$, $\Delta B_{1g}(k)$, $\Delta B_{2g}(k)$, $\Delta C_{1g}(k)$, $\Delta D_{1g}(k)$, and $\Delta D_{2g}(k)$ are the time-varying uncertainties in the system. Under the assumption that the premise variables do not explicitly depend on the control input, the overall T-S fuzzy model is inferred as

$$\begin{cases} x(k+1) = \sum_{g=1}^{r} \mu_g(\theta(x(k)))\{[A_g + \Delta A_g(k)]x(k) + [B_{1g} + \Delta B_{1g}(k)]\omega(k) + [B_{2g} + \Delta B_{2g}(k)]u(k)\} \\ \qquad = [A(\mu) + \Delta A(\mu,k)]x(k) + [B_1(\mu) + \Delta B_1(\mu,k)]\omega(k) + [B_2(\mu) + \Delta B_2(\mu,k)]u(k) \\ z(k) = \sum_{g=1}^{r} \mu_g(\theta(x(k)))\{[C_{1g} + \Delta C_{1g}(k)]x(k) + [D_{1g} + \Delta D_{1g}(k)]u(k) + [D_{2g} + \Delta D_{2g}(k)]u(k)\} \\ \qquad = [C_1(\mu) + \Delta C_1(\mu,k)]x(k) + [D_1(\mu) + \Delta D_1(\mu,k)]u(k) + [D_2(\mu) + \Delta D_2(\mu,k)]u(k) \\ y(k) = \sum_{g=1}^{r} \mu_g(\theta(x(k)))C_{2g}x(k) = C_2(\mu)x(k) \end{cases}$$

where $\chi_g(\theta(x(k))) = \prod_{t=1}^{p} J_t^g(\theta_t(x(k)))$, $\mu_g(\theta(x(k))) = \chi_g(x(k)) / \sum_{l=1}^{r} \chi_l(x(k)) \in [0,1]$,

$$\sum_{g=1}^{r} \mu_g(\theta(x(k))) = 1, \qquad A(\mu) = \sum_{g=1}^{r} \mu_g(x(k))A_g, \quad \Delta A(\mu,k) = \sum_{g=1}^{r} \mu_g(x(k))\Delta A_g(k),$$

$\theta(x(k)) = \left[\theta_1(x(k)), \ldots, \theta_p(x(k))\right]$. The definitions of other matrix are familiar with that of $A(\mu)$ and $\Delta A(\mu, k)$. Assume that the uncertainties satisfy the following assumption

$$\begin{bmatrix} \Delta A_g(k) & \Delta B_1(k) & \Delta B_2(k) \\ \Delta C_{1g}(k) & \Delta D_1(k) & \Delta D_2(k) \end{bmatrix} = \begin{bmatrix} E_{1g} \\ E_{2g} \end{bmatrix} F(k) [\, H_1 \quad H_2 \quad H_3 \,]$$

where H_1, H_2, H_3, E_{1g} and E_{2g} are known matrices which characterize the structure of the uncertainties; $F(k)$ is an unknown matrix function that satisfy $F^T(k)WF(k) \leq W$, where W is a positive definite matrix.

We consider the following fuzzy dynamic output feedback controller

$$\text{IF } \delta_1(\hat{x}(k)) \text{ is } N_1^h \text{ AND } \cdots \delta_q(\hat{x}(k)) \text{ is } N_q^h, \text{ THEN } \begin{cases} \hat{x}(k+1) = \hat{A}_h(i)\hat{x}(k) + \hat{B}_h(i)y(k-\tau_k) \\ u(k) = \hat{C}_h(i)\hat{x}(k) \end{cases}$$

where $\hat{x}(k)$ is the controller's state; $\hat{A}_h(i),\ \hat{B}_h(i),\ \hat{C}_h(i)$ are the controller matrices; h denotes the hth fuzzy inference rule; $h = 1, \ldots, c$, c is the number of inference rules; $\delta_1(\hat{x}(k)) \cdots \delta_q(\hat{x}(k))$ are the premise variables; q is the number of premise variables and $N_1^h \cdots N_q^h$ are the fuzzy terms; τ_k is the time delay.

Similar to the plant, the fuzzy output feedback controller is inferred as

$$\begin{cases} \hat{x}(k+1) = \sum_{h=1}^{r} \lambda_h(\delta(\hat{x}(k)))\{\hat{A}_h(r_k)\hat{x}(k) + \hat{B}_h(r_k)y(k-\tau_k)\} = \hat{A}(\lambda, r_k)\hat{x}(k) + \hat{B}(\lambda, r_k)y(k-\tau_k) \\ u(k) = \sum_{h=1}^{r} \lambda_h(\delta(\hat{x}(k)))\hat{C}_h(r_k)\hat{x}(k) = \hat{C}(\lambda, r_k)\hat{x}(k) \end{cases}$$

where $\delta(x(k)) = \left[\delta_1(\hat{x}(k)), \ldots, \delta_q(\hat{x}(k))\right], \phi_h(\delta(\hat{x}(k))) = \prod_{t=1}^{q} N_t^h \quad (\delta_t(\hat{x}(k))), \quad \lambda_h(\delta(\hat{x}(k))) = \phi_h(\hat{x}(k)) / \sum_{l=1}^{c} \phi_l(\hat{x}(k)) \in [0, 1], \quad \sum_{g=1}^{c} \lambda_h(\delta(\hat{x}(k))) = 1.$ The overall closed-loop system is

$$\begin{cases} \zeta(k+1) = [A_{\text{cl}}(\mu, \lambda, r_k) + \bar{E}_1(\mu)F(k)\bar{H}_1(\lambda, r_k)]\zeta(k) + B_{\text{cl}}(\lambda, r_k)\bar{C}_2(\mu)\zeta(k-\tau_k) \\ \qquad\qquad + [\bar{B}_1(\mu) + \bar{E}_1(\mu)F(k)H_2]\omega(k) \\ z(k) = [C_{\text{cl}}(\mu, \lambda, r_k) + E_2(\mu)F(k)\bar{H}_1(\lambda, r_k)]\zeta(k) + [D_1(\mu) + E_2(\mu)F(k)H_2]\omega(k) \end{cases} \tag{19.2}$$

where $A_{\text{cl}}(\mu, \lambda, r_k) = \begin{bmatrix} A(\mu) & B_2(\mu)\hat{C}(\lambda, r_k) \\ 0 & \hat{A}(\lambda, r_k) \end{bmatrix}$, $B_{\text{cl}}(\lambda, r_k) = \begin{bmatrix} 0 \\ \hat{B}(\lambda, r_k) \end{bmatrix}$, $\bar{B}_1(\mu) = \begin{bmatrix} B_1(\mu) \\ 0 \end{bmatrix}$, $\bar{C}_2 = [C_2(\mu)\, 0]$, $\bar{E}_1(\mu) = \begin{bmatrix} E_1(\mu) \\ 0 \end{bmatrix}$, $\bar{H}(\lambda, r_k) = \left[H_1\, H_3\hat{C}(\lambda, r_k)\right]$, $\zeta^T(k) = [x^T(k)\, \hat{x}^T(k)]$, $C_{\text{cl}}(\mu, \lambda, r_k) = \left[\, C_1(\mu) \quad D_2(\mu)\hat{C}(\lambda, r_k) \,\right]$. For brevity $\mu_g(\theta(x(k)))$,

$\lambda_h(\delta(\hat{x}(k)))$, $x(k)$, $\hat{x}(k)$ are denoted as $\mu_g(x)$, $\lambda_h(\hat{x})$, x, $\hat{x}$, respectively. Define $\Gamma_1(r_k) = [A_{\mathrm{cl}}(\mu,\lambda,r_k) \quad B_{\mathrm{cl}}(\mu,\lambda,r_k)\,\bar{C}_2(\mu)\,\bar{B}_1(\mu)\,\bar{E}_1(\mu)\,\bar{E}_2(\mu)]$ and $\tilde{\zeta}^T(k) = [[\,\zeta^T(k)\zeta^T(k-\tau(r_k)).\omega^T(k) \quad \zeta^T(k)\bar{H}_1^T(\lambda,r_k)F^T(k) \quad s\omega^T(k)H_2^T(\lambda,r_k)F^T(k)] \in R^l$ and $\Xi(r_k) = [C_{\mathrm{cl}}(\mu,\lambda,r_k)\,0\,D_1(\mu)\;E_2(\mu)\,D_1(\mu)]$. Define $\zeta_\ell = \zeta(\ell)$, $z_\ell = z(\ell)$, $\tilde{\zeta}_\ell = \tilde{\zeta}(\ell)$, and the closed system is

$$\zeta_{k+1} = \Gamma_1(r_k)\tilde{\zeta}_k,\; z_k = \Xi(r_k)\tilde{\zeta}_k \tag{19.3}$$

19.3 H_∞ Fuzzy Output Feedback Controller Design

The aim of this paper is to design a fuzzy dynamic output feedback controller such that, given a prescribed $\gamma > 0$, the controller will result such that the closed-loop system with $\omega(k) = 0$ is stochastically stable, that is, for all $x(0)$ and r_0 there exists a constant $0 < \vartheta < \infty$ such that

$$E\left\{\sum_{\ell=0}^{\infty} x^T(\ell)x(\ell)\right\} < \vartheta \tag{19.4}$$

Furthermore, under zero initial conditions, the following is to be satisfied

$$E\left\{\sum_{k=0}^{\infty} z^T(k)z(k)|r_0\right\} < \gamma \sum_{k=0}^{\infty} \omega^T(k)\omega(k) \tag{19.5}$$

We model the time delays $\tau(r_k)$ by using a discrete Markov chain. Let r_k be a discrete Markov chain taking values in a finite set $S = \{1, 2, \ldots, s\}$, with the transition probability from mode i at time k to mode j at time $k+1$, $P[\tau_{k+1} = j|\tau_k = i] = p_{ij}$, $\forall i,j \in S$, where $p_{ij} \geq 0$, $\sum_{j=1}^{N} p_{ij} = 1$, $\forall i \in S$. The proposed controller will always use the most recent data for feedback. This means that the delay τ_k can only increase at most by one at each step, therefore $\mathrm{Prob}\{\tau_{k+1} > \tau_k + 1\} = 0$.

In practice some of the elements in the transition probability matrix are unknown. Throughout the paper we use the following notations for $i, j \in S$

$$S_K^i = \{j : \text{if } p_{ij} \text{ is known}\},\; S_{UK}^i = \{j : \text{if } p_{ij} \text{ is unknown}\},\; p_K^i = \sum_{j \in S_K^i}^{i+1} p_{ij},\; p_{UK}^i = \sum_{j \in S_{UK}^i}^{i+1} p_{ij}\,.$$

YALMIP and SOSTOOLS can handle multivariate polynomial functions. So membership functions are approximated as below

$$\mu_g(x)\lambda_h(\hat{x}) = \sum_{k=1}^{D} \zeta(x.\hat{x})\left(\eta_{gh,s_k}(x.\hat{x}) + \Delta\eta_{gh,s_k}(x.\hat{x})\right),\ \alpha_{gh,s_k} \le \Delta\eta_{gh,s_k}(x.\hat{x}) \le \beta_{gh,s_k} \tag{19.6}$$

where $\eta_{gh,s_k}(x.\hat{x})$ are the polynomial function approximations, $\Delta\eta_{gh,s_k}(x.\hat{x})$ are the error terms in each subregion, $\zeta(x.\hat{x})$ is a scalar function which takes 1 if x and $\hat{x}$ are inside the subregion and 0 otherwise, $\alpha_{gh,s_k}, \beta_{gh,s_k}$ are known constants.

Theorem 19.1 [7] *For a given $\gamma > 0$, the closed-loop system will satisfy (19.4) and (19.5) if there exist sets of positive definite matrices $P(i), X(i), \tilde{R}_1(i), \tilde{R}_1, \tilde{R}_2(i), \tilde{R}_2, W_1(i), W_2(i), \tilde{W}_1(i), \tilde{Q}, Q, N_1, \tilde{Z}(i), S(i,j), \tilde{\Psi}_1^{gh}(i), \tilde{\Psi}_2^{gh}(i)$ and matrices $K_h(i), \hat{C}_h(i), \tilde{M}(i), J(i)$ for $i = 1, 2, \ldots, s$, $g = 1, 2, \ldots, r$, $h = 1, 2, \ldots, c$ satisfying*

$$\tilde{R}_1 > \tilde{R}_1(i),\ \tilde{R}_2 > \tilde{R}_2(i) \tag{19.7}$$

$$-v^T\left[\sum_{g=1}^{r}\sum_{h=1}^{c}\left(\eta_{gh,S_k}(x,\hat{x}) + \frac{1}{2}\alpha_{gh,S_k} + \frac{1}{2}\beta_{gh,S_k}\right)\tilde{T}^{gh}(i) + \tilde{V}^{gh,S_k\,gh}(i) - \tilde{\varepsilon}_{S_k}I\right]v \text{ is SOS} \tag{19.8}$$

$$\frac{1}{2}\tilde{T}^{gh}(i) - \tilde{\Psi}_1^{gh}(i) < 0,\ -\frac{1}{2}\tilde{T}^{gh}(i) - \tilde{\Psi}_2^{gh}(i) < 0 \tag{19.9}$$

$$\begin{bmatrix} \left(1 - p_{i(i+1)}\right)\tilde{R}_1(i) + \tilde{R}_2(i) & \tilde{M}(i) \\ * & \tilde{z}(i) \end{bmatrix} \ge 0;\ \begin{bmatrix} p_k^i\tilde{R}_1(i) + \tilde{R}_2(i) & \tilde{M}(i) \\ * & \tilde{z}(i) \end{bmatrix} \ge 0, \forall (i+1) \in S_{UK}^i \tag{19.10}$$

$$\begin{bmatrix} S(i,j) & J^T(i) \\ * & X(j) \end{bmatrix} > 0 \tag{19.11}$$

$$N_1\tilde{R}_1 = I,\ N_2\tilde{R}_2 = I,\ \tilde{W}_1(i)W_1(i) = I,\ Q\tilde{Q} = I,\ P(i)X(i) = I. \tag{19.12}$$

where v is a real vector and independent of x, $\tilde{\varepsilon}_{s_k}$ are predefined scalars;

$$\tilde{V}^{gh,s_k}(i) = \left(\beta_{gh,s_k} - \alpha_{gh,s_k}\right)\left(\tilde{\Psi}_1^{gh}(i) + \tilde{\Psi}_2^{gh}(i)\right),$$
$$\tilde{\Gamma}_3 = \left[\sqrt{\tau(s) - \tau(1) + 1} \quad 0 \quad 0 \quad 0 \quad 0\right],$$

$$\tilde{\tau}(i) = \sum_{j\in S_k^i}^{i+1} p_{ij}\tau(j) + (1-p_k^i)\sum_{j\in S_{Uk}^i}^{i+1}\tau(j),$$

$$\widetilde{\Upsilon}_1(i) = \tilde{M}^T(i)[\,\mathrm{diag}\{I,0\} \quad \mathrm{diag}\{-I,0\} \quad 0 \quad 0 \quad 0\,],$$

$$\tilde{A}_g = \begin{bmatrix} A_g & 0 \\ 0 & 0 \end{bmatrix},\ \bar{E} = \begin{bmatrix} 0 \\ I \end{bmatrix},\ \bar{R} = \begin{bmatrix} 0 & I \\ 0 & 0 \end{bmatrix},\ \hat{E} = \begin{bmatrix} 0 \\ I \end{bmatrix},\ \bar{B}_{2g} = \begin{bmatrix} B_{2g} \\ 0 \end{bmatrix},$$
$$\bar{E}_{1g} = \begin{bmatrix} 0 \\ E_{1g} \end{bmatrix},\ \bar{B}_{1g} = \begin{bmatrix} B_{1g} \\ 0 \end{bmatrix},$$

$$\bar{C}_{1g} = [\,C_{1g} \quad 0\,],\ \bar{C}_{2g} = [\,C_{2g} \quad 0\,],\ R = \mathrm{diag}\{N_1, N_2\},\ \tilde{H}_1 = [\,H_1 \quad 0\,],$$
$$\tilde{C}_h(i) = \begin{bmatrix} 0 & \hat{C}_h(i) \end{bmatrix},$$

$$\tilde{T}^{gh}(i) = \begin{bmatrix} \tilde{\Lambda}(i) & (\widetilde{\Gamma}_1^{gh}(i))^T & (\widetilde{\Gamma}_2^{gh}(i))^T & (\widetilde{\Gamma}_3)^T & (\widetilde{\Xi}^{gh}(i))^T & (\tilde{H}^h(i))^T \\ * & -\chi & 0 & 0 & 0 & 0 \\ * & * & -R & 0 & 0 & 0 \\ * & * & * & -\tilde{Q} & 0 & 0 \\ * & * & * & * & -I & 0 \\ * & * & * & * & * & -\tilde{W}_1(i) \end{bmatrix},$$
$$\widetilde{\Gamma}_2^{gh}(i) = \begin{bmatrix} \sqrt{\tilde{\tau}(i)}M \\ \sqrt{\tau(i)}M \end{bmatrix},$$

$$\tilde{\Lambda}(i) = \mathrm{diag}\{-P(i) \quad -Q \quad (H_2^T W_2(i) H_2 - \gamma I) \quad -W_1(i)\ -W_2(i)\} + \tilde{\Upsilon}_1^T(i) + \tilde{\Upsilon}_1(i) + \tau(i)\tilde{Z}(i),$$

$$\tilde{\Gamma}_1^{gh}(i) = \begin{bmatrix} \tilde{A}_g + \bar{E}K_h(i)\bar{R} + \bar{B}_{2g}\tilde{C}_h(i) & \bar{E}K_h(i)\hat{E}\bar{C}_{2g} & \bar{B}_{1g} & \bar{E}_{1g} & \bar{E}_{1g} \end{bmatrix},$$

$$M = [\,\tilde{A}_g \quad -\mathrm{diag}\{I \quad 0\} + \bar{B}_{2g}\tilde{C}_h(i)\ 0 \quad \bar{B}_{1g} \quad \bar{E}_{1g} \quad \bar{E}_{1g}\,],$$

$$\tilde{\Xi}^{gh}(i) = \begin{bmatrix} \bar{C}_{1g} + D_{2g}\bar{C}_{2g}\tilde{A}_g & 0 & D_{1g} & E_{2g} & E_{2g} \end{bmatrix},$$
$$\tilde{H}^h(i) = \begin{bmatrix} \tilde{H}_1 + H_3\tilde{C}_h(i) & 0 & 0 & 0 & 0 \end{bmatrix}$$

$$\chi(i,j) = J^T(i) + J(i) - \left\{ \sum_{j\in S_K^i}^{i+1} p_{ij}S(i,j) + (1-p_K^i)\sum_{j\in S_{UK}^i}^{i+1} S(i,j) \right\}.$$

The delay dependent dynamic fuzzy output feedback controller matrix is

$$\begin{bmatrix} \hat{A}_h(i) & \hat{B}_h(i) \end{bmatrix} = K_h(i).$$

Theorem 19.2 *According to the cone complementarity algorithm, the problem formulated by* (19.7–19.12) *can be converted into the following problem*

$$\text{Min } Tr\left(N_1\tilde{R}_1 + N_2\tilde{R} + N_2\tilde{R}_2^J + \tilde{W}_1(i)W_1(i) + \tilde{Q}Q + P(i)X(i)\right)$$

Subject to (19.7)–(19.11) and

$$\begin{bmatrix} N_1 & I \\ I & \tilde{R}_1 \end{bmatrix} > 0, \begin{bmatrix} N_2 & I \\ I & \tilde{R}_2 \end{bmatrix} > 0, \begin{bmatrix} \tilde{Q} & I \\ I & Q \end{bmatrix} > 0, \begin{bmatrix} \tilde{W}_1(i) & I \\ I & W(i) \end{bmatrix} > 0, \begin{bmatrix} P(i) & I \\ I & X(i) \end{bmatrix} > 0 \tag{19.13}$$

19.4 Simulations and Experiments

Consider a truck–trailer system shown in [8], a discrete time T-S fuzzy model of the plant above is obtained with two plant rules ($r = 2$) and two controller rules ($c = 2$). The subsystems are described as follows:

$$A_1 = \begin{bmatrix} 1.3636 & 0 & 0 \\ -0.3636 & 1 & 0 \\ 0.3636 & -2 & 1 \end{bmatrix}, A_2 = \begin{bmatrix} 1.3636 & 0 & 0 \\ -0.3636 & 1 & 0 \\ 0.0003 & -0.0018 & 1 \end{bmatrix}, B_{11} = \begin{bmatrix} 0 \\ 0.2 \\ 0.1 \end{bmatrix},$$

$$B_{21} = \begin{bmatrix} -0.7143 \\ 0 \\ 0 \end{bmatrix},$$

$B_{12} = B_{11}$, $B_{22} = B_{21}$, $C_{11} = C_{12} = [0 \quad 0 \quad 0], D_{11} = D_{12} = 0$, $D_{21} = D_{22} = -0.7143$, $C_{21} = C_{22} = [7 \quad -2 \quad 0.03]$. Define $\theta(t) = x_2(t) - 0.1818x_1(t)$, the membership functions are $\mu_1(\theta(t)) = \sin(\theta(t))/\theta(t), \mu_2(\theta(t)) = 1 - \sin(\theta(t))/\theta(t)$. The membership functions of the output feedback fuzzy controller are selected as $\lambda_1\left(\hat{\theta}(t)\right) = 1 - \sin\left(\hat{\theta}(t)\right)/\hat{\theta}(t), \lambda_2\left(\hat{\theta}(t)\right) = \sin\left(\hat{\theta}(t)\right)/\hat{\theta}(t)$. Figure 19.1 depicts the membership functions of the plant and the controller. We divide $\mu_g(\theta(t))\lambda_h\left(\hat{\theta}(t)\right)$ into four subregions. For every subregion polynomial approximation is obtained using cftool in Matlab which is shown in Table 19.1 with bounds of the error terms β_{gh,s_k}, α_{gh,s_k}.

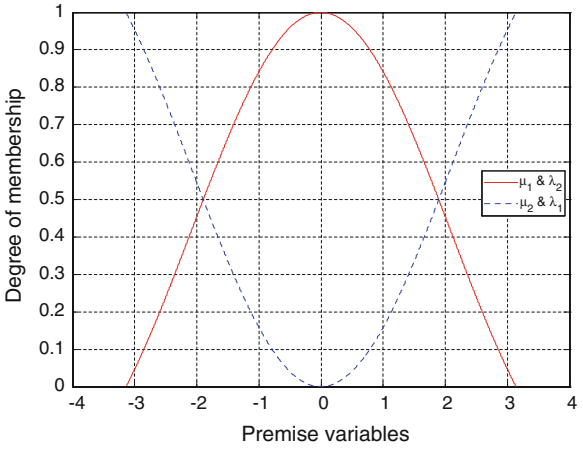

Fig. 19.1 Membership functions of truck–trailer example

Table 19.1 Polynomial approximation of membership functions and β_{gh,s_k}, α_{gh,s_k}

		$\eta_{gh,s_k}(\theta,\hat{\theta})$	β_{gh,s_k}	α_{gh,s_k}
$g=1$ $h=1$	1	$\left(-0.056(\theta-1.57)^2+1.188\right)\left(0.056(\hat{\theta}-1.57)^2-0.188\right)$	0.0584	−0.1081
	2	$\left(-0.056(\theta-1.57)^2+1.188\right)\left(0.056(\hat{\theta}+1.57)^2-0.188\right)$	0.0584	−0.1079
	3	$\left(-0.056(\theta+1.57)^2+1.187\right)\left(0.056(\hat{\theta}-1.57)^2-0.188\right)$	0.0589	−0.1074
	4	$\left(-0.056(\theta+1.57)^2+1.187\right)\left(0.056(\hat{\theta}+1.57)^2-0.188\right)$	0.0588	−0.1072
$g=1$ $h=2$	1	$\left(-0.056(\theta-1.57)^2+1.188\right)\left(-0.056(\hat{\theta}-1.57)^2+1.188\right)$	0.0581	−0.1022
	2	$\left(-0.056(\theta-1.57)^2+1.188\right)\left(-0.056(\hat{\theta}+1.57)^2+1.187\right)$	0.0582	−0.1016
	3	$\left(-0.056(\theta+1.57)^2+1.187\right)\left(-0.056(\hat{\theta}-1.57)^2+1.188\right)$	0.0585	−0.1015
	4	$\left(-0.056(\theta+1.57)^2+1.187\right)\left(-0.056(\theta+1.57)^2+1.187\right)$	0.0585	−0.1009
$g=2$ $h=1$	1	$\left(0.056(\theta-1.57)^2-0.188\right)\left(0.056(\hat{\theta}-1.57)^2-0.188\right)$	0.0525	−0.1140
	2	$\left(0.056(\theta-1.57)^2-0.188\right)\left(0.056(\hat{\theta}+1.57)^2-0.188\right)$	0.0525	−0.1138
	3	$\left(0.056(\theta+1.57)^2-0.188\right)\left(0.056(\hat{\theta}-1.57)^2-0.188\right)$	0.0525	−0.1137
	4	$\left(0.056(\theta+1.57)^2-0.188\right)\left(0.056(\hat{\theta}+1.57)^2-0.188\right)$	0.0524	−0.1136
$g=1$ $h=2$	1	$\left(-0.056(\theta-1.57)^2-0.188\right)\left(-0.056(\hat{\theta}-1.57)^2+0.188\right)$	0.0584	−0.1081
	2	$\left(-0.056(\theta-1.57)^2-0.188\right)\left(-0.056(\hat{\theta}+1.57)^2+0.187\right)$	0.0585	−0.1075
	3	$\left(0.056(\theta+1.57)^2-0.188\right)\left(-0.056(\hat{\theta}-1.57)^2+0.188\right)$	0.0584	−0.1079
	4	$\left(0.056(\theta+1.57)^2-0.188\right)\left(-0.056(\hat{\theta}+1.57)^2+0.187\right)$	0.0591	−0.1071

Utilizing Matlab, NS2 to simulate real-time control and network performance separately, we designed and realized a simulation platform [9] for NCS which is shown as Fig. 19.2. The communication between NS2 and Matlab is realized by Java application. Running for 30 min on the NCS platform with the sampling time of 0.1 s, the network performance of delay for a kind of network topology was obtained and shown in Fig. 19.3 for the first 5 min. So it is concluded that the time delays are $\tau_1 = T, \tau_2 = 2T$ and $P_\tau(1,1) = 0.6279$, $P_\tau(1,2) = 0.3721$.

Apply the theorem 2 and $\gamma = 1.3$, the controller can be obtained using YALMIP. When $\omega = 0$, initial state is $x = [0.5\pi \quad 0.75\pi \quad -10]^T$, the state response of the system is figured as Fig. 19.4a. Select $\omega(t) = \begin{cases} \text{rand} - 0.5 & t \le 50 \\ (\text{rand} - 0.5)/t & t > 50 \end{cases}$, the state response of the system is figured as Fig. 19.4b with the same initial conditions. Note that no feasible solution exists for this particular example when the theorem is reduced to $\tilde{T}^{gh}(i) < 0$. From the simulation results we can see that the system has good performance with the designed H_∞ output feedback controller.

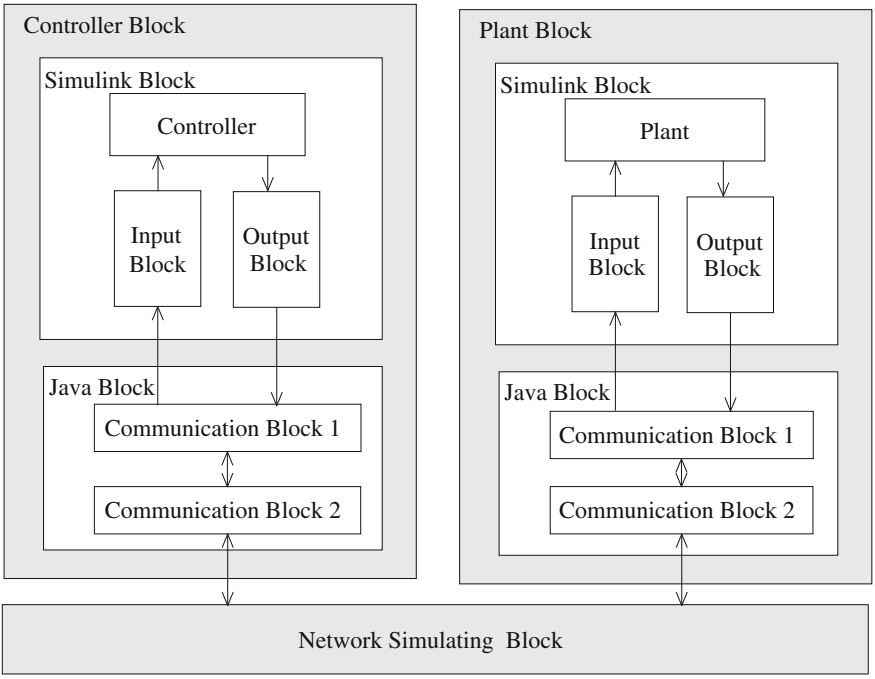

Fig. 19.2 Framework of simulation platform

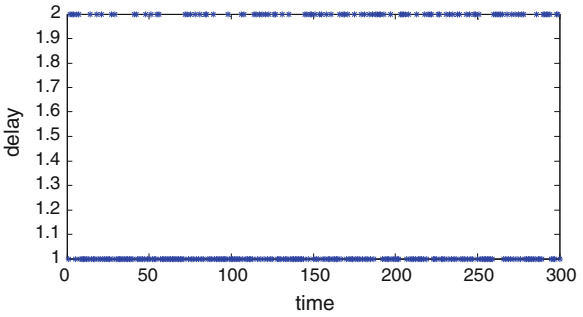

Fig. 19.3 Time delay

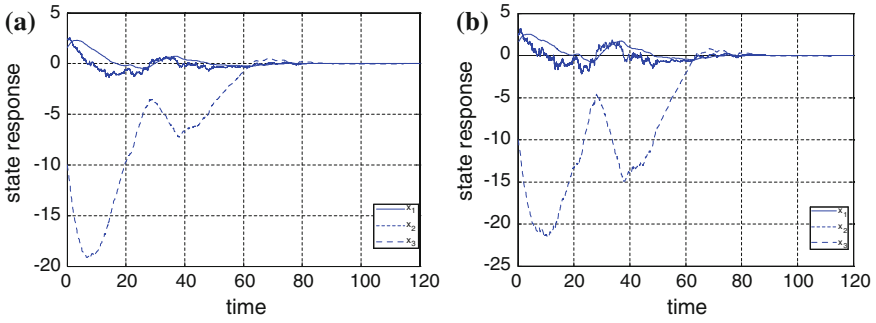

Fig. 19.4 The state of the truck–trailer system

19.5 Result

We investigated the fuzzy dynamic output feedback control of a class of nonlinear NCS with timed delay. Sufficient conditions for the existence of the controller are derived in terms of SOS inequalities which are then solved by YALMIP. A truck–trailer experiment was carried out on a real-time simulation platform and the simulations have demonstrated the effectiveness of the proposed approach.

References

1. Rasool F, Nguang SK (2009) Quantized robust output feedback control of discrete-time systems with random communication delays. In:s Proceedings IEEE ICCA 1399–1404
2. Goncalves APC, Fioravanti AR, Geromel JC (2009) H_∞ filtering of discrete-time markov jump linear systems through linear matrix inequalities. IEEE Trans Autom Control 54(6):1347–1351
3. Fioravanti AR, Goncalves APC, Geromel JC (2008) H_2 filtering of discrete-time markov jump linear systems through linear matrix inequalities. Int J Control 81:1221–1231

4. Nguang SK (2010) Comments on fuzzy tracking control for nonlinear networked control systems in T-S fuzzy model. IEEE Trans Syst Man Cybern B Cybern 40(3):957–957
5. Peng C, Yang TC (2010) Communication delay distribution dependent networked control for a class of T-S fuzzy systems. IEEE Trans Fuzzy Syst 18(2):326–335
6. Mahmoud M (2012) H_∞ control of uncertain fuzzy networked control systems with state quantization. Intell Control Autom 3(1):59–70
7. Chae S, Sing KN (2013) SOS based robust fuzzy dynamic output feedback conrol of nonlinear networked control systems. IEEE Trans Cybern 2168–2267
8. Kau SW, Lee HJ, Yang CM et al (2007) Robust H_∞ fuzzy static output feedback control of T-S fuzzy systems with parametric uncertainties. Fuzzy Sets Syst 158:135–146
9. Wang QF, Chen H, Wang P (2011) Design and implementation of simulation platform for networked control system based on NS2. J Syst Simul 23(2):270–274 (in Chinese)

Chapter 20
Study on the Control System of the Wheel Hanging Workbench

Chaokun Ma, Naijian Chen, Changchun Li and Longtao Liu

Abstract This paper describes a wheel hanging robot system that consists of a roller screw with a mounted 6 DOF manipulator and a visual workbench. It is designed to navigate autonomously and hangs wheels on the hook in the car wheel spray paint line. At the end of manipulator there is a holder used to catch and hang wheels. In order to achieve a better quality of spraying, a visual workbench can rotate the wheel to identify the rim's circumference. Thus the valve hole can be identified and positioned with the mounted camera automatically. The whole control system of the wheel hanging robot system includes the manipulator control system, the mobile platform control system, and the rotating platform control system. Experimental results are shown that the wheel hanging robot system can position the valve hole of the wheels and hang wheels automatically.

Keywords Wheel hanging robot · Visual workbench · Redundant manipulator

20.1 Introduction

With the rapid development of automobile industry, the demands of automobile wheel hub are also increasing. However, there are still many manufacturers done by worker in the car wheel spraying production line. Industrial robots are becoming an important part of flexible manufacturing systems. The advantage of this type of

C. Ma · N. Chen · C. Li (✉) · L. Liu
College of Mechanical Engineering, University of Jinan, Jinan, China
e-mail: me_licc@ujn.edu.cn

C. Ma
e-mail: m15966331433@163.com

N. Chen
e-mail: chnjian@126.com

L. Liu
e-mail: liulongtao12345@126.com

Z. Deng and H. Li (eds.), *Proceedings of the 2015 Chinese Intelligent Automation Conference*, Lecture Notes in Electrical Engineering 337,
DOI 10.1007/978-3-662-46463-2_20

robot is to adapt to various serious environments and can greatly improve efficiency. Thus we put forward the idea of using robots replace manual hanging wheel and designed a visual workbench. This paper describes how the whole control system control a complete set of equipment operation.

20.2 Physical Description and Design Specification

A car wheel suspension system consisting of redundant degrees of freedom carrying manipulator and car wheel hub valve hole visual measuring and positioning workbench is used in this paper to relieve workers of tedious, repetitive, and hazardous tasks [1]. The working process of the automobile wheel suspension system is shown in Fig. 20.1.

20.2.1 The Wheel Valve Hole Visual Measuring and Positioning Workbench

The car wheel hub valve hole visual measuring and positioning workbench is shown in Fig. 20.2.

The car wheel hub valve hole visual measuring and positioning workbench includes an image acquisition, storage and processing system, the test platform, the images processing software, etc. The equipment is divided into two parts: The following is a support base and on the base installation of a disk. Disk is driven by the middle of the servo motor and the sever motor was installed on the base through the bearing. On the disk there is a wheel gripper composed of three cylinders. Beside the disk there is the image acquisition system which is included by a linear array camera, lighting, and transmission device. Camera and lights installed on a bracket which can adjust the location that is benefit to obtain better image. The car wheel hub valve hole visual measuring and positioning workbench can complete the image processing, feature extraction, data processing, and other functions to get feature of the car wheel hub valve hole. Then through the data processing, we can

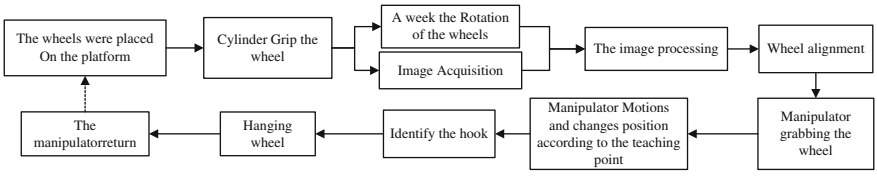

Fig. 20.1 The working process of the automobile wheel suspension system

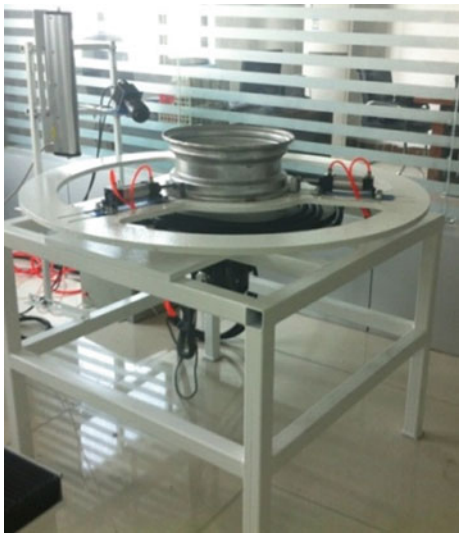

Fig. 20.2 The rim valve hole's measuring and positioning visual workbench

get the angle which the wheel needs to rotate. The working process of the visual measuring and positioning workbench is as follows:

1. Put the car wheel on the visual measuring and positioning system workbench.
2. The clamping cylinder which is mounted on the workbench grabs the wheel.
3. The car wheel rotates a week. Meanwhile, the center-line array camera scanning the wheel circumference and the collected images stored in the computer. And then the images processing software finish the image processing and find the location of the valve hole.
4. The computer calculates the angle that the valve hole should rotate. At the same time, we can get the pulse that required by the motor.
5. The information will be transmitted to the control system through the communication transmission of information.
6. After rotation to locate position, the wheel was loosened by the cylinder and waiting for fetching manipulator.

20.2.2 Carrying Manipulator

In manufacturing area, the industrial robots are widely used. The general industrial robot has six degrees of freedom. They include the base can rotate, the big arm can bobbing around the base, forearm bobbing around the big arm, the rotation of the forearm, wrist bobbing up and down, and turn of the wrist. In this paper, the industrial robot has six degrees of freedom and is mounted on the linear movement of the roller screw. Thus the manipulator includes six degrees of freedom

manipulator and roller screw moving workbench. The carrying manipulator can move with the ball screw. The carrying manipulator system working process is as follows:

1. Under the control system, the carrying manipulator grabs the wheel.
2. The manipulator movement along with the teaching way until it got to the place where the wheel can be hanging.
3. The roller screw drive the manipulator moving at the same speed of the catenary line hook, and at the same time manipulator hanging the wheel on the catenary line hook.
4. The manipulator movement back to grab point's accordance with the scheduled procedure for the next cycle.

20.2.3 Moving Workbench

Moving workbench is a platform that can driven manipulator move along with the hook. Moving workbench is composed of motor and roller screw. The roller crew is shown in the Fig. 20.3. Roller screw is installed in the middle of the base. The manipulator installed on the roller screw by sliding block.

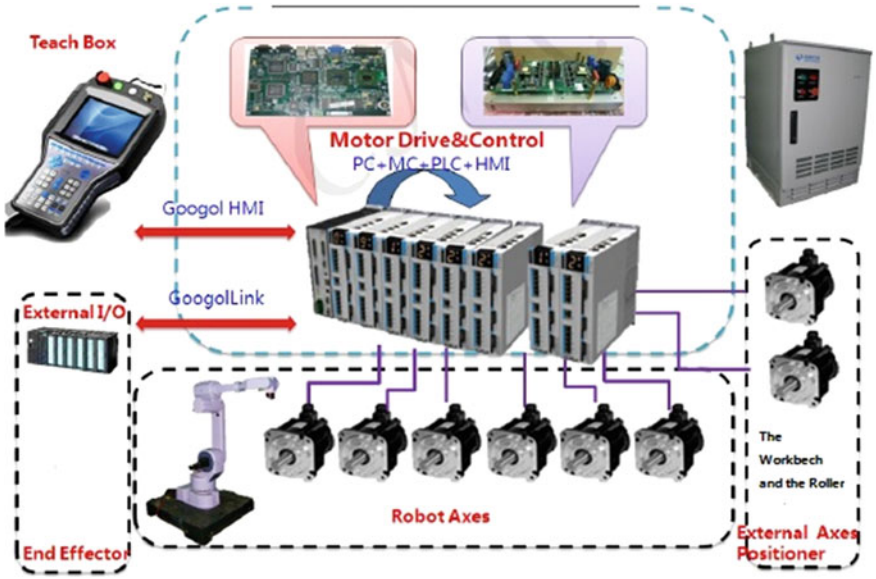

Fig. 20.3 The hardware architecture of the whole control system

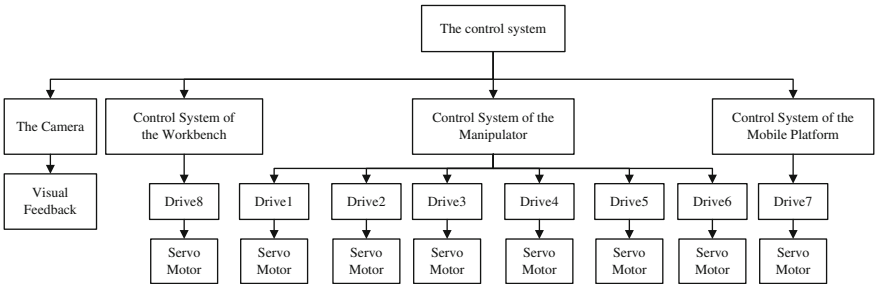

Fig. 20.4 The classification of control system

20.3 The Wheel Suspension Control System

The control system is the heart of whole wheel suspension process, which is detailed in a block diagram as given in Fig. 20.3.

The control system of automobile wheel hub suspension system uses the Google GUC series of eight axis integration motion controllers, which is the composition of embedded PC and motion control card. We can operate control using the man −machine interface or teach box. We can also control the motion controller card through the PC programming. The micro controller-based main board controls the motors. The hardware composition of control system comes in three configurations: Man−machine interface or teach box, GUC motor control card, and servo motor. Another aspect, our control system can be divided into three parts: The control system of the workbench, the control system of the manipulator, and the control system of the mobile platform.The classification of control system is shown in Fig. 20.4. We still can see the number of the servo motor used by the different system.

20.3.1 The Control System of the Workbench

Block diagram of workbench control system is shown in Fig. 20.5. The main purpose of the workbench control system is to drive the working platform wheels rotating. The GUC control card drives eight servo motors rotation under the control of the program. After obtained the angle data by processing the image, computer will send a signal to the controller and the GUC will drive motor to rotate the angle of corresponding data.

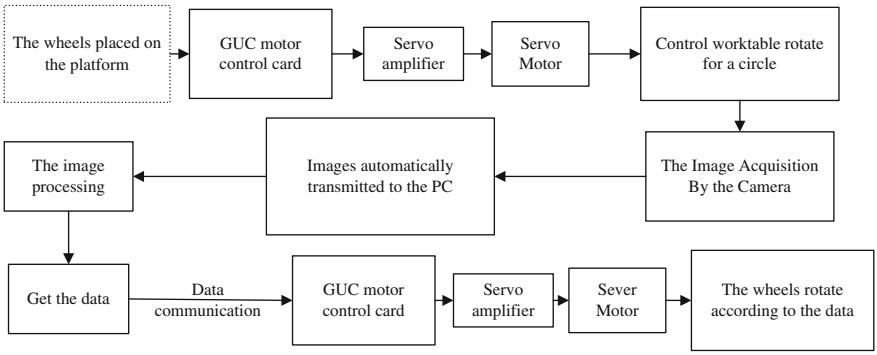

Fig. 20.5 Block diagram of workbench control system

20.3.2 The Control System of the Manipulator

In order to determine the relationship between the end of the manipulator hand the position and posture the manipulator grasping when the car wheel hub, and mechanical components, it is necessary to establish kinematics mathematical model of the manipulator. The car wheel suspension system is developing a seven degree of freedom manipulator. Seven degree of freedom manipulator has more than one solution. That is to say the robot has a lot of similar paths to reach a predetermined location. So there must be an additional decision-making program enables the robot to select the optimum one from a variety of methods. In this paper, the robot's seventh degree of freedom is installed roller screw on the bottom support. Due to the linear motion of the robot, it can move with the catenary at the same speed. That means the location of the base of the robot and the other coordinate system are known, so the redundant degree of freedom does not need to solve. In the kinematics analysis the number of degrees of freedom robot can still be classified as six, thus the solution is only one [2].

The robot of six joints needs to establish seven coordinate systems. In the base coordinate, the end of the robot coordinate system is $x_6y_6z_6$ (as shown in the figure below), the nth joint coordinate system is $x_{n-1}y_{n-1}z_{n-1}$ as shown in Fig. 20.6.

According to the function requirement analysis of the manipulator, the structure diagram of the manipulator control system is shown in Fig. 20.7.

According to the kinematics mathematical model that is established above, we transmitted the information of the location of the wheel to the robot motion planning system. According to the obtained all kinds of information about the wheel, The robot motion planning system calculated the optimal motion track points and the minimum rotation angle of each joint, and then make some point of interpolation. Then the ideal trajectory curve of every axis of manipulator can be acquired.

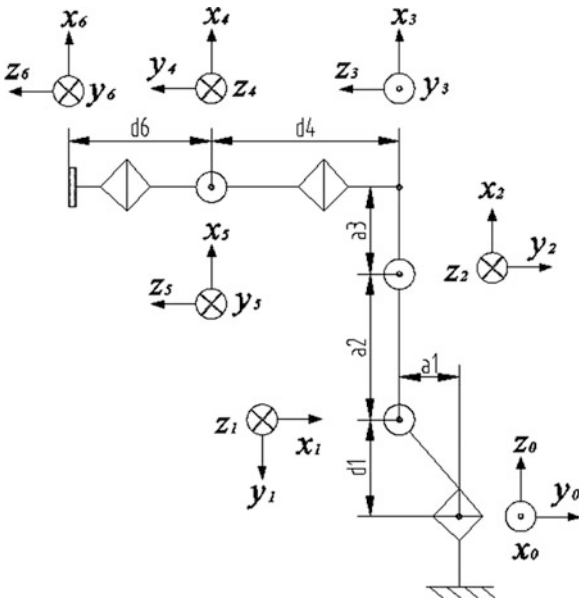

Fig. 20.6 Coordinate system of the manipulator

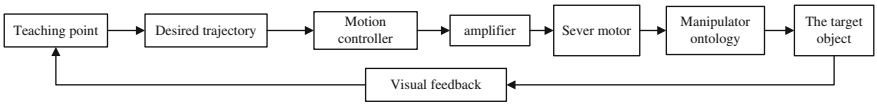

Fig. 20.7 The structure diagram of the manipulator control system

Taking the result of the motion planning as the foundation, the control system drives manipulator arm motion coordinately. Then the manipulator move with catenary suspension hook at the same speed, and eventually hanging the wheel on the hook. Then the manipulator returns to the start catching point accordance with the planning route. In the process, there also has inspection feedback of the visual platform camera. According to the visual platform of signals, the manipulator control system of the manipulator can take the grab action. In terms of automatic control, the working process of the manipulator is a complete closed loop.

20.3.3 The Control System of the Mobile Platform

The control system of the mobile platform is composed of four parts: The GUC control card, the seventh drive, severs motor, and the roller screw. The control

system of the mobile platform begins to work after the manipulator grabbed the wheel. The main purpose is to drive the manipulator moves along with catenary suspension hook. The main work flow is as follows:

- The industrial manipulator grabs the wheel.
- GUC control card control the motor rotation.
- Motor drives the roller screw rotation and the manipulator began to move.
- When the manipulator gets the same speed as the hook, the manipulator hangs the wheel on the hook.
- The last motor drives reversely the manipulator to return.

20.4 Experimental Results and Analysis

20.4.1 Experiments

Connect the GUC series motion controller to the standard input and output devices. The controller runs on 24 V DC. Hence a AC/DC converter is placed to convert 220 V AC to 24 V DC.

1. Install the motion controller driver.
2. Host communications with motion controller is established.
3. Connect the motor and drive.
4. Connect the motion controller and terminal board.
5. Connect the drive, input and output system and motion controller.

The processes of the system are as follows:

- First of all, put the wheel on the car wheel hub valve hole visual measuring and positioning workbench is shown in Fig. 20.2.
- The GUC control card issues instructions to the drives of the server motors. The wheels turn a week. The center-line array camera scans the wheel circumference and the collected images are stored in the computer as shown in Fig. 20.8 [3].
- The image will be processed through gray-scale threshold transform, morphological processing, cutting, edge detection, and so on, so that we can get the characteristic of the valve hole as shown in Fig. 20.9.
- The computer calculates the angle that the valve hole should rotate as shown in Fig. 20.10.
- The wheel rotates the corresponding Angle.
- According to working conditions, we determine the initial position and ending position of the manipulator.
- To avoid the problems such as collision with other devices, we set the start carrying manipulator posture as shown in Fig. 20.11.
- Then following the teaching of route hanging wheel. Figures 20.12 and 20.13 are two different demonstration points on the hanging wheel line. Figure 20.12

Fig. 20.8 The image of the rim circular

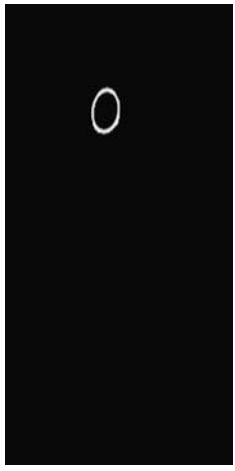

Fig. 20.9 Fit the contour of the valve hole

Fig. 20.10 The conclusion

shows it was transposing its position after catching up the wheels. Figure 20.13 shows that the manipulator was moving along the guide rail at the same speed of hanging hook. When the robot gets the destination, the position of the suspension time is as shown in the Fig. 20.14.

Fig. 20.11 The position of robot starts to grab the wheel

Fig. 20.12 The position after catching up the wheel

Fig. 20.13 The position when moving along the guide rail

Fig. 20.14 The position of the suspension time

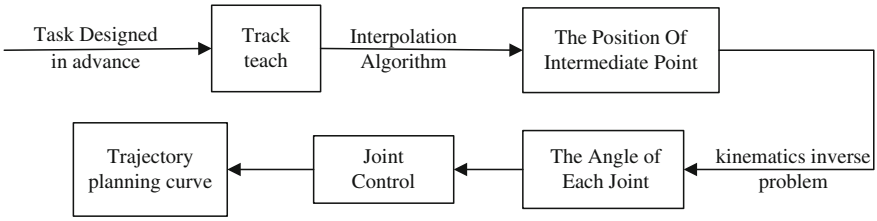

Fig. 20.15 The process of manipulator trajectory planning

- To set the path of a series of points, and then to work out each joint vector angle by the principle of kinematics inverse problem.
- The control system drive motor and every joint movements, make the actuator to complete the task.
- The purpose is to make the manipulator move along with the specific trajectory to complete the task.The process of manipulator trajectory planning is shown in Fig. 20.15.

20.5 Conclusion

In this paper, the author puts forward a design scheme of the wheel suspension system. In order to solve the problem of fetching and hanging of the wheels, incorporating various equipment as described above and making sure that it can work normally is a challenge by itself. The model takes into account the car wheel positioning and the grabbing and suspension of the wheel base, the detailed

dynamics of the manipulator. In addition, through the man−machine interface by operating the motion controller to realize further driving control, also reach control of robot, wheel positioning system, and moving workbench. The author has verified the feasibility and effectiveness of the control system of the wheel hanging equipment using a catenary line through the car wheel grab suspension experiments.

Overall, through the whole control system, we can complete operation of wheel measuring and positioning system to finish positioning of the car wheel valve hole and to control the manipulator trajectory planning to complete the car wheel scraping. Finally, the system can control the mobile platform to drive manipulator move to complete suspension of the wheel. The system is an efficacious architecture, so that it can make the work easier without worrying too much about its operational efficiency. This is particularly suitable in the grab and suspension process of the wheel.

References

1. Katz et al (2006) The UMass mobile manipulator uman: an experimental platform for autonomous mobile manipulation. In: Workshop on manipulation for human environments at robotics: science and systems. Philadelphia, USA
2. Datta S, Ray R, Banerji D (2008) Development of autonomous mobile robot with manipulator for manufacturing environment. Int J Adv Manuf Technol. doi:10.1007/s00170-007-1024-x
3. Wang F, Ma CK, Dai SQ, Li CC (2014) Study on the measuring and positioning of the rim valve hole based on machine vision. In: 2014 the 3rd international conference on mechanical engineering, materials science and civil engineering. Phuket Isl-ang, Thailang, 25–26 Oct 2014

Chapter 21
An Overview of Dynamic Equilibrium State Theory

Linjie Xin, Qinglin Wang and Yuan Li

Abstract The dynamic equilibrium state (DES) theory is a novel analysis method for control systems. It is considered that what the input of control system controls directly is the equilibrium state, not the output or state of system. The state moves under constrain of the system structure matrix. If the system structure matrix is stable, the state moves relatively to its equilibrium state. This idea gives new solutions for the steady-state analysis in the state space, and is applied in the nonlinear time-varying system design. It provides a new point of view for the control system design. The recent development of DES theory is reviewed in this paper, which is summarized by five issues. Furthermore, the future studies are pointed out.

Keywords Control system · Nonlinear system design · Steady state · Equilibrium state · Dynamic equilibrium state

21.1 Introduction

In classical control theory, the relationship between input and output is researched by the transfer function in frequency domain. It is considered that the input controls the output directly. The root locus and frequency response are used for system analysis and design. In modern control theory, the relationship among input, state, and output is discussed in the state space. It is considered that the input controls the state directly [1]. Both the regulating and tracking control are realized by controlling the state of deviation system to the origin which is regarded as the

This research is supported by National Natural Science Foundation of China (no. 61375100 and no. 61472037).

L. Xin · Q. Wang · Y. Li (✉)
School of Automation, Beijing Institute of Technology, Beijing 100081, China
e-mail: liyuan@bit.edu.cn

Z. Deng and H. Li (eds.), *Proceedings of the 2015 Chinese Intelligent Automation Conference*, Lecture Notes in Electrical Engineering 337,
DOI 10.1007/978-3-662-46463-2_21

equilibrium state. Although most of the control problems can be solved by the classical and modern control theory, there are still some theoretical issues which need further research.

The state transition matrix of linear systems reflects the control of input to the state, but the relationship among input, state, and equilibrium state is not clear enough. Besides, the equilibrium state is regarded as the steady state of freedom systems in the available literatures. It cannot describe the dynamic steady state of servo systems. In some uncertainty systems, there is no certain equilibrium state [2, 3]. The reason is that the system steady state is no longer a point.

The control affection of input is analyzed from a new point of view by Wang in 1997 [4]. It is considered that what the input of control system controls directly is the equilibrium state, not the output or state of system. The state moves under constrain of the system structure matrix A. If A is stable, the state moves relatively to its equilibrium state. So the state is indirectly controlled by the input. In addition, the concept of DES is proposed to describe the steady-state solution of driven systems by Wang in 1998 [5], which has a more general meaning than equilibrium state. It is considered that the state will asymptotically converge to the DES for an asymptotically stable system. And the indirect control to state and output can be realized when the movement of DES is controlled. As shown in Fig. 21.1, the control essence of input to the state is clearly reflected by introducing the DES $(x_e(t))$ to the modern system analysis. And the two theoretical issues above are solved.

The concept of DES, not only generalize the meaning of equilibrium state for driven systems, but more important is that it provides new valuable topics for control theory. In this paper, five issues are summarized from the available literatures. First, the analytic expression of DES is researched to reveal the relationship between input and the steady-state solution. Second, the stability of DES is studied to ensure that the state will move back to the DES after the disturbance disappears. Third, the controllability of steady state, which includes the controllability of equilibrium state and the controllability of DES, is an issue that whether the steady state could reach to any point in the state space. Fourth, the DES gives a new way to solve the steady-state output issues, including the controllability of steady-state output and the steady-state error. Fifth, the idea of DES has been applied in the nonlinear system design. The research of these issues has been developed and

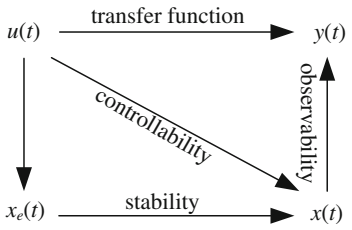

Fig. 21.1 System analysis framework based on DES

formed a systematic theory, named as DES theory. This paper gives a review of the recent development and suggests some subjects worthy for a further study.

21.2 Analytic Expression of DES

The analytic expression of DES reveals the control essence of input which considers that the input controls equilibrium state directly instead of the system state. In this section, this idea is interpreted, and then the main result of analytic expression of DES is summarized.

Consider a linear time-invariant (LTI) system:

$$\begin{aligned} \dot{x}(t) &= Ax(t) + Bu \\ y(t) &= Cx(t) \end{aligned} \tag{21.1}$$

First, we assume that the input u is a constant, and then the state solution is:

$$x(t) = e^{A(t-t_0)}x(t_0) + e^{At}\int_{t_0}^{t} e^{-A\tau}Bu\mathrm{d}\tau \tag{21.2}$$

Through certain mathematical process, Eq. (21.2) can be written as:

$$x(t) = e^{A(t-t_0)}(x(t_0) - x_e) + x_e, \quad x_e = -A^{-1}Bu \tag{21.3}$$

If A is Hurwitz, the state $x(t)$ will be stabilized on the point $-A^{-1}Bu$ in the state space. So x_e is the equilibrium state. Equation (21.3) shows that x_e is directly controlled by u, and $x(t)$ moves forward to x_e under condition of stable system matrix A. It also shows that x_e changes when u changes, and $x(t)$ will track new x_e.

Second, we assume that the input is a continuous function, and then the state solution is:

$$x(t) = e^{A(t-t_0)}x(t_0) + e^{At}\int_{t_0}^{t} e^{-A\tau}Bu(\tau)\mathrm{d}\tau \tag{21.4}$$

Through certain mathematical process, Eq. (21.4) can be written as:

$$x(t) = e^{A(t-t_0)}(x(t_0) - x_e(t_0)) + x_e(t) \tag{21.5}$$

$x_e(t)$ is the steady-state solution which is a time-varying function of input. $x_e(t)$ does not contain transient constituents. x_e and $x_e(t)$ are both the system steady states which have different forms for different inputs. Equation (21.5) shows that the

steady state is not a constant point. $x(t)$ moves forward to $x_e(t)$ with a stable A. $x_e(t)$ is defined as DES in [5]. It also shows that the indirect control to state can be realized when the movement of DES is controlled.

Definition 21.1 For driven dynamic system:

$$\dot{x} = f(t, x, u(t)) \tag{21.6}$$

where f is a sectional-continuous function about t and locally Lipschitz on x and $u(t)$.

The stable component $x_e(t)$ of the particular solution of system (21.6) is called the dynamic equilibrium state of system (21.6) driven by $u(t)$.

Because Definition 21.1 is different from the definition of equilibrium state. So the analytic expression of DES needs to be solved by other methods. The analytic expression of DES for typical input signals (step, ramp, and acceleration) is obtained through deviation transform for LTI systems in [5]. And the analytic expression of DES for general polynomial signals is obtained by [6, 7]. The input $u(t)$ is expanded through the Taylor series, and then the deviation transform and the additive property of linear systems are used to get the final result. If $u(t)$ is a polynomial function, and $u^{(j+1)}(t) = 0$. The analytic expression of DES is:

$$x_e(t) = -\sum_{i=0}^{j} A^{-(i+1)} B u^{(i)}(t) \tag{21.7}$$

According to the aircraft trajectory tracking problem in [8, 9], the analytic expression of DES for time-varying systems is discussed. The Eq. (21.8) presents the analytic expression of DES for time-varying systems, which depends on the Caratheodory solution $\phi(t) = e^{At}\Lambda$.

$$x_e(t) = \int_{-\infty}^{\infty} \phi(t-\tau)\left\{\tilde{A}(\tau)x(\tau) + B(\tau)u(\tau)\right\}\mathrm{d}\tau \tag{21.8}$$

21.3 Stability of DES

The stability of DES ensures that the state will move back to the DES after the disturbance disappears. The DES is the stable particular solution of the system equation. According to the stability definition of the particular solution in the theory of ordinary differential equation [10], the stability of DES is defined in sense of Lyapunov (i.s.L.).

Definition 21.2 The DES $x_e(t)$ $(t_0 \le t < +\infty)$ of system $\dot{x} = f(t, x, u(t))$ is

(1) i.s.L. stable if there exists $\delta(\varepsilon, t_0) > 0$, for all $\varepsilon > 0$, such that

$$\|x(t_0) - x_e(t_0)\| \le \delta(\varepsilon, t_0) \Rightarrow \|x(t) - x_e(t)\| \le \varepsilon, \forall t \ge t_0 \tag{21.9}$$

(2) i.s.L. uniformly stable if it is stable and δ is independent of t_0.

(3) i.s.L. asymptotically stable if there exists $\delta(\varepsilon, t_0) > 0$, for all $\varepsilon > 0$, such that

$$\|x(t_0) - x_e(t_0)\| \le \delta(\varepsilon, t_0) \Rightarrow \lim_{t \to \infty} \|x(t) - x_e(t)\| = 0 \tag{21.10}$$

(4) i.s.L. uniformly asymptotically stable if it is asymptotically stable and δ is independent of t_0.

When the steady state is equilibrium state, Definition 21.2 is the stability definition of equilibrium state. Being different from the attractiveness of equilibrium state, the stability of DES describes the attractiveness of a dynamic curve. As the linear systems can be carried out quantitative analysis, the available literatures research this problem in linear systems. According to [5, 10], the DES is a particular solution which satisfies the system equation, so its stability is equal to the origin stability of the disturbance system. It is obvious that $\dot{z} = A(t)z$ is the disturbance system of system $\dot{x} = A(t)x + B(t)u(t)$. So the stable conditions of DES are equal to the case of equilibrium state.

In addition, the impact of input to the system stability can be investigated in a new way, provided that the input can be allocated in the system structure matrix through some transform [11]. With this idea applied in LTI systems, the new equilibrium state can be obtained and coincides with the result in [4].

21.4 Controllability of Steady State

21.4.1 Controllability of Equilibrium State

The controllability of equilibrium state is proposed for LTI systems in [5]. This problem discusses that whether the equilibrium state could be regulated to any point in the state space.

If the input is constant, the equilibrium state is $x_e = -A^{-1}Bu$. For the single input case, $-A^{-1}B$ is one dimension, so the equilibrium state moves in direction of $-A^{-1}B$ following the input. For the multiple inputs case, if $\text{Rank}[B] = r$, the equilibrium state could be controlled in r dimensions in the state space. It is also pointed that the controllability of equilibrium state is not equal to the controllability of state in [5]. For linear single variable systems, if the state can be completely controllable, any point in the state space can be configured as the equilibrium state, but the stability will not be guaranteed.

21.4.2 Controllability of DES

Based on the controllability of equilibrium state, the controllability of DES is proposed in [6]. If the DES could be controlled to reach any point in the state space, then the DES is completely controllable. The controllability of DES means the controllability of steady-state response. It considers that whether the state could get to the appointed point after the system gets into the steady-state response.

The controllability of DES is discussed for the polynomial function signals in linear single variable systems in [6]. According to the analytic expression of DES, the DES is completely controllable, provided that $\text{rank}[A^{-1}BA^{-2}B\cdots A^{-n}B] = n$.

Furthermore, the discussion in [12] points out that the DES is one dimension controllable for an established ramp signal. In addition, it also gives a result for multiple variable systems. If the DES is n dimension controllable, the inputs are n dimensions at least, and $\text{rank}[A^{-1}BA^{-2}B\ldots A^{-n}B] = n$.

21.5 System Steady-State Output

21.5.1 Controllability of Steady-State Output

For many control systems, the steady-state output is expected to be a constant. And these problems are called constant steady-state output control issues in [13]. Consider system (21.1), if there always exists a control law satisfying $\lim_{t\to\infty} y(t) = c$, the system is steady-state output controllable.

An example in [13] shows that the controllability of steady-state output is different from the controllability of output. The necessary condition of the controllability of steady-state output is that the system is stable. The controllable condition for linear single variable systems is given, and it is equal to the existence condition for robust controller. If the system (21.1) is a single variable system, the steady-state output controllable condition is

$$\text{rank}\begin{vmatrix} A & B \\ C & 0 \end{vmatrix} = n + 1 \tag{21.11}$$

More research for the multiple variables systems is shown in [14, 15], the controllable condition is given, and it is also equal to the existence condition for robust controller.

21.5.2 Steady-State Error

Compared with the steady-state error analysis in classical control theory, the steady-state error could be easily analyzed in state space using the analytic expression of DES. The steady-state error for typical signals is studied in [5]. For a general polynomial function with $u^{(j+1)}(t) = 0$, the condition of zero steady-state error is:

$$CA^{-1}B = -1, CA^{-(i+1)}B = 0\,(i = 1, 2, \ldots, j) \tag{21.12}$$

In classical control theory, it is difficult to get the dynamic error coefficient for the high-order inputs. This problem is solved with the analytic expression of DES by [16]. The necessary and sufficient condition of zero steady-state error is proved to be equal to the result of internal model principle in [17].

21.6 Application in Nonlinear Systems

The DES theory considers that the indirect control to the state and output can be realized when the movement of DES is controlled. With this idea, a new design method for nonlinear system is proposed. First, design a control law to make the DES at the predetermined trajectory. Second, control the system state to converge to the DES.

21.6.1 Direct Method of Feedback Linearization

Based on the new idea, a direct method of feedback linearization for nonlinear time-varying systems is proposed in [18, 19]. According to the system design requirements, a linear time-invariant system is designed to be the reference model. Then, the state of the reference model is regarded as the optimal trajectory of DES. Using the Lyapunov direct method, a control law is designed to make the state of the object system asymptotically track the DES. This method has been applied in the single variable nonlinear systems, affine nonlinear systems and linear time-varying systems in [5].

21.6.2 Other Methods

A new backstepping method based on DES theory is proposed in [20–22]. The expected virtual control is regarded as the system DES. Then the backstepping method is used to design the control law for the tracking of DES. The concept of

DES, which is introduced to substitute the virtual control, makes the design process clearer. An adaptive fuzzy backstepping control method is presented for path tracking of underactuated ship in [23]. The direct method of feedback linearization, backstepping method, and sliding mode control method are compared in [24, 25]. These methods are applied to different classes of nonlinear systems, but they also have similarity. In addition, a robust adaptive controller is designed for underactuated systems [26, 27], in which the controller works for the tracking of the predetermined DES.

21.7 Conclusion and Prospect

The DES theory reveals the control essence of input to the control systems. It provides a new point of view for the control system design, especially the steady-state analysis in the state space. And it also gives a new way for the nonlinear time-varying system design. At the same time, it brings some new valuable research topics for control theory, such as analytic expression of DES, the controllability of steady state, and so on. Preliminary conclusions have been obtained for these issues, but there are still some subjects worthy for more study. Further research mainly includes (not limited to) the following points:

1. The analytic expression of DES for polynomial functions has been obtained, whereas the exponential and sinusoidal signals have not been analyzed. The stability of DES has been proved to be equal to the case of equilibrium state. The boundary stability could be researched by the DES. According to the steady-state analysis, the transient performance is worth to study through the DES.
2. All the nonlinear system design methods based on DES depend on the Lyapunov stability theory which ensures the convergence when time tends to infinity. But in the periodically control of servo systems, the learning control and repetitive control methods use the iterative learning. Whether the DES theory could solve the periodically control problems needs further study.
3. The available literatures of DES theory focus on the LTI systems. The relative analysis for time-varying systems is a great challenge.

References

1. Richard CD, Robert HB (2010) Modern control systems, 11th edn. Prentice Hall, New Jersey
2. Kofman E (2005) Non-conservative ultimate bound estimation in LTI perturbed systems. Automatic 41(10):1835–1838
3. Liu XC, Song CH, Chu EH (2013) Partial variable stabilization of a class of uncertain systems with uncertain equilibrium point. Acta Automatica Sin 39(1):1–10
4. Wang QL (1997) Control system equilibrium point and control. J Beijing Inst Tech 17(1):130
5. Wang QL (1998) Dynamic equilibrium state and nonlinear time-varying control systems design. Institute of automation, Chinese academy of sciences

6. Wang L (2005) Dynamic equilibrium state of control system and application in system analysis and design. Beijing Institute of Technology, Beijing
7. Wang L, Chen H (2007) Analysis of the dynamic equilibrium state in linear control system. Autom Instrum 22(3):21–25
8. Hunt LR, Meyer G, Ramakrishna V (1996) Output tracking and steady state for nonlinear systems. In: Proceedings of the 35th conference on decision and control, pp 2064–2068
9. Hunt LR, Meyer G, Su R (1996) Noncausal inverses for linear systems. IEEE Trans Autom Control 41(4):608–611
10. Lu QS, Peng LP, Yang ZQ (2010) Ordinary differential equation and dynamical systems, Beijing University of Aeronautics and Astronautics Press, Beijing
11. Wang QL (1998) The influence of control system input on system stability. J Beijing Inst Technol 18(4):453–455
12. Qiu DH, Wang QL, Zhou Y (2010) Dynamic equilibrium state controllability of linear time-invariant systems. In: Proceedings of the 8th world congress on intelligent control and automation, 3430–3434
13. Wang QL, Chen JD (1998) Steady-state output controllability of linear time-invariant SISO systems. Control Decis 13(1):91–94
14. Qiu DH (2011) Dynamic equilibrium state theory and its application on underactuated systems. Beijing Institute of Technology, Beijing
15. Qiu DH, Wang QL, Zhou Y (2009) Steady-state output controllability and output controllability of linear systems. In: The 2nd Asia-Pacific conference on computational intelligence and industrial applications, pp 147–150
16. Wang L, Wang QL, Chen H (2009) The steady-state error to control systems in state-space expression. Fire Control Command Control 34(6):28–31
17. Qiu DH, Wang QL, Zhou Y (2010) Mechanism analysis of steady-state error based on dynamic equilibrium state theory. Fire Control and Command Control 36(4):30–33
18. Wang QL (1996) Robust method for feedback linearization of nonlinear system. J Beijing Inst Technol 16(3):346
19. Wang QL, Chen Y (1999) Equilibrium control theory and direct method of feedback linearization for nonlinear time-varying systems. J Beijing Inst Technol 8(3):306–311
20. Wang L, Wang QL (2004) The analysis of the dynamic equilibrium in nonlinear control system. In: Proceedings of 2004 IEEE conference on cybernetics and intelligent systems, pp 1187–1191
21. Wang L, Wang QL (2006) The nonlinear system tracking design based on the dynamic equilibrium state theory. In: Proceedings of the 25th chinese control conference, pp 140–144
22. Wang L, Wang QL (2008) The nonlinear system design technique based on the dynamic equilibrium state theory. Fire Control Command Control 33(11):17–21
23. Qiu DH, Wang QL (2011) Adaptive fuzzy control for path tracking of underactuated ships based on dynamic equilibrium state theory. Int J Comput Intell Syst 4(6):1148–1157
24. Wang L, Wang QL (2004) Description and application of the backstepping design methods. Autom Panorama 21(6):57–61
25. Wang L, Wang QL (2004) Discussion of four nonlinear systems design methods. Autom Panorama 4(8):82–84
26. Qiu DH, Wang QL, Yang J (2011) Tracking control for the underactuated overhead crane system based on dynamic equilibrium state theory. Inf Technol J 10(12):2399–2405
27. Qiu DH, Wang QL, Zhou Y (2012) Tracking control for uncertain inverted pendulum systems based on the dynamic equilibrium state theory. J Basic Sci Eng 20(2):336–344

Chapter 22
RBFNN-Based Path Following Adaptive Control for Underactuated Surface Vessels

Wei Meng and Chen Guo

Abstract A robust adaptive control strategy is developed to force an underactuated surface vessel to follow a reference path at a desired speed with the unknown parameters, despite the presence of environmental disturbances induced by wave, wind, and ocean current. The proposed controller is designed by using RBF neural networks and the backstepping techniques. The proposed control system allows for both low- and high-speed applications since linear and nonlinear damping terms were considered in the control design. Numerical simulation results are provided to demonstrate the effectiveness of the proposed controller design and the accuracy of stability analysis.

Keywords Underactuated surface vessels · Path following · RBF neural networks · Adaptive control

22.1 Introduction

Robust path following is an issue of vital practical importance to the ship industry. For the path following problem, the main challenge is that most ships are usually equipped with one or two main propellers for surge motion control, and rudders for yaw motion control of the ship. There are no side thrusters, so the sway axis is not actuated. This configuration is mostly used in the marine vehicles [1]. Meanwhile, another challenge of path following issue is the inherent nonlinearity of the ship dynamics and kinematics with the uncertain parameters and unstructured

W. Meng (✉)
School of Information Engineering, Dalian Ocean University, Dalian 116023, China
e-mail: mengwei6699@126.com

C. Guo
School of Information Science and Technology, Dalian Maritime University, Dalian 116026, China
e-mail: guoc@dlmu.edu.cn

Z. Deng and H. Li (eds.), *Proceedings of the 2015 Chinese Intelligent Automation Conference*, Lecture Notes in Electrical Engineering 337,
DOI 10.1007/978-3-662-46463-2_22

uncertainties including external disturbances and measurement noise, etc. To overcome these challenges, many different nonlinear design methodologies have been introduced to the underactuated ships. By applying the Lyapunov's direct method, two constructive tracking solutions were developed in Jiang [2]. In [3–5], the controllers were designed to force an underactuated surface vessel to follow a predefined path. The stability analysis was investigated relying on the Lyapunov's direct method. A robust adaptive control scheme was proposed for point-to-point navigation of underactuated ships by using a general backstepping technique [6]. In [7], a simple control law was presented by using the novel backstepping and feedback dominance. Furthermore, the control design was verified using a model ship in a tank. By using intelligent control, Liu proposed a stable adaptive neural network algorithm for the path following of underactuated ship with parameters uncertainties and disturbances [8].

Motivated by these recent developments in path following of underactuated surface vessels, this paper presents an adaptive RBF neural networks control law. The stability analysis is performed based on the Lyapunov theory. The proposed controller can guarantee that all signals of the underactuated system are bounded. Numerical simulations are provided to validate the effectiveness of the proposed path following controller.

22.2 Problem Statements

Consider the path following problem of an underactuated surface vessel. Generally, for path following, the vessel is moving in the horizontal plane, the heave, roll, and pitch are normally neglected. The mathematical model of the underactuated surface vessel moving in three degrees of freedom can be described as [9]:

$$\begin{cases} \dot{x} = u\cos\psi - v\sin\psi \\ \dot{y} = u\sin\psi + v\cos\psi \\ \dot{\psi} = r \\ \dot{u} = f_u(u,v,r) + \tau_u/m_{11} + b_u/m_{11} \\ \dot{v} = f_v(u,v,r) + b_v/m_{22} \\ \dot{r} = f_r(u,v,r) + \tau_r/m_{33} + b_r/m_{33} \end{cases} \tag{22.1}$$

with $f_u = m_{22}vr/m_{11} - d_u u/m_{11} - \sum_{i=2}^{3} d_{ui}|u|^{i-1}u/m_{11}$, $f_v = -m_{11}ur/m_{22} - d_v v/m_{22} - \sum_{i=2}^{3} d_{vi}|v|^{i-1}v/m_{22}$, $f_r = (m_{11} - m_{22})uv/m_{33} - d_r r/m_{33} - \sum_{i=2}^{3} d_{ri}\,|r|^{i-1}r/m_{33}$, $[b_u, b_v, b_r]^T = R(\psi)^T\left[b_x, b_y, b_\psi\right]^T$, $R(\psi) = \begin{bmatrix} \cos\psi & -\sin\psi & 0 \\ \sin\psi & \cos\psi & 0 \\ 0 & 0 & 1 \end{bmatrix}$.

where x, y, and ψ are the surge displacement, sway displacement, and the yaw angle in the earth fixed frame, and u, v, and r are the velocities in surge, sway, and yaw, respectively. The constant parameters $m_{jj} > 0$, $1 \leq j \leq 3$, denote the ship's inertia and added mass effects. The positive terms d_u, d_v, d_r, d_{ui}, d_{vi}, and d_{ri}, $i = 2, 3$, are given by the hydrodynamic damping in surge, sway, and yaw. τ_u and τ_r denote the available control inputs, respectively, the surge force and the yaw moment. $b = \left[b_x, b_y, b_\psi\right]^T$ denote the low frequency interference in the earth fixed frame, $\dot{b} = 0$.

We now define the path following errors in a frame attached to the path as follows [8]:

$$(x_e, y_e, \psi_e)^T = R^T(\psi)(x - x_d, y - y_d, \psi - \psi_d)^T, \tag{22.2}$$

where ψ_d represents the desired yaw angle and was defined as $\psi_d = \arctan\left(y'_d(s)/x'_d(s)\right)$, $x'_d = \partial x_d/\partial s$, $y'_d = \partial y_d/\partial s$; x_d and y_d denote the desired displacement in path of the vessel.

Assumption 22.1 The parameters of underactuated surface vessels such as m_{jj}, d_u, d_v, d_r, d_{ui}, d_{vi}, and d_{ri}, $1 \leq j \leq 3$, $i = 2, 3$, are known.

Assumption 22.2 The reference path is regular, x_d, $\dot{x}_d$, $\ddot{x}_d$, y_d, $\dot{y}_d$, $\ddot{y}_d$, $\dot{\psi}_d$ and $\ddot{\psi}_d$ are all bounded.

Control objective: Under Assumptions 22.1 and 22.2, the objective of this paper is to seek the adaptive control laws τ_u and τ_r that force the vessel from the initial position and orientation to follow a reference path $\boldsymbol{\Omega}$.

22.3 Control Design

In this section, we develop an adaptive control law for underactuated surface vessels (22.1) with uncertain dynamics.

From (22.2), we have

$$\begin{cases} \dot{x}_e = u - u_d \cos(\psi_e) + r y_e \\ \dot{y}_e = v + u_d \sin(\psi_e) - r x_e \\ \dot{\psi}_e = r - r_d \end{cases} \tag{22.3}$$

where $u_d = \bar{u}_d \dot{s}$, $\bar{u}_d = \sqrt{x'^2_d(s) + y'^2_d(s)}$, $r_d = \frac{x'^2_d(s) y''^2_d(s) - x''^2_d(s) y'^2_d(s)}{x'^2_d(s) + y'^2_d(s)} \dot{s}$.

We define

$$u_e = u - \alpha_u, \bar{\psi}_e = \psi_e - \alpha_{\psi_e} \tag{22.4}$$

where α_u and α_{ψ_e} are virtual controls of u and ψ_e. Substituting (22.4) into (22.3) results in

$$\begin{cases} \dot{x}_e = \alpha_u + u_e - u_d \cos(\psi_e) + \Delta_1 + r y_e \\ \dot{y}_e = v + u_d \sin(\psi_e) + \Delta_2 - r x_e \end{cases} \tag{22.5}$$

where $\Delta_1 = -u_d\left(\left(\cos\left(\bar{\psi}_e\right) - 1\right)\cos\left(\alpha_{\psi_e}\right) - \sin\left(\bar{\psi}_e\right) \quad \sin\left(\alpha_{\psi_e}\right)\right), \Delta_2 = u_d \sin\left(\bar{\psi}_e\right)$ $\cos\left(\alpha_{\psi_e}\right) + \left(\cos\left(\bar{\psi}_e\right) - 1\right)\sin\left(\alpha_{\psi_e}\right)$.

We choose the virtual control α_u as

$$\alpha_u = -k_1 x_e + u_d \cos\left(\alpha_{\psi_e}\right) \tag{22.6}$$

where $k_1 > 0$. The derivative of the path parameter s satisfies

$$\dot{s} = \sqrt{u_{d0}^2 + (k_2 y_e + v_d)^2} \Big/ \bar{u}_d \tag{22.7}$$

where $k_2 > 0$, v_d is the filter of v, $v_e = v - v_d$. From (22.7), we have

$$u_d = \sqrt{u_{d0}^2 + (k_2 y_e + v_d)^2} \tag{22.8}$$

We choose the virtual control α_{ψ_e} as

$$\alpha_{\psi_e} = -\arctan((k_2 y_e + v_d)/u_{d0}) \tag{22.9}$$

Substituting (22.6), (22.7), and (22.9) into (22.5), we have

$$\begin{cases} \dot{x}_e = -k_1 x_e + u_e + \Delta_1 + r y_e \\ \dot{y}_e = -k_2 y_e + v_e + \Delta_2 - r x_e \end{cases} \tag{22.10}$$

And substituting (22.9) into (22.6), we have

$$\alpha_u = -k_1 x_e + u_{d0} \tag{22.11}$$

The time derivative of (22.4) using (22.3) and (22.9) can be derived as

$$\dot{\bar{\psi}}_e = r - r_d + \{[k_2(-k_2 y_e - r x_e + \Delta_2 + v_e) + \dot{v}_d]u_{d0} - (k_2 y_e + v_d)\dot{u}_{d0}\}/u_d^2 \tag{22.12}$$

We define the r_e as

$$r_e = r - \alpha_r \tag{22.13}$$

Substituting (22.13) into (22.12), we have

$$\dot{\bar{\psi}}_e = -k_3\bar{\psi}_e + f_x r_e + k_2 u_{d0} v_e / u_d^2 \tag{22.14}$$

where $k_3 > 0$, $f_x = 1 - k_2 x_e u_{d0}/u_d^2$.

Differentiating v_e, and substituting (22.1) into it, we have

$$v_e = g_v - \dot{v}_d \tag{22.15}$$

where $g_v = f_v(u, v, r) + b_v/m_{22}$.

According to the approximation property of NNs, the smooth function g_v can be approximated by RBF neural networks as follows

$$g_v = W_v^T \sigma(\eta) + \varepsilon_v \tag{22.16}$$

where W_v is the idea weight matrix, ε_v is the approximation error, $|\varepsilon_v| \leq \varepsilon_{vM}$, $\eta = [x, y, \psi, u, v, r]^T$.

Let $\hat{W}_v$ be the estimations of the weights W_v, $\hat{g}_v$ is the estimation of the g_v, and can be defined as

$$\hat{g}_v = \hat{W}_v^T \sigma(\eta) \tag{22.17}$$

In order to stabilize the v_e, the $\dot{v}_d$ can be chosen as

$$\dot{v}_e = \hat{W}_v^T \sigma(\eta) - k_6 v_e - k_2 u_{d0}\bar{\psi}_e / u_d^2 + \varepsilon_v \tag{22.18}$$

The time derivative of (22.4) can be derived

$$\dot{u}_e = g_u + \tau_u/m_{11} - \dot{\alpha}_u \tag{22.19}$$

with $g_u = f_u(u, v, r) + b_u/m_{11}$, $\dot{\alpha}_u = \dfrac{\partial \alpha_u}{\partial x_e}\dot{x}_e + \dfrac{\partial \alpha_u}{\partial u_{d0}}\dot{u}_{d0}$.

The smooth function g_u can also be approximated by RBF neural networks as follows

$$g_u = W_u^T \sigma(\eta) + \varepsilon_u \tag{22.20}$$

where W_u is the idea weight matrix, ε_u is the approximation error, $|\varepsilon_v| \leq \varepsilon_{vM}$, $\eta = [x, y, \psi, u, v, r]^T$.

Let $\hat{W}_u$ be the estimations of the weights W_u, $\hat{g}_u$ is the estimation of the g_u, and can be defined as

$$\hat{g}_u = \hat{W}_u^T \sigma(\eta) \tag{22.21}$$

The time derivative of (22.13) can be derived as

$$\dot{r}_e = g_r + \tau_r / m_{33} - \dot{\alpha}_r \tag{22.22}$$

where $g_r = f_r(u, v, r) + b_r / m_{33} + \dot{\hat{g}}_v$.

The smooth function g_u can be approximated by RBF neural networks as follows

$$g_r = W_r^T \sigma(\eta) + \varepsilon_r \tag{22.23}$$

where W_r is the idea weight matrix, ε_r is the approximation error, $|\varepsilon_r| \leq \varepsilon_{rM}$, $\eta = [x, y, \psi, u, v, r]^T$.

Let $\hat{W}_r$ be the estimations of the weights W_r, $\hat{g}_r$ is the estimation of the g_r, and can be defined as

$$\hat{g}_r = \hat{W}_r^T \sigma(\eta) \tag{22.24}$$

From (22.19) and (22.22), the adaptive NNs surge control law τ_u and the yaw moment control law τ_r can be presented as

$$\tau_u = m_{11}(-\hat{g}_u - k_4 u_e + \dot{\alpha}_u), \quad k_4 > 0 \tag{22.25}$$

$$\tau_r = m_{33}\left(-\hat{g}_r - k_5 r_e + \dot{\alpha}_r - f_x \bar{\psi}_e\right), \quad k_5 > 0 \tag{22.26}$$

The adaptive laws are given by

$$\dot{\hat{W}}_u = \Gamma_u \left[\sigma(\eta) u_e - k_u \hat{W}_u\right] \tag{22.27}$$

$$\dot{\hat{W}}_v = \Gamma_v \left[\sigma(\eta) v_e - k_v \hat{W}_v\right] \tag{22.28}$$

$$\dot{\hat{W}}_r = \Gamma_r \left[\sigma(\eta) r_e - k_r \hat{W}_r\right] \tag{22.29}$$

where $\Gamma_u = \Gamma_u^T > 0$, $\Gamma_v = \Gamma_v^T > 0$, $\Gamma_r = \Gamma_r^T > 0$ are constant design parameters.

22.4 Stability Analysis

Theorem 22.1 Assume that the Assumptions 1–2 hold, the adaptive NNs surge control law τ_u and the yaw moment control law τ_r are derived as in (22.25) and (22.26), and adaptation laws are given by (22.27–22.29), the control objective of

path following for underactuated surface vessels in the presence of uncertain parameters and unstructured uncertainties is solved, and the systems (22.1) are asymptotic stability.

Proof From (22.29) and (22.30), we have

$$\begin{cases} \dot{Z}_1 = f_1(Z_1, Z_2) \\ \dot{Z}_2 = f_2(Z_2) \end{cases}, \tag{22.30}$$

with $Z_1 = [x_e, y_e]^T$, $Z_2 = \left[\bar{\psi}_e, u_e, v_e, r_e, \tilde{W}_u, \tilde{W}_v, \tilde{W}_r\right]^T$

$$\begin{aligned} f_1 &= \left[-k_1 x_e + u_e + \Delta_1 + r y_e, -k_2 y_e + v_e + \Delta_2 - r x_e\right]^T, \\ f_2 &= \left[-k_3\bar{\psi}_e + f_x r_e + k_2 u_{d0} v_e / u_d^2, \tilde{W}_u^T \sigma(\eta) - k_4 u_e + \varepsilon_u, \tilde{W}_v^T \sigma(\eta)\right. \\ &\quad - k_6 v_e - k_2 u_{d0}\bar{\psi}_e / u_d^2 + \varepsilon_v, \tilde{W}_r^T \sigma(\eta) - k_5 r_e - f_x\bar{\psi}_e + \varepsilon_r, \\ &\quad \left.-\Gamma_u\left[\sigma(\eta)u_e - \sigma_u\hat{W}_u\right], -\Gamma_v\left[\sigma(\eta)v_e - \sigma_v\hat{W}_v\right], -\Gamma_r\left[\sigma(\eta)r_e - \sigma_r\hat{W}_r\right]\right]^T. \end{aligned}$$

To investigate stability of this subsystem, we consider the following Lyapunov function:

$$V_1 = \frac{1}{2}\bar{\psi}_e^2 + \frac{1}{2}u_e^2 + \frac{1}{2}r_e^2 + \frac{1}{2}\tilde{W}_u^T\Gamma_u^{-1}\tilde{W}_u + \frac{1}{2}\tilde{W}_v^T\Gamma_v^{-1}\tilde{W}_v + \frac{1}{2}\tilde{W}_r^T\Gamma_r^{-1}\tilde{W}_r, \tag{22.31}$$

Differentiating (22.32) along with (22.27–22.30), we have

$$\begin{aligned} \dot{V}_1 \le & -k_3\bar{\psi}_e^2 - k_4 u_e^2 - k_5 r_e^2 - k_6 v_e^2 + \sigma_u\tilde{W}_u^T\hat{W}_u + \sigma_v\tilde{W}_v^T\hat{W}_v + \sigma_r\tilde{W}_r^T\hat{W}_r \\ & + u_e\varepsilon_u + v_e\varepsilon_v + r_e\varepsilon_r \end{aligned} \tag{22.32}$$

The (22.33) can be described as

$$\begin{aligned} \dot{V}_1 \le & -k_3\bar{\psi}_e^2 - \left(k_4 - \frac{1}{4}\right)u_e^2 - \left(k_5 - \frac{1}{4}\right)v_e^2 - \left(k_6 - \frac{1}{4}\right)r_e^2 \\ & - \frac{1}{2}\sigma_u\left\|\tilde{W}_u\right\|^2 - \frac{1}{2}\sigma_v\left\|\tilde{W}_v\right\|^2 \\ & - \frac{1}{2}\sigma_r\left\|\tilde{W}_r\right\|^2 + \varepsilon_u^2 + \varepsilon_v^2 + \varepsilon_r^2 + \frac{1}{2}\sigma_u\|W_u\|^2 + \frac{1}{2}\sigma_v\|W_v\|^2 + \frac{1}{2}\sigma_r\|W_r\|^2 \\ \le & -\mu V_1 + \rho \end{aligned} \tag{22.33}$$

with

$\mu := \min\left\{2k_3, 2\left(k_4 - \frac{1}{4}\right), 2\left(k_5 - \frac{1}{4}\right), 2\left(k_6 - \frac{1}{4}\right), \min\left(\frac{\sigma_u}{\lambda_{\max}(\Gamma_u^{-1})}\right), \min\left(\frac{\sigma_v}{\lambda_{\max}(\Gamma_v^{-1})}\right),\right.$
$\left.\min\left(\frac{\sigma_r}{\lambda_{\max}(\Gamma_r^{-1})}\right)\right\}$, $\rho := \varepsilon_u^2 + \varepsilon_v^2 + \varepsilon_r^2 + \frac{\sigma_u}{2}\|W_u\|^2 + \frac{\sigma_v}{2}\|W_v\|^2 + \frac{\sigma_r}{2}\|W_r\|^2$

Let $\Phi = \frac{\rho}{\mu}$, the (22.34) can be rewritten as

$$0 \leq V(t) \leq \Phi + [V(0) - \Phi]e^{-\mu t} \tag{22.34}$$

Hence, all signals of the closed-loop system are uniformly ultimately bounded. The path following errors will converge to a small neighborhood of zero, and can be adjusted by the design parameters $k_3, k_4, k_5, k_6, \sigma_u, \sigma_v, \sigma_r$.

22.5 Numerical Simulations

In this section, some numerical simulations are provided to demonstrate the effectiveness of the proposed control laws and the accuracy of stability analysis. In this paper, we use a monohull ship with the length of 38 m, mass of 118×10^3 kg, the numerical values of the vessel are adapted from [6].

In the simulation, the reference path is generated by a virtual ship as follows:

$$\begin{cases} \dot{x}_d = u_d \cos(\psi_d) - v_d \sin(\psi_d) \\ \dot{y}_d = u_d \sin(\psi_d) + v_d \cos(\psi_d) \\ \dot{\psi}_d = r_d \\ \dot{v}_d = -\dfrac{m_{11}}{m_{22}} u_d r_d - \dfrac{d_{22}}{m_{22}} v_d - \displaystyle\sum_{i=2}^{3} \dfrac{d_{vi}}{m_{22}} |v_d|^{i-1} v_d \end{cases}$$

In the simulation we select $u_d = 5$, $r_d = 0.015$; the control parameters selected for the simulation are: $k_1 = 15$, $k_2 = 7.5$, $k_3 = 12$, $k_4 = 10$, $k_5 = 10$, $k_6 = 10$, $\Gamma_u = 10$, $\Gamma_v = 30$, $\Gamma_r = 0.5$, $\sigma_u = \sigma_v = \sigma_r = 0.01$,

The initial conditions are chosen as:

$$[x(0), y(0), \psi(0), u(0), v(0), r(0)] = [-100, 0, 0, 0, 0, 0].$$

The simulation results of ship path following control are plotted in Figs. 22.1 and 22.2. Figure 22.1 shows the position and the orientation of the vessel in the xy plane, and the control inputs τ_u and τ_r are plotted. The path following position errors are plotted in Fig. 22.2. It can be seen from these figures that all the signals of the closed-loop system are bounded. From Fig. 22.2, the path following position errors x_e, y_e, the velocity errors u_e, r_e, and the orientation error ψ_e converge to zero while the sway motion error v_e converges to a small value, since the reference path is generated by a virtual ship, the sway velocity error is always a constant value.

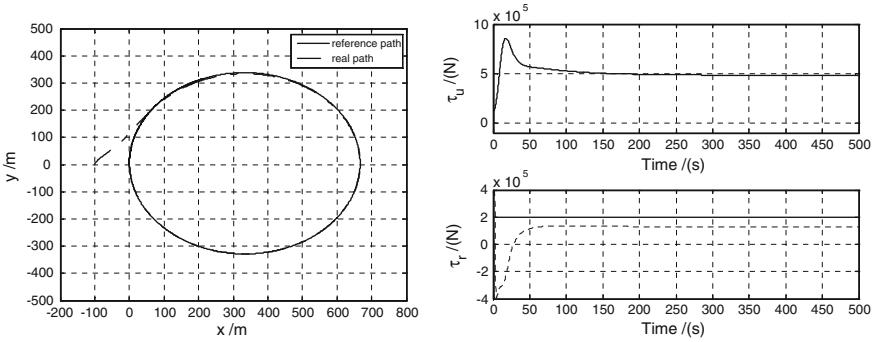

Fig. 22.1 Position and orientation and the inputs of the vessel

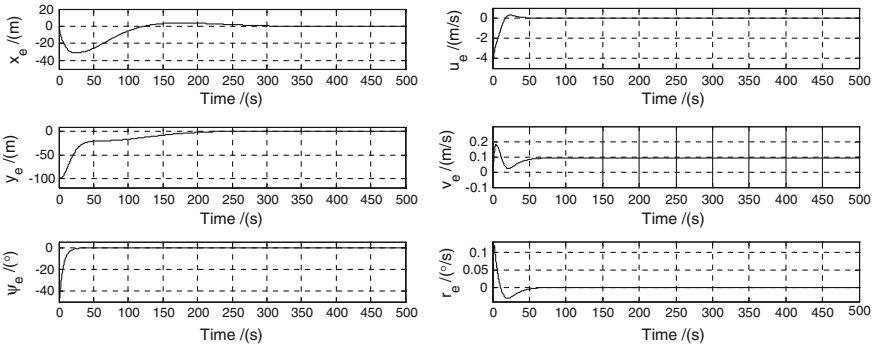

Fig. 22.2 Position, orientation, and velocity errors of the vessel

22.6 Conclusions

In this paper, we present an adaptive RBF neural networks scheme for path following of underactuated surface vessels with uncertain parameters and unstructured uncertainties including exogenous disturbances and measurement noise, etc. The proposed controller is designed by using RBF neural networks and the backstepping techniques. It is noted that the proposed control system allows for both low- and high-speed applications since linear and nonlinear damping terms were considered in the control design. The stability analysis is performed based on the Lyapunov theory. The effectiveness of the designed controller is also validated by the numerical simulations. Based on the ideas of this paper, the future work will consider the rudder saturation and rate limits.

Acknowledgments The work for this paper was financially supported by the National Natural Science Foundation of China (NSFC, Grant No: 61374114) and the Fundamental Research Funds for the Central Universities (Grant No: 3132014321).

References

1. Fossen TI (2002) Marine control systems. Marine Cybernetics, Trondheim
2. Jiang ZP (2002) Global tracking control of underactuated ships by Lyapunove's direct method. Automatica 38:301–309
3. Do KD, Jiang ZP, Pan J (2004) Robust adaptive path following of underactuated ships. Automatica 40:929–944
4. Do KD, Pan J (2004) State-and output-feedback robust path-following controllers for underactuated ships using Serret-Frenet frame. Ocean Eng 31:587–613
5. Do KD, Pan J (2006) Global robust adaptive path following of underactuated ships. Automatica 42:1713–1722
6. Li JH, Lee PM, Jun BH, Lim YK (2008) Point-to-point navigation of underactuated ships. Automatica 44:3201–3205
7. Li Z, Sun J, Oh SR (2009) Design, analysis and experimental validation of robust nonlinear path following control of marine surface vessels. Automatica 45:1649–1658
8. Liu Y, Guo C (2014) Control method of underactuated surface ship formation based on stable adaptive neural network control law. J Traffic Transp Eng 14(3):120–126
9. Perez T (2005) Ship motion control: course keeping and roll stabilisation using rudder and fins. Springer, Berlin

Chapter 23
Sliding Mode Tracking and Input Shaped Vibration Control of Flexible Hypersonic Vehicles

Xiaoyun Wang and Yingmin Jia

Abstract The combined sliding mode controller-observer equipped with the input shaper is designed and analyzed for the longitudinal dynamics of flexible hypersonic vehicles (FHVs). First, the input–output linearization is employed to decouple the velocity and altitude dynamics. Then, the sliding mode controller (SMD) with modified exponential approach law (MEAL) is designed, which can render the closed-loop system track the commands effectively. In order to estimate the states that are not available for measurement, a nonlinear sliding mode observer is proposed. Moreover, by applying the input shaping (IS) technique, flexible dynamics with less elastic deformation and vibration can be obtained without destroying the closed-loop performance. Simulation results verify the effectiveness of the proposed control scheme.

Keywords FHV · SMD · MEAL · Observer · IS

23.1 Introduction

The design and analysis for FHVs are highly challenging which stems from the peculiar characteristics of the vehicles, such as severe aeroheating and strong interactions among the elastic airframe, the propulsion system, and the structure dynamics [1]. Furthermore, it is difficult to measure the atmosphere properties and aerodynamic parameters at high flight altitude. Besides, the flight dynamics of FHVs are sensitive to the changes of flight condition and the aerodynamic parameters present large uncertainty. Therefore, advanced control approaches are needed to address these intractable problems.

X. Wang (✉) · Y. Jia
The Seventh Research Division and the Department of Systems and Control, Beijing University of Aeronautics and Astronautics F907, Xinzhu Building, NO. 37 Xueyuan Road, Haidian District, Beijing, China
e-mail: msbywxy@126.com

Z. Deng and H. Li (eds.), *Proceedings of the 2015 Chinese Intelligent Automation Conference*, Lecture Notes in Electrical Engineering 337,
DOI 10.1007/978-3-662-46463-2_23

Many control methods have been utilized on the control of the FHVs. Sliding mode control is widely utilized for its robustness to modeling inaccuracy and disturbance. Although this technique has good robustness properties, pure sliding mode control presents drawbacks that include chattering. In this paper, a modified exponential approach law-based SMD is proposed to solve that problem. However, a sliding mode controller can be implemented only if full states feedback is available, a requirement not readily achieved in a hypersonic flight. The state observer for the unmeasurable states is needed.

FHVs adopt the slender geometries and light structures, thus temperature-induced stiffness variations will lead to the flexible dynamics evidently, which should be considered in the controller design. Flexible dynamics have been considered as disturbances in [3, 4]. Despite excellent results of the present studies, the further research on the attenuation of the elastic vibrations for the FHVs is needed. The technique of IS [5, 6] to control flexible structures has received much attention during the past few years. It has been proved to be effective on flexible spacecrafts and maneuvering flexible structures.

The main contribution of this paper is devising a controller that combines sliding mode observers and MEAL-based SMD to obtain good tracking performance and to be robust to the parameter uncertainty. The elastic deformation and vibration of the flexible dynamics are reduced by the IS technique. The rest of the paper is organized as follows: Sect. 23.2 describes the longitudinal model of FHVs. The linearization of the vehicle dynamics, MEAL-based SMD, the sliding mode observer and IS technique are presented in Sect. 23.3. Simulation results are discussed in Sect. 23.4. Section 23.5 concludes the paper.

23.2 Hypersonic Vehicle Model

The hypersonic vehicle model developed by Bolender and Doman [7] is considered.

$$\dot{V} = \frac{T\cos\alpha - D}{m} - \frac{\mu\sin\gamma}{(R_E+h)^2};\quad \dot{\gamma} = \frac{L+T\sin\alpha}{mV} - \frac{(\mu - V^2(R_E+h))\cos\gamma}{V(R_E+h)^2}$$

$$\dot{h} = V\sin\gamma;\ \dot{\alpha} = q - \dot{\gamma};\ \dot{q} = \frac{M_{yy}}{I_{yy}};\ \ddot{\eta}_i = -2\varsigma_i\omega_i\dot{\eta}_i - \omega_i^2\eta_i + N_i, i = 1,2,3 \quad (23.1)$$

This model consists of five rigid-body states $x = [V, \gamma, \alpha, q, h]^T$ and six flexible states $\eta = [\eta_1, \dot{\eta}_1, \eta_2, \dot{\eta}_2, \eta_3, \dot{\eta}_3]^T$, in which V, γ, α, q, h are the vehicle speed, flight path angle, angle of attack, pitch rate, and altitude. η are represented by generalized model coordinates η_i and N_i are generalized forces. ς_i and ω_i are the damping factor and the natural frequency of the ith flexible mode, respectively. Besides, m is the vehicle mass, R_E is the radius of the earth, I_{yy} is the moment of inertia, μ is

gravitational constant. The lift L, drag D, thrust T, pitching moment M_{yy}, and the generalized forces N_i are complex algebraic functions of both the system states and inputs that must be simplified. The approximated analytical expressions are as given:

$$L = \frac{1}{2}\rho V^2 S C_L; \quad D = \frac{1}{2}\rho V^2 S C_{LD}; \quad M_{yy} = \frac{1}{2}\rho V^2 S\bar{c}[C_M(\alpha) + C_M(\delta_e) + C_M(q)]$$
$$T = \frac{1}{2}\rho V^2 S C_T; \quad N_i = \frac{1}{2}\rho V^2 S[N_i^{\alpha^2}\alpha^2 + N_i^{\alpha}\alpha + N_i^{\delta_e}\delta_e + N_i^0 + N_i^{\eta}\eta] \tag{23.2}$$

where ρ is the density of air, S is the reference area, $\bar{c}$ is the mean aerodynamic chord, and δ_e is the elevator deflection. And the specific expressions for the coefficients (i.e., $C_L(\cdot), C_D(\cdot)$, and so on) are:

$$C_L = C_L^{\alpha}\alpha + C_L^{\eta}\eta + C_L^0; \quad C_D = C_D^{\alpha^2}\alpha^2 + C_D^{\alpha}\alpha + C_D^{\eta^2}\eta^2 + C_D^{\eta}\eta + C_D^0$$
$$C_M(\alpha) = C_M^{\alpha^2}\alpha^2 + C_M^{\alpha}\alpha + C_M^0; \quad C_M(\delta_e) = c_e\delta_e;$$
$$C_M(q) = \left(\frac{\bar{c}}{2V}\right)q\left(C_M^{\alpha^2}\alpha^2 + C_M^{\alpha}\alpha + C_M^0\right); \quad C_T = C_T^{\alpha}\alpha + C_T^{\beta}\beta + C_T^{\delta_e}\delta_e + C_T^{\eta}\eta \tag{23.3}$$

Besides, the engine dynamics are modeled by a second-order system:

$$\ddot{\beta} = -2\varsigma\omega_n\dot{\beta} - \omega_n^2\beta + \omega_n^2\beta_c \tag{23.4}$$

where ω_n and ς are natural frequency and damping coefficient.

In this paper, the throttle setting β_c and the elevator deflection δ_e are chosen to be the control inputs. The control outputs are the velocity V and the altitude h. The commands of velocity and altitude are denoted by V_d and h_d, respectively. The objective of this paper is to design an appropriate controller that force the velocity and altitude to track desired trajectory and alleviate the flexible vibrations, when the vehicles are subject to the parametrical uncertainties.

23.3 Controller Design

23.3.1 Input/Output Linearization

According to [8], the open-loop dynamics of AHVs exhibit unstable short-period modes and a lightly damped phugoid mode. Therefore, it is difficult for traditional control methods to meet the performance requirements of the system. However, we can linearize the system and conduct the controller design based on the linearized system. Applying the Lie derivative to the model (2.1), the system can be linearized completely and the closed-loop system has no internal dynamics. As in [7], the linearized model is shown as follows:

$$\begin{bmatrix} \dddot{V} \\ h^{(4)} \end{bmatrix} = \begin{bmatrix} f_V \\ f_h \end{bmatrix} + B \begin{bmatrix} \beta_c \\ \delta_e \end{bmatrix}, \quad \text{where} \quad \mathrm{B} = \begin{bmatrix} b_{11} & b_{12} \\ b_{21} & b_{22} \end{bmatrix}$$

where the expressions of $f_V, f_h, b_{11}, b_{12}, b_{21}, b_{22}$ can be found in Ref. [7].

23.3.2 SMD with MEAL

SMD method provides a systematic approach to the problem of maintaining stability and consistent performance in the face of parametric uncertainties and external disturbances [7, 9]. In this paper, two decoupled sliding surfaces s_i are defined as:

$$\begin{aligned} \dot{s_1} &= \ddot{e_1} + 3\lambda_1 \dot{e_1} + 3\lambda_1^2 e_1 + \lambda_1^3 \int_0^t e_1(\tau)\mathrm{d}\tau \\ \dot{s_2} &= \dddot{e_2} + 4\lambda_2 \ddot{e_2} + 4\lambda_2^3 e_2 + 6\lambda_2^2 \dot{e_2} + \lambda_2^4 \int_0^t e_2(\tau)\mathrm{d}\tau \end{aligned} \tag{23.5}$$

where $e_1(t) = V - V_d, e_2(t) = h - h_d$ and $\lambda_i > 0, i = 1, 2$ define the bandwidth of the error dynamics. When the sliding surfaces $s_i, i = 1, 2$ equal to zero, the integral of the tracking errors will eliminate the steady-state error [7]. In this paper, we chose SMD with modified exponential approach law as sliding conditions:

$$\dot{s}_1 = -k_1 \mathrm{sat}\left(\frac{s_1}{\phi_1}\right) - k_3 s_1; \quad \dot{s}_2 = -k_2 \mathrm{sat}\left(\frac{s_2}{\phi_2}\right) - k_4 s_2 \tag{23.6}$$

where k_3 and k_4 are definitely positive. The modified sliding controller can be written as follows:

$$\begin{bmatrix} \beta_c \\ \delta_e \end{bmatrix} = B^{-1} \begin{bmatrix} -\vartheta_1(x,t) - k_1 \mathrm{sat}\left(\frac{s_1}{\phi_1}\right) - k_3 s_1 \\ -\vartheta_2(x,t) - k_2 \mathrm{sat}\left(\frac{s_2}{\phi_2}\right) - k_4 s_2 \end{bmatrix} \tag{23.7}$$

Remark 23.1 The matrix B inverse does exist for the entire flight envelope except on a vertical flight path [9].

23.3.3 Sliding Mode Observer Design

The SMD controller developed in the preceding sections assumes that full states are available for measurement. In practice, only the states that correspond to V, h, and q

are expected to be measured. The variables corresponding to α and γ are too small to be measured. Accurate measurements are costly and difficult. In this section, a sliding mode observer is designed to estimate α and γ based on the measurements of V, h, and q. Using the techniques in [2], the sliding mode observers are designed as:

$$\dot{\hat{h}} = V\sin\hat{\gamma} - \eta_1\tilde{h} - k_h\text{sgn}(\tilde{h}); \quad \dot{\hat{\gamma}} = \frac{\hat{L} + T\sin\hat{\alpha}}{mV} - \frac{(\mu - V^2 r)\cos\hat{\gamma}}{Vr^2} - \eta_3\tilde{h} - k_\gamma\text{sgn}(\tilde{h});$$
$$\dot{\hat{q}} = \frac{\hat{M}_{yy}}{I_0} - \eta_2\,\tilde{q} - k_q\text{sgn}(\tilde{q}); \quad \dot{\hat{\alpha}} = \hat{q} - \dot{\hat{\gamma}} - \eta_4\tilde{q} - k_\alpha\text{sgn}(\tilde{q}) \tag{23.8}$$

where $\hat{L} = \frac{1}{2}\rho_0 V^2 S_0 \times 0.011\,\hat{\alpha}$; $\tilde{h} = \hat{h} - h$; $\tilde{q} = \hat{q} - q$

$$\hat{M}_{yy} = \frac{\rho_0 V^2 S_0 \bar{c}_0}{2}\Big[\left(-10^{-5}\hat{\alpha}^2 + 7.6\times10^{-5}\hat{\alpha} + 0.004\right) + \left(\frac{\bar{c}_0}{2V}\right)q\left(-0.002\,\hat{\alpha}^2 + 0.005\,\hat{\alpha} - 0.2289\right) + 5.23\times10^{-4}(\delta_e - \hat{\alpha})\Big] \tag{23.9}$$

And η_1, η_2, η_3 and η_4 are positive constants selected as 2.0, 1.8, 0.0001, and 0.001, respectively. k_h, k_q, k_γ and k_α are the sliding gains chosen by the designer.

The sliding surfaces of the observer are defined by $s_0 = 0$, where $s_0 = \begin{bmatrix}\tilde{h} & \tilde{q}\end{bmatrix}^T$. The average error dynamics during sliding where $s_0 = 0$ and $\dot{s}_0 = 0$ are:

$$\tilde{h} = 0; \quad \tilde{q} = 0; \quad V(\sin\hat{\gamma} - \sin\gamma) - k_h\text{sgn}(\tilde{h}) = 0$$

$$\left(\frac{\rho_0 V^2 S_0 \bar{c}_0}{2I_0}\right)\left\{-10^{-5}\left(\hat{\alpha}^2 - \alpha^2\right) + \left[7.6\times10^{-5} - 0.005\left(\frac{\bar{c}_0}{2V}\right)q\right]\tilde{\alpha} - 0.002\left(\frac{\bar{c}_0}{2V}\right)q\left(\hat{\alpha}^2 - \alpha^2\right)\right\} - k_q\text{sgn}(\tilde{q}) = 0$$

$$\dot{\tilde{\gamma}} = \frac{0.0055\rho_0 V^2 S_0\,\tilde{\alpha} + T(\sin\hat{\alpha} - \sin\alpha)}{mV} - \frac{(\mu - V^2 r)(\cos\hat{\gamma} - \cos\gamma)}{Vr^2} - k_\gamma\text{sgn}(\tilde{h})$$
$$\dot{\tilde{\alpha}} = -\dot{\tilde{\gamma}} - k_\alpha\text{sgn}(\tilde{q}) \tag{23.10}$$

where $\tilde{\gamma} = \hat{\gamma} - \gamma$, $\tilde{\alpha} = \hat{\alpha} - \alpha$

The error dynamics are nonlinear and difficult to analyze, thus we have to make further simplification. Noting that V is high and α and γ are typically very small, which justifies the following approximations:

$$\sin\alpha \approx \alpha, \quad \sin\hat{\alpha} \approx \hat{\alpha}, \quad \cos\gamma, \cos\hat{\gamma} \approx 1, \quad \hat{\alpha}^2, \alpha^2 \approx 0, \quad \left(\frac{\bar{c}_0}{2V}\right)q \approx 0$$

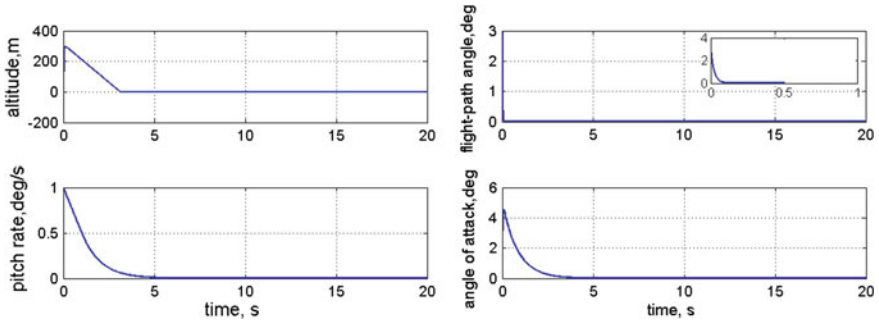

Fig. 23.1 Off-line sliding observer, initial state errors $\tilde{\gamma}(0) = 3.0\,\text{deg/s}$ and $\tilde{\alpha}(0) = 2.0\,\text{deg}$

When the trimmed conditions are substituted, the local error dynamics can be simplified as:

$$\dot{\tilde{\gamma}} \approx -4600\left(\frac{k_\gamma}{k_h}\right) + 0.005\,\tilde{\alpha} \tag{23.11}$$

$$\dot{\tilde{\alpha}} = -\left\{2.86 \times 10^{-3}\left(\frac{k_\alpha}{k_q}\right) + 0.005\right\}\tilde{\alpha} + 4600\left(\frac{k_\gamma}{k_h}\right)\tilde{\gamma} \tag{23.12}$$

The convergence of $\tilde{\gamma}$ and $\tilde{\alpha}$ depends on the ratio of $\frac{k_\gamma}{k_h}$ and $\frac{k_\alpha}{k_q}$, respectively. As a rule of thumb, the error dynamics of the observer on sliding surfaces $s_0 = 0$ should be much faster than the tracking error dynamics, that is,

$$\min\left\{4600\left(\frac{k_\gamma}{k_h}\right), 2.86 \times 10^{-3}\left(\frac{k_\alpha}{k_q}\right)\right\} \gg \max\{\lambda_1, \lambda_2\}$$

In this study, $\lambda_1 = 0.3, \lambda_2 = 0.5$, k_γ/k_h is chosen as 0.001, and k_α/k_q is 420. Thus, the poles of the reduced-order error dynamics of Eqs. (23.8) and (23.9) are at -4.6 and -1.2. The simulation results in Fig. 23.1 show the convergence behavior of the off-line observer. As we can see, the errors can converge to zero fast.

23.3.4 Input Shaping

Input shaping [5, 6] is proposed for suppressing residual vibration of flexible structure systems. It is implemented by convolving the command input with a sequence of impulses, also known as the input shaper. If amplitudes and instances of impulse application are accurate, the system performance will result in zero vibration. For more than one characteristic frequency and mode, the solution is to convolve the impulse sequences for each individual mode with one another. For a flexible structure

system with n modes, the amplitudes $I_{p,i}$, and instances $t_{p,i}, i = 1 \ldots M$ of impulse sequences for the pth mode can be expressed as:

$$I_{p,i} = \frac{\binom{M-1}{i-1} K_p^{i-1}}{\sum_{j=0}^{M-1} \binom{M-1}{j} K_p^j}, \quad t_{p,i} = (i-1)\frac{\pi}{\omega_p \sqrt{1-\zeta_p^2}}$$

$$K_p = \exp\left(-\frac{\zeta_p \pi}{\sqrt{1-\zeta_p^2}}\right) p = 1, \ldots, n; \quad i = 1, \ldots, M$$

where ω_p and ζ_p are the natural frequency and the damping ratio of the pth mode, respectively.

23.4 Simulation

In this section, simulations of the FHVs to track a desired trajectory and alleviate the flexible vibrations are given to illustrate the efficiency of the proposed method.

The coefficients of the vehicle dynamics in [7] are adopted here. The parameters of the controller are: $k_1 = 2, k_2 = 2, k_3 = 10, k_4 = 10, \phi_1 = 0.1, \phi_2 = 0.1$. Moreover, the parameter uncertainties have been considered to verify the robustness of

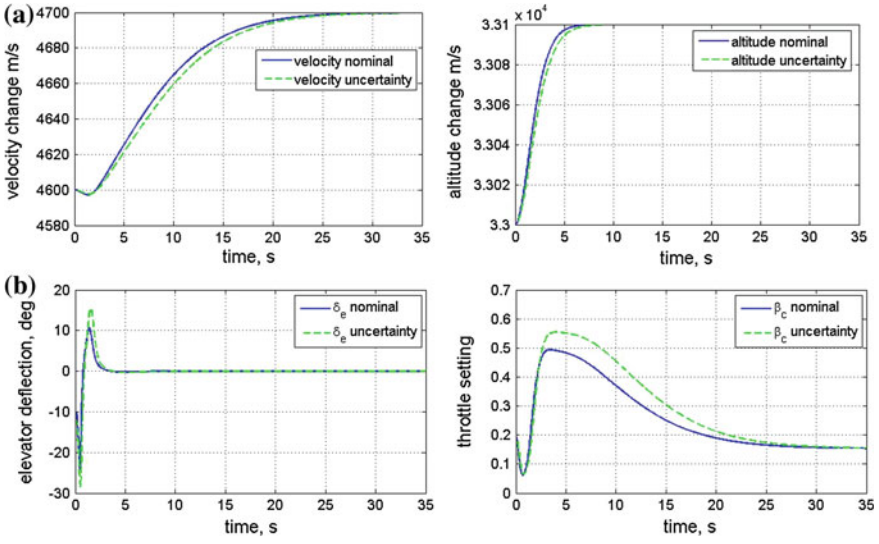

Fig. 23.2 Tracking response of SMD with MEAL. **a** *Left* velocity; *right* altitude. **b** *Left* elevator deflection; *right* throttle setting

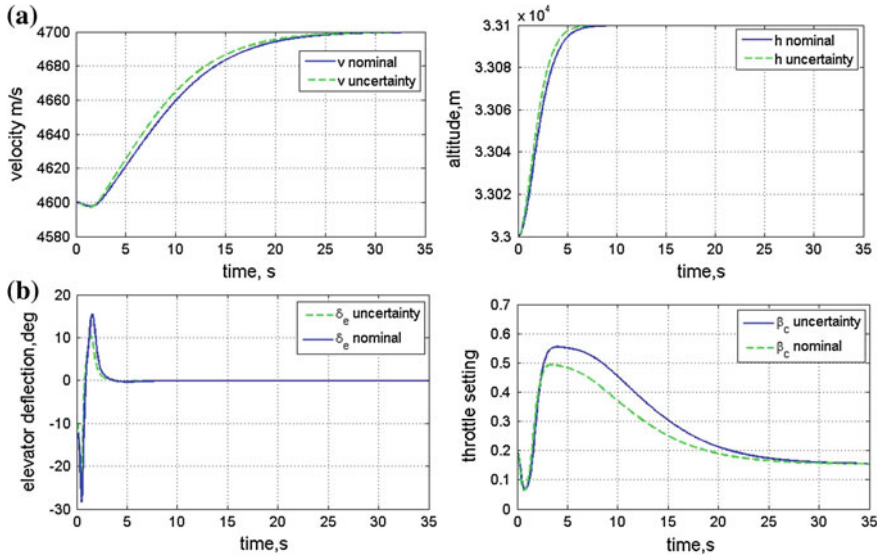

Fig. 23.3 Tracking response of sliding controller-observer. **a** *Left* velocity; *right* altitude. **b** *Left* elevator deflection; *right* throttle setting

the system. The blue lines and the green dash lines in Fig. 23.2 denote the nominal and uncertain systems, respectively. It can be observed that both the velocity and the altitude can follow the desired trajectories well despite the parameter uncertainties without obvious chattering. Then combine the controller with observers. The responses are shown in Fig. 23.3. We can see that the sliding mode controller-observer does provide good tracking performance despite the presence of parameter uncertainty and assumption of incomplete state measurement.

In order to attenuate the flexible vibrations, the system is equipped with inputs shaper. The zero vibration shaper is employed here to calculate the corresponding amplitudes I_{ij} and the instants t_{ij} of the impulse sequences, which are presented as:

$$L_1 = \begin{bmatrix} 0.8598 & 0.1402 \\ 0 & 3.627 \end{bmatrix}; \; L_2 = \begin{bmatrix} 0.956 & 0.044 \\ 0 & 3.9 \end{bmatrix}; \; L_3 = \begin{bmatrix} 0.9134 & 0.0866 \\ 0 & 2.4836 \end{bmatrix}$$

Then the shaped inputs can be expressed as $V_d * L_{\text{mult}}$ and $h_d * L_{\text{mult}}$, where L_{mult} denotes the composite-shaped impulse sequence which is defined as $L_{\text{mult}} = L_1 * L_2 * L_3$ and * is the convolution operator. Figures 23.4 and 23.5 show the system response of applying the inputs shaper to the closed-loop system. The vibrations have been attenuated to a certain extent while guaranteeing the performances without IS because IS is a feedforward part equipped in the system and it will not destroy the properties of the designed closed-loop system.

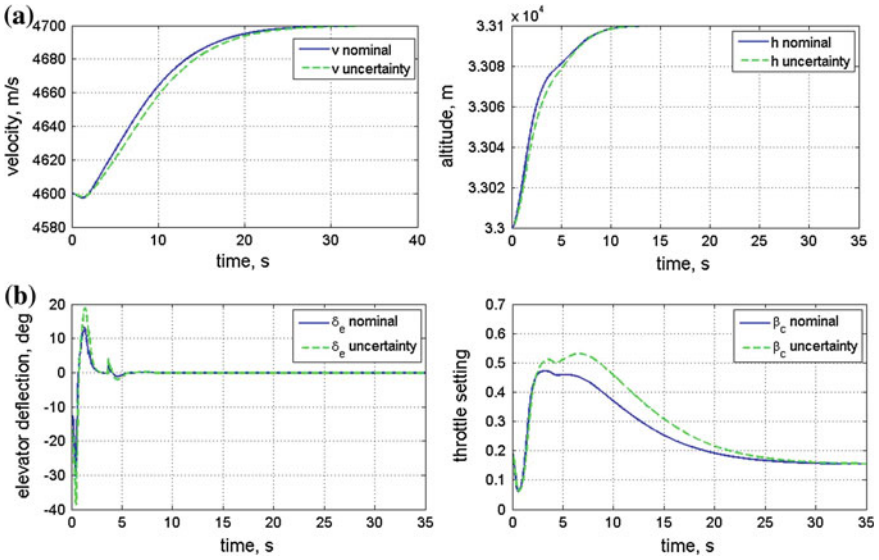

Fig. 23.4 Tracking response of the system equipped with IS. **a** *Left* velocity; *right* altitude. **b** *Left* elevator deflection; *right* throttle setting

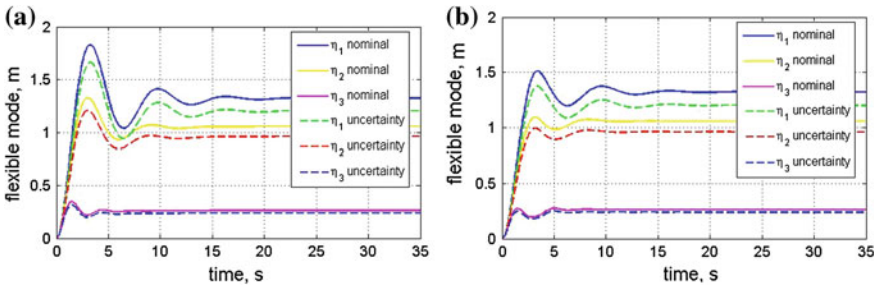

Fig. 23.5 Flexible dynamics responses. **a** Flexible modes: without IS. **b** Flexible modes: with IS

23.5 Conclusion

In this paper, a sliding controller-observer combined with IS technique is developed and applied to the nonlinear longitudinal model of FHVs with parameter uncertainties. A nonlinear sliding mode observer is developed to estimate the states that are not available for measurement as in a typical hypersonic flight. The IS technology is employed as a feedforward part to reduce the elastic vibrations. Simulation results demonstrate that the proposed control method has good tracking performance and robustness in the presence of parameter uncertainty and the assumption of partial state measurements and attenuates the vibration of the flexible modes to a certain extent.

References

1. Schmidt DK (1993) Integrated control of hypersonic vehicles-a necessity not just a possibility. AIAA 93(3761):539–549
2. Slotine JJE, Hedrick JK, Misawa EA (1987) On sliding observers for nonlinear systems. ASME J Dyn Syst Measur Contr 109:245–252
3. Zong Q, Wang J, Tian BL et al (2013) Quasi-continuous high-order sliding mode controller and observer design for flexible hypersonic vehicle. Aerosp Sci Technol 27(1):127–137
4. Wang J, Zong Q, Tian BL et al (2013) Flight control for a flexible air-breathing hypersonic vehicle based on quasi-continuous high-order sliding mode. J Syst Eng Electron 24(2):288–295
5. Singer NC, Seering WP (1990) Preshaping command inputs to reduce system vibration. J Dyn Syst Meas Contr 112(1):76–82
6. Singh T, Heppler G (1993) Shaped input control of a system with multiple modes. J Dyn Syst Meas Contr 115(3):341–347
7. Xu HJ, Mirmirani MD, Ioannou PA (2004) Adaptive sliding mode control design for a hypersonic flight vehicle. J Guid Control Dyn 27(5):829–838
8. Marrison Christopher I, Stengel Robert F (1998) Design of robust control systems for a hypersonic aircraft. J Guid Control Dyn 21(1):58–63
9. Chan ML, Tao CW, Lee TT (2000) Sliding mode controller for linear systems with mismatched time-varying uncertainties. J Franklin Inst 337(2):105–115

Chapter 24
An Application of Artificial Neural Networks in Crane Operation Status Monitoring

Jan-Li Yu, Rui-Fang Zhou, Man-Xiang Miao and Hong-Qi Huang

Abstract Crane as large mechanical equipment, plays an irreplaceable role in industrial production. Crane fault diagnosis technology, which improves safety and reliability of crane operation, becomes extremely important. The BP neural network has been utilized to study crane state monitoring and fault diagnosis. A BP neural network model was established to monitor tower crane running status online, and simulation experiments were made on the stability of the model. Results show that the BP neural network model can accurately monitor tower crane running status, give effectively fault prediction, and improve security and reliability of tower crane operation.

Keywords BP neural network · Status monitoring · Crane · Fault diagnosis

24.1 Introduction

As large-scale mechanical equipment of industrial manufacture, working range, lifting capacity, and monitoring level of crane stand-alone unceasingly develop in the direction of large scale and automation. Due to the structure and working characteristics of crane, it is a big risk factor for hidden construction machinery. To guarantee normal work of hoisting equipment, monitoring crane running status and crane fault diagnosis have become the research focus in crane safety design [1–7]. Much research is available in fault diagnosis neural network. Results show that neural network can not only detect known faults that have occurred, but can also recognize new faults that happened for the first time by learning new fault samples,

J.-L. Yu (✉) · M.-X. Miao · H.-Q. Huang
School of Management Science and Engineering Zhengzhou Institute of Aeronautical Industry Management, Zhengzhou 450015, China
e-mail: yjl837@163.com

R.-F. Zhou
School of Science, Zhongyuan University of Technology, Zhengzhou 450007, China
e-mail: topedis@126.com

Z. Deng and H. Li (eds.), *Proceedings of the 2015 Chinese Intelligent Automation Conference*, Lecture Notes in Electrical Engineering 337,
DOI 10.1007/978-3-662-46463-2_24

training and updating fault knowledge, building relationships between fault symptoms and fault states [8–16].

We utilized BP neural network to study online monitoring running status of tower crane. Online BP neural network model of monitoring tower crane running status had been built, simulation experiment was carried out to study model stability. Results show that BP neural network model can accurately judge tower crane running status, give effective fault prediction, and improve the security and reliability of tower crane operation.

24.2 BP Neural Network

BP neural network is a multilayer feedforward neural network trained by error back propagation algorithm. BP neural network can learn and store large amounts of input–output mode mappings, however, mathematical equation of this mapping is not needed (Fig. 24.1).

Learning method of BP neural network is the steepest descent method, which adjust weights and threshold value of neural network by back propagation, to minimize error sum squares of the BP neural network. The topology structure of BP neural network model consists of input layer, hidden layers, and output layer [17].

Forward-propagating and back propagation of BP neural network constitute its learning process. Forward-propagating means network computing, determining its output for given input; back propagation is used for error propagation layer by layer, modifying connection weight and threshold value. The algorithm step is given below:

(1) Set variables and parameters of training network:
$X_k = [x_{k1}, x_{k2}, \ldots, x_{kp}]$, $(k = 1, 2, \ldots, N)$ as input vector, i.e., training samples, total number of samples is N; $W_{PI}(n) = (w_{ij})_{M\times I}$ as the nth iterative weights vector between the hidden layer and input layer I; $W_{PI}(n) = (w_{ij})_{M\times I}$ as the nth iterative weights vector between the hidden layer J and the hidden layer I; $W_{PI}(n) = (w_{ij})_{M\times I}$ as the nth iterative weights vector between the hidden layer J and output; $O_k(n) = [O_{k1}(n), O_{k2}(n), \ldots, O_{kN3}(n)]$ as actual output of the nth iterative network; $d_k = [d_{k1}, d_{k2}, \ldots, d_{kN3}]$, $(k = 1, 2, \ldots, N)$ as expected output of trained network.

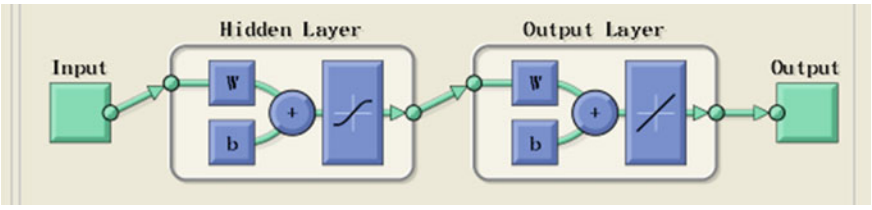

Fig. 24.1 BP neural network topology structure

(2) Initialize the settings. Assigned to small random nonzero values for $W_{MI}(0), W_{IJ}(0), W_{JN3}(0)$.
(3) Afterwards, input samples X_k, $n = 0$.
(4) About input samples X_k, compute BP neural network input signal u and output signal v of every layer neuron in forward direction.
(5) Compute error e according to actual output $O_k(n)$ and actual expected output d_k by last step, judge whether they meet the requirements, if they meet the requirements, go to (8); If they don't meet, go to (6).
(6) Judge if $n + 1$ greater than the maximum iterative number. If greater then turn to (8), otherwise, compute local gradient δ of every layer for input sample X_k

$$\begin{aligned} &\delta_p^{N3} = O_p(n)\big(1 - O_p(n)\big)\big(d_p(n) - O_p(n)\big) \\ &(p = 1, 2, \ldots, N3) \end{aligned} \tag{24.1}$$

$$\delta_j^J = f'\Big(u_j^J(n)\Big) \sum_{p=1}^{N3} \delta_p^{N3} w_{jp}(n), (j = 1, 2, \ldots, J) \tag{24.2}$$

$$\delta_i^I = f'\big(u_i^I(n)\big) \sum_{j=1}^{J} \delta_j^J w_{ij}(n), (i = 1, 2, \ldots, I) \tag{24.3}$$

(7) Compute weight amendment Δw according to formula below, and amend weight η is learning rate.

$$\begin{aligned} \Delta w_{jp}(n) &= \eta \delta_p^{N3}(n) v_j^J(n), \\ w_{jp}(n+1) &= w_{jp}(n) + \Delta w_{jp}(n), \ (j = 1, 2, \ldots, J; \ p = 1, 2, \ldots, P); \end{aligned} \tag{24.4}$$

$$\begin{aligned} \Delta w_{ij}(n) &= \eta \delta_j^J(n) v_i^I(n), \\ w_{ij}(n+1) &= w_{ij}(n) + \Delta w_{ij}(n), \ (i = 1, 2, \ldots, I; \ j = 1, 2, \ldots, J); \end{aligned} \tag{24.5}$$

$$\begin{aligned} \Delta w_{mi}(n) &= \eta \delta_i^I(n) x_{km}(n) \\ w_{mi}(n+1) &= w_{mi}(n) + \Delta w_{mi}(n), \ (m = 1, 2, \ldots, P; \ i = 1, 2, \ldots, I) \end{aligned} \tag{24.6)}$$

(8) Judge if whole samples be learned, if it is, turn to end, otherwise, go back (3).

24.3 Build BP Neural Network of Crane Running Status Monitor

Six variables of tower crane running status was chosen as observed variables, lifting weight, load moment, lifting altitude, lifting amplitude, wind velocity, and electromotor winding temperature, respectively. These six variables are variables collected by sensors in tower crane service.

Table 24.1 Trainning samples

Sample number	State observation variables						State type encoding
	Lifting weight	Load moment	Lifting altitude	Lifting amplitude	Electromotor wind velocity	Encoding winding temperature	
1	6,375	686	38.6	10.8	10.9	109	00100
2	6,565	666	39	10.1	15	88	00100
3	6,214	650	38.2	10.5	14.3	102	00100
4	6,483	650	39.4	10	15.7	114	00010
5	6,214	678	39.8	10.9	13.1	114	00010
6	6,565	666	39.8	10.1	14.3	118	00100
7	5,882	615	39.4	10.5	10.9	109	01000
8	5,882	686	38.6	11.7	14.3	88	00010
9	6,483	615	39	9.5	13.1	102	00100
10	5,882	678	39	11.5	15.6	102	00101
11	5,882	666	38.2	11.3	13.1	114	00101
12	6,375	650	38.6	10.2	10.9	118	00101
13	6,483	650	38.2	10	15	109	00101
14	6,214	686	39.8	11	15	114	00010
15	6,483	666	39.8	10.3	10.9	102	00101
16	5,882	615	38.6	9.4	14.3	114	00101
17	6,565	678	38.2	10.3	10.9	88	00010
18	6,565	615	38.6	9.4	14.3	114	00101
19	6,483	686	39	10.6	13.1	118	00010
20	6,375	678	39.4	10.6	14.3	102	00010
21	6,214	666	38.6	10.7	15.7	109	00010
22	6,130	640	39.2	10.4	12.4	86	01000
23	6,435	640	15	9.9	14.7	106	00101
24	6,400	640	15	10	14	100	01000
25	1,500	300	38.2	20	14	80	10000

Crane running status can be divided into five categories: safe state, quasi–safe state, transition state from safe to danger, quasi-danger state, and danger state. The code for the five states are: 10000, 01000, 00100, 00010, 0000, respectively.

Choose 25 group historical data of tower crane running status as trainning samples [18], shown in Table 24.1.

Set input layer, hidden layer, and output layer of BP neural network. Let observations of crane running state variables be input variable. Let crane state type encoding be output variable.

Weights and threshold values of BP neural network are obtained using BP neural network model by training samples.

Trainning method utilize steepest descent, by means of adjustment network weights and threshold values unceasingly, to make the square error of neural network be smaller and smaller, as shown in Fig. 24.2. BP neural network is trained in

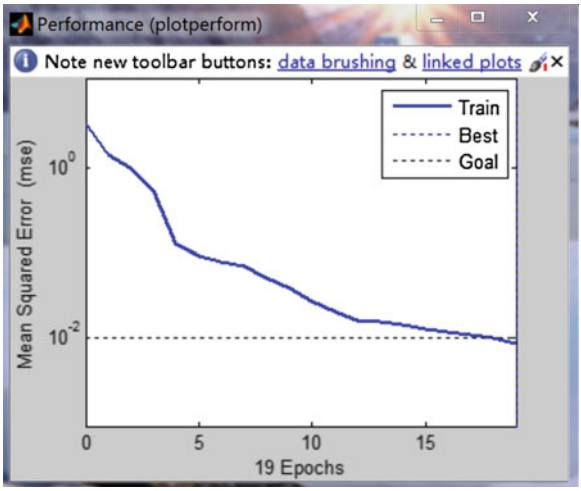

Fig. 24.2 Network trainning error

Matlab(net = train(net, p, t)), the neuron number of hidden layer is set as 10, p is input variable, and t is output target variable.

Neural network weights and threshold values are output by Matlab commands below: IW = net.IW{1,1}; LW = net.LW{2,1}; $b1$ = net.b{1,1}; $b2$ = net.b{2,1}.

Neural network weights are as below:

IW = 0.1067	0.0646	−0.1125	0.02450	1643	0.0571
−0.0002	−0.0206	−0.0718	−0.3071	−0.0496	0.1120
0.0002	0.0041	−0.1028	−0.1314	0.0100	0.0690
−0.0002	0.0223	0.0435	0.0136	−0.0083	−0.0554
−0.0365	0.3800	−0.5207	0.3660	−1.3808	0.0841
0.0062	−0.1071	0.5266	0.4779	0.1903	−0.0184
0.0002	−0.0193	−0.0489	−0.2360	−0.1359	0.1461
0.0039	−0.0340	−0.0318	−0.0501	−0.2325	−0.0897
−0.0004	−0.0118	−0.1971	0.5697	−0.2257	0.0674
−0.0005	0.0020	−0.0100	−0.2884	−0.0194	−0.0289

LW = 0.3688	−0.2433	0.2085	−0.0802	−0.1423
−0.5419	−1.0358	0.1921	0.2444	−0.4144
−0.0451	0.7692	−0.8836	0.0927	−0.0973
−0.7667	0.0299	0.2565	−0.0373	−0.1938
−0.0294	0.5902	−1.2631	0.6148	−0.0517
−0.0456	0.8632	−0.6285	−0.2706	-0.0862
0.0490	−0.4855	−0.6358	1.2044	0.1458
−0.6759	−0.4502	0.0860	−0.2969	−0.4888
−0.0098	0.3006	1.6465	−1.8921	−0.0124
0.1516	0.8135	−0.2395	−0.1729	0.4923

Trained threshold values of neural network are as below:

$b1$ = [9.7279, 6.4640, −6.6495, −6.6967, 7.4551, 4.4896, 2.4028, 7.9846, 7.8884, 7.5638]

$b2$ = [−0.7224, −0.1037, −0.1189, 0.1749, −0.2251]

24.4 Monitor Experiment of Crane Running Status

Among historical data of tower crane, which match the running state type encoding and running state observation variables, ten group samples are selected as monitor test samples, as shown in Table 24.2.

Input tower crane running state observation data of experiment into trained BP neural network by Matlab command t = sim(net, p), crane running status is recognized, output is as below:

t = 0.0061	0.0497	0.9657	0.0270	0.0127	0.0092	0.0453	1.0774	−0.1157	−0.0130
0.0124	0.1224	0.2970	0.6184	−0.0019	0.0089	1.0383	−0.0057	−0.0261	0.0052
0.0204	−0.0516	0.8702	0.2480	0.0497	−0.0021	0.1191	−0.1120	1.0303	0.0088
−0.0084	−0.0122	−0.1074	1.0437	−0.0586	−0.0154	0.9232	−0.0583	0.1573	0.0184
0.0127	0.9282	0.1122	−0.0035	0.0298	1.1944	0.8596	0.4673	−1.1309	0.0520

Set the BP neural network maximum corresponding component value of tower crane running state output vector as 1, other component as 0, crane running state

Table 24.2 Monitor test samples

Sample number	State observation variables						State type encoding
	Lifting weight	Load moment	Lifting altitude	Lifting amplitude	Wind velocity	Electromotor winding temperature	
1	6,375	686	38.6	10.8	10.9	109	00100
2	6,214	650	38.2	10.5	14.3	102	00100
3	6,483	650	39.4	10	15.7	114	00010
4	5,882	615	39.4	10.5	10.9	109	01000
5	5,882	666	38.2	11.3	13.1	114	00100
6	6,483	686	39	10.6	13.1	118	00010
7	6,375	678	39.4	10.6	14.3	102	00010
8	6,130	640	39.2	10.4	12.4	86	01000
9	6,400	640	15	10	14	100	01000
10	1,500	300	38.2	20	14	80	10000

identification results are obtained. Results show that BP neural network model identification accuracy rate is 100 % by comparing training samples sorting code number and origin code number.

24.5 Effectiveness and Stability Study of BP Neural Network

To study the effectiveness and stability of BP neural network model, disturbed experiment samples are simulated by add disturbance into input monitor experiment samples. Stability of BP neural network is studied by simulating running state identification using disturbed input data.

On the basis of monitoring experiment samples, for 10 group samples lifting weight, it is allowed to fluctuate by ±5, meanwhile, keep other data stay the same. The new disturbed experiment samples are employed by BP neural network using Matlab, running state identification are as shown below:

t1 = 0.0062	0.0502	0.9685	0.0240	0.0131	0.0130	−0.0359	1.2762	−0.2247	−0.0068
0.0123	0.1255	0.2905	0.6213	−0.0025	0.0084	1.0472	−0.0131	−0.0285	0.0038
0.0204	−0.0516	0.8692	0.2488	0.0495	−0.0022	0.1196	−0.1152	1.0327	0.0085
−0.0081	−0.0141	−0.1028	1.0415	−0.0578	−0.0177	0.9968	−0.2390	0.2579	0.0141
0.0120	0.9143	0.1372	−0.0154	0.0292	1.1946	0.8593	0.4669	−1.1299	0.0520

On the basis of monitoring experiment samples, for ten group samples load moment, it is allowed to fluctuate by ±3, meanwhile, keep other data stay the same. The new disturbed experiment samples are employed by BP neural network using Matlab, running state identification are as shown below:

t2 = 0.0092	0.0190	0.9693	0.0585	0.0206	−0.0005	0.2151	0.4386	0.3234	−0.0292
0.0118	0.0880	0.2795	0.6738	0.0009	0.0098	1.0893	−0.0435	−0.0522	−0.0034
0.0230	−0.0769	0.8719	0.2716	0.0538	−0.0015	0.1122	−0.0819	1.0064	0.0098
−0.0096	0.0200	−0.0992	1.0038	−0.0606	−0.0155	1.0336	−0.6708	0.6395	0.0171
0.0108	0.9949	0.0816	−0.0259	0.0304	1.2149	0.9343	0.4955	−1.2115	0.0623

Set the BP neural network maximum corresponding component value of tower crane running state output vector as 1, other component as 0, crane running state identification results are obtained. Results show that BP neural network model identification accuracy rate is 100 % by comparing training samples sorting code number and origin code number.

Similarly, on the basis of monitoring experiment samples, for ten group samples, other four observation variables, it is allowed to fluctuate up and down (0.7 %), meanwhile, keeping other data stay the same. The new disturbed experiment samples are employed by BP neural network using Matlab, disturbed experiment samples and running state identification results show that identification accuracy rate achieves 100 %.

24.6 Conclusion

Artificial neural network has strong ability of nonlinear mapping, autonomous learning, and generalization ability. We build tower crane running state monitor BP neural network using neural network based on steepest descent method, which adjusts network weights and threshold values unceasingly by means of error back propagations.

Six variables of tower crane running status observed variables are chosen as network input, which are lifting weight, load moment, lifting altitude, lifting amplitude, wind velocity, and electromotor winding temperature, respectively. Crane running status can be divided into five categories: safe state, quasi-safe state, transition state from safe to danger, quasi-danger state, and danger state. The five states are encoded as: 10000, 01000, 00100, 00010, 0000, respectively; The five codes are network output variables. Then network is trained by tower crane historical running data. Simulating test data using trained BP neural network results are identified. It is implied that identification accuracy reaches 100 %.

To study network model effectivity and stability, fluctuation is allowed in appropriate scope of one observation variable, meanwhile, keeping other data stay the same. The new disturbed experiment samples are employed by BP neural network using Matlab. Results of disturbed experiment samples and running state identification show that diagnosis accuracy is 100 %.

The above study shows that BP neural network model can effectively monitor change running status and forecast fault online by training historical data. Monitoring change running status by BP neural network is proved to have relatively high stability and efficiency, running safety and reliability can be attained by BP network.

Acknowledgments This work is supported by the Natural Science Foundation of Henan Province under Grant No. 132102210091 and No. 142102210077 and No.142102210105.

References

1. Chunying Z (2012) Failuere monitoring and diagnosis system based on artificial intelligence research. J Manufact Autom 34(4):52–54
2. Jing T, Chaoliang H, Zhiping C, Yang L, Hui C, Jinjin T (2013) Intelligent processing of the data tested out of crane safety inspection based on C++ builder. J Mod Sci Instrum 2:70–74
3. Jin-jie Y (2012) Implementation of monitoring system of monotower crane based on field bus. J Comput Meas Control 10(2):101–103
4. Mingdi W, Yannian R, Dunwen Z, Min W (2006) Based on the piezoelectric theory of wire rope working state intelligent monitoring method of tower crane. J Eng Mach 4:21–24
5. Chen W, Saif M (2011) Actuator fault diagnosis for a class of nonlinear systems and its application to a laboratory 3D crane. Automatica 47(7):1435–1442
6. Ying C, Wenliao D, Gen L, Wang S, Yanming L (2013) Crane remote monitoring and fault diagnosis system database. Mach Des Res 1:97–103 (in Chinese)

7. Jin-yu F, Si-qin L, Jia-liang H (2012) Gantry crane condition monitoring and fault diagnosis based on oil analysis. J Jimei Univ 2:122–125 (in Chinese)
8. Jian Z, Yannian R, Jie C (2005) Research on intelligent monitors and stoppage diagnoses of the mechancal system of crane based on the theory of manual nerve network. Mechatronics 6:41–44
9. Yuegang L, Xu H, Bangchun W (2001) Using neural network comprehensive diagnosis of the cylindrical supporting crane. J Lifting Transp Mach 7:8–10
10. Jun H (2002) Using neural network technology in the diagnosis of bridge crane bearng failure. J Lifting Transp Mach 1:35–37
11. Du W, Li Y,Yuan J, Liu C (2012) Denoising with advanced stepwise false discovery rate control and its application to fault diagnosis. J Measur 45(6):1343–1674
12. Zhang-ping Y, Jie J, Xiao-ping H, Xiao-ping Y (2010) Crane particle swarm neural network fault diagnosis of hydraulic system, Chinese. Hydraulics Pneumatics 8(3):348–352
13. Xing-zhou Y, Wen-ming C, Ming-heng X (2013) Gantry crane based on RBF neural network fault diagnosis system research, Chinese. J Constr Mach (4)
14. Chen D, Ye Y, Hua R (2013) Fault diagnosis system for npc inverter based on multi-layer principal component neural network. J Comput 8(6)
15. Jing-qiang S, Si-cong Y, Dong-dong W et al (2012) Application of genetic algorithm-based BP neural network in diagnosis to tower crane. J Hoisting Conveying Mach 4:61–64
16. Amirat Y, Benbouzid MEH, Al-Ahmar E, Bensaker B, Turri S (2009) A brief status on condition monitoring and fault diagnosis in wind energy conversion systems. Renew Sustain Energy Rev 13(9):2629–2636
17. Changhong D (2007) Matlab Neural networks and Applications. In: National defence industry press, Beijing
18. Xi-jian Z, Quan-yun H, Ye F (2005) The safety state model identification of tower crane based on RBF neural network and uniform design. J Mach Des Manuf 1:78–80

Chapter 25
Adaptive Fuzzy Dynamic Surface Control for Induction Motors via Backstepping

Fatao Shi, Yumei Ma, Jinfei Yu, Jinpeng Yu and Ziyang Qu

Abstract This paper addressed an adaptive fuzzy dynamic surface control (DSC) approach to speed regulation for induction motors. Fuzzy logic systems are used to approximate unknown nonlinear functions and the adaptive backstepping method is employed to construct controllers. By incorporating dynamic surface control technique into fuzzy control, we have developed an adaptive backstepping control design for induction motors. The proposed control method is able to overcome the problem of "explosion of complexity" inherent in the traditional backstepping design by introducing first-order low-pass filters. The adaptive fuzzy controllers guarantee the speed tracking error converges to a small neighborhood of the origin. Simulation results illustrate the effectiveness of the proposed approach.

Keywords Induction motors · Dynamic surface control · Fuzzy control · Backstepping

25.1 Introduction

Over the past few decades, induction motors (IMs) have been widely utilized for modern electrical drives due to their simple and robust construction, low cost, high reliability, and ruggedness. However, the control of IM is complex because of its highly nonlinear, multivariable dynamic model. Therefore, many nonlinear control methods have been proposed to control induction motor drive systems, such as sliding mode control [1], backstepping control [2, 3], and other control. The backstepping control is considered to be one of the popular techniques for controlling nonlinear

F. Shi · Y. Ma · J. Yu (✉) · Z. Qu
College of Automation Engineering, Qingdao University, No. 308 Ningxia Road, Qingdao 266071, China
e-mail: yjp1109@126.com

J. Yu
Zibo Technician College, Zibo 255013, China

Z. Deng and H. Li (eds.), *Proceedings of the 2015 Chinese Intelligent Automation Conference*, Lecture Notes in Electrical Engineering 337,
DOI 10.1007/978-3-662-46463-2_25

systems with linear parametric uncertainty. Nevertheless, when the virtual control is differentiated repeatedly, the problem of "explosion of complexity" has arisen. A dynamic surface control (DSC) technique was proposed by Swaroop et al. [4] to overcome this problem by introducing a first-order filtering of the synthesized input at each step of the backstepping design procedure. Despite these efforts using the DSC technique, the control method is not applied to nonlinear systems with unknown parameters. Recently, fuzzy logic control [5] has attracted great attention in induction motor drive systems. Fuzzy-approximation-based nonlinear control has been one of the conventional and popular methods to handle nonlinear systems with parameter uncertainties.

In this paper, an adaptive fuzzy dynamic surface control approach is proposed for induction motors. Finally, the proposed control method is able to overcome the problem of "explosion of complexity" inherent in the traditional backstepping design and the proposed controllers can assure that the speed tracking error converges to a small range of the origin and all the closed-loop signals are bounded. Simulation results illustrate the effectiveness of the proposed approach.

25.2 Mathematical Model of the Induction Motor Drive System

Induction motor's dynamic mathematical model can be described in the well-known $(d-q)$ frame as follows [6, 7]:

$$\begin{aligned}
&\frac{\mathrm{d}\omega}{\mathrm{d}t}=\frac{n_pL_m}{L_rJ}\psi_d i_q-\frac{T_L}{J},\frac{\mathrm{d}i_q}{\mathrm{d}t}=-\frac{L_m^2R_r+L_r^2R_s}{\sigma L_sL_r^2}i_q-\frac{n_pL_m}{\sigma L_sL_r}\omega\psi_d-n_p\omega i_d-\frac{L_mR_r}{L_r}\frac{i_qi_d}{\psi_d}+\frac{1}{\sigma L_s}u_q\\
&\frac{\mathrm{d}\psi_d}{\mathrm{d}t}=-\frac{R_r}{L_r}\psi_d+\frac{L_mR_r}{L_r}i_d,\frac{\mathrm{d}i_d}{\mathrm{d}t}=-\frac{L_m^2R_r+L_r^2R_s}{\sigma L_sL_r^2}i_d+\frac{L_mR_r}{\sigma L_sL_r^2}\psi_d+n_p\omega i_q+\frac{L_mR_r}{L_r}\frac{i_q^2}{\psi_d}+\frac{1}{\sigma L_s}u_d
\end{aligned}\tag{25.1}$$

where $\sigma=1-L_m^2/L_sL_r\cdot\ \omega, L_m, n_p, J, T_L$ and ψ_d denote rotor angular velocity, mutual inductance, pole pairs, inertia, load torque, and rotor flux linkage, respectively. i_d, i_q and u_d, u_q are the $d-q$ axis currents and voltages, respectively. R_s and L_s mean the resistance, inductance of the stator. R_r and L_r denote the resistance, inductance of the rotor. For simplicity, the following notations are introduced:

$$\begin{aligned}
&x_1=\omega,\quad x_2=i_q,\quad x_3=\psi_d,\quad x_4=i_d,\quad a_1=\frac{n_pL_m}{L_r},\quad b_1=-\frac{L_m^2R_r+L_r^2R_s}{\sigma L_sL_r^2},\\
&b_2=-\frac{n_pL_m}{\sigma L_sL_r},\quad b_3=n_p,\quad b_4=\frac{L_mR_r}{L_r},\quad b_5=\frac{1}{\sigma L_s},\quad c_1=-\frac{R_r}{L_r},\quad d_2=\frac{L_mR_r}{\sigma L_sL_r^2}
\end{aligned}\tag{25.2}$$

Lemma 25.1 [8] *Let $f(x)$ be a continuous function defined on a compact set Ω. Then for any scalar $\varepsilon > 0$, there exists a fuzzy logic system $W^T S(x)$ such that $\sup_{x\in\Omega} |f(x) - W^T S(x)| \le \varepsilon$, where $W = [W_1, \ldots, W_N]^T$ is the ideal constant weight vector, and $S(\mathrm{x}) = [p_1(\mathrm{x}), p_2(\mathrm{x}), \ldots, p_N(\mathrm{x})]^T / \sum_{i=1}^{N} p_i(\mathrm{x})$ is the basis function vector.*

By using these notations, the dynamic model of IM drivers can be described by the following differential equations:

$$\dot{x}_1 = \frac{a_1}{J} x_2 x_3 - \frac{T_L}{J}, \quad \dot{x}_2 = b_1 x_2 + b_2 x_1 x_3 - b_3 x_1 x_4 - b_4 \frac{x_2 x_4}{x_3} + b_5 u_q,$$
$$\dot{x}_3 = c_1 x_3 + b_4 x_4, \quad \dot{x}_4 = b_1 x_4 + d_2 x_3 + b_3 x_1 x_2 + b_4 \frac{x_2^2}{x_3} + b_5 u_d. \tag{25.3}$$

25.3 Adaptive Fuzzy Dynamic Surface Control Design

Step 1: For the reference signal x_{1d}, define the tracking error variable as $z_1 = x_1 - x_{1d}$. Consider the Lyapunov function candidate as $V_1 = \frac{J}{2} z_1^2$. Then the time derivative of V_1 is given as

$$\dot{V}_1 = J z_1 \dot{z}_1 = z_1 (a_1 x_2 x_3 - T_L - J \dot{x}_{1d}) \tag{25.4}$$

we assume T_L is unknown but its upper limit is $d > 0$. $z_1 T_L \le z_1^2 / 2\varepsilon_3^2 + \varepsilon_3^2 d^2 / 2$, where ε_3 is an arbitrary small positive constant. Then we can get

$$\dot{V}_1 \le \varepsilon_3^2 d^2 / 2 + z_1 (x_2 + a_1 x_2 x_3 + z_1 / 2\varepsilon_3^2 - J \dot{x}_{1d} - x_2) \tag{25.5}$$

To make backstepping simple, we design a fuzzy logic system as follows:

$$\begin{aligned} f_1(Z) &= a_1 x_2 x_3 + z_1 / 2\varepsilon_3^2 - J \dot{x}_{1d} - x_2 = W_1^T S_1(Z) + \delta_1(Z), \\ Z &= [x_1, x_2, x_3, x_4, x_{1d}, \dot{x}_{1d}]^T \end{aligned} \tag{25.6}$$

where $\delta_1(Z)$ is the approximation error and satisfies $|\delta_1| \le \varepsilon_1$. We can get

$$z_1 f_1 \le \frac{1}{2 l_1^2} z_1^2 ||W_1||^2 S_1^T S_1 + \frac{1}{2} l_1^2 + \frac{1}{2} z_1^2 + \frac{1}{2} \varepsilon_1^2 \tag{25.7}$$

Choose virtual control α_1 as $\alpha_1 = -k_1 z_1 - z_1/2 - z_1 \hat{\theta} S_1^T S_1 \Big/ 2l_1^2$ and define α_{1d}, then let α_1 pass through a first-order filter with time constant ς_1 to obtain α_{1d}

$$\varsigma_1 \dot{\alpha}_{1d} + \alpha_{1d} = \alpha_1, \alpha_{1d}(0) = \alpha_1(0) \tag{25.8}$$

Substituting (25.7) and (25.8) into (25.5), and defining $z_2 = x_2 - \alpha_{1d}$, we can obtain

$$\dot{V}_1 \leq -k_1 z_1^2 + \frac{1}{2}\varepsilon_3^2 d^2 + z_1(\alpha_{1d} - \alpha_1) + \frac{1}{2}l_1^2 + \frac{1}{2}\varepsilon_1^2 + \frac{1}{2l_1^2} z_1^2 (||W_1||^2 - \hat{\theta}) S_1^T S_1 + z_1 z_2 \tag{25.9}$$

Step 2: The Lyapunov function candidate V_2 is defined as $V_2 = V_1 + \frac{1}{2}z_2^2$, and the time derivative V_2 is

$$\dot{V}_2 \leq \dot{V}_1 + z_2\left(b_1 x_2 + b_2 x_1 x_3 - b_3 x_1 x_4 - b_4 x_2 x_4 / x_3 + b_5 u_q - \dot{\alpha}_{1d}\right) \tag{25.10}$$

where $f_2(Z) = z_1 + b_1 x_2 + b_2 x_1 x_3 - b_3 x_1 x_4 - b_4 x_2 x_4 / x_3 - \dot{\alpha}_{1d} = W_2^T S_2(Z) + \delta_2(Z)$. Then

$$z_2 f_2 \leq \frac{1}{2l_2^2} z_2^2 ||W_2||^2 S_2^T S_2 + \frac{1}{2}l_2^2 + \frac{1}{2}z_2^2 + \frac{1}{2}\varepsilon_2^2 \tag{25.11}$$

At this present stage, the control law u_q is designed as

$$u_q = \frac{1}{b_5}\left(-k_2 z_2 - \frac{1}{2}z_2 - \frac{1}{2l_2^2} z_2 \hat{\theta} S_2^T S_2\right) \tag{25.12}$$

By the Eqs. (25.11) and (25.12), we can get

$$\dot{V}_2 \leq \sum_{i=1}^{2}\left(-k_i z_i^2 + \frac{1}{2}l_i^2 + \frac{1}{2}\varepsilon_i^2 + \frac{1}{2l_i^2} z_i^2 (||W_i||^2 - \hat{\theta}) S_i^T S_i\right) + \frac{1}{2}\varepsilon_3^2 d^2 + z_1(\alpha_{1d} - \alpha_1) \tag{25.13}$$

Step 3: Similarly, for reference signal x_{3d}, choose the Lyapunov function candidate as $V_3 = V_2 + \frac{1}{2}z_3^2$. And the time derivative of V_3 is given by

$$\dot{V}_3 = \dot{V}_2 + z_3 \dot{z}_3 = \dot{V}_2 + z_3(c_1 x_3 + b_4 x_4 - \dot{x}_{3d}) \tag{25.14}$$

Similarly, α_2 is constructed as $\alpha_2 = (-k_3 z_3 - c_1 x_3 + \dot{x}_{3d})/b_4$ and let α_2 pass through a first-order filter with time constant ς_2 to obtain α_{2d}

$$\varsigma_2 \dot{\alpha}_{2d} + \alpha_{2d} = \alpha_2, \alpha_{2d}(0) = \alpha_2(0) \tag{25.15}$$

Defining $z_4 = x_4 - \alpha_{2d}$ and substituting (25.15) into (25.14) results in

$$\dot{V}_3 = \dot{V}_2 - k_3 z_3^2 + b_4 z_3(\alpha_{2d} - \alpha_2) + b_4 z_3 z_4 \tag{25.16}$$

Step 4: Choose the Lyapunov function candidate as $V_4 = V_3 + \frac{1}{2} z_4^2$, and the time derivative of V_4 is

$$\dot{V}_4 = \dot{V}_2 - k_3 z_3^2 + b_4 z_3(\alpha_{2d} - \alpha_2) + z_4(f_4 + b_5 u_d) \tag{25.17}$$

where $f_4(Z) = b_4 z_3 + b_1 x_4 + d_2 x_3 + b_3 x_1 x_2 + b_4 x_2^2/x_3 - \dot{\alpha}_{2d} = W_4^T S_4(Z) + \delta_4(Z)$. Similarly,

$$z_4 f_4 \leq \frac{1}{2l_4^2} z_4^2 ||W_4||^2 S_4^T S_4 + \frac{1}{2} l_4^2 + \frac{1}{2} z_4^2 + \frac{1}{2} \varepsilon_4^2 \tag{25.18}$$

We construct u_d as

$$u_d = \frac{1}{b_5}(-k_4 z_4 - \frac{1}{2} z_4 - \frac{1}{2l_4^2} z_4 \hat{\theta} S_4^T S_4) \tag{25.19}$$

Define $\theta = \max\{||W_1||^2, ||W_2||^2, ||W_4||^2\}$. $\tilde{\theta} = \hat{\theta} - \theta$. We can get

$$\begin{aligned} \dot{V}_4 \leq & -\sum_{i=1}^{4} k_i z_i^2 + z_1(\alpha_{1d} - \alpha_1) + b_4 z_3(\alpha_{2d} - \alpha_2) + \sum_{i=1,2,4} \left(\frac{1}{2} l_i^2 + \frac{1}{2} \varepsilon_i^2 \right) \\ & - \frac{1}{2l_1^2} z_1^2 \tilde{\theta} S_1^T S_1 - \frac{1}{2l_2^2} z_2^2 \tilde{\theta} S_2^T S_2 - \frac{1}{2l_4^2} z_4^2 \tilde{\theta} S_4^T S_4 + \frac{1}{2} \varepsilon_3^2 d^2 \end{aligned} \tag{25.20}$$

Define $y_i = \alpha_{id} - \alpha_i (i = 1, 2)$, and then we have

$$\dot{y}_i = \dot{\alpha}_{id} - \dot{\alpha}_i = -(\alpha_{id} - \alpha_i)/\varsigma_i - \dot{\alpha}_i = -y_i/\varsigma_i + B_i \tag{25.21}$$

Choose the Lyapunov function candidate as $V = V_4 + \frac{1}{2} y_1^2 + \frac{1}{2} y_2^2 + \frac{\tilde{\theta}^2}{2r_1}$. The time derivative of V along with (25.20) and (25.21) is given by

$$\begin{aligned} \dot{V} \leq & -\sum_{i=1}^{4} k_i z_i^2 + z_1 y_1 + b_4 z_3 y_2 + y_1 \dot{y}_1 + y_2 \dot{y}_2 + \sum_{i=1,2,4} \left(\frac{1}{2} l_i^2 + \frac{1}{2} \varepsilon_i^2 \right) + \frac{1}{2} \varepsilon_3^2 d^2 \\ & + \frac{\tilde{\theta}}{r_1} (\dot{\hat{\theta}} - \frac{r_1}{2l_1^2} z_1^2 S_1^T S_1 - \frac{r_1}{2l_2^2} z_2^2 S_2^T S_2 - \frac{r_1}{2l_4^2} z_4^2 S_4^T S_4) \end{aligned} \tag{25.22}$$

The corresponding adaptive law is chosen as $\dot{\hat{\theta}} = \sum_{i=1,2,4} (r_1 z_i^2 S_i^T S_i / 2l_i^2) - m_1 \hat{\theta}$, where r_1, m_1 and $l_i (i = 1, 2, 4)$ are positive constants.

25.4 Stability Analysis

To address the stability analysis of the resulting closed-loop system, substituting the corresponding adaptive law into (25.22), we have

$$\dot{V} \leq -\sum_{i=1}^{4} k_i z_i^2 + z_1 y_1 + b_4 z_3 y_2 + y_1 \dot{y}_1 + y_2 \dot{y}_2 + \sum_{i=1,2,4} \left(\frac{1}{2} l_i^2 + \frac{1}{2} \varepsilon_i^2 \right) - \frac{m_1 \tilde{\theta} \hat{\theta}}{r_1} + \frac{1}{2} \varepsilon_3^2 d^2 \tag{25.23}$$

By [9, 10], $|B_i|$ has a maximum B_{iM} on compact set $|\Omega_i|, i = 1, 2$, $|B_i| \leq B_{iM}$. Therefore, we can get $y_i \dot{y}_i \leq -y_i^2 / \varsigma_i + |B_{iM}||y_i| \leq -y_i^2 / \varsigma_i + 1/2\tau B_{iM}^2 y_i^2 + \tau/2$. With $\tau > 0$. Using Young's inequality, we can get the following inequalities:

$$z_1 y_1 \leq \frac{1}{4} y_1^2 + z_1^2, b_4 z_3 y_2 \leq \frac{b_4^2}{4} y_2^2 + z_3^2, -\tilde{\theta} \hat{\theta} \leq -\tilde{\theta}^2 / 2 + \theta^2 / 2 \tag{25.24}$$

Then by using these inequalities, (25.23) can be rewritten as

$$\dot{V} \leq -(k_1 - 1) z_1^2 - k_2 z_1^2 - (k_3 - 1) z_3^2 - k_4 z_4^2 - \frac{m_1 \tilde{\theta}^2}{2 r_1} - \left(\frac{1}{\zeta_1} - \left(\frac{1}{4} + \frac{1}{2\tau} B_{1M}^2 \right) \right) y_1^2 - \left(\frac{1}{\zeta_2} - \left(\frac{b_4^2}{4} + \frac{1}{2\tau} B_{2M}^2 \right) \right) y_2^2 + \frac{1}{2} \sum_{i=1,2,4} \left(l_i^2 + \varepsilon_i^2 \right) + \frac{m_1 \theta^2}{2 r_1} + \tau + \frac{1}{2} \varepsilon_3^2 d^2 \leq -a_0 V + b_0 \tag{25.25}$$

where $a_0 = \min\{2(k_1 - 1)/J, 2k_2, 2(k_3 - 1), 2k_4, m_1, 2(1/\zeta_1 - (1/4 + B_{1M}^2/2\tau)), 2(1/\zeta_2 - (b_4^2/4 + B_{2M}^2/2\tau))\}$ and $b_0 = \frac{1}{2} \sum_{i=1,2,4} (l_i^2 + \varepsilon_i^2) + \frac{m_1 \theta^2}{2 r_1} + \tau + \frac{1}{2} \varepsilon_3^2 d^2$. Then, (25.25) implies that

$$V(t) \leq (V(t_0) - b_0/a_0) e^{-a_0 (t - t_0)} + b_0/a_0 \leq V(t_0) + b_0/a_0, \forall t \geq t_0 \tag{25.26}$$

As a result, all $z_i(i = 1, 2, 3, 4)$ and $\tilde{\theta}$ belong to the compact set $\Omega = \left\{(z_i, \tilde{\theta}) | V \leq V(t_0) + b_0/a_0, \forall t \geq t_0\right\}$. Namely, all the signals in the closed-loop system are bounded. Especially, by (25.26) we can get $\lim_{t\to\infty} z_1^2 \leq 2b_0/a_0$. By the definitions of a_0 and b_0, it is proved that to get a small tracking error we can take r_1 large and l_i and ε_i small enough after giving the parameters k_i and m_1.

25.5 Simulation Results

To illustrate the effectiveness of the proposed adaptive fuzzy controller, the simulation is run for induction motors with the parameters: $J = 0.0586\,\text{Kg}\,\text{m}^2$, $R_s = 0.1\Omega$, $R_r = 0.15\Omega$, $L_s = L_r = 0.0699\,\text{H}$, $L_m = 0.068\,\text{H}$, $n_p = 1$. The controller parameters are chosen as $k_1 = 200, k_2 = 80, k_3 = 10, k_4 = 5, r_1 = 0.25, l_1 = l_2 = l_4 = 0.75, \varsigma_1 = 0.002, \varsigma_2 = 0.1$. The fuzzy membership functions are $\mu_{F_i^l} = \exp\left[-(x + l)^2 \Big/ 2\right], l \in N, l \in [-5, 5]$. The simulation is carried out under the zero initial condition for induction motor. Give the reference signal $x_{1d} = 4, 0 \leq t \leq 5$ or $x_{1d} = 6, t \geq 5$ and $T_L = 0.5, 0 \leq t \leq 5$ or $T_L = 1, t \geq 5$.

Simulation results are shown in Figs. 25.1, 25.2 and 25.3, where Fig. 25.1 shows the reference signal x_{1d} and ω curves. Figures 25.2 and 25.3 show the curves of u_q, u_d. From the simulations, it is clearly seen that the controllers can achieve a good tracking performance.

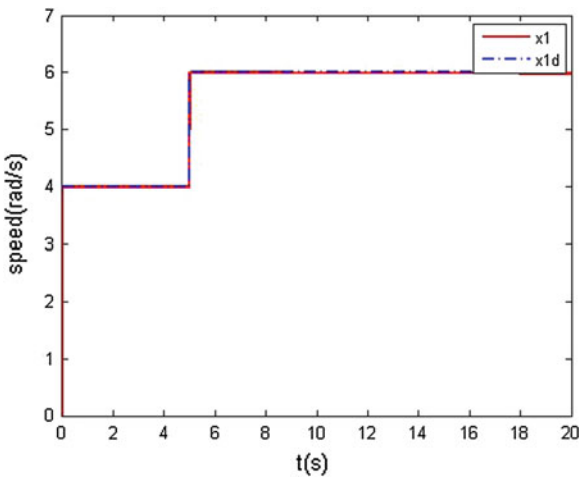

Fig. 25.1 Trajectories of x_1 and x_{1d}

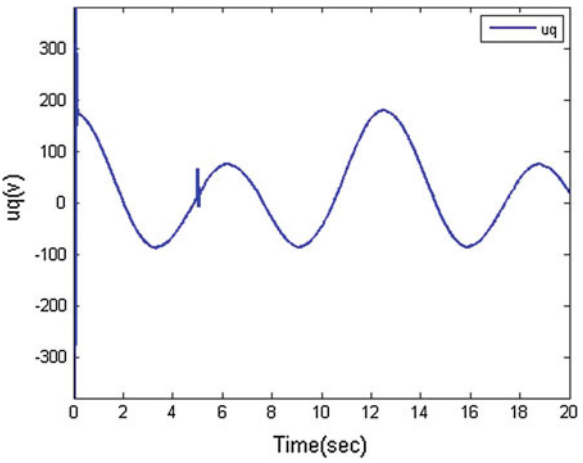

Fig. 25.2 Trajectory of u_q

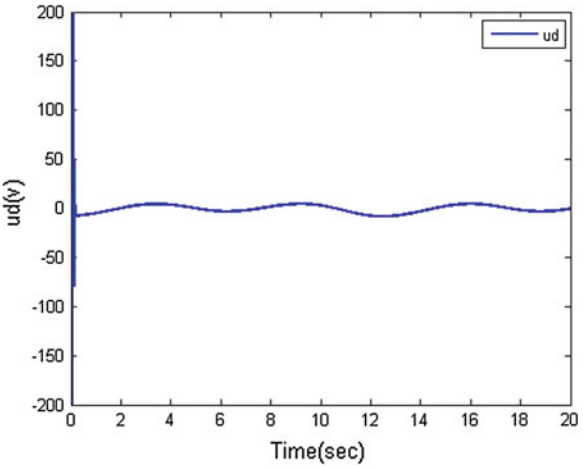

Fig. 25.3 Trajectory of u_d

25.6 Conclusions

Based on backstepping and DSC technique, an adaptive fuzzy dynamic surface control method is developed to control induction motors. The proposed controller is able to overcome the problems of "nonlinear systems with parameter uncertainties" and "explosion of complexity" inherent in the traditional backstepping design. In addition, it is proved that the proposed controllers guarantee the speed tracking error converge to a small neighborhood of the origin. Simulation results show that the controllers illustrate the effectiveness of the proposed approach.

Acknowledgments This work is supported by the Natural Science Foundation of China (61104076, 61174131, 61174033, 61473160) the China Postdoctoral Science Foundation (2014T70620, 2013M541881, 201303062) and Qingdao Postdoctoral Application Research Project.

References

1. Liu JK, Sun FC (2007) Research and development on theory and algorithms of sliding mode control. Control Theory Appl 24(3):407–418
2. Yu JP, Chen B, Yu HS (2010) Position tracking control of induction motors via adaptive fuzzy backstepping. Energy Convers Manag 51(11):2345–2352
3. Kwan CM, Lewis FL (2000) Robust backstepping control of induction motors using neural networks. IEEE Trans Neural Networks 11(5):1178–1187
4. Swaroop D, Hedrick JK, Yip PP (2000) Dynamic surface control for a class of nonlinear systems. IEEE Trans Autom Control 45(10):1893–1899
5. Tong SC, Li HH (2002) Direct adaptive fuzzy output tracking control of nonlinear systems. Fuzzy Sets Syst 128:107–115
6. Hassan AA (2002) Improving the Power Efficiency of a Rotor Flux-Oriented Induction Motor Drive. Electr Power Compon Syst 30(5):431–442
7. Ta CM, Hori Y (2001) Convergence Improvement of Efficiency Optimization Control of Induction Motor Drives. IEEE Trans Indus Appl 37(6):1746–1753
8. Wang LX, Mendel JM (1992) Fuzzy basis functions, universal approximation, and orthogonal least squares learning. IEEE Trans Neural Netw 3(5):807–814
9. Tong SC, Li YM, Feng G (2011) Observer-based adaptive fuzzy backstepping dynamic surface control for a class of MIMO nonlinear system. IEEE Trans Syst Man Cybern Part B: Cybern 41(4):1124–1135
10. Wang D, Huang J (2005) Neural network-based adaptive dynamic surface control for a class of uncertain nonlinear systems in strict-feedback form. IEEE Trans Neural Netw 16(1): 195–202

Chapter 26
Fault Tolerant Control with TSM for Spacecraft Formation Flying

Xiaoyu Han and Yingmin Jia

Abstract In this paper, a fault tolerant-based adaptive terminal sliding mode (TSM) control method is proposed for leader–follower spacecraft formation flying system in the presence of actuator fault. Unknown external disturbances and minimum fault information are adapted online and the great robustness is guaranteed. It has been proved that with this designed controller, the practical finite-time stability (PFS) of the closed-loop system can be guaranteed. Simulation results show the effectiveness of the proposed method.

Keywords Fault tolerant control · Spacecraft formation · Terminal sliding mode · Adaptive control

26.1 Introduction

Spacecraft flying in formation is revolutionizing our way of performing space-based operations, and brings out several advantages in space mission accomplishment, as well as new opportunities and applications for such missions. The major advantage of formation flying of spacecraft lies in flexibility and modularity, which also lead to a cost of increased complexity and technological challenges. In the early days, the model of relative motion between two spacecrafts is linear and multivariable, known as Hill equations or Clohessy-Wiltshire equations. Recently, the nonlinear model, with added terms for orbital perturbations, is built in [1–5]. Nonlinear adaptive tracking control was developed in [2], and an adaptive output feedback controller using relative position only, was proved in [6], a result which ensured semi-global asymptotic convergence of the relative translation errors.

X. Han (✉) · Y. Jia
The Seventh Research Division and the Department of Systems and Control,
Beijing University of Aeronautics and Astronautics, Xinzhu Building,
NO 37 Xueyuan Road, Beijing F907, Haidian District, China
e-mail: hanxy0810@163.com

Z. Deng and H. Li (eds.), *Proceedings of the 2015 Chinese Intelligent Automation Conference*, Lecture Notes in Electrical Engineering 337,
DOI 10.1007/978-3-662-46463-2_26

From what we introduced above, most previous works devoted to the system trajectories converge to the equilibrium with infinite time. However, finite-time stabilization of dynamical systems may lead to a better disturbance attenuation and a fast convergence to the origin. As far as author known, there is few finite-time control results applied in the problem of leader–follower spacecraft formation control. The terminal sliding mode (TSM) control was developed in [7–9], which was an effective scheme to guarantee finite-time convergence. For example, [10] used it to solve the finite time spacecraft formation control problem.

With more and more space missions asked for more control requirements, it poses tremendous challenges in spacecraft control, ranging from control performance, rapid response, and steady-state error to robustness. However, faults of actuators would occur frequently and the various external perturbations from the space cannot also be modeled accurately, which both greatly hinder the attitude control precision. Therefore, design of effective strategy to guarantee the safety of spacecraft and achieve fault tolerant control is the key in controller design [11–14].

Motivated by the above discussions, in this paper, an adaptive TSM-based fault-tolerate controller is proposed in relative translation tracking in a leader–follower spacecraft formation. In the presence of partial loss of actuator effectiveness and external disturbances, adaptive update laws are employed designed to estimate the minimum value of actuator faults, the bound of external disturbances. Through this approach, the system can convergent to a neighborhood of the origin in finite time.

26.2 Modeling

26.2.1 Relative Translational Motion

Earth centered inertial (ECI) frame is used throughout this paper and is given in Fig. 26.1 as follows: First, do linear interpolation on the X direction, finding the gray value of R1 and R2 as shown in Fig. 26.1.

The basis vectors of the frame can be defined as:

$$\boldsymbol{e}_l = \frac{\mathbf{r}_l}{r_l}, \quad \boldsymbol{e}_{\boldsymbol{\theta}} = \boldsymbol{e}_h \times \boldsymbol{e}_r, \quad \boldsymbol{e}_h = \frac{\mathbf{h}}{h} \tag{26.1}$$

where $\mathbf{h} = \mathbf{r}_l \times \dot{\mathbf{r}}_l$, is the angular momentum vector of the orbit, and $h = |\mathbf{h}|$. The general orbit equation for two-point masses m_1, m_2 (rf.3) is given as:

$$\ddot{\mathbf{r}} + \frac{\mu}{r^3}\boldsymbol{r} = 0 \tag{26.2}$$

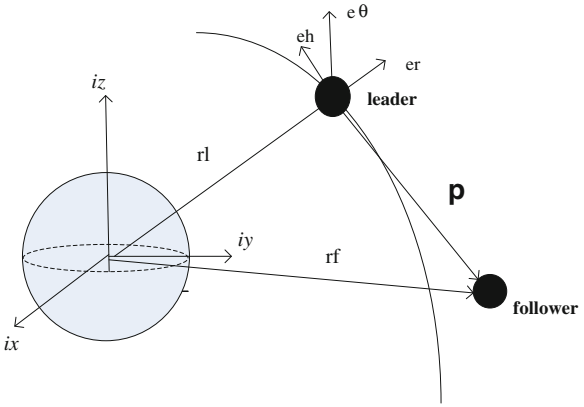

Fig. 26.1 Graphical description of reference frame

And (26.2) can be expressed for the leader and follower spacecraft as:

$$\ddot{\underset{l}{\mathbf{r}}} = -\frac{\mu}{r_l^3}\mathbf{r}_l \tag{26.3}$$

$$\ddot{\underset{f}{\mathbf{r}}} = -\frac{\mu}{r_f^3}\mathbf{r}_f + \frac{\mathbf{f}_{df}}{m_f} + \frac{\mathbf{u}_f}{m_f} \tag{26.4}$$

where $\mathbf{f}_{df} \in \mathbf{R}^3$ is the disturbance force term due to external perturbation effects and $\mathbf{u}_f \in \mathbf{R}^3$ is the actuator forces of the leader and follower, respectively. $\mu = \mathrm{GM}_e$. Taking the second-order derivative of the relative position vector $\mathbf{p} = \mathbf{r}_f - \mathbf{r}_l$, and using the true anomaly $v(t)$ of the leader the relative position dynamics can be written as [5]:

$$m_f\,\ddot{\mathbf{p}} + \mathbf{C}(\dot{v})\dot{\mathbf{p}} + \mathbf{D}\left(\dot{v},\, \ddot{v},\, r_f\right)\mathbf{p} + \mathbf{n}\left(r_l,\, r_f\right) = u_f + f_{df} \tag{26.5}$$

where

$$\mathbf{C}(\dot{v}) = 2m_f\begin{bmatrix} 0 & -\dot{v} & 0 \\ \dot{v} & 0 & 0 \\ 0 & 0 & 0 \end{bmatrix} \tag{26.6}$$

$$\mathbf{D}\left(\dot{v},\, \ddot{v},\, r_f\right) = m_f\begin{bmatrix} \frac{\mu}{r_f^3} - \dot{v}^2 & -\ddot{v} & 0 \\ \ddot{v} & \frac{\mu}{r_f^3} - \dot{v}^2 & 0 \\ 0 & 0 & \frac{\mu}{r_f^3} \end{bmatrix} \tag{26.7}$$

$$\mathbf{n}\left(r_l, r_f\right) = \mu\left[\frac{r_l}{r_f^3} - \frac{1}{r_l^2},\quad 0,\quad 0\right]^{\mathrm{T}} \tag{26.8}$$

Given a desired relative position $\mathbf{p}_d(t) = [x_d \ y_d \ z_d]^T$ of the follower spacecraft in the leader orbit frame, the position error can be written as: $\mathbf{e}(t) = [e_x \quad e_y \quad e_z]^T = \mathbf{p}(t) - \mathbf{p}_d(t)$. Then the relative position dynamics is rendered as:

$$m_f \ddot{\mathbf{e}} + \mathrm{C}(\dot{v})\dot{\mathbf{e}} + \mathrm{D}(\dot{v}, \ddot{v}, r_f)\mathbf{e} + \mathrm{N}(p_\mathrm{d}, \dot{p}_d, \ddot{p}_d, \dot{v}, \ddot{v}, r_f, r_l) = u_f + f_{df} \tag{26.9}$$

where $\mathrm{N}(p_d, \dot{p}_d, \ddot{p}_d, \dot{v}, \ddot{v}, r_f, \mathrm{r}_l) = m_f \ddot{p}_d + c(\dot{v})\dot{p}_d + \mathrm{n}(r_l, r_f)$.

26.2.2 The Dynamic Model of Fault Tolerant System

According to (26.9), the dynamic model of the leader–follower system can be written as:

$$m_f \ddot{\mathbf{e}} + \mathrm{C}(\dot{v})\dot{\mathbf{e}} + \mathrm{D}(\dot{v}, \ddot{v}, r_f)\mathbf{e} + \mathrm{N}(p_\mathrm{d}, \dot{p}_d, \ddot{p}_d, \dot{v}, \ddot{v}, r_f, r_l) = \mathbf{E}u_f + f_{df} \tag{26.10}$$

This model includes provisions for multiplicative faults represented by a diagonal matrix $\mathbf{E}$. Here, $\mathbf{E}$ is given by $\mathbf{E} = \mathrm{diag}(e_1(\mathrm{t}), e_2(\mathrm{t}), e_3(\mathrm{t}), 0 < e_i < 1$, $i = 1, 2, 3$. And $e_i = 1$ means no fault and $e_i = 0$ means the complete failure. We can written (26.10) as follows [14]:

$$m_f \ddot{\mathbf{e}} + \mathrm{C}(\dot{v})\dot{\mathbf{e}} + \mathrm{D}(\dot{v}, \ddot{v}, r_f)\mathbf{e} + \mathrm{N}(p_\mathrm{d}, \dot{p}_d, \ddot{p}_d, \dot{v}, \ddot{v}, r_f, r_l) = u_f - \Delta\mathbf{E}u_f + f_{df} \tag{26.11}$$

where $\Delta\mathbf{E} = \mathrm{diag}(1 - e_1(\mathrm{t}), 1 - e_2(\mathrm{t}), 1 - e_3(\mathrm{t}))$, then set $e_0 = \min e(t)$, so $\|\Delta\mathbf{E}\| = 1 - e_0 < 1$.

Define

$$\|\Delta\mathbf{E}\| \leq \eta \tag{26.12}$$

where η is unknown. f_{df} is the torque of outside interference, and

$$\left\|f_{df}\right\| \leq c_0 \tag{26.13}$$

where c_0 is unknown.

26.3 Controller Design

26.3.1 Preparation

Lemma 26.1 *If* $p \in (0, 1)$ *then the following inequality holds:*

$$\sum_{i=1}^{3} |x_i|^{1+p} \geq \left(\sum_{i=1}^{3} |x_i^2| \right)^{1+p/2} \tag{26.14}$$

Definition 26.1 [15, 16] Consider the nonlinear system $\dot{x} = f(x, u)$, where x is a state vector, u is the input vector. The solution is practical finite-time stable (PFS) if for all $x(t_0) = x_0$, there exists $\varepsilon > 0$ and $T(\varepsilon, x_0) < \infty$, such that $\|x(t)\| < \varepsilon$, for all $t \geq t_0 + T$.

Lemma 26.2 *For any real numbers* x_i, $i = 1, \ldots\ldots, n$ and $0 < b < 1$, *the following inequality holds:*

$$(|x_i| + \cdots + |x_n|)^b \leq |x_1|^b + \cdots + |x_n|^b$$

Lemma 26.3 [15, 16] *Consider the system* $\dot{x} = f(x, u)$ *suppose that there exists continuous function V(x),* scalars $\lambda > 0$, $0 < \alpha < 1$ and $0 < \eta < \infty$ *such that:*

$$\dot{\mathrm{V}}(x) \leq -\lambda V^{\alpha}(x) + \eta \tag{26.15}$$

Then the trajectory of system $\dot{x} = f(x, u)$ is PFS. The trajectories of the closed-loop system is bounded in finite times as

$$\lim_{\theta \to \theta_0} \mathrm{x} \in \left(\mathrm{V}^{\alpha}(x) \leq \frac{\eta}{(1-\theta)\lambda} \right) \tag{26.16}$$

where $0 < \theta_0 < 1$. And the time needed to reach is bound as $T \leq \frac{V^{1-\alpha}(x_0)}{\lambda\theta(1-\alpha)}$ where $\mathrm{V}(x_0)$ is the initial value of $V(x)$.

26.3.2 Adaptive Terminal Sliding Mode Control (ATSMC)

In this section, ATSMC is designed to implement on the leader–follower system. In order to reduce the influence of the unknown perturbations and actuator faults and improve the system robustness, the design idea is to adopt the adaptation laws to estimate the unknown parameters online.

Definition 1.2 Denote $\mathrm{sig}^{\alpha}(\mathrm{x}) = \mathrm{sign}(\mathrm{x})|x|^{\alpha}$, where $\alpha \geq 0, \mathrm{x} \in \mathbb{R}$, sign() is the standard sign function.

The follower is to construct a sliding mode surface in the system state space, which is given by:

$$\boldsymbol{s} = \dot{\boldsymbol{e}} + k_1 \boldsymbol{e} + k_2 \mathrm{sig}^{r} \boldsymbol{e} = 0 \tag{26.17}$$

where $k_1, k_2 > 0$, $r \in (0, 1)$.

When the controller made the system in the sliding mode, the closed-loop system is stable.

Theorem 26.1 *Consider the leader–follower spacecraft formation tracking error system in* (26.10)*, if the controller is given as in* (26.18) *with adaptive laws* (26.20–26.21)*, the trajectory of the closed-loop system can be driven onto a neighborhood of the sliding surface in finite time, where*

$$\begin{aligned} u_f = & \mathrm{C}(\dot{v})\dot{\mathbf{e}} + \mathrm{D}\left(\dot{v}, \ddot{v}, r_f\right)\mathbf{e} + \mathrm{N}\left(p_{\mathrm{d}}, \dot{p}_d, \ddot{p}_d, \dot{v}, \ddot{v}, r_f, r_l\right) \\ & - m_f k_1 \dot{\mathbf{e}} - m_f k_2 |\mathbf{e}|^{\dot{r}-1}\dot{\mathbf{e}} - (\hat{c}_0)\frac{s}{\|s\|} - r(t)\frac{s}{\|s\|} - \tau \mathrm{sig}(s)^{r} \end{aligned} \tag{26.18}$$

where

$$r(t) = -\varphi + \hat{\theta}\varphi \tag{26.19}$$

$$\dot{\hat{c}}_0 = q_0\|s\| - q_0\varepsilon_0\hat{c}_0 \tag{26.20}$$

$$\dot{\hat{\theta}} = q_1\varphi\|s\| - q_1\varepsilon_1\hat{\theta} \tag{26.21}$$

$$\theta = \frac{1}{1-\eta} \tag{26.22}$$

and

$$\begin{aligned} \varphi = & \|\mathrm{C}(\dot{v})\dot{\mathbf{e}} + \mathrm{D}\left(\dot{v}, \ddot{v}, r_f\right)\mathbf{e} + \mathrm{N}\left(p_{\mathrm{d}}, \dot{p}_d, \ddot{p}_d, \dot{v}, \ddot{v}, r_f, r_l\right) \\ & - m_f k_2 r |\mathbf{e}|^{r-1}\dot{\mathbf{e}} - m_f k_1 \dot{\mathbf{e}}\left(\dot{\hat{c}}_0\right)\frac{s}{\|s\|} - \tau \mathrm{sig}(s)^{r} + \varepsilon \end{aligned} \tag{26.23}$$

$\hat{c}_0$, $\hat{\theta}$ are estimated values q_0, q_1 (28) ε, ε_0, ε_1 are constant values.

Proof Consider the Lyapunov function candidate:

$$V = \frac{1}{2}m_f s^T s + \frac{1}{2}\frac{1}{q_0}\tilde{c}_0^2 + \frac{1}{2}\frac{1-\eta}{q_1}\tilde{\theta}^2 \tag{26.24}$$

where $\tilde{c}_0 = c_0 - \hat{c}_0$, $\tilde{\theta} = \theta = \hat{\theta}$.

In view of (26.17), (26.18–26.22), it follows that

$$\begin{aligned}\dot{V} &= s^T\left(m_e^{\cdot\cdot} + m_f k_1 \dot{e} + m_f k_2 \gamma |e|^{r-1}\dot{e}\right) - \frac{1}{q_0}\tilde{c}_0\dot{\hat{c}}_0 - \frac{1-\eta}{q_1}\tilde{\theta}\dot{\hat{\theta}} \\ &= s^T\left[-\left(C(\dot{v})\dot{e} + D\left(\dot{v},\, \ddot{v},\, r_f\right)e + N\left(p_{\mathrm{d}},\, \dot{p}_d,\, \ddot{p}_d,\, \dot{v},\, \ddot{v},\, r_f,\, r_l\right)\right)\right. \\ &\quad \left. + f_{df} + u_f + m_f k_1 \dot{e} + m_f k_2 r|e|^{r-1}\dot{e} - \Delta E u_f\right] - \frac{1}{q_0}\tilde{c}_0\dot{\hat{c}}_0 - \frac{1-\eta}{q_1}\tilde{\theta}\dot{\hat{\theta}}\end{aligned}$$

Substituting for u_f into the above equation, yields

$$\begin{aligned}\dot{V} &\le \mathrm{s}^T\left[(\hat{c}_0)\frac{\mathrm{s}}{\|s\|} - r(t)\frac{s}{\|s\|} - \tau \mathrm{sig}(s)^r - \Delta E u_f + f_{df}\right] - \frac{1}{q_0}\tilde{c}_0\dot{\hat{c}}_0 - \frac{1-\eta}{q_1}\tilde{\theta}\dot{\hat{\theta}} \\ &\le -s^T\Delta E u_f + \left(\varphi - \hat{\theta}\varphi\right)\|s\| + \varepsilon_0\hat{c}_0\tilde{c}_0 - \tau\sum_{i=1}^{3}|s_i|^{r+1} - \frac{1-\eta}{q_1}\tilde{\theta}\dot{\hat{\theta}} \\ &\le \|\mathrm{s}\|\left\|u_f\right\|\eta + \left(\varphi - \hat{\theta}\varphi\right)\|s\| - \tau\sum_{i=1}^{3}|s_i|^{r+1} - \frac{1-\eta}{q_1}\tilde{\theta}\dot{\hat{\theta}} + \varepsilon_0\hat{c}_0\tilde{c}_0\end{aligned}$$

Denote

$$\begin{aligned}u_1 = &\mathrm{C}(\dot{v})\dot{\mathbf{e}} + \mathrm{D}\left(\dot{v},\, \ddot{v},\, r_f\right)\mathbf{e} - m_f k_1\dot{\mathbf{e}} + \mathrm{N}\left(p_{\mathrm{d}},\, \dot{p}_d,\, \ddot{p}_d,\, \dot{v},\, \ddot{v},\, r_f,\, r_l\right) \\ &- m_f k_2 r|\mathbf{e}|^{r-1}\dot{\mathbf{e}} - (\hat{c}_0)\frac{s}{\|s\|} - \tau\mathrm{sig}(s)^r\|\end{aligned}$$

Then $\left\|u_f\right\| \le \|u_1\| + r(t) = \|u_1\| - \varphi + \hat{\theta}\varphi = -\varepsilon_0 + \hat{\theta}\varphi$. where (26.23) is applied. So, we have

$$\begin{aligned}\dot{V} &\le \|s\|\eta\left(-\varepsilon_0 + \hat{\theta}\varphi\right) + \left(\varphi - \hat{\theta}\varphi\right)\|s\| - \frac{1-\eta}{q_1}\tilde{\theta}\dot{\hat{\theta}} - \tau\sum_{i=1}^{3}|s_i|^{r+1} + \varepsilon_0\hat{c}_0\tilde{c}_0 \\ &= -\varepsilon_0\eta\|s\| + \left[1 - (1-\eta)\hat{\theta}\right]\varphi\|s\| + \varepsilon_0\hat{c}_0\tilde{c}_0 - \frac{1-\eta}{q_1}\tilde{\theta}\left(q_1\varphi\|s\| - q_1\varepsilon_1\hat{\theta}\right) - \tau\sum_{i=1}^{3}|s_i|^{r+1}\end{aligned}$$

From Eq. (26.22), we have:

$$\begin{aligned}\dot{V} \le &-\tau\sum_{i=1}^{3}|s_i|^{r+1} + \varepsilon_0\tilde{c}_0\hat{c}_0 + (1-\eta)\varepsilon_1\tilde{\theta}\hat{\theta} \le -\gamma\left(\frac{1}{2}m_f s^T s\right)^{\frac{r+1}{2}} + \varepsilon_0\tilde{c}_0\hat{c}_0 \\ &+ (1-\eta)\varepsilon_1\tilde{\theta}\hat{\theta}\end{aligned} \tag{26.25}$$

Note that for any positive scalars $\delta_0 > \frac{1}{2}$ and $\delta_1 > \frac{1}{2}$, the following inequalities hold:

$$\begin{aligned}\varepsilon_0\tilde{c}_0\hat{c}_0 &= \varepsilon_0\tilde{c}_0(-\tilde{c}_0+c_0) = \varepsilon_0\left(-\tilde{c}_0^2+\tilde{c}_0c_0\right)\\ &\le \varepsilon_0(-\tilde{c}_0^2+\frac{1}{2\delta_0}\tilde{c}_0^2+\frac{\delta_0}{2}c_0^2 \le \frac{-\varepsilon_0(2\delta_0-1)}{2\delta_0}\tilde{c}_0^2+\frac{\varepsilon_0\delta_0}{2}c_0^2\end{aligned} \tag{26.26}$$

$$(1-\eta)\varepsilon_1\tilde{\theta}\hat{\theta} \le \frac{-(1-\eta)\varepsilon_1(2\delta_1-1)}{2\delta_1}\tilde{\theta}^2+\frac{(1-\eta)\varepsilon_1\delta_1}{2}\theta^2 \tag{26.27}$$

Thus inequality (26.25) can be expressed as:

$$\begin{aligned}\dot{V} \le & -\gamma\left(\frac{1}{2}m_f s^T s\right)^{\frac{r+1}{2}}-\left(\frac{\varepsilon_0(2\delta_0-1)}{2\delta_0}\tilde{c}_0^2\right)^{r+1/2}-\left(\frac{(1-\eta)\varepsilon_1(2\delta_1-1)}{2\delta_1}\tilde{\theta}^2\right)^{r+1/2}\\ &+\left(\frac{\varepsilon_0(2\delta_0-1)}{2\delta_0}\tilde{c}_0^2\right)^{r+1/2}+\varepsilon_0\tilde{c}_0\hat{c}_0+\left(\frac{(1-\eta)\varepsilon_1(2\delta_1-1)}{2\delta_1}\tilde{\theta}^2\right)^{r+1/2}+(1-\eta)\varepsilon_1\tilde{\theta}\hat{\theta}\\ =&-\gamma\left[\left(\frac{1}{2}s^T s\right)^{\frac{r+1}{2}}+\left(\frac{1}{2q_0}\tilde{c}_0^2\right)^{\frac{r+1}{2}}+\left(\frac{1-\eta}{2q_1}\tilde{\theta}^2\right)^{\frac{r+1}{2}}\right]-\left(\frac{(1-\eta)\varepsilon_1(2\delta_1-1)}{2\delta_1}\tilde{\theta}^2\right)^{r+1/2}\\ &+\left(\frac{\varepsilon_0(2\delta_0-1)}{2\delta_0}\tilde{c}_0^2\right)^{r+1/2}+\left(\frac{(1-\eta)\varepsilon_1(2\delta_1-1)}{2\delta_1}\tilde{\theta}^2\right)^{r+1/2}+\varepsilon_0\tilde{c}_0\hat{c}_0+(1-\eta)\varepsilon_1\tilde{\theta}\hat{\theta}\end{aligned}$$

where

$$q_0=\frac{\delta_0\gamma^{r+1/2}}{\varepsilon_0(2\delta_0-1)},\ q_1=\frac{\delta_1\gamma^{r+1/2}}{\varepsilon_1(2\delta_1-1)},\ \gamma=\tau/m_f^{\frac{r+1}{2}} \tag{26.28}$$

Note Lemma 26.2, $\delta_0>\frac{1}{2}$, $\delta_1>\frac{1}{2}$ and $\frac{1}{2}<\frac{r+1}{2}<1$, the time derivative of Lyapunov function becomes:

$$\begin{aligned}\dot{V} \le & -\gamma V^{r+1/2}+\left(\frac{\varepsilon_0(2\delta_0-1)}{2\delta_0}\tilde{c}_0^2\right)^{r+1/2}+\left(\frac{(1-\eta)\varepsilon_1(2\delta_1-1)}{2\delta_1}\tilde{\theta}^2\right)^{r+1/2}+\varepsilon_0\tilde{c}_0\hat{c}_0\\ &+(1-\eta)\varepsilon_1\tilde{\theta}\hat{\theta}\end{aligned} \tag{26.29}$$

and

$$\left(\frac{\varepsilon_0(2\delta_0-1)}{2\delta_0}\tilde{c}_0^2\right)^{r+1/2}+\varepsilon_0\tilde{c}_0\hat{c}_0<\frac{\varepsilon_0(2\delta_0-1)}{2\delta_0}\tilde{c}_0^2+\varepsilon_0\tilde{c}_0\hat{c}_0\le\frac{\varepsilon_0\delta_0}{2}c_0^2 \tag{26.30}$$

Similarly to (26.29), the following inequality can be obtained:

$$\left(\frac{(1-\eta)\varepsilon_1(2\delta_1-1)}{2\delta_1}\tilde{\theta}^2\right)^{r+1/2}+(1-\eta)\varepsilon_1\tilde{\theta}\hat{\theta}\le\frac{(1-\eta)\varepsilon_1\delta_1}{2}\theta^2 \tag{26.31}$$

Thus, from (26.28) to (26.31), the time derivative of the Lyapunov function (26.29) becomes:

$$\dot{V} \leq -\gamma V^{r+1/2} + \eta_0 \tag{26.32}$$

where $\eta_0 = \frac{\varepsilon_0 \delta_0}{2} c_0^2 + \frac{(1-\eta)\varepsilon_1 \delta_1}{2} \theta^2$.

According to Lemma 26.3, it can be concluded now that the trajectory of the closed-loop system can be driven onto a neighborhood of the sliding surface in finite time.

26.4 Simulations

In order to demonstrate the effectiveness of the proposed control schemes, numerical simulations have been performed and presented in this subsection. The leader spacecraft is assumed to be following an elliptic orbit with $e = 0.6$. Both spacecrafts have mass $m = 1$ kg. The follower has initial values $p = [2, -5, 2]^T$, $\dot{p} = [0, 0, 0]$, and is further commanded to track sinusoidal trajectories around the leader, and the desired position is

$$p_d = \left[-10\cos\left(\frac{3\pi}{T_l}t\right),\ 10\sin\left(\frac{4\pi}{T_l}t\right),\ 5\cos\left(\frac{5\pi}{T_l}t\right) \right]^T$$

where T_l is the orbital period of the leader spacecraft. The disturbances that the follower spacecraft subject are set as $f_{df} = [0.02\sin(0.4t),\ 0.03\cos(0.5t),\ 0.04\ \mathrm{sim}(0.1t)]^T$.

The actuators faults are selected as:

$$\begin{cases} \tau_1(t) = 0.6 + 0.1\sin(0.5t) \\ \tau_2(t) = 0.7 + 0.2\sin(0.4t) \\ \tau_3(t) = 0.5 + 0.1cos(0.5t) \end{cases}$$

In (26.17) and (26.18), we set $k_1 = 0, 5$, $k_2 = 1$, $r = \frac{3}{5}$, $\tau = 0.01$. In the adaptive controller, we choose $\varepsilon_0 = 5$ and $\varepsilon_1 = 20$. The parameters q_i is according to (26.27) where $\delta_0 = 1$, $\delta_1 = 10$.

The relative position errors can be seen in Fig. 26.2, and the velocity errors are in Fig. 26.3, which shows that the trajectories of the leader–follower spacecraft formation (26.10) tend to a neighborhood of the origin in 10 s under the control law of (26.18–26.22) when considered unknown actuator faults and external disturbances. Figure 26.4 shows the simulation results of sliding surface. It is obvious that the sliding mode (26.17) is stable and the trajectories of the system also tend to a neighborhood of the origin in spite of unknown actuator faults and external

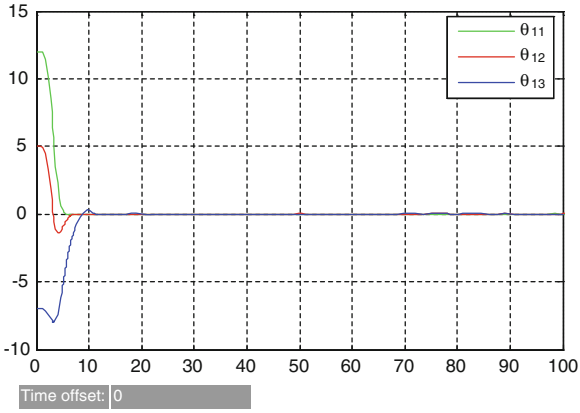

Fig. 26.2 Position error

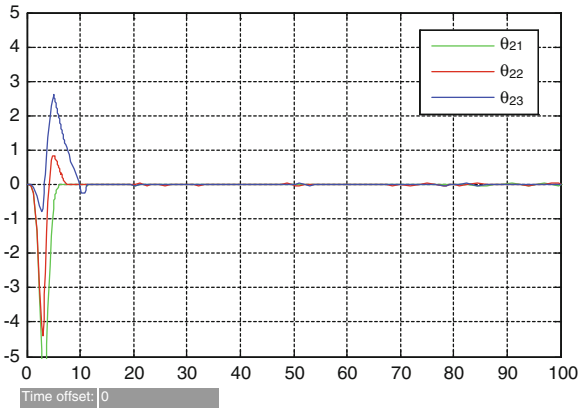

Fig. 26.3 Velocity error

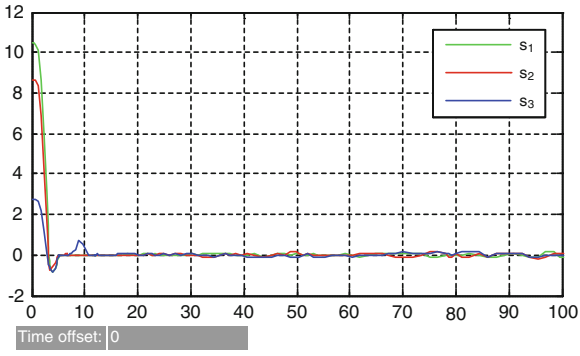

Fig. 26.4 Sliding surface

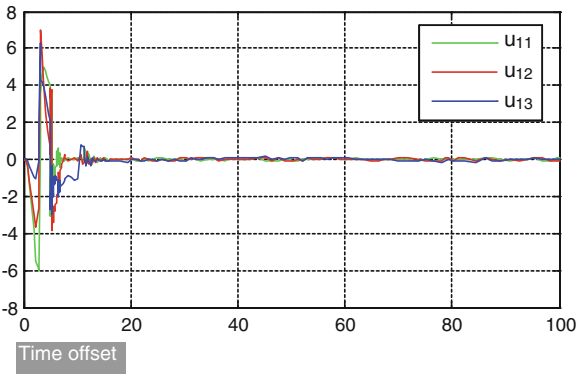

Fig. 26.5 Control input

disturbances. The input control signals are depicted in Fig. 26.5. In the first 10 s the undesired chattering emerged, for the adaptive algorithm (26.20–26.22) is adopted here to estimate and compensate the unknown actuator faults and external disturbances in the control input. Above all, the simulation results verify that the desired requirements of the closed-loop system have been achieved.

26.5 Conclusion

An adaptive terminal sliding mode control scheme was developed for the relative translation tracking in a leader–follower spacecraft formation system, in which the external disturbances and partial loss of actuator effectiveness faults are considered. The controller use adaptive laws to estimate the minimum value of actuator faults and the bounds of external disturbances. The resulting closed-loop system is proved in theory to be PFS. The control designs are evaluated using numerical simulation, in which an illustratively example has shown the effectiveness of the proposed control design methods. Hence, faults tolerance, robustness against the actuator faults, and high accuracy of system stabilization can be achieved.

References

1. Kapila V, Sparks AG, Buffington JM et al (2000) Spacecraft formation flying: dynamics and control. J Guidance Control Dyn 23(3):561–564
2. De Queiroz MS, Kapila V, Yan Q (2000) Adaptive nonlinear control of multiple spacecraft formation flying. J Guidance Control Dyn 23(3):385–390
3. Kristiansen R, Loría A, Chaillet A et al (2006) Adaptive output feedback control of spacecraft relative translation[C]. In: 2006 45th IEEE conference on decision and control, IEEE, pp 6010–6015
4. Liu X, Kumar KD (2011) Input-to-state stability of model-based spacecraft formation control systems with communication constraints. Acta Astronaut 68(11):1847–1859

5. Zhao L, Yan X, Hao Y et al (2011) Fault tolerant control for spacecraft based on adaptive fast terminal sliding mode[C]. In: 2011 international conference on mechatronic science, electric engineering and computer (MEC), IEEE, pp 2151–2155
6. Wong H, Kapila V, Sparks AG (2002) Adaptive output feedback tracking control of spacecraft formation. Int J Robust Nonlinear Control 12(2–3):117–139
7. Wu Y, Yu X, Man Z (1998) Terminal sliding mode control design for uncertain dynamic systems. Syst Control Lett 34(5):281–287
8. Feng Y, Yu X, Man Z (2002) Non-singular terminal sliding mode control of rigid manipulators. Automatica 38(12):2159–2167
9. Yu S, Yu X, Shirinzadeh B et al (2005) Continuous finite-time control for robotic manipulators with terminal sliding mode. Automatica 41(11):1957–1964
10. Hui L, Li J (2009) Terminal sliding mode control for spacecraft formation flying. IEEE Trans Aerosp Electron Syst 45(3):835–846
11. Jin J, Ko S, Ryoo CK (2008) Fault tolerant control for satellites with four reaction wheels. Control Eng Pract 16(10):1250–1258
12. Cai W, Liao X, Song DY (2008) Indirect robust adaptive fault-tolerant control for attitude tracking of spacecraft. J Guidance Control Dyn 31(5):1456–1463
13. Jiang Y, Hu Q, Ma G (2010) Adaptive backstepping fault-tolerant control for flexible spacecraft with unknown bounded disturbances and actuator failures. ISA Trans 49(1):57–69
14. Hu Q, Xiao B, Zhang Y (2011) Fault-tolerant attitude control for spacecraft under loss of actuator effectiveness. J Guidance Control Dyn 34(3):927–932
15. Yoo DS, Chung MJ (1992) A variable structure control with simple adaptation laws for upper bounds on the norm of the uncertainties. IEEE Trans Autom Control 37(6):860–865
16. Zhu Z, Xia Y, Fu M (2011) Attitude stabilization of rigid spacecraft with finite-time convergence. Int J Robust Nonlinear Control 21(6):686–702
17. Cao L, Chen XQ, Sheng T (2013) Fault tolerant small satellite attitude control using adaptive non-singular terminal sliding mode. Adv Space Res 51(12):2374–2393

Chapter 27
Position Control of Induction Motors via Adaptive Fuzzy Backstepping with Input Saturation

Wei Li, Yumei Ma, Jinfei Yu, Jinpeng Yu and Jiapeng Liu

Abstract This paper focuses on the problem of position tracking control for field-oriented induction motors with input saturation. In the scheme, an adaptive fuzzy control based on backstepping technique is designed. Fuzzy logic systems are used to approximate the unknown nonlinearities and the adaptive backstepping control is employed to construct controllers. The proposed adaptive fuzzy controllers guarantee the tracking error converge to a small neighborhood of the origin. Compared with the conventional backstepping, the designed fuzzy controllers' structure is very simple. The simulation results show that the new controller overcomes the influences of the parameter uncertainties and guarantee a tracking performance.

Keywords Induction motor · Fuzzy approximation · Adaptive control · Backstepping · Input saturation

27.1 Introduction

Induction motors are widely used in many industrial control fields because of their low cost, simple structure, high reliability, and ruggedness. However, induction motor's dynamic model is multivariable, strong coupling, and highly nonlinear in the control community [1]. In addition, the control of induction motor system preceded by saturation nonlinearities has been an active topic since the saturation nonlinearities are common in many practical systems.

W. Li · Y. Ma · J. Yu (✉) · J. Liu
College of Automation Engineering, Qingdao University, No. 308, Ningxia Road, Qingdao 266071, People's Rebublic of China
e-mail: yjp1109@126.com

J. Yu
Zibo Technician College, Zibo 255013, China

Z. Deng and H. Li (eds.), *Proceedings of the 2015 Chinese Intelligent Automation Conference*, Lecture Notes in Electrical Engineering 337,
DOI 10.1007/978-3-662-46463-2_27

Backstepping-based adaptive control [2] and fuzzy-approximation-based nonlinear control have become the popular approaches to handle nonlinear systems with the linear parametric uncertainties. Using the adaptive backstepping and fuzzy logic control, the problem of induction motor with input saturation can be solved more easily.

In this paper, during the controller design process, fuzzy logic systems [5] are employed to approximate the nonlinearities. And the adaptive technique and backstepping are used to construct fuzzy controllers. The simulation results show that the adaptive fuzzy control with input saturation guarantees a performance tracking performance even under the unknown parameters and load disturbances.

27.2 Mathematical Model of the IM Drive System

The Induction motor's dynamic mathematical model can be described in the well-known $(d-q)$ frame as follows [4]:

$$\begin{cases} \dfrac{\mathrm{d}\Theta}{\mathrm{d}t} = \omega, \dfrac{\mathrm{d}\omega}{\mathrm{d}t} = \dfrac{n_p L_m}{L_r J}\phi_d i_q - \dfrac{T_L}{J}, \dfrac{\mathrm{d}\phi_d}{\mathrm{d}t} = -\dfrac{R_r}{L_r}\phi_d + \dfrac{L_m R_r}{L_r} i_d \\ \dfrac{\mathrm{d}i_q}{\mathrm{d}t} = -\dfrac{L_m^2 R_r + L_r^2 R_s}{\sigma L_s L_r^2} i_q - \dfrac{n_p L_m}{\sigma L_s L_r}\omega\phi_d - n_p \omega i_d - \dfrac{L_m R_r}{L_r}\dfrac{i_q i_d}{\phi_d} + \dfrac{1}{\sigma L_s} u_q \\ \dfrac{\mathrm{d}i_d}{\mathrm{d}t} = -\dfrac{L_m^2 R_r + L_r^2 R_s}{\sigma L_s L_r^2} i_d + \dfrac{L_m R_r}{\sigma L_s L_r^2}\phi_d + n_p \omega i_q + \dfrac{L_m R_r}{L_r}\dfrac{i_q^2}{\phi_d} + \dfrac{1}{\sigma L_s} u_d \end{cases} \tag{27.1}$$

where: $\sigma = 1 - L_m^2 / L_s L_r$. Θ, ω, L_m, n_p, J, T_L, and ϕ_d denote the rotor position, rotor angular velocity, mutual inductance, pole pairs, inertia, load torque and rotor flux linkage. i_d and i_q stand for the $(d-q)$ axis currents. u_d and u_q are the $(d-q)$ axis voltages. R_s and L_s mean the resistance, inductance of the stator. R_r and L_r denote the resistance, inductance of the rotor. And in order to express more simple, the following notations are defined as:

$$\begin{cases} x_1 = \Theta,\ x_2 = \omega,\ x_3 = i_q,\ x_4 = \phi_d,\ x_5 = i_d,\ c_1 = -\frac{R_r}{L_r},\ c_2 = \frac{L_m R_r}{\sigma L_s L_r^2} \\ a_1 = \frac{n_p L_m}{L_r},\ b_1 = -\frac{L_m^2 R_r + L_r^2 R_s}{\sigma L_s L_r^2},\ b_2 = -\frac{n_p L_m}{\sigma L_s L_r},\ b_3 = n_p,\ b_4 = \frac{L_m R_r}{L_r},\ b_5 = \frac{1}{\sigma L_s} \end{cases} \tag{27.2}$$

The dynamic model of IM driver can be described by the following equations:

$$\begin{cases} \dot{x}_1 = x_2,\ \dot{x}_2 = \frac{a_1}{J} x_3 x_4 - \frac{T_L}{J},\ \dot{x}_3 = b_1 x_3 + b_2 x_2 x_4 - b_3 x_2 x_5 - b_4 \frac{x_3 x_5}{x_4} + b_5 u_q \\ \dot{x}_4 = c_1 x_4 + b_4 x_5,\ \dot{x}_5 = b_1 x_5 + c_2 x_4 + b_3 x_2 x_3 + b_4 \frac{x_3^2}{x_4} + b_5 u_d \end{cases} \tag{27.3}$$

Lemma 27.1 [7] *Let $f(x)$ be a continuous function defined on a compact set Ω.*

Then for any scalar $\varepsilon > 0$, there exists a fuzzy logic system $W^T S(x)$ such that $\sup_{x \in \Omega} |f(x) - W^T S(x)| \leq \varepsilon$.

27.3 Adaptive Fuzzy Controller Design with Backstepping Control

Step 1: Define the tracking error variables as $z_1 = x_1 - x_{1d}$, $z_2 = x_2 - \alpha_1$, $z_3 = x_3 - \alpha_2$, $z_4 = x_4 - x_{4d}$, $z_5 = x_5 - \alpha_3$. Where x_{1d} is the reference position signal, x_{4d} is the reference flux signal. Choose Lyapunov function candidate as $V_1 = \frac{1}{2}z_1^2$, then the time derivative of V_1 is given $\dot{V}_1 = z_1\dot{z}_1 = z_1(x_2 - \dot{x}_{1d})$.

The virtual control α_1 is constructed as $\alpha_1 = -k_1 z_1 + \dot{x}_{1d}$. Substituting α_1 into $\dot{V}_1$, we can obtain

$$\dot{V}_1 = -k_1 z_1^2 + z_1 z_2 \tag{27.4}$$

Step 2: Choose the Lyapunov function candidate as $V_2 = V_1 + \frac{J}{2}z_2^2$. Then the time derivative of V_2 is computed by $\dot{V}_2 = -k_1 z_1^2 + z_2(z_1 + a_1 x_3 x_4 - T_L - J\dot{\alpha}_1)$.

We assume T_L is unknown and there exists $0 \le T_L \le d$. Obviously, $z_2 T_L \le \frac{1}{2\varepsilon_2^2}z_2^2 + \frac{1}{2}\varepsilon_2^2 d^2$, $\varepsilon_2 > 0$. The derivative of V_2 can be rewritten as

$$\dot{V}_2 \le -k_1 z_1^2 + \frac{1}{2}\varepsilon_2^2 d^2 + z_2(z_1 + a_1 x_3 x_4 + \frac{1}{2\varepsilon_2^2}z_2 - J\dot{\alpha}_1) \tag{27.5}$$

Construct the virtual control α_2 as $\alpha_2 = \frac{1}{a_1 x_4}(-k_2 z_2 - z_1 + \hat{J}\dot{\alpha}_1)$.

Therefore, (27.5) can be rewritten as

$$\dot{V}_2 \le -k_1 z_1^2 - k_2 z_2^2 + \frac{1}{2}\varepsilon_2^2 d^2 + a_1 z_2 z_3 x_4 + (\hat{J} - J)\dot{\alpha}_1 z_2 \tag{27.6}$$

Step 3: Choose the Lyapunov function candidate as $V_3 = V_2 + \frac{1}{2}z_3^2$, then the time derivative of V_3 is computed by

$$\dot{V}_3 \le -k_1 z_1^2 - k_2 z_2^2 + \frac{1}{2}\varepsilon_2^2 d^2 + (\hat{J} - J)\dot{\alpha}_1 z_2 + z_3(f_3 + b_5 u_q) \tag{27.7}$$

To make the classical adaptive backstepping simply, we design a fuzzy logic system as $f_3(Z) = a_1 z_2 x_4 + b_1 x_3 + b_2 x_2 x_4 - b_3 x_2 x_5 - b_4 \frac{x_3 x_5}{x_4} - \dot{\alpha}_2 = W_3^T S_3(Z) + \delta_3(Z)$, where $Z = [x_1, x_2, x_3, x_4, x_5, x_{1d}, x_{4d}, \dot{x}_{1d}]^T$.

Consequently, a straightforward calculation produces the following inequality:

$$z_3 f_3(Z) \le \frac{1}{2l_3^2}z_3^2 ||W_3||^2 S_3^T S_3 + \frac{1}{2}l_3^2 + \frac{1}{2}z_3^2 + \frac{1}{2}\varepsilon_3^2 \tag{27.8}$$

u_q denotes the plant input subject to nonsymmetric input saturation nonlinearity described by $u_q = \mathrm{sat}(v_q) = \begin{cases} u_{q\max}, & v_q \ge u_{q\max} \\ v_q, & u_{q\min} < v_q < u_{q\max} \\ u_{q\min}, & v_q \le u_{q\min} \end{cases}$, where $u_{q\max} > 0$ and $u_{q\min} < 0$ are unknown constants of input saturation and v_q is the input signal of the

saturation nonlinearity. Similar to the method proposed in [6], a piecewise smooth function is used to approximate the saturation function and defined as

$$g(v_q) = \begin{cases} u_{q\max} \times \tanh(v_q/u_{q\max}), v_q \geq 0 \\ u_{q\min} \times \tanh(v_q/u_{q\min}), v_q \leq 0 \end{cases} = \begin{cases} u_{q\max} \times \frac{e^{v_q/u_{q\max}} - e^{-v_q/u_{q\max}}}{e^{v_q/u_{q\max}} + e^{-v_q/u_{q\max}}}, v_q \geq 0 \\ u_{q\min} \times \frac{e^{v_q/u_{q\min}} - e^{-v_d/u_{q\min}}}{e^{v_q/u_{q\min}} + e^{-v_q/u_{q\min}}}, v_q \leq 0 \end{cases} \tag{27.9}$$

Then $\text{sat}(v_q)$ can be described as $u_q = \text{sat}(v_q) = g(v_q) + d(v_q)$, where $d(v_q)$ is a bounded function, and its bound can be defined as $|d(v_q)| = |\text{sat}(v_q) - g(v_q)| \leq D_q$.

In addition, the mean value theorem [7] implies that there exists a constant $\mu (0 < \mu < 1)$ such that: $g(v_q) = g(v_{q0}) + g_{v_{q\mu}}(v_q - v_{q0})$, where $g_{v_{q\mu}} = \frac{\partial g(v_q)}{\partial v_q}|_{v_q = v_{q\mu}}$ and $v_{q\mu} = \mu v_q + (1-\mu)v_{q0}$. By choosing $v_{q0} = 0$, (27.10) can be written as: $g(v_q) = g_{v_{q\mu}} v_q$. To facilitate the control system design, the following assumptions are presented and will be used in the subsequent developments:

Assumption 27.1 [8] For the function $g_{v_{q\mu}}$ in [3], there exists an unknown positive constant g_m, such that $0 < g_m \leq g_{v_{q\mu}} \leq 1$.

Construct the control law $v_q = -k_3 z_3 - \frac{1}{2} z_3 - \frac{1}{2l_3^2} z_3 \hat{\theta}_1 S_3^T S_3$. Furthermore, substituting v_q into $g(v_q)$, we can obtain

$$\begin{aligned} \dot{V}_3 \leq & -\sum_{i=1}^{2} k_i z_i^2 + (\hat{J} - J)\dot{\alpha}_1 z_2 + \frac{1}{2l_3^2} z_3^2 ||W_3||^2 S_3^T S_3 \\ & + \frac{1}{2}\varepsilon_2^2 d^2 + \frac{1}{2} l_3^2 + \frac{1}{2} z_3^2 + \frac{1}{2}\varepsilon_3^2 + b_5 z_3 \big(g(v_q) + d(v_q)\big) \end{aligned} \tag{27.10}$$

Step 4: Choose Lyapunov function candidate as $V_4 = V_3 + \frac{1}{2} z_4^2$. Then the time derivative of V_4 is computed by $\dot{V}_4 = \dot{V}_3 + z_4 \dot{z}_4 = \dot{V}_3 + z_4(c_1 x_4 + b_4 x_5 - \dot{x}_{4d})$.

Construct the virtual control $\alpha_3 = \frac{1}{b_4}(-k_4 z_4 - c_1 x_4 + \dot{x}_{4d})$. Equation (27.11) shows that

$$\begin{aligned} \dot{V}_4 \leq & -k_1 z_1^2 - k_2 z_2^2 - k_4 z_4^2 + (\hat{J} - J)\dot{\alpha}_1 z_2 + \frac{1}{2} l_3^2 + \frac{1}{2l_3^2} z_3^2 ||W_3||^2 S_3^T S_3 \\ & + \frac{1}{2}\varepsilon_2^2 d^2 + \frac{1}{2} z_3^2 + \frac{1}{2}\varepsilon_3^2 + b_5 z_3 \big(g(v_q) + d(v_q)\big) + b_4 z_4 z_5 \end{aligned} \tag{27.11}$$

Step 5: Choose the Lyapunov function candidate as $V_5 = V_4 + \frac{1}{2} z_5^2$. Then the derivative of V_5 is given by

$$\begin{aligned} \dot{V}_5 \leq & -k_1 z_1^2 - k_2 z_2^2 - k_4 z_4^2 + (\hat{J} - J)\dot{\alpha}_1 z_2 + \frac{1}{2l_3^2} z_3^2 ||W_3||^2 S_3^T S_3 + \frac{1}{2}\varepsilon_2^2 d^2 + \frac{1}{2} l_3^2 \\ & + \frac{1}{2} z_3^2 + \frac{1}{2}\varepsilon_3^2 + b_5 z_3 \big(g(v_q) + d(v_q)\big) + z_5(f_5 + b_5 u_d) \end{aligned} \tag{27.12}$$

where $f_5(Z) = b_4 z_4 + b_1 x_5 + c_2 x_4 + b_3 x_2 x_3 + b_4 \frac{x_3^2}{x_4} - \dot{\alpha}_3 = W_5^T S_5(Z) + \delta_5(Z)$. Similarly,

$$z_5 f_5(Z) = z_5(W_5^T S_5 + \delta_5) \le \frac{1}{2l_5^2} z_5^2 ||W_5||^2 S_5^T S_5 + \frac{1}{2} l_5^2 + \frac{1}{2} z_5^2 + \frac{1}{2} \varepsilon_5^2 \tag{27.13}$$

u_d denotes the plant input subject to nonsymmetric saturation nonlinearity described by $u_d = \text{sat}(v_d) = \begin{cases} u_{d\max}, & v_d \ge u_{d\max} \\ v_d, & u_{d\min} < v_d < u_{d\max} \\ u_{d\min}, & v_d \le u_{d\min} \end{cases}$, where $u_{d\max}$ and $u_{d\min}$ are unknown positive constants of input saturation and v_d is the input signal of the saturation nonlinearity. Similar to Step 3, we define $g(v_d)$ as

$$g(v_d) = \begin{cases} u_{d\max} \times \tanh(v_d/u_{d\max}), v_d \ge 0 \\ u_{d\min} \times \tanh(v_d/u_{d\min}), v_d \le 0 \end{cases} = \begin{cases} u_{d\max} \times \frac{e^{v_d/u_{d\max}} - e^{-v_d/u_{d\max}}}{e^{v_d/u_{d\max}} + e^{-v_d/u_{d\max}}}, v_d \ge 0 \\ u_{d\min} \times \frac{e^{v_d/u_{d\min}} - e^{-v_d/u_{d\min}}}{e^{v_d/u_{d\min}} + e^{-v_d/u_{d\min}}}, v_d \le 0 \end{cases} \tag{27.14}$$

And $\text{sat}(v_d)$ can be expressed in the following form: $u_d = \text{sat}(v_d) = g(v_d) + d(v_d)$, where $d(v_d)$ is a bounded function, and its bounded can be defined as $|d(v_d)| \le D_d$.

Similar to Step 3, we can also obtain $g(v_d) = g_{v_{d\mu}} v_d$. And construct the control law $v_d = -k_5 z_5 - \frac{1}{2} z_5 - \frac{1}{2l_5^2} z_5 \hat{\theta}_2 S_5^T S_5$. Substituting v_d into (27.12), we can obtain

$$\begin{aligned} \dot{V}_5 \le & -k_1 z_1^2 - k_2 z_2^2 - k_4 z_4^2 + (\hat{J} - J)\dot{\alpha}_1 z_2 + \frac{1}{2l_3^2} z_3^2 ||W_3||^2 S_3^T S_3 + \frac{1}{2}\varepsilon_2^2 d^2 + \frac{1}{2} l_3^2 + \frac{1}{2} z_3^2 + \frac{1}{2}\varepsilon_3^2 \\ & + b_5 z_3 \big(g(v_q) + d(v_q)\big) + \frac{1}{2l_5^2} z_5^2 ||W_5||^2 S_5^T S_5 + \frac{1}{2} l_5^2 + \frac{1}{2} z_5^2 + \frac{1}{2}\varepsilon_5^2 + b_5 z_5 (g(v_d) + d(v_d)) \end{aligned} \tag{27.15}$$

Define $b_5\theta_1 = \max\{||W_3||^2/g_m, ||W_5||^2/g_m\}$, $b_5\theta_2 = \max\{||W_3||^2/g_m, ||W_5||^2/g_m\}$. Introduce variables $\tilde{J}$, $\tilde{\theta}_1$ and $\tilde{\theta}_2$ as $\tilde{J} = \hat{J} - J$, $\tilde{\theta}_1 = \hat{\theta}_1 - \theta_1$, $\tilde{\theta}_2 = \hat{\theta}_2 - \theta_2$. Choose the Lyapunov function candidate as $V = V_5 + \frac{1}{2r_1}\tilde{J}^2 + \frac{g_m}{2r_2}\tilde{\theta}_1^2 + \frac{g_m}{2r_3}\tilde{\theta}_2^2$. By differentiating V, and taking (27.15) into account, we can obtain

$$\begin{aligned} \dot{V} \le & -k_1 z_1^2 - k_2 z_2^2 - (k_3 b_5 g_m - \frac{1}{2}) z_3^2 - k_4 z_4^2 - (k_5 b_5 g_m - \frac{1}{2}) z_5^2 + \frac{1}{2}\varepsilon_2^2 d^2 + \frac{1}{2} l_3^2 \\ & + \frac{1}{2}\varepsilon_3^2 + \frac{1}{2} l_5^2 + \frac{1}{2}\varepsilon_5^2 + \frac{b_5}{g_m 2} D_q^2 + \frac{b_5}{2g_m} D_d^2 + \frac{g_m}{r_2}\tilde{\theta}_1 (-\frac{b_5 r_2}{2l_3^2} z_3^2 S_3^T S_3 + \dot{\hat{\theta}}_1) \\ & + \frac{g_m}{r_3}\tilde{\theta}_2 (-\frac{b_5 r_3}{2l_5^2} z_5^2 S_5^T S_5 + \dot{\hat{\theta}}_2) + \frac{1}{r_2}\tilde{J}\dot{\hat{J}} + \frac{g_m}{r_2}\tilde{\theta}_1\dot{\hat{\theta}}_1 + \frac{g_m}{2r_3}\tilde{\theta}_2\dot{\hat{\theta}}_2 \end{aligned} \tag{27.16}$$

The corresponding adaptive laws are chosen as $\dot{\hat{J}} = -r_1\alpha_1 z_2 - m_1\hat{J}$, $\dot{\hat{\theta}}_1 = \frac{b_5 r_2}{2l_3^2} z_3^2 S_3^T S_3 - m_2\hat{\theta}_1$, $\dot{\hat{\theta}}_2 = \frac{b_5 r_3}{2l_5^2} z_5^2 S_5^T S_5 - m_3\hat{\theta}_2$, where $r_i (i = 1, 2, 3)$, $m_i (i = 1, 2, 3)$ and $l_i (i = 3, 5)$ are positive constants.

27.4 Stability Analysis

For the term $-\tilde{J}\hat{J}$ one has $-\tilde{J}\hat{J} \leq -\frac{1}{2}\tilde{J}^2 + \frac{1}{2}J^2$. Similarly, $-\tilde{\theta}_1\hat{\theta}_1 \leq -\frac{1}{2}\tilde{\theta}_1^2 + \frac{1}{2}\theta_1^2$, $-\tilde{\theta}_2\hat{\theta}_2 \leq -\frac{1}{2}\tilde{\theta}_2^2 + \frac{1}{2}\theta_2^2$. Consequently, by using these inequalities, (27.16) can be rewritten in the following form:

$$\begin{aligned}\dot{V} \leq & -k_1 z_1^2 - k_2 z_2^2 - (k_3 b_5 g_m - \frac{1}{2}) z_3^2 - k_4 z_4^2 - (k_5 b_5 g_m - \frac{1}{2}) z_5^2 - \frac{m_1}{2r_1}\tilde{J}^2 \\ & - \frac{m_2 g_m}{2r_2}\tilde{\theta}_1^2 - \frac{m_3 g_m}{2r}\tilde{\theta}_2^2 + \frac{1}{2}\varepsilon_2^2 d^2 + \frac{1}{2}l_3^2 + \frac{1}{2}\varepsilon_3^2 + \frac{1}{2}l_5^2 + \frac{1}{2}\varepsilon_5^2 + \frac{b_5}{2g_m}D_q^2 \\ & + \frac{b_5}{2g_m}D_d^2 + \frac{m_1}{2r_1}J^2 + \frac{m_2}{2r_2}\theta_1^2 + \frac{m_3}{2r_3}\theta_2^2 \leq -a_0 V + b_0 \end{aligned} \tag{27.17}$$

where $a_0 = \min\{2k_1, \frac{2k_2}{J}, 2(k_3 b_5 g_m - \frac{1}{2}), 2k_4, 2(k_5 b_5 g_m - \frac{1}{2}), m_1, m_2, m_3\}$, and $b_0 = \frac{1}{2}\varepsilon_2^2 d^2 + \frac{1}{2}l_3^2 + \frac{1}{2}\varepsilon_3^2 + + \frac{1}{2}l_5^2 + \frac{1}{2}\varepsilon_5^2 + \frac{g_m}{2g_m}D_q^2 + \frac{g_m}{2g_m}D_d^2 + \frac{m_1}{2r_1}J^2 + \frac{m_2}{2r_2}\theta_1^2 + \frac{m_3}{2r_3}\theta_2^2$.

$$V(t) \leq (V(t_0) - \frac{b_0}{a_0}e^{-a_0(t-t_0)}) + \frac{b_0}{a_0} \leq V(t_0) + \frac{b_0}{a_0}, \forall t \geq t_0 \tag{27.18}$$

As a result, all $z_i (i = 1, 2, 3, 4, 5)$, $\tilde{J}$, $\tilde{\theta}_1$ and $\tilde{\theta}_2$ belong to the compact set $\Omega = \left\{(z_i, \tilde{J}, \tilde{\theta}_1, \tilde{\theta}_2) | V \leq V(t_0) + b_0/a_0, \forall t \geq t_0\right\}$. Namely, all the signals in the closed-loop system are bounded. Especially, from (27.18), we have $\lim_{t\to\infty} z_1^2 \leq \frac{2b_0}{a_0}$. By taking r_i sufficiently large and l_i and ε_i small enough after giving the parameters k_i and m_i, we can choose a suitable a_0 and b_0, then we can get a small tracking error.

27.5 Simulation Results

To illustrate the effectiveness of the proposed results, the simulation is run for induction motors with the parameters: $J = 0.0586\,\text{Kg m}^2$, $R_s = 0.1\,\Omega$, $R_r = 0.15\,\Omega$, $L_s = L_r = 0.0699\,\text{H}$, $L_m = 0.068\,\text{H}$, $n_p = 1$. Then, the control parameters are chosen as $k_1 = 40$, $k_2 = 64$, $k_3 = k_4 = k_5 = 80$, $r_1 = r_2 = r_3 = 2$, $m_1 = m_2 = 0.05$, $l_3 = l_5 = 2$.

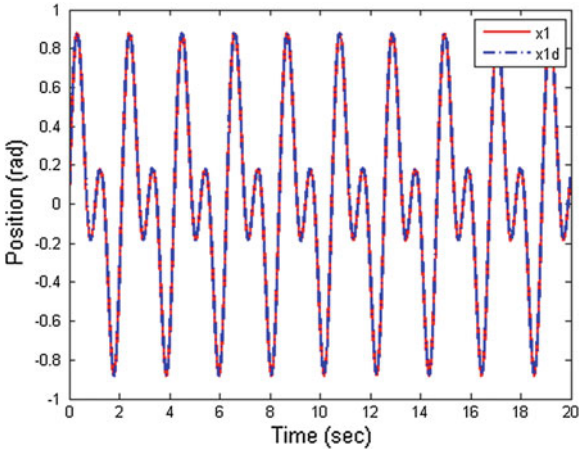

Fig. 27.1 Trajectories of x_1 and x_{1d}

The fuzzy membership functions are $\mu_{F_i^l} = \exp\left[-(x+l)^2/2\right]$, $l \in N$, $l \in [-5, 5]$. The simulation is carried out under the zero initial condition for the induction motor. Give the reference signal $x_{1d} = 0.5\sin(8t) + 0.5\sin(4t)$, and take T_L as $T_L = 1.5\,\mathrm{N\,m}$, $0 \le t \le 5$ or $T_L = 3\,\mathrm{N\,m}$, $\mathrm{t} > 5$. Figure 27.1 shows the tracking performance of x_1 and x_{1d}. Figures 27.2 and 27.3 show the final controllers v_d and v_q. From these figures, it is seen clearly that the tracking performance can be achieved very well.

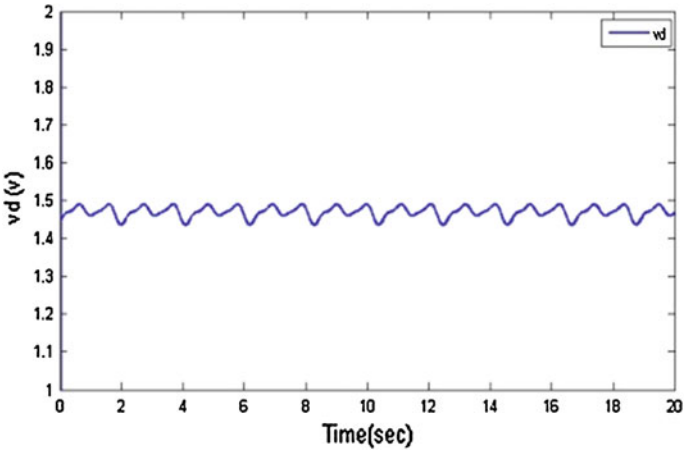

Fig. 27.2 Trajectory of v_d

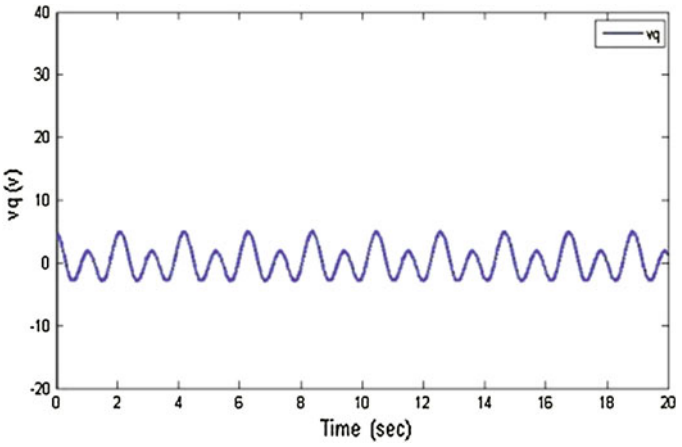

Fig. 27.3 Trajectory of v_q

27.6 Conclusions

An adaptive fuzzy controllers based on backstepping are designed to control induction motors with input saturation. This controllers overcome the problem of classical vector control which could not realize accurate control. The simulation results show that new controllers eliminate the influences of the parameter uncertainties and load disturbances. The position tracking control can be ideally accomplished.

Acknowledgments This work is supported by the Natural Science Foundation of China (61104076, 61174131, 61174033, 61473160), the China Postdoctoral Science Foundation (2014T70620, 2013M541881, 201303062) and Qingdao Postdoctoral Application Research Project.

References

1. Chen M, Ge SS, How B (2010) Robust adaptive neural network control for a class of uncertain MIMO nonlinear systems with input nonlinearities. IEEE Trans Neural Networks 21(5): 796–812
2. Yu JP, Chen B, Yu HS (2010) Position tracking control of induction motors via adaptive fuzzy backstepping. Energy Convers Manage 51(11):2345–2352
3. Pan ZG, Basar T (1999) Backstepping controller design for nonlinear stochastic systems under a risk-sensitive cost criterion. SIAM J Control Optim 37(3):957–995
4. Ta CM, Hori Y (2001) Convergence improvement of efficiency optimization control of induction motor drives. IEEE Trans Ind Appl 37(6):1746–1753
5. Tong SC, Li HH (2002) Direct adaptive fuzzy output tracking control of nonlinear systems. Fuzzy Sets Syst 128:107–115

6. Wang HQ, Chen B, Liu XP, Liu KF, Lin C (2013) Robust adaptive fuzzy tracking control for pure-feedback stochastic nonlinear systems with input constraints. IEEE Trans Cybern 43 (6):2093–2104
7. Wang LX, Mendel JM (1992) Fuzzy basis functions, universal approximation, and orthogonal least squares learning. IEEE Trans Neural Networks 3(5):807–814
8. Wen CY, Zhou J, Liu ZT, Su HY (2011) Robust adaptive control of uncertain nonlinear systems in the presence of input saturation and external disturbance. IEEE Trans Autom Control 56(7):1672–1678

Chapter 28
A Fault Detection and Isolation Method Based on R-Fast ICA and K-Fisher for Roller Bearings on the Urban Rail Vehicles

Linlin Kou, Yong Qin, Xiaoqin Cheng and Zhenyu Zhang

Abstract Operating status of roller bearings directly affects the safety of the urban rail vehicle, so accurate identification of the state has considerably practical significance. The fault detection and isolation method of the roller bearing operational was performed by the comprehensive utilization of fast independent component analysis (Fast ICA), and kernel fisher discriminant. Fast ICA method was used to denoise and extract signal with fault frequency. The fault characteristic signal separation used Fast ICA with the normal signal applied as a signal source. The Pearson product-moment correlation coefficient had been used to determine which component was the extracted one we needed. Then eight indicators were extracted as roller bearings' state features after Fast ICA. Based on the features under different states, the states of roller bearings on the urban rail vehicles were identified by the K-Fisher Discriminant. The experiment results indicated that the accuracies of the multiple states identification was more than 96 %, and verified the superiority of the proposed method.

Keywords Roller bearings · State identification · R-Fast ICA · K-fisher

28.1 Introduction

As the key component of urban rail vehicles' running gear [1], the roller bearings have been increasingly significant for satisfying the rail vehicles stable and reliable operation. According to statistics, only between 10 and 20 % of rolling bearings can work up to the normal design life [2]. Therefore, it is quite meaningful to exactly

L. Kou · Y. Qin (✉) · X. Cheng · Z. Zhang
State Key Laboratory of Rail Traffic Control and Safety, Beijing Jiaotong University, Beijing 100044, China
e-mail: koull01@163.com

Z. Deng and H. Li (eds.), *Proceedings of the 2015 Chinese Intelligent Automation Conference*, Lecture Notes in Electrical Engineering 337,
DOI 10.1007/978-3-662-46463-2_28

stabling and efficiently identifying the running state of rolling bearings. In this paper, a state identification method of the roller bearing operational was performed by the comprehensive utilization of R-Fast ICA and K-Fisher Discriminant. We presented an experiment and its results verified the superiority of the proposed method.

28.2 Basic Theroy

28.2.1 The Fast ICA Algorithm Using Negentropy

Fast ICA is an efficient and popular algorithm for independent component analysis, invented by Aapo Hyvärinen at Helsinki University of Technology [3]. The algorithm is based on a fixed-point iteration scheme maximizing non-Gaussianity as a measure of statistical independence, which is found faster than conventional gradient descent methods for ICA [4, 5].

A measure which is zero for a Gaussian variable and always nonnegative can be simply obtained from differential entropy, and is called negentropy. Negentropy J is defined by $J(y) = H(y_{\text{Gauss}}) - H(y)$. Entropy is the basic concept of information theory. The entropy of a random variable is related to the information that the observation of the variable gives. The differential entropy H of a random vector $y(t) = [y_1(t), y_2(t) \ldots, y_n(t)]^{\text{T}}$, with density $p(y)$ is defined by $H(y) = -\int p(y) \lg p(y) dy$. The advantage of using negentropy is that it is well justified by statistical theory. In fact, negentropy is in some sense the optimal estimator of non-Gaussianity. The problem is computationally difficult. In the case where we use only one nonlinear and nonquadratic function G, the approximation becomes $J(y) = \{E[G(y)] - E[G(y_{\text{Gauss}})]\}^2$ where y_{Gauss} is a Gaussian random vector of the same covariance matrix as y. The Fast ICA algorithm using negentropy combines the superior algorithmic properties resulting from the fixed-point iteration with the preferable statistical properties due to negentropy.

The Fast ICA algorithm can be described as follows.

(1) Center the data to make its mean zero, and whiten the data to provide z, which covariance matrix equals to the identity matrix: $E[zz^{\text{T}}] = I$.
(2) Choose N, the number of ICs. Set counter $p \leftarrow 1$.
(3) Choose an initial (e.g., random) vector w possessing a unit norm.
(4) Let $w_p \leftarrow E[zG'(w_p^{\text{T}} z)] - E[G''(w_p^{\text{T}} z)]w_p$.
(5) Do the following orthogonalization: $w_p \leftarrow w_p - \sum_{j=1}^{p-1} (w_p, w_j) w_j$.
(6) Normalize $w_p \leftarrow w_p / \|w_p\|$.
(7) If it is not converged, go back to Step(4).
(8) Let $p \leftarrow p + 1$. If p is not greater than the desired number of ICs N, go back to Step(3).
(9) Based on w, the independent signal is obtained by $y_i(t) = w_i^T z$.

28.2.2 Kernel Fisher Discriminant

Kernel Fisher's discriminant analysis (KFDA) [6] has been proposed for nonlinear binary classification. It is a hybrid method of the classical Fisher's linear discriminant analysis and a kernel machine.

Let $X_1 = \{x_1^1, \ldots, x_{l_1}^1\}$ and $X_2 = \{x_1^2, \ldots, x_{l_2}^2\}$ be samples from two different classes, with some abuse of notation $X = X_1 \cup X_2 = \{x_1, \ldots, x_l\}$. Fisher's linear discriminant is given by the vector ω which maximizes $J(\omega) = \frac{\omega^T S_B \omega}{\omega^T S_w \omega}$, where $S_B := (m_1 - m_2)(m_1 - m_2)^T$, $S_w := \sum_{i=1,2} \sum_{x \in X_i} (x - m_i)(x - m_i)^T$ are the between and within class scatter matrices, respectively, and m_i is defined by. The intuition behind maximizing $J(\omega)$ is to find a direction which maximizes the projected class means (the numerator) while minimizing the classes variance in this direction (the denominator). But there is also a well-known statistical way to motivate $J(\omega)$. Let Φ be a nonlinear mapping to some feature space F. To find the linear discriminant in F we need to maximize $J(\omega) = \frac{\omega^{\mathrm{T}} S_B^{\Phi} \omega}{\omega^{\mathrm{T}} S_w^{\Phi} \omega}$, where now $\omega \in F$ and S_B^{Φ} and S_w^{Φ} are the corresponding matrices in F, i.e., $S_B^{\Phi} := (m_1^{\Phi} - m_2^{\Phi})(m_1^{\Phi} - m_2^{\Phi})^{\mathrm{T}}$, $S_w^{\Phi} := \sum_{i=1,2} \sum_{x \in X_i} (\Phi(x) - m_i^{\Phi})(\Phi(x) - m_i^{\Phi})^{\mathrm{T}}$, with $m_i^{\Phi} := \frac{1}{l_i} \sum_{j=1}^{l_i} \Phi(x_j^i)$.

28.2.3 Features Extraction

Eight-time domain indexes had been used as the signal features, seen as below (Table 28.1).

28.3 Using R-Fast ICA Algorithm in Characteristic Signal Separation

28.3.1 R-Fast ICA Algorithm in Characteristic Signal Separation

Fast ICA method is commonly used in blind source separation, which requires multiple signals as the input matrix. But there is only one sensor to collect the real-time vibration acceleration signal. Bearing vibration can be caused by the structural characteristics of the bearing itself, the bearing assembly process and the bearing failure during operation [8]. Under normal operating condition, the collected vibration acceleration signal of bearing used on urban rail train, was caused by the first two factors. When the bearing fails, all the three factors made contribution to the bearing vibration, the signal caused by the third factor was added to the collected signal under

Table 28.1 Twelve time domain indexes

Serial	Name	Calculation formulas	Meaning
x_1	Root mean square (RMS)	$\sqrt{\frac{1}{N}\sum_{i=1}^{N}(x_i-\bar{x})^2}$	The vibration intensity and energy [7]
x_2	Peak	$\frac{1}{2}(\max(x_i)-\min(x_i))$	The maximum vibration
x_3	Crest factor	$Peak/RMS$	Signal strength [7]
x_4	Skewness	$\frac{1}{N}\sum_{i=1}^{N}(x_i-\bar{x})^3$	Asymmetric of signal's probability distribution
x_5	Skewness factor	$\left(\frac{1}{N}\sum_{i=1}^{N}(x_i-\bar{x})^3\right)/RMS^3$	Dimensionless factor related to skewness
x_6	Kurtosis	$\frac{1}{N}\sum_{i=1}^{N}(x_i-\bar{x})^4$	The distribution characteristics of signal
x_7	Kurtosis factor	$\left(\frac{1}{N}\sum_{i=1}^{N}(x_i-\bar{x})^4\right)/RMS^4$	Dimensionless factor related to kurtosis
x_8	Shape factor	$RMS/\left(\frac{1}{N}\sum_{i=1}^{N}\lvert x_i\rvert\right)$	A value that is affected by an object's shape

normal condition. So the signal collected under normal operating conditions of the bearing was treated as the reference signal source, the real-time monitoring signal with the same length of the reference signal is the other signal source.

Fast ICA algorithm method cannot determine which component of the extracted signal is corresponding to the original signal, so the output vector may appear upside down in the order. In order to solve this problem, the Pearson product-moment correlation coefficient had been used. Pearson product-moment correlation coefficient [9], a measure of the strength and direction of the linear relationship between two variables that is defined as the (sample) covariance of the variables divided by the product of their (sample) standard deviations.

$$\rho_{X,Y}=\frac{\operatorname{cov}(X,Y)}{\sigma_X\sigma_Y}=\frac{E((X-\mu_X)(Y-\mu_Y))}{\sigma_X\sigma_Y} \tag{28.1}$$

where E is the expectation, σ_X is the standard deviation of X, μ_X is the mean of X, cov is the covariance.

Steps of R-Fast ICA Algorithm in Characteristic signal separation are as follows:

(1) Select a reference signal source labeled as St. Intercept Signal to be processed as same length as the reference signal and symbolized as S. Input matrix of Fast ICA was [St; S].
(2) Do Fast ICA, obtained the separated two components, labeled as IC_1and IC_2.
(3) Calculate the Pearson product-moment correlation coefficient between IC_1, IC_2 and St.
(4) Select the component with low Pearson product-moment correlation coefficient.

28.3.2 Simulation and Verification

In order to verify the effectiveness of R-Fast ICA algorithm in the fault signal separation from the mixed signal, two sets of simulation experiment were designed.

1. Purpose: To verify the useful signals can be separated from the noise

To Simulate the real environment, noise contains white Gaussian noise, colored gaussian noise, and pink noise, and simulation experiment 2 is the same.

The original signal contains two frequency sinusoidal signals, as shown in the first picture of Fig. 28.1a.

$$\text{The Original signal} = \sin(20\pi \times t) + \sin(140\pi \times t)$$

We put white gaussian noise, colored gaussian noise, and pink noise into the original signal to obtain the mixed signal, which is shown in Fig. 28.1a second picture. Noise was completely covered the original signal.

$$\text{The Mixed signal} = \sin(20\pi \times t) + \sin(140\pi \times t) + \text{noise}$$

The reference signal was obviously the noise, shown in Fig. 28.1a third picture.

$$\text{Reference signal} = \text{noise}$$

2. Purpose: To verify certain frequency signals different from the reference signal can be separated from the noise

The original signal contains two frequency sinusoidal signals, as shown in the first picture of Fig. 28.1b.

$$\text{The Original signal} = \sin(140\pi \times t)$$

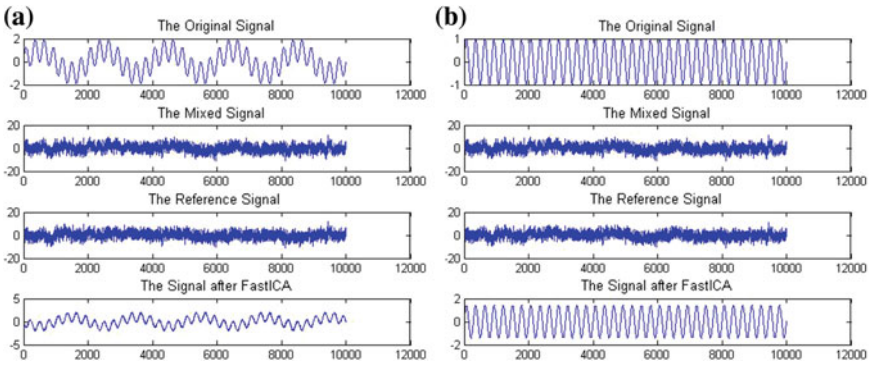

Fig. 28.1 The first and second simulation experiment results

the mixed signal is the same as experiment 1, which was shown in Fig. 28.1b second picture.

The reference signal was obviously the noise, shown in Fig. 28.1b third picture.

$$\text{Reference signal} = \sin(20\pi \times t) + \text{noise}$$

The result after R-Fast ICA can be seen in the last picture of Fig. 28.1a, b.

As we can see in Fig. 28.1a, the original signal can be separated from the noise, no matter how high the signal-to-noise ratio is, we can separate independent source signals from a mixed signal by using R-Fast ICA mentioned above, in the case of noise source is known. Figure 28.1b shows that, the single frequency's original signal has been separated from the noise and another frequency signal source successfully. We can come to a conclusion that R-Fast ICA mentioned in this paper can separate the specific frequency signal that we needed. Due to signals in failure cases being considered that fault characteristic frequency signal is superimposed on the normal signal, this method can be used to denoise and separate the fault frequency signal.

Figure 28.1 show that R-Fast ICA is effective in characteristic signal separation. Another thing worth noting is that, amplitude of no matter the mixed signal or the reference signal were higher than original, that is caused by the R-Fast ICA itself, but this phenomenon can be used as a way to enhance signals, which is meaningful for the next step, state identification.

28.4 A State Identification Method Based on R-Fast ICA and K-Fisher

Combining Sects. 28.2 and 28.3, the state identification method based on R-Fast ICA and K-Fisher can be implemented as the following steps for rolling bearings on the urban rail vehicles.

Step 1: Collect the vibration acceleration data of rolling bearings when the running state is normal or abnormal (including the faults of rolling elements, inner ring, and outer ring).

Step 2: According to appropriate time intervals, the data is divided into several parts which match with characteristic vectors. For example, if the total time and the time interval are, respectively, T_S and t_i, then the data can be divided into T_S/t_i parts.

Step 3: Choose a normal part of data as the reference signal. Every part of data (normal and abnormal parts) made a two-dimensional matrix with the reference signal as the input of Fast ICA, Do Fast ICA.

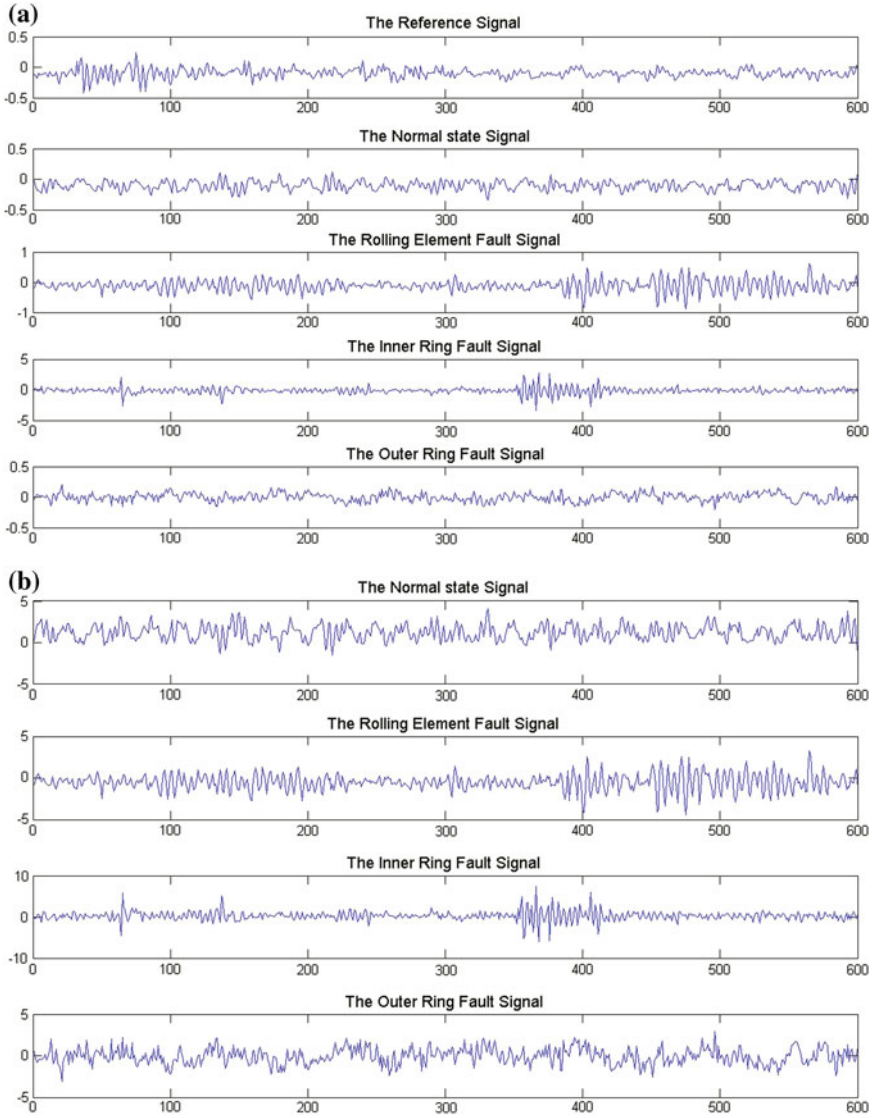

Fig. 28.2 One segment before and after R-Fast ICA

Step 4: Calculate the time domain feature values.
Step 5: Classify the fault state using the time domain feature values as the input of the K-Fisher algorithm.
Step 6: Analyze the classification performance.

28.5 Experiments and Results Analysis

28.5.1 Status Features Data Acquisition

The data was generated by the NSF I/UCR center for intelligent maintenance systems (IMS—www.imscenter.net) with a support from Rexnord Corp. in Milwaukee, WI. Four bearings were installed on a shaft. The rotation speed was kept constant at 2,000 RPM by an AC motor coupled to the shaft via rub belts. Senors sampling rate were set at 20 kHz. A radial load of 6,000 lbs is applied onto the shaft and bearing by a spring mechanism. All bearings are force lubricated [10].

The data in the normal and abnormal states were both divided into about 340 segments, each segment having about 600 data points, according to the rotation speed and sampling rate.

We presented a sample plot of one segment before and after Fast ICA, as seen in Fig. 28.2.

By Table 28.2, we presented part of features belongs to the four kinds of different states.

28.5.2 Identification Results Analysis

The data description and parameter options of clustering experiments are shown in Table 28.3. As mentioned earlier, the dimension of data samples is 12, and number of classes is 4, and samples numbers of each class are 339, 340, 340, and 340.

Table 28.2 Part of features belongs to the four kinds of different states

Features	x3	x5	x7	x8	Class
Train data	1.083369	0.628765	3.403065	0.628765	1
	0.715822	1.107851	3.605373	1.107851	2
	0.640965	1.463507	5.597999	1.463507	3
	0.704872	1.261612	3.482695	1.261612	4
	……				
Test data	1.069794	0.78097	3.576609	0.780970	1
	0.644665	1.256164	3.272290	1.256164	2
	0.776728	1.145849	3.197992	1.145849	3
	0.536010	1.235426	5.619299	1.235426	4
	……				

Table 28.3 Data description and parameter options

Feature data set	Time domain feature
Dimensions	8
Classes	4
Samples number in each class (N1/N2/N3/N4)	339/340/340/340
Train data in each class (N1/N2/N3/N4)	200/200/200/200
Test data in each class (N1/N2/N3/N4)	139/140/140/140
Classification result	132/136/135/137
Classification accuracy	96.6 %

28.6 Conclusion

In this paper, a state identification method of the roller bearing operational was performed by R-Fast ICA and K-Fisher Discriminant. The normal signal is applied as a reference signal, The characteristics signals under four conditions (normal bearing, ball fault, inner race fault, and outer race fault) were separated. twelve indicators extracted as roller bearings' state features were input into the K-Fisher Discriminant identified. The experiment results indicated that the accuracies of the multiple states identification was more than 96 %, and verified the superiority of the proposed method.

References

1. Choe HC, Wan Y, Chan AK (1997) Neural pattern identification of railroad wheel-bearing faults from audible acoustic signals: comparison of FFT, CWT, and DWT features. Proc SPIE Int Soc Opt Eng 3078:480–496
2. Qin TL, Yang Y, Cheng H (2008) Rolling bearing state identification based on intrinsic mode function energy moment and bp neural network. J Vibr Meas Diagn 28:229–232
3. Hyvarinen A, Oja EA (1999) Fast and robust fixed-point algorithms for independent component analysis. IEEE Trans Neural Networks 10(3):626–634
4. Hyvarinen A, Oja E (1997) A fast fixed-point algorithm for independent component analysis. Neural Comput 9(7):1483–1492
5. Lee TW, Girolami M, Sejnowski TJ (1999) Independent component analysis using an extended infomax algorithm for mixed subgaussian and supergaussian sources [J]. Neural Comput 11(2):417–441
6. Mikat S, fitscht G, Weston J, Scholkopft B (1999) Mullert K-R Fisher discriminant analysis with kernel. In: Hu Y-H, Larsen J, Wilson E, Douglas S (eds) Neural networks for signal processing, IX, IEEE pp 41–48
7. Nikias CL, Raghuveer MR (1987) Bispectrum estimation: a digital signal processing framework. Proc IEEE 75(5):869–891
8. Huang C, Fan x, Chen T (2006) Train's online fault diagnosis technology and its application. National defence industry press, Beijing, p 7
9. http://zh.wikipedia.org/wiki/%E7%9B%B8%E5%85%B3%E7%B3%BB%E6%95%B0
10. www.imscenter.net

Chapter 29
Finite-Time Synergetic Control of Mechanical System Based on Model-Free Friction Compensation

Shuangpo Zhai, Qiang Chen and Xiaoqing Tang

Abstract In this paper, a finite-time synergetic control scheme is proposed for a class of mechanical systems with friction compensation problem. Since the nonlinear parts in the friction model is difficult to be known in prior accurately, two neural networks are employed to approximate the static function and dynamic function of the friction model, respectively. Then, a finite-time synergetic controller is developed by combining synergetic control theory and nonsingular terminal sliding mode technique. The proposed control scheme can guarantee the finite-time convergence of tracking errors and avoid the singularity problem. Simulation results are provided to verify the effectiveness of the proposed scheme.

Keywords Finite-time control · Synergetic control · Friction compensation · Mechanical system

29.1 Introduction

In a mechanical control system, friction is one of the main factors which influence the system performance. Many dynamic friction models have been put forward, such as Karnopp model [1], Dahl model [2], Bliman-Sorine model [3], LuGre model [4, 5], generalized Maxwell-slip model (GMS), [6] and so on. In those friction models abovementioned, LuGre model is widely used to accurately describe the friction phenomenon in the machinery. However, since it is difficult to

This work was supported by the National Natural Science Foundation of China under Grant No. 61403343, the Scientific Research Foundation of the Education Department of Zhejiang Province under Grant No. Y201329260, and the Natural Science Foundation of Zhejiang University of Technology under Grant No.1301103053408.

S. Zhai · Q. Chen (✉) · X. Tang
Zhejiang University of Technology, Hangzhou 310023, Zhejiang, China
e-mail: sdnjchq@zjut.edu.cn

Z. Deng and H. Li (eds.), *Proceedings of the 2015 Chinese Intelligent Automation Conference*, Lecture Notes in Electrical Engineering 337,
DOI 10.1007/978-3-662-46463-2_29

know the nonlinear parts in the friction model accurately, some model-free compensation methods, such as, fuzzy logic [7], neural network [8, 9], and support vector networks [10], are developed to approximate the friction model.

Many control schemes have been proposed for designing tracking controllers of the mechanical system; for instance, adaptive control [11], sliding mode control (SMC) [12], nonsingular terminal sliding mode control (NTSMC) [13], synergetic control (SC) [14], and so on. SMC has been regarded as an effective robust control approach for handling the problem of system uncertainties and external disturbances. However, there are still some inherent drawbacks of SMC. For example, the high frequency switching control law will inevitably leads to chattering phenomena. Then, synergetic control theory (SCT) was first introduced by the Russian researcher Kolesnikov [15]. In [16], SC scheme was compared with SMC approach, and it pointed out that the synergetic control scheme operates at a constant switching frequency, which would cause less chattering problems.

In this paper, the static function and dynamic function of the friction model are approximated by employing two neural networks (NNs). Then, a finite-time synergetic tracking controller is designed based on NN approximations, and the finite-time convergence of tracking errors is guaranteed.

29.2 Problem Statement

The mechanical system under investigation is described as follows.

$$m\ddot{x} = -K_f x + u(t) - F \tag{29.1}$$

where $u(t)$ is the time-varying voltage, $x(t)$ is the position, K_f is the damping coefficient, m is the effective mass, and F is the friction force, which can be described by the following LuGre model

$$F = \sigma_0 z + \sigma_1 \dot{z} + \sigma_2 \dot{x}. \tag{29.2}$$

In the equation, σ_0 denotes the stiffness, σ_1 denotes the damping coefficient, and σ_2 denotes the viscous friction coefficient. Consider the contact surface effects which are lumped into an average asperity deflection z that is given by

$$\dot{z} = \dot{x} - \frac{|\dot{x}|}{h(\dot{x})} z \tag{29.3}$$

When $\dot{x}$ is constant, the deflection z approaches a steady- and bonded-state value z_s expressed as

$$z_s = h(\dot{x})\mathrm{sgn}(\dot{x}), \tag{29.4}$$

where the function $h(\dot{x})$ is

$$h(\dot{x}) = \frac{F_c + (F_s - F_c)e^{-(\dot{x}/\dot{x}_s)^2}}{\sigma_0}, \tag{29.5}$$

where F_s and F_s are both unknown constants. F_c is the Coulomb friction coefficient, and F_s is the Stribeck friction coefficient.

Defining a new error variable as

$$\varepsilon = z - z_s \tag{29.6}$$

the frictional force (29.2) can be rewritten as

$$F = \sigma_2 \dot{x} + F_1 \mathrm{sgn}(\dot{x}) + F_2 \tag{29.7}$$

where

$$F_1 \left[F_c + (F_s - F_c)e^{-(\dot{x}/\dot{x}_2)^2} \right] \tag{29.8}$$

which denotes a static function of the velocity, and F_2 is given by

$$F_2 = \sigma_0 \varepsilon \left[1 - \frac{\sigma_1}{F_c + (F_s - F_c)e^{-(\dot{x}/\dot{x}_2)^2}} |\dot{x}| \right] \tag{29.9}$$

which is a dynamic function scaled by the error ε, and satisfies

$$|F_2(\dot{x}, \varepsilon)| \leq \frac{\sigma_0 \sigma_1 \varepsilon_M}{F_c + (F_s - F_c)e^{-(\dot{x}/\dot{x}_s)^2}} |\dot{x}| + \Gamma, \tag{29.10}$$

where ε_M is the bounder of the error ε, i.e., $|\varepsilon| \leq \varepsilon_M$, and Γ is a constant. Hence, F is bounded satisfying $|F| \leq F_M$ with F_M being a positive constant.

Substituting (29.7–29.9) into (29.1) yields

$$m\ddot{x} = -\left(K_f + \sigma_2\right)\dot{x} + u(t) - \left[F_c + (F_s - F_c)e^{-(\dot{x}/\dot{x}_s)^2} \right] \mathrm{sgn}(x) - F_2(z, \dot{x}) \tag{29.11}$$

The control objective is to design a controller for a bounded smooth reference signal $x_d(t)$ with bounded time derivatives so that the controlled output $x(t)$ can track the reference $x_d(t)$ precisely.

29.3 Controller Design

29.3.1 Neural Network Approximation

Based on the approximation property of neural networks, the continuous function $H(x) : R^n \rightarrow R^p$ is represented as

$$H(x) = W\Phi(X) + \xi, \tag{29.12}$$

where $W \in R^{n\times p}$ is the ideal weight matrix and $\Phi(x) \in R^{n\times 1}$ is the radial basis function (RBF) of the NN, which can be chosen as the commonly used Gaussian function satisfying $0 < \Phi(X) < 1$, and ξ is the NN approximation error satisfying $\|\xi\| \leq \xi_M$.

Since F_1 and F_2 in (29.6) are unknown, in the paper, two NNs are used to approximate them, respectively, i.e.,

$$F_1 = W_1^T\Phi(\dot{x}) + \xi_{f1} \tag{29.13}$$

$$F_2 = W_2^T\Phi(\dot{x}) + \xi_{f2}, \tag{29.14}$$

where the approximation errors ξ_{f1} and ξ_{f2} satisfy the inequalities $|\xi_{f1}| \leq \xi_{M1}$ and $\xi_{f2} \leq \xi_{M2}$, respectively.

29.3.2 Finite-Time Synergetic Control

Define the tracking error and its time derivative as $e = x - x_d$ and $\dot{e} = \dot{x} - \dot{x}_d$, respectively.

Basically, the design procedure for the finite-time synergetic controller consists of the following steps:

Step 1: Defining the variable γ for the nonlinear system, we construct the synergetic manifold as:

$$M = \left\{\delta : \gamma = s(\delta) = 0, s(\delta) \in R^{m\times 1}\right\}, \tag{29.15}$$

where $\delta = \dot{e}$, and $[\gamma = \gamma_1, \gamma_2, \cdots, \gamma_m]^T$ is a function of the system states, and s is a function of δ.

Step 2: The system states would be driven to approach the specified manifold M exponentially within a finite time by the designed controller along with the following evolution constraint stated as:

$$\tau\dot{\gamma}^{p/r} + \gamma = 0, \tag{29.16}$$

where $\dot{\gamma}^{p/r} = \left[\dot{\gamma}_1^{p_1/r_1}, \dot{\gamma}_2^{p_2/r_2}, \cdots \dot{\gamma}_m^{p_m/r_m}\right]^T$, and τ is a nonsingular positive-definite diagonal matrix. p_i and r_i are positive odd numbers satisfying the condition $1 < p_i/r_i < 2, i = 1, 2, \cdots, m$. The variable γ and its derivative $\dot{\gamma}$ will be driven to zero at finite time by this constraint.

Step 3: From (29.16), we have

$$\dot{\gamma} = s_\delta \dot{\delta}, \tag{29.17}$$

where s_δ is the partial derivative respect to $\dot{\delta}$.

From (29.1), the error dynamic model of the mechanical system can be expressed as

$$m\ddot{e} + K_f \dot{e} - (m\ddot{x}_d + K_f \dot{x}_d + F) = -u(t) \tag{29.18}$$

with $\delta = \dot{e}$, and (29.18) becomes

$$m\dot{\delta} + K_f \delta - (m\ddot{x}_d + K_f \dot{x}_d + F) = -u(t) \tag{29.19}$$

Substituting (29.16) and (29.17) into (29.19) yields

$$u = -ms_\delta^{-1}(-\tau^{-1}\gamma)^{r/p} - K_f \delta + m\ddot{x}_d + K_f \ddot{x}_d + F \tag{29.20}$$

From (29.7), (29.13) and (29.14), the Eq. (29.20) can be rewritten as

$$\begin{aligned} u = &- ms_\delta^{-1}(-\tau^{-1}\gamma)^{r/p} - K_f \dot{e} + m\ddot{x}_d + K_f \ddot{x}_d + \sigma_2 x \\ &+ \hat{W}_1 \Phi(\dot{x})\mathrm{sgn}(\dot{x}) + \hat{W}_2 \Phi(\dot{x})|\dot{x}|\mathrm{sgn}(\gamma) \\ &+ (\mu_1 + \mu_2|\dot{x}|\mathrm{sgn}(\gamma), \end{aligned} \tag{29.21}$$

where $(\tau^{-1}\gamma(x))^{r/p} = [(\tau_1^{-1}\gamma_1)^{r_1/p_1}, (\tau_2^{-1}\gamma_2)^{r_2/p_2}, \cdots, (\tau_m^{-1}\gamma_m)^{r_m/p_m}]^T$, μ_1 and μ_2 are the NN estimation errors satisfying $\mu_i(i = 1, 2.) \geq ||\hat{W}_i(i = 1, 2.)\Phi(\dot{x})|| + F_M$. Furthermore, W_{M1}, W_{M2} are defined as the known largest value of W_1, W_2, respectively.

The weight update laws are given as follows.

$$\dot{\hat{W}}_1 = \mathrm{Pr}\ oj[\mathrm{I}_1 \Phi(\dot{x})\mathrm{sgn}(\dot{x})s, \hat{W}_1], |\dot{W}_1(0)| \leq W_{M1} \tag{29.22}$$

and

$$\dot{\hat{W}}_2 = \mathrm{Pr}\ oj[\mathrm{I}_2 \Phi(\dot{x})\mathrm{sgn}(\dot{x})s, \hat{W}_2], |\dot{W}_2(0)| \leq W_{M2}, \tag{29.23}$$

where $\mathrm{Pr}\ oj(y, \hat{k})$ is the smooth projection algorithm satisfying $\mathrm{Pr}\ oj(y, \hat{k}) \geq \tilde{k}y$.

Lemma 29.1 [17] *Suppose that a continuous, positive-definite function satisfies the following inequality*

$$\dot{V}(t) \leq -\alpha V^{\eta}(t), \forall t \geq t_0, V(t_0) \geq 0, \tag{29.24}$$

where $\alpha > 0$, $0 < \eta < 1$ *are constants. Then, for any given* t_0, $V(t)$ *satisfies the following inequality*:

$$V^{1-\eta} \leq V^{1-\eta}(t_0) - \alpha(1-\eta)(t-t_0), t_0 < t < t_1 \tag{29.25}$$

and

$$V(t) \equiv 0, \forall t \geq t_1 \tag{29.26}$$

With t_1 *given by*

$$t_1 = t_0 + \frac{V^{1-\eta}(t_0)}{\alpha(1-\eta)}. \tag{29.27}$$

Theorem 29.1 *Consider the nonlinear system with control law* (29.21) *and update laws* (29.22), (29.23), *the tracking error will converge to zero in the finite time with the convergence rate depending on the selected parameter* τ.

Proof Define a Lyapunov candidate function as $V = 0.5\gamma^T\gamma$, and then we have

$$\dot{V} = \frac{d}{dt}(0.5\gamma^T\gamma) = \gamma^T\dot{\gamma} \tag{29.28}$$

Substitute (29.16) into (29.28), and then

$$\begin{aligned} \dot{V} &= \gamma^T(-\tau^{-1}\gamma)^{r/p} \\ &= -\tau^{-1}||\gamma||^{(p+r)/p} \leq -\tau^{-1}2^{(p+r/2p)}\left(\frac{1}{2}\gamma^2\right)^{(p+r)/2p} \\ &\leq -\tau_1^{-1}V(t)^{(p+r)/2p} \end{aligned} \tag{29.29}$$

where $\tau_1^{-1} = \tau^{-1} \times 2^{(p+r)/2p}$

From Lemma 29.1, it can be obtained that the synergetic manifold γ can converge to zero in the finite time t_1 given by

$$t_1 = \frac{V^{[1-(p+r)/2p]}[0]}{\tau_1^{-1}(1-(p+r)/2p)}. \tag{29.30}$$

29.4 Simulation Results

In this section, the preceding theoretical development is applied to a simulation example. For this study, we assume that the nonlinear system (29.1) takes the parameters as $m = 0.59$, $K_f = 2.5$, and the parameters of the friction model (29.2) are selected as $\sigma_0 = 0.5$, $\sigma_1 = 0.3$, $\sigma_2 = 0.4$, $F_s = 0.5$, $F_c = 1$, and $v_s = 0.1$. The constraint $\tau \dot{y}^{p/r} + \gamma = 0$ takes the parameters as $\tau = 0.01$, $r = 5$, $p = 7$. Otherwise, $s_\delta = 1$ with $s = \dot{e} + \lambda e$ and $\delta = \dot{e}$.

In the employed NNs, the NN radial basis function is chosen as $\Phi(\dot{X}) = [\varphi_1, \varphi_2, \cdots, \varphi_N]^T$ with

$$\phi_i = \exp\left(\frac{\|\dot{x} - c_i\|^2}{2\sigma_i^2}\right) \tag{29.31}$$

The RBF NN contains 40 nodes with centers $c_i (i = 1, \cdots, N)$ evenly spaced in $[-8, 8]$ and widths $\sigma_1 = 0.5 (i = 1, \cdots, N)$. The initial NN weights $\hat{W}_1(0)$ and $\hat{W}_2(0)$ are selected as zeros. The NN weight update laws are given by (29.22–29.23) with the adaptation rates $I_1 = 10I$ and $I_2 = I$, where I is the positive unit diagonal matrix. The desired trajectory is given by

$$x_d = 0.5(\sin t + 0.5 \cos(0.5t)). \tag{29.32}$$

Figure 29.1 shows the tracking performance of system (29.1) with the proposed, where the parameters μ_1, μ_2 and λ are chosen as 0.05, 0.05, and 1, respectively. Through the NNs learning, Fig. 29.2 shows that the tracking error convergence to zero in a finite time, and bounded control signal is shown in Fig. 29.3. The two NN outputs are given in Fig. 29.4. From Figs. 29.1, 29.2, 29.3 and 29.4, we can see that

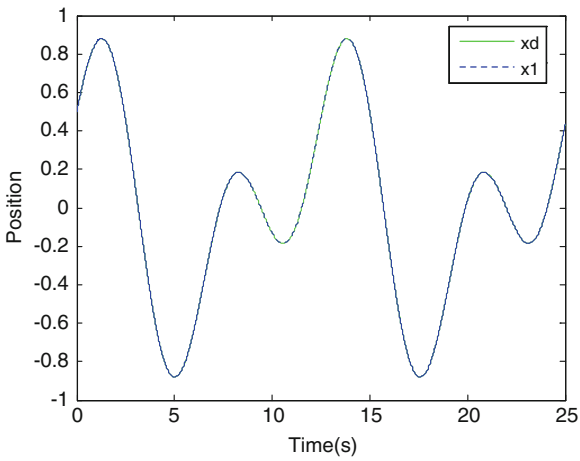

Fig. 29.1 Tracking performance

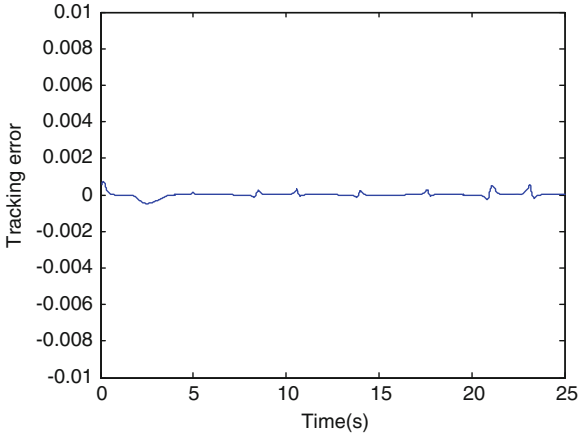

Fig. 29.2 Tracking error

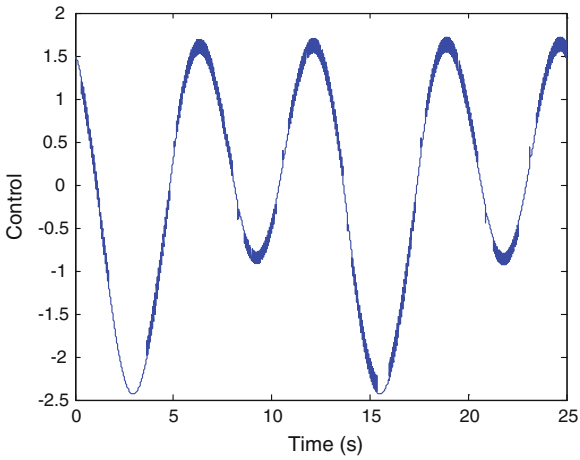

Fig. 29.3 Control signal

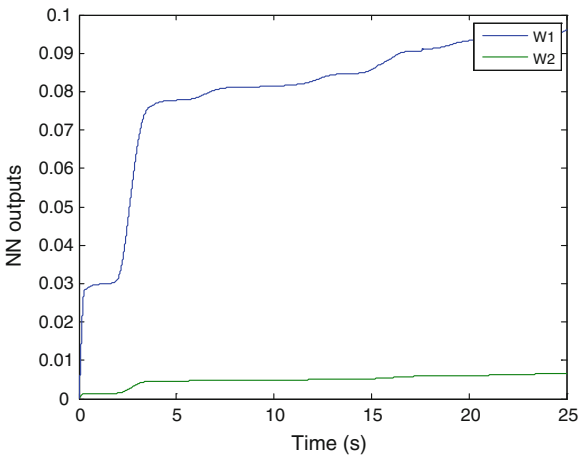

Fig. 29.4 NN outputs

the proposed control scheme is effective for the mechanical system (29.1) with nonlinear dynamical friction (29.2), and the controlled output $x(t)$ will track the desired trajectories $x_d(t)$ very quickly under the effect of the proposed controller.

29.5 Conclusion

This paper has presented a finite-time synergetic control for a class of mechanical nonlinear systems with the friction compensation. The static function and dynamic function of the friction model are approximated by employing two neural networks, respectively. Then, based on synergetic control theory and nonsingular terminal sliding mode technique, a finite-time synergetic controller is developed. Simulation results have verified the effectiveness of the proposed control scheme.

References

1. Karnopp D (1985) Computer simulation of stick-slip friction in mechanical dynamic systems. J Dyn Syst Meas Contr 107(1):100–103
2. Dahl PR (1968) A solid friction model. Aerospace corp, El Segundo
3. Olsson H, Åström KJ, de Canudas Wit C et al (1998) Friction models and friction compensation. Eur J Control 4(3):176–195
4. De Wit CC, Olsson H, Aström KJ et al (1995) A new model for control of systems with friction. IEEE Trans Autom Control 40(3):419–425
5. Freidovich L, Robertsson A, Shiriaev A et al (2010) LuGre-model-based friction compensation. IEEE Trans Control Syst Technol 18(1):194–200
6. Al-Bender F, Lampaert V, Swevers J (2005) The generalized Maxwell-slip model: a novel model for friction simulation and compensation. IEEE Trans Autom Control 50 (11):1883–1887
7. Lee CC (1990) Fuzzy logic in control systems: fuzzy logic controller. IEEE Trans II Syst Man Cybern 20(2):419–435
8. Huang S, Tan KK (2012) Intelligent friction modeling and compensation using neural network approximations. IEEE Trans Ind Electron 59(8):3342–3349
9. Na J, Chen Q, Ren XM, Guo Y (2014) Adaptive prescribed performance motion control of servo mechanisms with friction compensation. IEEE Trans Ind Electron 61(1):486–494
10. Wang GL, Li YF, Bi DX (2007) Support vector networks in adaptive friction compensation. IEEE Trans Neural Networks 18(4):1209–1219
11. Ge SS, Lee TH, Wang J (2000) Adaptive NN control of dynamic systems with unknown dynamic friction. In: Proceedings of the 39th IEEE conference on decision and control, vol 2, pp 1760–1765
12. Xie WF (2007) Sliding-mode-observer-based adaptive control for servo actuator with friction. IEEE Trans Ind Electron 54(3):1517–1527
13. Feng Y, Yu X, Man Z (2002) Non-singular terminal sliding mode control of rigid manipulators. Automatica 38(12):2159–2167
14. Liu CH, Hsiao MY (2012) A finite time synergetic control scheme for robot manipulators. Comput Math Appl 64(5):1163–1169
15. Tao G, Kokotovic PV (1994) Adaptive control of plants with unknown dead-zones. IEEE Trans Autom Control 39(1):59–68

16. Santi E, Monti A, Li D et al (2004) Synergetic control for power electronics applications: a comparison with the sliding mode approach. J Circuits Syst Comput 13(4):737–760
17. Chen Q, Yu L, Nan Y (2013) Finite-time tracking control for motor servo systems with unknown dead-zones. J Syst Sci Complexity 26(6):940–956

Chapter 30
Feedback Gain Scheduling Controller Design for Networked Control Systems with Accurate Measurement of QoS

Hong Yao, Jian-Qiu Deng, Cui Hao, Zeng-Qi Sun and Xin Lu

Abstract The networked control system was modeled in this paper. According to the actual network conditions, the networked-induced time delay is always varying in a certain range. So, the networked-induced time delay can be divided into the fixed time delay and the random time delay. The long time delay can be taken as packet dropout. What's more, the drive mode, packets disorder, sampling period, and some assumed conditions were considered carefully in this paper. In order to make the research close to the reality, the round-trip delay of the network between Tsinghua University and Yahoo is measured by sending and receiving data packet every 5 s from Tsinghua side. Simulation showed that the modeling method improved the effectiveness of the system.

Keywords Modeling · Analysis · NCSs · Long time delay

30.1 Introduction

Recently, NCSs have been extensively investigated. There are many research results in the NCSs field already. The NCSs model with time delay was established by Gao, and Lyapunov–Krasovskii function was used to analyze the stability of the system [1]. The maximum allowable delay was solved by Kim based on Lyapunov–Krasovskii function [2]. The time delay between controller and sensor and the time delay between controller and actuator are considered in this method. So, it has a broader application range than the perturbation method.

In the discrete NCSs with clock-driven, the stochastic optimal control method is proposed. Nilsson turned the NCSs with random time delay into the LQG (Linear Quadratic Gaussian) problem [3]. The stochastic optimal control problem of NCSs with linear quadratic cost function was researched by Zhu [4]. Besides, there are

H. Yao (✉) · J.-Q. Deng · C. Hao · Z.-Q. Sun · X. Lu
Beijing Institute of Technology, School of Aerospace, Beijing 100083, China
e-mail: lushanyaohong@163.com

Z. Deng and H. Li (eds.), *Proceedings of the 2015 Chinese Intelligent Automation Conference*, Lecture Notes in Electrical Engineering 337,
DOI 10.1007/978-3-662-46463-2_30

stochastic stabilization methods [5–7], stochastic H_∞ control method [8], stochastic H2 control method [9].

However, there are still some open problems to be addressed. To improve the universality of the networked method, the problems of analysis and design of NCSs with long time delay are studied.

30.2 Problem Formulation

In order to make the research close to the reality, the round-trip delay of the network between Tsinghua University and Yahoo is measured by sending and receiving data packet every 5 s from Tsinghua side. The Fig. 30.1 shows the continuous 10,000 times of time delay on the network between Tsinghua and Yahoo. The test date is September 7, 2010. Yahoo server's IP address is 66.94.230.34.

Several features are used to describe the NCSs. In this article, drive mode, time delay, packets disorder, packet dropout, sampling period, and some assumed conditions were considered.

30.2.1 Drive Mode

The sensor and the actuator are time driven. The controller is event driven.

30.2.2 Sampling Period

The results in Fig. 30.1 shows that time delay is varying in a small range near the average time delay in a certain period of time, and it is so long that we could not

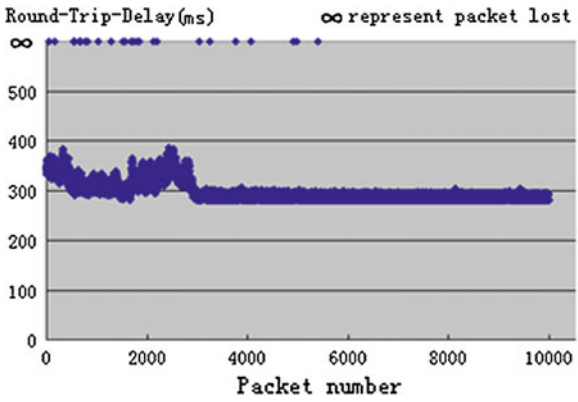

Fig. 30.1 Continuous 10,000 times of time delay on the network between Tsinghua and Yahoo

make them in one sampling period because of the poor control performance. It is more suitable to make the sampling period small, so the time delay is a few times of sampling period plus a time within a sampling period (i.e., the time delay τ is 320 ms, and the sampling period h is 60 ms. So, the time delay is $\tau = 5h + 20$).

30.2.3 Time Delay

There is time delay in the transmission of packet, so the actuator will use the old input value when the new one is not arriving. There are many time delays in the loop of NCSs, such as sensor-to-controller delay τ_{sc}, controller-to-actuator delay τ_{ca}, controller computing delay τ_{cc}. All these time delays can be considered together as: $\tau = \tau_{sc} + \tau_{ca} + \tau_{cc}$.

30.2.4 Packets Disorder and Packets Dropout

A packet disorder happens when a given packet arrives before another packet which was sent before. There is time stamp in every packet. So, the actuator can take packets by comparing their time stamps. The disordered packets will be taken as lost packets. Packet dropout is just like the time delay of this packet which is infinite. There is another kind of packet dropout that the packet is out of the available period. Take Fig. 30.1, for example, if the time delay is longer than $(5 + 1)h\,((N + 1))$, the packet will be considered as packet dropout. If the packet is in the available period, it will be considered as effective packet. i_m is used to represent the mth sampling instant number. $S \triangleq \{i_1, i_2, \ldots\} \subseteq N$ represents the set of effective sampling instants. An effective sampling instant is an instant when an effective packet arrives. N_{drop} represents the maximum number of continuous lost packages. $\Omega \triangleq \{0, 1, 2, \ldots, N_{\text{drop}}\}$ represents the set of continuous lost packages number. $\eta(i_m)$ represents the sampling periods between instant i_m and i_{m+1}. D represents the set of $\eta(i_m)$, $D \triangleq \{1, 2, \ldots, N_{\text{drop}} + 1\}$.

$$N_{\text{drop}} = \max\{\eta(i_m)\} - 1 \tag{30.1}$$

$$\eta(i_m) = i_{m+1} - i_m, i_m, i_{m+1} \in S, \eta(i_m) \in D \tag{30.2}$$

The diagram of the effective packets and the ineffective packets is shown in Fig. 30.2.

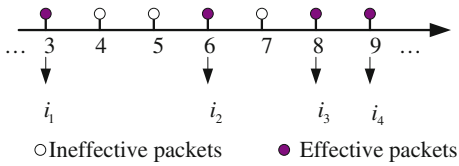

Fig. 30.2 The diagram of the effective packets and the ineffective packets

30.2.5 Assumptions

For simplicity, there are some assumptions to be raised.

(1) The state values of the NCSs are completely measured.
(2) There are no mistakes in the packets transmission process.
(3) There is no interference in the NCSs.
(4) Ignoring the graded effect of the sampling signal and control signal.
(5) The sampling signal and control signal adopt single packet transmission mechanism.
(6) The sensor and actuator are synchronous.

In the practical usage, these assumptions may not be satisfied strictly, but the control effect will not be changed a lot.

30.3 Design of Gain Scheduling Controller

30.3.1 Network Status Division and Monitor Design

There are many kinds of standards to evaluate the quality of the network service (QoS). The packet loss rate is taken as QoS parameter of the network in this paper for its stability in a period of time, and the status of the network is divided into many grades on the basis of the packet loss rate. The packet loss rate is defined as the ratio between the loss packets and the total packets in a period of time. The loss packet includes the packet whose time delay is longer than $(N + 1)h$. N can be any number in the natural numbers set.

30.3.2 Controller Design

The structure of the network controller with long time delay based on states feedback gain scheduling is shown in Fig. 30.3. The QoS Monitor is used to monitor the quality of the network service. The controller will call different parameters based on different QoS of the network.

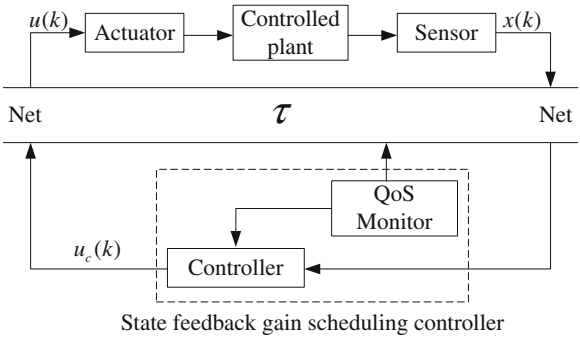

Fig. 30.3 The structure of the network controller with long time delay based on states feedback gain scheduling

Suppose that the current QoS is QoS_q, and the augmented vectors are shown as below:

$$z(i_m) = \left[\boldsymbol{x}(\boldsymbol{i_m})^{\boldsymbol{T}} \cdots \boldsymbol{x}(\boldsymbol{i_{m-k+j}})^{\boldsymbol{T}} \cdots \boldsymbol{x}(\boldsymbol{i_{m-k+n}})^{\boldsymbol{T}} \cdots \boldsymbol{x}(\boldsymbol{i_{m-k}})^{\boldsymbol{T}} \cdots \boldsymbol{x}(\boldsymbol{i_{m-N-1}})^{\boldsymbol{T}}\right]^T$$

$$z(i_{m+1}) = \left[\boldsymbol{x}(i_{m+1})^T \cdots \boldsymbol{x}(i_{m-k+j+1})^T \cdots \boldsymbol{x}(i_{m-k+n+1})^T \cdots \boldsymbol{x}(i_{m-k+1})^T \cdots \boldsymbol{x}(i_{m-N})^T\right]^T$$

So, the model of the NCSs is shown as below:

(1) If there is no new input effecting on the actuator, the transformational relationship from $z(i_m)$ to $z(i_{m+1})$ is

$$\boldsymbol{z}(\boldsymbol{i_{m+1}}) = \boldsymbol{M_{i,j,k,q}}\boldsymbol{z}(\boldsymbol{i_m}) \tag{30.3}$$

$$\boldsymbol{M}_{i,j,k,q} = \begin{bmatrix} \prod_0 & \delta(1,k)\prod_1 & \delta(2,k)\prod_1 & \cdots & \delta(N+1,k)\prod_1 \\ 1 & & & 0 & \\ & \ddots & & & \\ & & \ddots & & \\ 0 & & & 1 & 0 \end{bmatrix}, \quad \begin{aligned} \textstyle\prod_0 &= \boldsymbol{F}^{i_{m+1}-i_m} \\ \textstyle\prod_1 &= \sum_{l=0}^{i_{m+1}-i_m-1} \boldsymbol{F}^l \boldsymbol{G}\boldsymbol{L}_q \end{aligned}$$

$$i \in \{1, 2, \ldots, N_{\text{drop}} + 1\}, q \in W,$$

$$j = 0, k = \{1, 2, \ldots, N+1\}, \delta(n,k) = \begin{cases} 1, n = k \\ 0, n \neq k \end{cases}$$

(2) If there is new input effecting on the actuator, the transformational relationship from $z(i_m)$ to $z(i_{m+1})$ is shown in Eq. (30.4) which is listed below.

$$\boldsymbol{z}(i_{m+1}) = \boldsymbol{M}_{i,j,k,q}\boldsymbol{z}(i_m) \tag{30.4}$$

$$\boldsymbol{M}_{i,j,k,q}=\begin{bmatrix} \prod_0 & \overbrace{0\ \cdots\ 0}^{k-j-1} & \prod_{k-j} & \cdots & \prod_{k-n} & \cdots & \prod_k & \overbrace{0\ \cdots\ 0}^{N+1-k} \\ 1 & & 0 & & 0 & & 0 & \\ 0 & 1 & \vdots & & \vdots & & \vdots & \\ \vdots & \ddots & \vdots & & \vdots & & \vdots & \\ \vdots & 1 & 0 & & \vdots & & \vdots & \\ \vdots & & 1 & & \vdots & & \vdots & \\ \vdots & & 0 & \ddots & 0 & & \vdots & \\ \vdots & & \vdots & & 1 & & \vdots & \\ \vdots & & \vdots & & 0 & \ddots & 0 & \\ \vdots & & \vdots & & \vdots & & 1 & \\ \vdots & & \vdots & & \vdots & & 0 & \ddots \\ 0 & & 0 & & 0 & & 0 & 1\ 0 \end{bmatrix},$$

$$\prod_0 = \boldsymbol{F}^{i_{m+1}-i_m}$$

$$\prod_{k-j} = -\sum_{l=0}^{i_{m+1}-i_{m-k+j}-N-2} \boldsymbol{F}^l \boldsymbol{G} \boldsymbol{L}_q$$

$$\prod_{k-n} = -\boldsymbol{F}^{i_{m+1}-i_{m-k+n+1}-N-1} \sum_{l=0}^{i_{m-k+n+1}-i_{m-k+n}-1} \boldsymbol{F}^l \boldsymbol{G} \boldsymbol{L}_q$$

$$\prod_{k} = -\boldsymbol{F}^{i_{m+1}-i_{m-k+1}-N-1} \sum_{l=0}^{i_{m-k+1}+N-i_m} \boldsymbol{F}^l \boldsymbol{G} \boldsymbol{L}_q$$

$$i \in \left\{1, 2, \cdots, N_{\text{drop}}+1\right\}, q \in W,$$

$$1 \le k \le N+1, 0 < j \le k$$

In the same way, the transformational relationship from $z(i_m)$ to $z(i_m^p)$ $(i_m < i_m^p < i_{m+1})$ is shown as follows:

$$\boldsymbol{z}(i_m^p) = \left[\boldsymbol{x}(i_m^p)^T \quad \cdots \quad \boldsymbol{x}(i_{m-k+1})^T \quad \cdots \boldsymbol{x}(i_{m-N})^T\right]^T$$

(1) If there is no new input effecting on the actuator, the transformational relationship from $z(i_m)$ to $z(i_m^p)$ is

$$\boldsymbol{z}(i_m^p) = \bar{\boldsymbol{M}}_{p,j,k,q}\boldsymbol{z}(i_m) \tag{30.5}$$

$$\bar{\boldsymbol{M}}_{p,j,k,q} = \begin{bmatrix} \prod_0 & \delta(1,k)\prod_1 & \delta(2,k)\prod_1 & \cdots & \delta(N+1,k)\prod_1 \\ 1 & & & 0 & \\ & \ddots & & & \\ & & \ddots & & \\ 0 & & & 1 & 0 \end{bmatrix},$$

$$\prod_0 = \boldsymbol{F}^{i_m^p - i_m}$$

$$\prod_1 = \sum_{l=0}^{i_m^p - i_m - 1} \boldsymbol{F}^l \boldsymbol{G}\boldsymbol{L}_q$$

$$i_m < i_m^p < i_{m+1}$$

Thereinto, $i \in \{1, 2, \cdots, N_{\text{drop}}\}, q \in W, j = 0, k = \{1, 2, \cdots, N+1\}, \delta(n,k) = \begin{cases} 1, n = k \\ 0, n \neq k \end{cases}$

(2) If there is new input effecting on the actuator, the transformational relationship from $z(i_m)$ to $z(i_m^p)$ is

$$\boldsymbol{z}(i_m^p) = \bar{\boldsymbol{M}}_{p,j,k,q}\boldsymbol{z}(i_m) \tag{30.6}$$

$$\bar{\boldsymbol{M}}_{p,j,k,q}=\begin{bmatrix}
\prod_0 & \overbrace{0\ \cdots\ 0}^{k-j-1} & \prod_{k-j} & \cdots & \prod_{k-n} & \cdots & \prod_k & \overbrace{0\ \cdots\ 0}^{N+1-k} \\
1 & & 0 & & 0 & & 0 & \\
0 & 1 & \vdots & & \vdots & & \vdots & \\
\vdots & \ddots & \vdots & & \vdots & & \vdots & \\
\vdots & 1 & 0 & & \vdots & & \vdots & \\
\vdots & & 1 & & \vdots & & \vdots & \\
\vdots & & 0 & \ddots & 0 & & \vdots & \\
\vdots & & \vdots & & 1 & & \vdots & \\
\vdots & & \vdots & & 0 & \ddots & 0 & \\
\vdots & & \vdots & & \vdots & & 1 & \\
\vdots & & \vdots & & \vdots & & 0 & \ddots \\
0 & & 0 & & 0 & & 0 & 1\ \ 0
\end{bmatrix},$$

$$\prod_0 = \boldsymbol{F}^p$$

$$\prod_{k-j} = -\sum_{l=0}^{i_m^p-i_{m-k+j}-N-2}\boldsymbol{F}^l\boldsymbol{G}\boldsymbol{L}_q$$

$$\prod_{k-n} = -\boldsymbol{F}^{i_m^p-i_{m-k+n+1}-N-1}\sum_{l=0}^{i_{m-k+n+1}-i_{m-k+n}-1}\boldsymbol{F}^l\boldsymbol{G}\boldsymbol{L}_q$$

$$\prod_{k} = -\boldsymbol{F}^{i_m^p-i_{m-k+1}-N-1}\sum_{l=0}^{i_{m-k+1}+N-i_m}\boldsymbol{F}^l\boldsymbol{G}\boldsymbol{L}_q$$

Thereinto, $i \in \{1, 2, \cdots, N_{\text{drop}}\}$, $q \in W$, $1 \le k \le N+1$, $0 < j \le k$, $i_m < i_m^p < i_{m+1}$.

The stabilization and optimization problem of networked control system is analyzed with cone complementary linearization (CCL) approach and estimation of distribution algorithm (EDA).

30.4 Stability Analysis

Definition 30.1 Suppose that $\boldsymbol{L}_q$ is the state feedback gain of the controller which is scheduled right now. If there are positive matrixes $\boldsymbol{P}_i \in R^{(N+2)n\times(N+2)n}$ and $\boldsymbol{P}_j \in R^{(N+2)n\times(N+2)n}$ which satisfy in Eq. (30.7), the NCSs is stable under the network condition Ω.

$$\widetilde{\boldsymbol{M}}_i^T \boldsymbol{P}_j \widetilde{\boldsymbol{M}}_i - \boldsymbol{P}_i < 0 \quad \widetilde{\boldsymbol{M}}_i \in \boldsymbol{\Xi} \tag{30.7}$$

Thereinto, the set of parameter $\boldsymbol{M}_{i,j,k,q}$ is represented by $\boldsymbol{\Xi}$, so one element of the set is $\widetilde{\boldsymbol{M}}_i \in \boldsymbol{\Xi}$.

Certification:

The Lyapunov function of the NCSs is defined as:

$$\boldsymbol{V}(i_m) = \boldsymbol{z}^T(i_m)\boldsymbol{P}_i\boldsymbol{z}(i_m) \tag{30.8}$$

$$\boldsymbol{V}(i_{m+1}) = \boldsymbol{z}^T(i_m)\boldsymbol{M}_i^T\boldsymbol{P}_j\boldsymbol{M}_i\boldsymbol{z}(i_m) \tag{30.9}$$

$$\begin{aligned}\Delta\boldsymbol{V} &= \boldsymbol{V}(i_{m+1}) - \boldsymbol{V}(i_m) \\ &= \boldsymbol{z}^T(i_m)(\boldsymbol{M}_i^T\boldsymbol{P}_j\boldsymbol{M}_i - \boldsymbol{P}_i)\boldsymbol{z}(i_m) < 0\end{aligned} \tag{30.10}$$

Thereinto, $\boldsymbol{z}(i_m) \neq 0$.

We can infer that $\lim_{i_m\to\infty} \boldsymbol{z}(i_m) = 0$ based on Eq. (30.10). When $i_m < l < i_{m+1}$, $\|\boldsymbol{z}(l)\| = \|\bar{\boldsymbol{M}}_i\boldsymbol{z}(i_m)\| \le \alpha\|\boldsymbol{z}(i_m)\|$, $\lim_{l\to\infty}\|\boldsymbol{z}(l)\| = 0$ (thereinto, $l \neq i_m$). Summing up the above two kinds of case, we can infer that $\lim_{l\to\infty}\|\boldsymbol{z}(l)\| = 0$ ($l \in N$).

Based on the NCSs' stable definition, the NCSs are stable.

Inference 1:

Suppose that $\boldsymbol{L}_q$ is the state feedback gain of the controller which is scheduled right now. If there is a positive matrix $\boldsymbol{P} \in R^{(N+2)n\times(N+2)n}$ which satisfies inequation (30.11), the NCSs are stable under the network condition Ω.

$$\widetilde{\boldsymbol{M}}_i^T \boldsymbol{P} \widetilde{\boldsymbol{M}}_i - \boldsymbol{P} < 0 \quad \widetilde{\boldsymbol{M}}_i \in \boldsymbol{\Xi} \tag{30.11}$$

Thereinto, the set of parameter $\boldsymbol{M}_{i,j,k,q}$ is represented by $\boldsymbol{\Xi}$, so one element of the set is $\widetilde{\boldsymbol{M}}_i \in \boldsymbol{\Xi}$.

30.5 Feedback Gain Design

Definition 30.2 If there are positive matrixes P_i and Q_i which satisfy the NCSs' stable condition.

$$\begin{bmatrix} -\boldsymbol{P}_i & * \\ \widetilde{\boldsymbol{M}}_i & -\boldsymbol{Q}_{i+1} \end{bmatrix} < 0 \quad (\widetilde{\boldsymbol{M}}_i \in \boldsymbol{\Xi}) \tag{30.12}$$

$$\begin{bmatrix} -\boldsymbol{P}_i & * \\ \widetilde{\boldsymbol{M}}_i & -\boldsymbol{Q}_j \end{bmatrix} < 0 \quad (\widetilde{\boldsymbol{M}}_i \in \boldsymbol{\Xi}) \tag{30.13}$$

$$\boldsymbol{P}_j \boldsymbol{Q}_j = \boldsymbol{I} \tag{30.14}$$

Certification:

From Definition 30.1, we can obtain that: Suppose that $\boldsymbol{L}_q$ is the state feedback gain of the controller which is scheduled right now. If there are positive matrixes $\boldsymbol{P}_i \in R^{(N+2)n\times(N+2)n}$ and $\boldsymbol{P}_j \in R^{(N+2)n\times(N+2)n}$ which satisfy inequation (30.14), the NCSs are stable in the network condition Ω.

$$\widetilde{\boldsymbol{M}}_i^T \boldsymbol{P}_j \widetilde{\boldsymbol{M}}_i - \boldsymbol{P}_i < 0 \quad \widetilde{\boldsymbol{M}}_i \in \boldsymbol{\Xi} \tag{30.15}$$

Based on the Schur fill lemma, the inequation (30.15) is equal to the inequation (30.16).

$$\begin{bmatrix} -\boldsymbol{P}_i & * \\ \widetilde{\boldsymbol{M}}_i & -\boldsymbol{P}_j^{-1} \end{bmatrix} < 0 \tag{30.16}$$

From (30.14), we can infer that: $\boldsymbol{Q}_j = \boldsymbol{P}_j^{-1}$.

So, the inequation (30.16) can be represented as

$$\begin{bmatrix} -\boldsymbol{P}_i & * \\ \widetilde{\boldsymbol{M}}_i & -\boldsymbol{Q}_j \end{bmatrix} < 0 \tag{30.17}$$

So, the Definition 30.2 is right.

The inequations in definition 30.2 are not normal linear matrix inequations, so the CCL algorithm can be used to calculate the feedback gain $\boldsymbol{L}_q$. The main idea of the CCL algorithm is that the untypical linear matrix inequations can be changed to the nonlinear matrix minimization problem with restraint of linear matrix inequations.

$$\min \quad \mathrm{tr}\Big(\sum_{i=1}^{f((N+1),N_{QoS},(N_{\mathrm{drop}}+1))} \boldsymbol{P}_i \boldsymbol{Q}_i \Big) \tag{30.18}$$

where $f((N+1), N_{QoS}, (N_{\text{drop}}+1))$ is the function which represents the number of matrix $\boldsymbol{P_i}$ and $\boldsymbol{Q_i}$.

$$\text{Subject to} \begin{cases} \text{equation (30.16) and (30.17)} \\ \begin{bmatrix} \boldsymbol{P}_i & \boldsymbol{I} \\ \boldsymbol{I} & \boldsymbol{Q}_i \end{bmatrix} \geq 0 \end{cases} \tag{30.19}$$

30.6 Simulation Example

The servo motor NCSs can be taken as an illustrative example to demonstrate the effectiveness of the controller design method mentioned in this paper. The state of the system is $\boldsymbol{x}_p = [\theta, \omega]^T$, where θ and ω are the angular and angular velocity of the system, respectively. The dynamic equation of the servo motor is shown as below:

$$\dot{\boldsymbol{x}}_p(t) = \begin{bmatrix} 0 & 1 \\ 0 & -217.4 \end{bmatrix} \boldsymbol{x}_p(t) + \begin{bmatrix} 0 \\ 1669.5 \end{bmatrix} \boldsymbol{u}(t) \tag{30.20}$$

Owing to the transmission medium and heavy network load, there are time delay and packet loss in the transmission. Suppose that the sampling period of the NCSs is 50 ms. When the packet loss ratio is in the set $[0, 15\%)$, the QoS level is QoS_1, and when the packet loss ratio is in the set $(15, 30\%]$, the QoS level is QoS_2.

Figure 30.4 shows the simulation results of three different controllers: stabilization controller without parameters scheduling, stabilization controller with parameters scheduling, and optimized controller with parameters scheduling. The feedback gain of the stabilization controller without parameters scheduling is

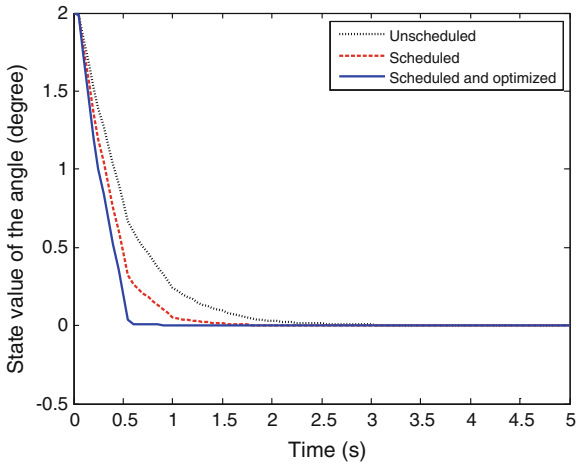

Fig. 30.4 The simulation results of three different controllers

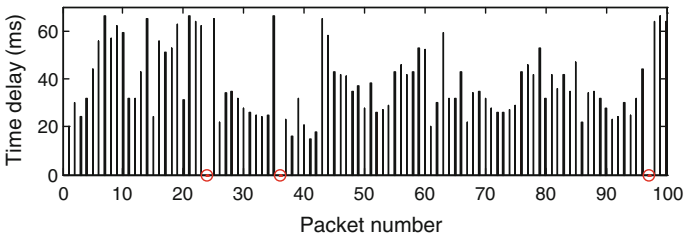

Fig. 30.5 The network condition of the simulation

$\boldsymbol{L}_1 = [0.223 \quad 0.0086]$. The feedback gain is obtained by CCL approach. The feedback gains of the stabilization controller with parameters scheduling are $\boldsymbol{L}_2^1 = [0.572 \quad 0.0088]$ under the network condition QoS_1, and $\boldsymbol{L}_2^2 = [0.302 \quad 0.0084]$ under the network condition QoS_2, respectively. The feedback gains of the optimized controller with parameters scheduling are $\boldsymbol{L}_3^1 = [0.582 \quad 0.0086]$ under the network condition QoS_1, and $\boldsymbol{L}_3^2 = [0.382 \quad 0.0086]$ under the network condition QoS_2, respectively.

Figure 30.5 shows the network condition of the simulation. The circle represents the lost packet. Most time delay is varying in the period [20 ms 66 ms]. So, we can conclude that $N = 0$ and the packet is lost when the time delay is more than 50 ms.

The simulation results show that the performance of the NCSs is prompted after parameters adjusting, and the performance of the NCSs is prompted a lot after parameters optimizing.

30.7 Conclusion

The network statuses are discussed carefully in this paper. The modeling of the NCSs and feedback gain scheduling controller design are investigated in the situation of network with long time delay. The network state QoS is divided into N grades and there are corresponding control parameter L_q for every network grade QoS_q. So, when the state of the network is different, different parameter is selected. In the end, for improving the performance of the system, the EDA algorithm is adopted to optimize the control parameter. The simulation results show that adopting different feedback gain of the system based on the different packet loss ratio can improve the performance of the NCSs, and the performance can be improved further after the parameters were optimized.

References

1. Gao H, Chen T, Lain J (2008) An new delay system approach to network-based control. Automatica 44(1):39–52
2. Kim DS, Lee YS, Kwon WH et al (2003) Maximum allowable delay bounds of networked control systems. Control Eng Pract 11(11):1301–1313
3. Nilsson J, Bernhardsson B, Wittenmark B (1998) Stochastic analysis and control of real-time systems with random time delays. Automatica 34(1):57–64
4. Zhu QX, Hu SS, Liu Y (2004) Infinite time stochastic optimal control of networked control systems with long delay. Control Theor Appl 21(3):321–326
5. Liu L, Tong C, Wu Y (2009) Markovian jump model of networked control systems with dynamic output feedback controllers. Acta Automatica Sinica 5:627–631
6. Yang F, Wang Z, Ho DWC et al (2007) Robust H∞ control with missing measurements and time delays. IEEE Trans Autom Control 52(9):1666–1672
7. Ma W, Shao C (2007) Stochastic stability for networked control systems. Acta Automatica Sinica 33(8):878–882
8. Wu J, Chen T (2007) Design of networked control systems with packet dropouts. IEEE Trans Autom Control 52(7):1314–1319
9. Wang W, Zhan Y, Yang F (2008) An H2 approach to networked control system. Acta Automatica Sinica 4(2):219–224

Chapter 31
Adaptive Fuzzy Control Based on Variable Universe for Ship Course

Yuchao Wang, Huixuan Fu and Sheng Liu

Abstract Aiming at the conventional fuzzy controller for ship course accuracy is not high and there is contradiction between the number of control rules and accuracy. Accordingly, a variable universe fuzzy controller algorithm for ship course was proposed. By analyzing the contraction–expansion factors, one of them was found able to satisfy the general contraction–expansion factor condition. The simulation results show that variable universe fuzzy controller for ship course has high performance, and the proposed control strategy has superior property in effectiveness and robustness than conventional controller.

Keywords Ship · Course-keeping · Variable universe · Fuzzy control

31.1 Introduction

The development of ship course (steering autopilot) is the field that control theories have been applied much earlier and achieved good results. In the early 1920s, the classical control theory was applied to course-keeping control, namely, PID autopilot, and at the end of 1970s, minimal variance self-tuning control and model reference adaptive control (MRAC), etc., were applied to ship course-keeping control [1].

With modern control theory and artificial intelligence control algorithm further, researchers began to focus on the research artificial intelligence control method is similar to steering by crew [2]. Reference [3] consider the impact of the external environment on cargo movement, an adaptive control method combines with optimal control compensator were proposed. Robust tracking controller is proposed for ship course nonlinear systems were presented in reference [4]. Aiming at underactuated path tracking problem of ship model uncertain parameters, design a

Y. Wang (✉) · H. Fu · S. Liu
College of Automation, Harbin Engineering University, Nantong Street 145, Harbin, China
e-mail: wangyuchao@hrbeu.edu.cn

Z. Deng and H. Li (eds.), *Proceedings of the 2015 Chinese Intelligent Automation Conference*, Lecture Notes in Electrical Engineering 337,
DOI 10.1007/978-3-662-46463-2_31

stable adaptive neural network controller [5]. In reference [6] proposed the path tracking control algorithm consider constraint of the ship's position and velocity point. The sliding mode robust adaptive control algorithm was discussed in references [7]. Fuzzy control is easy to achieve without precise mathematical model and clearly physical meaning, and in the field of ship control applications [8]. Reference [9] first proposed the idea of variable universe by selecting the appropriate contraction–expansion factors. Contraction–expansion factors select and design the key factor for variable universe fuzzy control, a lot of literatures are doing useful discussion [10].

In this paper fuzzy control adaptive algorithm based on variable universe for ship course-keeping were proposed. Variable universe adaptive fuzzy controller with three-input and single-output, and contraction–expansion factors selection of relevant parameters were discussed in this paper. The digital variable universe adaptive fuzzy controller system differential was shown. Simulation results of our proposed ship course control algorithm verified high precision and strong adaptability.

31.2 Nonlinear Mathematical Model of Ship Motion

31.2.1 Mathematical Model of Rudder

Steering servo system drives command rudder angle δ_r to the actual rudder angle δ, servo characteristics usually is as follows:

$$\dot{\delta} = -\frac{1}{T_E}\delta + \frac{1}{T_E}\delta_r \tag{31.1}$$

where the actual rudder angle is δ, command rudder angle is δ_r, time constant of the steering gear is T_E.

31.2.2 Responding Nonlinear Mathematical Model

Nomoto model obtains nonlinear differential equations that may retain characteristic dynamics of ship course to get the simulation accuracy requirements of the model. The ship yaw dynamics was chosen as a first-order Nomoto model with actuator dynamics [8]:

$$T\ddot{\psi} + \dot{\psi} + \alpha\dot{\psi}^3 = K\delta \tag{31.2}$$

where yaw velocity is $\dot{\psi}$, rudder angle is δ, stability parameter is T, K is parameter of rotation, α is nonlinear coefficient.

If we considered errors of control system modeling and external disturbances, model would be modified as following:

$$T\ddot{\psi} + \dot{\psi} + \alpha\dot{\psi}^3 + \Delta(\psi, \dot{\psi}) + w = K\delta \tag{31.3}$$

where modeling errors are $\Delta(\psi, \dot{\psi})$, it came from model parameter errors, and ignores some of the higher order dynamic characteristics of ships outside uncertain disturbance being w, including uncertainties wind, wave, currents and so on. Usually, $\Delta(\psi, \dot{\psi})$ and w are difficult to accurately described by a mathematical expression.

31.3 Design of Variable Universe Fuzzy Controller

Variable universe fuzzy controller is actually an adaptive fuzzy controller, universe contraction with the error becomes smaller with the form of rules unchanged, contraction of universe is equivalent to an increase in terms of fuzzy control rules to improve the control precision of the system.

31.3.1 Structure Design of Controller

Variable universe fuzzy control system with three-input and single-output for ship course is shown in Fig. 31.1.

In Fig. 31.1, output angle of fuzzy control steering is δ_r, where ship course angle and heading angle desired output is ψ_d and ψ, respectively.

Let $X = [-E, E]$, $Y = [-EC, EC]$ and $Z = [-EI, EI]$ be the universes of input variables and $V = [-U, U]$ be the universe of output variable. $A = \{A_i\}_{1 \le i \le p}$, $B = \{B_j\}_{1 \le j \le q}$, $C = \{C_j\}_{1 \le s \le r}$, $D = \{D_{ijs}\}_{1 \le i \le p,\ 1 \le j \le q, 1 \le s \le r}$ are, respectively,

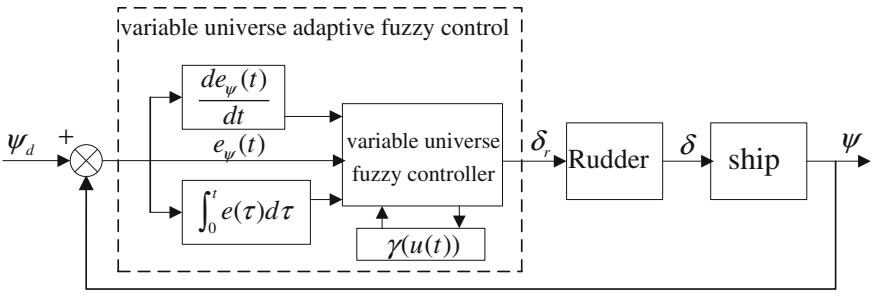

Fig. 31.1 Structure of variable universe adaptive fuzzy controller

fuzzy sets denoted by X, Y, Z, $V.x_i$, y_j, z_s, u_{ijs} is the peak point of A_i, B_i, C_s, D_{ijs}, satisfying condition under $-E \le x_1 < x_2 < \cdots < x_p \le E$, $-EC \le y_1 < y_2 < \cdots < y_q \le EC$, $-EI \le z_1 < z_2 < \cdots < z_r \le EI$, $-U \le u_{111} < u_{112} < \cdots < u_{pqr} \le U$. Let $x_i(0) = x_i$, $y_j(0) = y_j$, $y_s(0) = y_s$, and $u_{ijs}(0) = u_{ijs}$ as linguistic variables. The control rule base $R(\mathrm{A}, \mathrm{B}, \mathrm{C})$ of a fuzzy controller is usually written as follows:

$$\text{if } x \text{ is } A_i \text{ and } y \text{ is } B_j \text{ and } z \text{ is } C_s \text{ then } u \text{ is } D_{ijs} \tag{31.4}$$

The fuzzy controller is approximately a binary piecewise interpolation function:

$$u(t) \triangleq F(x(t), y(t), z(t)) = \sum_{i=1}^{p} \sum_{j=1}^{q} \sum_{s=1}^{r} A_i(x(t)) B_j(y(t)) C_s(z(t)) u_{ijs} \tag{31.5}$$

31.3.2 Contraction–Expansion Factor

Definition 31.1 A function $\alpha : X \to [0,\ 1]$, is called a contraction–expansion factor on universe X, if it satisfies the following conditions:

(1) Evenness: $(\forall\, x \in X)\ (\alpha(x) = \alpha(-x))$;
(2) zero-preserving: $\alpha(0) = 0$;
(3) monotonicity: $\alpha(x)$ is strictly monotonically increasing on $[0, E]$;
(4) corizpatibility: $(\forall\, x \in X)\ (|x| \le \alpha(x)E)$.
From the compatibility of Definition 31.1, it is easy to know that contraction–expansion factors satisfy the following condition:
(5) Normality: $\alpha(\pm E) = 1$, $\upsilon(\pm E) = 1$.

For any $x \in X$, write $X = [-\alpha(x)E, \alpha(x)E]$, and $\alpha(x)$ called contraction–expansion factors, we can use one of the following two expressions of references [10]:

$$\alpha(x) = \left(\frac{|x|}{E}\right)^{\tau} + \varepsilon \quad \tau > 0, \varepsilon \textit{ is} \text{ small positive number} \tag{31.6}$$

$$\alpha(x) = 1 - \lambda \exp(-kx^2) \quad \lambda \in (0, 1),\ k > 0 \tag{31.7}$$

For contraction–expansion factors formula, it will be choice reasonable for λ and k, and can ensure the compatibility of contraction–expansion factors to satisfy the compatibility conditions as following:

$$\alpha(x) = 1 - 0.8 \cdot \exp(-10x^2) - x \ge 0 \tag{31.8}$$

Output of contraction–expansion factors is:

$$\beta(t) = K_i \sum_{i=0}^{n} P_i \int_0^t e_n(\tau)\mathrm{d}\tau + \beta(0) \tag{31.9}$$

where K_i and P_i is the adjustable parameters, n is the number of input variable, $\beta(0)$ is general admission $(\beta(0) = 1.0)$.

31.3.3 Differential Format of Adaptive Fuzzy Controller with Variable Universe

Set $(k = 0, 1, 2, \ldots)$ as points of sampling time, T is sampling period, conventional approximation as following:

$$\frac{de(t)}{dt} \approx \frac{e(k) - e(k-1)}{T} \triangleq \frac{e(kT) - e[(k-1)T]}{T} \tag{31.10}$$

$$\int_0^t e(\tau)d\tau \approx T \sum_{i=0}^{k} e(k) \triangleq \sum_{i=0}^{k} e(kT)T \tag{31.11}$$

To facilitate the writing, omitting $e(kT)$ the abbreviated T, let contraction–expansion factors are recorded as: $\alpha(x)$, $\beta(y)$, $\phi(z)$.

Specific steps for ship course fuzzy controller based on variable universe are as follows:

$$\delta(1) = F(x(0), y(0), z(0)) = \sum_{i=1}^{p} \sum_{j=1}^{q} \sum_{s=1}^{r} A_i(x(0))B_j(y(0))C_s(z(0))\delta_{ijs}(0) \tag{31.12}$$

Step 0: For an arbitrarily given initial input value $x(0) \in X$, $y(0) \in Y$ and $z(0) \in Z$, calculate the output value of the controller $\delta(1)$:

$$\delta(1) = F(x(0), y(0), z(0)) = \sum_{i=1}^{p} \sum_{j=1}^{q} \sum_{s=1}^{r} A_i(x(0))B_j(y(0))C_s(z(0))\delta_{ijs}(0) \tag{31.13}$$

Step 1: The output of the system emerges after $\delta(1)$ acts on the object. Then get the input of the controller $x(1)$, $y(1)$ and $z(1)$ after the output compares with

the reference input $x_i(1) = \alpha(x(1))x_i(0)$, $y_j(1) = \beta(x(1), y(1))y_j(0)$, $z_s(1) = \phi(x(1), y(1), z(1))z_s(0)$ and calculate:

$$\begin{aligned}\delta_{ijs}(1) &= F(x_i(1), y_j(1), z_s(1)) \\ &= \sum_{m=1}^{p}\sum_{t=1}^{q}\sum_{n=1}^{r} A_m(x_i(1))B_t(y_j(1))C_n(z_j(1))\delta_{m\,tn}(0)\end{aligned} \tag{31.14}$$

$$\delta(2) = F(x(1), y(1), z(1)) = \sum_{i=1}^{p}\sum_{j=1}^{q}\sum_{s=1}^{r} A_i(x(1))B_j(y(1))C_s(z(1))\delta_{ijs}(1) \tag{31.15}$$

...

Step k: The output of the system emerges after $\delta(k)$ acts on the object. Then get the input of the controller $x(k)$, $y(k)$ and $z(k)$, after the output compares with the reference input $x_i(k) = \alpha(x(k))x_i(0)$, $y_j(k) = \beta(x(k), y(k))y_j(0)$ and $z_s(k) = \phi(x(k), y(k), z(k))z_s(0)$ and calculate

$$\begin{aligned}\delta_{ijs}(k) &= F(x_i(k), y_j(k), z_s(k)) \\ &= \sum_{m=1}^{p}\sum_{t=1}^{q}\sum_{n=1}^{r} A_m(x_i(k))B_t(y_j(k))C_n(z_j(k))\delta_{mtn}(0)\end{aligned} \tag{31.16}$$

$$\delta(k+1) = F(x(k), y(k), z(k)) = \sum_{i=1}^{p}\sum_{j=1}^{q}\sum_{s=1}^{r} A_i(x(k))B_j(y(k))C_s(z(k))\delta_{ijs}(k) \tag{31.17}$$

The three-input and single-output variable universe fuzzy controller from formula (31.5) as following:

$$\begin{aligned}\delta(k+1) = F(x(k), y(k), z(k)) = &\sum_{m=1}^{p}\sum_{t=1}^{q}\sum_{n=1}^{r}\sum_{i=1}^{p}\sum_{j=1}^{q}\sum_{s=1}^{r}\{A_i(x(k)/\alpha(x(k)))A_m(\alpha(x(k))x_i(0))\bullet \\ &B_j(y(k)/\beta(x(k), y(k)))B_t(\beta(x(k), y(k))y_j(0))y_j(0)\bullet \\ &C_s(z(k)/\phi(x(k), y(k), z(k)))C_n(\phi(x(k), y(k), z(k)))\delta_{mtn}(0)\end{aligned} \tag{31.18}$$

Remark 31.1 $F(x, y, z)$ corresponding monotonic with $x(k), y(k), z(k)$. That is, when $x(k) \to 0$, $y(k) \to 0$, $z(k) \to 0$ and $u(k+1) \to 0$, $\to$, it can ensure the effectiveness of control function.

31.4 Results and Analysis of Simulation

In this section, simulation results will be resented to verify the performance of the proposed adaptive fuzzy controller base on variable universe for ship course. For this purpose, it is interesting to compare the simplex method PID controller and the proposed in this paper, respectively.

The main parameters of the real ship: waterline length is 105 m, breadth is 12 m, draft is 3.3 m, displacement 2050 t, area of rudder is 15.4 m^2, speed is 18 kn. Contraction–expansion factor is $\alpha(x) = 1 - 0.8 \cdot \exp(-10\mu^2)$, simplex method PID parameters: $k_p = 2.24079$, $k_i = 0.02128$ and $k_d = 0.60533$. Under wave height $h = 2\,\text{m}$ and encounter angle $\alpha = 90°$, Figs. 31.2a, b are shown that simulation

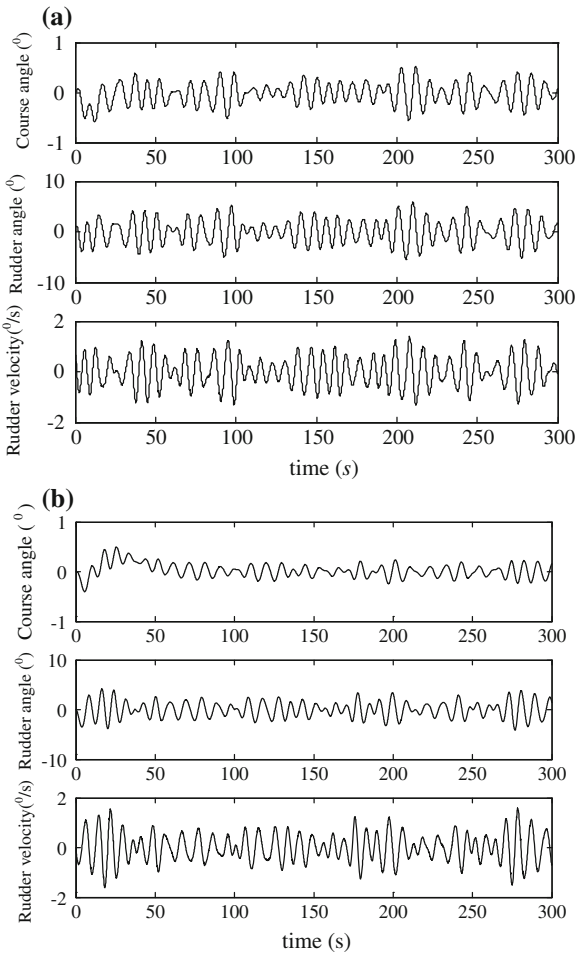

Fig. 31.2 Compare control for ship course ($h = 2\,\text{m}$, $\alpha = 90°$. **a** Simplex method PID control. **b** Fuzzy control with variable universe

Table 31.1 Statistics of simplex method PID and adaptive fuzzy control with variable universe

Statistics control method	Encounter angle	$E(\psi)$	STD(ψ)	$E(\delta)$	STD(δ)	$E(\dot{\delta})$	STD($\dot{\delta}$)
Simplex method PID	30°	–0.0079	0.5202	–0.0363	1.4760	–0.0077	0.9764
	90°	0.0018	0.3627	0.0039	1.0762	–0.0029	0.6511
	150°	0.0013	0.2790	0.0036	0.8366	0.0065	0.5027
Variable universe fuzzy control	30°	–0.0120	0.3134	0.0221	1.4382	–0.0092	0.9637
	90°	0.0091	0.1555	0.0180	0.9420	0.0032	0.6346
	150°	0.0082	0.0715	0.0058	0.8145	0.0065	0.5107

curve of the simplex method PID control and adaptive variable universe fuzzy control, respectively, simulation sampling time is 0.1 s.

Table 31.1 shows the ship course statistical values and simulation results by simplex method PID control and adaptive variable universe fuzzy control under different suffered waves, where $E(\cdot)$ is the mean, STD$(\cdot)$ is standard deviation, ψ is course angle, δ is rudder angle, $\dot{\delta}$ is rudder angle velocity, and angular dimension are degrees.

Figure 31.2 illustrates simulation results of simplex method PID controller for ship course when complex disturbances act on the ship. In Fig. 31.2, the first graph shows the desired and actual ship course, the second graph shows the rudder angle of steering; and the third graph shows response of the velocity of rudder angles. In this case the simplex method PID control performs bad ship course. In Fig. 31.2b, the comparison between adaptive fuzzy controller base on variable universe and simplex method PID control for ship course is presented. From Table 31.1, the results show that adaptive fuzzy controller base on variable universe has better performance in comparison with simplex method PID controller.

31.5 Conclusion

A simplex method PID control method and an adaptive fuzzy controller base on variable universe for the ship course are developed and compared. Simulations suggest that, in the presence of sea wave disturbances, ship angle standard deviation reduced by an average 10.82 %, while the rudder angle rudder angular velocity standard deviation and standard deviation change is not obvious, the steering is more reasonable. Simulation results have shown that this variable universe adaptive fuzzy method has better performance in comparison with simplex method PID controller for ship course especially in the presence of environmental disturbances (sea waves), it not only has high control accuracy, but have a more good adaptability and robustness. The benefits of the proposed approach that an adaptive fuzzy controller base on variable universe to better adjust to external disturbances and to

be insensitive to mathematical model(s) of the ship course. An adaptive fuzzy controller base on variable universe algorithm design process is simple, clearly physical meaning.

Acknowledgments This work is supported by the National Natural Science Foundation of China (No. 51409064, 51279036), and the Fundamental Research Funds for the Central Universities (HEUCF041565).

References

1. Fossen TI (2011) Handbook of marine craft, hydrodynamics, and motion control. Wiley, Chichester
2. Jianchuan YIN, Fang DONG, Tieshan LI et al (2010) Ship motion predictive PID control based on variable structure radial basis function network. Control Theor Appl 10 (27):1564–1568
3. Kahveci NE, Ioannou PA (2013) Adaptive steering control for uncertain ship dynamics and stability analysis. Automatica 49(3):685–697
4. Luo WL, Zou ZJ, Li TS (2009) Robust tracking control of nonlinear ship steering. Control Theor Appl 26(8):893–895
5. Liu Y, Guo C, Shen ZP et al (2010) Stable adaptive neural network control of path following for underactuated ships. Control Theor Appl (27)2:169–174
6. Peymani E, Fossen TI (2011) A lagrangian framework to incorporate positional and velocity constraints to achieve path-following control. In: 50th IEEE conference on decision and control and European control conference (CDC-ECC), Orlando, USA, PP 3940–3945
7. Yuan L, Wu HS (2010) Multiple-sliding-mode robust adaptive design for ship course tracking control. Control Theor Appl 27(12):1618–1622
8. Li TS, Yang YS, Hong BG et al (2007) Robust adaptive fuzzy design for ships track-keeping control. Control Theor Appl 24(3):445–448
9. Li HX (1999) Variable universe adaptive fuzzy controller. Sci China (Ser E) 29(1):10–20
10. Zhang W, Wang J, Wang H et al (2011) Research on the variable universe fuzzy algorithm of chaotic systems. Acta Phys Sin 60(1):10511-1–10511-9

Chapter 32
Alignment of MEMS in Civilian Vehicle Navigation

Yun Wang, Chun Yang and Lei Zhang

Abstract The integration of low-cost MEMS with GPS provides a more reliable velocity and position solution as the MEMS are able to propagate navigation state information during GPS outages in the urban environment. A convenient, practical method is proposed in this paper to implement the alignment of MEMS with the vehicle body frame. Special maneuvers of vehicle are restricted to estimate the mounting angles of roll, pitch, and yaw and the error analysis is implemented. Two classes of inertial sensors (SPAN-CPT and MTw) were tested in the repeated experiments to evaluate the property of aligning method. The testing experiments provide the alignment of roll and pitch within 1° and yaw within 2°, which is able to propagate navigation state information during the outages of GPS in civilian vehicle and improve the effectiveness of the integrated navigation system.

Keywords GPS · MEMS · Alignment · Integrated navigation

32.1 Introduction

GPS provides precise position and velocity information but narrowband radio frequency interference and signal attenuation will observably affect the steadiness of navigating process [1]. The advantages of MEMS are well known: position and velocity in high accuracy, high update rates within a short time. However, the data accuracy rapidly degrades with time due to the effect of various factors such as sensor biases, position drifts, and noises.

As these two systems possess complementary error characteristics, while GPS and MEMS are integrated [2], an accurate, drift-free, and high-resolution navigation system can be achieved for most outdoor situations.

Y. Wang (✉) · C. Yang · L. Zhang
College of Automation, Nanjing University of Science and Technology, Nanjing 210094, China
e-mail: wangyun2118@126.com

Z. Deng and H. Li (eds.), *Proceedings of the 2015 Chinese Intelligent Automation Conference*, Lecture Notes in Electrical Engineering 337,
DOI 10.1007/978-3-662-46463-2_32

Inertial Measurement Unit (IMU) requires alignment, some vehicle including factory-installed navigation systems that can contain IMU with known mounting angles. The present research applies to the large majority of vehicles without permanently installed navigation systems. The MEMS is aligned with the vehicle body frame (VBF), the first set of accelerometer and gyroscope is pointing in the forward/backward direction, the second set associates with the sides of the vehicle, and, finally, the third set is in the vertical direction [3].

A rapid transfer alignment method with linear models and linear filtering for arbitrary misalignment angles is presented in [4]. In reference [5], full observable Kalman filter is applied so that the horizontal attitudes (pitch, roll) errors and yaw error can be exactly evaluated within 80 and 100 s, respectively, while the random constant biases of gyroscopes and accelerometers can be precisely evaluated within 120 s. In reference [6], a new rapid transfer alignment method is implemented to improve the property of alignment.

Although some methods of alignment are proposed, they are presented with simulation. A practical method with experimental verification is proposed in this paper to verify the effectiveness of alignment.

32.2 Mounting Angle Estimation Methods

The angles that we need to estimate between the VBF and sensor frame are shown in Fig. 32.1. The first is yaw (ψ), followed by the pitch (θ), and the third is roll (ϕ) rotations.

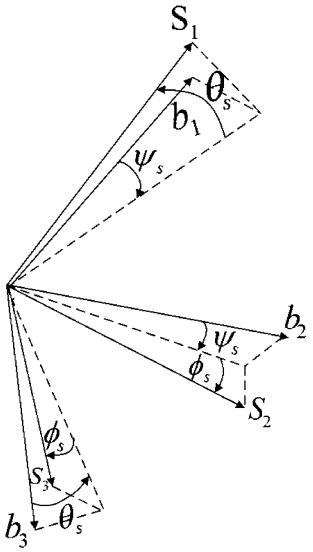

Fig. 32.1 Body to sensor frame angular rotations

The coordinate transformation matrix (CTM) which is used to translate body frame accelerations into the sensor frame is

$$C_b^s = \begin{bmatrix} c\theta_s c\psi_s & c\theta_s s\psi_s & -s\theta_s \\ c\psi_s s\theta_s s\phi_s - s\psi_s c\phi_s & c\psi_s c\phi_s + s\psi_s s\theta_s s\phi_s & c\theta_s s\phi_s \\ c\psi_s s\theta_s c\phi_s + s\psi_s s\phi_s & s\psi_s s\theta_s c\phi_s - c\psi_s s\phi_s & c\theta_s c\phi_s \end{bmatrix} \tag{32.1}$$

In Eq. (32.1) and in the subsequent section, s, c, and t separately represent sine, cosine, and tangent.

The vehicle is supposed to keep in contact with the road surface constrained so that the velocity is always in the forward (or lateral) direction. Gravity is close to act in the local down direction. So the specific force in the VBF is

$$f_b = \vec{a_b} + C_n^b \begin{bmatrix} 0 \\ 0 \\ -g \end{bmatrix} = \begin{bmatrix} A_{\text{forward}} \\ A_{\text{lateral}} \\ 0 \end{bmatrix} + C_n^b \begin{bmatrix} 0 \\ 0 \\ -g \end{bmatrix} \tag{32.2}$$

Translating the specific force to the sensor frame shows as

$$f_s = \begin{bmatrix} f_{s1} \\ f_{s2} \\ f_{s3} \end{bmatrix} = C_b^s f_b = C_b^s \begin{bmatrix} A_{\text{forward}} \\ A_{\text{lateral}} \\ 0 \end{bmatrix} + C_b^s C_n^b \begin{bmatrix} 0 \\ 0 \\ -g \end{bmatrix} \tag{32.3}$$

To estimate the roll and pitch mounting angle conveniently, the movement of the vehicle is restricted to make the roll and pitch of VBF with respect to the navigation frame extraordinary close to zero, which will be described in detail in the next section. To estimate the yaw mounting angle (ψ_S), the movement of the vehicle is restricted as follows:

1. Forward or backward on the horizontal road surface
2. Approximately known the orientation of the road surface.

32.2.1 Pitch and Roll Angle Estimation

While estimating the pitch and roll mounting angles, we restrict the vehicle to keep stationary on a horizontal road surface or traveling on a horizontal road surface without acceleration. As given in [7], pitch and roll angle are determined by

$$\theta_s = -a\tan\left(\frac{f_{s1}}{\sqrt{f_{s2}^2 + f_{s3}^2}}\right) \tag{32.4}$$

$$\phi_s = a\tan 2(f_{s2}, f_{s3}) \tag{32.5}$$

where f_{s1}, $f_{s2,}$ and f_{s3} are the forward, lateral, and down sensor frame accelerometer values. When these equations are used, errors in the mounting angle estimation are derived from an accelerating vehicle, biased sensor measurements, a tilted road surface. The magnitude of these errors is discussed in Sect. 32.3.

32.2.2 Yaw Angle Estimation

Once the roll and pitch mounting angles have been determined, they can be used to estimate the yaw mounting angle with two methods.

32.2.2.1 The First Method

While the vehicle is accelerating on an assumed horizontal road surface, with known forward acceleration, we can use the following method to estimate the yaw mounting angle. We must restrict the movement so that the lateral acceleration is close to zero. GPS components are used to identify whether the road surface is horizontal and also to identify the forward acceleration.

After translating acceleration from VBF to the sensor frame, the special force measurements on this occasion are modeled as

$$\begin{bmatrix} f_{s1} \\ f_{s2} \\ f_{s3} \end{bmatrix} = \begin{bmatrix} A_{\text{forward}} c\theta_s c\psi_s + g s\theta_s \\ A_{\text{forward}} c\psi_s s\theta_s s\phi_s - A_{\text{forward}} s\psi_s c\phi_s - g c\theta_s s\phi_s \\ A_{\text{forward}} c\psi_s s\theta_s c\phi_s + A_{\text{forward}} s\psi_s s\phi_s - g c\theta_s c\phi_s \end{bmatrix} \tag{32.6}$$

By eliminating $c\psi_s$ between the second and third equations, the yaw angle could be isolated as

$$s\psi_s = \frac{-f_{s2} + t\phi_s(f_{s3} + g c\theta_s c\phi_s) - g c\theta_s s\phi_s}{A_{\text{forward}} c\phi_s (1 + t^2 \phi_s)} \tag{32.7}$$

Forward GPS velocity component is applied to measure and calculate the value for A_{forward}.

32.2.2.2 The Second Method

If GPS velocity components are not available, we can use an alternate method (method 2) that does not explicitly require A_{forward}. Equation (32.8) is rearranged as follows:

$$\begin{bmatrix} \frac{f_{s1}-gs\theta_s}{c\theta_s} \\ f_{s2}+gc\theta_s s\phi_s \\ f_{s3}+gc\theta_s c\phi_s \end{bmatrix} = \begin{bmatrix} 1 & 0 \\ s\theta_s s\phi_s & -c\phi_s \\ s\theta_s c\phi_s & s\phi_s \end{bmatrix} \begin{bmatrix} B \\ C \end{bmatrix} \tag{32.8}$$

$$B = A_{\text{forward}} c\psi_s \tag{32.9}$$

$$C = A_{\text{forward}} s\psi_s \tag{32.10}$$

$$\psi_s = a\tan\left(\frac{C}{B}\right) \tag{32.11}$$

Methods 1 and 2 apply equally well to forward or backward acceleration cases. Only the value represented by A_{forward} would change.

32.3 Error Analysis

In this section, the effect of biased IMU and tilt of road on pitch, roll, and yaw from VBF to the sensor frame are assessed.

The pitch mounting angle error sensitivity to accelerometer bias while the road surface is horizontal could be derived from (32.4) as

$$\delta\theta_s \approx \frac{\delta f_{s1}}{g} \tag{32.12}$$

$\delta\theta_s$ is the resulting pitch mounting angle error (in radians) and δf_{s1} is the forward accelerometer bias (in g).

The roll mounting angle error sensitivity to accelerometer bias while the sensor is on a horizontal road surface is derived from (32.5) as

$$\delta\phi_s \approx \frac{-\delta f_{s2}}{g} \tag{32.13}$$

$\delta\phi_s$ is the resulting roll mounting angle error (in radians) and δf_{s2} is the lateral accelerometer bias (in g).

The estimation of the yaw mounting angle will be affected by the estimation of the roll and pitch mounting angles. The yaw mounting angle sensitivity errors during method 1 maneuver is found from (32.6) as

$$\delta\psi_s \approx \frac{-g\delta\phi_s}{A_{\text{forward}}} \tag{32.14}$$

$\delta\psi_s$ is the resulting yaw mounting angle error (in radians), $\delta\phi_s$ is the roll mounting angle estimation error (in radians), and A_{forward} is the magnitude of forward acceleration (in g).

32.4 Experiment

Static and dynamic movements of vehicle data were collected to evaluate the mounting angle estimation methods. There are two classes of accelerometers: consumer grade MEMS and tactical grade. The tactical grade accelerometers are part of NovAtel's SPAN (Synchronized Position Attitude Navigation) GPS/IMU system, which have a bias of ±1 mg. Accelerometers in MTw are uesd as consumer grade MEMS which are the focus of this research and they have a bias of ±50 mg.

Before estimating the mounting angle, the actual angle must be determined, a three-dimensional motion controller was used to producing pitch, yaw, and roll mounting angles relative to the VBF.

To evaluate the mounting angle estimation methods, the special repeated maneuvers were carried out to collect the export of IMU and GPS. The collection was performed on September 25, 2014 on a horizontal campus in Nanjing University of Science and Technology. The special repeated maneuvers are composed of a 30 s static portion and a forward acceleration on a horizontal road surface. Two experiments were separately repeated 10 times to test the mounting methods.

32.5 Results and Conclusion

This section presents experimental results from the collections, utilizing the proposed pitch, roll, and yaw mounting angle estimation methods.

Figure 32.2 shows values of three accelerometers of MTi 100-series while the MEMS sensors were static on a horizontal road. Table 32.1 shows the accelerometer triad roll and pitch mounting angle estimations from a 30 s static collection for both the SPAN-CPT and MTi 100-series accelerometers. The accelerometer readings were averaged prior to the roll (32.5) and pitch (32.4) estimation.

Figure 32.3 shows the values of one time of ten of 20 s forward accelerating MTi 100-series. Table 32.2 shows the results of yaw mounting angle estimation. Three estimating angles in Tables 32.1 and 32.2 are the average of ten times of experiment.

From the result in collection, we can find out that SPAN-CPT accelerometer output is more accurate than MTi accelerometer. Method 1 assumes knowledge of the forward acceleration, method 2 assumes estimation without that knowledge. Although method 1 seems to utilize more information in the form of acceleration from GPS than method 2, its results are not more accurate. An inspection of (32.7) shows that if the roll mounting angle is close to zero, the contribution of f_{s3} is

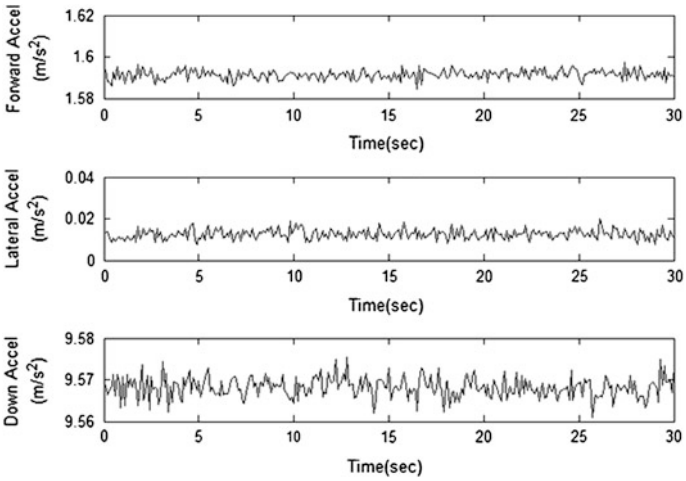

Fig. 32.2 Values of three accelerometers of 30 s static MTi 100-series

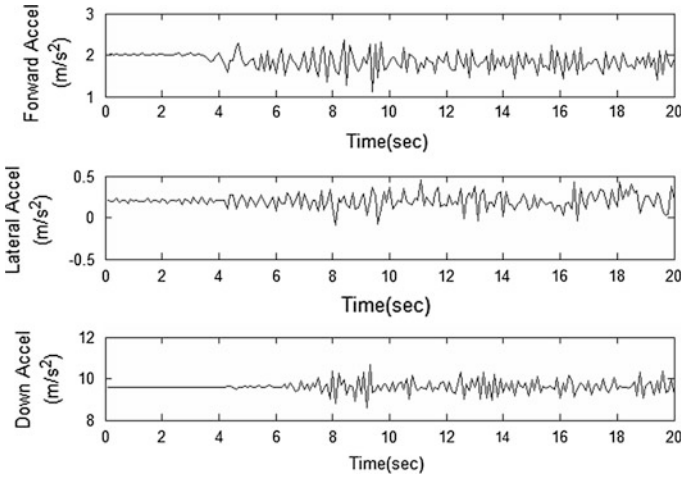

Fig. 32.3 Values of 20 s forward accelerating MTi 100-series

Table 32.1 Pitch and roll angle estimates

	Truth	SPAN	MTi
Pitch (°)	−9.43	−9.32	−8.57
Roll (°)	0.067	0.114	0.282

negligible, so only the f_{s1} sensor measurement is utilized. Method 2 efficiently cancels out A_{forward} at three sensor frame measurement and utilizes all accelerometers components.

Table 32.2 Yaw mounting angle estimates of 16.82° ture value using forward acceleration

	Ture	SPAN			MTi		
		Mean	STD	Mean	Mean	STD	Mean
Method 1	16.82	15.57	0.98	1.25	14.49	1.82	2.33
Method 2	16.82	17.62	-0.64	0.8	14.85	1.44	1.97

From the research of reference [6], ±15° misalignments with VBF which is allowable will cause less than 20 % of degradation as compared with the perfectly aligned IMU. The testing experiments provide the alignment of roll and pitch within 1° and yaw within 2°, which are well below ±15° so that MEMS are able to improve the effectiveness of the integrated navigation system.

References

1. Liu F, Liang L, Gao J (2014) Fuzzy PID control of space manipulator for both ground alignment and space applications. Int J Autom Comput 11:353–360
2. Chen Juming, Lin Yingchieh, Tsai MengHsiun, Lin Hsiaowei, Kuncheng Wu, Chen Muyen (2013) An automation system for bological squence agnment. Planet Sci Res Cent Conf Proc 37:18–22
3. Xu J, Wang Y, Xiao Z (2013) Rapid transfer alignment for SINS of carrier craft. J Syst Eng Electron 24(2):125–130
4. Zhao C (2014) New rapid transfer alignment method for SINS of airborne weapon systems. J Syst Eng Electron 25(2):111–117
5. Song L, Zhang C, Lu J (2014) Self-alignment of full skewed RINS: observability analysis and full-observable Kalman filter. J Syst Eng Electron 25(1):108–118
6. Syed Z, Aggarwal P, Niu X, El-Sheimy N (2008) Civilian vehicle navigation: required alignment of the inertial sensors for acceptable navigation accuracies. IEEE Trans Veh Technol 57(6):3402–3412
7. Groves P (2008) Principles of GPS, inertial, and multisensor integrated navigation systems. Artech House, Norwood

Chapter 33
Simulation Study of General Cargo Yard Layout

Lu Wu, Yu Zhang, Dongdong Wang and Zhixiong Liu

Abstract General cargo terminal operation system is a discrete event dynamic system with low operating efficiency. Aiming at solving the problem of low loading efficiency, this paper studied it from the perspective of yard layout. First, the yard's handling characteristics were analyzed and the status of the yard was summarized. Second, the current situations of terminals in China and abroad were reviewed. Then a simulation model was established using the block-based design method, whose research object is handling time. Lastly, it took an actual port cargo terminal as an example to test the simulation model. Based on the cargo layout and equipment configuration of the port, two kinds of yard layout schemes based on storage strategies were proposed. Analysis results show that allocating storage space can improve operation efficiency and save time.

Keywords Cargo terminal · Loading efficiency · Handling time · Yard layout · Simulation modeling

33.1 Introduction

Cargo handling efficiency is an important feature of a port. Generally speaking, according to its use and cargo characteristics, a modern port can be roughly organized into three categories: container terminal, bulk terminal, and general cargo wharf. Container terminal is a discrete operating system that takes containers as transport units and its types are standard, stacking simple, and operating equipment

L. Wu (✉) · Y. Zhang · D. Wang
Department of Logistics Engineering, Wuhan University of Technology, 1178#, Heping Road, Wuhan 430063, People's Republic of China
e-mail: 1226943050@qq.com

Z. Liu
School of Automobile and Traffic Engineering, Wuhan University of Science and Technology, 947#, Heping Road, Wuhan 430081, People's Republic of China

Z. Deng and H. Li (eds.), *Proceedings of the 2015 Chinese Intelligent Automation Conference*, Lecture Notes in Electrical Engineering 337,
DOI 10.1007/978-3-662-46463-2_33

specialization with high mechanization and automation efficiency. Bulk terminal is a continuous operating system, having specialized continuous transport machinery and equipment, transports granular or liquid cargo that are stacking simple, because it has continuous operation, working time is not affected by yard shift, and loading efficiency is higher. General cargo wharf is a discrete operating system whose cargoes are of various kinds, different sizes, and different ways to stack. In addition, unloading equipment, working tools, and unloading craft flow are multiple, with the random arriving time of ships, which makes the productive system of general cargo wharves diverse, comprehensive, uncertain, and dynamic [1], developing a problem confronted by many academic fields and port operators.

Luo [2] found that the planning and management of the warehouse is the weakest link and the general cargo yard is the bottleneck for the development of the whole port logistics system. The yard is the most complex part of a terminal [3]. The location of the general cargo yard and its internal structure are keys to the system's efficiency. Therefore, it is necessary to use advanced technology to study the general cargo yard.

Currently, research on container yard and bulk cargo terminal yard layout is relatively mature [4]. Several authors [5–8] have studied the container terminal and bulk terminal yard layout using planning technology that combines greedy construction, enumeration, and integer programming.

However, research on the general cargo yard is few. Handling efficiency is a key indicator of general cargo operations closely related with the yard layout [9]. In the domestic general cargo wharf, yard management level is still relatively backward. Authors [10] conclude goods stacking disorder in existing general cargo yards, without proper and effective function division of the yard. By contrast, the foreign port of groceries warehouse is better than the domestic situation, such as in Japan and the United States. A part of groceries warehouse storage spaces have been partitioned. Although computers are used to manage functions like planning and management, yet it has failed to achieve a systematic and standardized level [2].

General cargo wharf yard is the main place for goods handling and storage. Yard storage capacity and distribution capacity have important impacts on the general cargo wharf production capacity [10]. How to effectively use the resource in yard is one of the hot research topics. This paper proposed different general cargo yard layout schemes based on the research results of container yard and bulk terminal yard. Its impact on the general cargo terminal system was also studied.

33.2 Operating Characteristics of General Cargo

General cargo transport is an unsophisticated mode of transport with low levels of standardization and automation. The main characteristics are as follows:

(1) Drop and pull transport characteristics of horizontal transportation.

Drop and pull transport is a unique mode of transport that exists in general cargo terminals. It is defined as a trailer towing as a cycle with multiple carriages: a tractor

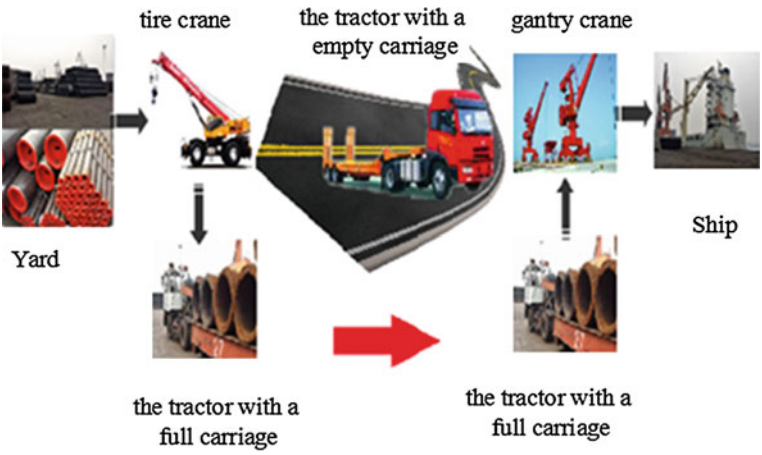

Fig. 33.1 Drop and pull transportation diagram

pulls a full carriage to the location where the gantry crane can reach. Then the tractor and full carriage are divided through the drop and pull function, the full carriage waits for unloading while the tractor moves to the empty carriage and pulls it to the location where the tire crane can reach. Thus, it works in a cycle. The schematic diagram is shown in Fig. 33.1.

(2) Operating lines distribution

After ship mooring, based on the hatches and the number of gantry cranes on the berth, the number of operating lines are determined. There is a limitation on the number of operating lines on the same yard because it will cause interference if many tire cranes are working in a yard at the same time.

(3) Berth distribution

The parameters of gantry cranes are so different that we have to distribute berths according to the rated capacity when ships arrive at port, to ensure that every gantry crane does not exceed the rated parameters. For example, the Tianjin Port general cargo terminal has specialized berths for handling large-scale machinery and equipment.

(4) Stacking standards

General cargoes are of various kinds, different sizes, and some of them cannot be pressed, which makes stacking complex. There are different ways to stack as shown in Fig. 33.2. On the other hand, we must consider the carrying capacity per unit area of the yard to limit the stacking height.

(5) Spreader replacement

There is no uniform standard that each good must have a corresponding spreader. If the loading cargoes change, the spreader will also be changed. Therefore, spreader standardization has become a hot issue worldwide.

Fig. 33.2 Stacking standards diagram

(6) Tire crane transitions

An operating line may be loading and unloading different kinds of goods or one kind of good, which have been distributed in different yards, so tire cranes need to move to another yard to complete the handling tasks.

(7) Gantry crane shifting berths

A hatch is equipped with an operating line, but if the number of gantry cranes on the berth is less than the number of hatches of a ship, there are still hatches waiting for service after opening all operating lines. In such circumstance, gantry cranes need to move to the adjacent hatch once they have completed the task.

33.3 Simulation Modeling

This paper uses eM-Plant software and adopts the block-based design method to establish simulation model. The whole operating process is divided into four modules as shown in Fig. 33.3.

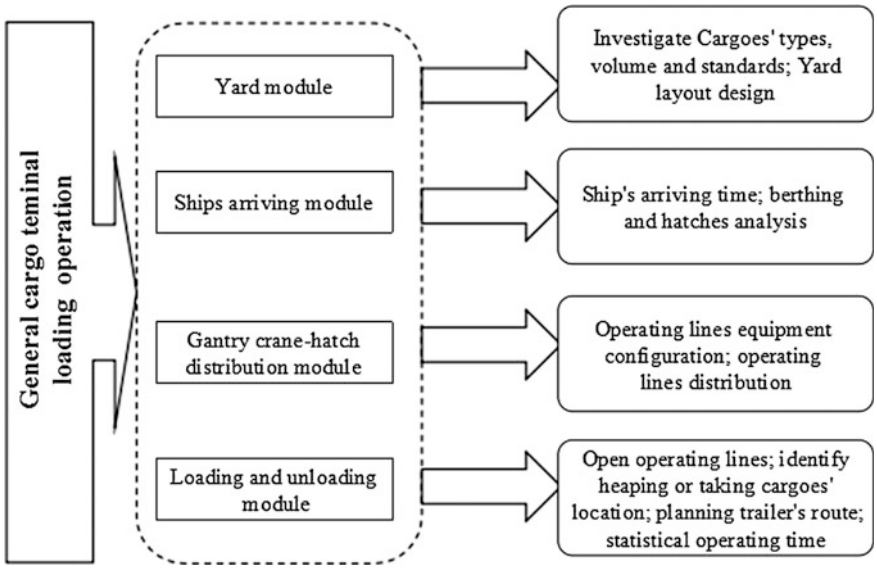

Fig. 33.3 Modeling ideas

33.3.1 Yard Module

In order to simplify the model, this paper only considered shipment processing, without considering the cargo collection process. After designing the yard layout, initialize the yard filled with goods. After working, if the quantity of goods cannot meet the requirement, the model will produce goods to make the yard filled with goods again.

(1) Goods analysis

Calculate the category and quantity, and then get the weight and number of each goods using formulas (33.1) and (33.2).

$$W_i = R \times p_i \tag{33.1}$$

$$N_i = \left\lfloor \frac{W_i}{w_i} \right\rfloor \tag{33.2}$$

W_i total weight of the goods
R yard's capacity
w_i single weight
p_i percentage of goods
N_i the number of goods

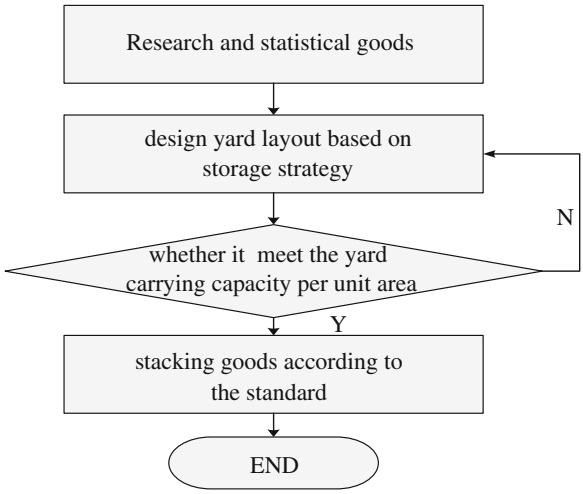

Fig. 33.4 Yard modeling process

(2) Storage strategy

Storage strategy is defined as the rules of goods stored in the storage area. There are two typical strategies for material storage in the warehouse space: fixed storage strategy and random storage strategy [11]. Fixed storage strategy refers to each type of goods stored in one (or more) fixed area, while random storage strategy refers to any kind of goods that can be stored in any vacant storage space.

(3) Modeling process

After analyzing the goods, the yard layout is designed based on the storage strategy. The modeling process is shown in Fig. 33.4.

33.3.2 Ship Arriving Module

This paper discusses the statistics parameters (arriving time, loading weight, hatch numbers, and so on.) of ships at port analyzes their distribution function. Then based on queuing theory it allows ships into port, allocates berths, and shows the loading requirements in the form of order. It is assumed that ships arrive at their scheduled times [12] without considering the natural phenomena during the sea journey [13]. The modeling process is shown in Fig. 33.5.

33.3.3 Gantry Crane-Hatch Distribution Module

Based on the ship's parameters berths are distributed, the number of operating lines is determined, mechanical equipment is deployed, and planning carried out. The modeling process is shown in Fig. 33.6.

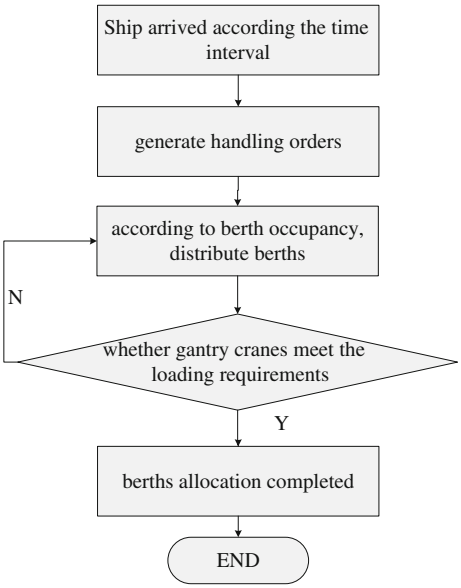

Fig. 33.5 Ships arriving module process

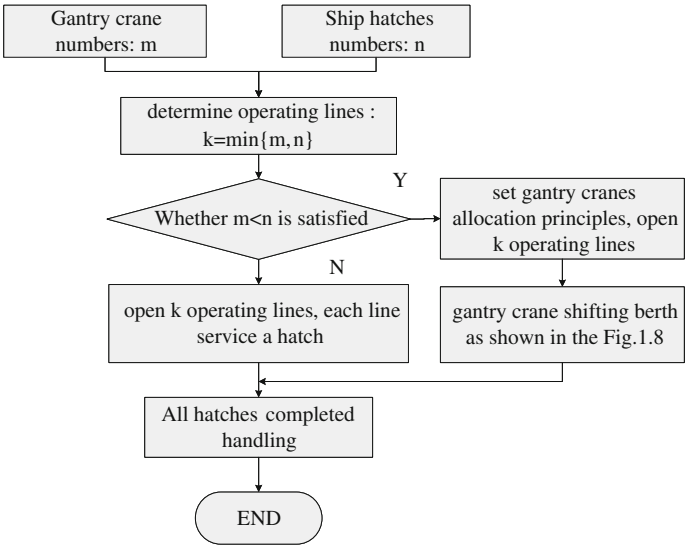

Fig. 33.6 Gantry crane-hatch distribution process

33.3.4 Loading and Unloading Module

This paper only studied the shipping process. The modeling process is shown in Fig. 33.7. In this module, gantry crane shifting berths and tire crane transition will appear. Their processes are shown in Figs. 33.8 and 33.9, respectively.

It was assumed that ships could be handled all day. The operating time is calculated using formulas from (33.3) to (33.6). After completing the handling task, the ships leave port.

$$t_{\text{trailer}} = \sum_{i=1}^{N} \left(\left\lceil \frac{N_i}{M_i} \right\rceil \times t_3 \right) \tag{33.3}$$

$$t_{\text{tire}}/t_{\text{gantry}} = t_{\text{hang}} + t_{\text{translate}} \tag{33.4}$$

$$t_{\text{hang}} = \sum_{\text{i}=1}^{N} \left(\left\lceil \frac{N_i}{k} \right\rceil \times t_2 \right) \tag{33.5}$$

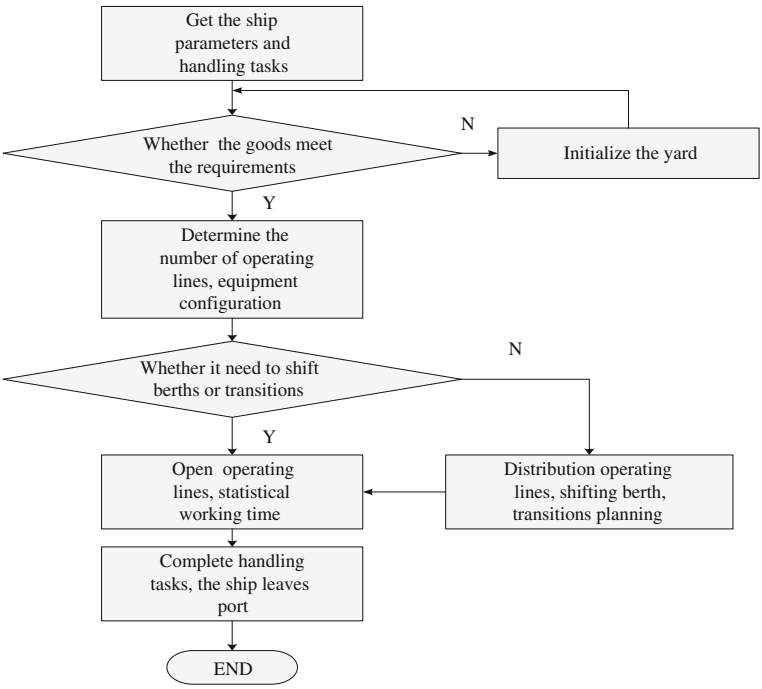

Fig. 33.7 Ship loading and unloading process

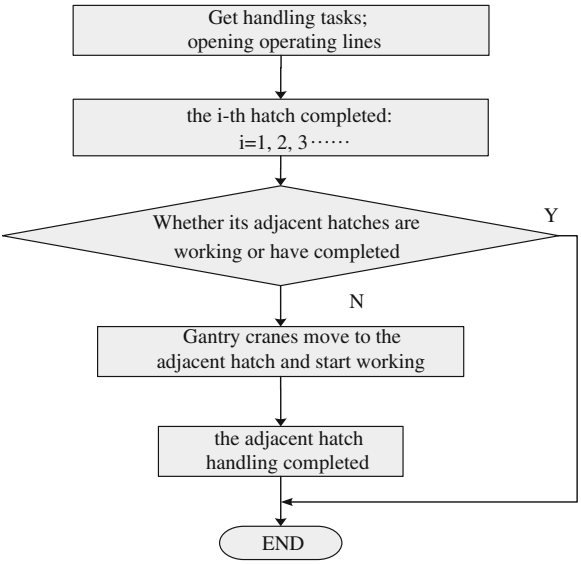

Fig. 33.8 Gantry crane shifting berths process

$$t_{\text{translate}} = \sum (n \times t_1) \tag{33.6}$$

N	the number of goods categories
$t_{\text{tire}}/t_{\text{trailer}}$	tire crane's working time/trailer's transport time
$t_{\text{translate}}/t_{\text{hang}}$	translating time/hanging time
n/k	transition times/lifting numbers
$t_1/t_2/t_3$	single transition time/single-hook operation time/horizontal transport time
N_i	the quantity of goods
M_i	trailer's rated load

A simulation model was established by linking each module. It sets the simulation time and records the loading and unloading time of operating lines. Then it accumulates the operation time of all ships that arrive in the simulation time, thus obtaining the total time of ship handling under different yard layout schemes. Lastly, it analyzes the simulation results and compares the efficiency of different schemes.

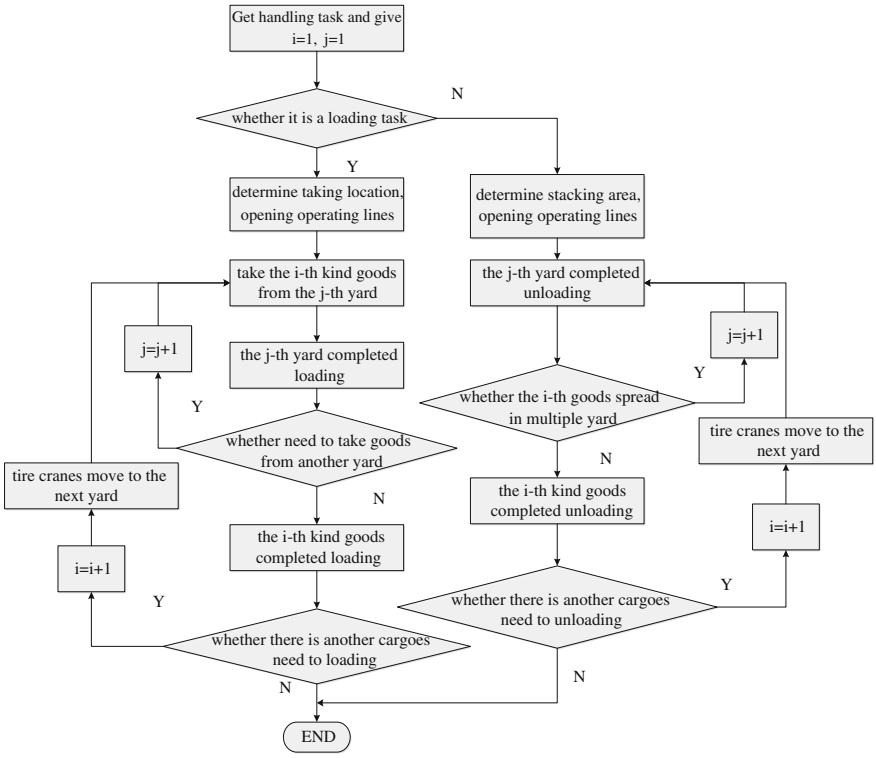

Fig. 33.9 Tire crane transition process

33.4 Case Study

33.4.1 Examples of Modeling

The actual port is a large comprehensive port that mainly transports bulk cargo, general cargo, and containers; general cargoes occupy the dominant position [14]. The general cargo terminal has 24 pieces of yard, which has already worked in overload status and "free to put" situation, making it more difficult to manage and reduce the handling efficiency. Therefore, studying the yard layout is of practical significance. It is possibly a powerful guideline for stockyard design. Yard layout picture is shown in Fig. 33.10.

Through investigation and analysis is obtained the simulation input data: 16 kinds of typical groceries and its properties; ship's arrival event obeys poisson flow, and its arrival time interval obeys negative exponential distribution: $\lambda = 6.5212$ h; loading weight obeys normal distribution with the average value of 7835.3872 *t* and standard deviation of 229.39568; the trailer full traveling at the speed of 25 km/h and empty driving at the speed of 15 km/h. After examination, hatch numbers do

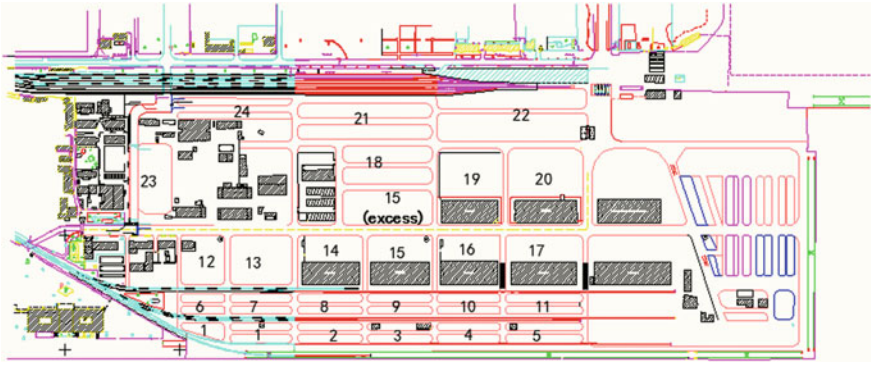

Fig. 33.10 Yard layout of the actual port general cargo terminal

not obey any normal distribution, to simplify the model, assuming it obeys the uniform distribution. According to the collected data, put forward two yard layout schemes, set the simulation parameters, and run the simulation model to get the corresponding simulation results.

33.4.2 Analysis of Simulation Results

In this paper, sequential procedure method [15] is used to determine the minimum number of simulations. Through calculation, we can draw the conclusion that the minimum number of simulations is $n = 7$. The simulation results are shown in Table 33.1.

Table 33.1 Simulation results records

Times Time(s) Yard layout	Random storage strategy	Fixed storage strategy
1	31300963.2	28493213.28
2	31203540.24	29123194.8
3	31367860.56	28786372.08
4	31119225.12	29183876.88
5	31439993.76	29545380.96
6	31462257.36	29524113.12
7	31203540.24	29123194.8

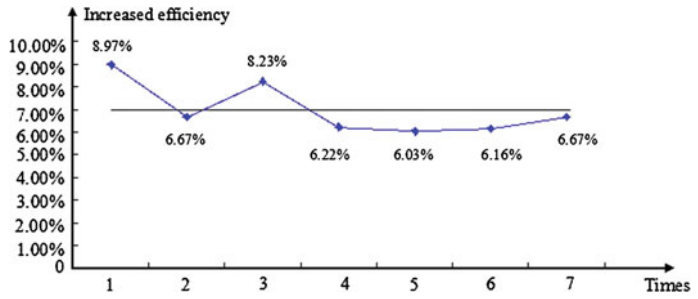

Fig. 33.11 Increased efficiency by changing the storage strategy

The analysis results show that the working time of fixed storage strategy is shorter than the random storage strategy. If we change the random storage strategy into fixed storage strategy, the loading efficiency can be increased to about 7 % as shown in Fig. 33.11.

33.5 Conclusion

This paper studied the general cargo terminal from the perspective of yard layout using the block-based design method. It proposed two methods to stack cargoes and simulate the actual production terminal for 1 year. The simulation results verified the feasibility of the model and provided a decision support for the yard layout design. However, this paper only studied the shipment process; further research can be carried out from the following aspects: (1) the time interval of cars and trains; (2) trailer's circular towing operation visualization problems; (3) traffic flow analysis; and (4) machine scheduling and allocation.

Acknowledgments This research has been partially funded by NSFC (No. 71372202).

References

1. Yang M (2009) General cargo port management practices[M]. Shanghai Press, Shanghai, pp 122–161 (in Chinese)
2. Luo H (2005) General cargo warehouse storage and optimize ship arrangement management [D]. A thesis Submitted to South China University of Technology (in Chinese)
3. Yong G, Dong M-w, Liu J-t, Huang H (2007) Simulation model of operation process in container yard and its application in design of container yard[j]. J Wuhan Univ Technol 31 (4):633–636 (in Chinese)
4. Mo Z-p, Wang Q-m (2003) Thinking about optimizing handling technology and reducing costs of General cargo terminal[J]. Port handling 3:15–18 (in Chinese)

5. Boland N, Gulczynski D, Savelsbergh M (2012) A stockyard planning problem[J]. Eur J Transp Logist 1:197–236
6. Kemme N et al (2013) Design and operation of automated container storage systems[M]. Springer-Verlag, Berlin, pp 52–86
7. Lee BK, Kim KH (2013) Optimizing the yard layout in container terminals[J]. OR Spectrum 35:363–398
8. Savelsbergh M, Smith O (2014) Cargo assembly planning. Eur J Transp Logist 3:20–34
9. Liu C (2013) Study of on operation optimization of Loading and Unloading of General cargo terminal[D]. A thesis submitted to Dalian Maritime University (in Chinese)
10. Yi Y-q, Liu Z-x (2012) Running analysis of storage yard operation for general cargo terminal [J]. Port technol 7:6–7 (in Chinese)
11. Zhou J (2011) Production system simulation: plant simulation application tutorial[M]. Publishing House of Electronics Industry, Beijing (in Chinese)
12. Jagerman D, Altiok T (2003) Vessel arrival process and queuing in marine ports handling bulk materials[J]. Queuing Syst 45:223–243
13. van Vianen T, Ottjes J, Lodewijks G (2014) Simulation-based determination of the required stockyard size for dry bulk terminals[J]. Simul Model Pract Theory 42:119–128
14. Zhang P (2011) Research on loading and unloading efficiency of general cargo terminal in Tianjin port[D]. A thesis submitted to Tianjin University (in Chinese)
15. Li W-F, Yuan B, Zhang Y (2010) Logistics system modeling and simulation [M]. Science and Technology Press, Beijing (in Chinese)

Chapter 34
Stowage Plan Research Based on Hierarchical Decomposition

Dongdong Wang, Yu Zhang, Lu Wu and Guangwei Tian

Abstract Based on the irregularity structure of the containership's bay and the characteristics of the container stowage problem with multiconstraint and multiobjective, the container stowage problem is divided into the master bay plan problem (MBPP) and the slot plan problem (SPP) by using the principle of hierarchical batch decomposition algorithm. For MBPP, the matching model between bay collection and container collection is developed, aiming to minimize the rehandles rate and trim moment. For SPP, it is major to confirm the specific stowage sequence with the aim of minimizing the expected rehandles rate and the specific stowage position in view of heeling moment in one bay. Then, a case of Port A terminal is testified via simulation. The result demonstrates that the simulation-driven model can follow the relevant strategy of shipment and achieve the goal of zero rehandles rate with satisfying related constraints of stowage.

Keywords Hierarchical batch decomposition · MBPP · SPP · Rehandles

34.1 Background

34.1.1 Introduction

Containership stowage is a multiconstrained and multiobjective combinatorial optimization problem. First, the safety of ship during sailing, such as stability, draft, strength, etc., needs to be put into consideration. Second, the size, weight, and

D. Wang (✉) · Y. Zhang · L. Wu
Department of Logistics Engineering, Wuhan University of Technology,
1178#, Heping Road, Wuhan 430063, China
e-mail: 775192278@qq.com

G. Tian
Department of Mechanical and Energy Engineering, Shanghai Tongji University,
4800#, CaoAn Road, Shanghai 200240, People's Republic of China

Z. Deng and H. Li (eds.), *Proceedings of the 2015 Chinese Intelligent Automation Conference*, Lecture Notes in Electrical Engineering 337,
DOI 10.1007/978-3-662-46463-2_34

destination of containers are also important factors. The unreasonable stowage will lead to the rehandles, which increase the large cost and time. So the reasonable arrangement of the container loading sequence and position, that is stowage plan, is extremely important [1].

Traditional stowage plan depends on the experience of workers and with the help of assistant check by computer (named as "Semi-automatic mode loading"). However, with the wide use of containers in the world and the size of containership constantly becoming larger, the container stowage problem becomes more complex, and the traditional stowage plan could not meet the actual demand anymore. The intelligent optimization and automation of container stowage have become the focus of research in related fields [2].

In recent years, many scholars try to solve the stowage plan with the use of the probabilistic simulation method [3], heuristic algorithm [4], integer linear programming model [5], and ant colony algorithm [6]. Their solutions have some shortcomings, like only considering a single target, simplifying structure of bay, and ignoring some constraints. However, the stowage plan is an actual application problem, the fundamental way is not only to optimize in theory, but also to realize intelligence.

In this paper, we studied the stowage problem under the irregular structure of bay in vessel.

34.1.2 Making the Stowage Plan

The hierarchical batch decomposition algorithm is used in this paper. The theory of algorithm is to break the large computing capacity and complex problem down into simple submodule layer. Each layer undertakes the task relatively independent, and a low-level layer can be called by a high-level layer to complete a specific function. Based on this theory, containership stowage problem is divided into MBPP and SPP.

MBPP is an NP-hard problem, it takes bay as research object under constraints that contain local strength, longitudinal strength, draft, principle of container stowage, then, achieves a reasonable match with the set of bays and the group of containers with low rehandles rate. MBPP is divided into two steps including getting initial overall stowage plan and optimizing the trim moment of vessel.

SPP is based on MBBP, which takes any of bays as the research object and ensures the containers load reasonably in the bay. The factors include stability, transverse strength, and the principle of container stowage. The SPP is broken down into two phases that are determining the initial stowage plan and optimizing heeling moment of each bay.

Combining two submodules, a reasonable match between collection of bays and a set of containers is obtained. The specific idea is shown in Fig. 34.1.

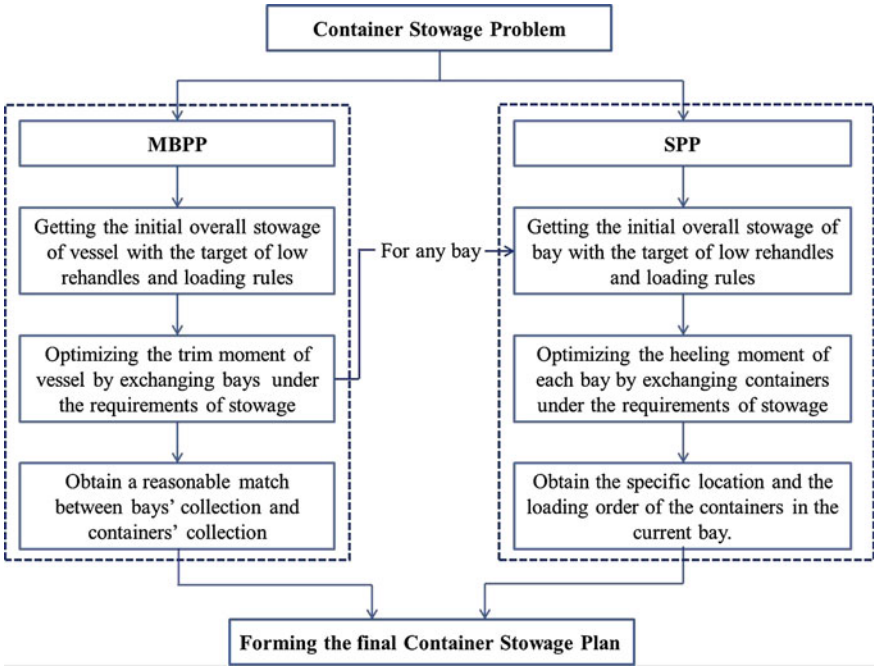

Fig. 34.1 Specific idea of making stowage plan

34.2 MBPP

MBPP is to make a minimum rehandles rate based on making full use of bay's weight and capacity, at the same time, it should meet the constraints including local strength, draft, and the principle of stowage.

34.2.1 The Initial Loading of MBPP

To simplify the MBPP, it can assume that the containership is empty, containers are 20′ or 40′, and the special containers are ignored. On the basis of the principles of stowage, the sequence rules of stowing containers are determined as follows:

Rule 1: the containers of far destination are loaded first.
Rule 2: load the 20′ containers first.
Rule 3: load the heavy containers first.
Rule 4: the bay in the middle of ship is loaded first.
Rule 5: leave 2 ∼ 3 bays as the interval, when the containers of the same port need to take up several bays.

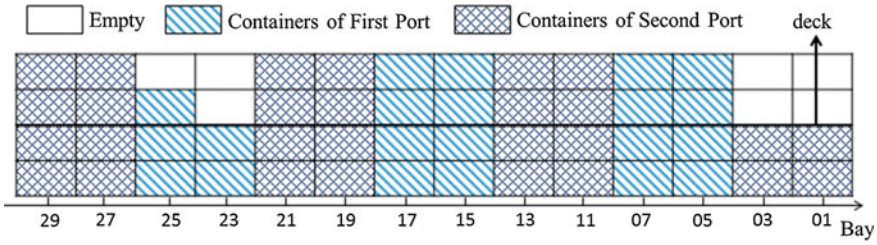

Fig. 34.2 Loading sequence with rules 4 and 5

Example with rule 4 and 5 in Fig. 34.2, it is cited in [5].

To sum up, the process chart of the loading is shown in Fig. 34.3. In Figure *A* presents the size of the container, and $j = 1, 2$.

34.2.2 Optimization of Ship Trim Moment

In the second step, reducing the trim moment of vessel is the goal; the local strength and the capacity of bay are regarded as the constraints. Meeting the conditions of the exchange and also exchanging the containers on the deck in any two different bays can reduce trim moment, until it finds the smallest trim moment of stowage scene. The conditions of the exchange are as follows:

$$\text{Objective}: \sum_{1}^{n/2} M_L - \sum_{n/2}^{n} M_R \propto 0 \tag{34.1}$$

$$\text{S.t.}: \text{Max}\left\{\sum\nolimits_{S_i}, \sum\nolimits_{S_j}\right\} \leq \text{Min}\{V_i, V_j\}; S_i, S_j, V_i, V_j \geq 0; i \neq \quad j; i,j \in B_i; \tag{34.2}$$

$$\text{Max}\left\{\sum\nolimits_{W_i'}, \sum\nolimits_{W_j'}\right\} \leq \text{Min}\{W_i, W_j\}; W_i', W_j', W_i, W_j \geq 0; i \neq \quad j; i, j \in B_i; \tag{34.3}$$

$$\sum_{1}^{n/2} M_L^m - \sum_{n/2}^{n} M_R^m \leq \sum_{1}^{n/2} M_L^{m-1} - \sum_{n/2}^{n} M_R^{m-1}; \tag{34.4}$$

Among them: M_L: trim moment of portside in ship; M_R: trim moment of starboard in ship; W_i, W_j: theoretical loading weight; V_i, V_j: theoretical capacity of Bay; $\sum_{S_i}$, $\sum_{S_j}$: the actual number of loaded containers; $\sum_{W_i'}$, $\sum_{W_j'}$: the actual loading weight of the containers; m: the number of exchanged containers; M_L^m: trim

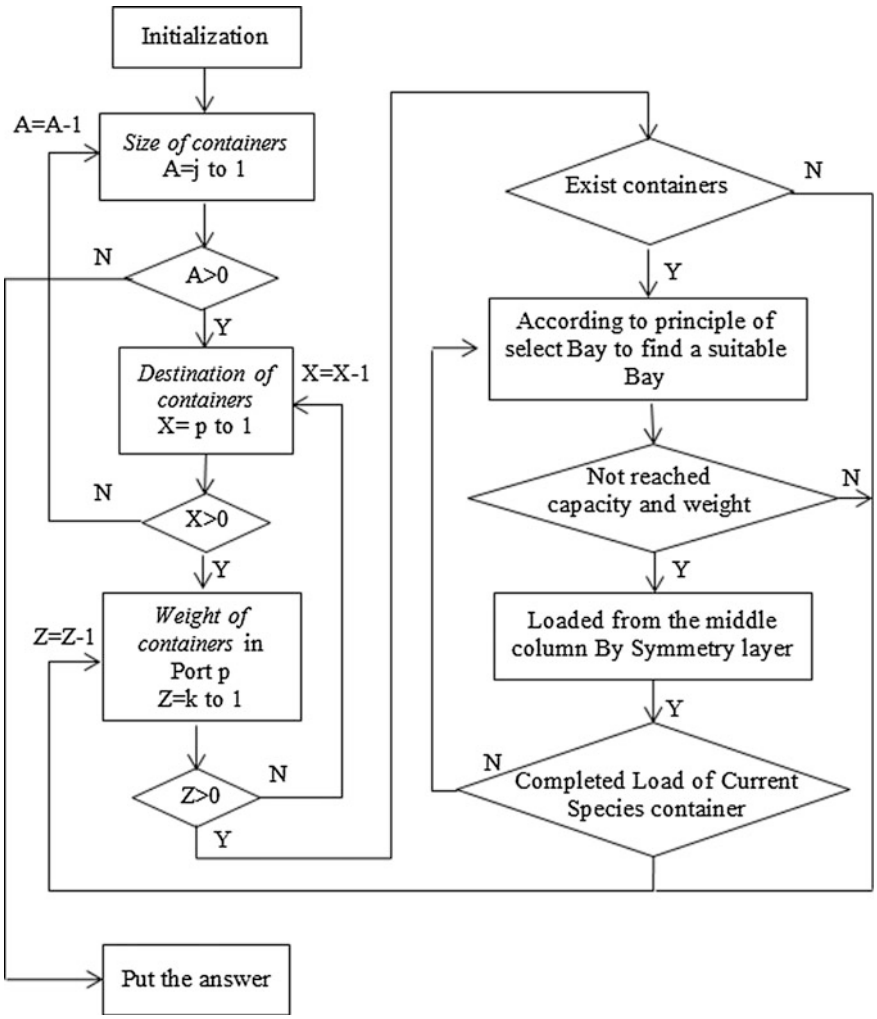

Fig. 34.3 The flow of the load

moment of portside after exchange m times; M_R^m: trim moment of starboard after exchange m times.

34.3 SPP

SPP is to determine the specific location and the loading order of the containers in the current bay.

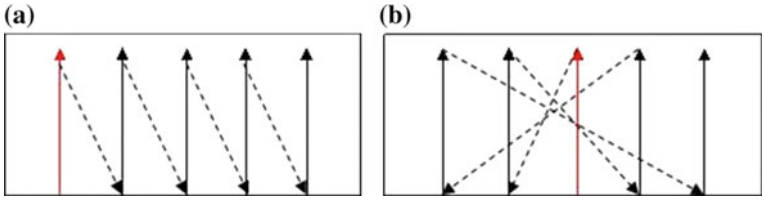

Fig. 34.4 **a** Loading strategy 1, **b** loading strategy 2

34.3.1 The Initial Loading of SPP

To meet the low rehandles rate and principle of loading containers, the process of loading in SPP is the same as in MBPP. In SPP, two kinds of loading strategy are proposed to find the better stowing plan. One is loading containers from left to right by column of bay, the principle of Fig. 34.4a. Another is loading containers from the middle by columns of bay, its principle is shown in Fig. 34.4b.

34.3.2 Optimization of the Bay Heeling Moment

The containers in different positions of bay will produce different heeling moment, so it can swap containers' positions in different columns to change heeling moment. The exchanging columns must meet the conditions as follows:

- The exchanging columns cannot be same.
- The number of containers must be less than the capacity of the new column.
- The columns must satisfy requirements of the local strength.
- Exchanging columns can reduce the value of heeling moment.

34.4 Examples of Verification and Analysis

In order to validate the feasibility and effectiveness of the model, an actual container terminal is used to test. The idea is shown in the Fig. 34.5.

34.4.1 Simulation and Analysis the Results of MBPP

The original loading list of actual container terminal is shown in the Table 34.1. According to the idea of the MBPP, test the simulation model. The changing trim moment is shown in Fig. 34.6.

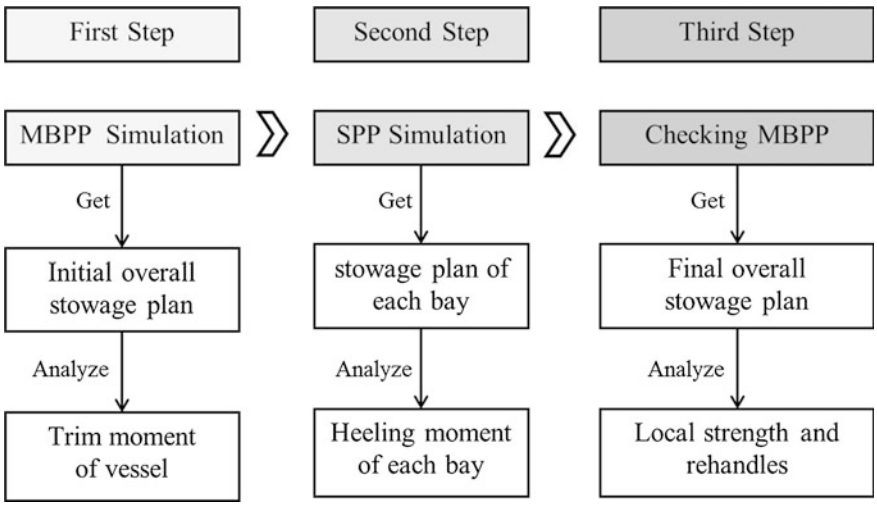

Fig. 34.5 The idea of simulation analysis

Table 34.1 The original loading list of actual container terminal

Destination	Total number (TEU)	Size (ft)	Number (TEU)	Light (TEU)	Medium (TEU)	Heavy (TEU)	TEUs
1	593	20	227	68	136	23	959
		40	366	109	220	37	
2	5	20	3	1	2	0	7
		40	2	0	2	0	
3	13	20	13	4	8	1	13
		40	0	0	0	0	
4	276	20	221	66	133	22	331
		40	55	17	32	6	
5	96	20	17	5	10	2	175
		40	79	24	47	8	

From Fig. 34.6, the trim moment is gradually decreasing and tending to zero. After 23 times optimization, it gets the smallest trim moment 772.42 F m.

34.4.2 Simulation and Analysis the Results of SPP

Considering the structure of bay as irregular, design the different kinds of stacking strategy simulation model of the SPP, and the model is tested by any of the bay. The weight attribute of containers in a bay is such as Table 34.2.

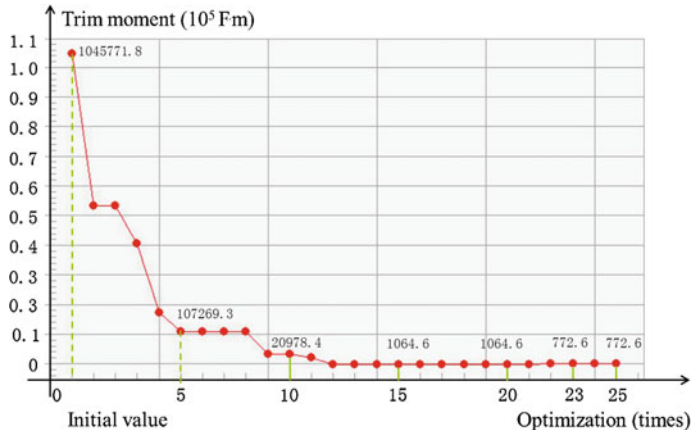

Fig. 34.6 Simulation result of the trim moment

Table 34.2 Container weight attribute in any of the bay

Container No	Weight	Container No	Weight	Container No	Weight	Container No	Weight
C1	22	C11	7	C21	24	C31	17
C2	16	C12	10	C22	10	C32	5
C3	27	C13	8	C23	27	C33	10
C4	23	C14	17	C24	20	C34	13
C5	11	C15	5	C25	21	C35	18
C6	16	C16	29	C26	23	C36	23
C7	17	C17	23	C27	9	C37	17
C8	8	C18	23	C28	27	C38	9
C9	24	C19	17	C29	24	C39	18
C10	19	C20	21	C30	23	C40	24

The simulation results are shown in Figs. 34.7 and 34.8 and the statistical result is shown in Table 34.3. The results showed that the heeling moment is obviously different with different stacking strategies, and loading containers from the middle is better than another, such as the initial and the final value of the heeling moment are smaller, and the number of optimizations is less.

34.4.3 Checking of MBPP

After optimizing each bay by the model of SPP, it is also need to check the requirement of MBPP. The local strength and the number of rehandles are shown in the Figs. 34.9 and 34.10, respectively.

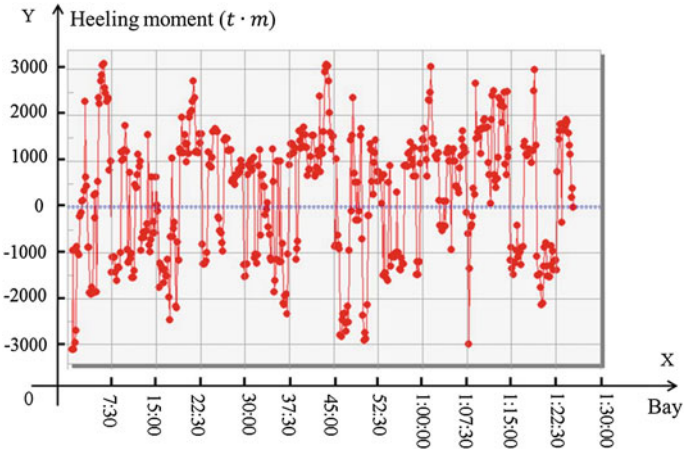

Fig. 34.7 Result of loading strategy 1

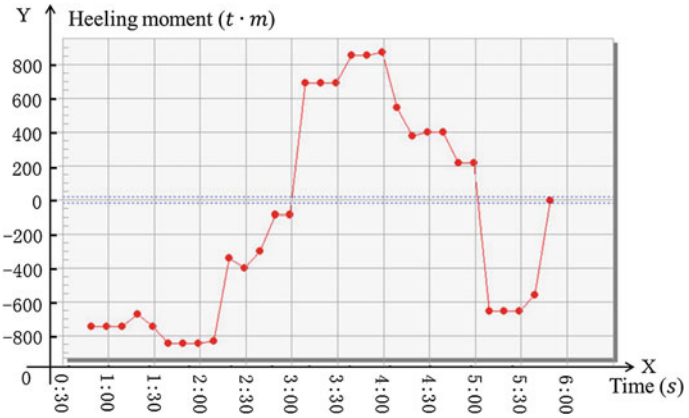

Fig. 34.8 Result of stacking strategy 2

Table 34.3 Statistical simulation results of different stacking strategy

Heeling moment	Stacking strategy 1	Stacking strategy 3
Before optimization (t m)	−3102.36	−774.81
Optimized (t m)	−18.285	−3.657
Refinements	509	31

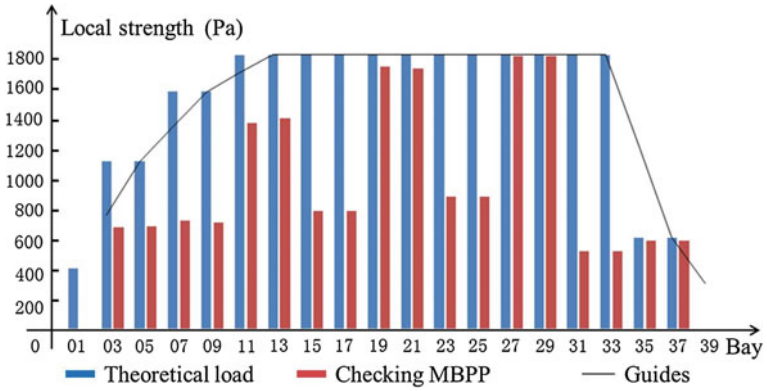

Fig. 34.9 The result of local strength

Fig. 34.10 The result of rehandles

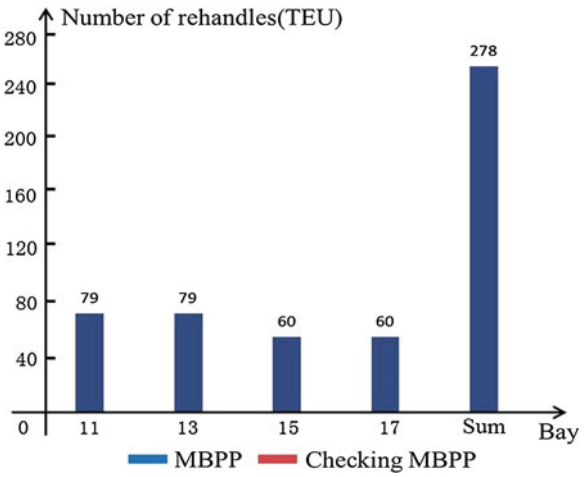

From Fig. 34.9, the local strength of each bay does not exceed the theoretical strength after optimization. From Fig. 34.10, it exists rehandles after MBPP, the numbers of rehandles reach to 278. But, the number is down to zero after SPP.

34.5 Conclusion

In this paper, the containership stowage issue is divided into two subproblems: MBPP and SPP by using the principle of hierarchical batch decomposition algorithm. An actual container terminal is testified via simulation. The results verify that the driver model is reasonable, and a stowage plan that can meet the

requirements of stowage is obtained. At the same time, After loading optimization, the trim moment of vessel, the heeling moment of vessel, and the local strength are all within a reasonable range and the rehandle rate drops from 28 to 0 %. Also, we find that the stowage strategy of loading in the middle can get a satisfactory value of heeling moment with less iterations. In addition, as the stowage plan is a part of the shipping line, this issue could be further studied on multiport stowage on the route in future.

Acknowledgments This research has been partially funded by NSFC (No. 71372202).

References

1. Pacino D (2013) An LNS approach for container stowage multi-port master planning. Comput Logist 8197:35–44
2. Yang J (2011) Stowage planning and integrating algorithm research in large container terminal. J Ocean Univ Chin 41(10):121–127 (in Chinese)
3. Hernández PH et al (2013) An ant colony algorithm for improving ship stability in the containership stowage problem. Advances in Artificial Intelligence, Springer, Berlin, vol 8266, pp 93–104
4. de Tavares AA, de Fernandes AE, de Leduino SNL et al (2013) Solution of the 3D stochastic stowage planning for container ships through representation by rules. In: Fourth international workshop proceedings. Atlantis Press, pp 120–129
5. Ambrosino D, Sciomachen A, Tanfani E (2006) A decomposition heuristics for the containership stowage problem. J Heuristics Springer Sci Bus Media LLC 12:211–233
6. Sun W (2013) An adaptive parallel genetic algorithm and its application in container ship stowage. Dalian maritime university (in Chinese)

Chapter 35
Decentralized Robust Predictive Control for Convex Polyhedral Uncertain Large-Scale Systems

Wenwen Guan, Chaoyong Jin and Liping Xie

Abstract When the system states are unmeasurable, the problem of decentralized robust predictive control with output feedback is studied for convex polyhedral uncertain large-scale system. By constructing the Lyapunov function, and with the idea of variable transformation and LMI methods, the infinite time domain "min-max" optimization problems are converted into convex programming problems. The sufficient conditions for the existence of this controller are derived. The controller enables the closed-loop large-scale systems robust stable. A simulation example shows the effectiveness of the control algorithm.

Keywords Robust predictive control · Uncertain large-scale systems · Decentralized control · Output feedback · Linear matrix

35.1 Introduction

Predictive control, a kind of optimal control algorithm, has to solve the optimization problem to get the controlled variable at each sample instant. However, it is different from the discrete optimal control algorithm. Instead of taking a global optimization target, predictive control applies the optimization strategy in which its time rolls forward on the limited time domain. The procedure is an iterative process [1]. Owing to the limited information structure, the centralized control often generates the problem of insufficient information. The predictive control can solve this problem well. As a result, centralized predictive control becomes a powerful tool for dealing with large system control. Many scholars have studied this problem and obtained good results [2, 3]. In [2], the author has studied the scattered generalized predictive algorithm of the interconnected large-scale systems by estimating the

W. Guan (✉) · C. Jin · L. Xie
School of Applied Mathematics, Guangdong University of Technology,
No 161 Ying Long Road, Guangzhou City, TianHe, China
e-mail: guanwenwen0725@163.com

Z. Deng and H. Li (eds.), *Proceedings of the 2015 Chinese Intelligent Automation Conference*, Lecture Notes in Electrical Engineering 337,
DOI 10.1007/978-3-662-46463-2_35

states of the subsystem. And in [3], the scholar puts forward the design method of decentralized predictive controller for time-delay large-scale systems. Robust predictive control is a kind of robust predictive control method which combines the fuse robust control of uncertainty processing method with the rolling optimization principle of predictive control. Many scholars have studied the robust control for a variety of uncertain systems with output feedback form or the form of state feedback, such as [4–8]. In [4], the author has studied the problem of robust predictive control of linear continuous-time norm-bounded parameter uncertain system by adopting variable change ideas and output feedback form. The essence of robust predictive control is online to solve a min-max optimization problem regarding the future of state and input system. In this paper, we will considerate the robust predictive control problem of convex polyhedral uncertain large-scale system. One of the important parts in this article is to show the specific derivation process of the expression on decentralized output feedback controllers by variable transformation method. Furthermore, the simulation effect is slightly better than Ref. [6], which is the most relevant to this paper. The stabilized time of system is shorter than literature [6] for nearly 1 s.

35.2 Problem Description and Lemma

Consider a convex polyhedral uncertain large-scale system S composed of L interconnected subsystems S_i. Each subsystem S_i is described as

$$\begin{cases} \dot{x}_i(t) = A_{ii}(t)x_i(t) + B_i(t)u_i(t) + \sum\limits_{j=1,j\neq i}^{L} A_{ij}(t)x_j(t) \\ y_i(t) = C_i(t)x_i(t) \\ \left[A_{ij}(t)|B_i(t)\right] \in \Omega \end{cases} \tag{35.1}$$

or $i = 1, 2, \ldots, L$, where $x_i(t)$, $u_i(t)$, and $y_i(t)$ are the state, control, and output vectors, respectively. $A_{ii}(t)$, $A_{ij}(t)$, $B_i(t)$, and $C_i(t)$ denote the system matrix, input matrix, and output matrix with appropriate dimensions, respectively. $A_{ij}(t)$ represents the interconnection matrix between the ith and the jth subsystems. Ω denote polyhedral model, and its concrete form is as follows:

$$\Omega = \left\{ \begin{bmatrix} A_{ij} & B_i \end{bmatrix} \middle| \left[A_{ij}(t)|B_i(t)\right] = \sum_{i=1}^{K} \lambda_i(t)\left[A_{ijl}(t)|B_{il}(t)\right], \sum_{i=1}^{K} \lambda_i(t) = 1, \lambda_i(t) \geq 0 \right\}$$

In this paper, our aim is to design a strictly real output feedback controller for each subsystems to guarantee the asymptotical stability of the closed-loop large-scale system. The form of the controller is as follows:

$$\begin{cases} \dot{\tilde{x}}_i(t) = A_{ci}\tilde{x}_i(t) + B_{ci}y_i(t) \\ u_i(t) = C_{ci}\tilde{x}_i(t) \qquad\qquad \tilde{x}_i(0) = x_i(0) \end{cases} \tag{35.2}$$

where $\tilde{x}_i(t) \in R^{n_i}$ is the state vector of the ith controller, A_{ci}, B_{ci}, C_{ci} are the pending coefficient matrix.

Substituting (35.2) into (35.1), we can get the closed-loop subsystem as follows:

$$\dot{\bar{x}}_i(t) = \bar{A}_i(t)\bar{x}_i(t) \tag{35.3}$$

where

$$\bar{x}_i(t) = \begin{bmatrix} x_i(t) \\ \tilde{x}_i(t) \end{bmatrix}, \quad \bar{A}_i(t) = \begin{bmatrix} \sum_{i=1}^{L}((A_{ii})_{ii}) + \sum_{j=1,j\neq i}^{L}((A_{ij})_{ij}) & B_iC_{ci} \\ B_{ci}C_i & A_{ci} \end{bmatrix}.$$

Then we chose the trundle optimization performance index of robust predictive control for large-scale system (35.1) as follows:

$$\begin{aligned} \min_{u(kT+\tau,kT),\tau\geq 0} J_k = \min\max \sum_{i=1}^{L} \int_0^{\infty} & (x_i^T(kT+\tau,kT)Q_ix_i(kT+\tau,kT) \\ & + u_i^T(kT+\tau,kT)R_iu_i(kT+\tau,kT))\mathrm{d}\tau \end{aligned} \tag{35.4}$$

where $Q_i > 0$, $R_i > 0$ are given symmetric positive definite matrixes.

Substituting $u_i(kT+\tau,kT) = C_{ci}\tilde{x}_i(kT+\tau,kT)$ into (35.4), then the optimization problems attribute to follows:

$$\min_{u(kT+\tau,kT),\tau\geq 0} J_k = \min\max \sum_{i=1}^{L} \int_0^{\infty} \left(\bar{x}_i^T(kT+\tau,kT)\bar{C}_i^T\bar{C}_i\bar{x}_i(kT+\tau,kT)\right)\mathrm{d}\tau \tag{35.5}$$

where

$$\bar{x}_i(kT+\tau,kT) = \begin{bmatrix} x_i(kT+\tau,kT) \\ \tilde{x}_i(kT+\tau,kT) \end{bmatrix}, \quad \bar{C}_i = \begin{bmatrix} Q_i & 0 \\ 0 & R_i^{\frac{1}{2}}C_{ci} \end{bmatrix}.$$

Construct a Lyapunov function with parameters of the independent in the following form:

$$V(\bar{x}_i(t)) = \bar{x}_i^T(t)P_i(\lambda)\bar{x}_i(t)$$

where $P_i(\lambda) = \sum_{i=1}^{L} \lambda_i(t) P_i$ and P_i is given symmetric positive definite matrix with appropriate dimensions. And ρ_1, ρ_2 meet the conditions as follows [9]:

$$\rho_1 \leq \lambda_{\min}(P_i(\lambda)) \leq \rho_2, \rho_1 > 0, \rho_2 > 0$$

At each sampling time kT, we assume that V satisfies following condition:

$$\frac{\mathrm{d}}{\mathrm{d}\tau} V(\bar{x}_i(kT + \tau, kT)) \leq -\bar{x}_i^T(kT + \tau, kT)\bar{C}_i^T \bar{C}_i \bar{x}_i(kT + \tau, kT) \tag{35.6}$$

In order to ensure that the performance index is a limited value, we let $\bar{x}_i(\infty, kT) = 0$, then $V(\bar{x}_i(\infty, kT)) = 0$. And we do the integration for τ from 0 to T for formula (35.6) of both sides and when $T \to \infty$, we can have

$$\bar{x}_i^T(kT + \tau, kT) P_i(\lambda) \bar{x}_i(kT + \tau, kT) \to 0$$

then

$$V(\bar{x}_i(kT)) \geq \int_0^{\infty} \left(-\bar{x}_i^T(kT + \tau, kT)\bar{C}_i^T \bar{C}_i \bar{x}_i(kT + \tau, kT)\right) d\tau.$$

Obviously, $\sum_{i=1}^{L} V(\bar{x}_i(kT))$ is the least upper bounds of max J_k.

Let

$$V(\bar{x}_i(kT)) = \bar{x}_i^T(kT) P_i(\lambda) \bar{x}_i(kT) \leq TrP_i(\lambda) \tag{35.7}$$

where $TrP_i(\lambda)$ is the trace of $P_i(\lambda)$. Then the problem of minimizing the optimization performance index is converted to figure out the minimization num of $\sum_{i=1}^{L} TrP_i(\lambda)$. Equivalently, it is min $\sum_{i=1}^{L} TrP_i(\lambda)$.

Lemma 35.1 (Schur complement lemma) *F is the given symmetric positive definite matrixes as follows*:

$$F = \begin{bmatrix} A & B^T \\ B & C \end{bmatrix}$$

where $A \in R^{n \times n}$, $B \in R^{m \times n}$, $C \in R^{m \times m}$, $F = F^T \in R^{(n+m) \times (n+m)}$, and the following conditions are equivalent:

$$(1)F > 0, (2)A > 0, C - B^T A^{-1} B > 0, (3)C > 0, A - B^T C^{-1} B > 0$$

35.3 Main Result

Theorem 35.1 *Consider system* (35.1). *If the inequality constraints* (35.6) *were established at each sampling time kT, then the closed-loop optimization problem* (35.5) *can be converted into optimization problems* (35.8–35.10):

$$\min_{\lambda, M_i, \bar{A}_i, \bar{C}_i} \sum_{i=1}^{L} TrP_i(\lambda) \tag{35.8}$$

$$\text{s.t} \quad \begin{bmatrix} 1 & \bar{x}_i^T(kT) \\ \bar{x}_i(kT) & M_i \end{bmatrix} > 0 \tag{35.9}$$

$$\begin{bmatrix} M_i^T \bar{A}_i^T + \bar{A}_i M_i & M_i^T \bar{C}_i^T \\ \bar{C}_i M_i & TrP_i(\lambda) \end{bmatrix} > 0 \tag{35.10}$$

where

$$\bar{A}_i = \begin{bmatrix} \sum_{i=1}^{L} ((A_{ii})_{ii}) + \sum_{j=1, j\neq i}^{L} ((A_{ij})_{ij}) & B_i C_{ci} \\ B_{ci} C_i & A_{ci} \end{bmatrix}, \quad M_i = (TrP_i(\lambda)) P_i^{-1}(\lambda)$$

In Theorem 35.1, since A_{ci}, B_{ci}, C_{ci} with other variables in the form of nonlinear coupled together, therefore, it is difficult to determine them directly. Hence we convert them to linear relationship by the variable transformation thought [10]. First, do the following decomposition of M_i and M_i^{-1}, as follows:

$$M_i(\lambda) = \begin{bmatrix} M_{i1}(\lambda) & M_{i2}(\lambda) \\ M_{i2}^T(\lambda) & M_{i3}(\lambda) \end{bmatrix}, M_i^{-1}(\lambda) = \begin{bmatrix} N_{i1}(\lambda) & N_{i2}(\lambda) \\ N_{i2}^T(\lambda) & N_{i3}(\lambda) \end{bmatrix}$$

where $M_{i1}(\lambda)$ and $N_{i1}(\lambda)$ are symmetric positive definite matrixes. By $M(\lambda)M^{-1}(\lambda) = I$, we have

$$M_{i2}(\lambda) N_{i2}^T(\lambda) = I - M_{i1}(\lambda) N_{i1}(\lambda) \tag{35.11}$$

Therefore, we can get $N_{i2}^T(\lambda)$ and $M_{i2}(\lambda)$.

Definite new variables as follows:

$$\begin{cases} \hat{A}_i = N_{i1} A_i M_{i1} + N_{i2} A_{ci} M_{i2}^T + \hat{B}_i C_i M_{i1} + N_{i1} B_i \hat{C}_i \\ \hat{B}_i = N_{i2} B_{ci} \\ \hat{C}_i = C_{ci} M_{i2}^T \end{cases} \tag{35.12}$$

Theorem 35.2 *Consider system* (35.1). *At each sampling time kT, adopting the output feedback controller* (35.3), *the optimization problems* (35.8–35.10) *can be converted into following optimization problems*:

$$\min_{\lambda,\hat{A}_i,\hat{C}_i,M_{i1},N_{i1}} \sum_{i=1}^{N} TrP_i(\lambda). \tag{35.13}$$

$$s.t \quad \begin{bmatrix} 1 & \bar{x}_i^T(kT) \\ \bar{x}_i(kT) & M_i \end{bmatrix} > 0 \tag{35.14}$$

$$\begin{bmatrix} J_{11} & J_{12} \\ J_{12}^T & J22 \end{bmatrix} < 0 \tag{35.15}$$

where

$$J_{11} = \begin{bmatrix} J_1 & A_i^T + \hat{A}_i \\ A_i + \hat{A}_i^T & J_2 \end{bmatrix}, \; J_1 = N_{i1}A_i + A_i^T N_{i1} + \hat{B}_i C_i + C_i^T \hat{B}_i^T$$
$$J_2 = M_{i1}A_i + A_i^T M_{i1} + B_i \hat{C}_i + \hat{C}_i^T B_i^T$$
$$J_{12} = \begin{bmatrix} Q_i & 0 \\ M_{i1}Q_i^{\frac{1}{2}} & M_{i2}C_{ci}^T R_i^{\frac{1}{2}} \end{bmatrix}, J_{22} = \begin{bmatrix} -\frac{1}{TrP_i(\lambda)}I & 0 \\ 0 & -\frac{1}{TrP_i(\lambda)}I \end{bmatrix}$$

Proof By Lemma 35.1, we can get formula (35.10)

equivalently,

$$M_i\bar{A}_i^T + \bar{A}_i M_i + M_i^T \bar{C}_i^T (TrP_i(\lambda))^{-1} \bar{C}_i M_i < 0$$

then the above inequality is multiplied by $(\bar{C}_i M_i)^{-T}$ on left side and $(\bar{C}_i M_i)^{-1}$ on right side as well, we have

$$\bar{C}_i^{-T}\left(\bar{A}_i^T M_i^{-1} + M_i^{-T}\bar{A}_i\right)\bar{C}_i^{-1} - \left(-\frac{1}{TrP_i(\lambda)}I\right) < 0.$$

Substituting the decompose matrixes of M_i and M_i^{-1} into above inequality, then

$$\begin{bmatrix} Q_i^{-\frac{T}{2}} & 0 \\ 0 & R_i^{-\frac{T}{2}} C_{ci}^{-T} \end{bmatrix} \begin{bmatrix} Z_{11} & Z_{12} \\ Z_{21} & Z_{22} \end{bmatrix} \begin{bmatrix} Q_i^{-\frac{1}{2}} & 0 \\ 0 & C_{ci}^{-1} R_i^{-\frac{1}{2}} \end{bmatrix} - \begin{bmatrix} -\frac{1}{TrP_i(\lambda)} & 0 \\ 0 & -\frac{1}{TrP_i(\lambda)} \end{bmatrix} < 0$$

where

$$Z_{11} = A_i^T N_{i1} + C_i^T B_{ci}^T N_{i2}^T + N_{i1}^T A_i + N_{i2} B_{ci} C_i \; ; \quad Z_{12} = A_i^T N_{i2} + C_i^T B_{ci}^T N_{i3}^T + N_{i1}^T B_i C_{ci} + N_{i2} A_{ci};$$
$$Z_{21} = C_{ci}^T B_i N_{i1} + A_{ci}^T N_{i2}^T + N_{i2}^T A_i + N_{i3}^T B_{ci} C_i; \quad Z_{22} = C_{ci}^T B_i N_{i2} + A_{ci}^T N_{i2} + N_{i2}^T B_i C_{ci} + N_{i3}^T A_{ci}$$

Let

$$J_{12} = \begin{bmatrix} Q_i & 0 \\ M_{i1}Q_i^{\frac{1}{2}} & M_{i2}C_{ci}^T R_i^{\frac{1}{2}} \end{bmatrix}, J_{22} = \begin{bmatrix} -\frac{1}{TrP_i(\lambda)} & 0 \\ 0 & -\frac{1}{TrP_i(\lambda)} \end{bmatrix}$$

then the above inequality is multiplied by J_{12} on left side, meanwhile, multiply J_{12}^T on right side, we have

$$\begin{bmatrix} I & 0 \\ M_{i1} & M_{i2} \end{bmatrix} \begin{bmatrix} Z_{11} & Z_{12} \\ Z_{21} & Z_{22} \end{bmatrix} \begin{bmatrix} I & M_{i1}^T \\ 0 & M_{i2}^T \end{bmatrix} - J_{12}J_{22}J_{12}^T < 0$$

By

$$M_{i1}N_{i1} + M_{i2}N_{i2}^T = I,\ M_{i2}^T N_{i2} + M_{i3}N_{i3} = I, M_{i1}N_{i2} + M_{i2}N_{i3} = 0\ ,\ M_{i2}^T N_{i1} + M_{i3}N_{i2}^T = 0,$$
$$N_{i1}M_{i1} + N_{i2}M_{i2}^T = I,\ N_{i2}^T M_{i2} + N_{i3}M_{i3} = I\ ,\ N_{i1}M_{i2} + N_{i2}M_{i3} = 0,\ N_{i2}^T M_{i1} + N_{i3}M_{i2}^T = 0.$$

then we can get

$$J_{11} - J_{12}J_{22}J_{12}^T < 0$$

By Lemma 35.1, we can get formula (35.15). Hence, Theorem 35.2 is proved.

Hence, we can conclude the algorithm of output feedback decentralized robust predictive control as follows:

Step1: Selecting $t_k (k = 0, 1, 2, 3, \ldots)$ and T which satisfy $t_k = kT$, then let $k = 0$

Step2: At sampling time kT, by solving optimization problems (35.13), we obtain the variables $\hat{A}_i, \hat{B}_i, \hat{C}_i\ , M_{i1}, N_{i1}$, and the variables M_{i2}, N_{i2} can be figured out by formula (35.11)

Step3: Substituting the matrixes $\hat{A}_i, \hat{B}_i, \hat{C}_i\ , M_{i1}, N_{i1}, M_{i2}, N_{i2}$ into formula (35.12), we can figure out A_{ci}, B_{ci}, C_{ci} of controller (35.3)

Step4: Substituting $A_{ci}, B_{ci,} C_{ci}$ into formula (35.2), based on system (35.1), we can figure out the state prediction $x_i(kT + \tau, kT)$, output prediction $y_i(kT)$, and the state prediction of the controller (35.3) for the sampling period $kT + \tau$

Step5: Based on the prediction of $\tilde{x}_i(kT + \tau, kT)$ and $y_i(kT)$, repeat Step1–Step4.

35.4 Stability Analysis

Lemma 35.2 [11] There is symmetric positive matrix $P \in R$, and the formula $A^T P + PA < 0$ is set up, then the system $\dot{x}(t) = A(t)x(t)$ is stable.

Lemma 35.3 [9] Any feasible solution of the optimization in Theorem 35.2 for time kT is also feasible for all sampling time $NT(N > K)$.

By Theorem 35.2, we can get the output feedback controller matrices $A_{ci}^k, B_{ci}^k, C_{ci}^k$, when k changes from 0 to ∞, we can receive the output feedback control sequence $\left\{A_{ci}^k, B_{ci}^k, C_{ci}^k\right\}$ orderly. By Lemma 35.3, we can know that the feasibility of the solution of optimization problem (35.13) can be guaranteed by the feasible solution of the sampling time. Substituting $\left\{A_{ci}^k, B_{ci}^k, C_{ci}^k\right\}$ into system (35.1), we can get the closed-loop subsystem as follows:

$$\dot{\bar{x}}_i(t) = \bar{A}_i(t)\bar{x}_i(t) \tag{35.16}$$

Theorem 35.3 *Assume that the solution of optimization problem* (35.13) *is feasible. Then the closed-loop system* (35.14) *is stable.*

Proof The piecewise continuous Lyapunov function of closed-loop system is

$$V(\bar{x}_i(t)) = \bar{x}_i^T(t)P_i(\lambda)\bar{x}_i(t)$$

By Theorem 35.2, we have

$$\bar{A}_i^T P_i(\lambda) + P_i(\lambda)\bar{A}_i + \bar{C}_i^T \bar{C}_i \leq 0$$

thus

$$\bar{A}_i^T P_i(\lambda) + P_i(\lambda)\bar{A}_i < 0$$

By Lemma 35.2, we can conclude that the closed-loop system (35.14) is stable. Hence, Theorem 35.3 is proved.

35.5 Simulation Example

Consider subsystems 1 with

$$\begin{aligned}&\left[A_{11}, A_{12}, B_1\right] \in \Omega_1 \\ &= \left\{\left(\begin{bmatrix}1 & 2.5\\ 2 & 2\end{bmatrix}, \begin{bmatrix}-1 & 0.5\\ 1 & 1\end{bmatrix}, \begin{bmatrix}0.5\\ -1.5\end{bmatrix}\right), \left(\begin{bmatrix}1 & 0.5\\ -0.5 & 2\end{bmatrix}, \begin{bmatrix}1 & -0.5\\ -0.5 & 1\end{bmatrix}, \begin{bmatrix}1.5\\ 4.5\end{bmatrix}\right)\right\},\end{aligned}$$

and subsystems 2 with

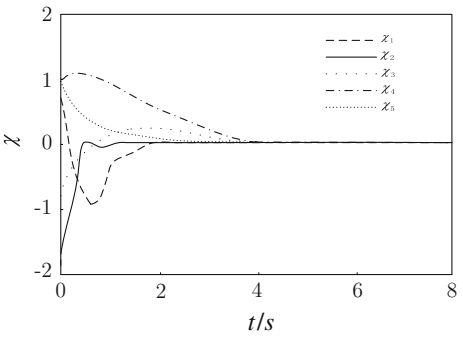

Fig. 35.1 The state of closed-loop system curve

$$[A_{22}, A_{21}, B_2] \in \Omega_2 = \left\{ \left(\begin{bmatrix} 0 & 0.3 & 1 \\ -1 & 0.5 & 2 \\ 0.1 & -1 & 1 \end{bmatrix}, \begin{bmatrix} 1.5 & -1 & 0 \\ 0 & 2 & 1 \\ -1 & -1 & 0.5 \end{bmatrix}, \begin{bmatrix} -1 & 0.5 \\ -0.5 & 1 \\ 1 & -0.5 \end{bmatrix} \right), \left(\begin{bmatrix} 2 & 0.1 & 0.2 \\ 1 & 1.5 & 0 \\ 0.3 & 1 & 1 \end{bmatrix}, \begin{bmatrix} 0.5 & 0.6 & 0.4 \\ 2 & 0 & 1 \\ 1 & 3 & 2 \end{bmatrix}, \begin{bmatrix} 1 & 0.5 \\ -1.5 & -1 \\ 0 & -1 \end{bmatrix} \right) \right\}$$

$$C_1 = [1 \quad 0], C_2 = \begin{bmatrix} 0 & 0.5 & 1 \\ 1 & 0.5 & 1 \end{bmatrix}, x_{10} = [1.8 \quad 0.6 \quad 1.2 \quad 0.4]^T,$$

$$x_{20} = [1 \quad 0.2 \quad 1.2 \quad 0.9 \quad 0.6 \quad 0.9]^T$$

Choose the sampling period

$$T = 0.3\text{s}, Q_1 = I_{2\times 2}, R_1 = I, Q_2 = I_{3\times 3}, Q_2 = I_{3\times 3}, R_2 = 0.5I_{2\times 2}$$

by the above algorithm and the toolkit of LMI of *Matlab* [12], we can obtain

$$A_{c1} = \begin{bmatrix} -6.6624 & 5.4446 \\ -38.6415 & 31.5699 \end{bmatrix}, B_{c1} = \begin{bmatrix} -1.9816 \\ -11.4934 \end{bmatrix}, C_{c1} = [-0.6469 \quad -5.5310]$$

$$A_{c2} = \begin{bmatrix} -5.5591 & 3.7821 & 7.5585 \\ -29.6653 & -1.2207 & -1.9320 \\ -15.1346 & -16.8271 & -34.2251 \end{bmatrix}, B_{c2} = \begin{bmatrix} 0.9653 & -0.3310 \\ 1.8933 & -2.3847 \\ -1.6327 & -1.6834 \end{bmatrix},$$

$$C_{c2} = \begin{bmatrix} 0.1046 & 1.0415 \\ 0.3957 & -0.0013 \end{bmatrix}$$

The following simulations reveal that the output feedback robust predictive control algorithm, which is designed on the method of LMI, can solve the problem of the unpredictable system parameter uncertainty effectively by selecting the proper sampling period and make the closed-loop system achieve stability under meeting the constraint condition (Figs. 35.1, 35.2 and 35.3).

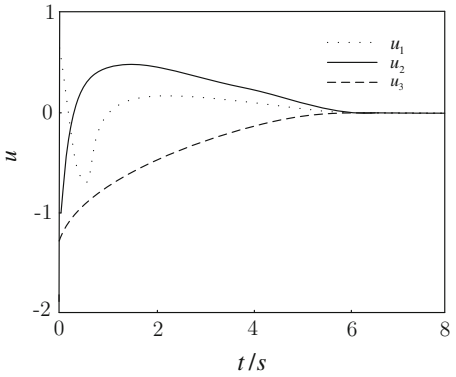

Fig. 35.2 The input graph

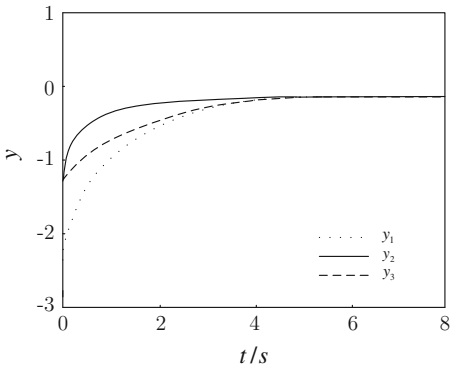

Fig. 35.3 Closed-loop system output curve

35.6 Conclusion

In this paper, we study the design problem of the convex polyhedral uncertain large-scale system with state matrix and the associated matrix is convex polyhedral uncertain. We can deduce matrix inequality conditions for the existence of the controller from adopting the variable transformation thought. By solving the linear matrix inequality, the controller can make the closed-loop system robust stability. The simulation results verify the effectiveness of the algorithm.

References

1. Chen H (2013) Model predictive control. Science Press, Beijing
2. Katebi MR, Johnson MA (1997) Predictive control design for large-scale systems. Automatica 33(3):421–425
3. Yang YH, Liu XH (2007) Decentralized predictive control for interconnected time-delay system based on LMI. Ludong Univ J (Nat Sci Ed) 32(2):111–113 (in Chinese)

4. Han CY, Liu XH (2006) Robust predictive control for uncertain continuous-time system based on output feedback. Inf Control 35(6):721–725 (in Chinese)
5. Liu XH, Wang LJ (2009) Robust model predictive control for uncertain singular systems via dynamic output feedback. Control Decis 24(9):1371–1376 (in Chinese)
6. Liu XH, Jing YF, Yang YH (2014) Decentralized robust predictive control for uncertain singular large-scale systems. Control Decis 29(4):719–724 (in Chinese)
7. Ding BC, Xi YG, Cycowskii MT, O'Mahony T (2008) A synthesis approach for output feedback robust constrained model predictive control. Automatica 44(1):258–264
8. Zhang LQ, Huang B (2004) Robust model predictive control of singular systems. IEEE Trans Autom Control 49(6):1000–1006
9. Jamal D, Jacques B (2001) Parameter dependent Lyapunov functions for discrete time systems with time varying parametric uncertainties. Syst Control Lett 43(5):355–359
10. Evn TJ, Do CO, Jong HK, Hong BP (1996) Robust controller design for uncertain systems with time delays: LMI approach. Automatica 32(8):1229–1231
11. Wu M, He Y, Yu JH (2010) Robust control theory. Higher Education Press, Beijing
12. Yu L (2002) Robust control linear matrix inequality approach. Tsinghua University Press, Beijing

Chapter 36
Research on Natural Gas Pipeline Leak Detection Algorithm and Simulation

Daiyong Zhou

Abstract In order to improve detection accuracy and reduce false alarm rate, research on gas pipeline leakage algorithm has extremely important significance. In this paper based on long pipe negative pressure wave algorithm, the adaptive Kalman filter detection method is proposed, which can overcome the shortage of wavelet transform method. An adaptive detection model is established using the data collected by pressure sensor. The location of leakage point can be calculated by time difference between the upstream and downstream through the Kalman Filter. The relative error and false alarm rate are estimated. Experimental results show that the improved method can reduce the false alarm rate. The adaptive Kalman filter detection method provides a useful method for the detection of natural gas pipeline leakage.

Keywords Negative pressure wave · Wavelet transform · Adaptive Kalman filtering · Detection technology

36.1 Introduction

Natural gas is a necessary energy in people's daily life, and is closely related to people's life. As energy fuel distributed by the state it has received immense social attention today; natural gas is the most important energy being a clean green energy and being supplied directly to millions of households through gas pipelines. Because of the flammable characteristics of natural gas, it is mainly transported by pipelines [1]. The safe transportation of natural gas is a problem that must be solved as it has become the focus of people's worry and the country attaches great

D. Zhou (✉)
College of Automation, Chongqing University of Posts and Telecommunications, Chongqing no. 2 Chongwen Road, Nan'an District, Chongqing 400065, People's Republic of China
e-mail: zhoudaiyong123@163.com

Z. Deng and H. Li (eds.), *Proceedings of the 2015 Chinese Intelligent Automation Conference*, Lecture Notes in Electrical Engineering 337,
DOI 10.1007/978-3-662-46463-2_36

importance to this concern. Because there are unavoidable pipeline transportation potential factors such as pipeline corrosion, aging pipes, and accidental damage that may cause gas leaks to occur at any time, normal delivery cannot be allowed from the pipeline as it may cause heavy casualties. Recent news reports convey that pipeline leaks can have serious impacts on people's liveswith heavy financial loss to the country; thus the study of natural gas pipeline leak detection technology has become a hotspot.

The natural gas pipeline transport can be divided into long pipeline transportation for cities; different pipeline leak detection method are used which makes a great difference. This article is a study of the leak methods for long natural gas pipelines. The long gas pipeline always uses negative pressure wave leak detection algorithm, this method being simple in principle with the ability to apply strong, high sensitivity without the establishment of relevant mathematical model on detection [2]. However, the negative pressure wave detection algorithm is particularly sensitive to rapid sudden leakage situation, such as large leaks or man-made destruction. In the tiny leakage or slow leakage situation it is not very sensitive. In such detection methods where there are a lot of potential crises, the following visible problems exist:

(1) Pipeline in negative pressure wave propagation velocity v is not constant, in addition to the propagation velocity and also the compressibility of the gas, the elastic wall of the pipe and the pipe wall friction factor closely linked.

(2) Noise interference in the natural environment, using the pressure sensor to accurately detecting negative pressure wave singularity is difficult and leads to the lack of negative pressure wave propagation time Δt which is the difference accuracy.

(3) Long pipeline during normal operations such as start–stop switch will cause negative pressure wave propagation conditions; the algorithm can distinguish normal identify switch start–stopped the negative pressure wave, which can effectively reduce the rate of false positives and provide the basis to improve detection accuracy [3].

To solve the problems mentioned above, and taking into account the pressure within the gas flow velocity that will affect the situation, can be gradually an iterative approximation algorithm that locate leak points with a small parameter as evaluation criteria, it is possible to improve the accuracy of location. For natural gas pipeline the inspection method is as follows. Ge and Wang [4] used a physical model based on gas pipeline, combined with the negative pressure wave amplitude along the pipeline approximate exponential decay mechanism, an assessment of the proposed gas pipeline leak detection, and location system performance index method (minimum detectable amount of leakage). This method can solve the situation of small leaks in gas pipeline. Niu and Zhang [5] proposed a real-time model on natural gas long pipeline detection, leak location to locate the pipeline. Zhang and Gao [6] used wavelet transform negative pressure wave signal which occurs when the acquired pipeline leak has noise reduction, captures the negative pressure wave signal singularity, calculates the location of the leak points, and improves the positioning accuracy. Methods in the literature are from the detection accuracy of performance evaluation system.

However, for long gas pipeline algorithm based on negative pressure wave pipeline leak studies, this paper is based on negative pressure wave adaptive Kalman filter algorithm with performance of the natural gas pipeline from the detection accuracy and false alarm rate evaluation system.

36.2 Adaptive Kalman Filtering Algorithm

Adaptive Kalman filter realizes the basic tasks of filtering and prediction information processing, time domain filter parameters also need to be able to track over time to update and adapt to the dynamic environment, where the parameters are updated using recursive way [7]. In the adaptive filter, statistical capacity algorithm, statistical power tracking systems, ability to adapt to the dynamic changes of the environment, in practical application are important [8]. Thus, for natural gas pipeline leak detection, in addition to the natural gas pipeline has a lot of noise outside, but also has a data flow when gas pressure sensor to collect gas concentration changes cannot accurately detect or measure in case of false positives and prone to leakage, in order to solve this series of questions, the use of adaptive Kalman filter effectively avoids these problems. The algorithm can track changes in the system or the environment to detect leaks and optimize system performance. The Kalman filter prediction process is

$$x(k+1) = H(k+1,\, k)x(k) + v(k) \tag{36.1}$$

The observation process is

$$y(k) = C(k)x(k) + w(k) \tag{36.2}$$

where $v(k)$ is the process noise vector, $w(k)$ is the observation noise vector, $v(k)$ and $w(k)$ are white noise and uncorrelated.

Adaptive Kalman filter prediction method uses an even number to predict an odd number of sequences, the prediction method constructs an odd number of sequences and is original even sequence linear minimum mean square error estimation. Based on Formulas (36.1) and (36.2) the prediction equation is obtained.

$$x_j(2n+1) = H(2n+1,\ 2n)x_j(2n) + v(2n) \tag{36.3}$$

we can get the observation equation as

$$y(2n) = C(2n)x_j(2n) + w(2n) \tag{36.4}$$

In the least squares even sequence given observation $y(0),\ y(2), \ldots, y(2n-2)$ can be obtained and observation vector $y(2n)$ is estimated as

$$\overline{y_1}(2n) = \overline{y_1}(2n|y(0),\ y(2), \ldots, y(2n-2)) \tag{36.5}$$

Updating of prediction data is found in the following expression:

$$a(2n) = y(2n) - \overline{y_1}(2n) \qquad n = 0, 1, 2, \ldots \tag{36.6}$$

Thus the data update sequence $a(2n)$ and observational data are orthogonally related and the correlation matrix is expressed as

$$R(2n) = E\{a(2n)a^H(2n)\} \tag{36.7}$$

Calculate the even number sequence forecast estimates that predict to estimate the observation data using an even number sequence linear combination structure of an odd number of forecast update process [9], forecast an odd sequence in which the minimum mean square estimate is

$$\hat{s}_{j,1} = H(2n+1, 2n)\hat{s}_{j,1}(2n) + G(2n)a(2n) \tag{36.8}$$

By the above formula, the error covariance of adaptive Kalman filter is

$$P_{k+1|k+1} = (I - K_{k+1}H)P_{k+1|k} \tag{36.9}$$

Formula (36.8) by using an even number sequence adaptive Kalman filter prediction methods of odd number of columns visible, $H(2n+1,\ 2n)\hat{s}_{j,1}(2n)$ determining the value of the nonadaptive, $G(2n)$ is adaptive gain matrix, and $G(2n)a(2n)$ determines the value of a nonadaptive.

36.3 The Experimental Results and Analysis

The gas pipeline inspection system is for performance evaluation, in addition to precision leak detection and location, as well as pipeline inspection false positive rate, which are the essential performance evaluation parameters of natural gas pipeline inspection system. This paper uses the adaptive Kalman filter compared with the literature [3] wavelet transform method. Where the literature [3] used wavelet transform pressure sensor to the data processing, the corresponding simulation results are as follows (Fig. 36.1).

In the natural gas pipeline based on adaptive Kalman filter leak detection method, the acquisition by the pressure sensor to the pressure signal, and the pressure signal collected for storage, adaptive Kalman filter pressure signal for data analysis and filtering, detected are their leaks case. When leaks occur early warning system is not only timely, but can also be able to find the location of pipeline leaks and provide important information to repair the pipeline. Pipeline leaks detection using adaptive Kalman algorithm flowchart is shown in Fig. 36.2.

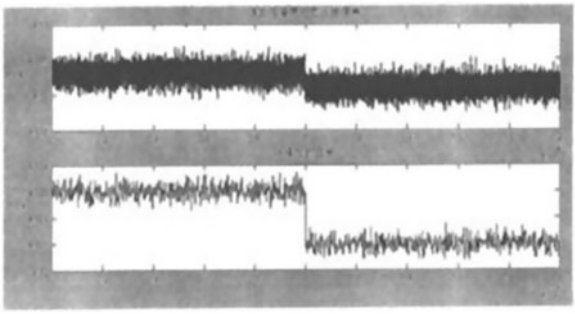

Fig. 36.1 Wavelet transform of the simulation

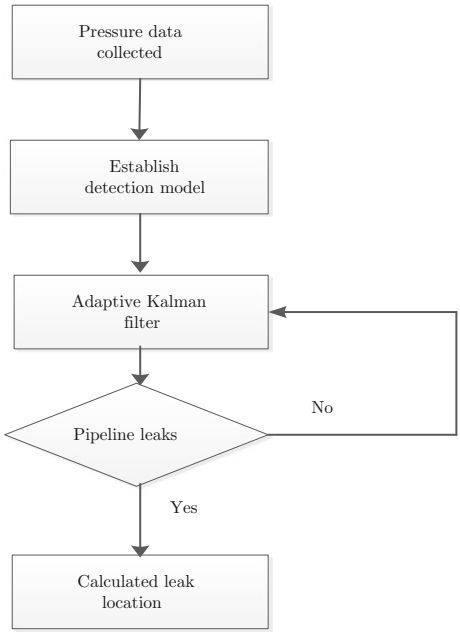

Fig. 36.2 The adaptive algorithm flowchart

After pipeline leak, the upstream end of the negative pressure wave signals received are nonstationary signals with noise. The use of adaptive Kalman filter for signal denoising and tracking can accurately locate the leak, and accurately detect leak onto the downstream sensor negative pressure wave propagation time. Adaptive filter algorithm gas pipeline leakage detection simulation is shown in Fig. 36.3.

The experiment results analysis shows that the error of the algorithm to detect pipeline leakage point and the rate of false positives are shown in Table 36.1.

Figures 36.1 and 36.3 and Table 36.1 show that natural gas pipeline detection method based on negative pressure wave is prone to false positives, pipeline leak point accuracy is not good enough, but based on adaptive Kalman filter method

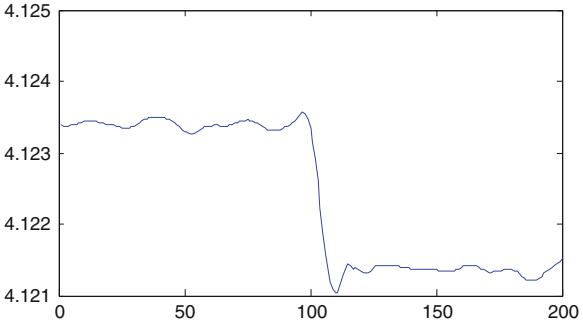

Fig. 36.3 The simulation of adaptive algorithm

Table 36.1 The result of experimental data

	The evaluation index	
	Positioning error (%)	The rate of false positives (%)
Negative pressure wave	1.99	1.5
The adaptive method	0.11	0.4

used to detect natural gas pipeline, whether from false positives situation or from the positioning accuracy is better than the negative pressure wave method. So the adaptive Kalman filter method can get the desired effect.

36.4 Conclusion

This article is the use of adaptive Kalman filter to detect natural gas pipeline leaks. The adaptive filter can accurately detect the exact time and location of the leak negative pressure waveform signal transmitted from the leak point to the difference between the upstream and downstream relative error which can be calculated leak points and false alarm rate. Regardless of the method or positioning accuracy is better than on the issue of false positives based on negative pressure wave detection of gas pipeline.

References

1. Sun DH, Wang HY (2013) Control system of the pipeline leakage test system. Fifth international conference on intelligent human-machine systems and cybernetics, vol 4, issue 13, pp 470-473
2. Dong LJ, Chun CS (2011) Leak detection and localization of gas pipeline system based on wavelet analysis. In: The 2nd international conference on intelligent control and information processing, pp 478–483

3. Ye YC, Zhang LB (2012) Study on leakage acoustic signal in natural gas pipeline. In: Fourth international conference on computational and information sciences, vol 3, issue 12, pp 1244–1247
4. Ge CH, Wang GH (2008) Analysis of the smallest detectable leakage flow rate of negative pressure wave based leak detection systems for liquid pipelines. Comput Chem Eng 8 (32):1669–1680
5. Niu HC, Zhang HB (2012) Research on the real-time leak monitoring model of the long distance natural gas pipeline. In: Fourth international conference on computational and information sciences, vol 3, issue 12, pp 1368–1370
6. Zhang SQ, Gao TY (2009) Study on new methods of improving the accuracy of leak detection and location of natural gas pipeline. In: International conference on measuring technology and mechatronics automation, vol 8, issue 9, pp 360–363
7. Joshi A, Udpa L (2006) Adaptive wavelets for characterizing magnetic flux leakage signals from pipeline inspection. IEEE Trans Magn 10(42):3168–3170
8. Jiang CL, Wang Y (2013) The Research of natural gas pipeline leak detection based on adaptive filter technology. In: 2nd international conference on measurement, information and control, vol 3, issue 13, pp 1229–1233
9. Chen GG, Liu LL (2014) Chaotic improved PSO-based multi-objective optimization for minimization of power losses and L index in power systems. Energy Convers Manag 86: 548–560

Chapter 37
H_∞ Filtering for Network-Based Systems with Time-Varying Delay

Duanjin Zhang and Xiaojing Jie

Abstract This paper is concerned with the problem of H-infinity filtering for network-based systems with time-varying delay. The performance analysis of network-based H-infinity filtering-error systems is proposed by constructing a suitable Lyapunov-Krasovskii functional which can retain some useful time-delay terms. A sufficient condition of exponential stability for filtering error system is derived in terms of linear matrix inequality approach, and the design method of H-infinity filter is also given. A numerical example shows the effectiveness of the proposed approach.

Keywords Time-varying delay · H_∞ filtering · Networked control systems · Linear matrix inequality approach

37.1 Introduction

State estimation has a significant role in signal processing and control systems. Compared with Kalman filtering, the advantage of H_∞ filtering is that the noise sources can be arbitrary signal instead of Gaussian noise. Besides, H_∞ filtering has high estimation precision and robustness. As a result, H_∞ filtering approach has received growing attention to deal with the estimation problem [1–4]. Networked control systems (NCSs), which can realize large system control and remote control through complex data network or wireless network, bring new functionalities such as good interactive performance, reduced system wiring, simple system diagnosis and maintenance, and high reliability. However, the insertion of communication networks makes the NCS analysis complex, as network system may be time-varying delay, packet dropouts, packet disorder, etc. Time-varying delay is usually regarded as the fundamental cause of system dynamic performance or system instability.

D. Zhang (✉) · X. Jie
School of Information Engineering, Zhengzhou University, Zhengzhou 450001, China
e-mail: djzhang@zzu.edu.cn

Z. Deng and H. Li (eds.), *Proceedings of the 2015 Chinese Intelligent Automation Conference*, Lecture Notes in Electrical Engineering 337,
DOI 10.1007/978-3-662-46463-2_37

The problem of H_∞ filtering for the systems over network with time-varying delay is challenging and meaningful. Therefore, this paper concerns network-based H_∞ filtering for time-varying delay systems.

Many useful results on filtering with time-varying delay system have been reported [5–7]. For example, Ref. [5] studied the H_∞ performance analysis criterion using linear matrix inequality (LMI). References [6] and [7] focus on the stability of filtering error system with free weighting matrix method. Nevertheless, the presented results use the time-varying-delay upper bound instead of the time delay. Therefore, the methods in the existing literature [5–7] ignore part of the time-delay information, which makes the results conservative. In this paper, to reduce the conservative of the existing results, an available Lyapunov function is constructed. Based on integral inequality approach, the stability criteria are derived by considering the whole variation interval of the delay. By the given examples, it can be seen that the range for time delay can be wider, which makes the derived criteria less conservative.

37.2 Problem Formulation

Consider the following continuous time system with time-varying delay:

$$\begin{aligned} \dot{x}(t) &= Ax(t) + A_d x(t-\tau(t)) + Bw(t) \\ y(t) &= Cx(t) + C_d x(t-\tau(t)) + Dw(t-\tau(t)) \\ z(t) &= Lx(t) \\ x(0) &= \phi_0 \end{aligned} \tag{37.1}$$

where $x(t) \in \Re^n$ is the state vector, $y(t) \in \Re^r$ is the measurement output, $z(t) \in \Re^q$ is the objective signal to be estimated, and $w(t) \in \Re^p$ is the disturbance input. A, A_d, B, C, C_d, D and L are known constant real matrices of appropriate dimensions. ϕ_0 is the initial condition. $\tau(t)$ is time-varying delay, where $\tau(t)$ satisfies:

$$0 < \tau_m \le \tau(t) \le \tau_M \tag{37.2}$$

We design an H_∞ filter described as follows:

$$\begin{aligned} \dot{x}_f(t) &= A_f x_f(t) + B_f y_f(t) \\ z_f(t) &= L_f x_f(t) \end{aligned} \tag{37.3}$$

where $x_f(t) \in \Re^n$, $y_f(t) \in \Re^r$ are the inputs of the filter, A_f, B_f and L_f are filter parameters to be determined.

Define

$$\xi(t) = \left[x^T(t), x_f^T(t)\right]^T,\ e(t) = z(t) - z_f(t),\ \alpha(t) = \begin{bmatrix} w(t) \\ w(t-\tau(t)) \end{bmatrix}.$$

Combining (37.1) and (37.2), we obtain the filtering-error system

$$\begin{aligned} \dot{\xi}(t) &= \overline{A}\xi(t) + \overline{A}_1\xi(t-\tau(t)) + \overline{B}\alpha(t) \\ e(t) &= \overline{L}\xi(t) \\ \xi(t) &= \phi(t), t \in [t_0 - \tau_M, t_0] \end{aligned} \tag{37.4}$$

where

$$\overline{A} = \begin{bmatrix} A & 0 \\ B_f & A_f \end{bmatrix}; \overline{A}_1 = \begin{bmatrix} A_d & 0 \\ B_f C_d & 0 \end{bmatrix}; \overline{B} = \begin{bmatrix} B & 0 \\ 0 & B_f D \end{bmatrix}; \overline{L} = [L \quad -L_f].$$

To give an H_∞ performance analysis result for the filtering-error system (37.4), the following definition is introduced first.

Definition 37.1 System (37.4) is said to be exponentially stable with an H_∞ norm bound γ, if the following hold:

(1) System (37.4) is exponentially stable with $\alpha(t) \equiv 0$, that is, there exist a small enough positive $\eta > 0$, such that $V(t)$ satisfies:

$$\dot{V}(t) < -\eta\|\xi(t)\|^2 \tag{37.5}$$

(2) Under the assumption of zero initial condition, the performance of H_∞ satisfies:

$$\|e(t)\|_2 \le \gamma\|\alpha(t)\|_2, \alpha(t) \in L_2[t_0, \infty)$$

For the following use, we need four lemmas.

Lemma 37.1 [8] *Let $x(t) \in \Re^n$ be a vector-valued function with first-order continuous-derivative entries. For any positive definite matrix $R \in \Re^{n\times n}$ and $Y = [M_1 \quad M_2] \in \Re^{n\times 2n}$, and a scalar function $h \ge 0$, the following integral inequality holds*:

$$\begin{aligned} -\int_{t-h}^{t} \dot{x}^T(s)R\dot{x}(s)\mathrm{d}s &\le h\xi^T(t)Y^{\mathrm{T}}R^{-1}Y\xi(t) \\ &+\xi^T(t)\begin{bmatrix} M_1^T + M_1 & -M_1^T + M_2 \\ * & -M_2^T - M_2 \end{bmatrix}\xi(t) \end{aligned} \tag{37.6}$$

Lemma 37.2 [9] *For any constant matrix* $W \in \Re^{n\times n}$, $W = W^T > 0$, *scalar* $\tau > 0$, *and vector function* $x(\cdot) : [-\tau, 0] \to \Re^n$, *such that the following integration holds*:

$$-\tau \int_{t-\tau}^{t} \dot{x}^T(s)\, W\, \dot{x}(s)\mathrm{d}s \le \begin{pmatrix} x(t) \\ x(t-\tau) \end{pmatrix}^T \begin{pmatrix} -W & W \\ W & -W \end{pmatrix} \begin{pmatrix} x(t) \\ x(t-\tau) \end{pmatrix} \tag{37.7}$$

Lemma 37.3 [10] (*Schur complement*) *For given real symmetric matrices* A_{11}, A_{22} *and* A_{12} *of appropriate dimensions, the following three conditions are equivalent*:

(I) $\begin{pmatrix} A_{11} & A_{12} \\ A_{12}^T & A_{22} \end{pmatrix} < 0;$

(II) $A_{11} < 0, A_{22} - A_{12}^T A_{11}^{-1} A_{12} < 0;$

(III) $A_{22} < 0, A_{11} - A_{12} A_{22}^{-1} A_{12}^T < 0.$

Lemma 37.4 [10] Ξ_1, Ξ_2 *and* Ω *are constant matrix of appropriate dimensions. Suppose* $\tau_m \le \tau(t) \le \tau_M$, *where* $\tau(t)$ *is time-varying function. Then, the inequality* (37.8) *holds, if and only if inequality* (37.9) *holds*:

$$\Omega + (\tau(t) - \tau_m)\Xi_1 + (\tau_M - \tau(t))\Xi_2 < 0 \tag{37.8}$$

$$\Omega + (\tau_M - \tau_m)\Xi_2 < 0;\ \ \Omega + (\tau_M - \tau_m)\Xi_1 < 0 \tag{37.9}$$

37.3 Main Results

37.3.1 H_∞ Filter Stability Analysis

In this section, we will present a sufficient condition for the stability analysis of networked control systems using integral inequality approach.

Theorem 37.1 *For given scalars* $\tau_m > 0$, $\tau_M > 0$, $\gamma > 0$, *the filtering error system* (37.4) *is exponentially stable if there exist real matrices*

$$P = \begin{bmatrix} P_1 & P_2 \\ * & P_3 \end{bmatrix} > 0, \quad Q_i = Q_i^{\mathrm{T}} \ge 0, \quad R_i = R_i^{\mathrm{T}} > 0 (i = 1, 2), \quad \overline{N} = [N_1 \quad N_2],$$

$N = [0 \quad 0 \quad N_1 \quad N_2 \quad 0 \quad 0 \quad 0], \overline{M} = [M_1 \quad M_2], M = [0 \quad 0 \quad 0 \quad M_1 \quad M_2 \quad 0 \quad 0]$, satisfying:

$$\Phi_1 = \begin{bmatrix} \overline{\Phi}_1 & * & * \\ \Xi_{21} & \Xi_{22} & * \\ \Xi_{31}^i & 0 & \Xi_{33} \end{bmatrix} < 0, \quad i = 1, 2 \tag{37.10}$$

where

$$\overline{\Phi}_1 = \begin{bmatrix} \Pi & * & * & * & * & * & * \\ \Phi_{12} & \Phi_{13} & * & * & * & * & * \\ R_1 & 0 & -Q_1 - R_1 + N_1^{\mathrm{T}} + N_1 & * & * & * & * \\ \Phi_{21} & \Phi_{22} & -N_1 + N_2^{\mathrm{T}} & M_1^{\mathrm{T}} + M_1 - N_2 - N_2^{\mathrm{T}} & * & * & * \\ 0 & 0 & 0 & -M_1^{\mathrm{T}} + M_2 & -Q_2 - M_2^{\mathrm{T}} - M_2 & * & * \\ \Phi_{31} & \Phi_{32} & 0 & 0 & 0 & -\gamma^2 I & * \\ \Phi_{33} & \Phi_{34} & 0 & 0 & 0 & 0 & -\gamma^2 I \end{bmatrix}$$

$$\Xi_{21} = \begin{bmatrix} \tau_m R_1 \Lambda \\ \sqrt{\tau_M - \tau_m} R_2 \Lambda \\ \Gamma \end{bmatrix}; \quad \Xi_{22} = \mathrm{diag}(-R_1, -R_2, -I); \quad \Xi_{33} = -R_2;$$

$$\Xi_{31}^1 = \sqrt{\tau_M - \tau_m} M^T; \quad \Xi_{31}^2 = \sqrt{\tau_M - \tau_m} N^T;$$

$$\Pi = Q_1 + Q_2 - R_1 + P_1 A + A^T P_1 + P_2 B_f C + C^T B_f P_2; \quad \Phi_{12} = P_2 A + P_2 A_f + P_3 B_f C;.$$

$$\Phi_{13} = P_3 A_f + A_f^T P_3; \quad \Phi_{21} = P_1 A_d + A_d^T P_1 + P_2 B_f C_d + C_d^T B_f^T P_2;$$

$$\Phi_{22} = A_d^T P_2 + P_2 A_d + P_3 B_f C_d + C_d^T B_f^T P_3; \quad \Phi_{31} = P_1 B + B^T P_1;$$

$$\Phi_{32} = P_2 B + B^T P_2; \quad \Phi_{33} = P_2 B_f D + D^T B_f^T P_2; \quad \Phi_{34} = P_3 B_f D + D^T B_f^T P_3;$$

$$\Gamma = [L \quad L_f \quad 0 \quad 0 \quad 0 \quad 0 \quad 0]; \; \Lambda = [A \quad 0 \quad 0 \quad A_d \quad 0 \quad B \quad 0];$$

Proof Define Lyapunov-Krasovskii functional as:

$$\begin{aligned} V(t) = {} & \xi^T(t) P \xi(t) + \int_{t-\tau_m}^{t} x^T(s) Q_1 x(s) \mathrm{d}s + \int_{t-\tau_M}^{t} x^{\mathrm{T}}(s) Q_2 x(s) \mathrm{d}s \\ & + \tau_m \int_{t-\tau_m}^{t} \int_{s}^{t} \dot{x}^T(s) R_1 \dot{x}(s) \mathrm{d}v \mathrm{d}s + \int_{t-\tau_M}^{t-\tau_m} \int_{s}^{t} \dot{x}^T(s) R_2 \dot{x}(s) \mathrm{d}v \mathrm{d}s \end{aligned} \tag{37.11}$$

Take a derivative of $V(t)$ with respect to t along the trajectory of (37.4) yields:

$$\begin{aligned} \dot{V}(t) = {} & 2\xi^T(t) P \dot{\xi}(t) + x^T(t)(Q_1 + Q_2) x(t) - x^T(t - \tau_m) Q_1 x(t - \tau_m) \\ & - x^T(t - \tau_M) Q_2 x(t - \tau_M) + \dot{x}^T(t)(\tau_m^2 R_1 + (\tau_M - \tau_m) R_2) \dot{x}(t) \\ & - \tau_m \int_{t-\tau_m}^{t} \dot{x}^T(s) R_1 \dot{x}(s) \mathrm{d}s - \int_{t-\tau_M}^{t-\tau(t)} \dot{x}^{\mathrm{T}}(s) R_2 \dot{x}(s) \mathrm{d}s - \int_{t-\tau(t)}^{t-\tau_m} \dot{x}^T(s) R_2 \dot{x}(s) \mathrm{d}s \end{aligned} \tag{37.12}$$

By using Lemma 37.1, we have:

$$-\int_{t-\tau(t)}^{t-\tau_m} \dot{x}^T(s)R_2\dot{x}(s)\mathrm{d}s \le \xi_1^T(t)\begin{bmatrix} N_1^T+N_1 & -N_1^T+N_2 \\ * & -N_2^T-N_2 \end{bmatrix}\xi_1(t) + (\tau(t)-\tau_m)\xi_1^T(t)\overline{N}^T R_2^{-1}\overline{N}\xi_1(t) \tag{37.13}$$

$$-\int_{t-\tau_M}^{t-\tau(t)} \dot{x}^T(s)R_2\dot{x}(s)\mathrm{d}s \le \xi_2^T(t)\begin{bmatrix} M_1^T+M_1 & -M_1^T+M_2 \\ * & -M_2^{\mathrm{T}}-M_2 \end{bmatrix}\xi_2(t) + (\tau_M-\tau(t))\,\xi_2^T(t)\overline{M}^T R_2^{-1}\overline{M}\,\xi_2(t) \tag{37.14}$$

where

$$\xi_1^T(t) = \begin{bmatrix} x^T(t-\tau_m) & x^T(t-\tau(t)) \end{bmatrix} \xi_2^T(t) = \begin{bmatrix} x^T(t-\tau(t) & x^T(t-\tau_M) \end{bmatrix}$$

By Lemma 37.2, we have:

$$-\tau_m\int_{t-\tau_m}^{t} \dot{x}^T(s)R_1\dot{x}(s)\mathrm{d}s \le \begin{pmatrix} x(t) \\ x(t-\tau_m) \end{pmatrix}^T \begin{pmatrix} -R_1 & R_1 \\ R_1 & -R_1 \end{pmatrix}\begin{pmatrix} x(t) \\ x(t-\tau_m) \end{pmatrix} \tag{37.15}$$

Suppose $\dot{x}(t) = \Lambda\mu(t)$,

$$\mu(t) = [\,x^T(t) \quad x_f^T(t) \quad x^T(t-\tau_m)\; x^T(t-\tau(t)) \quad x^T(t-\tau_M) \quad w^T(t) \quad w^T(t-\tau(t))\,].$$

Adding (37.13–37.15) into (37.12) yields:

$$\dot{V}(t) + e^T(t)\,e(t) - \gamma^2\alpha^T(t)\,\alpha(t) \le \mu^T(t)(\Phi_1 + \Lambda^T(\tau_m^2R_1 + (\tau_M-\tau_m)R_2)\Lambda + \Gamma^T\Gamma)\mu(t) + (\tau(t)-\tau_m)\mu^T(t)MR_2^{-1}M^T\mu(t) + (\tau_M-\tau(t))\,\mu^T(t)NR_2^{-1}N^T\mu(t) \tag{37.16}$$

By Lemma 37.3, the inequality (37.10) is equivalent to:

$$\Phi_1 + \Lambda^T(\tau_m^2R_1 + (\tau_M-\tau_m)R_2)\Lambda + \Gamma^T\Gamma + (\tau_M-\tau_m)MR_2^{-1}M^T < 0 \tag{37.17}$$

$$\Phi_1 + \Lambda^{\mathrm{T}}(\tau_m^2R_1 + (\tau_M-\tau_m)R_2)\Lambda + \Gamma^{\mathrm{T}}\Gamma + (\tau_M-\tau_m)NR_2^{-1}N^{\mathrm{T}} < 0 \tag{37.18}$$

By Lemma 37.4, combining (37.17) and (37.18), we can obtain:

$$\dot{V}(t) + e^T(t)e(t) - \gamma^2\alpha^T(t)\alpha(t) < 0$$

That is,

$$e^T(t)e(t) - \gamma^2\alpha^T(t)\alpha(t) \leq -\dot{V}(t) \tag{37.19}$$

Under the zero condition, integrating both sides to (37.19), we obtain

$$\int_0^\infty e^T(s)e(s)\mathrm{d}s - \int_0^\infty \gamma^2\alpha^T(s)\alpha(s)\mathrm{d}s \leq V(0) - V(\infty) < 0$$

The inequality above is equivalent to:

$$\int_0^\infty e^T(s)e(s)\mathrm{d}s \leq \int_0^\infty \gamma^2\alpha^T(s)\alpha(s)\mathrm{d}s \tag{37.20}$$

Under zero initial condition, for all nonzero $w(t)$ satisfies:

$$\|e(t)\|_2 \leq \gamma\|\alpha(t)\|_2$$

Therefore, system (37.4) has a guaranteed H_∞ noise attenuation performance. As for the proof of Theorem 37.1, we reserve the time-varying delay information instead of the upper bound, which makes the result less conservativeness.

37.3.2 H_∞ Filter Design

Theorem 37.2 *For given scalar* $\tau_m > 0$, $\tau_M > 0$, $\gamma > 0$, *if there exist matrices* $P_1 = P_1^T > 0$, $Q_i = Q_i^T \geq 0$, $R_i = R_i^{\mathrm{T}} > 0\,(i = 1, 2)$, $Y = P_2P_3^{-1}P_2^T > 0$, $N = [0 \quad 0 \quad N_1 \quad N_2 \quad 0 \quad 0 \quad 0]$, $M = [0 \quad 0 \quad 0 \quad M_1 \quad M_2 \quad 0 \quad 0]$ *such that*

$$\Phi_1 = \begin{bmatrix} \overline{\Phi}_1^{'} & * & * \\ \Xi_{21}^{'} & \Xi_{22} & * \\ \Xi_{31}^{i} & 0 & \Xi_{33} \end{bmatrix} < 0, i = 1, 2 \tag{37.21}$$

$$\Phi_1' = \begin{bmatrix} \Gamma & * & * & * & * & * & * \\ \Phi_{12}' & \Phi_{13}' & * & * & * & * & * \\ R_1 & 0 & -Q - R_1 + N_1^T + N_1 & * & * & * & * \\ \Phi_{21} & \Phi_{22}' & -N_1 + N_2^T & M_1^T + M_1 - N_2 - N_2^T \rightarrow & * & * & * \\ 0 & 0 & 0 & -M_1^T + M_2 & -Q - M_2^T - M_2 & * & * \\ \Phi_{21} & \Phi_{32}' & 0 & 0 & 0 & -\gamma^2 I & * \\ \Phi_{21} & \Phi_{34}' & 0 & 0 & 0 & 0 & -\gamma^2 I \end{bmatrix}$$

$$\Xi_{21} = \begin{bmatrix} \tau_m R_1 \Lambda \\ \sqrt{\tau_M - \tau_m} R_2 \Lambda \\ \Gamma' \end{bmatrix};$$

$$\Phi_{12}' = YA + A^T Y + YA_f + A_f^T Y + \overline{B}_f C + C^T \overline{B}_f;\ \Phi_{13}' = \overline{A}_f + \overline{A}_f^T;$$
$$\Phi_{22}' = YA_d + A_d^T Y + \overline{B}_f C_d + C_d^T \overline{B}_f; \quad \Phi_{32}' = YB + B^T Y;$$
$$\Phi_{34}' = \overline{B}_f D + D^T \overline{B}_f^T; \quad \Gamma' = \begin{bmatrix} L & -L_f P_3^{-1} P_2 & 0 & 0 & 0 & 0 & 0 \end{bmatrix}.$$

Moreover, the filter parameters of an admissible filter of form (37.3) are given by

$$A_f = \overline{A}_f Y^{-1}; B_f = P_2^{-1} \overline{B}_f; L_f = \overline{L}_f P_2^{-1} P_3.$$

Proof Let $V = \mathrm{diag}(I \quad P_2 P_3^{-1} \quad I \quad I \quad I \quad I \quad I \quad I \quad I \quad I \quad I)$, pre- and post-multiplying form (37.10) with V and V^T. Let $\overline{A}_f = P_2 P_3^{-1} P_2^T A_f$; $\overline{B}_f = P_2 B_f$; $\overline{L}_f = L_f P_3^{-1} P_2$. Then we can obtain the form (37.21). □

37.4 Number Example

Consider the system (37.1) with the following parameters:

$$A = \begin{bmatrix} 0 & 3 \\ -4 & -5 \end{bmatrix}; A_d = \begin{bmatrix} -0.5 & 0 \\ 0.9 & 0 \end{bmatrix}; B = \begin{bmatrix} 0.5 & 0 \\ 0 & 0 \end{bmatrix}; C = \begin{bmatrix} 0.2 & 0.6 \end{bmatrix};$$
$$C_d = \begin{bmatrix} 0 & 1 \end{bmatrix}; D = \begin{bmatrix} 0 & 1 \end{bmatrix}; L = \begin{bmatrix} 1 & 1 \end{bmatrix}.$$

Here, the time-varying delay $\tau(t)$ satisfies (37.2). By using Theorem 37.2, we can compute the corresponding allowable upper bounds of the delay for different τ_m by the LMI toolbox in MATLAB. The computed results are shown in Table 37.1. From Table 37.1, we can obtain larger allowable upper bound of time-delay, which lead to less conservative results (Table 37.1).

By Theorem 37.2 with $\tau_m = 0.2$ and $\tau_M = 0.48$, we can obtain H_∞ performance $\gamma = 0.1607$, while applying the method in [12], the H_∞ performance is given by $\gamma = 0.2309$. Clearly, our method can improve the H_∞ performance. The parameter matrices A_f, B_f and C_f of the filter as

Table 37.1 The upper bound of τ_M for different τ_m

τ_m	0	0.5	1.0	1.5
Reference [11]	1.34	1.49	1.74	2.08
Theorem 37.2	1.69	2.12	2.59	3.08

$$A_f = \begin{bmatrix} -0.8073 & 0 \\ 0 & -0.8073 \end{bmatrix}; B_f = \begin{bmatrix} 0.0084 \\ -0.0019 \end{bmatrix};$$
$$L_f = [0.0485 \quad -0.0508]$$

37.5 Conclusions

We have addressed the problem of network-based H_∞ filtering for time-varying delay system. When we take a derivative of Lyapunov-Krasovskii functional with respect to t along the trajectory of filtering error system, we did not ignore the variation interval of the delay. Some numerical examples have been given to show the effectiveness and less conservativeness.

Acknowledgments This work was supported by the National Nature Science Foundation of China under Grant 61471323 and the Key Program of Science and Technology of the Education Department of Henan of China under Grant 14A120004.

References

1. Zhang XM, Han QL (2012) Network-based H_∞ filtering for discrete-time systems. IEEE Trans Signal Process 60(2):956–961
2. Jie XJ, Zhang DJ, Wang AJ (2013) Network-based filtering for discrete-time Markov jumping systems. J Central S Univ Sci Technol 44(s1):119–122 (in Chinese)
3. Zhang XM, Han QL (2008) Robust H_∞ filtering for a class of uncertain linear systems with time-varying delay. Automatica 44(1):157–166
4. Schnato L (2008) Optimal estimation in networked control systems subject to random delay and packet drop. IEEE Trans Autom Control 53(5):1311–1317
5. Yue D, Han QL (2006) Network-based H_∞ filtering for uncertain linear systems. IEEE Trans Signal Process 54(11):4293–4301
6. Lien CH, Cheng WC, Tsai CH et al (2007) Non-fragile observer-based control of linear system via LMI approach. Solitons Fractal 32(4):1530–1537
7. Chen JD, Yang CD, Lien CH et al (2008) New delay-dependent non-fragile H_∞ observer-based control for continuous time-delay systems. Inf Sci 187(24):4699–4706
8. Zhang XM, Wu M, She JH (2005) Delay-dependent stabilization of linear systems with time-varying state and input delays. Automatica 41(8):1405–1412
9. Han QL (2005) Absolute stability of time-delay systems with sector-bounded nonlinearity. Automatica 41(12):2171–2176
10. Boyd S, Ei-Ghaoui L, Feron E et al (1994) Linear matrix inequalities in systems and control theory. SIAM, Philadelphia

11. He Y, Wang QG, Lin C et al (2007) Delay-range-dependent stability for systems with time-varying delay. Automatica 43(2):371–376
12. Chen G, Zhu HQ, Yang CH et al (2012) Robust H_∞ filtering for networked control systems with time-delay. J Central S Univ Sci Technol 43(10):3886–3893 (in Chinese)

Chapter 38
A Comparative Study of Pricing Control Algorithms in Deregulated Electricity Market

Zhi-Yu Xu, Wei-Hui Shao, Hai-Ni Qu, Ke Sun and Wei-Sheng Xu

Abstract In the future smart grid, both sides of the generation and the demand participate in the real-time electricity market, and their activities are responsive to the electricity price. Thus it is proposed the concept of "pricing control." Considering the numerous algorithms of pricing control which are reported in literature, this paper performs a comparative study and evaluates their effectiveness and advantages. The pricing control scheme of electricity market is formulated. The control algorithms are presented, i.e., info-fusion-based control, multiperiod optimal control, adaptive estimation, proportional-integral, and moving average estimation. The differences are clarified; from the model description to the solving technique. The quality of the solution is computationally compared and analyzed.

Keywords Smart grid · Electricity market · Real-time pricing · Control algorithm · Comparative study

38.1 Introduction

In the recent decades, the smart grid is attracting the interest from academy to industry [1]. Such a large-scale informatization of the conventional power system is making both the generation companies (GenCos) and the demand-side more intelligent, thus more responsive to the market situation [2]. Meanwhile the time-scale of power trade is greatly shortened and the real-time electricity market is required. The electricity price plays a significant role in the future real-time electricity market [3]. Since GenCos and demand side are price taker and reactor, the price could be adopted as the incentive or the control signal to affect their activities. If the market operator (MO) could figure out the "proper" price, both GenCos and demand-side are financially motivated to behave as required. As a sequel the market

Z.-Y. Xu (✉) · W.-H. Shao · H.-N. Qu · K. Sun · W.-S. Xu
School of Electronics & Informatics, Cao'an Highway. 4800, Shanghai 201804, China
e-mail: xuzhiyu@tongji.edu.cn

Z. Deng and H. Li (eds.), *Proceedings of the 2015 Chinese Intelligent Automation Conference*, Lecture Notes in Electrical Engineering 337,
DOI 10.1007/978-3-662-46463-2_38

stability and the system reliability could be ensured. That is the principle of the "pricing control."

Adopting the framework of the pricing control, numerous researches have been devoted for the derivation of such "proper" price. Considering these inherent feedback dynamics, [4] proposes a novel idea which formulates competitive bidding as a feedback system. A proportional-integral (PI) controller is developed to ensure the supply-demand balance in a steady state meanwhile each GenCO gains maximal profit. Estrada-Cruz et al. [5] models the bidding behavior of GenCOs as a discrete-time linear system and utilizes expectation methods, e.g., adaptive estimation (AE), moving average estimation (MAE), etc. and numerically investigates their output equilibrium and price convergence within various cases and scenarios. Liu and Wu [6] emphasizes the benefit of long-term optimization in the global view. The multiperiod optimal control (MPC) on the generation quantity is computed via backward induction and simulation results indicate that GenCo could obtain more profit by applying multiperiod optimization. These works assume the supply–demand balance in steady state and the coefficients of demand function are fixed known [4, 7, 8] or periodically predictable in the hour timescale [6]. The price is implicit in the model and GenCo makes decision on estimating the rivals' behavior and market demand function. The info-fusion-based pricing control (IFC) is reported in [9], the pricing control on generation-side is formulated as a linear constrained quadratic optimal tracking problem and the info-fusion technique is applied for solving the problem. In this paper, we attempt to provide insight and evaluation on the aforementioned algorithms of pricing control through a comparative study.

38.2 Model Comparison

38.2.1 Adaptive Estimation and Moving Average Estimation

Most of the existing researches assume that demand–supply intrinsic balance and market clearing price is negative-linearly dependent on the total demand. Gutierrez-Alcaraz and Sheble [7] formulate the generation decision as the constrained optimization problem

$$\max \pi_i^k = u^k \cdot Tx_i^k - C_S(Tx_i^k) \tag{38.1}$$

$$\text{st.} \begin{cases} u^k = a^k - b^k y_*^k \\ y_*^k = y^k \\ y^k = \sum_{i=1}^{n} x_i^k \\ C_S(Tx_i^k) = d_i + e_i \cdot Tx_i^k + f_i/2 \cdot (Tx_i^k)^2 \end{cases} \tag{38.2}$$

where π is the profit of GenCo, u is the electricity price, T is the control period, x is the output power of GenCo, y^* is the total demand, y is the total generation, C_S is the generation cost, a, b, d, e, f are relevant coefficients.

The dynamic model of GenCoi is

$$x_i^k = -\frac{b^k}{2b^k + f_i} \sum_{j=1,\, j\neq i}^{n} x_j^k + \frac{1}{T}\frac{a^k - e_i}{2b^k + f_i} \tag{38.3}$$

Gutierrez-Alcaraz and Sheble [7] present some methods for estimating opponents' behaviors, i.e., $\hat{x}_j^k, \forall j \neq i$.

The estimation is called "adaptive" if GenCoi assumes

$$\hat{x}_j^k = \hat{x}_j^{k-1} + \beta_i(x_j^{k-1} - \hat{x}_j^{k-1}) \tag{38.4}$$

The estimation is called "moving average" if GenCoi assumes

$$\hat{x}_j^k = \omega_i x_j^{k-1} + (1 - \omega_i)x_j^{k-2} \tag{38.5}$$

where β and ω are the estimation weights. Notice that the electricity price is implicit in GenCoi's decision model (38.3) because of the strong assumption of supply–demand balance in (38.2). From (38.3), we can say GenCoi makes generation decision according to predicted market structure and estimated behaviors of all opponents. The effectiveness and accuracy of the model greatly rely on those estimations, which are actually time-variant and highly uncertain.

38.2.2 Multiperiod Optimal Control (MPC)

Liu and Wu [6] employ the same GenCo model as [7] moreover, it is believed that each GenCo performs multiperiod optimization could gain more profit than the sum of single-period optimization, i.e.,

$$\max_{\{x_i^k\}_{k=1}^N} \sum_{k=1}^{N} \pi_i^k > \sum_{k=1}^{N} \max_{\{x_i^k\}} \pi_i^k \tag{38.6}$$

Also applying $\partial \pi_i^k / \partial x_i^k = 0$ on (38.3), [6] gives

$$x_i^k = \left[1 - \beta_i\left(2b^{k-1} + f_i\right)\right]x_i^{k-1} - \beta_i 2b^{k-1}x_j^{k-1} + \beta_i\left(a^{k-1} - e_i\right) \qquad i = 1, 2; j \neq i \tag{38.7}$$

for 2-GenCo (symmetric) market. Notice that electricity price is not explicit factor for GenCoi's decision either.

38.2.3 Proportional-Integral Control (PI)

Syothert and MacLeod [4] present an alternative approach and designs the PI (with saturation) controller for MO which modifies electricity price according to the current and accumulated error between supply and demand. The quantity–price mapping is

$$x_i^k = \frac{u^k - e_i}{2f_i T} \tag{38.8}$$

$$x_{i\min} \le x_i^k \le x_{i\max} \tag{38.9}$$

The error of current period is

$$\varepsilon^k = y_*^k - \sum_{i=1}^{n} T x_i^k \tag{38.10}$$

The bidding price of GenCoi is

$$\hat{u}_i^{k+1} = \frac{d_i}{T x_i^k} + e_i + f_i \cdot T x_i^k \tag{38.11}$$

MO applies saturated PI control to update the electricity price

$$u^{k+1} = \max_{i=1,\ldots,n} \hat{u}_i^{k+1} + K_{\mathrm{P}} \varepsilon^k + K_{\mathrm{I}} \sum_{j=1}^{k} \varepsilon^j \tag{38.12}$$

In the model of [4], the electricity price is first bid by GenCos and then modified by MO according to the tracking error. Since the output feedback is evolved, the supply could meet the demand after a transient process.

38.2.4 Info-Fusion Based Control (IFC)

In [9], the net-profit of GenCoi is presented as

$$\pi_i^k = u^{k-1} \cdot T x_i^k - C_{\mathrm{S}}\left(T x_i^k\right) - C_{\mathrm{V}}\left(T \Delta x_i^k\right) \tag{38.13}$$

Notice that the costs of both generation status (C_{S}) and variation (C_{V}) are taken in account. The former is the same as (38.2) and the latter is

$$C_{\mathrm{V}}\left(T\Delta x_i^k\right) = \alpha_i\left(Tx_i^k - Tx_i^{k-1}\right)^2 \tag{38.14}$$

where α is the constant coefficient.

The pricing control is formulated as the linear constrained quadratic optimization problem

$$\min\left\|y^N - y_*^N\right\|_{\mathbf{S}}^2 + \sum_{k=0}^{N-1}\left\|y^k - y_*^k\right\|_{\mathbf{Q}}^2 + \left\|u^k - u_*^k\right\|_{\mathbf{R}}^2 \tag{38.15}$$

$$\text{s.t.} \quad \begin{cases} \mathbf{x}^{k+1} = \mathbf{A}\mathbf{x}^k + \mathbf{B}u^k - \mathbf{w} \\ y^k = \mathbf{C}\mathbf{x}^k \end{cases} \quad k = 0, 1, \ldots, N-1 \tag{38.16}$$

where $\mathbf{A} = \mathrm{diag}\left(\frac{2\alpha_i}{2\alpha_i + f_i}\right)$, $\mathbf{B} = \mathrm{col}\left(\frac{1/T}{2\alpha_i + f_i}\right)$, $\mathbf{C}^{\mathrm{T}} = \mathrm{col}(1)$, $\mathbf{w} = \mathrm{col}\left(\frac{e_i/T}{2\alpha_i + f_i}\right)$.

38.3 Performance Comparison

38.3.1 Simulation Setups

Considering the fairness of competition, the benchmark problem should be defined. Here we adopt the 24-h demand data from California day-ahead market on April 16, 1998, which is also utilized in [6]. The estimated coefficients are provided in [6] (See Table 38.1). The five algorithms of pricing control are applied to track this benchmark demand trajectory over 24-h time horizon. The initial condition is each GenCo equally shares the initial demand, and T = 1/6 h in IFC.

Consider that MPC, AE, PI, and MAE, respectively, incorporate with Case 1, 2, 3, and 4 in the literatures, we carry out four groups for comparison: (i) IFC versus MPC under Case 1, (ii) IFC versus AE under Case 2, (iii) IFC versus PI under Case 3, and (iv) IFC versus MAE under Case 4. The parameter setups are listed in Table 38.2, which are identical to those in the literatures.

38.3.2 Computational Results

The tracking performances are demonstrated by Figs. 38.1, 38.2, 38.3, and 38.4, in which the 24-h demand, results of IFC, and other methods (MPC, AE, PI, and MAE) are shown with circled, thick solid, and thin solid lines, respectively. Since the effectiveness of AE, PI, and MAE are realized via repeated bidding; the x-axis of their trajectories in Figs. 38.2, 38.3, and 38.4 should be bidding count rather than the time. Thus it is only necessary to concentrate on the final steady-state

Table 38.1 24-h historical data of demand, price, and periodically estimated coefficients

Hour	1	2	3	4	5	6	7	8
Demand (MWh)	17280	16832	16611	16631	16911	17780	19647	20808
Price ($/MWh)	16.056	14.64	13.573	13.749	15.453	24.7	26.493	27.09
a	34.547	24.093	21.114	21.617	26.463	53.341	56.883	57.47
b ($\times 10^{-4}$)	9.4162	5.6148	4.5372	4.7304	6.5062	16.103	15.456	14.599
Hour	9	10	11	12	13	14	15	16
Demand (MWh)	21235	21819	22238	22391	22333	22344	22172	21874
Price ($/MWh)	27.079	27.492	28.398	28.991	28.505	28.201	27.75	27.023
a	57.055	57.682	60.013	61.585	60.184	59.295	58.085	56.256
b ($\times 10^{-4}$)	14.104	13.831	14.205	14.556	14.184	13.908	13.68	13.351
Hour	17	18	19	20	21	22	23	24
Demand (MWh)	21166	20639	20798	22110	22409	21374	19861	17847
Price ($/MWh)	26.49	26.116	26.045	27.815	27.987	26.49	26.208	20.494
a	55.347	54.771	54.346	58.37	58.565	55.11	55.763	34.283
b ($\times 10^{-4}$)	13.624	13.87	13.605	13.812	13.643	13.387	14.881	9.1075

Table 38.2 Parameter setup for performance comparison

Case	Market structure	Control algorithm	Control parameters
1	2-GenCo (symmetric)	MPC	Optimization horizon: 24 h; control period: 1 h; $\beta_1 = \beta_2 = 60$
2	2-GenCO	AE	Bidding rounds: 10; $\beta_1 = 0.3, \beta_2 = 0.6$
3	3-GenCO	PI	Bidding rounds: 30; $K_P = 10^{-4}, K_I = 8 \times 10^{-3}$
4	5-GenCO	MAE	Bidding rounds: 10; $\omega_1 = 0.2, \omega_2 = 0.5, \omega_3 = 0, \omega_4 = 1, \omega_5 = 0$

equilibrium and ignore the transient. We summarize the comparison results and present our remarks as follows.

MPC, AE, and MAE could generate the output and price similar to the historical data in the shape of trajectories but the errors of amplitude could be quite large. MPC provides supply around 5 % higher than demand (Fig. 38.1), the bidding equilibriums of AE and MAE are less than 20 % of the demand (Figs. 38.2 and 38.4). (Note: Their supply reaches the demand at the first round of bidding only because the initial condition is each GenCo generates y^*/n). The reason is that none of them has the closed loop of supply. They simply assume that supply is equal to demand. However such assumption strictly relies on the estimation of the demand function coefficients, i.e., the accuracy of a and b. Through repeated bidding of the algorithms, the market could settle at the equilibrium and each GenCo could obtain maximal profit but the total supply volume could not be guaranteed.

PI could accurately track the varying demand (Fig. 38.3), because it employs supply closed-loop so that price could be adjusted by the tracking error. But PI

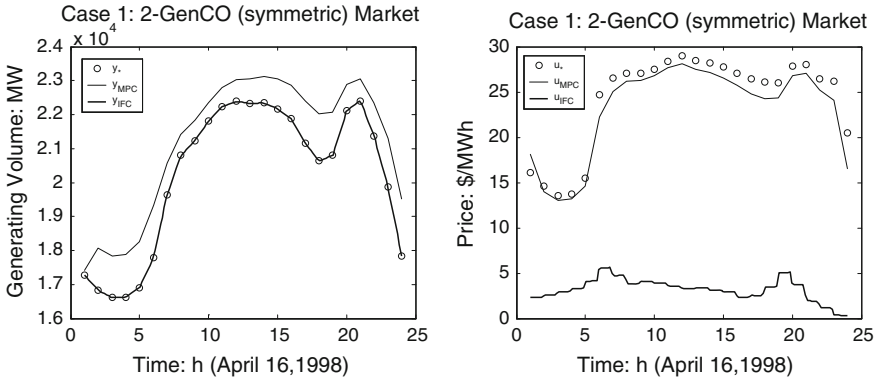

Fig. 38.1 Tracking performance and price level of IFC and MPC under Case 1

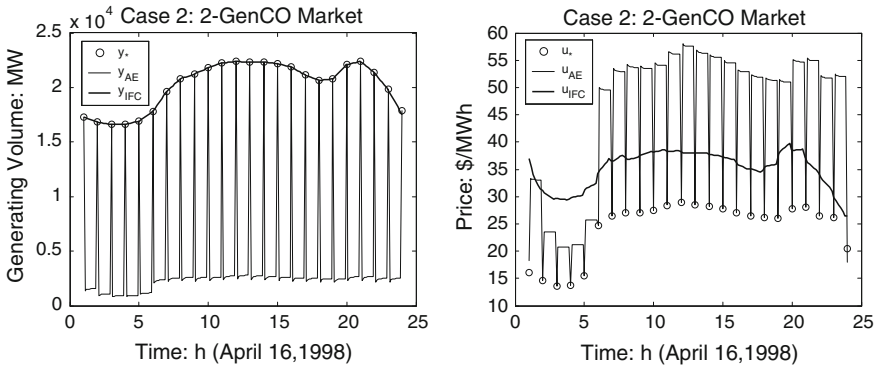

Fig. 38.2 Tracking performance and price level of IFC and AE under Case 2

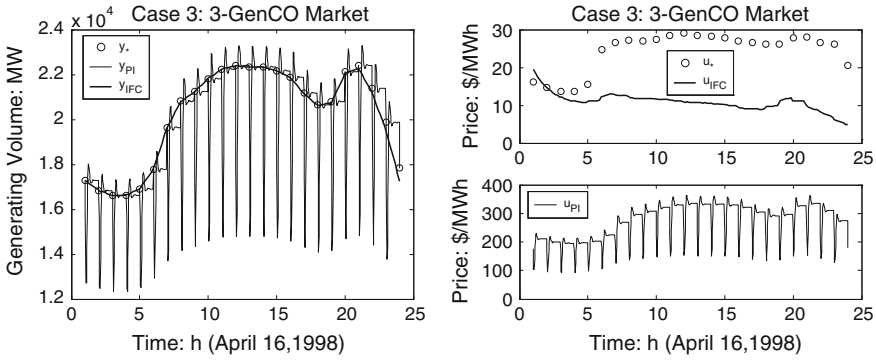

Fig. 38.3 Tracking performance and price level of IFC and PI under Case 3

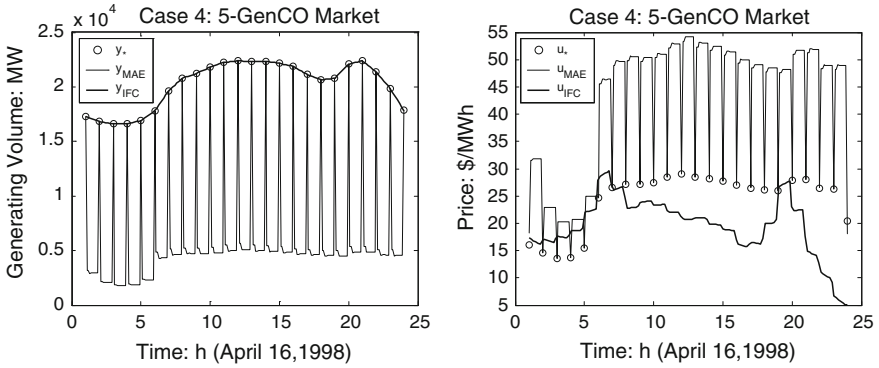

Fig. 38.4 Tracking performance and price level of IFC and MAE under Case 4

requires multiple rounds of bidding (see the damped oscillation in Fig. 38.3) and reaches the demand in steady state. The reason is that PI merely uses output feedback and only considers the demand of next single period, thus it behaves as a series of independent step responses over sequential hours.

Due to the inherent mechanism of state-feedback and multiperiod optimization, the pricing decision of IFC is derived by information fusion of all the future demand so that IFC dynamically tracks the demand under all four cases. Besides, IFC achieves the lowest electricity price as compared to MPC, AE, PI, and MAE. As a result, IFC should be more appreciated by MO. Meanwhile the profit of each GenCo is also reduced since the price is brought down. However, GenCo still could benefit from accepting and adopting IFC. The reason is that given other control strategies, GenCo has to make its bidding decision by predicting electricity price and estimating rivals' behaviors, which are highly uncertain and risky. While in IFC, GenCo makes its optimal option only by considering the MO-offered price and its own operation status, thus the profit becomes more deterministic and ensured.

38.4 Conclusion

This paper conducts a comparative study on five algorithms of pricing control, i.e., PI, MPC, AE, MAE, and IFC. The model formulations are presented and the differences are clarified. The performances of these algorithms are compared by numeric simulations under various cases. Computational results indicate that the IFC could derive the solution which achieves the minimal power imbalance and the lowest price. Both GenCos and MO could benefit from adopting IFC.

Acknowledgments This work was supported by the National Natural Science Foundation of China under Grant No. 71401125, 51475334 and the Doctoral Program Foundation of Higher Education of China under Grant no. 20130072110045.

References

1. Kolhe M (2012) Smart grid: charting a new energy future: research, development and demonstration. Electr J 25:88
2. Lampropoulos I, Baghină N, Kling WL, Ribeiro PF (2013) A predictive control scheme for real-time demand response applications. IEEE Trans Smart Grid 4:2049
3. Roozbehani M, Dahleh MA, Mitter SK (2012) Volatility of power grids under real-time pricing. IEEE Trans Power Syst 27:1926
4. Syothert A, MacLeod I (2000) Competitive bidding as a control problem. IEEE Trans Power Syst 15:88
5. Estrada-Cruz O, Gutierrez-Alcaraz G, Tovar-Hernandez H (2008) Modeling dynamic generation companies' bidding strategies. In: IEEE 2nd international conference on power and energy (PECon 2008), p 1317
6. Liu Y, Wu FF (2006) Generator bidding in oligopolistic electricity markets using optimal control: fundamentals and application. IEEE Trans Power Syst 21:1050
7. Gutierrez-Alcaraz G, Sheble GB (2010) Generation companies decision-making modeling by linear control theory. Electric Power System Research 80:815
8. Gutierrez-Alcaraz G, Ramos-Trujillo RA (2010). GenCos' strategic behavior monitoring on auction bidding based on state variables formulation. In: International conference on power system technology (POWERCON2010), p 1
9. Xu ZY, Xu WS, Shao WH, Zeng ZY (2014) Real-time pricing control on generation-side: optimal demand-tracking model and information fusion estimation solver. IEEE Trans Power Syst 29:1522

Chapter 39
Adaptive Output Feedback Control of Nonlinear Systems with States and Input Unmodeled Dynamics

Xiaonan Xia, Tianping Zhang and Qin Wang

Abstract In this paper, an adaptive output feedback neural control strategy is investigated for a class of nonlinear systems with states and input unmodeled dynamics based on dynamics surface control method. States unmodeled dynamics is described by introducing a kind of Lyapunov function, and the nonlinear input unmodeled dynamics is dealt with by using a normalization signal. The unknown control gain sign is solved with the help of Nussbaum function. By the theoretical analysis, all the signals in the closed-loop system are proved to be semi-globally uniformly ultimately bounded. A numerical example is provided to illustrate the effectiveness of the proposed approach.

Keywords Adaptive control · Output feedback control · Dynamic surface control · State unmodeled dynamics · Input unmodeled dynamics

39.1 Introduction

In past decades, dynamics surface control (DSC) has been widely used for the design of adaptive controller for nonlinear systems in [1–6] since it does not need to repeat derivation to virtual control. In addition, the circular argument in back-stepping can be avoided using DSC, i.e., DSC does not need to assume that the approximation error is bounded before the stability analysis is proved in [4]. In [2], robust adaptive neural control was investigated for a class of uncertain strict-feedback nonlinear systems. In [3, 4], adaptive DSC control was proposed for nonlinear pure-feedback system with input dead zone. In [5, 6], using K-filter, two adaptive output feedback control schemes were designed for uncertain nonlinear systems.

X. Xia · T. Zhang (✉) · Q. Wang
Department of Automation, College of Information Engineering, Yangzhou University, Yangzhou 225127, China
e-mail: tpzhang@yzu.edu.cn

Z. Deng and H. Li (eds.), *Proceedings of the 2015 Chinese Intelligent Automation Conference*, Lecture Notes in Electrical Engineering 337,
DOI 10.1007/978-3-662-46463-2_39

Commonly, states unmodeled dynamics is used to generalize modeling error, measure error and extra disturbance when modeling controlled systems, and input unmodeled dynamics also expresses the similar factors in actuator. These unmodeled dynamics may bring about unstable influence to systems. Both Lyapunov function method and dynamic signal method were presented to handle unmodeled dynamics in [7, 8], respectively. Utilizing these methods, adaptive output feedback control was designed for a class of nonlinear systems with uncertain dynamics in [9–12]. Using backstepping method and dynamic nonlinear damping design, global asymptotic stability problem was solved for systems with stable linear input unmodeled dynamics in [13, 14]. When the zero dynamics subsystem of uncertain nonlinear system was input-state stable and high-frequency gain was known, input unmodeled dynamics was dealt with by redesign nominal backstepping control law in [15]. A linear high gain observer was designed for a class of nonlinear output feedback systems with input unmodeled dynamics in [16].

Inspired of [15], adaptive neural DSC is developed for a class of uncertain output feedback nonlinear systems with states and input unmodeled dynamics. A novel description of unmodeled dynamics based on Lyapunov function is employed. The unstable influence of input unmodeled dynamics on the whole closed-loop system is counteracted by introducing a normalization signal. Compared with literature [15], nonlinear functions and constants used to describe input unmodeled dynamic subsystem in this paper are unknown except $d_\Delta \neq 0$, whereas, the sign of d_Δ and input gain sign need to be known in [15].

39.2 Problem Description and Basic Assumptions

Consider a class of output feedback nonlinear systems with state and input unmodeled dynamics in the following form:

$$\begin{cases} \dot{z} = q(z, y, t) \\ \dot{x} = Ax + f(y) + Gv + \Delta(z, y, t) \\ y = e_1^T x \end{cases} \tag{39.1}$$

where the input unmodeled dynamics subsystem is described as follows:

$$\dot{\zeta} = A_\Delta(\zeta) + b_\Delta \sigma(y)u \tag{39.2}$$

$$v = c_\Delta(\zeta) + d_\Delta \sigma(y)u \tag{39.3}$$

$x = [x_1, x_2, \ldots, x_n]^T \in R^n$ is the unmeasurable state, $y \in R$ is the measurable output of the system. $f(y) = [f_1(y), \ldots, f_n(y)]^T$, $f_i(y)$ are the unknown smooth functions. $z \in R^{n_0}$ is the unmodeled dynamics, $\Delta(z, y, t) = [\Delta_1(z, y, t), \ldots, \Delta_n(z, y, t)]^T$, $\Delta_i(z, y, t)$ are the uncertain nonlinear dynamic disturbances, and $\Delta_i(z, y, t)$ and

$q(z, y, t)$ are the unknown smooth functions satisfying the Lipschitz condition. $G = [0_{1\times(n-m-1)}, b^T]^T$, $b = [b_m, \ldots, b_1, b_0]^T \in R^{m+1}$ is the unknown constant vector, $B(s) = b_m s^m + \cdots + b_1 s + b_0$ is a Hurwitz polynomial. $A = \begin{bmatrix} 0 & I_{n-1} \\ 0 & 0 \end{bmatrix}$, $e_i \in R^n$ denotes the n dimension vector in which the ith component is 1 and the others are 0. $\zeta \in R^q$ is the state of unmodeled dynamics driven by the input $\sigma(y)u$, $u \in R$, $\sigma(y) \neq 0$ is a known positive continuous function; $v \in R$ is the input of system (1), which acts as the output of ζ-subsystem, i.e., if $v = \sigma(y)u$, system (1) is a nominal system. $A_\Delta(\cdot)$ and b_Δ are unknown vectors, $c_\Delta(\cdot)$ is an unknown function and d_Δ is an unknown constant.

The control objective is to design adaptive output feedback control $u(t)$ for system (1) such that the output y follows the specified desired trajectory y_d, and all the signals in the closed-loop system are semi-globally uniformly ultimately bounded.

Assumption 39.1 The unknown nonlinear dynamic disturbances $\Delta_i(z, y, t)$, $i = 1, 2, \ldots, n$ satisfy $|\Delta_i(z, y, t)| \leq \rho_{i1}(|y|) + \rho_{i2}(y)||z||$, where $\rho_{i1}(|y|)$ and $\rho_{i2}(y)$ are the unknown nonnegative smooth functions, and $||\cdot||$ denotes the Euclidian norm of a vector.

Assumption 39.2 The system $\dot{z} = q(z, 0, t) - q(0, 0, t)$ is global asymptotic stable when $z = 0$, i.e., there exists a Lyapunov function $W(z, t)$ satisfying

$$c_1||z||^4 \leq W(z,t) \leq c_2||z||^4, \left|\frac{\partial W}{\partial z}(z,t)\right| \leq c_4||z||^3$$

$$\frac{\partial W}{\partial t}(z,t) + \frac{\partial W}{\partial z}(z,t)(q(z,0,t) - q(0,0,t)) \leq -c_3||z||^4$$

where c_1, c_2, c_3, c_4 are positive constants, and there exists $c_5 \geq 0$, $||q(0, 0, t)|| \leq c_5$, $\forall t \geq 0$.

Assumption 39.3 There exists an unknown smooth function ψ_0 and $\psi_0(0) = 0$ such that $||q(z, y, t) - q(z, 0, t)|| \leq \psi_0(|y|)$.

Assumption 39.4 The desired trajectory vector X_d is smooth and available, and $X_d = [y_d, \dot{y}_d, \ddot{y}_d]^T \in \Omega_d$, where $\Omega_d = \{x_d : y_d^2 + \dot{y}_d^2 + \ddot{y}_d^2 \leq B_0\}$, and B_0 is a known constant.

Assumption 39.5 The input unmodeled dynamics subsystem has relative degree zero, that is, $d_\Delta \neq 0$, and there exists a known smooth function $\bar{c}_\Delta(\cdot)$ of class K such that $|c_\Delta(\zeta(t))| \leq \bar{c}_\Delta|\zeta(t)|$.

Assumption 39.6 The input unmodeled dynamics subsystem composed of (39.2) and (39.3) is globally exponential stable (GES) with the convergence rate δ when $u = 0$, and the input unmodeled dynamics composed of (39.2) and (39.3) is also GES when $A_\Delta(\cdot)$ is globally Lipschitz, i.e., there exists a Lyapunov function $V(\zeta)$ satisfying

$$\beta_1|\zeta|^2 \le V(\zeta) \le \beta_2|\zeta|^2$$
$$\frac{\partial V}{\partial \zeta}A_\Delta(\zeta) \le -2\delta V(\zeta),\ \left|\frac{\partial V}{\partial \zeta}\right| \le \beta_3|\zeta|$$

Assumption 39.7 There exists a known constant $b_{\max}$ such that $0 < b_m \le b_{\max}$.

Lemma 39.1 *Consider the system composed of* (39.2) *and* (39.3) *and construct a first-order system* $\dot{\bar{m}} = -\delta\bar{m} + |\sigma(y)u|$. *If Assumption* 39.6 *holds and suppose* $u(t) \in L_\infty[0,T]$, *then there exist constants* α_1 *and* $\alpha_2 > 0$ *such that, for all* $t \in [0,T]$,

$$\|\zeta(t)\| \le \alpha_1(\|\zeta(0)\| + |\bar{m}(0)|)e^{-\delta t} + \alpha_2|\bar{m}(t)| \tag{39.4}$$

Let $\Omega_y = \{y||y| \le M_y\}$ *be a compact set with* $M_y > 0$ *being a design constant. We use radial basis function neural networks to approximate unknown continuous function* $f_i(y)$ *on the compact set* Ω_y *as discussed in* [17], *i.e.,* $f_i(y) = \phi_i^T(y)\theta_i^* + \delta_i(y)$, *where* $\theta_i^* = [\theta_{i1}^*, \theta_{i2}^*, \ldots, \theta_{iM_i}^*]^T$, $\theta_i^* = \arg\min_{\theta_i \in R^{M_i}}[\sup_{y\in\Omega_y}|\theta_i^T\phi_i(y) - f_i(y)|]$, $\delta_i(y)$ *is an approximation error, and* $\phi_i(y) = [\phi_{i1}(y), \ldots, \phi_{iM_i}(y)]^T$, *and* $\phi_{ij}(y)$ *is called as radial basis function, which is chosen as* $\phi_{ij}(y) = \exp[-(y-\mu_{ij})^2/d_{ij}]$ *with* μ_{ij} *being its center and* d_{ij} *being its width,* $j = 1, \ldots, M_i$, $i = 1, \ldots, n$ and M_i *is the node number of the ith neural networks. Substituting* (39.3) *into system* (39.1), *we obtain*

$$\begin{cases} \dot{z} = q(z,y,t) \\ \dot{x} = Ax + f(y) + F^T(y,u)\theta + \delta(y) + \Delta(z,y,t) + Gc_\Delta(\zeta) \\ y = e_1^T x \end{cases} \tag{39.5}$$

where

$$F^T(y,u) = \left[\begin{bmatrix} 0_{(\rho-1)\times(m+1)} \\ I_{m+1} \end{bmatrix}\sigma(y)u,\ \Phi^T(y)\right],\ \Phi^T(y) = \begin{bmatrix} \phi_1^T(y) & & \\ & \ddots & \\ & & \phi_n^T(y) \end{bmatrix}$$

$$\theta_\Delta = bd_\Delta \in R^{m+1},\ \theta_f = [\theta_1^{*T}, \ldots, \theta_n^{*T}]^T,\ \theta = [\theta_\Delta^T, \theta_f^T]^T \in R^{(m+1+N_1)}$$

$$N_1 = \sum_{i=1}^{n} M_i,\ \delta(y) = [\delta_1(y), \delta_2(y), \ldots, \delta_n(y)]^T,\ n = \rho + m$$

39.3 Filter Design Based on Neural Networks

The neural network filters are designed as follows:

$$\begin{cases} \dot{\xi} = A_0\xi + Ly,\ \xi \in R^n \\ \dot{\vartheta} = A_0\vartheta + \Phi^T(y),\ \vartheta \in R^{n\times N_1} \\ \dot{\lambda} = A_0\lambda + e_n\sigma(y)u,\ \lambda \in R^n \end{cases} \tag{39.6}$$

where $A_0 = A - Le_1^T$ and $L = [l_1, \ldots, l_n]^T$, A_0 is a Hurwitz matrix satisfying the Lyapunov equation $PA_0 + A_0^T P = -hI$, $P = P^T > 0$ and $h > 0$.

Define the state estimate as $\hat{x} = \xi + \Omega^T\theta$, and the state observer error as $\varepsilon = x - \hat{x}$, then

$$\dot{\varepsilon} = A_0\varepsilon + \delta(y) + Gc_\Delta(\zeta) + \Delta \tag{39.7}$$

where $\Omega^T = [v_m, \ldots, v_1, v_0, \vartheta]$, $v_i \in R^n$.

$$\dot{v}_i = A_0 v_i + e_{n-i}\sigma(y)u,\ i = 0, 1, \ldots, m \tag{39.8}$$

Since $A_0^i e_n = e_{n-i}, i = 0, 1, \ldots, n-1$, we have

$$v_i = A_0^i\lambda,\quad i = 0, 1, \ldots, m \tag{39.9}$$

$$x_2 = b_m d_\Delta v_{m,2} + \xi_2 + [0,\ v_{m-1,2}, \ldots,\ v_{1,2},\ v_{0,2},\ \vartheta_{(2)}]\theta + \varepsilon_2 \tag{39.10}$$

where $\vartheta_{(2)}$ represents the second row of matrix ϑ, and $\xi_2, v_{i,2}$ and ε_2 represent the second element of vector ξ, v_i and ε, respectively.

$$\dot{y} = b_{m\Delta}v_{m,2} + \xi_2 + \bar{\omega}^T\theta + \varepsilon_2 + \delta_1(y) + \Delta_1 \tag{39.11}$$

where $\omega^T = \left[v_{m,2}, \ldots, v_{1,2}, v_{0,2}, \vartheta_{(2)} + \Phi_{(1)}^T\right]$, $\bar{\omega}^T = [0, v_{m-1,2}, \ldots, v_{1,2}, v_{0,2}, \vartheta_{(2)} + \Phi_{(1)}^T]$, and $\Phi_{(1)}^T$ is the first row of Φ^T, $b_m d_\Delta = b_{m\Delta}$.

39.4 Adaptive Dynamic Surface Control Design

In this section, we propose adaptive output feedback control using dynamic surface control method. The whole design needs ρ steps.

Define $V_\varepsilon = \varepsilon^T P\varepsilon$, then

$$\begin{aligned} \dot{V}_\varepsilon \le & -(h-3)\varepsilon^T\varepsilon + \sum_{j=1}^{n}\|P\|^2\delta_j^2(y) + \|P\|^2\|G\|^2|c_\Delta(\zeta)|^2 + 2\sum_{j=1}^{n}\|P\|^2\bar{\rho}_{j1}^2(|y|) \\ & + \frac{16n\lambda_0}{c_3}\sum_{j=1}^{n}\|P\|^4\rho_{j2}^4(y) + \frac{c_3}{16\lambda_0}\|z\|^4 \end{aligned} \tag{39.12}$$

According to Assumptions 39.5, 39.6 and Lemma 39.1, we know

$$|c_\Delta(\zeta(t))| \le \bar{c}_\Delta \|\zeta(t)\| \le \bar{c}_\Delta \alpha_1(\|\zeta(0)\| + |\bar{m}(0)|)e^{-\delta t} + \bar{c}_\Delta \alpha_2 |\bar{m}(t)|$$

Using $1 + |m(t)|$ to divide two sides of the above equation, it yields

$$|c_\Delta(\zeta)|(1 + \bar{m}(t))^{-1} \le H_{\bar{m}}$$

where $H_m = \max\{\bar{c}_\Delta \alpha_1(\|\zeta(0)\| + |\bar{m}(0)|), \bar{c}_\Delta \alpha_2\}$. Furthermore, we obtain

$$\|P\|^2 \|G\|^2 |c_\Delta(\zeta)|^2 \le (1 + |\bar{m}(t)|)^2 H_c$$

where $H_c = \|P\|^2 \|G\|^2 H_{\bar{m}}^2$. If let $H = H_c/\varepsilon^*$, where ε^* is a design constant, $P_{\bar{m}} = (1 + |\bar{m}|)^2$, then

$$\|P\|^2 \|G\|^2 |c_\Delta(\zeta)|^2 \le P_{\bar{m}} s_1 H + (1 - s_1/\varepsilon^*) P_{\bar{m}} H_c \tag{39.13}$$

From (39.12) and (39.13),

$$\begin{aligned} \dot{V}_\varepsilon \le & -(h-3)\varepsilon^T \varepsilon + \sum_{j=1}^{n} \|P\|^2 \delta_j^2(y) + P_{\bar{m}} s_1 H + (1 - \frac{s_1}{\varepsilon^*}) P_{\bar{m}} H_c \\ & + 2\sum_{j=1}^{n} \|P\|^2 \bar{\rho}_{j1}^2(|y|) + \frac{16n\lambda_0}{c_3} \sum_{j=1}^{n} \|P\|^4 \rho_{j2}^4(y) + \frac{c_3}{16\lambda_0} \|z\|^4 \end{aligned} \tag{39.14}$$

Define $V_W = \lambda_0^{-1} W(z,t)$, $\lambda_0 > 0$, then

$$\dot{V}_W \le -5c_3 \|z\|^4 \lambda_0^{-1}/8 + 16c_4^4 \psi_0^4(|y|) \lambda_0^{-1} c_3^{-3} + 16c_4^4 c_5^4 \lambda_0^{-1} c_3^{-3} \tag{39.15}$$

Step 1: Let $\omega_1 = y_d$ and $s_1 = x_1 - \omega_1$, then the derivation of s_1 with respect to time t is

$$\dot{s}_1 = b_{m\Delta} v_{m,2} + \xi_2 + \bar{\omega}^T \theta + \varepsilon_2 + \delta_1(y) + \Delta_1 - \dot{y}_d \tag{39.16}$$

Define $V_{s_i} = s_i^2/2$, and s_i will be given later. Then

$$\dot{V}_{s_1} = s_1 b_{m\Delta} v_{m,2} + s_1(\xi_2 + \bar{\omega}^T \theta + \varepsilon_2 + \delta_1(y) + \Delta_1 - \dot{y}_d) \tag{39.17}$$

Design a virtual control law as

$$\alpha_1 = N(\varsigma)(k_1 s_1 + \xi_2 + \bar{\omega}^T \hat{\theta} + s_1 \hat{\theta}_1^T \psi_1(X) + P_{\bar{m}} \hat{H}) \tag{39.18}$$

$$\dot{\varsigma} = s_1(k_1 s_1 + \xi_2 + \bar{\omega}^T \hat{\theta} + s_1 \hat{\theta}_1^T \psi_1(X) + P_{\bar{m}} \hat{H}) \tag{39.19}$$

where $k_1 > 0$ is a design constant, $\hat{\theta}$, $\hat{\theta}_1$, $\hat{H}$ are the estimate of θ, θ_1, H at time t, respectively, θ_1, $\psi_1(X)$ will be given later, $N(\varsigma) = \varsigma^2 \cos(\varsigma)$. Define the estimate errors $\tilde{\theta} = \theta - \hat{\theta}$, $\tilde{\theta}_1 = \theta_1 - \hat{\theta}_1$, $\tilde{H} = H - \hat{H}$.

A first-order filter with τ_2 being a time constant and ω_2 being the output is designed as follows:

$$\tau_2 \dot{\omega}_2 + \omega_2 = \alpha_1, \ \omega_2(0) = \alpha_1(0) \tag{39.20}$$

Let $y_2 = \omega_2 - \alpha_1$ and define $s_i = v_{m,i} - \omega_i$, then $v_{m,2} = s_2 + \alpha_1 + y_2$. According to (39.20), we have

$$\begin{aligned} \dot{V}_{s_1} \leq & -(k_1 - 2b^*_{\max} - 2)s_1^2 + \frac{b^*_{\max}}{4}s_2^2 + \frac{b^*_{\max}}{4}y_2^2 - s_1\hat{\theta}_1^T\psi_1(X) + s_1\bar{\omega}^T\tilde{\theta} \\ & - s_1 P_{\bar{m}}\hat{H} + (b_{m\Delta}N(\varsigma) + 1)\dot{\varsigma} + 0.25(\varepsilon_2^2 + \delta_1^2) + s_1\Delta_1 - s_1\dot{y}_d \end{aligned} \tag{39.21}$$

where $b^*_{\max} = b_{\max} d_\Delta$.

From Assumption 39.2 and using Young's inequality, we get

$$|s_1\Delta_1| \leq s_1^2\rho_{11}^2(|y|) + 0.25 + s_1^2\rho_{12}^2(y) + c_3\lambda_0^{-1}\|z\|^4/16 + 0.25\lambda_0 c_3^{-1} \tag{39.22}$$

Define $V_{sW\varepsilon} = V_{s_1} + V_\varepsilon + V_W$, then

$$\begin{aligned} \dot{V}_{sW\varepsilon} \leq & -(h - 3.25)\varepsilon^T\varepsilon - (k_1 - 2b^*_{\max} - 2)s_1^2 - 0.5c_3\lambda_0^{-1}||z||^4 \\ & + (b_{m\Delta}N(\varsigma) + 1)\dot{\varsigma} + s_1H_1(x) + (1 - s_1^2/\varepsilon^*)P_{\bar{m}}H_c \ - s_1\hat{\theta}_1^T\psi_1(X) \\ & + (1 - s_1^2/\varepsilon^*)Q(y) + s_1P_{\bar{m}}\tilde{H} + s_1\bar{\omega}^T\tilde{\theta} + 0.25b^*_{\max}(s_2^2 + y_2^2) + D \end{aligned} \tag{39.23}$$

where $H_1(X) = s_1\rho_{11}^2(|y|) + s_1\rho_{12}^2(y) - \dot{y}_d + s_1Q(y)/\varepsilon^*$, $X = [s_1, y_d, \dot{y}_d]^T$, $D = 16c_4^4c_5^4\lambda_0^{-1}c_3^{-3} + 0.25\lambda_0c_3^{-1} + 0.25$, $Q(y) = ||P||^2\sum_{j=1}^{n}\delta_j^2 + 2||P||^2\sum_{j=1}^{n}\rho_{j1}^2(|y|)$ $+16n\lambda_0c_3^{-1}||P||^4\sum_{j=1}^{n}\rho_{j2}^4(y)] + 16c_4^4\lambda_0^{-1}c_3^{-3}\psi_0^4(|y|)$.

Let $\Omega_X = \{X| \ \|X\| \leq M_X\} \subset R^3$ be a given compact set with $M_X > 0$ being a design constant, and ${\theta_1}^T\psi_1(X)$ be the approximation of the radial basis function neural networks on the compact set Ω_X to $H_1(X)$. Then, we have $H_1(X) = {\theta_1}^T\psi_1(X) + B_1(X)$, where $B_1(X)$ denotes the approximation error, and $\psi_1(X) = [\psi_{11}(X), \ldots, \psi_{1N_2}(X)]^T \in R^{N_2}$ denotes the basis function vector with $\psi_{1j}(X)$ being chosen as the commonly used Gaussian functions, which have the form $\psi_{1j}(X) = exp[-||X - \mu_{1j}||^2/b_{1j}^2]$, $j = 1, \ldots, N_1$, μ_{1j} is the center of the receptive field and b_{1j} is the width of the Gaussian function; θ_1 is an adjustable parameter vector. There exists a nonnegative continuous function $\kappa(s_1, y_d, \dot{y}_d)$ satisfying $|B_1(X)| \leq \kappa(s_1, y_d, \dot{y}_d)$. From (39.26), it yields

$$\begin{aligned}\dot{V}_{sW\varepsilon} \leq & -(h-3.25)\varepsilon^T\varepsilon-(k_1-2b^*_{\max}-3)s_1^2-0.5c_3\lambda_0^{-1}\|z\|^4\\ & +(b_{m\Delta}N(\varsigma)+1)\dot{\varsigma}+0.25\kappa+(1-s_1^2/\varepsilon^*)P_{\bar{m}}H_c \ +s_1\tilde{\theta}_1^T\psi_1(X)\\ & +(1-s_1^2/\varepsilon^*)Q(y)+s_1P_{\bar{m}}\tilde{H}+\ s_1\bar{\omega}^T\tilde{\theta}+0.25b^*_{\max}(s_2^2+y_2^2)+D\end{aligned} \tag{39.24}$$

There exists a nonnegative continuous function $\eta_2(\bar{s}_2, y_2, \varepsilon_2, \hat{\theta}_b, \xi, \vartheta, \bar{\lambda}_{m+2}, y_d, \dot{y}_d, \ddot{y}_d)$ such that

$$|\dot{y}_2+\tau_2^{-1}y_2| \leq \eta_2(\bar{s}_2, y_2, \varepsilon_2, \hat{\theta}_b, \xi, \vartheta, \bar{\lambda}_{m+2}, y_d, \dot{y}_d, \ddot{y}_d) \tag{39.25}$$

where $\bar{s}_i = [s_1, s_2, \ldots, s_i]^T, i = 1, \ldots, \rho$.

$$y_2\dot{y}_2 \leq -y_2^2/\tau_2+y_2^2+\eta_2^2/4 \tag{39.26}$$

Step i ($2 \leq i \leq \rho-1$): Define $s_i = v_{m,i}-\omega_i$, then

$$\dot{s}_i = \dot{v}_{m,i}-\dot{\omega}_i = \dot{v}_{m,i+1}-l_iv_{m,1}-\dot{\omega}_i \tag{39.27}$$

Design a virtual control law as:

$$\alpha_i = -k_is_i+l_iv_{m,1}+\dot{\omega}_i \tag{39.28}$$

A first order filter with τ_i being a time constant is defined as follows:

$$\tau_{i+1}\dot{\omega}_{i+1}+\omega_{i+1} = \alpha_i,\ \omega_{i+1}(0) = \alpha_i(0)$$

Let $y_{i+1} = \omega_{i+1}-\alpha_i$, then

$$\dot{V}_{s_i} \leq -(k_i-2)s_i^2+\frac{1}{4}s_{i+1}^2+\frac{1}{4}y_{i+1}^2 \tag{39.29}$$

and there exists a nonnegative continuous function $\eta_{i+1}(\bar{s}_{i+1}, \bar{y}_{i+1}, \varepsilon_2, \hat{\theta}_b, \xi, \vartheta, \bar{\lambda}_{m+2}, y_d, \dot{y}_d, \ddot{y}_d)$ such that

$$|\dot{y}_{i+1}+\tau_{i+1}^{-1}y_{i+1}| \leq \eta_{i+1}(\bar{s}_{i+1}, \bar{y}_{i+1}, \varepsilon_2, \hat{\theta}_b, \xi, \vartheta, \bar{\lambda}_{m+2}, y_d, \dot{y}_d, \ddot{y}_d) \tag{39.30}$$

where $\bar{y}_j = [y_2, \ldots, y_j]^T, j = 2, \ldots, \rho$. Therefore,

$$y_{i+1}\dot{y}_{i+1} \leq -y_{i+1}^2/\tau_{i+1}+y_{i+1}^2+\eta_{i+1}^2/4 \tag{39.31}$$

Step ρ: Define $s_\rho = v_{m,\rho}-\omega_\rho$, then

$$\dot{s}_\rho = \sigma(y)u+v_{m,\rho+1}-l_\rho v_{m,1}-\dot{\omega}_\rho \tag{39.32}$$

Choose the control law u as follows:

$$u = (-k_\rho s_\rho - v_{m,\rho+1} + l_\rho v_{m,1} + \dot{\omega}_\rho)/\sigma(y) \tag{39.33}$$

then

$$\dot{V}_{s_\rho} = s_\rho \sigma(y) u + s_\rho (v_{m,\rho+1} - l_\rho v_{m,1} - \dot{\omega}_\rho) \leq -k_\rho s_\rho^2 \tag{39.34}$$

Select the adaptive laws as follows:

$$\dot{\hat{\theta}} = \gamma_1(\bar{\omega} s_1 - \sigma_1 \hat{\theta}) \tag{39.35}$$

$$\dot{\hat{\theta}}_1 = \gamma_2(s_1 \psi_1(X) - \sigma_2 \hat{\theta}_1) \tag{39.36}$$

$$\dot{\hat{H}} = \gamma_3(P_m s_1 - \sigma_3 \hat{H}) \tag{39.37}$$

where $\gamma_1, \gamma_2, \gamma_3$ and $\sigma_1, \sigma_2, \sigma_3$ are design constants. Define

$$V_1 = s_1^2 + 2V_\varepsilon + \tilde{\theta}^T \tilde{\theta}/\gamma_1 + \tilde{\theta}_1^T \tilde{\theta}_1/\gamma_2 + \tilde{H}^2/\gamma_3 + c_3 ||z||^4/\lambda_0$$

$$V_i = \sum_{j=1}^{i} s_j^2 + 2V_\varepsilon + \sum_{j=2}^{i} y_j^2 + \tfrac{1}{\gamma_1}\tilde{\theta}^T \tilde{\theta} + \tfrac{1}{\gamma_2}\tilde{\theta}_1^T \tilde{\theta}_1 + \tfrac{1}{\gamma_3}\tilde{H}^2 + \tfrac{c_3}{\lambda_0}||z||^4, i = 2, \ldots, \rho$$

Define some compact sets $\Omega_1 = \{(s_1, \varepsilon^T, \bar{m}, \hat{\theta}^T, \hat{\theta}_1^T, \hat{H}, ||z||) : V_1 \leq p\} \subset R^{p_1}$ and $\Omega_i = \{(\bar{s}_i^T, \bar{y}_i^T, \varepsilon^T, \bar{m}, \hat{\theta}^T, \theta_1^T, \hat{H}, ||z||) : V_i \leq p\} \subset R^{p_i}$, where $i = 2, \ldots, \rho$, $p_i = n + N_1 + N_2 + m + 2i + 3$, $p > 0$ is a design constant that can be determined by a given arbitrary positive constant c. $\Omega_1 \times R^{p_\rho - p_1} \supset \Omega_2 \times R^{p_\rho - p_2} \supset \cdots \supset \Omega_{\rho-1} \times R^{p_\rho - p_{\rho-1}} \supset \Omega_\rho$. The maximum value of the continuous function $\kappa(s_1, y_d, \dot{y}_d)$ is N_0 on the compact set $\Omega_1 \times \Omega_d$, and the maximum value of the continuous function $\eta_{i+1}(\bar{s}_{i+1}, \bar{y}_{i+1}, \varepsilon_2, \hat{\theta}_b, \xi, \vartheta, \bar{\lambda}_{m+2}, y_d, \dot{y}_d, \ddot{y}_d)$ on the compact set $\Omega_{i+1} \times \Omega_d$ is N_{i+1} when $\xi, \vartheta, \bar{\lambda}_{m+2}$ is bounded.

Theorem 39.1 *Consider the closed-loop system consisting of the plant* (1) *under Assumptions* 39.1–39.7, *the controller* (39.33) *and adaptation laws* (39.35)-(39.37). For $V(0) \leq c$, *choose appropriate positive constants* $k_i, \tau_i, h, \gamma_1, \gamma_2, \gamma_3$ *and* $\sigma_1, \sigma_2, \sigma_3$ *such that the closed-loop system is semi-globally uniformly ultimately bounded and the tracking error converges to a small residual error set, and* k_i, τ_i *and* h *satisfy*

$$\begin{cases} k_i \geq 3 + 2b_{\max}^* + 0.5\alpha_0, i = 1, 2, \ldots, \rho \\ \tau_i^{-1} \geq 0.25 b_{\max}^* + 1.25 + 0.5\alpha_0, i = 2, \ldots, \rho \\ \alpha_0 = \min\{\gamma_1\sigma_1, \gamma_2\sigma_2, \gamma_3\sigma_3, c_3/(2c_2), (h - 13/4)\lambda_{\max}^{-1}(P)\} \end{cases} \tag{39.38}$$

To save space, simulation results are omitted.

39.5 Conclusions

By using neural network filters to estimate unmeasurable states, adaptive output feedback dynamic surface control has been proposed for a class of nonlinear systems with state and input unmodeled dynamics. The unknown control gain sign is handled by using Nussbaum function. State unmodeled dynamics is dealt with by introducing a Lyapunov function, and input unmodeled dynamics is solved by using a normalization signal. By theoretical analysis, all the signals in the closed-loop system are shown to be semi-globally uniformly ultimately bounded.

Acknowledgments This work was partially supported by the National Natural Science Foundation of China (61174046 & 61473250).

References

1. Swaroop D, Hedrick JK, Yip PP et al (2000) Dynamic surface control for a class of nonlinear systems. IEEE Trans Autom Control 45(10):1893–1899
2. Wang D, Huang J (2005) Neural network-based adaptive dynamic surface control for a class of uncertain nonlinear systems in strict feedback form. IEEE Trans Neural Networks 16(1):195–202
3. Chen WS, Jiao LC (2010) Adaptive tracking for periodically time-varying and nonlinearly parameterized systems using multilayer neural networks. IEEE Trans Neural Networks 21 (2):345–351
4. Zhang TP, Ge SS (2008) Adaptive dynamic surface control of nonlinear systems with unknown dead zone in pure feedback form. Automatica 44(7):1895–1903
5. Liu YJ, Wang W (2012) Adaptive output feedback control of uncertain nonlinear systems based on dynamic surface control technique. Int J Robust and Nonlinear Control 22:945–958
6. Wang Q, Zhang TP (2009) Adaptive fuzzy output feedback control using dynamic surface control. Systems Engineering and Electrics 31(3):647–652 (in Chinese)
7. Jiang ZP, Praly L (1998) Design of robust adaptive controllers for nonlinear systems with dynamic uncertainties. Automatica 34(7):825–840
8. Jiang ZP, Hill DJ (1999) A robust adaptive backstepping scheme for nonlinear systems with unmodeled dynamics. IEEE Trans Autom Control 44(9):1705–1711
9. Xia XN, Zhang TP (2014) Adaptive Output Feedback Control for Uncertain Nonlinear Systems with Unknown Dead-Zone Input. Proceedings of the 33rd Chinese Control Conference. Nanjing, China, pp 8729–8734
10. Tong SC, Li YM (2009) Fuzzy adapitive robust control for a class of nonlinear system with unmodeled dynamics. Control and Decision 24(3):417–422 (in Chinese)
11. Zhang TP, Gao ZY (2013) Adaptive dynamic surface control with uncertain dynamics. Control and Decision 28(10):1541–1546 (in Chinese)
12. Zhang XY, Lin Y (2011) Adaptive tracking control for a class of pure-feedback nonlinear systems including actuator hysteresis and dynamic uncertainties. IET Control Theor Appl 5 (16):1868–1880
13. Krstic M, Sun J, Kokotovic PV (1995) Robust control of strict and output feedback system with unmodeled dynamics. In: Proceedings of the 34 IEEE Conference on Decision and Control, New Orleans, USA, pp 2257-2262
14. Krstic M, Sun J, Kokotovic PV (1996) Robust control of nonlinear systems with input unmodeled dynamics. IEEE Trans Autom Control 41(6):913–920

15. Arcak M, Kokotovic P (2000) Robust nonlinear control of systems with input unmodeled dynamics. Syst Control Lett 41(2):115–122
16. Hou MZ, Wu AG, Duan GR (2008) Robust output feedback control for a class of nonlinear systems with input unmodeled dynamics. Int J Automation and Computing 5(3):307–312
17. Ge SS, Hang CC, Le TH, Zhang T (2001) Stable Adaptive Neural Network Control. Kluwer Academic, Boston

Chapter 40
Control of Powered Knee Joint Prosthesis Based on Finite-State Machine

Guoxing Chen, Zuojun Liu, Lingling Chen and Peng Yang

Abstract In order to make the powered knee joint prosthesis to provide the required power for walking, a driving motor control approach based on finite-state machine is proposed. According to the periodicity and repeatability of the human body movement characteristic, the gait phase is divided into four states by foot pressure signals. With the reference of healthy limb gait information, a movement database for powered prosthesis is established for different terrain and speed conditions. The finite-state machine is used to control powered prosthesis, and a stateflow module structure is build in the controller, making prosthesis limb to move to coordinate with the healthy limb. Finally, the experiment using the prosthesis prototype verified the feasibility of this method.

Keywords Finite-state machine · Powered prosthesis · Knee joint · Movement database

40.1 Introduction

As the passive lower limb prosthesis lack the ability to generate the required power for the amputees walking, the powered lower limb prosthesis became the inevitable trend of prosthesis development [1]. However, compared with traditional passive prosthesis, the research of powered prosthesis still faces the challenges in weight, energy consumption, especially in motion control [2].

The studies of powered prosthesis have been widely reported. In 1970s, Flowers et al. developed a hydraulically actuated knee prosthesis joints [3]. In 1990, a British company developed a world's first microprocessor control intelligent prosthesis called IP [4]. Akin and Yucenur invented a powered knee joint using

G. Chen · Z. Liu (✉) · L. Chen · P. Yang
School of Control Science and Engineering, Hebei University of Technology,
No. 8 Guangrong Road, Hong Qiao, Tianjin 300130, China
e-mail: liuzuojun@hebut.edu.cn

Z. Deng and H. Li (eds.), *Proceedings of the 2015 Chinese Intelligent Automation Conference*, Lecture Notes in Electrical Engineering 337,
DOI 10.1007/978-3-662-46463-2_40

motor as a driving mechanism in 2006 [5]. The first commercially available powered knee prosthesis was developed by Ossur, called Power Knee. In 2009, the second-generation power knee has been developed with many great improvements in terms of weight, height, and noise reduction as well as in power autonomy. In 2011, Sup et al. extended a previously developed walking control methodology to enable an above-knee amputee to walk up slopes using a powered knee and ankle prosthesis [6–8]. He Huang and her team are committed to the research of locomotion-mode identification and control method for prosthesis, and they designed a low-power mobile CPU-based embedded system for artificial leg control in 2013 [9, 10]. In China, more and more researchers also worked in this field. Jin designed an intelligent knee prosthesis that used EMG signal to identify terrain conditions [11]. Tan et al. developed a kind of intelligent prosthesis CIP-I legs based on nonlinear PID control [12]. And Yang made a model of powered lower limb prosthesis which designed on the basis of robotics, and also successfully identified the different movement patterns [13]. So the control method for the prosthesis limb moving coordinates with the healthy limb becomes the focus at present stage.

Generally, the key in the control of powered prosthesis is to regulate knee joint's angle correctly. A finite-state machine approach is described in this paper. Although some preliminary studies had mentioned the control method based on FSM, which is potentially useful for the powered prosthesis [14, 15], the applications for different terrain conditions and speed had not been discussed deeply. Via the anglicizing of healthy limb gait information, a knee joint movement database is established to provide control signals. According to the periodicity and repeatability of the human movement characteristic, a finite-state machine is used to control the powered knee prosthesis motor. The control principle diagram of powered knee prosthesis is shown in Fig. 40.1. The method described in this paper is easy to be implemented for practical application.

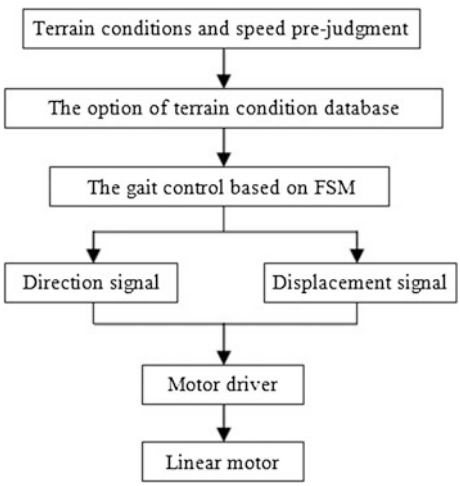

Fig. 40.1 The control principle diagram of powered knee prosthesis

40.2 Movement Database

Powered prosthesis movement research is mainly composed of terrain conditions prejudgment and knee joint angle control. According to the different terrain conditions, such as level ground, upslope or down slope, stairs ascent or descent [16, 17], different knee angle swing modes are outputted in the prosthesis control. A movement database is established through using the movement data from the healthy knee joint as reference. The database contains the motor's pulse control signal of direction and displacement in the different gait phase under a variety of terrain conditions. As shown in Fig. 40.2, the gait phase divides a walking cycle into four phases, which are early stance phase, middle stance phase, late stance phase, and swing phase, respectively. The phases can be recognized via two pressure switches mounted under the sole of the prosthesis foot, one under the ball flat and another under the heel.

The prosthesis knee joint used in this paper is shown in Fig. 40.3. The four connecting rods driven by the motor make the change of knee joint's angle. The relationship between prosthesis knee joint angle (θ) and motor shaft displacement (L) is described in Eq. 40.1. And the motor shaft displacement is 0.0508 mm for each pulse of signal. So the number of pulse signal can be calculated by knee joint angle's change for establishing the displacement database.

$$\theta = 2.188 * L \tag{40.1}$$

When the knee joint sways in reverse direction, the direction of the driving motor should change at the same time. The direction signal pulse (dir) is set as 1 when knee joint angle increases. Conversely, the direction signal pulse (dir) is set as −1 when knee joint angle decreases.

Taking the level walking as an example, the motor displacement and direction movement is shown in Fig. 40.4. There are information of knee joint angle, toe pressure, heel pressure, direction signal, and displacement pulse control signal of motor movement from top to bottom. In the figure, it can be seen that the dense part

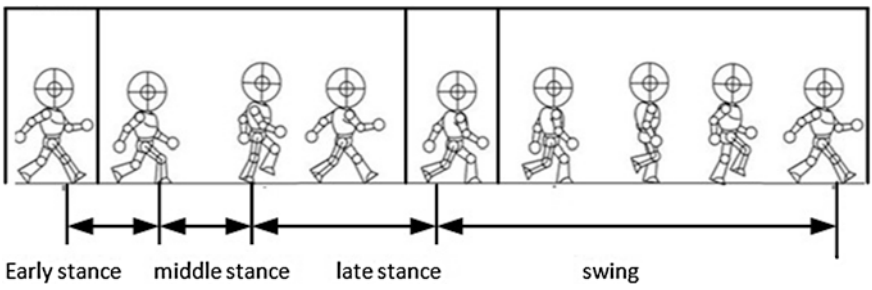

Fig. 40.2 The different phases in a walking cycle

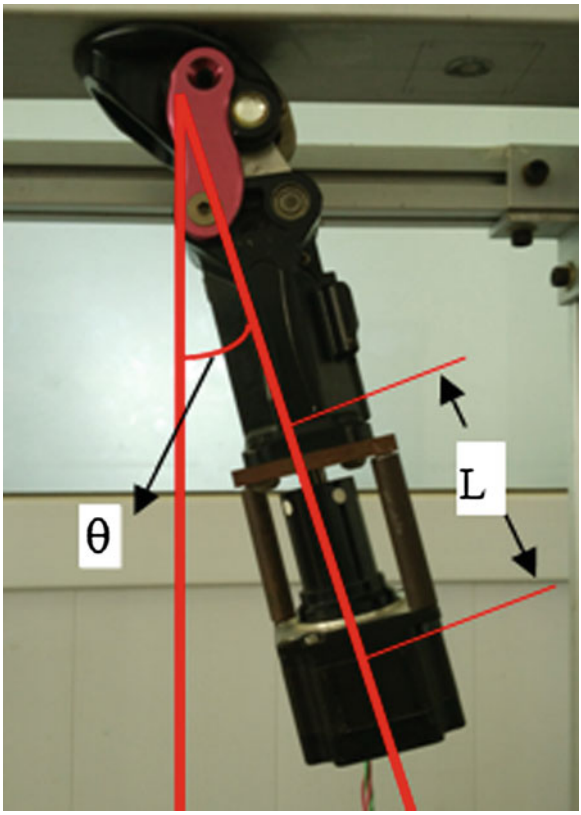

Fig. 40.3 The prototype of powered knee prosthesis

of pulse control signal of motor displacement is the moment that knee joint angle changes fast. While the sparse part of pulse control signal of motor displacement is the moment that knee joint angle changes slowly.

The four different gait phases are divided according to the information of toe pressure and heel pressure. Different gait phase corresponds to different waveform sequence in the control database of displacement and direction. Four parts constitute the movement database of level walking.

As far as the different speeds of walking are concerned, the database of each terrain condition contains three types of different speed information, 2, 3, and 4 km/h, respectively, for slow, medium and fast speed in a fuzzy way for average adult amputees. The database of level walking established above is in the case of 3 km/h, as a typical example. And the biggest difference among three types of speed information is that the required time is different when output the same amount of pulse signals. In addition, for stairs ascent and descent, upslope and down slope motions, the database establishing method is similar to that of level ground.

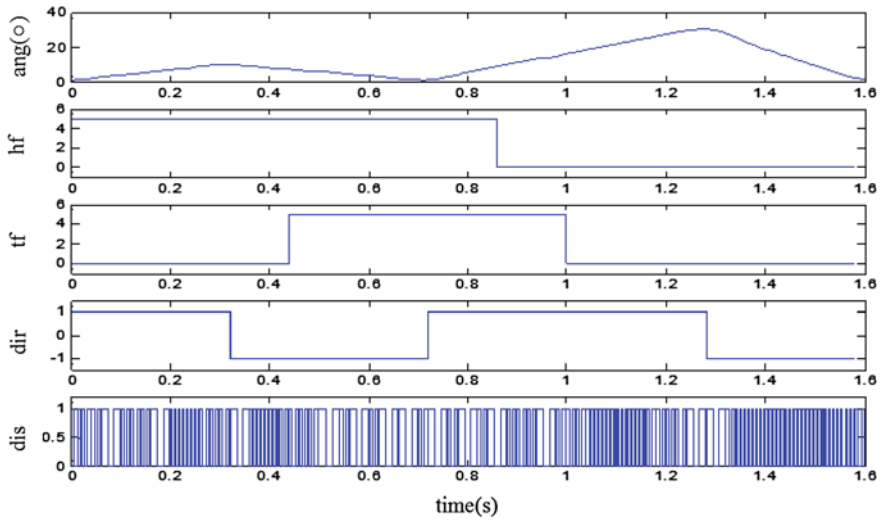

Fig. 40.4 The pulse control signal of motor displacement and direction

40.3 Control Method

In this paper, a finite-state machine (FSM) is used in a walking cycle control for the transformation process of different gait phase, due to the control system of powered knee prosthesis has some limit state (early stance, middle stance, late stance, and swing). Each state of the knee joint's movement behaviour keeps similar in walking. The control system of powered knee prosthesis always stays in a fixed state at any period. Besides, the trigger condition between two states is fixed too. Such a regular nature is consistent with the application condition of FSM [18].

According to the mathematical definition of FSM, the corresponding relation between walking cycle and FSM's five elements (Q, Σ, δ, $q0$, F) of mathematical definition is described as below:

1. Q is a finite set of all states, which are corresponding to the early stance phase, middle stance phase, late stance phase, and swing phase.
2. Σ is a finite set of all input symbols, which are corresponding to the signals of foot pressure (toe force, heel force).
3. $\delta: Q \times \Sigma \rightarrow Q$ is the transfer function between different gait phases.
4. $q0 \in Q$ is the starting state, defined as early stance in this paper. The default initial condition is early stance.
5. $F \subseteq Q$ is accepting state sets. In this paper, $F = Q$.

A stateflow module structure is build in the FSM controller, in which the transition conditions between different gait phases are determined according to the foot pressure signals. When the heel touches the ground and the toe is off the

Table 40.1 The option of gait phase database

Tf\Hf	0	1
0	Swing	Early stance
1	Late stance	Middle stance

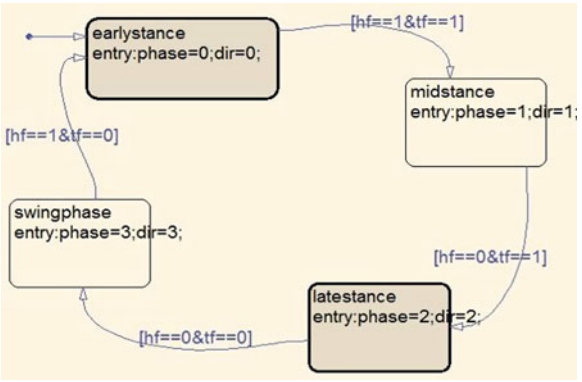

Fig. 40.5 The stateflow diagram in FSM

ground (hf = 1, tf = 0), it is the transition condition from swing state to early stance state. Similarly when (hf = 1, tf = 1), it is the transition condition of early stance state to middle stance state. When (hf = 0, tf = 1), it is the transition condition of middle-stance state to late stance state. When (hf = 0, tf = 0), it is the transition condition of late stance state to swing state, as shown in Table 40.1.

So a stateflow diagram is created, as shown in Fig. 40.5. The foot pressure is the input signals. And the transition condition is the change of foot pressure as described above. Namely, when different foot pressure signals are changed, the corresponding state is triggered. As the corresponding control database for different terrain conditions and states have already been established, the control signal sequence of direction and displacement of corresponding state is indexed and outputted to control the movement of the knee joint motor. As a result, the angle of knee joint would change with the demand of real-time movement in the process of walking.

40.4 Experiment

In the experiment, a prototype of powered knee prosthesis is used, and the PMW control signals are provided by the QuaRc platform. The FSM transition conditions of foot pressure come from outer signal sequence. The control models of five terrain conditions are saved in the database of QuaRC system. The relationship between motor displacement and prosthesis knee joint angle has been described above.

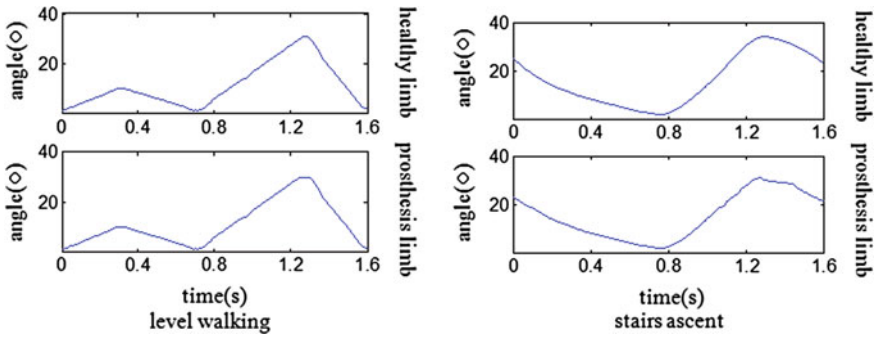

Fig. 40.6 The experiment data comparison of level walking movement and stairs ascent movement

Table 40.2 The error of knee joint's movement experiment

Terrain conditions	Level ground (%)	Up slope (%)	Down slope (%)	Stairs ascent (%)	Stairs descent (%)
Error (2 km/h)	1	2	1	3	3
Error (3 km/h)	1	3	2	5	3
Error (4 km/h)	2	3	3	6	5

The knee joint's angles are recorded through gyroscope in the process of experiment, and the angle signals are sampled at 500 Hz and synchronized with the measurements from powered knee prosthesis. For example, the prosthesis knee joint's angles in the level ground and stairs ascent at the speed of 3 km/h are compared with the healthy knee joint's angle in Fig. 40.6. It shows that the matching degree of two curves is high with a slight difference.

Totally, 20 groups of experiment are carried out for each of the five terrain conditions at different speeds. In order to guarantee the reliability of the experiment, all of the healthy knee joint's data used to compare not only contain the data that already contain reference to create the movement database, but also the data that contain reference from other healthy subjects. The average knee curve errors are shown in Table 40.2. As can be seen, the errors of all the five typical terrain conditions are in a tolerance scope. So the FSM control can obtain relatively well by the effect for prosthesis limb to move coordinate with the healthy limb in different terrain conditions. However, there are still something need to be improved, such as reducing the error rate and improving the structure of the knee joint. The results of this study can guide the further optimization of control design for powered knee prosthesis.

40.5 Conclusion

This paper analyzed the regularity of the human knee joint's angle under different terrain conditions and speed. And the gait phase was divided into four states by foot pressure switches. A standard database was set up to provide the displacement and direction control signals sequence of the gait phase under different terrain conditions and speed. A FSM model was established for achieving the coordinate motion of prosthesis with the healthy limb. The experiments verified the feasibility of this method.

Acknowledgments This paper was supported by the National Natural Science Foundation of China (61174009 and 61203323). The authors would like to thank Bin Gou and Lina Zhao for assisting with experiment and Fengqing Zhao for assisting with data collection.

References

1. Geng YL, Xu XY, Chen LL, Yang P (2011) Design and analysis of active transfemoral prosthesis. J Hebei Univ Techonl 40(5):32–35 (in Chinese)
2. Martinez-Villalpando EC, Weber J, Elliott G, Herr H (2008) Design of an agonist-antagonist active knee prosthesis. In: Proceedings of the 2nd Biennial IEEE/RAS-EMBS international conference on biomedical robotics and biomechatronics, Scottsdale, AZ, USA, 19–22 Oct 2008, pp 529–534
3. Flowers WC, Mann RW (1977) Electrohydraulic knee-torque controller for a prosthesis simulator. SAME J Biomech Eng 99(4):3–8
4. Popovic D, Stein RB (1991) Optimal control for the active above-knee prosthesis. Ann Biomed Eng 19(2):131–150
5. Akin OK, Yucenur MS (2006) Design and control of an active artificial knee. Mech Mach Theory 41(12):1477–1485
6. Sup F, Bohara A, Goldfarb M (2007) Design and control of a powered knee and ankle prosthesis. In: IEEE international conference on robotics and automation, Roma, Italy, 10–14 April 2007, pp 4134–4139
7. Kahle JT, Highsmith MJ, Hubbard SL (2008) Comparison of nonmicroprocessor knee mechanism versus C-leg on prosthesis evaluation questionnaire, stumbles, falls, walking tests, stair descent, and knee preference. J Rehabil Res Dev 45(1):1–14
8. Sup F, Varol HA, Goldfarb M (2011) Upslope walking with a powered knee and ankle prosthesis: initial results with an amputee subject. IEEE Trans Neural Syst Rehabil Eng 19(1):71–78
9. Huang H, Zhang F, Hargrove LJ, Dou Z, Rogers DR, Englehart KB (2011) Continuous locomotion-mode identification for prosthetic legs based on neuromuscular-mechanical fusion. IEEE Trans Biomed Eng 58(10):2867–2875
10. Hernandez R, Yang Q, Huang H, Zhang F, Zhang XR (2013) Design and implementation of a low power mobile CPU based embedded system for artificial leg control. In: 35th annual international conference of the IEEE EMBS, Osaka, Japan, 3–7 July 2013, pp 5769–5772
11. Jin DW, Yang JK, Zhang RH, Wang RC, Zhang JC (2006) Terrain identification for prosthetic knees based on electromyographic signal features. Tsinghua Sci Technol 11(1):74–79 (in Chinese)

12. Tan GZ, Cai GC, Zeng QD, Yan BL, He SH (2006) Study and design of handhold controller system of CIP-I intelligent bionic artificial leg. Comput Meas Control 14(1):47–50 (in Chinese)
13. Yang P, Liu ZJ, Geng YL, Zhao LN (2013) Research advance on key technology of intelligent lower limb prosthesis. J Hebei Uni Techonl 42(1):76–80 (in Chinese)
14. Lawson B, Varol HA, Huff A, Erdemir E, Goldfarb M (2013) Control of stair ascent and descent with a powered transfemoral prosthesis. IEEE Trans Neural Syst Rehabil Eng 21(3):466–473
15. Young AJ, Simon AM, Hargrove LJ (2014) A training method for locomotion mode prediction using powered lower limb prostheses. IEEE Trans Neural Syst Rehabil Eng 22(3):671–676
16. Gou B, Liu ZJ, Zhao LN, Yang P (2013) Walking mode pre-judgment of lower limb prosthesis based on correlation analysis. J Southeast Univ 43(s1):192–196 (in Chinese)
17. Zhao LN, Liu ZJ, Gou B, Yang P (2014) Gait recognition pre-judgment of dynamic lower limb prosthesis based on Hidden Markov model. Robot 36(3):337–341 (in Chinese)
18. Sun HX, Wei X, Lin T (2012) Research of model transformation approaches based on Finite State Machine. Comput Technol Dev 22(2):10–17 (in Chinese)

Chapter 41
Robust PI-Type Position Controller Design for Permanent Magnet Synchronous Motor Using LMI Techniques

Xiaokang Sun, Yang Yi, Songyin Cao, Heqing Liu and Tianping Zhang

Abstract In this paper, a novel proportional-integral (PI) rotor position tracking controller-based linear matrix inequality (LMI) technique is designed for the permanent magnet synchronous motor (PMSM) system. Different from the results on structure control for PMSM, the PI-type gain parameters can be obtained by solving a series of LMIs instead of by manual debugging repeatedly. As a result, more control requirements for PMSM system including stability, position tracking, and robustness can be guaranteed based on systemic analysis method. Moreover, when considering the motor model without position sensor, a reduced-order Luenberger observer is constructed to estimate the rotor position.

Keywords PI-type position controller · PMSM · Robust control · LMI · Luenberger observer

41.1 Introduction

In recent years, the permanent magnet synchronous motor (PMSM) has received increasing interest in the field of industrial application [1]. Compared with other drive devices, the PMSM model can obtain higher power density, larger torque to inertia, and higher efficiency which makes the PMSM a prior choice in certain applications [2, 3]. It is noted that both the rotor position and the angular speed in PMSM system are the two main controlled objectives and have obtained widespread concerns (see [4–9]). However, the existence of nonlinearities, unknown disturbances, and load torque will influence the control performance of PMSM system [1, 2]. In order to solve these difficulties, some advanced control algorithms have been presented for the PMSM system, such as predictive control [2], adaptive control [3], backstepping method [8], sliding mode control [9], and so on.

X. Sun · Y. Yi (✉) · S. Cao · H. Liu · T. Zhang
College of Information Engineering, Yangzhou University, Yangzhou 225127, China
e-mail: yiyangcontrol@163.com

Z. Deng and H. Li (eds.), *Proceedings of the 2015 Chinese Intelligent Automation Conference*, Lecture Notes in Electrical Engineering 337,
DOI 10.1007/978-3-662-46463-2_41

It is well known that PI/PID control is widely applied in practical systems and some theoretical algorithms have also been discussed based on both the frequency-domain and time-domain approaches [10]. With the popularity of linear matrix inequality (LMI) techniques, the PI/PID controller-based LMI optimization algorithm has been designed to achieve satisfactory control performance in the scope of time domain [11]. For the control problem of PMSM system, the control gains in some traditional PI/PID algorithms can be obtained only by debugging repeatedly or depending on experience, which seriously affects the system performance of PMSM [3, 5]. Moreover, not enough sensors applied in PMSM system [7] will bring more difficulties in controlling the rotor position or the angular speed in PMSM system.

In this paper, a PI-type position controller based on LMIs is proposed for PMSM system. Instead of manual debugging repeatedly, the control gains can be computed by solving a series of convex LMIs and rigorous proof is given such that the closed-loop PMSM system can be guaranteed to be stable and the tracking error of rotor position can also converge to zero. At the same time, in order to deal with the immeasurable position problem when lacking position sensors, a linear Luenberger observer based on PMSM system is constructed to estimate the position variable. Furthermore, the peak-to-peak index is used to formulate the disturbance attenuation performance of PMSM system.

41.2 Mathematical Model of Surface-Mounted PMSM

After making some standard assumptions, the dynamical model of a surface-mounted PMSM can be written as follows: [1–3]

$$\begin{pmatrix} \dot{i}_q \\ \dot{i}_d \\ \dot{\omega} \\ \dot{\theta} \end{pmatrix} = \begin{pmatrix} -\frac{R}{L} & -p\omega & -\frac{p\phi_f}{L} & 0 \\ p\omega & -\frac{R}{L} & 0 & 0 \\ \frac{K_t}{J} & 0 & -\frac{B}{J} & 0 \\ 0 & 0 & 1 & 0 \end{pmatrix} \begin{pmatrix} i_q \\ i_d \\ \omega \\ \theta \end{pmatrix} + \begin{pmatrix} \frac{u_q}{L} \\ \frac{u_d}{L} \\ -\frac{T_L}{J} \\ 0 \end{pmatrix} \tag{41.1}$$

where i_d and i_q are the $d-q$ axis currents, u_d and u_q are the $d-q$ axis voltages, ω is the angular velocity, θ is the rotor angle position, R is the stator resistance, L is the stator inductor, p is the pole pair, B is the viscous friction coefficient, J is the rotor moment of inertia, ϕ_f is the rotor flux linkage, T_L is the load torque, $K_t = 1.5\,p\phi_f$ is the torque constant.

In order to eliminate the influence of the coupling terms between angular velocity and currents, the d-axis reference current is usually assumed as $i_d^* = 0$. If

the current controllers work well, the output term $i_d = i_d^* = 0$. As a result, the PMSM system (41.1) can be simplified in the following form:

$$\begin{pmatrix} \dot{i}_q \\ \dot{\theta} \\ \dot{\omega} \end{pmatrix} = \begin{pmatrix} -\frac{R}{L} & 0 & -\frac{p\phi_f}{L} \\ 0 & 0 & 1 \\ \frac{K_t}{J} & 0 & -\frac{B}{J} \end{pmatrix} \begin{pmatrix} i_q \\ \theta \\ \omega \end{pmatrix} + \begin{pmatrix} \frac{u_q}{L} \\ 0 \\ -\frac{T_L}{J} \end{pmatrix} \tag{41.2}$$

which makes the position controller design simpler.

With the desired angular position θ^*, $\zeta(t)$ is a designed auxiliary variable based on tracking error with the expression $\dot{\zeta}(t) = \theta^* - \theta(t)$. To achieve good control objective, the augmented state variable is defined as $x(t) = [\,\theta(t), \quad i_q(t), \quad \zeta(t), \quad \omega(t)\,]^T$. Assuming $u(t) = u_q(t)$ as the control input and $d(t) = [\,\theta^*, \quad T_L\,]^T$ as the disturbance term, the state equation can be given in the following augmented form:

$$\begin{cases} \dot{x} = Ax(t) + Bu(t) + B_1 d(t) \\ z(t) = Cx(t) + Dd(t) \end{cases} \tag{41.3}$$

where $z(t)$ is the reference output with known matrices C and D, and

$$A = \begin{bmatrix} 0 & 0 & 0 & 1 \\ 0 & -\frac{R}{L} & 0 & -\frac{p\phi_f}{L} \\ -1 & 0 & 0 & 0 \\ 0 & \frac{3p\phi_f}{2J} & 0 & -\frac{B}{J} \end{bmatrix}, \quad B = \begin{bmatrix} 0 \\ \frac{1}{L} \\ 0 \\ 0 \end{bmatrix}, \quad B_1 = \begin{bmatrix} 0 & 0 \\ 0 & 0 \\ 1 & 0 \\ 0 & -\frac{1}{J} \end{bmatrix}$$

41.3 PI-Type Controller Design

For the position tracking problem, a novel PI-type position controller is proposed as follows:

$$u(t) = K_{P1}\theta(t) + K_{P2} i_q(t) + K_I \int_0^t (\theta^* - \theta(\tau))d\tau + K_{P3}\omega(t) \tag{41.4}$$

where K_{P1}, K_{P2}, K_{P3} and K_I are controller gains to be determined later.

Substituting $u(t) = Kx(t)$ into augmented system (41.3), the corresponding closed-loop PMSM system can be described as

$$\begin{cases} \dot{x}(t) = (A + BK)x(t) + B_1 d(t) \\ z(t) = Cx(t) + Dd(t) \end{cases} \tag{41.5}$$

where $K = [\, K_{P1} \quad K_{P2} \quad K_I \quad K_{P3} \,]$.

41.4 Stability Analysis with Disturbance Attenuation Performance

The following result provides a criterion for the performance analysis of the unforced PMSM system of (41.3).

Theorem 41.1 *For the known parameters $\lambda, \mu_i (i = 1, 2), \alpha > 0$, suppose there exist matrices with appropriate dimensions $P, T > 0$, and parameter $\gamma > 0$ such that the following LMIs*

$$\begin{bmatrix} \mathrm{sym}(A^T P) + \mu_1^2 T & PB_1 \\ B_1^T P & -\mu_2^2 I \end{bmatrix} < 0 \tag{41.6}$$

$$\begin{bmatrix} \mu_1^2 T & 0 & C^T \\ 0 & (\gamma - \mu_2^2) I & D^T \\ C & D & \gamma I \end{bmatrix} > 0 \quad \begin{bmatrix} \alpha I & T \\ T & T \end{bmatrix} > 0 \quad \begin{bmatrix} T & 0 & C^T \\ 0 & (\gamma - \alpha x_m^T x_m) I & D^T \\ C & D & \gamma I \end{bmatrix} > 0 \tag{41.7}$$

are solvable, then the unforced system of (41.3) is stable, and the output satisfies the disturbance attenuation performance $\sup_{\|d(t)\|_\infty \le 1} \|z(t)\|_\infty < \gamma^2$.

Proof Defining a typical Lyapunov function as

$$V(x(t), t) = x^T(t) P x(t) \tag{41.8}$$

Obviously it is noted that $V(x(t), t) \ge 0$. Furthermore, we can get

$$\dot{V}(x(t), t) \le x^T(t) \Phi_1 x(t) + \|\mu_2 d(t)\|^2 \tag{41.9}$$

where $\Phi_1 = \mathrm{sym}(A^T P) + \mu_2^{-2} P B_1 B_1^T P$.

Based on Schur complement formula, (41.6) implies that $\Phi_1 + \mu_1^2 T < 0$ holds. With (41.10), it can be seen that for any $\|d(t)\|_\infty \leq 1$, we can get

$$\dot{V}(x(t), t) \leq -\mu_1^2 x^T(t) T x(t) + \mu_2^2 \tag{41.10}$$

So for any $x(t)$, it can be seen that

$$x^T(t) T x(t) < \max\left\{\mu_1^{-2}\mu_2^2, x_m^T T x_m\right\}, \quad \|x_m\| = \sup_{-d \leq t \leq 0} \|x(t)\| \tag{41.11}$$

which also implies that the unforced PMSM system of (41.3) is stable.

The proof of disturbance attenuation performance is omitted here to save space. □

41.5 Position Tracking with Peak-to-Peak Performance

The following theorem provides an effective solution for the PI-type position tracking problem of closed-loop PMSM system (41.5).

Theorem 41.2 *For the known parameters $\mu_i (i = 1, 2), \alpha > 0$, suppose there exist matrices with appropriate dimensions $Q = P^{-1} > 0, M = T^{-1}, R > 0$, and parameter $\gamma > 0$ such that the following LMIs*

$$\begin{bmatrix} \mathrm{sym}(AQ + BR) & B_1 & Q \\ B_1^T & -\mu_2^2 I & 0 \\ Q & 0 & -\mu_1^{-2} M \end{bmatrix} < 0 \tag{41.12}$$

$$\begin{bmatrix} \mu_1^2 M & 0 & MC^T \\ 0 & (\gamma - \mu_2^2) I & D^T \\ CM & D & \gamma I \end{bmatrix} > 0 \quad \begin{bmatrix} \alpha I & I \\ I & M \end{bmatrix} > 0 \quad \begin{bmatrix} M & 0 & MC^T \\ 0 & (\gamma - \alpha x_m^T x_m) I & D^T \\ CM & D & \gamma I \end{bmatrix} > 0 \tag{41.13}$$

are solvable, then the closed-loop PMSM system (41.5) under the PI-type control law (41.4) is stable and satisfies both $\lim_{t\to\infty} \theta(t) = \theta^*$ and $\sup_{\|d(t)\|_\infty \leq 1} \|z(t)\|_\infty < \gamma^2$. In this case, the control gains K_{P1}, K_{P2}, K_{P3} and K_I can be solved via $R = KQ$.

The proof of Theorem 41.2 is omitted here to save space.

41.6 Reduced Luenberger Observer Design

In this section, we focus on the motor model without position sensor. As a result, the position status of the rotor cannot be measured directly. So a typical reduced-order Luenberger observer needs to be constructed to observe the state variables of PMSM system and further to estimate the position values.

Based on the PMSM system (41.2), the reduced Luenberger observer is designed as follows:

$$\begin{bmatrix} \dot{\hat{i}}_q \\ \dot{\hat{\omega}} \end{bmatrix} = \begin{bmatrix} -\frac{R}{L} & -\frac{p\phi_f}{L} \\ \frac{3p\phi_f}{2J} & -\frac{B}{J} \end{bmatrix} \begin{bmatrix} \hat{i}_q \\ \hat{\omega} \end{bmatrix} + \begin{bmatrix} \frac{1}{L} \\ 0 \end{bmatrix} u + \begin{bmatrix} \varepsilon \\ 0 \end{bmatrix} (i_q - \hat{i}_q) \tag{41.14}$$

where $\hat{i}_q$ and $\hat{\omega}$ represent the estimate values of i_q and ω, respectively.

Combining (41.2) with (41.14), we can get

$$\begin{bmatrix} \frac{\mathrm{d}e_q}{\mathrm{d}t} \\ \frac{\mathrm{d}e_\omega}{\mathrm{d}t} \end{bmatrix} = \begin{bmatrix} -\frac{R}{L} - \varepsilon & -\frac{p\phi_f}{L} \\ \frac{3p\phi_f}{2J} & -\frac{B}{J} \end{bmatrix} \begin{bmatrix} e_q \\ e_\omega \end{bmatrix} \tag{41.15}$$

where $e_q = i_q - \hat{i}_q, e_\omega = \omega - \hat{\omega}$ represent the observation errors of i_q and ω. From (41.15), the observer gain ε can be designed to make the continuous error dynamics converge to zero asymptotically. It is shown that the proposed observer is of first order, so the computation burden is relatively light. Hence, the position of the rotor can be calculated by $\theta = \int \hat{\omega} dt$.

41.7 Simulation Results

The specification of the PMSM system is shown in Table 41.1.

From $t = 0$ to 20 s, the position command is designed as π rad, and after $t = 20$ s, the position command is changed as 4 rad. Defining parameters $\varepsilon = 5, T_L = 5\,\mathrm{N\,m}$. By using the LMI box, the PI-type controller can be computed as $K_{P1} = -1.5968, K_{P2} = 0.5192, K_{P3} = 0.1498, K_I = 1.1481$.

Table 41.1 Specification of the PMSM system

Stator resistance R	0.54 Ω	Viscous coefficient B	0.0001 Nm/rad/s
Stator inductance L	0.0096 H	Rotor inertia J	0.016 kgm^2
Pole pairs p	4	Flux of linkage ϕ_f	0.61 wb

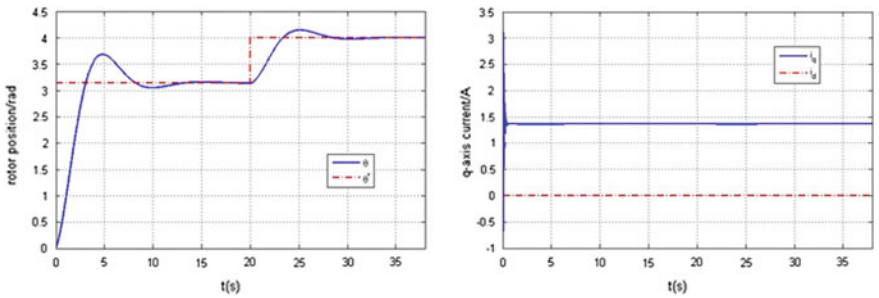

Fig. 41.1 Position responses of with Luenberger observer and responses of the q-axis current

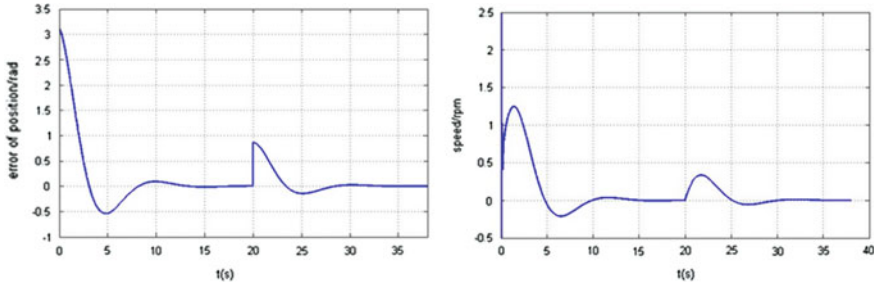

Fig. 41.2 Error between desired position and actual position and responses of angular speed

The above four figures show the dynamical responses of PMSM in combination with the PI-type controller and the Luenberger observer. From Fig. 41.1, the rotor position and the d-axis current are correct and rapidly converge to their reference values, respectively. The satisfactory position tracking and speed control are embodied in Fig. 41.2.

41.8 Conclusion

This paper considers the tracking problem for the rotor position of PMSM system by combining a generalized PI-type controller with a reduced-order Luenberger observer. Based on convex optimization LMI techniques, some typical control objectives including stabilization, position tracking, and robustness for PMSM system can be guaranteed simultaneously.

Acknowledgments This paper is supported by the National Natural Science Foundation of China under Grants (61473249, 61174046 and 61203195).

References

1. Krishnan R (2001) Electric motor drives: modelling, analysis and control. Prentice-Hall, Upper Saddle River
2. Liu H, Li S (2012) Speed control for PMSM servo system using predictive function control and extend state observer. IEEE Trans Ind Electron 59:1171–1183
3. Li S, Gu H (2012) Fuzzy adaptive internal model control schemes for PMSM speed-regulation system. IEEE Trans Ind Inf 8:767–779
4. Kim WH, Shin D, Chung CC (2012) The Lyapunov-based controller with a passive nonlinear observer to improve position tracking performance of microstepping in PMSM. Automatica 48:3064–3074
5. Jung JW, Choi YS, Leu VQ, Choi HH (2011) Fuzzy PI-type current controllers for permanent magnet synchronous motors. IET Electr Power Appl 5:143–152
6. Xu JX, Panda SK, Pan YJ, Lee TH, Lam BH (2004) A modular control scheme for PMSM speed control with pulsating torque minimization. IEEE Trans Ind Inf 51:526–536
7. Jang LH, Ha LI, Ohto M, Sul SK (2004) Analysis of permanent magnet machine for sensorless control based on high-frequency signal injection. IEEE Trans Ind Appl 40:1595–1604
8. Zhou J, Wang Y (2003) Adaptive backstepping speed controller design for PMSM. IEEE Proc Electr Appl 2:165–172
9. Zhang XG, Sun LZ, Zhao K, Sun L (2013) Nonlinear speed control for PMSM system using sliding-mode control and disturbance compensation techniques. IEEE Trans Power Electron 28:1358–1365
10. Astrom KJ, Hagglund IT (1994) PID controllers: theory, design and tuning, 2nd edn. Instrument Society of America, Research Triangle Park
11. Yi Y, Guo L, Wang H (2009) Constrained PI tracking control for output probability distributions based on two-step neural networks. IEEE Trans Circuits Syst I 56:1416–1426

Chapter 42
Reviews to the Research on Building Electrical Intelligent Fault Self-diagnosis

Jiajun Wang and Yahui Wang

Abstract We summarize some methods of the fault diagnosis in the paper, based on the Fault Self-diagnosis researching. Because of the Building Electrical Fault Self-diagnosis System is not researched in depth, our group found the problem of Fault Self-diagnosis and propose taking the artificial intelligence method. Especially in this few years, we discussed the applying of many kinds of extensions in Building Electrical Fault Self-diagnosis System based on the neural network and the result of discussing can provide some new ideas for further researching of Fault Self-diagnosis.

Keywords Fault self-diagnosis · Building electrical · Detection technology

42.1 Introduction

The electrical and electronic equipment in buildings brings the convenience to people's life and work, and has also improved the quality of life. However, it will be a huge disaster if the electrical and electronic equipment break down. In order to prevent the accident in building of electrical equipment, First, the equipment's production, installation, operation conform to the corresponding design specification and process, it can fundamentally enhance equipment reliability and decrease the failure rate. Second, an effective management measure includes the equipment's maintenance and care when the abnormal situation can be found earlier, for avoiding this preventing accidents before they occur.

J. Wang (✉)
Department of Electrical Engineering, University of New South Wales, Sydney, Australia
e-mail: wjiajun1990@sina.com

Y. Wang
Beijing University of Civil Engineering and Architecture, Zhanlan Rd. No.1, Beijing 10044, China
e-mail: yahui-wang@vip.sina.com

Z. Deng and H. Li (eds.), *Proceedings of the 2015 Chinese Intelligent Automation Conference*, Lecture Notes in Electrical Engineering 337,
DOI 10.1007/978-3-662-46463-2_42

Early, the way of detecting the building electrical equipment fault is through the maintenance workers to check up. There are a lot of subjectivity and uncertainty in this way. It cannot satisfy the requirements through the factitious empirical maintenance along with the electrical equipment were become more and more complicated and their kinds are becoming more and more. Self-diagnosis system becomes realistic demand. At present, the countries in all over the world pay a lot of money for equipment's maintenance every year because of the maintenance systems that be used on the construction of electrical equipment have serious defects, such as the frequent temporary repair, inadequate maintenance or superfluous maintenance and blind maintenance, etc. It is an important problem that how to save maintenance's cost to construction of electrical equipment and at the same time ensure that the system has high reliability for the system's operation personnel [1]. The fault's maintenance research based on the equipment's state monitoring and advanced fault diagnosis technology developing became an important research in the construction of electrical system, because of the sensing technology, microelectronics, computer hardware and software, digital signal processing technology, artificial neural network, expert system, fuzzy set theory and other comprehensive intelligent system ware applied to condition monitoring and fault diagnosis [2]. Specific to the construction of electrical field, there are five kinds of direct benefits to carry out the self-diagnosis of fault in construction of electrical equipment system: 1. save a lot of electrical equipment's maintenance fee; 2. increase the available coefficient of electric energy; 3. extend the service life of electrical equipment; 4. ensure reliability of the power supply for electrical equipment; 5. reduce the maintenance coast of electrical equipment fault and the maintenance risk. This paper mainly introduces system evolution, the general situation and state of development and the problem of self-diagnosis maintenance [3–5].

This project adopts methods that are based on the method of classification, and considered about people need to have an accurate fault classification and fault location in the construction of electrical failure. Neural network, a kind of classification method, has the good pattern recognition ability and neural network is good at dealing with the problem that has some strong coupling nonlinear correlation about mapping of symptom set or fault set. Then, we decided to have a further study about the theory and practice based on the fault diagnosis of neural network.

42.2 The Main Types and Progress of the Application of Fault Diagnosis Theory

The development of the theory of fault diagnosis has come to a new stage now. The core is that the modern knowledge system of various disciplines was synthesized. The fault diagnosis theory about control theory and control engineering involved the modern control theory, signal and system, power electronic technology, modern statistics, system identification and pattern recognition and other kinds of discipline.

Table 42.1 The common methods of fault diagnosis

The methods of fault diagnosis	The applied occasion	The selection of parameters	Advantage
The methods of signal processing	The system's modeling is difficult but the output state can be measured	High order statistics, correlation function, spectrum, etc.	The difficulty of setting up the mathematical model to the abstract objects was avoided
The methods of analytic model	A more accurate mathematical model can be established for the diagnosis object	The physical fault that is possibility in the detecting system of physical parameters' change predicting system	The inherent sensitivity for unknown fault
The methods based on the classification	The model can deal with the input and output signal that be measured	A large number of knowledge about system failure and all kinds of fault sample data that have been measured	Ability of recognition pattern, good real-time performance and learning on line
The methods based on reasoning	Acquiring a lot of fault's information except the mathematic model but depend on the experts' practical experience	Production rule, framework representation, logic representation	The sample data of system fault model diagnosed was not needed

In recent years, with the research scope of fault diagnosis continues to expand, it formed that some mainstream methods of fault diagnosis [6, 7].

Some basic methods [8–13] of fault diagnosis were given and their application and advantages were summarized in the Table 42.1.

42.2.1 The Application of Artificial Intelligence in the Electrical System's Fault Self-diagnosis

The Artificial Intelligence (AI) system was developed and applied in the fault self-diagnosis of electrical equipment field. Therefore the Expert System and Artificial Neural Network are the most conspicuous [14]. The electrical equipment fault self-diagnosis expert system that has been developed has the knowledge base, database, reasoning machine, interpretation system and man-machine interface five parts. The electrical equipment fault self-diagnosis expert system's knowledge base uses the modular structure. As the Fig. 42.1 shows: The artificial neural network also uses the modular structure. It uses the RBF radial basis function neural network, bring in the fuzzy logic theory and judge some fault in electrical equipment to prevent the

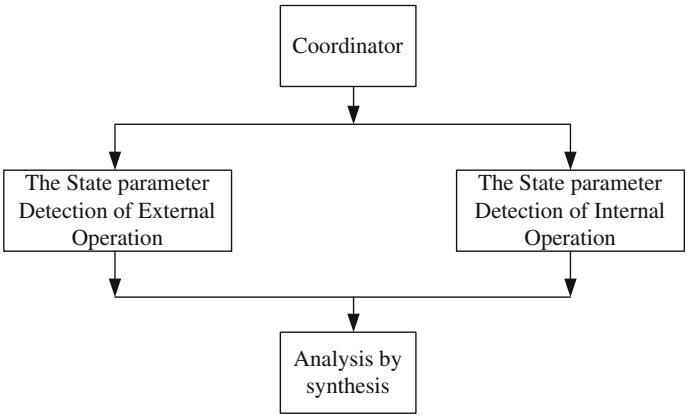

Fig. 42.1 Electrical equipment fault self-diagnosis system knowledge base module chart

occurrence of failure. The electrical equipment system can make early anticipation for internal latent failure of operational electrical equipment and it can provide "consultation" to the operating personnel who operate the electrical equipment.

The characteristics of fault self-diagnosis expert system are shown in Fig. 42.1.

1. At present, the fault self-diagnosis system of electrical equipment using the produce type model system that is the most common, and the knowledge base use the modular structure. The knowledge base module is mutually independent and it is advantageous in the modification, extension and renewal of knowledge base. It takes a great convenience to the knowledge base's maintenance of in the fault self-diagnosis system of electrical equipment.
2. Using the characteristics of the expert system programming language to realize the reverse inference of electrical equipment fault self-diagnosis system's object and bring in the fuzzy logic reasoning model and successfully dealing with the problem of some fuzziness.
3. Electrical equipment fault self-diagnosis system database consists of electrical parameter analysis and dynamic database.

42.2.2 The Method Based on the Theory Model of Electrical Testing Estimate's Fault Self-diagnosis

As everyone knows, people usually use the state equation of single continuous variation to accurately describe when the electrical equipment system sends failure. The random hybrid system model [15] is more accurate mathematical model in the fault self-diagnosis system of electrical equipment. This random hybrid system model is different with stochastic system, because the state of random hybrid

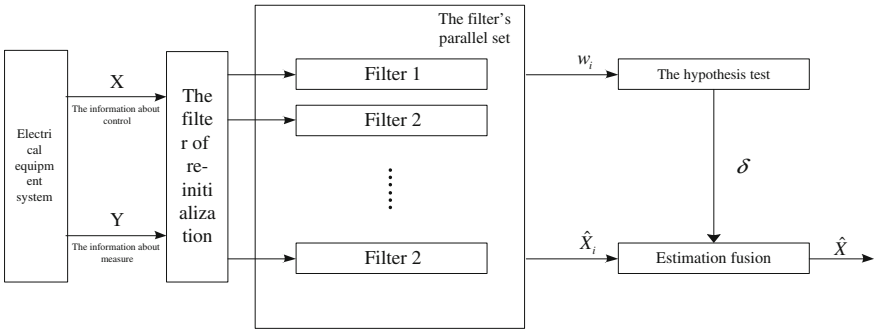

Fig. 42.2 The multiple model estimation algorithm's principle diagram in electrical testing system

system can be discrete and continuous, so we can know that the random hybrid system has characteristic of random. The passive failure mode control system that is a kind of electrical test system is a kind of typical random hybrid system model and they are different between the failure mode's structures of the internal electrical test system, and we can know that are different between the failure mode's structure and normal mode's structure.

In the electrical test system, the multiple model estimation algorithm include the random hybrid system model's design, filter's selection, the reinitialization of estimation fusion and filter. The principle block diagram of electrical test system's random hybrid system model estimation algorithm is shown in Fig. 42.2.

Multiple model estimation algorithm [15] is brought out by Maigl when he researched the optimization self-adaption estimation of random sample data processing. But in the early, multiple model algorithm did not consider about the models switching and it belong the multiple model algorithm with static zero input. In the few years, China and other countries began to research the Multiple Model Self-adaptive Estimate and Multiple Model Self-adaptive Control, they are a kind of multiple model approach of typical zero input interaction. The method of Multiple Model Self-adaptive Estimation maybe generate the electrical equipment system's estimation performance deterioration and even make the electrical equipment system's estimator appear the divergence, because of the method of Multiple Model Self-adaptive Estimation lack the necessary input mutual information.

42.2.3 The Electrical System's Fault Self-diagnosis Based on Fuzzy Neural Network

When the electrical equipment system is doing the fault self-diagnosis, the fuzzy neural network can extract the current electrical equipment system's fuzzy model's description with nonlinearity and compare with each reference model, thus people can get the accurate fault diagnosis [16]. The system model of fuzzy neural network

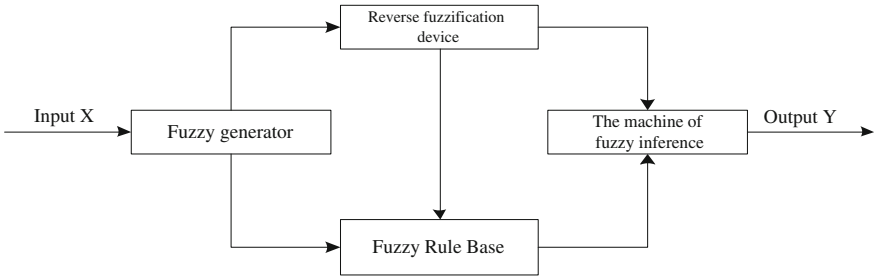

Fig. 42.3 The system's model block diagram of fuzzy neural network

as the Fig. 42.3 shows. The method of electrical equipment system's fault self-diagnosis by using neural network, although we can get the data of failure characteristics through the network self-learning but it is tardiness to compare with some complex electrical equipment system learning. And the neural network is not fully in the network's structure, so it is difficult to extract the performance of neural network through to analysis the data of training characteristics. In addition, mostly the results of neural network training are selected by neural network's initial value, and some expert knowledge is hard to be effectively used in the electrical equipment system.

This is the deficiencies when people doing the fault self-diagnosis in the method of neural network. As everyone knows, they can be conversed each other between neural network and fuzzy system in the theory, the neural network's simulation is based on the biological cranial nerve network and want to close the function about biological brain's self-organization and the parallel processing information in the 'hard' structure (refers to the permutation and combination between the each neuron cell in the biological brain and the collocation of 'individual features'). The fuzzy system makes the human's fuzziness characteristics to be a starting point and simulates the biological action's thinking from 'soft' structure (soft structure's essence is the management structure or the coordination structure between the biological groups) based on the fuzzy logic thinking. The fuzzy neural network technology that combined with the common features of neural network and fuzzy system reflects the dominance along with the electrical equipment system's technology of processing the fuzzy information and the neural network were researched deeply. Here, we use this kind of application which can use the new fuzzy neural network to do the fault self-diagnosis to the electrical equipment system. This application not only has the characteristic of network's sample structure but also training and learning is fast. It can extract the electrical equipment system's fault state model by self-adaptive, doing the fault self-diagnosis to electrical equipment system online.

42.3 The Fault Diagnosis Methods Based on Neural Network

The neural network is used by a lot of complicated system because of the neural network have the excellent ability of learning sample and simulation's ability of nonlinear function. There are four aspects about the neural network's function in the fault diagnosis.

42.3.1 Pattern Classification and Fault Reasoning

The pattern classification and fault reasoning is the method that is usually used by fault diagnosis. First of all, to set up the neural network model through the diagnosis object, the number that is network input node should respond to the fault symptom type and the output node should respond to the cause of the fault [17]. Collecting the fault samples to train the model. When the neural network training is finished, according to the given omen, people can realize the nonlinear mapping from omen to fault. This process is the aim to use the neural network's characteristics to diagnose the fault. Figure 42.4 shows the process.

42.3.2 The Residual

The residuals are mean using the neural network to change the system model of normal state. As Fig. 42.5 shows, the processing is the actual input data of measuring system and using the data to train the neural network, after training, the residual can be produced on line [18].

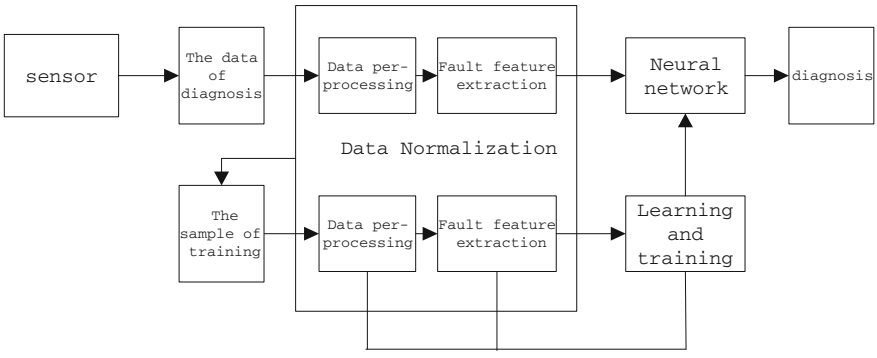

Fig. 42.4 The fault diagnosis structure model's diagram based on neural network

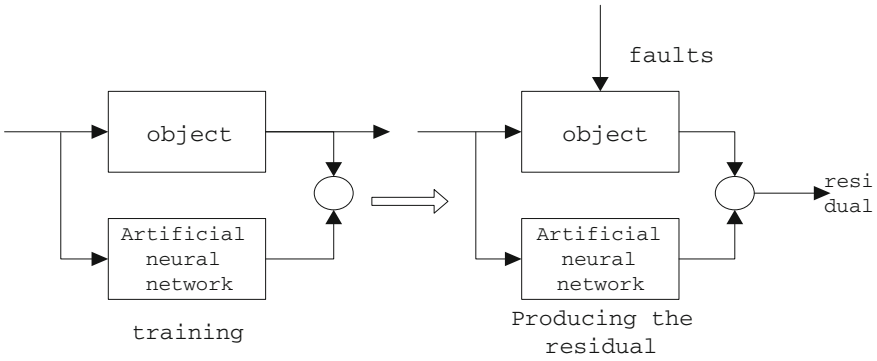

Fig. 42.5 The neural network training and producing the residual on line and evaluating the residual

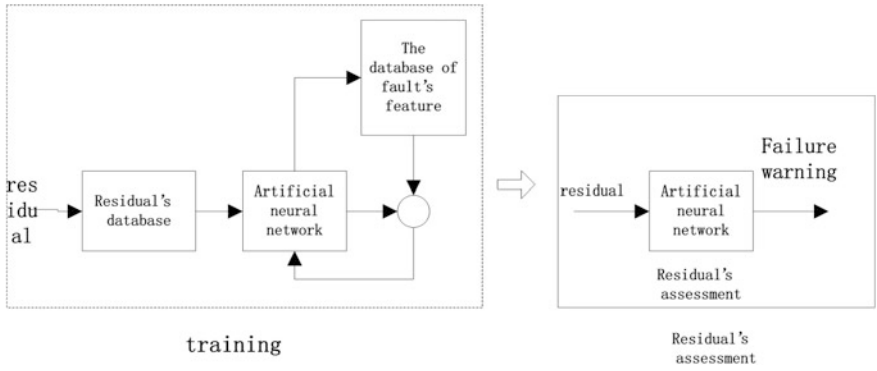

Fig. 42.6 The neural network training and assessment of residual on line

Using the neural network to estimate the residual, the first of all, people need to train network. And it needs to artificially collect a lot of data to establish the residual database and the corresponding fault's characteristic database. As is shown in Fig. 42.6. To complete the training, the neural network can estimate the residual on line and judge whether the system's running status is normal and find the cause of fault.

42.4 The Advantage and Feasibility of Construction of Electrical Apply the Neural Network

The construction of electrical system can't create a precise mathematical model, is not able to use based on method of analysis; Correlation function spectrum characteristics is not typical, also can't the application of signal processing methods;

And based on the method of reasoning rules expression in difficulty bigger, critical state is not easy to judge.

Application of neural network in fault diagnosis based on the basic ideas from the pattern classification of fault reasoning method to fault characteristics as network input, diagnosis as network output, with already measured more sets of historical fault data and training the neural network, enabling the network through the right value memory fault symptom and the corresponding fault type of the corresponding relationship between specific [16].

Fault characteristic value, middle layer obtain input layer information by internal learning into targeted solutions, complete the input to the output of the nonlinear mapping. Output layer output for failure mode vector, through the neuron output and threshold value comparison diagnosis results, this paper diagnosis fault of the total number of nodes is 22, fault type are line impedance fault, continuity failure, grounding resistance anomaly, ground resistivity anomaly, insulation resistance is too small, five kinds of fault is corresponding to the 22 fault location. Fault vector, with 0 means no failure, 1 if the malfunction.

42.5 Conclusion

This paper put forward about the necessity, feasibility and reality of doing the fault self-diagnosis in construction of electrical system at first. Then, it reviews the common fault diagnosis algorithm. At last, this paper selects the neural network that has the most application value to be the point of application diagnosis algorithm in many of methods of fault diagnosis. It completed the experimental research based on the measured data and put forward the performance evaluation index of the fault diagnosis.

References

1. Yun G, Yuanbin H (2005) Based on rough set of fault diagnosis and fault-tolerant control theory and method research. China's outstanding Ph.D. thesis full text database (in Chinese)
2. Jing X, Wang J (2008) Electrical equipment state inspection technology research review. Technol Dyn 2:31 (in Chinese)
3. Hao Y, Minfang P (2009) Tolerance analogy circuit fault diagnosis methods. China's outstanding master's degree thesis full text database (in Chinese)
4. Zhen-yu L, Xi-dong L (1996) Electrical equipment diagnosis technology: an introduction. Water Conservancy Power Press, Beijing (in Chinese)
5. Li X (2005). Electronic control element fault self-diagnosis function application analysis. J Inner Mongolia Sci Technol Econ (2):137–114 (in Chinese)
6. Zhipeng W (2001) Base and information fusion technology of fault diagnosis methods of research and application. Dalian University of Technology, Dalian (in Chinese)
7. Chao Z, Junchang Z (2001) Control system fault detection and multiple model hybrid estimation method. J Syst Eng Electron (7):63–65 (in Chinese)

8. Reimann P, Dausend A, Schutze A (2008) A self-monitoring and self-diagnosis strategy for semiconductor gas sensor systems. Sensors 53:192–195
9. Shu-Yen L, Chan-Cheng H, An-Yeu W (2009) A scalable built-in self-test/self-diagnosis architecture for 2D-mesh based chip multiprocessor systems. Circ Syst 2317–2320
10. Aktouf C, Mazare G, Robach C, Velazco R. (1992) A practical approach for the diagnosis of a MIMD network. In: Test symposium, pp 182–186
11. Elhadef M, Das S, Nayak A (2006) A novel artificial-immune-based approach for system-level fault diagnosis. Availab Reliab Secur 2006:8
12. Hongjun W, Qiushi H, Xiaoli X (2009) Study of the intelligent fault diagnosis system based on rough set. In: 2009 international forum on information technology and applications
13. Huang W, Wang W, Meng Q (2008) Fault diagnosis method for power transformers based on rough set theory. In: Chinese Control and Decision Conference
14. Khomfoi S, Tolbert LM (2007) Fault diagnosis and reconfiguration for multilevel inverter drive using AI-based techniques. IEEE Trans Ind Electron 54(6):2954–2968
15. Lee CF, Xu YP (2001) A multi-sensor based temperature measuring system with self-diagnosis, electrical and electronic technology. In: Proceedings of IEEE region 10 international conference, vol 2, pp. 19–22
16. Ruijuan J, Chunxia X (2008) Mechanical Fault diagnosis and signal feature extraction based on fuzzy neural network. In: Proceedings of the 27 Chinese control conference Kunming, Yunnan, China
17. Pomeranz I (2010) Equivalence, dominance, and similarity relations between fault pairs and a fault pair collapsing process for fault diagnosis. IEEE Trans Comput 59(2):150–158
18. Vemuri AT, Polycarpou MM, Ciric AR (2001) Fault diagnosis of differential-algebraic systems. IEEE Trans Syst Man Cybern-Part A: Syst Humans 31:143–152

Chapter 43
Output Feedback for Networked Control Systems with Time-Delay and Data Packet Dropout

Wang Yan-Feng, Li Zu-Xin, Chen Hui-Ying and Qian Yi

Abstract For networked control systems (NCSs) with time-delay and random data packet dropout, the model is established as a kind of stochastic control system which contains Bernoulli distributed stochastic variable. Furthermore, the existence conditions of the output feedback controller are derived, such that the closed-loop NCSs are exponentially stable in the mean-square sense. Then a linear matrix inequality (LMI) approach for designing output feedback controller is presented. Finally, a numerical example is employed to demonstrate the validity of the proposed method.

Keywords Time-delay · Data packet dropout · Output feedback

43.1 Introduction

The vast progress in network technology over the past decade has influenced the area of system control. Nowadays, it is becoming more and more common to use networks in systems, especially in those that are large and physically distributed or that require expensive cabling. Networked control systems are feedback control systems with control loops closed via digital communication channels [1]. Compared with the traditional point-to-point wiring, the use of communication channels can reduce the costs of cables and power, simplify the installation and maintenance of the whole system, and increase the reliability. Because of these advantages, networked control systems (NCSs) have many industrial applications in automobiles, manufacturing plants, aircraft [2, 3]. NCSs receive much attention in the field of control theory and application. The insertion of communication network in the feedback control loop makes stability analysis and controller design very complex. The delays could potentially deteriorate the stability and control performance of the

W. Yan-Feng (✉) · L. Zu-Xin · C. Hui-Ying · Q. Yi
School of Engineering, Huzhou University, Huzhou, Zhejiang 313000, China
e-mail: wyf2013@hutc.zj.cn

Z. Deng and H. Li (eds.), *Proceedings of the 2015 Chinese Intelligent Automation Conference*, Lecture Notes in Electrical Engineering 337,
DOI 10.1007/978-3-662-46463-2_43

system. Another interesting problem in networked control systems is the data packet dropout issue. Because of uncertainties and noise in the communication channels, there may exist unavoidable errors in the transmitted packet or even loss. If this happens, the corrupted packet is dropped and the receiver uses the packet that it received most recently. In addition, packet dropout may occur when one packet reaches the destination later than its successors; in such situation, the old packet is dropped, and its successive packet is used instead. Many researchers have paid attention to the study of the modeling, stability analysis, and controller design of NCSs under the existence of network-induced delay and data packet dropout. The stochastic control problem for NCSs was studied by the time-stamp technique [4, 5]. A model of NCSs with time-delay was proposed, and then the guaranteed cost control was discussed in terms of Lyapunov theories and linear matrixin-equality (LMI) method [6]. However, the above literatures only focus on the problem of time-delay without consideration of the data packet dropout issue. Some literatures focus on the problem of data packet dropout without consideration of time-delay [7–9]. The problem of modeling and controller design for NCSs with both time-delay and data packet dropout has not been adequately studied. NCSs with time-delay and data packet dropout were modeled as asynchronous dynamical systems or switched systems, and the sufficient conditions for stability were given, but solving nonlinear matrix inequalities was needed [1, 10, 11].

In this paper, we aim to tackle modeling and controller design of NCSs with both time-delay and data packet dropout. Both the stability analysis and the controller synthesis problems are thoroughly investigated. It is shown that the controller design problem under consideration is solvable if certain linear matrix inequalities are feasible. A simulation example is exploited to demonstrate the effectiveness of the proposed approach.

43.2 Problem Formulation

We only consider that the network exists between sensor and controller and τ_k stands for network time-delay. We use a switch to describe the transmission of the data packet. A data packet dropout happens when the switch is open, otherwise the data packet is transmitted successfully.

Consider the following controlled plant:

$$\begin{cases} \dot{x}(t) = Ax(t) + Bu(t) \\ y(t) = Cx(t) \end{cases} \tag{43.1}$$

where $x(t) \in R^n$, $u(t) \in R^m$, $y(t) \in R^r$ are the system state vector, control input, and output vector, respectively. Without loss of generality, we make the following assumption for technical convenience.

Assumption 43.1 The sensor works at time-driven mode and the controller works at event-driven mode and the actuator works at time-driven mode.

Assumption 43.2 Network only exists between the sensor and the controller, the controller and the actuator are at one network node. And the total time-delay $\tau_k = \tau_k^{sc} + \tau_k^{ca}$ is no larger than one sampling period h, i.e.,$\tau_k \leq h$.

Assumption 43.3 The matrix C^T is of full-column rank, i.e., rank $(C^T) = r$, then there exist two orthogonal matrices $U \in R^{n\times n}$ and $V \in R^{r\times r}$, such that

$$UC^T V = \begin{bmatrix} U_1 \\ U_2 \end{bmatrix} C^T V = \begin{bmatrix} \Sigma \\ 0 \end{bmatrix}$$

where $U_1 \in R^{r\times n}$, $U_2 \in R^{(n-r)\times n}$ and $\Sigma = \text{diag}\{\sigma_1, \sigma_2, \ldots, \sigma_r\}$, where $\sigma_i (i = 1, 2, \ldots, r)$ are nonzero singular values of C^T. Integration of system (43.1) in one sampling period h, and considering the network-induced delay, the discrete time representation of system (43.1) is as follows:

$$\begin{cases} x_{k+1} = \Phi x_k + \Gamma_0 u_k + \Gamma_1 u_{k-1} \\ y_k = C x_k \end{cases} \tag{43.2}$$

where $\Phi = e^{Ah}$, $\Gamma_0 = \int_0^{h-\tau_k} e^{As} ds B$, $\Gamma_1 = \int_{h-\tau_k}^{h} e^{As} ds B$. Noting that $\Gamma_0 = \int_0^{h-\tau_k} e^{As} ds B = \int_0^{h/2} e^{As} ds B + \int_{h/2}^{h-\tau_k} e^{As} ds B$. Let $H_0 = \int_0^{h/2} e^{As} ds B$, $E = I$, $F_{\tau_k} = \int_{h/2}^{h-\tau_k} e^{As} ds$. Then we get $\Gamma_0 = H_0 + E F_{\tau_k} B$. According to [12], the uncertain matrix F_{τ_k} satisfies $\sigma_{\max}(F_{\tau_k}) \leq (e^{\sigma_{\max}(\Phi)h} - e^{\sigma_{\max}(\Phi)h/2})/\sigma_{\max}(\Phi) := \delta$

When data packet dropout occurs, the actuator uses the control signal of last period, thus the system representation is:

$$\begin{cases} x_{k+1} = \Phi x_k + H u_{k-1} \\ y_k = C x_k \end{cases} \tag{43.3}$$

where $H = \int_0^h e^{As} ds B$. Define a stochastic variable $\alpha_k = \begin{cases} 0 \\ 1 \end{cases}$, when a data packet dropout occurs, we let $\alpha_k = 0$; otherwise $\alpha_k = 1$. Then α_k is a Bernoulli distributed white sequence with $\Pr ob\{\alpha_k = 1\} = \varepsilon\{\alpha_k\} := a$; $\Pr ob\{\alpha_k = 0\} = 1 - \varepsilon\{\alpha_k\} := 1 - a$;

$\text{Var}\{\alpha_k\} = \varepsilon\{(\alpha_k - a)^2\} = a(1-a) := b^2$. Combining (43.2) and (43.3), NCSs with time-delay and data packet dropout can be described by the stochastic control system below:

$$\begin{cases} x_{k+1} = \Phi x_k + \alpha_k \Gamma_0 u_k + (1-\alpha_k)\Gamma_0 u_{k-1} + \Gamma_1 u_{k-1} \\ y_k = C x_k \end{cases} \tag{43.4}$$

Because of the physical or economical restriction, the whole state information of the controlled plant is often hard to get, so the output feedback control law is adopted:

$$u_k = Ky_k = KCx_k \tag{43.5}$$

Then the closed-loop control system representation is:

$$x_{k+1} = \Phi x_k + \alpha_k \Gamma_0 KCx_k + (1 - \alpha_k)\Gamma_0 KCx_{k-1} + \Gamma_1 KCx_{k-1} \tag{43.6}$$

By defining augmented vector

$$\eta_k = \begin{bmatrix} x_k \\ x_{k-1} \end{bmatrix}$$

the system (43.6) can be written as:

$$\eta_{k+1} = \begin{bmatrix} \Phi + \alpha_k \Gamma_0 KC & (H - \alpha_k \Gamma_0)KC \\ I & 0 \end{bmatrix} \eta_k = \mathrm{A}_k \eta_k \tag{43.7}$$

It should be pointed out that in the closed-loop control system (43.7), there appears stochastic variable α_k. This differs from the traditional deterministic systems without random data packet dropout. To deal with the stochastic parameter system (43.7), we need to introduce the notion of stochastic stability in the mean-square sense.

Definition 43.1 The closed-loop networked control system (43.7) is said to be exponentially mean-square stable if, there exist constants $\beta > 0$ and $0 < \zeta < 1$ such that $\varepsilon\{\| \eta_k \|^2\} < \beta\sigma^k \varepsilon\{\| \eta_0 \|^2\}, \forall k \in \mathrm{I}^+$.

To proceed, we will need the following two lemmas.

Lemma 43.1 *Xie* [13] *Given matrices G, L and N of compatible dimensions with G symmetric, inequality $G + LF(\tau_k)N + N^T F(\tau_k)^T L^T < 0$ holds for $\sigma_{\max}(F_{\tau_k}) \leq \delta$, if and only if there exists a constant $\varepsilon > 0$, such that $G + \varepsilon\delta^2 LL^T + N^T N/\varepsilon < 0$.*

Lemma 43.2 *Ho et al.* [14] *For the matrix $C^T \in R^{n\times r}$ that is of full-column rank, if matrix X is of the following structure*:

$$X = U^T \begin{bmatrix} X_{11} & 0 \\ 0 & X_{22} \end{bmatrix} U = U_1^T X_{11} U_1 + U_2^T X_{22} U_2 \ \text{ where } \ X_{11} \in R^{r\times r} > 0, \ X_{22} \in R^{(n-r)\times(n-r)} > 0, \ U_1 \text{ and } U_2 \text{ are defined in assumption } 43.3, \text{ then there exists a nonsingular matrix } Y \in R^{r\times r}, \text{ such that } XC^T = C^T Y$$

43.3 Controller Design

Now we give the main results of this paper.

Theorem 43.1 *Take as given the communication channel parameters* $0 \le \tau_k \le h$ *and* $0 \le 1 - a \le 1$, *the closed-loop networked control system* (43.7) *is exponentially mean-square stable if there exist positive-definite matrices* P, Q *such that*

$$\begin{bmatrix} \Sigma & \Psi^T \\ \Psi & \Lambda \end{bmatrix} < 0 \tag{43.8}$$

where

$$\begin{aligned}
\Sigma &= (\Phi + a\Gamma_0 KC)^T P(\Phi + a\Gamma_0 KC) + b^2(\Gamma_0 KC)^T P(\Gamma_0 KC) + Q - P \\
\Psi &= (HKC - a\Gamma_0 KC)^T P(\Phi + a\Gamma_0 KC) - b^2(\Gamma_0 KC)^T P\Gamma_0 KC \\
\Lambda &= (HKC - a\Gamma_0 KC)^T P(HKC - a\Gamma_0 KC) + b^2(\Gamma_0 KC)^T P\Gamma_0 KC - Q
\end{aligned}$$

Proof Define a Lyapunov functional $V_k = \eta_k^T M \eta_k = \eta_k^T \begin{bmatrix} P & 0 \\ 0 & Q \end{bmatrix} \eta_k = x_k^T P x_k + x_{k-1}^T Q x_{k-1}$, where P and Q are positive-definite matrices to be determined. Obviously, we have $V_k > 0$. It follows from (43.7) that

$$\begin{aligned}
\varepsilon\{V_{k+1}\} - \varepsilon\{V_k\} &= \eta_k^T \varepsilon\{A_k^T M A_k\} \eta_k - \varepsilon\{\eta_k^T M \eta_k\} \\
&= \varepsilon\{((\Phi + a\Gamma_0 KC)x_k + (\alpha_k - a)\Gamma_0 KCx_k + (H - a\Gamma_0)KCx_{k-1} \\
&\quad - (\alpha_k - a)\Gamma_0 KCx_{k-1})^T P((\Phi + a\Gamma_0 KC)x_k + (\alpha_k - a)\Gamma_0 KCx_k \\
&\quad + (H - a\Gamma_0)KCx_{k-1} - (\alpha_k - a)\Gamma_0 KCx_{k-1})\} + x_k^T Q k - x_k^T P x_k - x_{k-1}^T Q x_{k-1} \\
&= \eta_k^T \begin{bmatrix} \Sigma & \Psi^T \\ \Psi & \Lambda \end{bmatrix} \eta_k
\end{aligned}$$

Thus, if (43.8) holds, we can get $\varepsilon\{A_k^T M A_k\} - M < 0$. Since $M > 0$, it is easy to obtain $\lambda_{\min}(M) I \le M \le \lambda_{\max}(M) I$. Thus we can get

$$\lambda_{\min}(M)\varepsilon\{\| \eta_k \|^2\} \le \varepsilon\{\eta_k^T M \eta_k\} \le \lambda_{\max}(M)(1 - \frac{\phi}{\lambda_{\max}(M)})^k \varepsilon\{\| \eta_k \|^2\}$$

That is, $\varepsilon\{\| \eta_k \|^2\} < \beta\sigma^k \varepsilon\{\| \eta_0 \|^2\}$, where $\beta = \frac{\lambda_{\max}(M)}{\lambda_{\min}(M)}$, $\zeta = 1 - \frac{\phi}{\lambda_{\max}(M)}$. □

According to Definition 43.1, the system (43.7) is exponentially mean-square stable.

Theorem 43.2 *Take as given the communication channel parameters* $0 \le \tau_k \le h$ *and* $0 \le 1 - a \le 1$, *if there exist positive-definite matrices* X_{11}, X_{22}, N, *matrix* Z *and scalar* $\mu > 0$, *such that the following LMI holds*:

$$\begin{bmatrix} N-X & * & * & * & * \\ 0 & -N & * & * & * \\ \Phi X + aH_0ZC & (H-aH_0)ZC & -X+\mu\delta^2a^2E & * & * \\ bH_0ZC & -bH_0ZC & \mu\delta^2abE & -X+\mu\delta^2b^2E & * \\ BZC & BZC & 0 & 0 & -\mu I \end{bmatrix} < 0 \tag{43.9}$$

where $X = U_1^T X_{11} U_1 + U_2^T X_{22} U_2$, then closed-loop system (43.7) is exponentially mean-square stable, and the controller gain matrices are given by $K = ZV\Sigma^{-1}X_{11}^{-1}\Sigma V^T$.

Proof Using Schur complement, we can get the following inequality from (43.8):

$$\begin{bmatrix} Q-P & * & * & * \\ 0 & -Q & * & * \\ \Phi + a\Gamma_0KC & (H-a\Gamma_0)KC & -P^{-1} & * \\ b\Gamma_0KC & -b\Gamma_0KC & 0 & -P^{-1} \end{bmatrix} < 0$$

which can be written as

$$\begin{bmatrix} Q-P & * & * & * \\ 0 & -Q & * & * \\ \Phi + aH_0KC & (H-aH_0)KC & -P^{-1} & * \\ bH_0KC & -bH_0KC & 0 & -P^{-1} \end{bmatrix} + \begin{bmatrix} (BK)^T \\ (BK)^T \\ 0 \\ 0 \end{bmatrix} F_{\tau_k}^T \begin{bmatrix} 0 \\ 0 \\ aE \\ bE \end{bmatrix}^T + \begin{bmatrix} 0 \\ 0 \\ aE \\ bE \end{bmatrix} F_{\tau_k} \begin{bmatrix} (BK)^T \\ (BK)^T \\ 0 \\ 0 \end{bmatrix}^T < 0$$

□

By using Lemma 43.1, we can obtain

$$\begin{bmatrix} Q-P & * & * & * \\ 0 & -Q & * & * \\ \Phi + aH_0KC & (H-aH_0)KC & -P^{-1}+\mu\delta^2a^2E & * \\ bH_0KC & -bH_0KC & \mu\delta^2abE & -P^{-1}+\mu\delta^2b^2E \end{bmatrix} + \begin{bmatrix} (BK)^T \\ (BK)^T \\ 0 \\ 0 \end{bmatrix} \begin{bmatrix} (BK)^T \\ (BK)^T \\ 0 \\ 0 \end{bmatrix}^T \mu^{-1}$$

Using Schur complement again, we can obtain

$$\begin{bmatrix} Q-P & * & * & * & * \\ 0 & -Q & * & * & * \\ \Phi+aH_0KC & (H-aH_0)KC & -P^{-1}+\mu\delta^2a^2E & * & * \\ bH_0KC & -bH_0KC & \mu\delta^2abE & -P^{-1}+\mu\delta^2b^2E & * \\ BKC & BKC & 0 & 0 & -\mu I \end{bmatrix} < 0$$

Consequently, pre- and post-multiplying the inequality above with $\mathrm{diag}\{P^{-1}, P^{-1}, I, I, I\}$, and let $X = P^{-1}$, $N = XQX$, we can get

$$\begin{bmatrix} N-X & * & * & * & * \\ 0 & -N & * & * & * \\ \Phi X+aH_0KCX & (H-aH_0)KCX & -X+\mu\delta^2a^2E & * & * \\ bH_0KCX & -bH_0KCX & \mu\delta^2abE & -X+\mu\delta^2b^2E & * \\ BKCX & BKCX & 0 & 0 & -\mu I \end{bmatrix} < 0$$

Since $X = U^T \begin{bmatrix} X_{11} & 0 \\ 0 & X_{22} \end{bmatrix} U = U_1^T X_{11} U_1 + U_2^T X_{22} U_2$, there exists a matrix Y such that $XC^T = C^T Y$ from Lemma 43.2. It follows from $XC^T = C^T Y$ and $C^T = U^T \begin{bmatrix} \Sigma \\ 0 \end{bmatrix} V^T$ that $XU^T \begin{bmatrix} \Sigma \\ 0 \end{bmatrix} V^T = U^T \begin{bmatrix} \Sigma \\ 0 \end{bmatrix} V^T Y$, that is, $U^T \begin{bmatrix} X_{11} & 0 \\ 0 & X_{22} \end{bmatrix} UU^T \begin{bmatrix} \Sigma \\ 0 \end{bmatrix} V^T = U^T \begin{bmatrix} \Sigma \\ 0 \end{bmatrix} V^T Y$, which implies that $X_{11}\Sigma V^T = \Sigma V^T Y$, that is $Y = V\Sigma^{-1} X_{11} \Sigma V^T$. Let $KY = Z$, since $KCX = (XC^T K^T)^T = (C^T Y K^T)^T = (C^T Z^T)^T = ZC$, so we get $K = ZV\Sigma^{-1} X_{11}^{-1} \Sigma V^T$, this completes the proof.

43.4 Numerical Example

Consider the following controlled plant:

$$\begin{cases} \dot{x}(t) = \begin{bmatrix} 0 & 1 \\ -3 & 0.2 \end{bmatrix} x(t) + \begin{bmatrix} 2 \\ -2 \end{bmatrix} u(t) \\ y(t) = \begin{bmatrix} 1 & 3 \\ 1 & -2 \end{bmatrix} x(t) \end{cases}$$

Assuming the sampling period $h = 0.1$ s, the possibility of data packet dropout $\Pr ob\{\alpha_k = 0\} = 0.1$. We can get the following parameters after some mathematic computations:

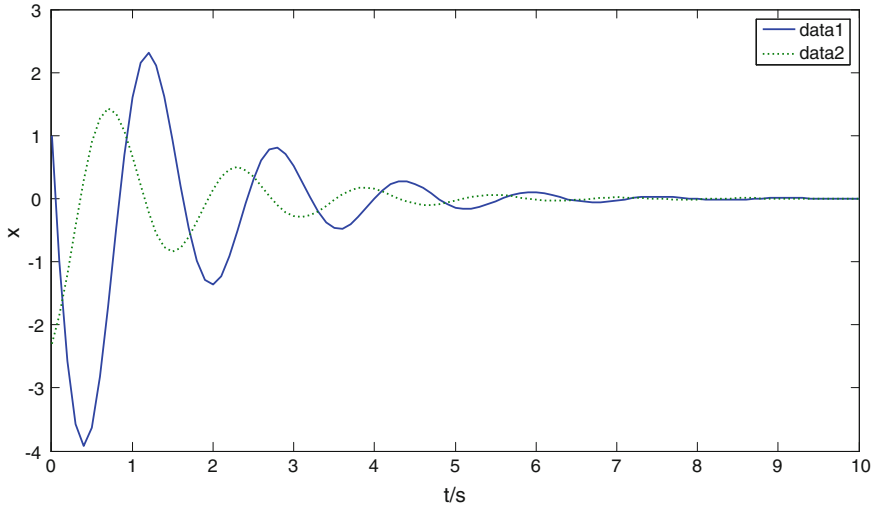

Fig. 43.1 State responses of the closed-loop system

$$\Phi = \begin{bmatrix} 0.9909 & 0.0861 \\ -0.1722 & 0.7326 \end{bmatrix}, H_0 = \begin{bmatrix} 0.0976 \\ -0.0976 \end{bmatrix}, H = \begin{bmatrix} 0.1904 \\ -0.1904 \end{bmatrix}, \delta = 0.0503$$

According to Theorem 43.2, we can obtain the following solutions using Matlab LMI tool box:

$$Z = [\,-0.1683 \quad -1.0318\,], X_{11} = \begin{bmatrix} 161.5070 & -1.7381 \\ -1.7381 & 189.4742 \end{bmatrix}$$

So the state feedback controller gain is given by:

$$K = [\,-0.0007 \quad -0.0056\,]$$

Assuming the system initial state is $x(0) = [\,1 \quad 0.8\,]^T$, the state responses of the closed-loop system is shown in the figure below, then, we can see the closed-loop system is stable (Fig. 43.1).

43.5 Conclusion

In this paper, a new model for NCSs with time-delay and data packet dropout is proposed as a kind of stochastic control system which contains Bernoulli distributed stochastic variable. Sufficient conditions for the existence of an output feedback controller have been obtained to stabilize the closed-loop NCSs exponentially

stable in mean-square sense. The controller has been given by solving certain LMI. Simulation results have demonstrated the effectiveness of the proposed method.

Acknowlegments This work is supported by the National Natural Science Foundation of China under grant 61174029 and the Natural Science Foundation of Huzhou under grant No. 2014YZ07 and the Public Technology Application Research Project of Zhejiang Province in Social Development under grant No. 2014C33004.

References

1. Zhang W, Branicky MS, Philips SM (2001) Stability of networked control system. IEEE Control Syst Mag 21(1):84–99
2. Lu RQ, Xu Y, Xue AK, Zheng JC (2013) Networked control with state reset and quantized measurements: observer-based case. IEEE Trans Ind Electron 60(11):5206–5213
3. Li JG, Yuan JQ, Lu JG (2010) Observer-based H_∞ control for networked nonlinear systems with random packet losses. ISA Trans 48:39–46
4. Nilsson et al (1998) Stochastic analysis and control of real-time systems with random time-delays. Automatica 34(1):57–64
5. Hu SS, Zhu QX (2003) Stochastic optimal control and analysis of stability of networked control systems with long delay. Automatica 39:1877–1884
6. Liu HL, Zhu QX (2008) Guaranteed cost control of networked control systems with long time-delay. In: IEEE Pacific-Asia workshop on computational intelligence and industrial application, pp 175–179
7. Sahebsara M, Chen T, Shala SL (2008) Optimal H_∞ filtering in networked control systems with multiple packet dropouts. Syst Control Lett 57(9):696–702
8. Wang Z, Liu X, Yang F, Ho DWC, Liu X (2007) Robust H_∞ control for networked systems with random packet losses. IEEE Trans Syst Man Cybern B Cybern 37(4):916–924
9. Xie DX, Han XD (2009) H_∞ state feedback control with data packet dropout. Syst Eng Electron 31(3):629–633
10. Ge Y, Chen QG, Jiang M (2008) Stability analysis of networked control systems with data dropout and transmission delays. In: Proceedings of the 7th world congress on intelligent control and automation, Chongqing, pp 7986–7991
11. Li W, Wang Q, Dong CY (2014) Robust H_∞ control of networked control systems with short delays and packet dropouts. J Northeast Univ 35(6):774–779
12. Xie GM, Wang L (2004) Stabilization of networked control systems with time-varying network-induced delay. In: Proceedings of 43rd IEEE conference on decision and control, pp 3551–3556
13. Xie LH (1996) Output feedback H_∞ control of systems with parameter uncertainty. Int J Control 63(4):741–750
14. Ho DWC, Lu G (2003) Robust stabilization for a class of discrete-time non-linear systems via output feedback. Int J Control 76(2):105–115

Chapter 44
Design of an Improved Variable Universe Fuzzy Control System and Its Stability Analysis

Weihua Huang and Haiyan Long

Abstract An improved function-type contraction-expansion factor is designed in this paper. Optimization criterion rules of contraction-expansion factor are designed by analyzing the changing relationship between the input signals of fuzzy controller and contraction-expansion factor. And then, an improved contraction-expansion factor is designed to optimize the structure and improve the control quality of the system. Based on Lyapunov stability theory, the stability of variable universe fuzzy control system with designed contraction-expansion factor is proved. Simulation results show that the design of variable universe fuzzy control method can effectively improve system performance.

Keywords Improved contraction-expansion factor · Variable universe fuzzy control · Lyapunov stability

44.1 Introduction

The idea of variable universe fuzzy control was first proposed to regulate the universe by a set of nonlinear contraction-expansion factor. That is, the universe is changed with actual error. With the fix fuzzy rule-base, change of contraction-expansion factor is equal to decrease or increase the number of fuzzy rules. It is proven that the variable universe fuzzy controller is a high-precision controller with self-organization, self-learning and self-adaption characters [1].

Generally, there are three basic types of variable universe fuzzy controllers, which are based on function, fuzzy inference and intelligent searching algorithm, respectively. A contraction-expansion factor of exponential type is deduced and applied successfully in the control of four-level-inverted pendulum in [2]. After the

W. Huang (✉) · H. Long
Information Science and Engineering School, Wuhan University of Science and Technology, Wuhan, China
e-mail: hwh1108@wust.edu.cn

Z. Deng and H. Li (eds.), *Proceedings of the 2015 Chinese Intelligent Automation Conference*, Lecture Notes in Electrical Engineering 337,
DOI 10.1007/978-3-662-46463-2_44

change law of contraction-expansion factor is analyzed, a contraction-expansion factor of proportional type is presented to be not only as the antecedent of rules but also the consequent in [3]. In order to overcome large amount of calculation and difficulty of realization, the weighted sum is used to replace the integral calculation in contraction-expansion factor of integral type on the basis of the previous research [4]. For the various plants, it is difficult to construct contraction-expansion factor by normal function type. So some contraction-expansion factors of inference type are proposed in [5], with the consideration of the advantage of fuzzy language inference mechanism. For example, according to the inference classification of error, a contraction-expansion factor of inference type is designed to improve the control precision in [6]. Clearly, the selection of contraction-expansion factor is important for the performance of fuzzy controller. With the consideration of stability of control system, which is realized by contraction-expansion factor, an improved contraction-expansion factor of function type is designed on the analysis of the relationship between contraction-expansion factor and change of universe. Meanwhile, its stability is proved by Lyapunov method. Simulation results show that the fuzzy controller with the improved contraction-expansion factor is effective in comparison with the results of normal factors.

44.2 Definition of Improved Contraction-Expansion Factor

The following practical contraction-expansion factors [2, 6] are commonly used in fuzzy system, which are,

$$\alpha(x) = (|x|/E)^{\tau} + \varepsilon, \quad \tau \in (0,1), \ \varepsilon \text{ is a very small positive constant;} \tag{44.1}$$

$$\beta(x) = 1 - \lambda \exp(-kx^2), \qquad \lambda \in (0,1), \ \ k > 0; \tag{44.2}$$

Suggest the input universes of SISO fuzzy controller is expressed as $[-E, E]$, and its contraction-expansion factor is $\alpha(x)$. Let the initial universe $X = [-2, 2]$. For Eq. (44.1), $\tau = 0.85$ and for Eq. (44.2), $\lambda = 0.97, k = 1$. The relationship between contraction-expansion factor and universe is shown in Fig. 44.1.

Supposed that there are there terms: big, medium and small for the description of universe and $\alpha(x)$. With the Fig. 44.1, the relationship between contraction-expansion factor and universe, $x \to \alpha(x)$, can be concluded by the following rules: (44.1) if error x is big then $\alpha(x)$ is big; (44.2) if error x is medium then $\alpha(x)$ is medium; (44.3) if error x is small then $\alpha(x)$ is small. When x is big, the number of control rules need not be added, so the change rate of $\alpha(x)$ is small. If x is small, the system is near stable state, the system need more fuzzy rules to enhance the performance of convergence, i.e., the change rate of $\alpha(x)$ should be big to make error close to zero rapidly. Based on the above analysis, the rules for $x \to \Delta\alpha(x)$ can be concluded by: (44.1) if error x is big then $\Delta\alpha(x)$ is big; (44.2) if error x is medium then $\Delta\alpha(x)$ is medium; (44.3) if error x is small then $\Delta\alpha(x)$ is small. The rules for

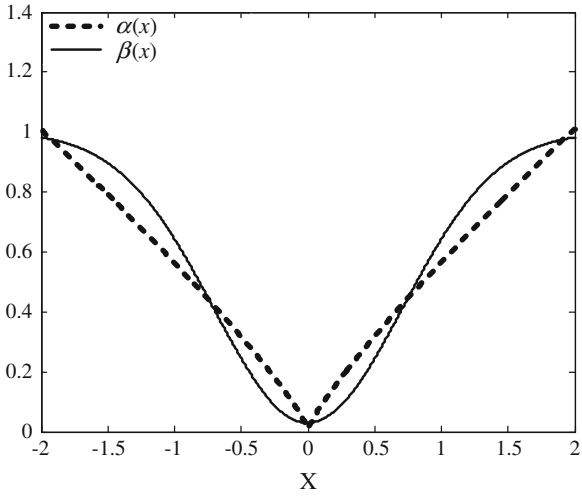

Fig. 44.1 Relationship between contraction-expansion factor and universe

$\alpha(x)$ and $\Delta\alpha(x)$ are called as designing criterion. With the consideration of coordination and zero avoidance of contraction-expansion factor, $\Delta\alpha(x)$ is denoted by

$$\Delta\alpha(x) = 2 \cdot k \cdot \Delta x \cdot (E - |x|) \cdot (1 - \alpha(x))/E \tag{44.3}$$

After solving differential equation, Eq. (44.3) becomes,

$$\alpha(x) = 1 - \lambda e^{-2k|x| + kx^2/E},\ k > 0, \lambda > 0 \tag{44.4}$$

Let $k_1 = 2k$, Eq. (44.3) becomes

$$\alpha(x) = 1 - \lambda e^{-k_1|x| + k_2 x^2}, \quad k_1 > 0, k_2 > 0, \lambda > 0 \tag{44.5}$$

where λ is the adjusted parameter. Equation (44.4) is the improved contraction-expansion factor designed in the paper, and its performance of improved contraction-expansion factor is discussed as follows,

(1) According to the basic definition of contraction-expansion factor, as to Eq. (44.4), when $|x| \to E$, $\alpha \to 1$ and $|x| \to 0$, $\alpha \to 1 - \lambda$. Obviously, Eq. (44.4) is satisfying to the requirements of definition of contraction-expansion factor, which are duality, monotonicity, zero avoidance and coordination.

(2) According to the designing criterion for contraction-expansion factor, there is

$$\mathrm{d}\alpha(x)/\mathrm{d}x = -\lambda(-k_1 + k_2|x|)e^{-k_1|x| + k_2 x^2} \tag{44.6}$$

For Eq. (44.6), when $|x| \to E$, $\mathrm{d}\alpha(x)/\mathrm{d}x \to 0$; and when $|x| \to 0$, $\mathrm{d}\alpha(x)/\mathrm{d}x \to \lambda k_1$, which can be adjusted by the adapt value of k_1. So the improved contraction-expansion factor, denoted by Eq. (44.4), satisfies the designing criterion. Additionally, $\alpha(x)$ can be proportional-type and exponential-type [2, 7] with the change of k_1 and k_2. Let the initial universe $X = [-E, E]$, and then compare the improved contraction-expansion factor with other two types of typical ones, which are generally called as proportional factor and exponential factor and denoted by Eqs. (44.1) and (44.2), respectively,

$$\alpha(x) = (|x|/E)^{\tau} + \varepsilon \tag{44.7}$$

where $\tau \in (0, 1)$, ε is a very small positive constant.

$$\alpha(x) = 1 - \lambda \exp(-kx^2), \tag{44.8}$$

where $\lambda \in (0, 1)$, $k > 0$.

Suggest $X = [-2, 2]$ and the figures of $\alpha(x)$ and $\mathrm{d}\alpha(x)/\mathrm{d}x$ are shown in Figs. 44.2 and 44.3.

It is obvious to find that the change rate of improved factor is bigger when error is small, which leads to fast change of universe and makes system arrive at stable state quickly. Additionally, the figure of improved factor is smoother than other two ones and without jump like exponential factor.

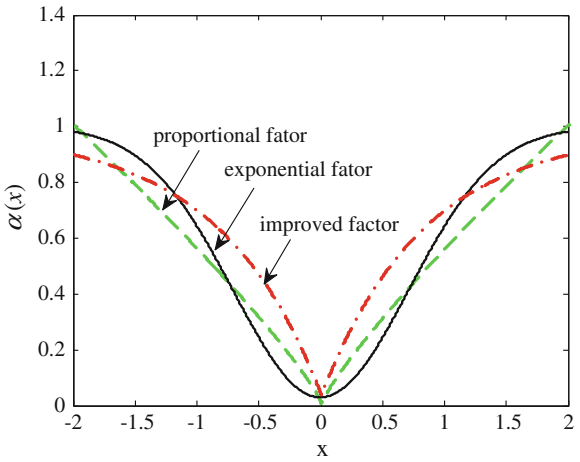

Fig. 44.2 Output of $\alpha(x)$

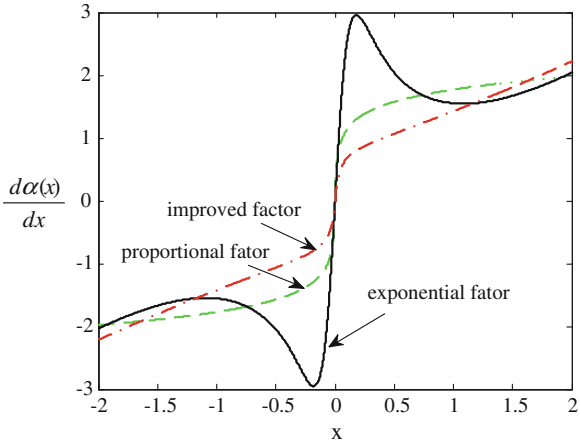

Fig. 44.3 Output of $\mathrm{d}\alpha(x)/\mathrm{d}x$

44.3 Stability Analysis of Fuzzy System with Improved Contraction Expansion Factor

Think of the following n-order continuous nonlinear system,

$$\begin{aligned} &\dot{x}_1 = x_2, \dot{x}_2 = x_3, \ldots, \dot{x}_n = f(x_1, x_2 \ldots x_n) + bu + d \\ &y = x_1 \end{aligned} \tag{44.9}$$

where $f(x_1, x_2 \ldots x_n)$ is an unknown nonlinear continuous function, and $|f(\boldsymbol{x})| \leq f_0(\boldsymbol{x})$, $0 < b_1 < b < b_2, d \leq D_N$, $f_0(\boldsymbol{x})$ is a known continuous function, b is an unknown constant, d is a disturbance variable, b_1, b_2 are constants, u, y are control input and system output, respectively, and $u, y \in R$. Let $\boldsymbol{x} = [x_1, x_2 \ldots x_n]^T \triangleq (x, \dot{x} \ldots x^{(n-1)})^T$, then Eq. (44.9) can be expressed by

$$\begin{aligned} &\dot{\boldsymbol{x}} = \hat{A}\boldsymbol{x} + \hat{B}(f(\boldsymbol{x}) + bu + d) \\ &y = \hat{C}^T\boldsymbol{x} \end{aligned} \tag{44.10}$$

where $\hat{A} = \begin{bmatrix} 0 & 1 & 0 & 0 & \cdots & 0 & 0 \\ 0 & 0 & 1 & 0 & \cdots & 0 & 0 \\ \vdots & \vdots & \vdots & \vdots & \ddots & \vdots & \vdots \\ 0 & 0 & 0 & 0 & \cdots & 0 & 1 \\ 0 & 0 & 0 & 0 & 0 & 0 & 0 \end{bmatrix}$, $\hat{B} = \begin{bmatrix} 0 \\ 0 \\ \vdots \\ 0 \\ 1 \end{bmatrix}$, $\hat{C} = \begin{bmatrix} 1 \\ 0 \\ 0 \\ \vdots \\ 0 \end{bmatrix}$.

Let r be input of system, and error $e = r - y$, denoted by $\boldsymbol{e} = (e_1, e_2 \ldots e_n)^T \triangleq (e, \dot{e} \ldots e^{(n-1)})^T$. In order to realize the control target, that is, $\lim_{t \to \infty} \|\boldsymbol{e}\| = 0$, select a Hurwitz polynomial, which is,

$$h(s) = s^n + k_1 s^{n-1} + \cdots + k_{n-1} s + k_n \tag{44.11}$$

Because the system, denoted by Eq. (44.9), is stable if and only if all roots of Eq. (44.10) belongs to left half-plane, an equation about error can be structured as;

$$e^{(n)} + k_1 e^{(n-1)} + \cdots + k_{n-1} \dot{e} + k_n e = 0 \tag{44.12}$$

Obviously, e is approximately stable if Eq. (44.11) has a solution. Let $\boldsymbol{k} \triangleq [k_n, k_{n-1} \ldots k_1]^T$, then Eq. (44.12) can be expressed by

$$e^{(n)} = -\boldsymbol{k}^T \boldsymbol{e} \tag{44.13}$$

and there is,

$$u = \frac{1}{b}(-f(\boldsymbol{x}) + r^{(n)} + \boldsymbol{k}^T \boldsymbol{e}) \tag{44.14}$$

Let u_f is the output of the fuzzy controller with the improved contraction-expansion factor, and u_s is offset variable for the output of the fuzzy controller, so there is

$$u = u_f + u_s \tag{44.15}$$

Substituting Eq. (44.15) into (44.10) gives

$$x^{(n)} = f(x) + b(u_f + u_s) + d \tag{44.16}$$

With Eqs. (44.13) and (44.16), the error is

$$e^{(n)} = -k^T e + b(u^* - u_f - u_s) \tag{44.17}$$

Let $A = \begin{bmatrix} 0 & 1 & 0 & \cdots & 0 \\ 0 & 0 & 1 & \cdots & 0 \\ \vdots & \vdots & \vdots & \ddots & \vdots \\ 0 & 0 & 0 & \cdots & 1 \\ -k_n & -k_{n-1} & -k_{n-2} & \cdots & -k_1 \end{bmatrix}$, $B = \begin{bmatrix} 0 \\ 0 \\ \vdots \\ 1 \end{bmatrix}$, then Eq. (44.11) is,

$$\dot{\boldsymbol{e}} = A\boldsymbol{e} + B(u^* - u_f - u_s - d) \tag{44.18}$$

Theorem 44.1 *The system expressed by Eq. (44.18) is a approximately stable system with the adaptive selection of* u_s.

Prove According to Lyapunov equation, there is a positive definite matrix P to satisfy the following condition with arbitrary selected positive definite matrix Q.

$$A^T P + PA = -Q \tag{44.19}$$

Construct energy function $V(\boldsymbol{e}) = \boldsymbol{e}^T P\boldsymbol{e}/2$, and then $\dot{V}(\boldsymbol{e})$ is

$$\dot{V}(\boldsymbol{e}) = -\boldsymbol{e}^T Q\boldsymbol{e}/2 + \boldsymbol{e}^T PB(u^* - u_f - u_s) = -\boldsymbol{e}^T Q\boldsymbol{e}/2 + \boldsymbol{e}^T P_n B(u^* - u_f - u_s)$$

where $P_n = [p_1, p_2 \ldots p_n]^T$.

$$\text{Let} \quad u_s = I^* \text{sgn}(e^T P)[(f_0 + \left|r^{(n)}\right| + \left|\boldsymbol{k}^T\boldsymbol{e}\right|)/b + \left|u_f\right| + D_N] \tag{44.20}$$

Where $I^* = \begin{cases} 1, & |\boldsymbol{e}P|(f_0 + |r^n| + \left|\boldsymbol{k}^T\boldsymbol{e}\right| + b_2\left|u_f\right|) < \boldsymbol{e}^T P\boldsymbol{e}/2 \\ 0, & \text{otherwise} \end{cases}$.

With Eqs. (44.8) and (44.14), there is

$$\begin{aligned} \dot{V}(\boldsymbol{e}) &\le -\boldsymbol{e}^T Q\boldsymbol{e} + \left|\boldsymbol{e}^T P_n\right| b(|u^*| + \left|u_f\right| + D_N)/2 - \boldsymbol{e}^T P_n b u_s \\ &\le -\boldsymbol{e}^T Q\boldsymbol{e} + \left|\boldsymbol{e}^T P_n\right| b(f_0 + \left|r^{(n)}\right| + \left|\boldsymbol{k}^T\boldsymbol{e}\right| + b\left|u_f\right| + D_N)/2 - \boldsymbol{e}^T P_n b u_s \end{aligned}$$

When $I^* = 0$, $\dot{V}(\boldsymbol{e}) \le 0$; When $I^* = 1$, $\dot{V}(\boldsymbol{e}) \le -\boldsymbol{e}^T Q\boldsymbol{e}/2 \le 0$, and if and only if $\|\boldsymbol{e}\| = 0$, $\dot{V}(\boldsymbol{e}) = 0$. So the system expressed by Eq. (44.18) is a approximately stable system with the adaptive selection of u_s.

Deduction 44.1 The error vector is bounded after adding of Compensator u_s to the system, i.e., $\exists E_0 > 0$, make $\|e\| \le E_0$. Additionally, If the inference input r is bounded, the state variable x is also bounded.

Prove Because of $V(e) \ge 0$ and $\dot{V} \le 0$, st. $\forall t$, $V(e) \le V_0$. Let $\lambda_{\min}$ is the minimum eigenvalue of P, there exists $\frac{1}{2}\|e\|^2 \lambda_{\min} \le \frac{1}{2} e^T Pe = V(e) \le V_0$. Because P is positive definite matrix, $\lambda_{\min} > 0$, $\|e\|$ is :$\|e\| \le \sqrt{2V_0/\lambda_{\min}(P)}$.

Let $E_0 = \sqrt{2V_0/\lambda_{\min}}$, then $\|e\| \le E_0$. Supposed that the system input r is bounded, $\exists \Omega_r > 0$ and $\forall t$, make $\|r\| \le \Omega$, where $r = (r, \dot{r}, \ldots, r^{(n-1)})$. Obviously, $\|x\| \le \|r\| + \|e\| \le \Omega_r + E_0$. Let $\Omega_x = \Omega_r + E_0$, then $\|x\| \le \Omega_x$, that is, x is bounded.

44.4 Simulations

Consider the non-minimum phase system $G(s) = 1/s^2 - 0.65\text{s} + 1$. Without any control, the system denoted by Eq. (44.6) is divergent and unstable, shown in Fig. 44.4. The sampling time $T = 0.01$.

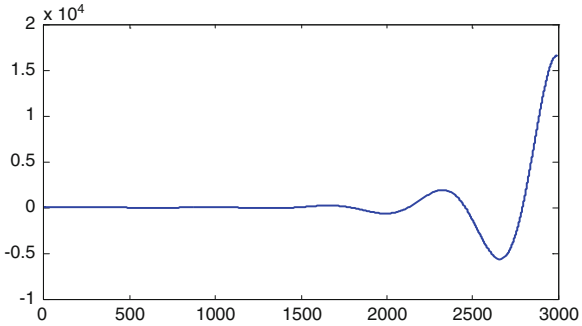

Fig. 44.4 Step responding figure of the system without control

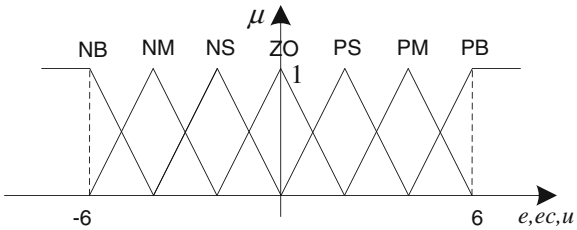

Fig. 44.5 Distribution of fuzzy sets for e, ec and u

Parameters of fuzzy controller are: Universes of error e, change of error ec and output u are $[-6, 6]$. Scale factors of e, ec and u are $k_e = 5$, $k_{ec} = 2$, $k_u = 1$ respectively. Fuzzy partitions of e, ec and u are $\{\text{NB}, \text{NM}, \text{NS}, \text{ZO}, \text{PS}, \text{PM}, \text{PB}\}$ respectively, Here, the membership functions are all taken triangle membership functions, shown as Fig. 44.5 and fuzzy rules are shown in Table 44.1.

Three kinds of contraction-expansion factors are selected as followings: proportional contraction-expansion factor: $\alpha(x) = (|x|/E)^{\tau}$, where $\tau = 0.5$; exponential contraction-expansion factor: $\alpha(x) = 1 - \lambda_1 \exp(-k_1 x^2)$, where $\lambda_1 = 0.88, k_1 = 0.8$,

Table 44.1 Fuzzy rules

EC u E	NB	NM	NS	ZO	PS	PM	PB
NB	−6	−6	−4	−2	0	0	2
NM	−6	−6	−4	−2	0	2	4
NS	−6	−4	−2	−2	0	4	4
ZO	−6	−4	−2	0	2	4	6
PS	−4	−2	0	2	2	4	6
PM	−4	−2	0	2	4	6	6
PB	−2	0	0	2	4	6	6

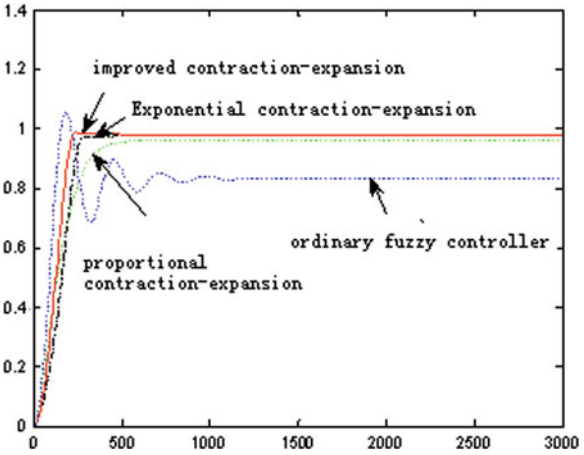

Fig. 44.6 Step responding figures

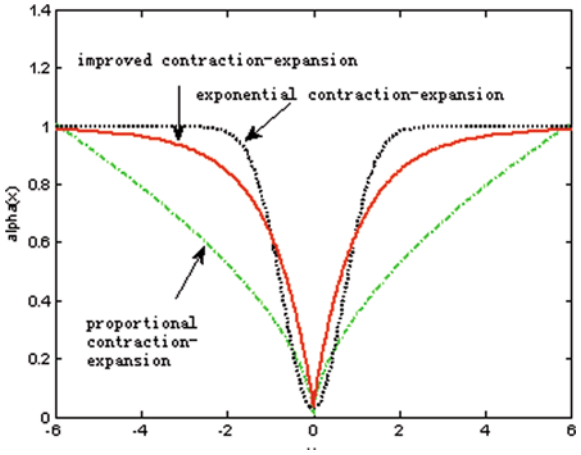

Fig. 44.7 Changes of expansion factors with error

and improved contraction-expansion factor: $\alpha(x) = 1 - \lambda_2 \exp(-k_2|x| + k_3 x^2)$, where $\lambda_2 = 0.98$, $k_2 = 0.9$, $k_3 = 0.01$. With the same structure of fuzzy controller, figures for fuzzy control system with the above three kinds of expansion factors are shown in Figs. 44.6 and 44.7.

With Figs. 44.6 and 44.7, the fuzzy system with improved contraction-expansion factor is of some good characteristics, such as short setting time, little overshot, small stable error, strong robustness. Meanwhile, the simulation results also manifest the effective design and optimal designing criterion.

44.5 Conclusion

An improved contraction-expansion factor is designed in the paper. With the discussion of the relationship between error, weight of university and contraction-expansion factor, optimal designing criterion for contraction-expansion factor is deduced, which gives the basis for design of an improved contraction-expansion factor. And then, stability of fuzzy system with improved contraction-expansion factor is proved by Lyapunov stability theorem. Finally, simulations for a non-minimum phase system are manifested that the performance of the fuzzy system with an improved contraction-expansion factor is more effective than that with proportional contraction-expansion factor and exponential contraction-expansion factor.

Acknowledgments This work is supported by Natural Science Foundation of Hubei provincial (2013CFC077) and Engineering Research Center of for Metallurgical Automation and Detecting Technology of Ministry of Education.

References

1. Li H, Zhihong M (2002) Variable universe stable adaptive fuzzy control of a nonlinear system. Comput Math Appl 44:799–815
2. Li H, Zhihong M, Jiayin W (2002) Variable universe adaptive fuzzy control on the quadruple inverted pendulum. Sci China Ser E Technol Sci 45(2):213–224 (in Chinese)
3. Li H (1999) Adaptive fuzzy controllers based on variable universe. Sci China Ser E Technol Sci 42(1):10–20 (in Chinese)
4. Long Z, Liang X, You K, Chen L (2008) Double-input and single-output fuzzy control algorithm with potentially-inherited variable universe and its convergence. Control Theor Appl 25(4):683–687 (in Chinese)
5. Cao Ming, Chen XinChu (2012) Design of fuzzy controller based on variable universe of discourse. Mech Electrical Technol 35(4):2–4
6. TAN Bing-wen, LI Chun-wen (2013) Comparative study of several selection methods of the expansion factor for variable universe. Sci Technol Eng (4):908–911
7. Hongxin Li (1999) Adaptive fuzzy control based on variable universe of discourse. Sci China 29(1):32–42 (in Chinese)

Chapter 45
Experimental Study on Adaptive Iterative Control for Lower Limb Prostheses

Yu-liang Ma, Xiao-hui Ding, Ming Meng and Qing-shan She

Abstract In order to adapt to the personalized parameters and to the change of tempo in user's lower limb prosthesis, taking these factors such as nonlinear model and parameter uncertainty of human prosthetic system into consideration, adaptive iterative learning controller has been designed to implement imputation control on it. First, the dynamic model of lower limb prosthesis is created. Then, adaptive iterative learning controller is designed to implement imputation control on it, using Lyapunov function method to prove the stability and convergence of tracking error. Finally, the knee trajectory simulation results are obtained. The final results show that the designed controller has excellent tracking results on the lower limb prosthetic knee.

Keywords Lower limb prosthetic · Kinetic model · Iterative learning adaptive control · Trajectory tracking

45.1 Introduction

Human legs have a strong ability to adapt to the complicated external environment during walking. With the development of technology, the study of human lower limb prostheses is also increasingly focused on how to let the users walk more easily and naturally, and the research on lower limb prostheses knee is particularly important. A good lower limb prosthetic knee can guarantee patients walk flexibly and most close to the maximum state of natural gait in the period of support phase (the period from the heel contacts the ground to the toes leave the ground) and swing phase (from the toes leave the ground to the heel contacts the ground), which are also the key factors in the performance and life cycle of the entire lower limb prostheses [1]. So it is of great significance to the research on lower limb prosthetic knee control.

Y. Ma · X. Ding (✉) · M. Meng · Q. She
Institute of Intelligent Control and Robotics, Hangzhou Dianzi University, Hangzhou 310018, China
e-mail: 131060063@hdu.edu.cn

Z. Deng and H. Li (eds.), *Proceedings of the 2015 Chinese Intelligent Automation Conference*, Lecture Notes in Electrical Engineering 337,
DOI 10.1007/978-3-662-46463-2_45

Today, people have developed a lot of new intelligent artificial legs, making intelligent prostheses develop toward a climax. But the relevant theoretical study has been mainly focused on general intelligent control theory, such as ordinary BP neural network control, rule-based expert control, and general fuzzy control, although the neural network adaptive control, fuzzy expert control, and other compound intelligent control technology have been used relatively less. Kalanovic and others have researched on Neural network supervisory control based on feedback-error learning (FEL), combined BP neural network controller with PD controller, but the real-time performance is poor for the BP neural network controller [2].

Adaptive Iterative Learning Control is a compound intelligent control method with rapid asymptotic convergence, taking full advantage of adaptive control and iterative learning control, and the method has been used to control lower limb prosthetic knee in this paper. The experiment results show that the algorithm can not only effectively reduce the tracking error of the prosthetic knee but also get well tracking effect.

45.2 Normal Human Gait Characteristics and Lower Limb Prosthesis Control Requirements

Normal gait refers to healthy human feel the most natural and comfortable posture during walking, which is also with the characteristics of well-coordinated and balanced cyclical. The process of human normal walk is a circular motion of their lower limb, besides a complete cycle includes two phases: single stand phase and double stand phase. Single stand phase refers to one leg swing while the other leg touchdown with a maximum vertical load at the end of it, and soon after the knee begins to bend preparing for the swing phase, at the same time with minimum bending resistance. Therefore, knee prostheses should start to move at the minimum bending resistance to automatically adapt to a range of gait speed.

Controlled above-knee prostheses (AKP) is artificial limb mounted below the amputee's hip. Usually, the ideal lower limb prosthesis control is expected to achieve the following requirements: lower limb prosthesis not only has sufficient stability to support weight and being with automatic security response in support phase, but also has the ability of automatic bending lock when tripped, control the walking mode during the entire gait cycle such as sitting, standing, downstairs, respond to transient changes in walking speed, can adapt to different wearer's personalized configuration requirements, realize adaptive control without training, have the ability to absorb shocks when the heel contacts the ground [3].

45.3 Dynamics Model of Lower Limb Prosthesis Control

To get the results of the simulation based on adaptive iterative learning control method, IPL is established as a control object of mathematical model. Traditional inverse problem of dynamics can be summarized as follows: the motion path and various points speed and acceleration are known according to trajectory planning, solving the generalized driving force of drive element that must be provided to the joint, which changes with time (or displacement). So as to get ankle, knee, and hip joint torques, inverse kinetic equation is directly solved in light of the kinematic parameters. However, joint torque calculated in this method cannot be used in the actual control of prosthetic leg, because the joint torque that influences the thigh gait is usually controlled by the nonlinear damping indirectly and the output of the controlling microprocessor cannot trace the torque directly only according to the calculated the results of this mathematical model [4].

Therefore, the research is based on lower limb prosthesis system of two rigid body two degrees of freedom (see Fig. 45.1), and the Newton–Euler algorithm is used for dynamic analysis. In the figure, l_1 and l_2 represent the length of thigh and the length of calf. d_1 and d_2 represent the links mass; θ_1 and θ_2 indicate generalized angle coordinate variables of the link, which conforms to the right-hand rule; M_1 and M_2 are outer drive torque applied to the joints; m_1 and m_2 represent the weight of the link, X_i represents position coordinate $(i = 1, 2)$

$$\begin{aligned} M_1 &= (m_1 d_1^2 + m_2 d_2^2 + m_2 l_1^2 + 2m_2 l_1 d_2 \cos\theta_2)\,\ddot{\theta}_1 + (m_2 d_2^2 + m_2 l_1 d_2 \cos\theta_2)\,\ddot{\theta}_2 \\ &\quad + (-2m_2 l_1 d_2 \sin\theta_2)\,\dot{\theta}_1\,\dot{\theta}_2 + (-m_2 l_1 d_2 \sin\theta_2)\,\dot{\theta}_2^2 + (m_1 d_1 + m_2 d_1) g * \sin\theta_1 \\ &\quad + m_2 g p_2 \sin(\theta_1 + \theta_2) \\ M_2 &= (m_2 d_2^2 + m_1 l_1 d_2 \cos\theta_2)\,\ddot{\theta}_1 + m_2 d_2^2\,\ddot{\theta}_2 + (-m_2 l_1 \sin\theta_2 + m_2 l_1 d_2 \sin\theta_2)\,\dot{\theta}_1\,\dot{\theta}_2 \\ &\quad + (m_2 l_1 d_2 \sin\theta_2)\,\dot{\theta}_1^2 + m_2 g p_2 \sin(\theta_1 + \theta_2) \end{aligned} \tag{45.1}$$

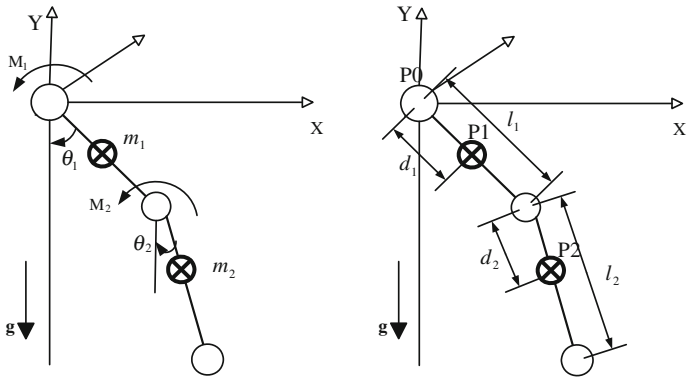

Fig. 45.1 The thigh two rigid body two degrees of freedom

Suppose hip joints P_0 is the origin of coordinates and establishes kinematics equation, then calculate $x1$ and $x2$ coordinates

$$\begin{cases} X_{p1} = X_{p0} + d_1 \sin\theta_1 \\ Y_{p1} = Y_{p0} - d_1 \cos\theta_1 \end{cases} \tag{45.2}$$

$$\begin{cases} X_{p2} = X_{p0} + l_1 \sin\theta_1 + d_2 \sin\theta_2 \\ Y_{p2} = Y_{p0} - l_1 \cos\theta_1 - d_2 \cos\theta_2 \end{cases} \tag{45.3}$$

Through derivation to the position equations, so as to get velocity equations of the swing leg

$$V_{p1} = \begin{pmatrix} \dot{X}_{p1} \\ \dot{Y}_{p1} \end{pmatrix} = \begin{pmatrix} d_1 \cos\theta_1 \\ d_1 \sin\theta_1 \end{pmatrix} \dot{\theta}_1 \tag{45.4}$$

$$V_{p2} = \begin{pmatrix} \dot{X}_{p2} \\ \dot{Y}_{p2} \end{pmatrix} = \begin{pmatrix} l_1 \cos\theta_1 \\ l_1 \sin\theta_1 \end{pmatrix} \dot{\theta}_1 + \begin{pmatrix} d_2 \cos\theta_2 \\ d_2 \sin\theta_2 \end{pmatrix} \dot{\theta}_2 \tag{45.5}$$

45.4 Lower Limb Prosthetic Knee Trajectory Control Based on Adaptive Iterative Learning Control

45.4.1 Problem Description

Considering the effects, such as the existing uncertainties, friction, internal knee damping, and external disturbances, Formula (45.1) can be changed to [5]:

$$M(q_i(t))\ddot{q}_i(t) + C\left(q_i(t), \dot{q}_i(t)\right)\dot{q}_i(t) + G(q_i(t)) = \tau_i(t) - d_i(t) \tag{45.6}$$

Therein, $q_i(t) = \theta_i(t), i = 1, 2, \ldots, t \in [0, T]$ is the time variable, $i \in Z_+$ is the number of iterations, $q_i(t) \in R^n$, $\dot{q}_i(t) \in R^n$, $\ddot{q}_i(t) \in R^n$ denotes the ith iteration joint angle, angular velocity, angular acceleration. $M(q_i) \in R^{n\times n}$ is robot inertia matrix, $C(q_i, \dot{q}_i)\, \dot{q}_i \in R^n$ is centrifugal Coriolis force, $G(q_i) \in R^n$ is the gravity, $\tau_i \in R^n$ is the rotational torque of joints, $d_k \in R^n$ is knee damping and external disturbances.

45.4.2 Convergence Analysis

Suppose the position and velocity of the knee can be obtained through the feedback, the control task is to design a control rate $\tau_i(t)$ to guarantee $q_i(t)$ bounded in any [0, T] and any $i \in Z_+$, and if $i \to \infty$, $q_i(t)$ can always converge to the corresponding desired trajectory in any $t \in [0, T]$. Therefore, the basic assumptions are as follows [6]:

1. For $\forall t \in [0, T]$ and $\forall i \in Z_+$, then $q_i(t)$, $\dot{q}_i(t)$, $\ddot{q}_i(t)$ and $d_i(t)$ are bounded;
2. for $\forall i \in Z_+$, and satisfies initial condition $q_d(t) - q_i(t) = \dot{q}_d(t) - \dot{q}_i(t) = 0$;

also satisfies the following four characteristics [7]:

(1) $M(q_i) \in R^{n\times n}$ is bounded positive definite symmetric matrix;

(2) $M\left(\dot{q}_i\right) - 2C\left(q_i, \dot{q}_i\right)$ is skew-symmetric matrix, and also we can know that $X^T\left(M\left(\dot{q}_i\right) - 2C\left(q_i, \dot{q}_i\right)\right)X = 0, \forall X \in R^n$;

(3) $G(q_i) + 2C\left(q_i, \dot{q}_i\right)\dot{q}_d(t) = \psi\left(q_i, \dot{q}_i\right)\xi^T(t), \psi\left(q_i, \dot{q}_i\right) \in R^{n\times m-1}$ is a known vector, $\xi^T(t) \in R^{m-1}$ is an unknown vector;

(4) $\left\|C\left(q_i, \dot{q}_i\right)\right\| \le k_c\left\|\dot{q}_i\right\|, \|G(q_i)\| < k_g, \forall t \in [0, T]$, therein, k_c and k_g are positive real numbers.

Position tracking error and velocity tracking error of the joint are respectively set as follows: $e(t) = q_d(t) - q_i(t), \dot{e}(t) = \dot{q}_d(t) - \dot{q}_i(t)$. On the basis of the classical PD feedback control, lower limb prosthesis system unknown parameters and disturbance caused by uncertainty can be removed through iteration, and the convergence analysis is given below [8].

$$\tau_i(t) = K_p e_i(t) + K_d \dot{e}_i(t) + \varphi\left(q_i, \dot{q}_t, \dot{e}_i(t)\right)\overset{\cap}{\theta}_i(t) \tag{45.7}$$

$$\overset{\cap}{\theta}_i(t) = \overset{\cap}{\underset{i-1}{\theta}}(t) + \Gamma\varphi^T\left(q_i, \dot{q}_t, \dot{e}_i(t)\right)e_i(t) \tag{45.8}$$

Therein, $\overset{\cap}{\theta}_i(0) = 0, \varphi\left(q_i, \dot{q}_t, \dot{e}_i\right) \in R^{n\times n}, \varphi\left(q_i, \dot{q}_t, \dot{e}_i\right) = \left[\psi\left(q_i, \dot{q}_i\right)\mathrm{sgn}\left(\dot{e}_i\right)\right]$ matrix K_P, K_D and Γ are all symmetric positive definite matrix, thereby $e_i(t)$ and $\dot{e}_i(t)$ are bounded, and also can infer that $\lim\limits_{i\to\infty} e_i(t) = \lim\limits_{i\to\infty} \dot{e}_i(t) = 0, \forall t \in [0, T]$.

Proof construct Lyapunov function at the *i*th iteration [9]:

$$W_i\left(\dot{e}_i(t), e_i(t), \tilde{\theta}_i(t)\right) = V_i\left(\dot{e}(t), e_i(t)\right) + \frac{1}{2}\int_0^t \tilde{q}_i(t)\Gamma^{-1}\tilde{\theta}_i(t)\mathrm{d}\tau \tag{45.9}$$

Therein, $\widetilde{\theta}_i(t) = \theta_i(t) - \hat{\theta}_i(t)$, $\theta_i(t) = \left[\xi^T(t) \quad \beta\right]$, $\hat{\theta}(t) = \left[\hat{\xi}_i^T(t) \quad \hat{\beta}_i(t)\right]^T$ stands for the estimates of $\theta(t)$, $\left\|M(q_i)\ddot{q}_d - d_i\right\| \leq \beta$.

$$V_i\left(\dot{e}_i(t), e_i(t)\right) = \frac{1}{2}\dot{e}_i^T(t)M(q_i)\dot{e}_i(t) + \frac{1}{2}e_i(t)^T K_p e_i(t) \tag{45.10}$$

In the formula, if $\bar{\theta}_i = -\theta + \hat{\theta}_{i+1} - \hat{\theta}_i + \theta = \hat{\theta}_{i+1}(t) - \hat{\theta}_i(t)$, that is, the equation: $\hat{\theta}_{i+1}(t) = \hat{\theta}_i(t) + \bar{\theta}_i(t)$, then the formula can be changed to:

$$\widetilde{\theta}_i(t)^T\Gamma^{-1}\widetilde{\theta}_i(t) - \underset{i-1}{\widetilde{\theta}}(t)^T\Gamma^{-1}\widetilde{\theta}_{i-1}(t) = -2\,\bar{\theta}_i(t)^T\Gamma^{-1}\widetilde{\theta}_i(t) - \bar{\theta}_i(t)^T\Gamma^{-1}\bar{\theta}_i(t) \tag{45.11}$$

45.4.2.1 $W_i(t)$ Non-incremental Proof [10]

$$\Delta W_i = V_i - V_{i-1} - 1/2\int_0^t \left(\bar{\theta}_i(t)^T\Gamma^{-1}\bar{\theta}_i(t) - \underset{i-1}{\bar{\theta}}(t)^T\Gamma^{-1}\bar{\theta}_{i-1}(t)\right)\mathrm{d}\tau \tag{45.12}$$

Therein, $\bar{\theta}_i(t) = \hat{\theta}_i(t) - \underset{i-1}{\hat{\theta}}(t)$, according to that $\int_0^t \dot{V}(t)d\tau = V_i(t) - V_i(0)$, that is, $V_i(t) = V_i(0) + \int_0^t \dot{V}(t)d\tau$, $\dot{V}_i(t) = \dot{e}_i(t)M(q_i)\ddot{e}_i(t) + 1/2\dot{e}_i^T(t) \times \dot{M}(q_i)\dot{e}_i(t) + \dot{e}_i^T(t)K_p e_i(t)$, then it can be changed to:

$$\begin{aligned} V_i\left(\dot{e}_i(t), e_i(t)\right) =& V_i\left(\dot{e}_i(0), e_i(0)\right) \\ &+ \int_0^t \left[\dot{e}_i^T(t) \times \dot{M}(q_i)\ddot{e}_i(t) + \dot{e}_i^T(t) \times M(q_i)\dot{e}_i(t) + \dot{e}_i^T(t)K_p\dot{e}_i(t)\right]\mathrm{d}\tau \end{aligned}$$

According to Formula (45.6) and features B_2, B_3, the results are given as follows:

$$\begin{cases} \dot{e}_i^T M\ddot{e}_i = \dot{e}_i^T M\left(\ddot{q}_d - \ddot{q}_i\right) = \dot{e}_i^T M\ddot{q}_d - \dot{e}_i^T\left(-C\dot{q}_i - G + \tau_i + d_i\right) \\ 1/2\,\dot{e}_i^T\dot{M}\dot{e}_i = \dot{e}_i^T C\dot{e}_i = \dot{e}_i^T C\left(\dot{q}_d - \dot{q}_i\right) = \dot{e}_i^T C\dot{q}_d - \dot{e}_i^T C\dot{q}_i \end{cases} \tag{45.13}$$

We can conclude from the known results that [11]:

$$\dot{e}_i^T\left(M(q_i)\,\ddot{q}_d - d_i\right) \le \beta\left\|\dot{e}_i^T\right\| = \left[\psi\left(q_i,\dot{q}_i\right)\mathrm{sgn}\left(\dot{e}_i\right)\right]\left[\,\xi^T \quad \beta\,\right]^T = \phi\left(q_i,\dot{q}_i,\dot{e}_i\right)\theta \tag{45.14}$$

$$\begin{aligned} V_i\left(\dot{e}_i(t),e_i(t)\right) &= V_i\left(\dot{e}_i(0),e_i(0)\right) + \int_0^t \dot{e}_i^T\left(M(q_i)\,\ddot{q}_d - d_i + C\left(\dot{q}_i,q_i\right)\dot{q}_d + G(q_i) + K_p e_i - \tau_i\right)\mathrm{d}\tau \\ &\le V_i\left(\dot{e}_i(0),e_i(0)\right) + \int_0^t \dot{e}_i^T\left(\phi\left(q_i,\dot{q}_i,\dot{e}_i\right)\theta - K_p e_i - \tau_i\right)\mathrm{d}\tau \end{aligned} \tag{45.15}$$

Combine control rate formula (45.7) and the formula (45.15), the result can be changed to [12]:

$$V_i\left(\dot{e}_i(t),e_i(t)\right) \le V_i\left(\dot{e}_i(0),e_i(0)\right) + \int_0^t \dot{e}_i^T\left(\varphi\left(\dot{q}_i,q_i,e_i\right)\tilde{\theta}_i + K_D\,\dot{e}_i\right)\mathrm{d}\tau \tag{45.16}$$

In formula (45.8): $\bar{\theta}_i^T(t) = \left(\Gamma\phi^T\dot{e}_i\right)^T = \dot{e}_i^T\,\phi\Gamma$, it can be changed as the equation below: $\bar{\theta}_i^T\Gamma^{-1}\bar{\theta}_i = \dot{e}_i^T\,\phi\Gamma\Gamma^{-1}\Gamma\phi^T\dot{e}_i$, then

$$\bar{\theta}_i^T\Gamma^{-1}\tilde{\theta}_i = 2\,\dot{e}_i^T\,\phi\Gamma\Gamma^{-1}\Gamma\tilde{\phi}_i = 2\,\dot{e}_i^T\,\phi\tilde{\phi}_i \tag{45.17}$$

According to assumption two $V_i\left(\dot{e}_i(0),e_i(0)\right) = 0$ and formulas (45.17) and (45.12):

$$\begin{aligned} \Delta W_i &= -V_{i-1} + V_i - 1/2\int_0^t \left(\bar{\theta}_i^T\Gamma^{-1}\bar{\theta}_i + 2\bar{\theta}_i^T\Gamma^{-1}\tilde{\theta}_i\right)d\tau \\ &\le -V_{i-1} - 1/2\int_0^t \left(\dot{e}_i^T\left(\phi\Gamma\phi^T + 2K_D\right)\dot{e}_i\right)d\tau \le 0 \end{aligned} \tag{45.18}$$

Because V_{i-1}, Γ, K_D are positive definite matrix and $\Delta W_i \le 0$, W_i must be nonincreasing sequence, and the conclusion can be drawn: if W_0 is bounded, then W_i must also be bounded.

45.4.2.2 $W_0(t)$ Continuous and Bounded Proof [13]

Combine formula (45.9) with formula (45.15), the formula can be changed to:

$$\dot{W}_0(t) \le \left(\dot{e}_0^T \varphi\left(q_0, \dot{q}_0, \ddot{q}_0,\right) \tilde{\theta}_0 - K_D \dot{e}_0 \right) + 1/2 \tilde{\theta}_0^T \Gamma^{-1} \tilde{\theta}_0 \tag{45.19}$$

For $\theta^T \Gamma^{-1} \overset{\cap}{\theta}_0 \le K \left\| \Gamma^{-1} \overset{\cap}{\theta}_0 \right\|^2 + \frac{1}{4K} \|\theta\|^2$ and $K > 0$, formula (45.19) can be changed to:

$$\dot{W}_0(t) \le -\beta_1 \left\| \dot{e}_0 \right\|^2 - \beta_2 \left\| \overset{\cap}{\theta}_0 \right\|^2 + \frac{1}{4K} \|\theta\|^2 \tag{45.20}$$

Therein, $\beta_1 = \lambda_{\min}(K_D), \beta_2 = 1/2 \lambda_{\min}\left(\Gamma^{-1}\right) - K \lambda_{\max}^2\left(\Gamma^{-1}\right), K \le \frac{\lambda_{\min}\left(\Gamma^{-1}\right)}{2\lambda_{\max}^2\left(\Gamma^{-1}\right)}$, then

$$\dot{W}_0(t) \le \frac{1}{4K} \|\theta\|^2, \quad \forall t \in [0, T] \tag{45.21}$$

Because $\theta(t)$ is bounded and continuous, $W_0(t)$ must be bounded and continuous.

45.4.2.3 $W_i(t)$ Continuous and Bounded Proof

Because $W_i(t)$ can be expressed as $W_i(t) = W_0 + \sum_{j=1}^{i} \Delta W_j$ and formula (45.22), then

$$W_i \le W_0 - \sum_{j=1}^{i} V_{j-1} \le W_0 - 1/2 \sum_{j=1}^{i} e_{j-1}^T K_P e_{j-1} - 1/2 \sum_{J=1}^{I} \dot{e}_{j=1}^T K_P \dot{e}_{j-1} \tag{45.22}$$

Because $\left(\sum_{j=1}^{i} e_{j-1}^T K_P e_{j-1} - \sum_{J=1}^{I} \dot{e}_{j=1}^T K_P \dot{e}_{j-1} \right) \le 2W_0$, that is, $W_i(t)$ is bounded. Also, due to $\lim_{i \to t} e_i(t) = \lim_{i \to t} \dot{e}_i(t) = 0, \forall t \in [0, T]$, and theorem has been proved.

45.5 Simulation Results and Analysis

According to the lower limb prosthesis kinetic equation formula (45.6) and the controller designed by formulas (45.7) and (45.8), the simulation system parameters are set as follows: $l_1 = l_2 = 0.5, d_1 = d_2 = 0.25, g = 9.81$ (Fig. 45.2). The damping and external interference of the two joints are unified set as: $d(t) = d_m \sin(t)$, where d_m is

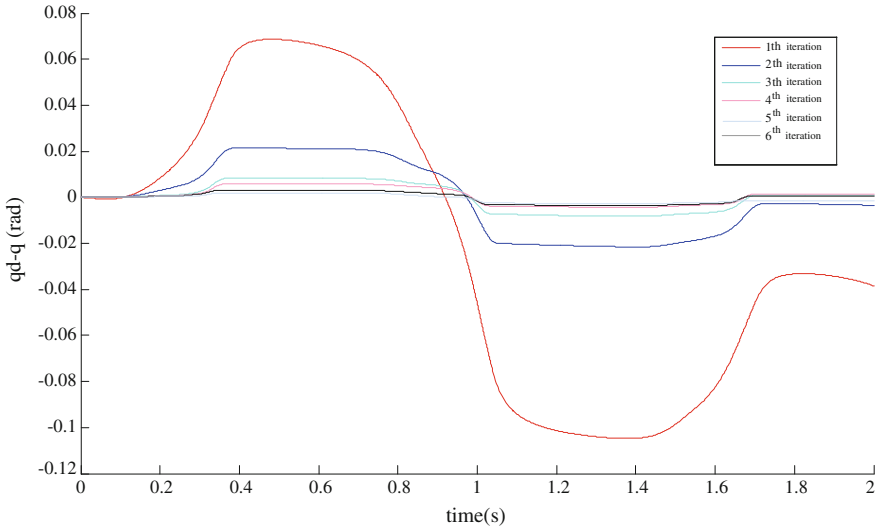

Fig. 45.2 Position tracking error of sixth iteration

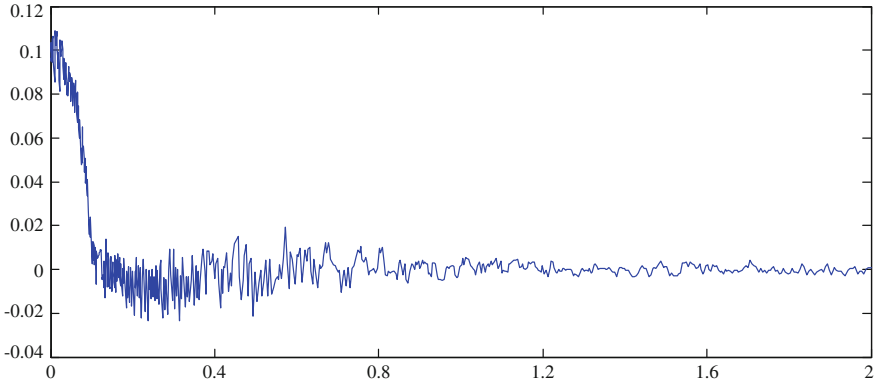

Fig. 45.3 The tracking speed error of sixth iteration

the random signal with amplitude of one, PD controller parameters of formula (45.7) is set as diag[20, 20], adaptive law arguments are taken as $\Gamma = \text{diag}[10, 10, 10, 10, 10]$, the number of iterations is set to 20, the simulation time is set to 20 s. Figure 45.3 shows that after the 6th iteration it has excellent effect of the speed of tracking; Fig. 45.4 shows the position tracking error of six iterations; Fig. 45.5 shows speed tracking error of six iterations, and the tracking error both gradually decrease with the increase in the number of iterations.

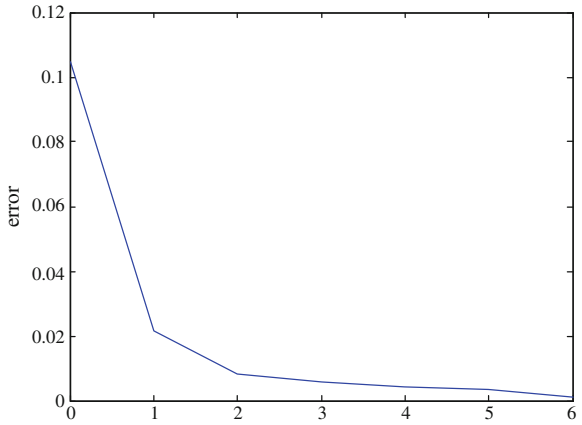

Fig. 45.4 Six iterations convergence process during absolute speed error

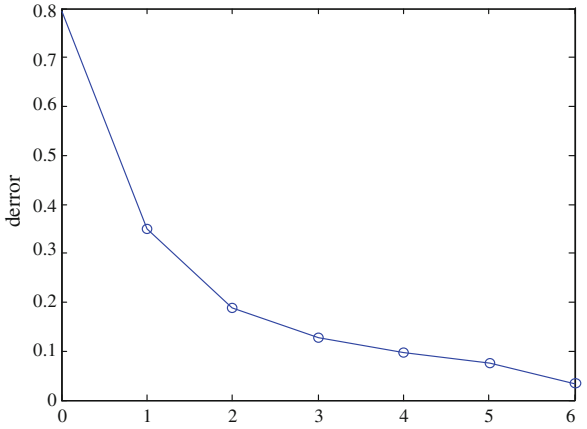

Fig. 45.5 Six iterations convergence process during absolute position error

45.6 Conclusion

Based on the Newton–Euler algorithm to conduct dynamic analysis of lower limb prostheses, and due to the uncertainty of damping and external disturbances, adaptive iterative learning controller has been implemented for tacking the trajectory. Simulation results show that the use of adaptive iterative learning control algorithm to trajectory tracking lower limb prosthetic knee can stably reduce the tracking error within a certain time and can achieve good tracking performance, and also fully verify the validity and feasibility of the algorithm.

Acknowledgments The authors would like to acknowledge the financial support from the Zhejiang Provincial Natural Science Foundation of Chin (Grant No. LY14F030023), and the National Natural Science Foundation of China (Grant No. 6137202361201300, 61201302, 61172134), and the Construction of Postgraduate Brand Course of Hangzhou Dianzi University (Grant No. PPKC2013YB006).

References

1. Wang R, Shen Q, Jin D (2007) Research and development of intelligent prosthetic knee. Chin J Rehabil Med 22(12):1093–1094 (in Chinese)
2. Yu H, Xu Z, Lu B et al (2012) Study on Intelligent control of human body prosthetic leg based on fuzzy-CMAC. Chin J Biomed Eng 31(1):83–88 (in Chinese)
3. Rao DH, Bitner D, Engineer IOEA (1994) Feedback-error learning scheme using recurrent neural networks for nonlinear dynamic systems. In: IEEE International Conference on Neural Networks. vol 6, issue 1, pp 175–178
4. Yu H, Hu J et al (2010) Dynamics modeling of artificial legs system based on knee joint damper characteristics. J Mach Des 27(2):40–42 (in Chinese)
5. Wang Y, Hou Z, LI X (2008) A novel automatic train operation algorithm based on iterative learning control theory. Institute of Electrical and Electronics Engineering Computer Society, Beijing
6. Li R, Han Z (2005) Survey of iterative learning control. Control Decis 20(9):19–24 (in Chinese)
7. Sun M, Huang B (1999) Iterative learning control. National Defense Industry Press, Beijing (in Chinese)
8. Q CY, L MK (2002) A practical iterative learning path-following control of an omni-directional vehicle 4(1):90–98
9. Sun Y, Li J (2009) Adaptive learning control of nonlinear systems with iteration-varing trajectory. Sys Eng Electron 31(7):1715–1719 (in Chinese)
10. Li J, Hu Y (2012) Direct adaptive learning control of time-varying nonlinear systems tems. Syst Eng Electron 34(1):154–159 (in Chinese)
11. Sun M (2009) A Barbalat-1ike lemma with its application to learning control. IEEE Trans Autom Control 54(9):2222–2225
12. Marino R, Tomei P (2009) An iterative learning control for a class of partially feedback linearizable systems. IEEE Trans Autom Control 54(8):1991–1996
13. Mingxuan S, Xiongxiong H (2007) Iterative learning identification and control of discrete time-varying systems. Institute of Electrical and Electronics Engineering Computer Society, China, pp 520–552

Chapter 46
Dynamic Surface Control for a Class of Nonlinear Systems in the Presence of Input Saturation

Cao Pi and Jinkun Liu

Abstract In this technical note, we present a novel control approach based on dynamic surface for single input nonlinear systems in the presence of input saturation. The control algorithm is constructed by introducing first-order filtering of the virtual input at each step of the traditional backstepping approach. To deal with the problem of input saturation, we incorporate a new auxiliary design system and Nussbaum gain functions into the control scheme. Compared with the early backstepping approach, the dynamic surface control scheme has greatly simplified the design process. It is proved that the global stability of the closed-loop system can be guaranteed by the proposed control algorithm.

Keywords Nonlinear systems · Saturation · Dynamic surface · Stability analysis

46.1 Introduction

In many practical systems, physical input saturation on actuators indicates that the magnitude of the control signal is constrained. Saturation nonlinearity is unavoidable in most actuators. Saturation is a problem for actuators of control systems. It often severely degrades the performance of system, raises undesirable inaccuracy or even leads to instability [1, 2].

For this problem, much attention has led to saturation and a lot of work has been done in these years. In [3, 4], model reference adaptive control law was proposed for a linear plant in the presence of input saturation, where the plant poles lie entirely on the left side of the complex plane. For nonlinear systems, the analysis and design of control systems with saturation have been studied in [5–8]. Among them, a based-backstepping robust adaptive control technique was presented in [8] in the presence of saturation.

C. Pi · J. Liu (✉)
Beihang University, XueYuan Road No. 37, HaiDian District, Beijing 100191, China
e-mail: ljk@buaa.edu.cn

Z. Deng and H. Li (eds.), *Proceedings of the 2015 Chinese Intelligent Automation Conference*, Lecture Notes in Electrical Engineering 337,
DOI 10.1007/978-3-662-46463-2_46

However, a drawback with the backstepping technique is the problem of "explosion of complexity" [9–11]. That is, the complexity of controller grows drastically as the order of the system increases. This "explosion of complexity" is caused by the repeated differentiations of certain nonlinear functions.

Motivated by the backstepping approaches in saturation, a dynamic surface control approach is presented for a class of SISO nonlinear systems in the presence of input saturation in this paper. With this technique, the control design process has been simplified a lot. It is proved that the proposed control approach can guarantee that all the signals of the closed-loop system are bounded. Besides showing global stability, transient performance can also be adjusted by tuning certain design parameters.

46.2 System Description and Preliminaries

Consider the following single input single output nonlinear dynamic system:

$$\begin{cases} \dot{x}_1 = x_2 + f_1(x,t) \\ \dot{x}_2 = f_2(x,t) + bu(v) \\ y = x_1 \end{cases} \tag{46.1}$$

where $b \neq 0$. $x = [x_1, x_2]$ represents the configuration variable vector, $y = x_1$ is the flat output, $f_1(x,t)$, $f_2(x,t)$ are given smooth functions. $u(v)$ expresses the limited control input, which has an explicit definition as follows:

$$u(v) = \text{sat}(v) = \begin{cases} \text{sgn}(v(t))u_{\text{M}}, & |v(t)| \geq u_{\text{M}} \\ v(t), & |v(t)| < u_{\text{M}} \end{cases} \tag{46.2}$$

where u_M is the upper bond of $u(t)$.

The control object is to force the output y tracking the desired trajectory x_{1d}.

It can be easily checked there exists a nonsmooth point between the physical control input and the theoretical one when $|v(t)| = u_M$. The nonsmooth point prevents the direct accessibility of standard backstepping control.

In order to use this technique, we introduce a smooth function to approximate the saturation defined as

$$g(v) = u_M \tanh\left(\frac{v}{u_M}\right) = u_M \frac{e^{v/u_M} - e^{-v/u_M}}{e^{v/u_M} + e^{-v/u_M}}$$

Then we obtain:

$$u(v) = \text{sat}(v) = g(v) + d(v) = u_M \tanh\left(\frac{v}{u_M}\right) + d(v)$$

where $d(v) = \text{sat}(v) - g(v)$ is a bounded function and its bound can be obtained as:

$$|d(v)| = |\text{sat}(v) - g(v)| \leq 0.2785u_M$$

So the system can be written as:

$$\begin{cases} \dot{x}_1 = x_2 + f_1(x,t) \\ \dot{x}_2 = f_2(x,t) + bg(v) + d \\ y = x_1 \end{cases} \tag{46.3}$$

where $d = bd(v)$, $|d| \leq D$.

Assumption 46.1 The desired trajectory x_{1d} and its nth order derivatives are known and bounded.

Assumption 46.2 The plant is input-to-state stable.

A function $N(s)$ is called a Nussbaum-type function if it has properties as follows:

$$\lim_{k\to\pm\infty} \sup \frac{1}{k} \int_0^k N(s)\mathrm{d}s = \infty$$

$$\lim_{k\to\pm\infty} \inf \frac{1}{k} \int_0^k N(s)\mathrm{d}s = -\infty$$

Lemma 46.1 [8] *Let $V(\cdot)$ and $\chi(\cdot)$ be smooth functions, which are defined on $[0, t_f)$ with $V(t) \geq 0$, $\forall t \in [0, t_f)$, and $N(\chi)$ be a Nussbaum gain function. If the following inequality holds, $V(\cdot)$ and $\chi(\cdot)$ must be bounded on $[0, t_f)$.*

$$V \leq V(0)e^{-Ct} + \frac{M}{C}\left(1 - e^{-Ct}\right) + \frac{e^{-Ct}}{\gamma_\chi} \int_0^t (\xi N(\chi)\dot{\chi} - \dot{\chi})e^{C\tau} d\tau$$

where $C > 0$, $M > 0$, $\gamma_\chi > 0$ are constants, and ξ is a positive variable.

46.3 Control Design

In this section, a dynamic surface method is to be constructed.

Step 1: We define the position error as follows:

$$z_1 = x_1 - x_{1d} \tag{46.4}$$

Then the derivative of z_1 is

$$\dot{z}_1 = \dot{x}_1 - \dot{y}_r = x_2 + f_1(x,t) - \dot{x}_{1d} \tag{46.5}$$

$\bar{x}_2$ is the virtual control variable and was defined as:

$$\bar{x}_2 = -c_1 z_1 + \dot{x}_{1d} - f_1(x,t) \tag{46.6}$$

where $c_1 > 0$.

Let $\bar{x}_2$ pass through a first-order low-pass filter, where the time constant is τ. Then we obtain the new state variable x_{2d} and it meets the following mathematic relation:

$$\begin{aligned} \tau \dot{x}_{2d} + x_{2d} &= \bar{x}_2 \\ x_{2d}(0) &= \bar{x}_2(0) \end{aligned} \tag{46.7}$$

From formula (46.4), we obtain $\dot{x}_{2d} = \frac{\bar{x}_2 - x_{2d}}{\tau}$, and the filter error is $y_2 = x_{2d} - \bar{x}_2$.

Step 2: We define the new variable as:

$$z_2 = x_2 - x_{2d} \tag{46.8}$$

We define a positive Lyapunov function as follows:

$$V_1 = \frac{1}{2} z_1^2 \tag{46.9}$$

Then the derivative of $\dot{V}_1$ pass is

$$\dot{V}_1 = z_1 \dot{z}_1 = z_1(x_2 + f_1(x,t) - \dot{x}_{1d}) = z_1(z_2 + x_{2d} + f_1(x,t) - \dot{x}_{1d}) \tag{46.10}$$

From (46.4) to (46.9), we obtain:

$$\dot{V}_1 = -c_1 z_1^2 + z_1 z_2 + z_1 y_2 \tag{46.11}$$

Define $z_3 = g(v) - \bar{x}_3$,

Then

$$\dot{z}_2 = \dot{x}_2 - \dot{x}_{2d} = b(z_3 + \bar{x}_3) + f_2(x,t) + d - \dot{x}_{2d} \tag{46.12}$$

We consider a positive Lyapunov function given by:

$$V_2 = V_1 + \frac{1}{2} z_2^2 \tag{46.13}$$

Then the derivative of $\dot{V}_2$ pass is:

$$\dot{V}_2 = \dot{V}_1 + z_2\dot{z}_2 = -c_1 z_1^2 + z_1 z_2 + z_1 y_2 + z_2[b(z_3 + \bar{x}_3) + f_2(x,t) + d - \dot{x}_{2d}] \tag{46.14}$$

We design the virtual control law $\bar{x}_3$ as follows:

$$\bar{x}_3 = \frac{1}{b}(-(c_2 + l)z_2 - f_2(x,t) + \dot{x}_{2d}) \tag{46.15}$$

where $l > 0$, $c_2 > 0$.

Then, we obtain:

$$\begin{aligned} \dot{V}_2 =& -c_1 z_1^2 + z_1 z_2 + z_1 y_2 + z_2[b(z_3 + \bar{x}_3) + f_2(x,t) + d - \dot{x}_{2d}] \\ =& -c_1 z_1^2 - (c_2 + l)z_2^2 + z_2 d + b z_2 z_3 + z_1 z_2 + z_1 y_2 \end{aligned} \tag{46.16}$$

Then, it yields:

$$\dot{V}_2 \leq -c_1 z_1^2 - c_2 z_2^2 + b z_2 z_3 + z_1 z_2 + z_1 y_2 + \frac{1}{4l} d^2 \tag{46.17}$$

Step 3: Define an auxiliary system

$$\dot{v} = -cv + \omega \tag{46.18}$$

where c is a positive constant, and ω is an auxiliary signal.

Then the design of control law v turns to be the design of ω.

We can find that

$$\dot{z}_3 = \frac{\partial g}{\partial v}(-cv + \omega) - \dot{\bar{x}}_3 \tag{46.19}$$

Note that $\frac{\partial g}{\partial v}$ is varying, which makes the design and analysis difficult. To deal with it, we use a Nussbaun function

$$N(\chi) = \chi^2 \cos(\chi) \tag{46.20}$$

The control law for ω is designed as follows:

$$\begin{aligned} \omega =& N(\chi)\bar{\omega} \\ \dot{\chi} =& \gamma_\chi z_3 \bar{\omega} \\ \bar{\omega} =& -c_3 z_3 + cv\frac{\partial g}{\partial v} + \dot{\bar{x}}_3 \end{aligned} \tag{46.21}$$

where $c_3 > 0$.

46.4 Stability Analysis

Taking account of the filtering error, we define:

$$V = V_2 + \frac{1}{2}z_3^2 + \frac{1}{2}y_2^2 \tag{46.22}$$

Then, we have:

$$\dot{V} \leq -c_1 z_1^2 - c_2 z_2^2 + b z_2 z_3 + z_1 z_2 + z_1 y_2 + \frac{1}{4l}d^2 + z_3 \dot{z}_3 + y_2 \dot{y}_2 \tag{46.23}$$

where

$$\dot{y}_2 = -\frac{y_2}{\tau_2} + B_2(z_1, z_2, y_2, \ddot{x}_{1d}) \tag{46.24}$$

$$\begin{aligned} B_2 &= c_1(x_2 - \dot{x}_{1\mathrm{d}}) - \ddot{x}_{1\mathrm{d}} = c_1(z_2 + \alpha_1 - \dot{x}_{1\mathrm{d}}) - \ddot{x}_{1\mathrm{d}} \\ &= c_1(z_2 + y_2 + \bar{x}_2 - \dot{x}_{1\mathrm{d}}) - \ddot{x}_{1\mathrm{d}} = c_1(z_2 + y_2 - c_1 z_1) - \ddot{x}_{1\mathrm{d}} \end{aligned} \tag{46.25}$$

Theorem 46.1 *Consider the nonlinear system* (46.1) *satisfying Assumptions* 46.1–46.2 *and Lemma* 46.1. *With the application of virtual controllers* (46.6), (46.15), (46.21), *parameters selected rightly. When* $V(0) \leq p, p > 0$, *the closed-loop system is stable.*

Proof When $V = p$, $V = \frac{1}{2}z_1^2 + \frac{1}{2}z_2^2 + \frac{1}{2}z_3^2 + \frac{1}{2}y_2^2 = p$, B_2 is bounded as M_2, then we get $\frac{B_2^2}{M_2^2} - 1 \leq 0$. □

The derivative of V is given as follows:

$$\begin{aligned} \dot{V} &\leq -c_1 z_1^2 - c_2 z_2^2 + b z_2 z_3 + z_1 z_2 + z_1 y_2 + \frac{1}{4l}d^2 + z_3 \dot{z}_3 + y_2 \dot{y}_2 \\ &\leq -c_1 z_1^2 - c_2 z_2^2 + b z_2 z_3 + z_1 z_2 + z_1 y_2 + \frac{1}{4l}d^2 + y_2 \dot{y}_2 - c_3 z_3^2 + \left[\frac{\partial g}{\partial v}N(\chi) - 1\right] z_3 \bar{\omega} \\ &\leq -\frac{1}{\tau}y_2^2 + |y_2||B_2| - c_1 z_1^2 - c_2 z_2^2 - c_3 z_3^2 + b|z_2||z_3| \\ &\quad + |z_1||z_2| + |z_1||y_2| + \frac{1}{4l}d^2 + \left[\frac{\partial g}{\partial v}N(\chi) - 1\right] z_3 \bar{\omega} \\ &= (1 - c_1)z_1^2 + \left(\frac{1}{2} + \frac{b}{2} - c_2\right)z_2^2 + \left(\frac{b}{2} - c_2\right)z_3^2 + \left(\frac{1}{2}B_2^2 + \frac{1}{2} - \frac{1}{\tau}\right)y_2^2 \\ &\quad + \frac{1}{2} + \frac{1}{4l}d^2 + \left[\frac{\partial g}{\partial v}N(\chi) - 1\right] z_3 \bar{\omega} \end{aligned} \tag{46.26}$$

where we choose

$$c_1 \geq 1 + r,\ r > 0,\ c_2 \geq \frac{1}{2} + \frac{b}{2} + r,\ c_3 \geq \frac{b}{2} + r,\ \frac{1}{\tau} \geq \frac{1}{2}M_2 + \frac{1}{2} + r \tag{46.27}$$

Then, we obtain:

$$\begin{aligned}
\dot{V} &\leq -rz_1^2 - rz_2^2 - rz_3^2 + \left(\frac{1}{2}B_2^2 - \frac{M_2^2}{2} - r\right)y_2^2 + \frac{1}{2} + \frac{1}{4l}d^2 + \left[\frac{\partial g}{\partial v}N(\chi) - 1\right]z_3\bar{\omega} \\
&= -2rV + \left(\frac{M_2^2}{2M_2^2}B_2^2 - \frac{M_2^2}{2}\right)y_2^2 + \frac{1}{2} + \frac{1}{4l}d^2 + \left[\frac{\partial g}{\partial v}N(\chi) - 1\right]z_3\bar{\omega} \\
&\leq -2rV + \frac{1}{2} + \frac{1}{4l}d^2 + \left[\frac{\partial g}{\partial v}N(\chi) - 1\right]z_3\bar{\omega} \\
&= -2rV + \frac{1}{2} + \frac{1}{4l}d^2 + \frac{1}{\gamma_\chi}\left(\frac{\partial g}{\partial v}N(\chi) - 1\right)\dot{\chi}
\end{aligned} \tag{46.28}$$

Thus, it yields:

$$\dot{V} \leq -2rV + \frac{1}{\gamma_\chi}\left(\frac{\partial g}{\partial v}N(\chi) - 1\right)\dot{\chi} + \frac{1}{4l}D^2 + \frac{1}{2} \tag{46.29}$$

By direct integrations of the differential inequality (46.29), we have:

$$V \leq V(0)e^{-2rt} + \frac{D^2}{8rl}\left(1 - e^{-2rt}\right) + \frac{1}{4r}\left(1 - e^{-2rt}\right) + \frac{e^{-2rt}}{\gamma_\chi}\int_0^t \left(\frac{\partial g}{\partial v}N(\chi) - 1\right)\dot{\chi}e^{2r\tau}d\tau \tag{46.30}$$

46.5 Simulation Example

Consider a two-order system as follows:

$$\begin{aligned}
\dot{x}_1 &= x_2 \\
\dot{x}_2 &= -a_1x_1 - a_2x_2 + b\text{sat}(v)
\end{aligned} \tag{46.31}$$

where $a_1 = 8$, $a_2 = 2$, $b = 1$, $u_M = 2$ $y = x_1$. The desired trajectory is given as $x_{1d} = 0.1 \sin t$.

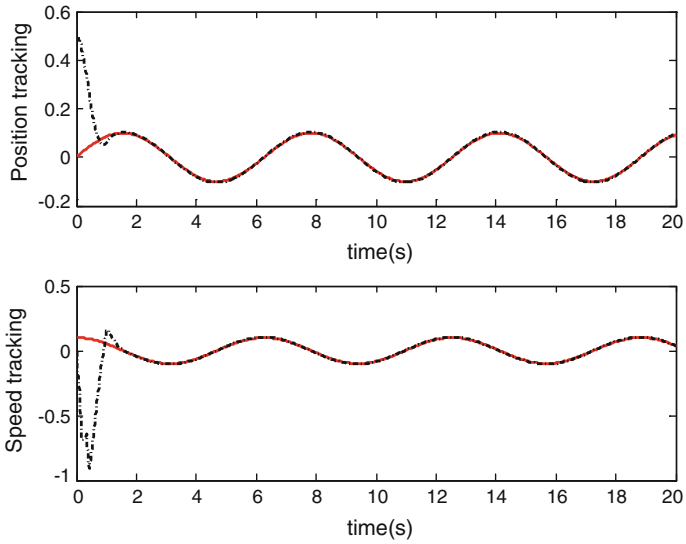

Fig. 46.1 Trajectories of x_1, x_2

Parameters in controller are chosen as: $c_1 = 10$, $c_2 = 15$, $c_3 = 10$, $c = 5$, $l = 10$. The initial conditions are chosen as: $x_1 = 0.5$, $x_2 = 0$, $x_{2d} = -4.9$.

The simulation results are shown in Figs. 46.1, 46.2 and 46.3, where Fig. 46.1 expresses the trajectories of x_1, x_2; Fig. 46.2 expresses the trajectory of v; Fig. 46.3 expresses the trajectory of $\mathrm{sat}(v)$.

Fig. 46.2 Trajectory of v

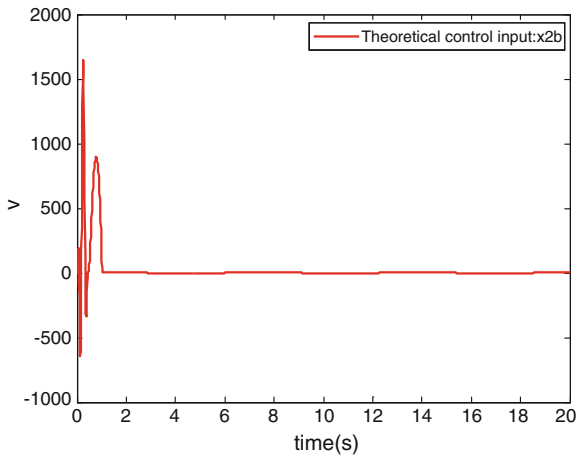

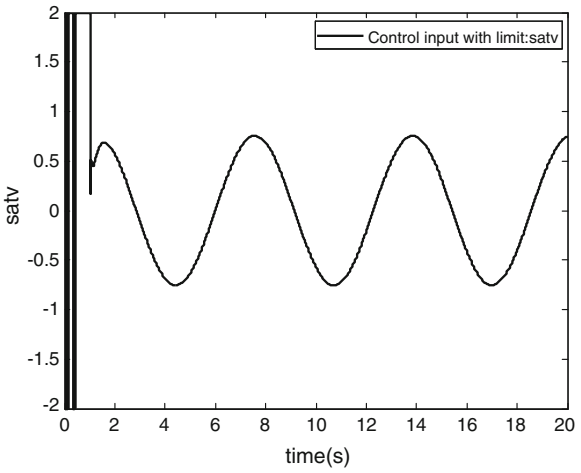

Fig. 46.3 Trajectory of sat(v)

46.6 Conclusion

In this paper, a novel dynamic surface control approach has been presented for second-order nonlinear systems in the presence of input saturation. This technique has eliminated the problem of "explosion of complexity" caused by the traditional backstepping approach. Compared with the earlier backstepping approach, the dynamic surface control scheme has greatly simplified the design process. Besides showing global stability, transient performance can also be adjusted by tuning certain design parameters.

Acknowledgments This work was supported by the National Natural Science Foundation of China (Grant No. 61374048) and the Research Fund for Doctoral Program of Higher Education of China (Grant No. 20121102110008).

References

1. Perez-Arancibia NO, Tsao T-C, Gibson JS (2010) Saturation-induced instability and its avoidance in adaptive control of hard disk drives. IEEE Trans Control Syst Technol 2:368–382
2. Kapila V, Grigoriadis K (eds) (2002) Actuator saturation control (automation and control engineering). CRC Press, Orlando
3. Annaswamy AM, Evesque S, Niculescu SI, Dowling AP (2001) Adaptive control of a class of time-delay systems in the presence of saturation. Adapt Control Nonsmooth Dyn Syst 333–348
4. Karason SP, Annaswamy AM (1994) Adaptive control in the presence of input constraints. IEEE Trans Autom Control 39(11):2325–2330
5. Zhou J (2008) Decentralized adaptive control for large-scale time-delay systems with dead-zone input. Automatic 44(7):1790–1799

6. Li YM, Tong SC, Li TS (2013) Direct adaptive fuzzy backstepping control of uncertain nonlinear systems in the presence of input saturation. Neural Comput Appl 23:1207–1216
7. Ting CS (2008) A robust fuzzy control approach to stabilization of nonlinear time-delay systems with saturating inputs. Int J Fuzzy Syst 10(1):50–60
8. Wen CY, Zhou J, Liu ZT, Su HY (2011) Robust adaptive control of uncertain nonlinear systems in the presence of input saturation and external disturbance. IEEE Trans Autom Control 66(7):1672–1678
9. Swaroop D, Gerdes JC, Yip PP, Hedrick JK (1997) Dynamic surface control of nonlinear systems. In: Proceedings American control conference, Albuquerque, NM, pp 3028–3034
10. Swaroop D, Hedrick JK, Yip PP, Gerdes JC (2000) Dynamic surface control for a class of nonlinear systems. IEEE Trans Autom Control 45(10):1893–1899
11. Yip PP, Hedrick JK (1998) Adaptive dynamic surface control: a simplified algorithm for adaptive backstepping control of nonlinear systems. Int J Control 71(5):959–979

Chapter 47
Sliding-Mode Control of a Class of Nonlinear Systems in the Presence of Input Saturation

Jinkun Liu and Cao Pi

Abstract In this paper, we present a sliding-mode control approach for a two-order nonlinear system in the presence of input saturation and external disturbance. A robust control algorithm is constructed by using backstepping design techniques. Two well-defined smooth functions are introduced to approximate the primary functions so that they could be differential. To overcome the problem of input saturation, a new auxiliary design system and a Nussbaum function are incorporated into the control method. It is proved that the global stability of the closed-loop system can be guaranteed by the proposed control algorithm. A simulation example is included at last.

Keywords Nonlinear systems · Saturation · Backstepping design · Sliding-mode control

47.1 Introduction

Saturation, deadzone, and hysteresis are the most common actuator nonlinearities in practical control system applications. Saturation nonlinearity is unavoidable in most actuators. When an actuator has reached such an input limit, it is said to be "saturated," since efforts to further increase the actuator output would not result in any variation in the output. It often severely degrades the performance of system, giving rise to undesirable inaccuracy or even leading to instability [1, 2].

In recent years, a lot of research has been done on saturation issues. For linear systems with input saturation, there are many research results so far. Among them the representative approach is to use the LMI method to solve the problem of

J. Liu (✉) · C. Pi
Beihang University, XueYuan Road No. 37, HaiDian District, Beijing 100191, China
e-mail: ljk@buaa.edu.cn

Z. Deng and H. Li (eds.), *Proceedings of the 2015 Chinese Intelligent Automation Conference*, Lecture Notes in Electrical Engineering 337,
DOI 10.1007/978-3-662-46463-2_47

saturation [3–6]. However, for the nonlinear systems with input saturation, little work has been done. A representative approach among them is to combine the backstepping technique with the smooth hyperbolic tangent function to achieve the control of the nonlinear systems in the presence of input saturation [7–10].

On the basis of reference [10], a sliding-mode control approach for single input nonlinear systems in the presence of an external disturbance and input saturation is introduced in this paper. Note that saturation is a nonsmooth function but the dynamic surface technique requires all functions differentiable. To handle this problem, a smooth function is used to approximate the saturation. Another smooth function is introduced again to approximate the sliding-mode function for the same reason. The stability of the closed-loop is proved and simulation illustrate the effectiveness of the proposed method.

47.2 System Description and Preliminaries

Consider the following single input single output nonlinear dynamic system with input noise:

$$\begin{cases} \dot{x}_1 = x_2 \\ \dot{x}_2 = f(x,t) + bu(v) + \bar{d}(t) \\ y = x_1 \end{cases} \tag{47.1}$$

where $b \neq 0$, $\left|\bar{d}(t)\right| \leq d_{\max}$. $x = [x_1, x_2]$ represents the configuration variable vector, $y = x_1$ is the flat output, $f(x,t)$ is a given smooth function. $u(v)$ expresses the limited control input, which has a explicit definition as follows:

$$u(v) = \text{sat}(v) = \begin{cases} \text{sgn}(v(t))u_M, & |v(t)| \geq u_M \\ v(t), & |v(t)| < u_M \end{cases} \tag{47.2}$$

where u_M is the upper bond of $u(t)$.

The control object is to force the output y tracking the desired trajectory y_r.

It can be easily checked there exists a nonsmooth point between the physical control input and the theoretical one when $|v(t)| = u_M$. The nonsmooth point prevents the direct accessibility of standard backstepping control (Fig. 47.1).

In order to use this technique, we introduce a smooth function to approximate the saturation defined as

$$g(v) = u_M \tanh\left(\frac{v}{u_M}\right) = u_{\text{M}} \frac{e^{v/u_M} - e^{-v/u_M}}{e^{v/u_M} + e^{-v/u_M}}$$

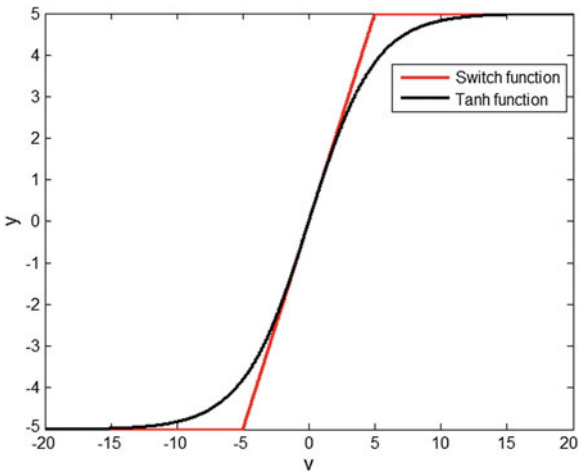

Fig. 47.1 Saturation and smooth function

Then we obtain

$$u(v) = \text{sat}(v) = g(v) + d(v) = u_M \tanh\left(\frac{v}{u_M}\right) + d_1(v)$$

where $d_1(v) = \text{sat}(v) - g(v)$ is a bounded function and its bound can be obtained as

$$|d_1(v)| = |\text{sat}(v) - g(v)| \leq 0.2785\, u_M$$

So the system can be written as

$$\begin{cases} \dot{x}_1 = x_2 \\ \dot{x}_2 = f(x,t) + bg(v) + d(t) \end{cases} \tag{47.3}$$

where $d(t) = bd_1(t) + \bar{d}(t)$, $|d| \leq D$, $D = |0.2785\, bu_M| + d_{\max}$.

Assumption 47.1 The desired trajectory y_r and its nth order derivatives are known and bounded.

Assumption 47.2 The plant is input-to-state stable.

A function $N(s)$ is called a Nussbaum-type function if it has properties as follows:

$$\lim_{k \to \pm\infty} \sup \frac{1}{k} \int_0^k N(s)\mathrm{d}s = \infty \tag{47.4}$$

$$\lim_{k\to\pm\infty} \inf \frac{1}{k} \int_0^k N(s)\mathrm{d}s = -\infty \tag{47.5}$$

Lemma 47.1 [10] *Let $V(\cdot)$ and $\chi(\cdot)$ be smooth functions, which are defined on $[0, t_f)$ with $V(t) \geq 0$, $\forall t \in [0, t_f)$, and $N(\chi)$ be a Nussbaum gain function. If the following inequality holds, $V(\cdot)$ and $\chi(\cdot)$ must be bounded on $[0, t_f)$.*

$$V \leq V(0)e^{-Ct} + \frac{M}{C}\left(1 - e^{-Ct}\right) + \frac{e^{-Ct}}{\gamma_\chi} \int_0^t (\xi N(\chi)\dot{\chi} - \dot{\chi})e^{C\tau}\mathrm{d}\tau$$

where $C > 0$, $M > 0$, $\gamma_\chi > 0$ are constants, and ξ is a positive variable.

47.3 Sliding-Mode Control Design and Stability Analysis

In this section, a sliding-mode control method is to be constructed in the framework of backstepping technique, so that all the signals in the closed-loop system are bounded. The detailed design procedure can be divided into three steps.

Step 1: Define the position error

$$z_1 = x_1 - y_r \tag{47.6}$$

and take its derivative with respect to the time.

$$\dot{z}_1 = \dot{x}_1 - \dot{y}_\mathrm{r} = x_2 - \dot{y}_\mathrm{r} \tag{47.7}$$

Define the first virtual control input

$$\alpha_1 = -c_1 z_1 \tag{47.8}$$

where the coefficient $c_1 > 0$.

Choose the tracking error between $\dot{z}_1$ and α_1 as z_2.

$$z_2 = x_2 - \alpha_1 - \dot{y}_\mathrm{r} \tag{47.9}$$

As a result, we take the following Lyapunov function:

$$V_1 = \frac{1}{2} z_1^2 \tag{47.10}$$

Calculate its derivative along the solution of (47.7).

$$\dot{V}_1 = z_1 \dot{z}_1 = z_1(x_2 - \dot{y}_r) = z_1(z_2 + \alpha_1) \tag{47.11}$$

then substitute (47.8) into (47.11).

$$\dot{V}_1 = -c_1 z_1^2 + z_1 z_2 \tag{47.12}$$

Step 2: The Lyapunov function V_2 is defined as

$$V_2 = V_1 + \frac{1}{2} z_2^2 \tag{47.13}$$

With regard to the transformative control plant (47.5), $g(v)$ is the new control input. Follow the same line in step 1, $g(v)$ is designed by introducing another virtual control input α_2. The expression of α_2 will give in (47.16) taking into account the robustness.

After defining the error $z_3 = g(v) - \alpha_2$, It can be readily get

$$\dot{z}_2 = \dot{x}_2 - \dot{\alpha}_1 - \ddot{y}_r = b(z_3 + \alpha_2) + f(x,t) + d - \dot{\alpha}_1 - \ddot{y}_r \tag{47.14}$$

As a consequence, the derivative of (47.13) turns into (47.15).

$$\dot{V}_2 = \dot{V}_1 + z_2 \dot{z}_2 = -c_1 z_1^2 + z_1 z_2 + z_2[b(z_3 + \alpha_2) + f(x,t) + d - \ddot{y}_r - \alpha_1] \tag{47.15}$$

To overcome the composite disturbance d, the switch item is added into α_2 where z_2 is considered as the sliding function. Hence, the virtual control α_2 is designed as follow:

$$\alpha_2 = \frac{1}{b}(-c_2 z_2 + \ddot{y}_r - z_1 - f(x,t) + \dot{\alpha}_1 - D\,\mathrm{sgn}(z_2)) \tag{47.16}$$

where the coefficient $c_2 > 0$.

Nevertheless, the discontinuous of $\mathrm{sgn}(\cdot)$ function gives rise to non-differentiable problem. It canot carry out the next *design* procedure. To solve the problem, we introduce the smooth tangent function replacing the discontinuous function $\mathrm{sgn}(\cdot)$. Ultimately, the virtual control α_2 is verified as the following:

$$\alpha_2 = \frac{1}{b}\left(-c_2 z_2 + \ddot{y}_r - z_1 - f(x,t) + \dot{\alpha}_1 - D\,\tanh\left(\frac{z_2}{\varepsilon}\right)\right) \tag{47.17}$$

where the boundary layer coefficient $\varepsilon > 0$.

Therefore, the (47.15) can be rewritten as

$$\begin{aligned}\dot{V}_2 &= -c_1 z_1^2 + z_1 z_2 + z_2\left[bz_3 - c_2 z_2 + \ddot{y}_r - z_1 - f(x,\,t) + \dot{\alpha}_1 - D\,\tanh\left(\frac{z_2}{\varepsilon}\right)\right. \\ &\quad \left. + f(x,t) + d - \ddot{y}_r - \dot{\alpha}_1\right] \\ &= -c_1 z_1^2 - c_2 z_2^2 - D z_2\,\tanh\left(\frac{z_2}{\varepsilon}\right) + z_2 d + b z_2 z_3 \end{aligned} \tag{47.18}$$

Note that

$$|z_2| - z_2 \tanh\left(\frac{z_2}{\varepsilon}\right) \le \mu\varepsilon, \quad \mu = 0.2785$$

After some arrangement, the following inequality can be obtained

$$-Dz_2 \tanh\left(\frac{z_2}{\varepsilon}\right) + z_2 d \le -D|z_2| + z_2 d + D\mu\varepsilon \le D\mu\varepsilon \tag{47.19}$$

Associating with (47.19), (47.18) is formulated as

$$\dot{V}_2 \le -c_1 z_1^2 - c_2 z_2^2 + b z_2 z_3 + D\mu\varepsilon \tag{47.20}$$

Step 3: Define an auxiliary system

$$\dot{v} = -cv + \omega \tag{47.21}$$

where c is a positive constant, and ω is an auxiliary signal. Consequently, the control law design switch to design ω.

Expanding (47.17), it can be show that

$$\alpha_2 = \frac{1}{b}\left(-c_2(c_1 x_1 + x_2 - c_1 y_r - \dot{y}_r) + \ddot{y}_r - (x_1 - y_r) - f(x,\,t) - c_1(x_2 - \dot{y}_r) - D\tanh\left(\frac{c_1 x_1 + x_2 - c_1 y_r - \dot{y}_r}{\varepsilon}\right)\right) \tag{47.22}$$

Hence one can see that α_2 is a function of x_1, x_2, y_r, $\dot{y}_r$ and $\ddot{y}_r$.

$$\dot{\alpha}_2 = \frac{\partial \alpha_2}{\partial x_2}(f(x,t) + bg(v) + d) + \frac{\partial \alpha_2}{\partial x_1} x_2 + \frac{\partial \alpha_2}{\partial y_r}\dot{y}_r + \frac{\partial \alpha_2}{\partial \dot{y}_r}\ddot{y}_r + \frac{\partial \alpha_2}{\partial \ddot{y}_r}\dddot{y}_r \tag{47.23}$$

After further derivation, we have

$$\begin{aligned}\dot{z}_3 &= \frac{\partial g}{\partial v}(-cv + \omega) - \dot{\alpha}_2 \\ &= \frac{\partial g}{\partial v}(-cv + \omega) - \frac{\partial \alpha_2}{\partial x_2}(f(x,t) + bg(v) + d) - \frac{\partial \alpha_2}{\partial x_1} x_2 - \frac{\partial \alpha_2}{\partial y_r}\dot{y}_r - \frac{\partial \alpha_2}{\partial \dot{y}_r}\ddot{y}_r - \frac{\partial \alpha_2}{\partial \ddot{y}_r}\dddot{y}_r \end{aligned} \tag{47.24}$$

Note that $\frac{\partial g}{\partial v}$ is varying, which makes the design and analysis difficult. To deal with it, we use a Nussbaun function

$$N(\chi) = \chi^2 \cos(\chi) \tag{47.25}$$

The control law for ω is designed as follows:

$$\omega = N(\chi)\bar{\omega} \tag{47.26}$$

$$\dot{\chi} = \gamma_\chi z_3 \bar{\omega} \tag{47.27}$$

$$\begin{aligned}\bar{\omega} = &- c_3 z_3 + \frac{\partial \alpha_2}{\partial x_1} x_2 + \frac{\partial \alpha_2}{\partial y_r}\dot{y}_r + \frac{\partial \alpha_2}{\partial \dot{y}_r}\ddot{y}_r + \frac{\partial \alpha_2}{\partial \ddot{y}_r}\dddot{y}_r + cv\frac{\partial g}{\partial v} \\ &+ b\frac{\partial \alpha_2}{\partial x_2} g(v) - bz_2 + \frac{\partial \alpha_2}{\partial x_2} f - l\left(\frac{\partial \alpha_2}{\partial x_2}\right)^2 z_3\end{aligned} \tag{47.28}$$

where the coefficient $c_3 > 0$.

Define the Lyapnov function

$$V_3 = V_2 + \frac{1}{2} z_3^2 \tag{47.29}$$

Then

$$\begin{aligned}\dot{V}_3 \leq &- c_1 z_1^2 - c_2 z_2^2 + b z_2 z_3 + D\mu\varepsilon + z_3 \dot{z}_3 \\ &= -c_1 z_1^2 - c_2 z_2^2 + b z_2 z_3 + D\mu\varepsilon + z_3(\dot{z}_3 + \bar{\omega} - \bar{\omega}) \\ &= -c_1 z_1^2 - c_2 z_2^2 + b z_2 z_3 + D\mu\varepsilon + z_3\left\{\frac{\partial g}{\partial v}\omega - c_3 z_3 - b z_2 - \frac{\partial \alpha_2}{\partial x_2} d - l\left(\frac{\partial \alpha_2}{\partial x_2}\right)^2 z_3\right\} - z_3\bar{\omega} \\ &\leq - c_1 z_1^2 - c_2 z_2^2 - c_3 z_3^2 + D\mu\varepsilon + \left(\frac{\partial g}{\partial v} N(\chi) - 1\right) z_3\bar{\omega} - z_3 \frac{\partial \alpha_2}{\partial x_2} d - l\left(\frac{\partial \alpha_2}{\partial x_2}\right)^2 z_3^2\end{aligned} \tag{47.30}$$

We obtain:

$$\dot{V}_3 \leq - CV_3 + D\mu\varepsilon + \frac{1}{\gamma_\chi}(\xi N(\chi) - 1)\dot{\chi} + \frac{1}{4l} D^2 \tag{47.31}$$

where $C = 2\min\{c_1, c_2, c_3\}$.

Define $\frac{\partial g}{\partial v} = \xi$, and $\left|\frac{\partial g(v)}{\partial v}\right| = \left|\frac{4}{\left(e^{v/u_{\mathrm{M}}} + e^{-v/u_{\mathrm{M}}}\right)^2}\right| \leq 1$.

By direct integrations of the differential inequality (47.31), we have

$$V_3 \leq V_3(0)e^{-Ct} + \frac{1}{C}\left(D\mu\varepsilon + \frac{D^2}{4l}\right)\left(1 - e^{-Ct}\right) + \frac{e^{-Ct}}{\gamma_\chi}\int_0^t (\xi N(\chi) - 1)\dot{\chi}e^{C\tau}\mathrm{d}\tau \quad (47.32)$$

We can conclude that the closed-loop system is stable from Lemma 47.1.

47.4 Simulation Example

Consider a two-order system as follows:

$$\begin{aligned} \dot{x}_1 &= x_2 \\ \dot{x}_2 &= -a_1 x_1 - a_2 x_2 + b\mathrm{sat}(v) + \bar{\mathrm{d}}(t) \end{aligned} \quad (47.33)$$

where $a_1 = 8$, $a_2 = 2$, $b = 1$, $u_M = 2$, $y = x_1$. The desired trajectory is given as $y_r = 0.1\sin t$. $\bar{\mathrm{d}}(t) = 0.1\sin(t)$.

Parameters in controller are chosen as $c_1 = 10$, $c_2 = 10$, $c_3 = 10$, $c = 5$, $l = 10$.

The initial conditions are chosen as $x_1 = 0.4$, $x_2 = 0$.

The simulation results are shown in Figs. 47.2 and 47.3, where Fig. 47.2 expresses the trajectories of x_1, x_2; Fig. 47.3 expresses the trajectory of v.

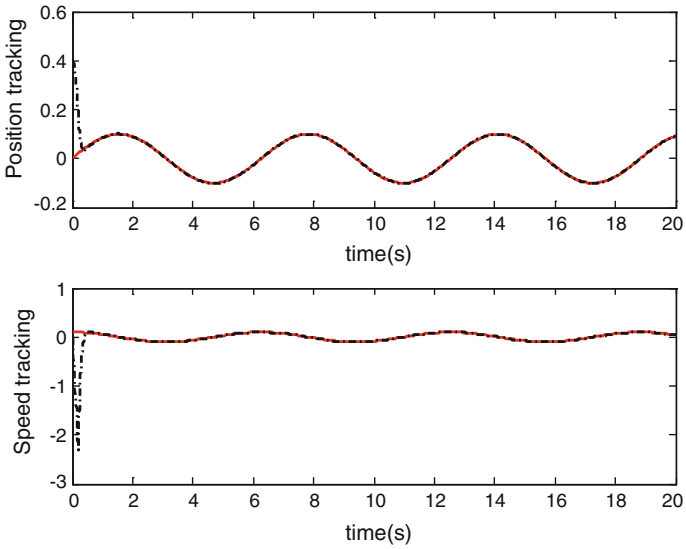

Fig. 47.2 Trajectories of x_1, x_2

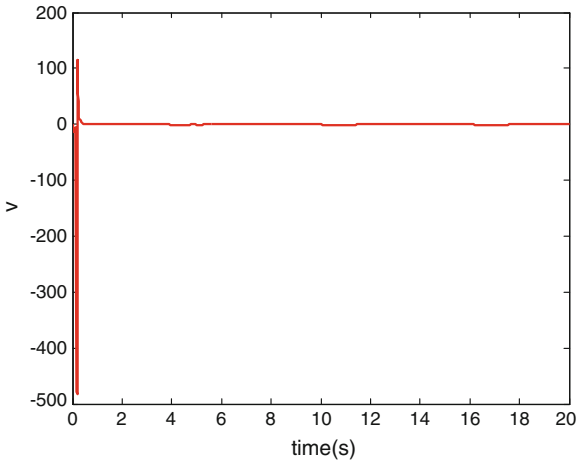

Fig. 47.3 Trajectory of v

47.5 Conclusion

In this paper, a sliding-mode control approach has been presented for the two-order nonlinear systems in the presence of input saturation and external disturbance. Two well-defined smooth functions are introduced to approximate the primary functions to solve the problem of nondifferentiability. The Nussbaum function is introduced to deal with the problem of saturation. The stability analysis has proved the stability of the whole closed-loop system.

Acknowledgments This work was supported by the National Natural Science Foundation of China (Grant No. 61374048) and the Research Fund for Doctoral Program of Higher Education of China (Grant No.20121102110008).

References

1. Perez-Arancibia NO, Tsao T-C, Gibson JS (2010) Saturation-induced instability and its avoidance in adaptive control of hard disk drives. IEEE Trans Control Syst Technol 2: 368–382
2. Kapila V, Grigoriadis K (eds) (2002) Actuator saturation control (automation and control engineering). CRC Press, Orlando
3. Grimm G, Hatfield J, Postlethwaite I et al (2003) Antiwindup for stable linear systems with input saturation: an LMI-based synthesis. IEEE Trans Autom Control 48(9):1509–1525
4. Forni F, Galeani S, Zaccarian L (2012) Model recovery anti-windup for continuous-time rate and magnitude saturated linear plants. Automatica 48(8):1502–1513
5. Herrmann G, Turner MC, Menon P et al (2006) Anti-windup synthesis for nonlinear dynamic inversion controllers. Robust Control Des 5(1):471–476
6. Gomes da Silva JM Jr, Ghiggi I, Tarbouriech S (2008) Non-rational dynamic output feedback for time-delay systems with saturating inputs. Int J Control 81(4):557–570

7. Zhou J (2008) Decentralized adaptive control for large-scale time-delay systems with dead-zone input. Automatic 44(7):1790–1799
8. Li YM, Tong SC, Li TS (2013) Direct adaptive fuzzy backstepping control of uncertain nonlinear systems in the presence of input saturation. Neural Comput Appl 23:1207–1216
9. Ting CS (2008) A robust fuzzy control approach to stabilization of nonlinear time-delay systems with saturating inputs. Int J Fuzzy Syst 10(1):50–60
10. Wen CY, Zhou J, Liu ZT, Su HY (2011) Robust adaptive control of uncertain nonlinear systems in the presence of input saturation and external disturbance. IEEE Trans Autom Control 66(7):1672–1678

Chapter 48
Fault Diagnosis with Adaptive Projection Algorithms for Complex Non-Gaussian Stochastic Distribution Systems

Yangfei Ye, Yang Yi, Xiaokang Sun and Tianping Zhang

Abstract This paper discusses the fault diagnosis problem for a class of non-Gaussian stochastic processes with unknown fault. By using the spline function and T-S model simultaneously, the probability density function (PDF) control problem can be transformed into the control problem of T-S fuzzy weight dynamics. In this framework, an adaptive fuzzy filter based on output PDF is designed to estimate the size of system fault. Meanwhile, in order to solve the bounded problem of the fault, an adaptive projection algorithm is applied into adjust the estimated value for the fault. As a result, the satisfactory stability and fault diagnosis ability can be guaranteed by rigorous theoretical proof.

Keywords Non-gaussian stochastic processes · Fault diagnosis · Adaptive projection algorithm · T-S fuzzy model

48.1 Introduction

All along, the fault detection and diagnosis (FDD) is an important technique to improve the security of system and has received considerable attention in the field of control engineering [1]. Many significant results have also been presented and applied into different control systems [2, 3]. On the other hand, the T-S model was viewed as a powerful modeling tool since it is a powerful solution that bridges the gap between linear and nonlinear control systems [4]. Many complex nonlinear models can be described by T-S fuzzy model [2, 5, 6]. In order to further enhance the stability of T-S fuzzy models with unknown fault, the FDD algorithms based on T-S fuzzy models have been discussed [2].

With the higher requirements for process control, the control for output probability density functions (PDFs) in different actual processes has become a chal-

Y. Ye · Y. Yi (✉) · X. Sun · T. Zhang
College of Information Engineering, Yangzhou University, Yangzhou 225127, China
e-mail: yiyangcontrol@163.com

Z. Deng and H. Li (eds.), *Proceedings of the 2015 Chinese Intelligent Automation Conference*, Lecture Notes in Electrical Engineering 337,
DOI 10.1007/978-3-662-46463-2_48

lenging task [7–9] and it is also called as non-Gaussian stochastic distribution control (SDC) problem. Recently, some meaningful approaches have also been discussed to solve the system modeling and shape control difficulties existed in those non-Gaussian SDC systems [10, 11]. On the other hand, due to the complexity and uncertainty in SDC systems, some unknown faults and disturbances may exist. Since 2000, the FDD algorithm for SDC systems has begun to be considered based on filter theory [8, 9, 12, 13]. In these results, the modeling problem is ignored and only linear models or general nonlinear models are considered in FDD [8, 12, 13]. Technically, some control algorithms need to be designed to guarantee the bounded of the estimated value of unknown fault.

Motivated by the above observations, the objective is to develop an effective fault diagnosis algorithm for non-Gaussian stochastic distribution systems with unknown fault. In the two-step modeling framework, the T-S fuzzy weight model is established to model the nonlinear dynamical relationship between the control input and the output PDFs. Instead of common nonlinear filter, an adaptive fuzzy diagnostic filter is designed by combining the measurable output PDF with the T-S fuzzy weight dynamics. Meanwhile, the projection algorithm is applied to guarantee the bounded of the estimated value of fault. Moreover, a group of linear matrix inequalities (LMIs)-based solution is presented such that the estimation error system is stable and the error converges to a small region.

48.2 System Modeling with Spline Function and T-S Model

Denote $u(t) \in R^m$ as the control input, $y(t) \in [a, b]$ is the output of the non-Gaussian stochastic system, F is supposed as a constant vector and represents the unknown fault. Similar to previous results, the conditional probability of output $y(t)$ on $[\alpha, \beta]$ can be defined as follows:

$$P\{\alpha \le y(t) \le \beta\} = \int_{\alpha}^{\beta} \gamma(z, u(t), F)\mathrm{d}z \tag{48.1}$$

where $\gamma(z, u(t), F)$ represents the output PDF.

In the following, a spline expansion is imported to approximate the out PDFs, where $b_i(z)$ are basis functions. $\upsilon_i(z, u(t), F)$ are the corresponding weight values. Due to the constraint $\int_a^b \gamma(z, u(t), F)\mathrm{d}z = 1$, only $n - 1$ weights are independent.

$$\sqrt{\gamma(z, u(t), F)} = \sum_{i=1}^{n} \upsilon_i(u(t), F) b_i(z) \tag{48.2}$$

Thus, the output PDF can be further rewritten as

$$\sqrt{\gamma(z,u(t),F)} = B(z)V(u(t),F) + h(V(u(t),F))b_n(z) \tag{48.3}$$

where $V(u(t),F) = [\upsilon_1(u,F)\ldots\upsilon_{n-1}(u,F)]^T$, $B(z) = [b_1(z)\ldots b_{n-1}(z)]$. $V(t) := V(u(t),F)$ can be described as a function, that is, $h(V(t))$ (see [8, 10] for details). It can be concluded that the following Lipschitz condition can be satisfied within its operation region, for any $V_1(t)$ and $V_2(t)$, there exists a known matrix U such that

$$\|h(V_1(t)) - h(V_2(t))\| \le \|U(V_1(t) - V_2(t))\| \tag{48.4}$$

The next step is to find the dynamic relationship between the control input and the weight vectors. T-S fuzzy model is applied into approximate the weighting dynamics. The expression of T-S fuzzy weight model can be showed as follows:

Plant Rule i: If θ_1 is $\mu_{i1},\ldots,$ θ_p is μ_{ip}, then

$$\begin{cases} \dot{x}(t) = A_i x(t) + B_i u(t) + J_i F \\ V(t) = E_i x(t) \end{cases} \tag{48.5}$$

where $x(t) \in R^m$ are the unmeasured states, $V(t) := V(u(t),F) \in R^{n-1}$ is the independent weights vector. A_i, B_i, J_i and E_i represent the known parameter matrices. $\theta_j(x)$ and $\mu_{ij}(i = 1,\ldots,r, j = 1,\ldots,p)$ are the premise variables and the fuzzy sets respectively. r is the number of the if-then rules and the number of the premise variables is p. The T-S fuzzy weight model can be redefined as

$$\begin{cases} \dot{x}(t) = \sum_{i=1}^{r} h_i(\theta)(A_i x(t) + B_i u(t) + J_i F) \\ V(t) = \sum_{i=1}^{r} h_i(\theta) E_i x(t) \end{cases} \tag{48.6}$$

It is noted that for any θ, $h_i(\theta)$ satisfies $h_i(\theta) \ge 0, \sum_{i=1}^{n} h_i(\theta) = 1$.

48.3 Fault Diagnosis with Adaptive Projection Algorithm

In order to estimate the fault, we construct the following adaptive fuzzy filter:

$$\begin{cases} \dot{\hat{x}}(t) = \sum_{i=1}^{r} h_i(\theta)\left(A_i\hat{x}(t) + B_i u(t) + L\varepsilon(t) + J_i\hat{F}(t)\right) \\ \varepsilon(t) = \int_a^b \sigma(z)\left(\sqrt{\gamma(z,u(t),F)} - \sqrt{\hat{\gamma}(z,u(t))}\right)\mathrm{d}z \\ \sqrt{\hat{\gamma}(z,u(t))} = \sum_{i=1}^{r} h_i(\theta)B(z)E_i\hat{x}(t) + h\left(\sum_{i=1}^{r} h_i(\theta)E_i\hat{x}(t)\right)b_n(z) \end{cases} \tag{48.7}$$

where $\hat{x}(t)$ is the estimated state, L is the gain to be determined, and $\sigma(z)$ can be regarded as the pre-specified vector. Different from some traditional filter design methods, the residual signal $\varepsilon(t)$ is formulated as an integral with respect to the difference of the measured FDF and the estimated FDF.

By defining $\bar{E} = \sum_{i=1}^{r} h_i(\theta)E_i$, $e(t) = x(t) - \hat{x}(t)$. The residual signal can be shown to satisfy

$$\begin{aligned}\varepsilon(t) &= \int_a^b \sigma(z)B(z)\bar{E}e(t)dz + \int_a^b \sigma(z)[h(\bar{E}x(t)) - h(\bar{E}\hat{x}(t))]b_n(z)\mathrm{d}z \\ &= \Gamma_1 e(t) + \Gamma_2[h(\bar{E}x(t)) - h(\bar{E}\hat{x}(t))]\end{aligned} \tag{48.8}$$

In order to guarantee the bounded of the estimated value for the fault, an adaptive law with projection algorithm is designed as follows:

$$\dot{\hat{F}}(t) = \begin{cases} -C_1\hat{F}(t) + C_2\varepsilon(t), \\ \text{if} \left\|\hat{F}(t)\right\| < M/2 \text{ or } \left\|\hat{F}(t)\right\| = M/2 \text{ and } \hat{F}^T(t)C_1\hat{F}(t) - \hat{F}^T(t)C_2\varepsilon(t) \geq 0 \\ -C_1\hat{F}(t) + C_2\varepsilon(t) + \left(\hat{F}^T(t)C_1\hat{F}(t) - \hat{F}^T(t)C_2\varepsilon(t)\right)\frac{\hat{F}(t)}{\left\|\hat{F}(t)\right\|^2}, \\ \text{if} \left\|\hat{F}(t)\right\| = M/2 \text{ and } \hat{F}^T(t)C_1\hat{F}(t) - \hat{F}^T(t)C_2\varepsilon(t) < 0 \end{cases} \tag{48.9}$$

where $\hat{F}$ is the estimated value of the fault, $C_i > 0$ are the designed learning rate.

48.4 System Analysis and Theorem Proof

In this section, the stability and diagnosis performance will be discussed by the following theorems.

Theorem 48.1 *Suppose the initial value of $\hat{F}(t)$ satisfies the inequality $\left\|\hat{F}(0)\right\| \leq M/2$, where M is a known positive constant. If the adaptive projection algorithm (48.9) is applied into adjust the $\hat{F}(t)$, we can get the conclusion that the inequality $\left\|\hat{F}(t)\right\| \leq M/2$ can be satisfied during the whole control process.*

The proof of theorem is omitted here to save space.

Denoting $\tilde{F}(t) = F(t) - \hat{F}(t)$, the error system can be expressed as

$$\begin{cases} \dot{e}(t) = \sum_{i=1}^{r} h_i(\theta)\big((A_i - L\Gamma_1)e(t) - L\Gamma_2(h(\bar{E}x(t)) - h(\bar{E}\hat{x}(t))) + J_i\tilde{F}\big) \\ \dot{\tilde{F}} = C_1\hat{F} - C_2\varepsilon(t) - I\cdot\big(\hat{F}^T C_1\hat{F} - \hat{F}^T C_2\varepsilon(t)\big)\frac{\hat{F}}{\|\hat{F}\|^2} \end{cases} \tag{48.10}$$

Theorem 48.2 *Suppose* $\|\hat{F}(0)\| \le M/2$, $\|F\| \le M/2$. *For the known parameters* $\lambda_1 > 0$ *and the known matrix* $C_i (i = 1, 2)$, *there exist matrices* $P > 0$, R *and constant* $k_1 > 0$ *satisfying*

$$\begin{bmatrix} \Pi_{1i} + k_1 I & PJ_i - \Gamma_1^T C_2^T & R\Gamma_2 & 0 \\ J_i^T P^T - C_2\Gamma_1 & -2C_1 & 0 & C_2\Gamma_2 \\ \Gamma_2^T R^T & 0 & -\lambda_1^{-2} I & 0 \\ 0 & \Gamma_2^T C_2^T & 0 & -\frac{1}{2} I \end{bmatrix} < 0, \quad i = 1, 2 \ldots r \tag{48.11}$$

$$\Pi_{1i} = \mathrm{sym}(PA_i - L\Gamma_1) + \big(\big(2\lambda_1^2 + 1\big)/\lambda_1^2\big)\bar{E}^T U^T U\bar{E}$$

then the error system (48.10) can be proved as stable in presence of fault. For any t, the error satisfies the inequality $\|e(t)\|^2 \le k_1^{-1}\|C_1\|M^2$. The gain L of fuzzy filter is computed by $L = P^{-1}R$.

Proof Define the Lyapunov function as follows:

$$\Psi\big(e(t), x(t), \hat{x}(t), \tilde{F}, t\big) = \Phi(e(t), x(t), \hat{x}(t), t) + \tilde{F}^T(t)\tilde{F}(t) \tag{48.12}$$

Based on (48.10), we can get

$$\begin{aligned} \dot{\Psi} = & \sum_{i=1}^{r} h_i(\theta) e^T(t)\big(P(A_i - L\Gamma_1) + (A_i - L\Gamma_1)^T P\big)e(t) + 2\sum_{i=1}^{r} h_i(\theta) e^T(t) P J_i \tilde{F}(t) \\ & + \frac{1}{\lambda_1^2}\Big(e^T(t)\bar{E}^T U^T U\bar{E}e(t) - \|h(\bar{E}x(t)) - h(\bar{E}\hat{x}(t))\|^2\Big) - 2e^T(t)PL\Gamma_2(h(\bar{E}x(t)) - h(\bar{E}\hat{x}(t))) \\ & + 2\big(\tilde{F}^T C_1\hat{F} - \tilde{F}^T C_2\varepsilon(t)\big) - 2I\cdot\big(\tilde{F}^T C_1\hat{F} - \tilde{F}^T C_2\varepsilon(t)\big)\Big(\tilde{F}^T\hat{F}\Big/\|\hat{F}\|^2\Big) \end{aligned} \tag{48.13}$$

By using Schur complement formula with respect to (48.11), the inequality (48.11) means $\Omega_i < \mathrm{diag}\{-k_1 I, 0\}$. So we can get

$$\dot{\Psi} \le -k_1\|e(t)\|^2 + 2\tilde{F}^T C_1 F \le -k_1\|e(t)\|^2 + \|C_1\|M^2 \tag{48.14}$$

Thus $\dot{\Psi} < 0$, if $k_1\|e(t)\|^2 \ge \|C_1\|M^2$ holds. So for any t, it can be seen that $\|e(t)\|^2 \le k_1^{-1}\|C_1\|M^2$, which also implies the error system (48.10) is stable in the presence of the fault. □

48.5 Simulation Results

Suppose that the output PDFs can be approximated using the following spline function:

$$b_i = \begin{cases} |\sin 2\pi z|, z \in [0.5(i-1), 0.5i] \\ 0, z \in [0.5(j-1), 0.5j] \end{cases} \quad i \neq j,\ i = 1, 2, 3,\ z \in [0, 1.5]$$

The fault F is defined as $F(t) = 0$, when $t \leq 5$ and if $t > 5$, $F(t) = 1$. When the rule $i = 2$, the model parameters are given as follows:

$$J_1 = [1.45; 1.1] \qquad B_1 = [-0.6; -0.65] \quad A_1 = [-2 \quad 0.83; -0.8 \quad -1.5]$$
$$E_1 = [-1 \quad 0; 0.2 \quad 1\ ] \quad J_2 = [1.45; 1.1] \qquad B_2 = [-0.65; -0.6]$$
$$A_2 = [-2 \quad 0.525; -0.4 \quad -1.3\ ] \quad E_2 = [-1 \quad 0; 0.2 \quad 1\ ]$$

It is noted that the member functions are defined as the Gaussian type function. By selecting the parameters $\lambda = \eta = 1$, $\theta_i = 1$, $\Gamma_1 = [1.6 \quad 6.88\,]$, $\Gamma_2 = 0.33$, we can get

$$P = [3.6690 \quad -1.1809; -1.1809 \quad 15.3658\ ] \quad R = [-0.0248; -1.8607]$$
$$L = [-0.0469; -0.1247]$$

Figure 48.1 is the fault and its estimated value that shows the estimation error can be converge in a small field and also describes the responses of the system state. It can be clearly seen when t = 5 s, the fault will occur. Figure 48.2 represents the residual signal and the 3D mesh plot of the output PDF.

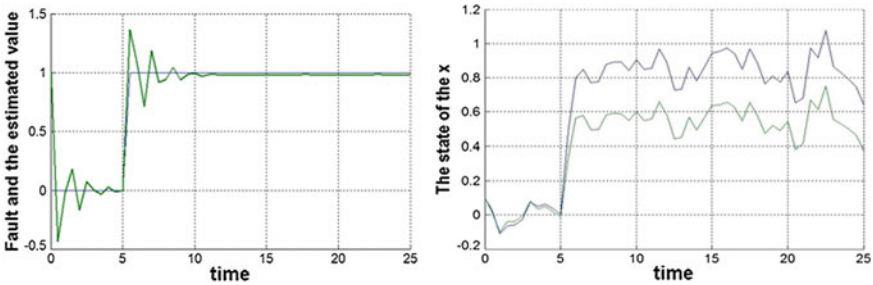

Fig. 48.1 Responses of the fault and its estimated value and responses of the system state

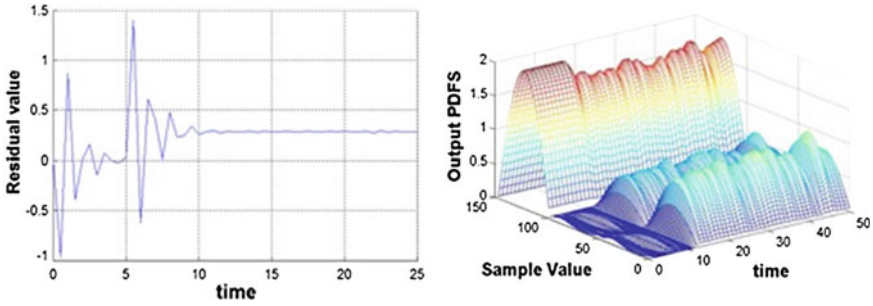

Fig. 48.2 Responses of the residual signal and 3-D mesh plot of the output PDFs

48.6 Conclusion

The main research of this paper is the fault diagnosis problem for a class of non-Gaussian stochastic distribution systems. By combining spline approximation with fuzzy modeling, a novel fuzzy filter based on output PDF is designed to estimate the system state and the unknown fault. Moreover, the adaptive projection algorithm is considered to guarantee the bounded of the estimated value of the fault and the satisfactory diagnosis ability can also further be verified by using optimization algorithm.

Acknowledgments This paper is supported by the National Natural Science Foundation of China under Grants (61473249, 61174046, 61203195).

References

1. Ding SX (2008) Model-based fault diagnosis techniques: design schemes, algorithms and tools. Springer, London
2. Zhang K, Jiang B, Shi P (2012) Fault estimation observer design for discrete-time Takagi-Sugeno fuzzy systems based on piecewise lyapunov functions. IEEE Trans Fuzzy Syst 20 (1):192–200
3. Chen RH, Mingori DL, Speyer JL (2003) Optimal stochastic fault detection filter. Automatica 39:377–390
4. Takagi T, Sugeno M (1985) Fuzzy identification of systems and its applications to modeling and control. IEEE Trans Syst Man Cyber 15(1):116–132
5. Tong SC, Li YM, Shi P (2012) Observer-based adaptive fuzzy backstepping output feedback control of uncertain MIMO pure-feedback nonlinear systems. IEEE Trans Fuzzy Syst 20 (4):771–785
6. Tong SC, Li YM (2011) Adaptive fuzzy output feedback tracking backstepping control of strict-feedback nonlinear systems with unknown dead zones. IEEE Trans Fuzzy Syst 20 (1):168–180
7. Wang H (2000) Bounded dynamic stochastic systems: modeling and control. Springer, London

8. Guo L, Wang H (2010) Stochastic distribution control system design: a convex optimization approach. Springer, London
9. Xu CH, Gui WH, Yang CH, Zhu HQ, Lin YQ, Shi C (2013) Flotation process fault detection using output PDF of bubble size distribution. Miner Eng 26:5–12
10. Yi Y, Guo L, Wang H (2009) Constrained PI tracking control for output probability distributions based on two-step neural networks. IEEE Trans Circuits Syst I 56(7):1416–1426
11. Yi Y, Zheng WX, Guo L (2013) Improved results on statistic information control with a dynamic neural network identifier. IEEE Trans Circuits Syst II 60(11):816–820
12. Li T, Guo L (2009) Optimal fault-detection filtering for non-gaussian systems via output PDFs. IEEE Trans Syst Man Cyber A 39(2):476–481
13. Yao L, Qin J, Wang A (2013) Fault diagnosis and fault-tolerant control for non-gaussian non-linear stochastic systems using a rational square-root approximation model. IET Control Theory Appl 7(1):116–124

Chapter 49
Multimode Anomaly Detection Under the Multiscale Framework

Funa Zhou, Yu Zhang, Xiaoliang Feng, Chenglin Wen and Juan Wang

Abstract Multiscale characteristic of fault signals determines the necessity of multiscale analysis in multimode anomaly detection. Firstly, mode identification is implemented. Then, multiscale MSPCA detection modeling and multiscale time-varying rolling balls anomaly detection model is, respectively, established to each steady state and transition mode. Simulation result shows that the multimode monitoring method under multiscale framework can significantly reduce the missing detection rate of critical faults, which can effectively avoid major accidents.

Keywords Multimode · Transition mode · Multiscale · Anomaly detection

49.1 Introduction

Traditional multivariate statistical monitoring method assumes that process running with single operating mode. Multimode process abnormal monitoring should take both the stable mode and transition mode into consideration [1]. Existed multimode process monitoring mainly focuses on multiple model method [2] and method based on Gaussian mixture model [3, 4]. Since statistic feature extraction fails to well describe the dynamic characteristics of the transition process [1], missing or false alarm during monitoring is inevitable. Paper [5] proposed an anomaly

F. Zhou · Y. Zhang (✉) · J. Wang
Institute of Advanced Control and Intelligent Information Processing, He'nan University, Kaifeng, China
e-mail: zhangyu_henu@163.com

X. Feng
Xiaoliang Feng College of Information Science and Technology, He'nan University of Technology, Zhengzhou, China

C. Wen
Chenglin Wen Institute of System Modeling and Control, Hangzhou Dianzi University, Hangzhou, China

Z. Deng and H. Li (eds.), *Proceedings of the 2015 Chinese Intelligent Automation Conference*, Lecture Notes in Electrical Engineering 337,
DOI 10.1007/978-3-662-46463-2_49

detection method based on differential geometry feature extraction (Differential Geometry Feature Extraction, DGFE) techniques. But unique rolling ball anomaly detection model cannot well detect abnormal in time-varying transition mode.

On the other hand, the multiscale characteristic of fault signals during the multimode monitoring process determines the necessity of introducing the idea of multiscale analysis into multimode anomaly detection, which can enhance the ability of detecting abnormal signal, thus effectively avoid major accidents [6–8].

For the reasons mentioned above, multimode anomaly detection under the mutiscale framework is developed in the following parts of this paper.

49.2 Anomaly Detection Model Based on Improved Rolling Balls

For the dynamic transition process, paper [5] proposed a DGFE method to depict the dynamic characteristic of transition process. This method assumes that ideal transition mode corresponding to the observation of each sensor is a dynamic curve with random fluctuation. The position, slope, and curvature matrix of the offline and online transition data is P_0, S_0, K_0 and P, S, K, respectively. With n samples, m variables and $i = 1, 2, \ldots, n-2$, The statistic R of transition process of statistics can be calculated via Eq. (49.1).

$$R_i = \sum_{j=1}^{m} \sqrt{\left(P_{i,j} - P_{0(i,j)}\right)^2 + \left(S_{i,j} - S_{0(i,j)}\right)^2 + \left(K_{i,j} - K_{0(i,j)}\right)^2} \tag{49.1}$$

where the subscript of $P_{i,j}$, $P_{0(i,j)}$ or $S_{i,j}$, $S_{0(i,j)}$ or $K_{i,j}$, $K_{0(i,j)}$ denote the corresponding values of online and offline of the ith samples of jth variables.

Since the randomness of observational data, the value of statistic R is random. Statistic R should vary in some range decided by the variance of R itself while system is well functioned. The calculation method of the control limit of statistic R in Literature [5], assumes that the deterministic ideal transition curve is available, $r(r > 100)$ set of normal transition data under normal conditions is generated. For any two groups of normal transition data, calculated by Eq. (49.1), $V = C_r^2$ times calculation.

$$\Delta P^v = P_0^s - P_0^t,\ \Delta S^v = S_0^s - S_0^t,\ \Delta K^v = K_0^s - K_0^t \tag{49.2}$$

$$T_{i,j}^v = \sqrt{(\Delta P_{i,j}^v)^2 + (\Delta S_{i,j}^v)^2 + (\Delta K_{i,j}^v)^2} \tag{49.3}$$

where $v = 1, 2, \ldots, V$, $s, t = 1, 2, \ldots, r$ and $s \neq t$. Calculate the maximum in each column for every matrix T, which can get V groups of maximum vector, then construct a new matrix B with the V vectors.

$$b_v = \max_{1 \le i \le n-2} \mathrm{T}_{i,j}^{v}, v = 1, 2, \ldots, V, \quad B^T = \left[b_1^T, b_2^T, \ldots, b_V^T\right] \tag{49.4}$$

The control limit for each observed variables:

$$\tau_j = \max_{1 \le v \le V} B_{v,j}, \quad (j = 1, 2, \ldots, m) \tag{49.5}$$

The control limit of transition process is calculated via Eq. (49.6):

$$\Gamma = \sum_{j=1}^{m} \tau_j \tag{49.6}$$

For transition process, variance of the observed data can be time varying. Unique rolling balls anomaly monitoring model can inevitably lead to missing and false alarm for time-varying transition process. We need longitudinal statistical analysis with the multiple sets of normal working condition observations, find out statistical characteristics of the data on each observation point, and establish time-varying control limit of online anomaly detection model accordingly.

$$\Gamma_i = \sum_{j=1}^{m} \left(\frac{1}{V} \sum_{v=1}^{V} T_{i,j}^{v} \right) \tag{49.7}$$

where Γ_i denotes the control limit of ith samples.

Sphere radius $r_i = \Gamma$ in Fig. 49.1, each sphere radius $r_i = \Gamma_i$ in Fig. 49.2. The figures show that when the variance of a certain point of transition process is different, sphere radius calculated with Eq. (49.6) is not suitable to all sample points, establish time-varying rolling ball model can well detect abnormal occurred in the transition dynamic characteristics.

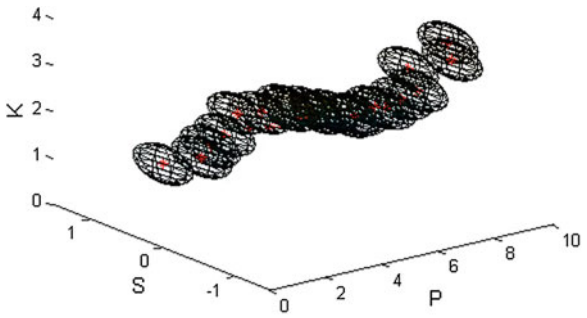

Fig. 49.1 Time-invariant rolling balls model

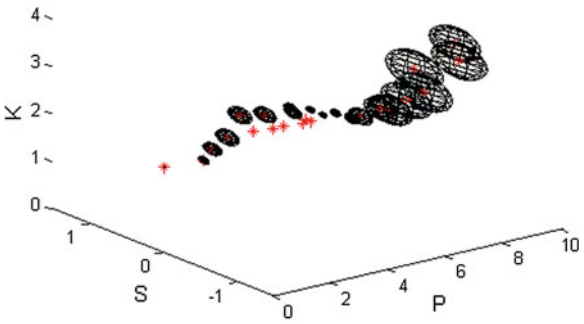

Fig. 49.2 Time-varying rolling balls model

49.3 DGFE Multiscale Modeling for Transition Mode

DGFE-based anomaly detection method proposed in paper [5] is modeled on single scale without considering the multiscale feature of the observation. Combining multiscale method with DFGE method, the algorithm proposed in this section can effectively extract the multiscale feature of the dynamic transition mode as well as noise suppression.

Firstly, wavelet decomposition is used firstly to extract the multiscale feature. Then improved Differential Geometry Feature Extraction (IDGFE) in Sect. 49.2 is used to establish the rolling balls model on each scale. Since L times decomposition to the observation is implemented, $L+1$ models on all scale's detail and smoothing on the coarsest scale is included to establish the final anomaly detection model.

By extracting feature of the history data of $r(r > 100)$ times operation of the system's transition process, which is generated by Monte Carlo simulation in this paper, the control limit on each scale is established via Eq. (49.7). Then multiscale filtering for history and online data is implemented.

In the last step, r sets of reconstructed data are used to model the final multiscale $IDGFE(MSIDGFE)$ detection algorithm. The total modeling and detection process can be depicted in Fig. 49.3.

Multiscale IDGFE history data modeling is an online-data-driven modeling process. The detailed modeling process follows as:

(1) Wavelet decomposition is implemented to all r sets of history data. Wavelet transforms coefficients of smoothing A_{0L}^{r} and detail D_{0k}^{r}.

$$A_{0L} = [A_{0L}^{1}, A_{0L}^{2}, \ldots, A_{0L}^{r}], \quad r = 1, 2, \ldots, V \tag{49.8}$$

$$D_{0k} = [D_{0k}^{1}, D_{0k}^{2}, \ldots, D_{0k}^{r}] \tag{49.9}$$

where $k = 1, 2, \ldots, L$, $r = 1, 2, \ldots, V$.

(2) Similar wavelet decomposition is implemented to the online observation, the wavelet transform coefficients A_L and $D = [D_1, D_2, \ldots, D_L]$ is obtained.

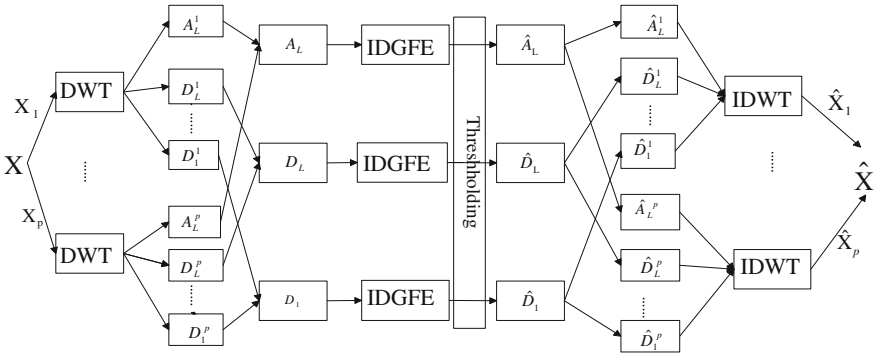

Fig. 49.3 Main idea of MSIDGFE

(3) Control limit $\Gamma_i^k (k = 1, 2, \ldots, L,\ \ i = 1, 2, \ldots, n-2)$ of the for the detail coefficients D_{0i}^r is established via Eq. (49.10). The value of R^k is also calculated on each scale.
If DGFE detection is significant, i.e., $R^k(i) \geq \Gamma_i^k (i = 1, 2, \cdots, n-2)$, the filtered detail coefficients is equal to the original detail coefficients. Otherwise, i.e., $R^k(i) < \Gamma_i^k$, the filtered detail coefficients are equal to zeros, i.e., $D_k(i,:) = \text{zeros}(1, m)$, $D_{0k}^r(i,:) = \text{zeros}(1, m)$.

(4) Implement inverse discrete wavelet transform (IDWT), the filtered observation $\hat{X}$ can be reconstructed. The reconstructed R and the reconstructed control limit Γ_i is calculated to implement the final multiscale IDGFE anomaly detection.

49.4 Multimode Online Monitoring Under the Multiscale Framework

49.4.1 Mode Identification

Partitioning the offline data and online data, respectively, based on Gaussian Mixture Model algorithm [3]. First, determine the posteriori probability of monitoring samples belongs to each Gaussian component [3]: $P\left(x_i \in C_j\right)$ (the posteriori probability of sample ith sample belongs to the jth Gaussian component). If posteriori probability of the monitoring sample belongs to each Gaussian component is very small, close to zero, then classify the sample as transitional process data (Figs. 49.4 and 49.5).

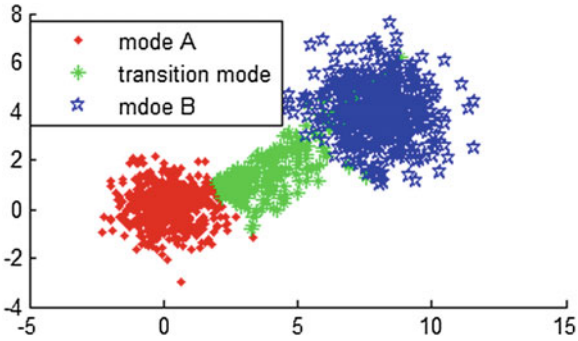

Fig. 49.4 Modes partition figure

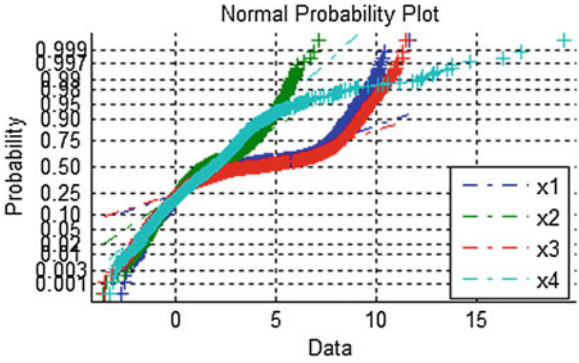

Fig. 49.5 Normal distribution test

49.4.2 Different Mode Anomaly Detection Are Carried Out with Different Detection Model

Online steady state data using multiscale PCA filtering scheme, online transition mode using the filtering scheme described in Sect. 49.3. For the data after filtering, each steady state mode monitored with the corresponding MSPCA model. As for the transition mode, calculate the transition mode statistic R according to Eq. (49.1) with the reconstituted offline and online data. According to Eq. (49.7) calculate control limit threshold Γ_i, and according whether R_i greater than Γ_i to judge whether a transition mode is abnormal.

49.5 Simulation

In this paper, simulation experiment is designed for multimode with two stable modes (A, B), and the transition mode: $A \rightarrow B$. Mode A, B takes 512 sample points, respectively, transition mode takes 256 sample points. The observable variables of mode A set as $X_0 = [x_1, x_2, x_3, x_4]$,

$$x_1 = \text{normrnd}(0, 0.8, n, 1), \quad x_2 = \text{normrnd}(0, 0.8, n, 1) \tag{49.10}$$

$$x_3 = (x_1 + x_2)./\text{sqrt}(2) + 0.6\text{randn}(n, 1) \tag{49.11}$$

$$x_4 = (x_1 - x_2)./\text{sqrt}(2) + 0.4\text{randn}(n, 1) \tag{49.12}$$

transition mode $Y_0 = [y_1, y_2, y_3, y_4]$,

$$\begin{bmatrix} y_1 \\ y_2 \\ y_3 \\ y_4 \end{bmatrix} = \begin{bmatrix} 0 & 0 & 0 & 0 & 0 \\ -0.5 & 0 & 0 & 0 & 0 \\ 0 & -0.5 & 0 & 0 & 0 \\ 3 & 0 & -0.1 & 0 & 0 \end{bmatrix} \begin{bmatrix} y_1 \\ y_2 \\ y_3 \\ y_4 \end{bmatrix} + \begin{bmatrix} 1 & 0 & 0 \\ 0 & 1 & 0 \\ 0 & 0 & 1 \\ 0 & 0 & -1.5 \end{bmatrix} U + \begin{bmatrix} e_1 \\ e_2 \\ e_3 \\ e_4 \end{bmatrix} \tag{49.13}$$

where $t = \text{linspace}(0.1, 2\pi, n)$, $U = [0.5\sin(t) + t, -\log(t), \ln(n) + t, t]'$, $e_i = 0.2t \times N(0, 1)$, $(i = 1, 2, 3, 4, 5)$ is time-varying.

The observable variables of mode B set as $Z_0 = [z_1, z_2, z_3, z_4]$, add the white noise with 0.2 variance to the first 400 points of z_3, z_4.

$$z_1 = \text{normrnd}(8, 1.2, n, 1), \quad z_2 = \text{normrnd}(4, 1.2, n, 1) \tag{49.14}$$

$$z_3 = (z_1 + z_2)./\text{sqrt}(2) + 0.6\text{randn}(n, 1) \tag{49.15}$$

$$z_4 = (z_1 - z_2)./\text{sqrt}(2) + 0.4\text{randn}(n, 1) \tag{49.16}$$

Generate fault signal Add high-frequency fault to variable 1 between 101 and 200th samples. Add constant deviation fault to variable 2 between 301 and 400th samples. Add slow variation interference to variable 1 between 613 and 712th samples. Add high-frequency fault and constant deviation fault to variable 1 and variable 2 between 869 and 968th samples, respectively. Add slow variation interference to variable 2 between 1,169 and 1,280th samples. Then the abnormal observations shown in Fig. 49.6.

Normal distribution test of the multimode data is shown in Fig. 49.5, which shows that all observation variables of multimode are not subject to Gaussian distribution, and cannot adopt global method for unified modeling. Multimode process needs to establish different anomaly detection model for each stable mode and transition mode. Figures 49.7 and 49.8 show the anomaly detection result of global PCA and global MSPCA, respectively.

Using the method of literature [5], establishes single scale anomaly detection model. Multiscale features of multimode data is not considered in this method. The monitoring results are shown in Fig. 49.9.

Figures 49.7, 49.8 and 49.9 show that neither global method nor single scale multimode method can well detect abnormal. Figure 49.10 shows that the multi-scale multimode anomaly detection method proposed in this paper can significantly reduce the missing detection rate of critical faults, which can effectively avoid major accidents.

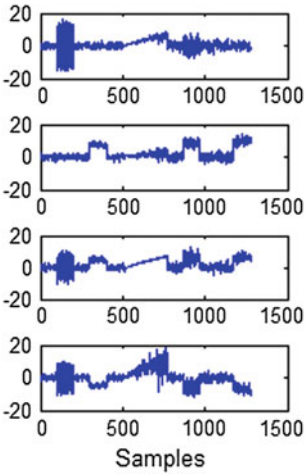

Fig. 49.6 Abnormal signal observations

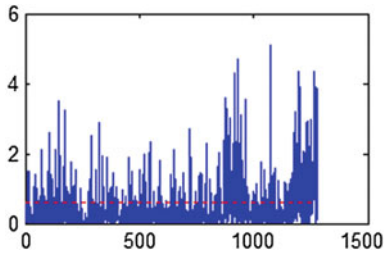

Fig. 49.7 Global PCA

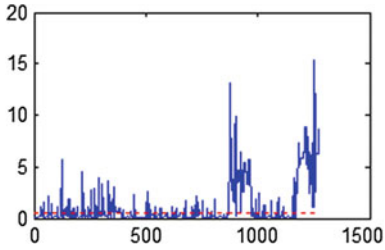

Fig. 49.8 Global MSPCA

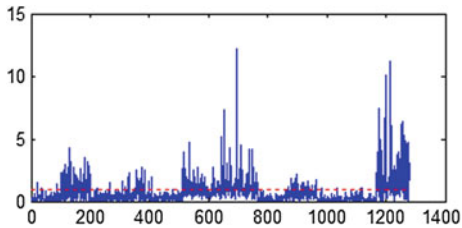

Fig. 49.9 Single scale multimode detection

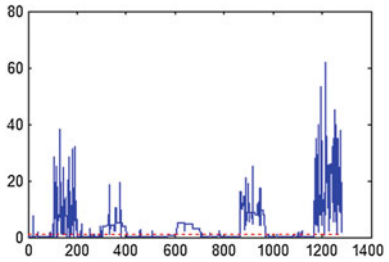

Fig. 49.10 Multiscale multimode detection

Table 49.1 Comparison of missed alarm rate and false alarm rate

Detection methods	Missed alarm points	Missed alarm rate	False alarm points	False alarm rate
GPCA	353	0.6895	127	0.1654
SSM	270	0.5273	88	0.1146
GMSPCA	164	0.3203	115	0.1497
MSM	13	0.0254	71	0.0924

Table 49.1 shows the missing and false alarm rate of the four methods described in this paper. The global PCA (GPCA), global MSPCA (GMSPCA), and single scale multimode detection methods (SSM) cannot achieve ideal effect of detection with high missing or false alarm rate. While multimode anomaly detection under the framework of multiscale (MSM) can well detect abnormal occurred in multimode process with multiscale characteristics.

49.6 Conclusions

This paper introduces multiscale analysis into multimode monitoring process. For multimode system with time-varying transition process, multiscale model combining with time-varying rolling balls model can significantly reduce the missing detection rate without increasing the false detection rate.

Acknowledgments The authors greatly appreciate the support of National Natural Science Foundation of China (Grant Nos. 61174112, 61203094).

References

1. Tan S, Wang FL, Chang YQ (2010) Fault detection of multi-mode process using segmented PCA based on differential transform. Acta Automatica Sin 36(11):1626–1636 (in Chinese)
2. Zhao SJ, Zhang J, Xu YM (2006) Performance monitoring of processes with multiple operating modes through multiple PLS models. J Process Control 16(7):763–772

3. Xu XZ, Xie L, Wang SQ (2011) Multi-mode process monitoring method based on PCA mixture model. CIESC J 03:743–752 (in Chinese)
4. Ge ZQ, Song ZH (2010) Mixture bayesian regularization method of PPCA for multimode process monitoring. AIChE J 56(11):2838–2849
5. Zhou FN, Zhang Y, Yang SN (2014) Multimode process monitoring based on correlative principal components and differential geometry feature extraction. In: 26th Chinese control and decision conference (CCDC), Changsha, China, (in Chinese)
6. Bakshi BR (1998) Multiscale PCA with application to multivariate statistical process monitoring. AIChE J 44(7):1596–1610
7. Zhang YY (2012) Study on multi-scale adaptive PCA and its application in process monitoring. Beijing University of Chemical Technology (in Chinese)
8. Ferracuti F, Giantomassi A, Sauro L (2011) Multi-scale PCA based fault diagnosis on a paper mill plant. In: IEEE 16th conference on emerging technologies and factory automation, ETFA 2011, Toulouse, France

Chapter 50
Mixed H_2/H_∞ Robust Controller with Degree Constraint in Angular Metric

Bin Liu, Yangyang Cui and Jiuqiang Sun

Abstract In the framework of the angular metric, robust stability margin is used to characterize the stability robustness of the closed-loop system. The mixed H_2/H_∞ robust controller with degree constraint is designed, whose degree is not larger than that of the plant. The characteristics of mixed H_2/H_∞ controller with degree constraint are discussed, and the form of the controller is parameterized. After that, we get the constraint conditions and the interpolation equations. The mixed H_2/H_∞ controller can be synthesized by solving the nonlinear equations, where a group preserving scheme is adapted. In comparison with the LMI controller and the central controller, the mixed H_2/H_∞ robust controller has the best LQG performance when the robust stability margin is given.

Keywords Angular metric · Mixed H_2/H_∞ control · Degree constraint · Group preserving scheme

50.1 Introduction

The main task of the mixed H_2/H_∞ control is to minimize the H_2 norm of one transfer function, while imposing restriction on H_∞ norm of the other transfer function [1, 2]. There have been quite many researches to solve the mixed H_2/H_∞ control problem [3–5]. An overwhelming majority of the methods are based on linear matrix inequality (LMI) technique. Numerical experiences show this framework is quite conservative, even not as good as the central controllers [6, 7]. In this paper, we will study a special and yet important mixed H_2/H_∞ control with

B. Liu (✉) · Y. Cui · J. Sun
Northeast Petroleum University, Daqing 163318, Heilongjiang Province, China
e-mail: liubin.nepu@hotmail.com

B. Liu · Y. Cui · J. Sun
University of California at Berkeley, Berkeley, CA 94720, USA

Z. Deng and H. Li (eds.), *Proceedings of the 2015 Chinese Intelligent Automation Conference*, Lecture Notes in Electrical Engineering 337,
DOI 10.1007/978-3-662-46463-2_50

degree constraint, where the robust stability margin is used to characterize the stability robustness in the metric framework [8].

The organization of the paper is as follows: In Sect. 50.2, the suboptimal H_∞ controller with degree constraint and the mixed H_2/H_∞ controller with degree constraint are discussed; Sect. 50.3 proposes a modified Newton method to solve nonlinear equations induced by mixed H_2/H_∞ control problem; In Sect. 50.4, a numerical example is presented to illustrate the efficiency of the new method.

50.2 Mixed H_2/H_∞ Robust Control in Angular Metric

Consider the standard feedback configuration shown in Fig. 50.1, where P, C represent the plant and the controller, respectively.

According to the definition of the robust stability margin in angular metric [9],

$$\sin \kappa_{P,C} = \inf_{\omega \in \mathbf{R}} \frac{|1 - P(j\omega)C(j\omega)|}{\sqrt{1 + |P(j\omega)|^2}\sqrt{1 + |C(j\omega)|^2}},$$

where $\kappa_{P,C}$ is defined as the robust stability margin. When the controller can stabilize the plant set with uncertainty maximally, we call the feedback control system has the optimal robust stability in the angular metric. If the robust stability margin is given by θ, the mixed H_2/H_∞ control problem can be stated as follows.

Problem description: For a given k-th degree plant $P(s) = p_n(s)/p_m(s)$ and the robust stability margin θ in angular metric, design the controller $C(s)$ satisfying

$$\min_{\kappa_{P,C} > \theta, \deg C(s) \le k} \left\| \boldsymbol{T}_{\boldsymbol{yw}} \right\|_2,$$

where $\boldsymbol{T}_{\boldsymbol{yw}}$ is the transfer function matrix from $[\boldsymbol{w}_1 \quad \boldsymbol{w}_2]^T$ to $[\boldsymbol{y}_1 \quad \boldsymbol{y}_2]^T$.

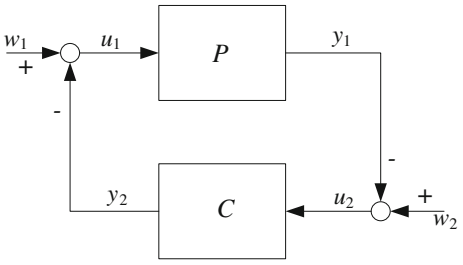

Fig. 50.1 Configuration of the feedback system

Algorithm Mixed H_2/H_∞ controller design with degree constraint.

Step 1. Spectral factorization. Find the monic and stable polynomial $p_d(s)$ such that

$$p_m(-s)p_m(s) + p_n(-s)p_n(s) = p_d(-s)p_d(s).$$

Step 2. Central controller design. According to [11–13], compute the central controller

$$C_c(s) = h_c(s)/g_c(s).$$

Step 3. Initial condition. Compute $p_c(s)$,

$$p_c(s) = p_m(s)g_c(s) - p_n(s)h_c(s),$$

and

$$\boldsymbol{\psi}_c = \boldsymbol{G}(\boldsymbol{p}_c);$$

then, apply Routh table to calculate $\boldsymbol{r}_c = \Phi(\boldsymbol{\psi}_c)$, which is the initial condition of H_2 optimization [10].

Step 4. H_2 optimization.

(a) For $\boldsymbol{x} \in \mathbf{R}^{2k}$, compute $\boldsymbol{r} = \begin{bmatrix} 1 \\ \boldsymbol{x} \end{bmatrix}$, $\psi = \Phi^{-1}(\boldsymbol{r})$, respectively;

(b) solve the equation

$$\boldsymbol{G}(\boldsymbol{p}) = \boldsymbol{\psi}, \tag{50.1}$$

to obtain $p(s)$;

(c) solve Diophantine equation

$$p_m(s)g(s) - p_n(s)h(s) = p(s)$$

to obtain $g(s)$, $h(s)$, and

$$C(s) = g(s)/h(s);$$

(d) find the optimal $\boldsymbol{x}_{\text{opt}} \in \mathbf{R}^{2k}$ that minimizes $\left\|\boldsymbol{T}_{\boldsymbol{yw}}\right\|_2$. Let

$$\boldsymbol{r}_{\text{opt}} = \begin{bmatrix} 1 \\ \boldsymbol{x}_{\text{opt}} \end{bmatrix},$$

and compute

$$p = G^{-1}\left(\Phi^{-1}\left(\boldsymbol{r}_{\text{opt}}\right)\right).$$

Step 5. Robust stability margin and H_2 norm computation:

$$\kappa_{P,C} = \arcsin \frac{1}{\sqrt{1+\left\|\frac{P(-s)+C(s)}{1-P(s)C(s)}\right\|_\infty^2}},$$

$$\left\|\boldsymbol{T}_{yw}\right\|_2 = \left\| \begin{bmatrix} P(1-CP)^{-1} & PC(1-PC)^{-1} \\ CP(1-CP)^{-1} & C(1-PC)^{-1} \end{bmatrix} \right\|_2.$$

Thus the resulting controller can provide better nominal performance than that of the central controller, which is the initial condition of the optimization. In above steps, the key one is to solve the nonlinear algebraic Eq. (50.1). Here, we introduce a modified Newton method to solve the nonlinear Eq. (50.1).

50.3 Group Preserving Scheme to Solve the Nonlinear Equations

50.3.1 Variable Transformation

The Eq. (50.1) can be rewritten as the nonlinear algebra equation

$$\boldsymbol{F}(\boldsymbol{p}) = \boldsymbol{G}(\boldsymbol{p}) - \boldsymbol{\psi} = \boldsymbol{0}.$$

We introduce a fictitious time-like variable τ in the following transformation of variable from $\boldsymbol{p}$ to $\boldsymbol{y}$ [14]:

$$\mathbf{y}(\tau) = (1+\tau)\boldsymbol{p}, \tag{50.2}$$

where τ and $\boldsymbol{p}$ are independent variables. Hence

$$\frac{\mathrm{d}\boldsymbol{y}}{\mathrm{d}\tau} = \boldsymbol{p}. \tag{50.3}$$

If the parameter $v \neq 0$, the Eq. (50.1) is equivalent to

$$\boldsymbol{0} = v\boldsymbol{F}(\boldsymbol{p}). \tag{50.4}$$

Adding Eq. (50.3) to Eq. (50.4),

$$\frac{\mathrm{d}\boldsymbol{y}}{\mathrm{d}\tau} = \boldsymbol{p} - v\boldsymbol{F}(\boldsymbol{p}). \tag{50.5}$$

By using Eq. (50.2), we derive

$$\frac{\mathrm{d}\boldsymbol{y}}{\mathrm{d}\tau} = \frac{\boldsymbol{y}}{1+\tau} - v\boldsymbol{F}\left(\frac{\boldsymbol{y}}{\boldsymbol{1}+\boldsymbol{\tau}}\right), \tag{50.6}$$

Further,

$$\frac{\mathrm{d}}{\mathrm{d}\tau}\left(\frac{\boldsymbol{y}}{1+\tau}\right) = -v\boldsymbol{F}\left(\frac{\boldsymbol{y}}{1+\tau}\right). \tag{50.7}$$

that is,

$$\frac{\mathrm{d}\boldsymbol{p}}{\mathrm{d}\tau} = -\frac{v}{1+\tau}\boldsymbol{F}(\boldsymbol{p}). \tag{50.8}$$

The roots of (50.1) are the fixed points of (50.8), which can also be rewritten as the following form:

$$\dot{\boldsymbol{p}} = \boldsymbol{f}(\boldsymbol{p}). \tag{50.9}$$

50.3.2 Augmentation of the Nonlinear Equations

The Euclidean norm of the vector $\boldsymbol{p}$ is

$$\|\boldsymbol{p}\| = \sqrt{\langle \boldsymbol{p}, \boldsymbol{p} \rangle} = \sqrt{\boldsymbol{p}^T\boldsymbol{p}}. \tag{50.10}$$

where $\langle \cdot, \cdot \rangle$ denotes the inner product of two n-dimension vectors.

Obviously, if $\boldsymbol{p} \neq \boldsymbol{0}$, $\|\boldsymbol{p}\| > 0$. Taking the derivatives of both the sides of (50.10) with respect to τ, we have

$$\frac{\mathrm{d}\|\boldsymbol{p}\|}{\mathrm{d}\tau} = \frac{\dot{\boldsymbol{p}}^T\boldsymbol{p}}{\sqrt{\boldsymbol{p}^T\boldsymbol{p}}} = \frac{\mathbf{f}^T\boldsymbol{p}}{\|\boldsymbol{p}\|}. \tag{50.11}$$

Equation (50.9) and Eq. (50.11) can be combined together into a simple matrix equation:

$$\frac{\mathrm{d}}{\mathrm{d}\tau}\begin{bmatrix} \boldsymbol{p} \\ \|\boldsymbol{p}\| \end{bmatrix} = \begin{bmatrix} \boldsymbol{0}_{2k\times 2k} & \boldsymbol{f}/\|\boldsymbol{p}\| \\ \boldsymbol{f}^T/\|\boldsymbol{p}\| & 0 \end{bmatrix}\begin{bmatrix} \boldsymbol{p} \\ \|\boldsymbol{p}\| \end{bmatrix}. \tag{50.12}$$

It is obvious that the first row in (50.12) is the same as (50.19), but the inclusion of the second row in (50.12) gives a Minkowskian structure of the augmented state variables of $\boldsymbol{K} := \begin{bmatrix} \boldsymbol{p}^T & \|\boldsymbol{p}\| \end{bmatrix}^T$, which satisfies the cone condition:

$$\boldsymbol{K}^T \boldsymbol{\zeta} \boldsymbol{K} = \boldsymbol{p}^T \boldsymbol{p} - \|\boldsymbol{p}\|^2 = \|\boldsymbol{p}\|^2 - \|\boldsymbol{p}\|^2 = 0, \tag{50.13}$$

where $\boldsymbol{\zeta} = \begin{bmatrix} \mathbf{I}_{2k} & \mathbf{0}_{2k\times 1} \\ \mathbf{0}_{1\times 2k} & -1 \end{bmatrix}$ is a Minkowski metric.

Consequently, we have an $n+1$-dimensional augmented differential equations system:

$$\dot{\boldsymbol{K}} = \boldsymbol{A}\boldsymbol{K}, \tag{50.14}$$

where $\boldsymbol{A} = \begin{bmatrix} \mathbf{0}_{2k\times 2k} & \boldsymbol{f}/\|\boldsymbol{p}\| \\ \boldsymbol{f}^T/\|\boldsymbol{p}\| & 0 \end{bmatrix}$ satisfying $\boldsymbol{A}^T\boldsymbol{\zeta} + \boldsymbol{\zeta}\boldsymbol{A} = \mathbf{0}$ is a Lie algebra $so(n,1)$ of the proper orthochronous Lorentz $SO_o(n,1)$.

50.3.3 Group Preserving Scheme

Because of $\boldsymbol{A} \in so(2k,1)$, we can get

$$\boldsymbol{K}_{l+1} = \boldsymbol{D}_l \boldsymbol{K}_l, \tag{50.15}$$

by discretized mapping $\boldsymbol{D}_l$, where

$$\boldsymbol{D}_l = \exp[t\boldsymbol{A}_l] = \begin{bmatrix} \boldsymbol{I}_{2k} + \frac{(\alpha_l - 1)}{\|\boldsymbol{f}_l\|}\boldsymbol{f}_l\boldsymbol{f}_l^T & \frac{\beta_l \boldsymbol{f}_l}{\|\boldsymbol{f}_l\|} \\ \frac{\beta_l \boldsymbol{f}_l^T}{\|\boldsymbol{f}_l\|} & \alpha_l \end{bmatrix}, \tag{50.16}$$

$$\alpha_l := \cosh\left(\frac{t\|\boldsymbol{f}_l\|}{\|\boldsymbol{g}_l\|}\right),\ \beta_l := \sinh\left(\frac{t\|\boldsymbol{f}_l\|}{\|\boldsymbol{g}_l\|}\right),\ t = \tau_{l+1} - \tau_l.$$

Substituting 50.16 for $\boldsymbol{D}_l$ into 50.15, we obtain

$$\boldsymbol{p}_{l+1} = \boldsymbol{p}_l + \eta_l \boldsymbol{f}_l, \tag{50.17}$$

$$\|\boldsymbol{p}_{l+1}\| = \alpha_l \|\boldsymbol{p}_l\| + \frac{\beta_l}{\|\boldsymbol{f}_l\|}\langle \boldsymbol{f}_l, \boldsymbol{p}_l \rangle, \tag{50.18}$$

where

$$\eta_l := \frac{\beta_l \|\boldsymbol{p}_l\| \|\boldsymbol{f}_l\| + (\alpha_l - 1)\langle \boldsymbol{f}_l, \boldsymbol{p}_l \rangle}{\|\boldsymbol{f}_l\|^2} \tag{50.19}$$

is the adjustment factor.

In every iterative, when $\boldsymbol{K}_l$ is mapped to the $\boldsymbol{K}_{l+1}$, the discretized mapping $\boldsymbol{D}_l$ preserves the following properties: $\boldsymbol{D}_l^T \boldsymbol{\zeta} \boldsymbol{D}_l = \boldsymbol{\zeta}$, $\det \boldsymbol{D}_l = 1$, $\boldsymbol{D}_{l,00} > 0$, where $\boldsymbol{D}_l \in SO_0(2k, 1)$ is the group value of $\boldsymbol{D}_l$ at τ_l; $\boldsymbol{D}_{l,00}$ is the 00-th component of $\boldsymbol{D}_l$; $\boldsymbol{K}_l$ denotes the numerical value of $\boldsymbol{K}$ at τ_l and $\boldsymbol{K}_l$ satisfies (50.13). The group properties are preserved in this scheme for all $t > 0$, so the method is called a group preserving scheme.

According to the expression of η_l in (50.19) and the Schwartz inequality,

$$\eta_l \geq \left[1 - \exp\left(1 - \frac{t\|\boldsymbol{f}_l\|}{\|\boldsymbol{p}_l\|}\right)\right] \frac{\|\boldsymbol{p}_l\|}{\|\boldsymbol{f}_l\|} > 0, \quad \forall t > 0. \tag{50.20}$$

So the equivalent condition of $\boldsymbol{p}_{l+1} = \boldsymbol{p}_l$ is $\boldsymbol{f}_l = \boldsymbol{0}$, which means (50.17) has the same equilibrium point as the (50.1). The stopping criterion of the above iterative algorithm can be determined by $\|\boldsymbol{p}_{l+1} - \boldsymbol{p}_l\| \leq \varepsilon_1$, where $\|\cdot\|$ denotes the 2-norm of the vector, ε_1 is a given convergent error.

The above numerical iterative algorithm (50.17)–(50.19) is in agreement with Euler method. Hence, the one-step iterative formula has the first order convergence.

50.4 Numerical Example

Denote the robust stability margin corresponding to the optimal H_2 controller and optimal H_∞ controller by $b_2(P)$ and $b_{\text{opt}}(P)$ respectively, and denote the optimal H_2 norm by $\|\boldsymbol{T}_{\boldsymbol{yw}}\|_2^*$, where $\boldsymbol{T}_{\boldsymbol{yw}}$ denotes the transfer function from $\boldsymbol{w} = [w_1 \quad w_2]^T$ to $\boldsymbol{y} = [y_1 \quad y_2]^T$. Obviously, $b_{\text{opt}}(P)$ is the upper bound of $\kappa_{P,C}$, and there will be no solution to the problem with given $\theta > b_{\text{opt}}(P)$.

Consider the plant [15]

$$P(s) = \frac{-6.475s^2 + 4.0302s + 175.77}{s(5s^3 + 3.5682s^2 + 139.5021s + 0.0929)},$$

which is the transfer function of the flexible beam, and we can get that

$$b_{\text{opt}}(P) = 0.3646, \quad b_2(P) = 0.2234, \quad \|\boldsymbol{T}_{\boldsymbol{yw}}\|_2^* = 3.3067.$$

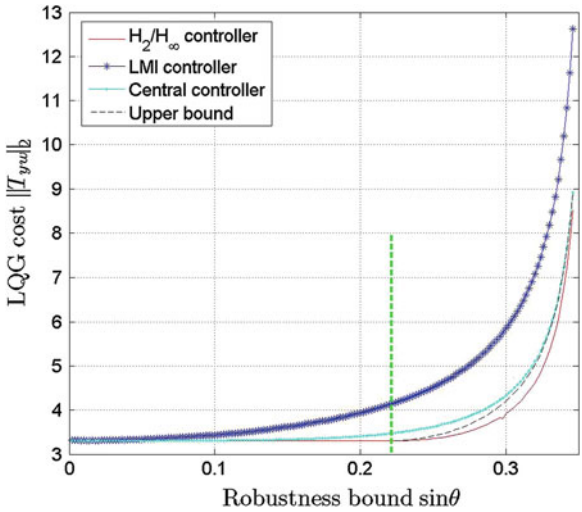

Fig. 50.2 Comparison of controllers

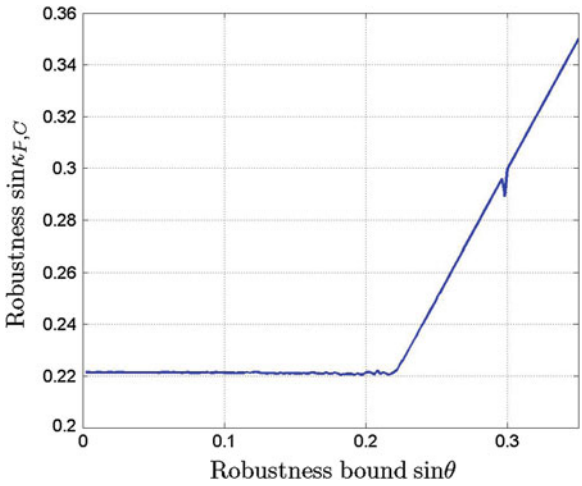

Fig. 50.3 Relationship between robustness bound and robustness

Simulation results show that for the given same conditions, mixed H_2/H_∞ controller has the best LQG cost performance, comparing with the LMI robust controller and the central controller. Figure 50.2 gives the comparisons between various controllers, and Fig. 50.3 gives the actual robust stability margin $\kappa_{P,C}$ of the mixed H_2/H_∞ controller corresponding to different prespecified θ.

Acknowledgments This work is supported by Project of the Specialized Research Fund for Doctoral Program of the University in China 20132322120003, Youth Academic Backbone Project of University in Heilongjiang Province under Grant 1253G012, Youth Science Foundation of

Heilongjiang Province under Grant QC2011C043, Science and Technology Research Project of Heilongjiang Province under Grant 12531058. This word is also supported by the Reserve Talents of Universities Overseas Research Program of Heilongjiang under Grant HEI GAO JIAO [2013]350.

References

1. Bernstein DS, Haddad WM (1989) LQG control with an H_∞ performance bound: a riccati equation approach. IEEE Trans Autom Control 34(3):293–305
2. Zhou KM, Glover K, Bodenheier B et al (1994) Mixed H_2 and H_∞ performance objective i: robust performance analysis. IEEE Trans Autom Control 39(8):1564–1574
3. Khargonekar PP, Rotea MA (1991) Mixed H_2/H_∞ control: a convex optimization approach. IEEE Trans Autom Control 36(7):824–837
4. Rotea MA, Khargonekar PP (1991) H_2 optimal control with an H_∞ constraint: the state feedback case. Automatica 27(2):307–316
5. Zhang W, Chen BS (2006) State feedback H_∞ control for a class of nonlinear stochastic systems. SIAM J Control Optim 44(6):1973–1991
6. Scherer CW (1995) Multiobjective H_2/H_∞ control. IEEE Trans Autom Control 40(6): 1054–1062
7. Scherer CW, Gahinet P, Chilali M (1997) Multiobjective output-feedback control via LMI optimization. IEEE Trans Autom Control 42(7):896–911
8. Yu NB, Qiu L (2006) A mixed H_2/H_∞ control problem with controller degree constraint. In: Proceedings of the 45th IEEE conference on decision and control, San Diego, CA, pp 5365–5370
9. Liu B, Ci WF, Huo BW (2013) Stability robustness of control system in angular metric. In: Proceedings of the 25th Chinese control and decision conference, Guiyang, Guizhou, pp 3302–3307
10. Qiu L, Zhou KM (2003) Pre-classical tools for post-modern control. In: Proceedings of the 42nd IEEE conference on decision and control, Maui, Hawaii, pp 4945–4950
11. Glover K, Mustafa D (1989) Derivation of the maximum entropy H_∞-controller and a state-space formula for its entropy. Int J Control 50(3):899–916
12. Mustafa, & D., Glover, K. (1988). Controllers which satisfy a closed-loop H_∞-norm bound and maximize an entropy integral. In: Proceedings of 27th IEEE conference on decision and control, Austin, Texas, pp 959–964
13. Qiu L, Zhou KM (2010) Introduction to feedback control. Prentice Hall, Upper Saddle River
14. Liu CS (2001) Cone of non-linear dynamical system and group preserving schemes. Int J Non-Linear Mech 36:1047–1068
15. Doyle JC, Francis B, Tannenbaum A (1992) Feedback control theory. Macmillan Publishing Company, New York, pp 93–168

Chapter 51
ADRC Based Attitude Control of a Quad-rotor Robot

Yi Li, Zengqiang Chen, Mingwei Sun, Zhongxin Liu and Qing Zhang

Abstract In this paper, active disturbance rejection control (ADRC) technique is described in detail. Typical algorithms for each component are given as well. In order to control the attitudes of a quad-rotor robot as we desired, two kinds of continuous ADRC controllers are designed. The satisfactory real-time control experimental results indicate that the continuous ADRC can not only meet the control accuracy requirement but also can achieve rapid and effective response for the nonlinear coupled systems. Eventually, the advantages and scopes of application of the two controllers are summarized.

Keywords ADRC · Extended state observer · Quad-rotor · Nonlinear dynamics

51.1 Introduction

Nowadays, the advanced control algorithms have the potential to achieve better dynamic performance and stronger robustness than the conventional ones. Although the classical PID controller has been extensively applied to the automation of industrial process due to its weak dependence on the exact dynamics model of the controlled plant, its disadvantages and deficiencies are still clear when dealing with the control process with remarkable uncertainties or subject to intensive perturbations. Under these circumstances, active disturbance rejection control (ADRC), which was proposed by Prof. Han [1, 2] almost three decades ago, has become a novel and effective control strategy in the field of nonlinear systems. A detailed design and tuning method for the linear extended state observer which

Y. Li · Z. Chen (✉) · M. Sun · Z. Liu
Tianjin Key Laboratory of Intelligent Robotics, College of Computer and Control Engineering, Nankai University, Tianjin 300071, China
e-mail: chenzq@nankai.edu.cn

Z. Chen · Q. Zhang
College of Science, Civil Aviation, University of China, Tianjin 300300, China

Z. Deng and H. Li (eds.), *Proceedings of the 2015 Chinese Intelligent Automation Conference*, Lecture Notes in Electrical Engineering 337,
DOI 10.1007/978-3-662-46463-2_51

was proposed by Prof. Gao [3, 4] is demonstrated in [4]. The ADRC control approach has a lot of attractive characteristics such as swift response, accurate control, active rejection disturbance, strong robustness, etc. Also with the advantage of simple structure, it is easy to be applied in practice. Till now, ADRC has been successfully and widely used in many experimental installations and industrial processes.

The quad-rotor robot is an underactuated dynamic system composed of six output coordinates (fully spatial movements) and four input forces (the thrust provided by each propeller). This multivariable, nonlinear, high-order, and strong-coupling system imposes severe difficulties for flight control design. However, attitude control is the backbone of flight control. To date, there are many control approaches have been used to control the attitudes of the quad-rotor robot, such as backstepping control [5], linear quadratic (LQ) control [6], and so on.

In this paper, we propose a new methodology for motion control applications. It is based upon the recent development in ADRC. Through hardware tests, it is demonstrated that this is a promising new technology. It is a more powerful method in controlling the attitude of the quad-rotor robot than any other approaches we have ever used and is easy to use.

The organization of the paper is as follows. Section 51.2 gives an introduction to active disturbance rejection technique. The experimental results and a comparison of dynamic performance measures for using the two sorts of continuous ADRC are presented in Sect. 51.3. Eventually, concluding remarks are given in Sect. 51.4.

51.2 ADRC Algorithm

The ADRC control approach consists of three important components: Tracking differentiator (TD), extended state observer (ESO), and nonlinear state error feedback (NLSEF). The structure of ADRC strategy is shown in Fig. 51.1.

51.2.1 Tracking Differentiator

Here, the smooth trajectory of the given signal and its high-order derivatives can be obtained through arranging a transition process by the use of tracking differentiator. One feasible nonlinear second-order TD can be designed as

$$\begin{cases} \dot{v}_1 = v_2 \\ \dot{v}_2 = \mathrm{f\,han}(v_1 - v, v_2, r, h_1) \end{cases} \tag{51.1}$$

Besides the above algorithm, another effective linear second-order TD can be represented as

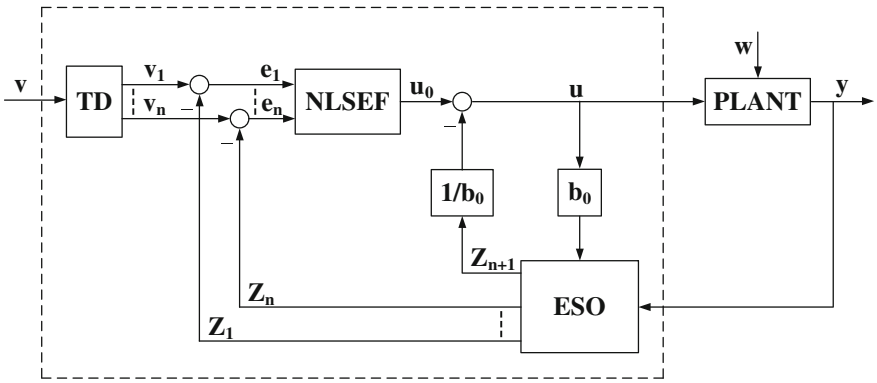

Fig. 51.1 Block diagram of ADRC

$$\begin{cases} \dot{v}_1 = v_2 \\ \dot{v}_2 = -1.76\,Rv_2 - R^2(v_1 - v) \end{cases} \tag{51.2}$$

where v denotes the input signal; v_1 is the tracking signal of v and v_2 is the tracking signal of the derivative of v; h_1 is an adjustable filter factor; both r and R represent the adjustable speed factors. And the greater the value of speed factor is, the shorter the transition process will be. The TD also can be seen as a filter if there is any noise in the input signal. fhan(x_1, x_2, r, h) is defined as

$$\begin{cases} d = rh \\ d_0 = hd \\ y = x_1 + hx_2 \\ a_0 = \sqrt{d^2 + 8r|y|} \\ a = \begin{cases} x_2 + \dfrac{a_0 - d}{2}\mathrm{sign}(y), & |y| > d_0 \\ x_2 + y/h, & |y| \le d_0 \end{cases} \\ \mathrm{fhan}(x_1, x_2, r, h) = \begin{cases} -r\mathrm{sign}(a), & |a| > d \\ -ra/d, & |a| \le d \end{cases} \end{cases} \tag{51.3}$$

51.2.2 Extended State Observer

The system states and the comprehensive disturbance, which include external unknown disturbance and internal uncertainties that determined by the system itself, can be estimated in real time by the ESO, which is the core part of the ADRC technique. The estimated sum of disturbance will be regarded as compensation and

added into the controller. Hence, the original nonlinear system will turn into a new linear cascade integrator control system, which is more easily to control. One feasible continuous ESO can be designed as

$$\begin{cases} e = z_1 - y \\ \dot{z}_1 = z_2 - \beta_{01}\text{fal}(e, a_1, \delta) \\ \dot{z}_2 = z_3 - \beta_{02}\text{fal}(e, a_2, \delta) \\ \qquad\vdots \\ \dot{z}_n = z_{n+1} - \beta_{0n}\text{fal}(e, a_n, \delta) + b_0 u \\ \dot{z}_{n+1} = -\beta_{0(n+1)}\text{fal}(e, a_{n+1}, \delta) \end{cases} \tag{51.4}$$

where $z_1, z_2, \ldots, z_n$ are the observer outputs and stand for the estimated system states, respectively; z_{n+1} is the extended state variable and denotes the estimated comprehensive disturbance; e is the difference between z_1 and the system output y; β_{01}, $\beta_{02}, \ldots, \beta_{0(n+1)}$ are the observer gains; $a_1, a_2, \ldots, a_{n+1}$ are the adjustable parameters; δ represents the length of linear interval; fal(e, a, δ) can be expressed as

$$\text{fal}(e, a, \delta) = \begin{cases} |e|^a \text{sign}(e), & |e| > \delta \\ \frac{e}{\delta^{1-a}}, & |e| \le \delta \end{cases} \tag{51.5}$$

51.2.3 Nonlinear State Error Feedback

The NLSEF will combine the tracking signals provided by TD and the observer estimation system states offered by ESO appropriately by using special nonlinear functions to obtain the virtual control u_0. Take the second-order system for instance, the errors of system states are defined as

$$\begin{cases} e_1 = v_1 - z_1 \\ e_2 = v_2 - z_2 \end{cases} \tag{51.6}$$

There are two approaches to calculate the virtual control u_0 as follows:

(*I*) $u_0 = \beta_0\text{fal}(e_0, a_0, \delta) + \beta_1\text{fal}(e_1, a_1, \delta) + \beta_2\text{fal}(e_2, a_2, \delta)$
where the error $e_0 = \int_0^t e_1(\tau)d\tau$; β_0, β_1 and β_2 are integral, proportional, and derivative adjustable parameters, respectively.

(*II*) $u_0 = -\text{fhan}(e_1, c \cdot e_2, r, h)$
where c, r and h are adjustable parameters.
Eventually, the control law can be represented as

$$u = u_0 - \frac{z_3}{b_0} \text{ or } u = \frac{u_0 - z_3}{b_0} \tag{51.7}$$

where the compensating factor b_0 is an adjustable parameter.

51.3 Experiments of Attitude Control

In this part, two kinds of continuous ADRC controllers will be applied in real-time controlling the attitude [7] of the quad-rotor hover system, which is produced by a Canadian company named Quanser. To complete the real-time experiments, the following hardwares are required: Power amplifier, data acquisition board, hover specialty plant. Quarc, the real-time control software, is used to control and monitor the plant in real time. Finally, the advantages and drawbacks of each strategy are summarized.

51.3.1 Dynamics Model

The hover system [8] consists of a frame with four propellers mounted on a three DOF pivot joint such that the body can freely yaw, pitch, and roll, as seen in Fig. 51.2. When a positive voltage is applied to any motor, a positive thrust force is generated and this causes the corresponding propeller assembly to rise. The thrust force generated by the front, back, right, and left motors are denoted by v_f, v_b, v_r and v_l, respectively. So the system can be written in state space form as

Fig. 51.2 Three-degree-of-freedom quad-rotor hover plant

Table 51.1 Parameters of the quad-rotor robot

Symbol	Description	Value	Unit
$K_{t,n}$	Normal rotation propeller torque-thrust constant	0.0036	N m/V
$K_{t,c}$	Counter rotation propeller torque-thrust constant	−0.0036	N m/V
K_f	Propeller force-thrust constant	0.1188	N/V
J_y	Equivalent moment of inertia about the yaw axis	0.1104	Kg m^2
J_p	Equivalent moment of inertia about the pitch axis	0.0552	Kg m^2
J_r	Equivalent moment of inertia about the roll axis	0.0552	Kg m^2
l	Distance between pivot to each motor	0.1969	m

$$\begin{bmatrix} \ddot{y} \\ \ddot{p} \\ \ddot{r} \end{bmatrix} = \begin{bmatrix} 0 & 0 & 0 & 0 & 0 & 0 \\ 0 & 0 & 0 & 0 & 0 & 0 \\ 0 & 0 & 0 & 0 & 0 & 0 \end{bmatrix} \begin{bmatrix} \dot{y} \\ \dot{p} \\ \dot{r} \end{bmatrix} + \begin{bmatrix} \frac{k_{t,c}}{J_y} & \frac{k_{t,c}}{J_y} & \frac{k_{t,n}}{J_y} & \frac{k_{t,n}}{J_y} \\ \frac{lk_f}{J_p} & -\frac{lk_f}{J_p} & 0 & 0 \\ 0 & 0 & \frac{lk_f}{J_r} & -\frac{lk_f}{J_r} \end{bmatrix} \begin{bmatrix} v_f \\ v_b \\ v_r \\ v_l \end{bmatrix} \quad (51.8)$$

where y, p and r denote the angle of yaw, pitch, and roll, respectively. Table 51.1 below lists the main parameters associated with the quad-rotor helicopter.

51.3.2 Experiments

The system can be divided into yaw channel, pitch channel, and roll channel. The block diagram of the controlled system with the ADRC controllers will be as shown in (Fig. 51.3):

The initial state of the system is set to zero. And the real-time control will last for 40 s. The set point in each channel will be a square wave of 3° amplitude and 0.05 Hz frequency. The experimental parameters of two controllers are shown in Tables 51.2 and 51.3.

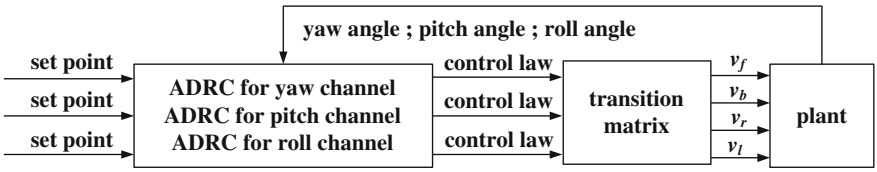

Fig. 51.3 Block diagram of the controlled system

Table 51.2 Experimental parameters of type I controller

Block	TD	ESO	NLSEF
Yaw	R = 2	$a_1 = 1$, $a_2 = 0.5$, $a_3 = 0.25$, $\delta = 0.001$,	$a_0 = 0.6$, $a_1 = 0.1$, $a_2 = 0.4$, $\delta = 0.035$,
		$\beta_{01} = 36$, $\beta_{02} = 432$, $\beta_{03} = 1728$	$\beta_0 = 35$, $\beta_1 = 300$, $\beta_2 = 180$, $b_0 = 0.008$
Pitch	R = 2	$a_1 = 1$, $a_2 = 0.5$, $a_3 = 0.25$, $\delta = 0.001$,	$a_0 = 0.6$, $a_1 = 0.1$, $a_2 = 0.4$, $\delta = 0.035$,
		$\beta_{01} = 36$, $\beta_{02} = 432$, $\beta_{03} = 1728$	$\beta_0 = 25$, $\beta_1 = 200$, $\beta_2 = 130$, $b_0 = 0.008$
Roll	R = 2	$a_1 = 1$, $a_2 = 0.5$, $a_3 = 0.25$, $\delta = 0.001$,	$a_0 = 0.6$, $a_1 = 0.1$, $a_2 = 0.4$, $\delta = 0.035$,
		$\beta_{01} = 36$, $\beta_{02} = 432$, $\beta_{03} = 1728$	$\beta_0 = 25$, $\beta_1 = 200$, $\beta_2 = 130$, $b_0 = 0.008$

Table 51.3 Experimental parameters of type II controller

Block	TD	ESO	NLSEF
Yaw	$R = 2$	$a_1 = 1$, $a_2 = 0.5$, $a_3 = 0.25$, $\delta = 0.001$,	$c = 50$, $r = 100$, $h = 0.001$, $b_0 = 0.009$
		$\beta_{01} = 42$, $\beta_{02} = 588$, $\beta_{03} = 2744$	
Pitch	$R = 2$	$a_1 = 1$, $a_2 = 0.5$, $a_3 = 0.25$, $\delta = 0.001$,	$c = 100$, $r = 70$, $h = 0.001$, $b_0 = 0.004$
		$\beta_{01} = 30$, $\beta_{02} = 300$, $\beta_{03} = 1000$	
Roll	$R = 2$	$a_1 = 1$, $a_2 = 0.5$, $a_3 = 0.25$, $\delta = 0.001$,	$c = 100$, $r = 70$, $h = 0.001$, $b_0 = 0.004$
		$\beta_{01} = 30$, $\beta_{02} = 300$, $\beta_{03} = 1000$	

Figures 51.4 and 51.5 show that each continuous ADRC controller can achieve the performance we expected rapidly and stably. Depending on the real-time experimental data, we can have the dynamic performance measures of the two kinds of controllers, as listed in Tables 51.4 and 51.5. T_d, T_r, T_p and σ stand for the delay time, the rise time, the peak time and the percent overshoot, respectively. The settling time, T_s, is defined as the time required for the system to settle within 5 % of the input amplitude. The delay time $T_d < 0.9$ s, the rise time $T_r < 1.4$ s and the peak time $T_p < 2.2$ s imply that the system has an excellent performance in terms of the swiftness of response. Meanwhile, The settling time $T_s < 2.1$ s and the percent overshoot $\sigma < 4.6$ % indicate that the ADRC controllers can achieve the

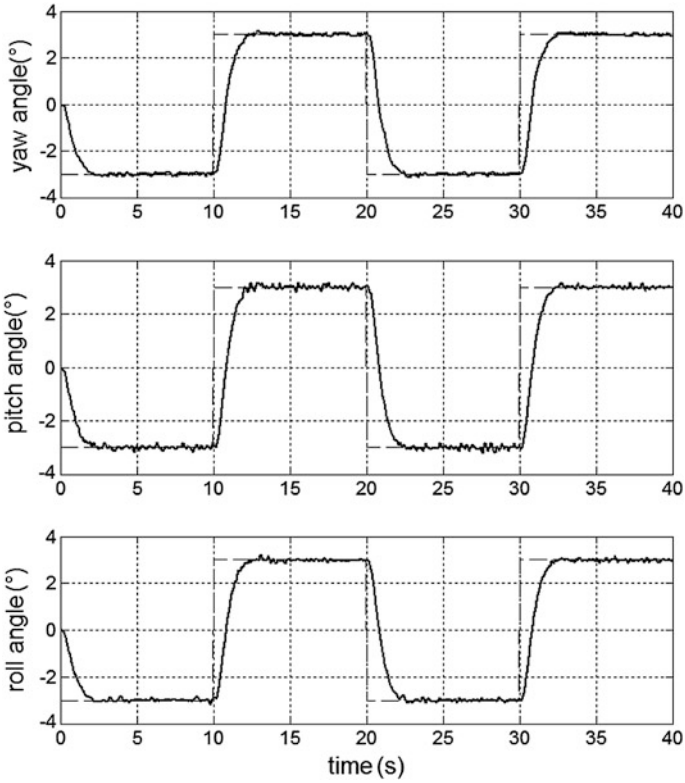

Fig. 51.4 Real-time control results of type I controller

performance in terms of the robustness and the closeness of the response to the desired response.

By comparison with the two kinds of continuous ADRC controllers, we can draw the conclusion that the type I ADRC controller are more suitable if our goal is to achieve the fastest and the most accurate response to the input. Obviously, the type II ADRC controller is very convenient for the adjustment of parameters.

Overall, the real-time attitude control is completely successful by using the two sorts of continuous ADRC controllers.

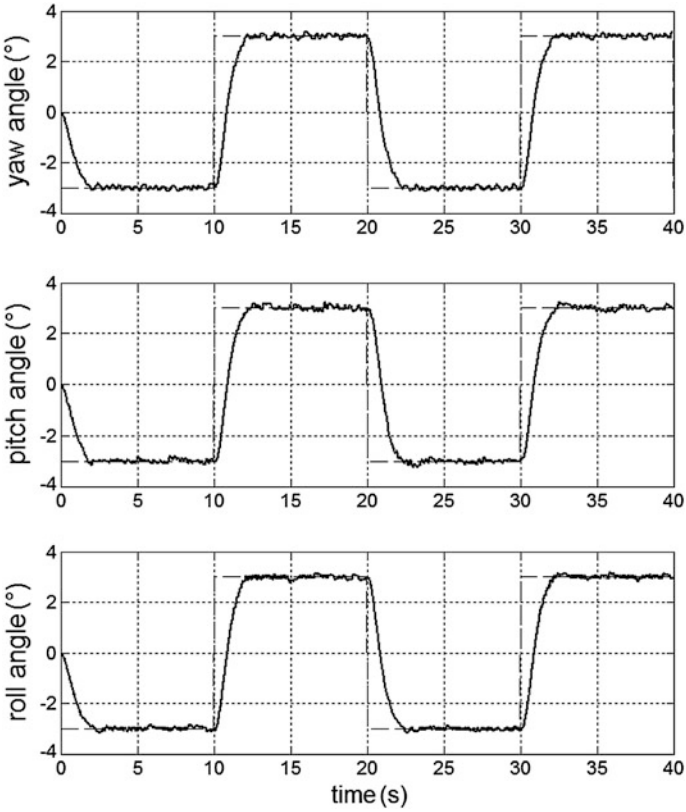

Fig. 51.5 Real-time control results of type II controller

Table 51.4 Dynamic performance measures of type I controller in real-time control

Performance measure	T_d (s)	T_r (s)	T_p (s)	T_s (s)	σ (%)
Yaw	0.828	1.259	2.344	2.008	2.002
Pitch	0.859	1.215	2.459	1.956	3.125
Roll	0.853	1.219	2.546	1.964	3.467

Table 51.5 Dynamic performance measures of type II controller in real-time control

Performance measure	T_d (s)	T_r (s)	T_p (s)	T_s (s)	σ (%)
Yaw	0.841	1.307	2.123	1.979	3.467
Pitch	0.895	1.300	2.404	1.952	4.199
Roll	0.887	1.295	2.113	1.858	3.857

51.4 Conclusion

In this paper, we have designed two kinds of continuous ADRC controllers to achieve the attitude control of a quad-rotor hover system, which has a unique mechanical structure. With the effective and efficient adjustment of parameters, two controllers have been successfully applied in the real-time control and all the dynamic performance measures have been summarized and analyzed. The experimental results have demonstrated that the continuous ADRC control approaches have a strong robustness and antidisturbance performance and the ability to decouple a complicated nonlinear coupled system.

References

1. Han J (2008) Active disturbance rejection control technique (in Chinese). National Defense Industry Press, Beijing
2. Han J (2009) From PID to active disturbance rejection control. Proc IEEE Int Conf Ind Electron 56(3):900–906
3. Gao Z (2006) Active disturbance rejection control: a paradigm shift in feedback control system design. In: Proceedings of the 2006 American control conference, pp 2399–2405
4. Gao Z (2003) Scaling and bandwidth-parameterization based controller tuning. In: Proceedings of the 2003 American control conference, pp 4989–4996
5. Bouabdallah S, Siegwart R (2005) Backstepping and sliding-mode techniques applied to an indoor micro quadrotor. In: Proceedings of the 2005 IEEE international conference on robotics and automation, pp 2247–2252
6. Bouabdallah S, Noth A, Siegwart R (2004) PID vs LQ control techniques applied to an indoor micro quadrotor. In: Proceedings of the 2004 IEEE/RSJ international conference on intelligent robots and systems, vol 3, pp 2451–2456
7. Bouchoucha M, Seghour S, Osmani H, Bouri M (2011) Integral backstepping for attitude tracking of a quadrotor system. Electron Electr Eng 10(116):75–81
8. Huang H, Hoffmann GM, Waslander SL, Tomlin CJ (2009) Aerodynamics and control of autonomous quadrotor helicopters in aggressive maneuvering. In: Proceedings of the 2009 IEEE international conference on robotics and automation, pp 3277–3282

Chapter 52
Design and Implementation of a PMSM Rotor Position Detecting System with High Speed and High Precision

Bo Zhu, Huailin Zhao, Jihong Zhu and Yang He

Abstract To solve the problem of detecting motor rotor position accurately of the Permanent Magnet Synchronous Motor (PMSM), this paper designs and realizes a method of demodulating the signal of PMSM rotor position based on Δ-Σ modulation and Cascade Integrator Comb (CIC) filter. This method uses Δ-Σ modulation chip ADS1205 and specially designed filter chip AMC1210 for motor control. With the combination of ADS1205 and AMC1210, the PMSM rotor position information is demodulated, and the 16-bit demodulated angle data are got. The actual system validation shows that the decoding circuits have high precision, PMSM can be stable and reliable when running at 10,000 RPM, proving the feasibility of the design. Compared with the conventional A/D sampling method, this method is more stable and reliable, cheaper, and has higher signal-to-noise ratio.

Keywords PMSM · Δ-Σ modulation · CIC filter · High precision

52.1 Introduction

The PMSM is rapidly becoming a hot researching field of AC speed regulating system because of its small size, light weight, high efficiency, compact structure, good stability, fewer rotor problem, no mechanical commutator and brushes, etc. [1]. In PMSM control system, the PMSM vector control has high control accuracy, which is determined by the accuracy of the resolver and its decoding circuits [2]. The resolver gets more and more applications in PMSM driving system because of

B. Zhu (✉) · H. Zhao
School of Electrical and Electronic Engineering, Shanghai Institute of Technology, Shanghai 201418, China
e-mail: supermoon2008@126.com

J. Zhu · Y. He
Department of Computer Science and Technology, Tsinghua University, Beijing 100084, China

Z. Deng and H. Li (eds.), *Proceedings of the 2015 Chinese Intelligent Automation Conference*, Lecture Notes in Electrical Engineering 337,
DOI 10.1007/978-3-662-46463-2_52

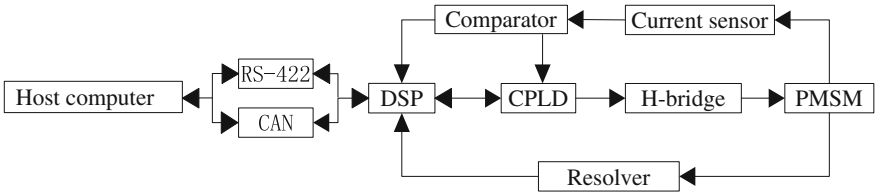

Fig. 52.1 The overall block diagram of the PMSM control system

its stability, high resolution, antishock vibration, strong adapting temperature and humidity change ability, and so on. In this paper, we introduce the Δ-Σ modulation and CIC extraction filter method to detect the rotor position. After verification of the actual system, it is shown that this method can greatly improve the accuracy of detecting the rotor position and is very suitable for high-speed, high-precision control of the PMSM. Compared with the conventional A/D sampling method, this method is more stable and reliable, cheaper, and has higher signal-to-noise ratio.

52.2 Overall Design of the PMSM Control System

The overall block diagram of the PMSM control system is shown in Fig. 52.1. DSP mainly completes the master controller and host computer communication, control algorithms, current closed loop, speed closed loop, current and voltage detection, and other tasks. CPLD mainly completes the logical combination, timing control, driving topologies reconfigurable logic, gate driving, fault isolation, overcurrent protection, reducing the burden of DSP logic control arithmetic and other tasks of the motor.

The master controller DSP communicates with the host computer via RS-422 bus or CAN bus. The host computer transmits the speed command to DSP, DSP transmits the detected motor rotor speed, phase current and motor rotor position signal to the host computer. DSP generates SPWM to CPLD, CPLD drives the H-bridge to control the motor work after logic control. Current sensor transmits the detected phase current to DSP to do vector control algorithm to CPLD to do current protection. The resolver decoding circuits transmit the detected rotor position and speed information to DSP, and DSP generates corresponding control voltage according to the received rotor position and velocity information to achieve synchronous rotation of the permanent magnet rotor's magnetic field and the armature's magnetic field.

52.2.1 Principle Analysis of the Resolver

The variable reluctance resolver has no rotor winding, the primary and secondary windings are located on the stator, but the special design of the rotor makes the

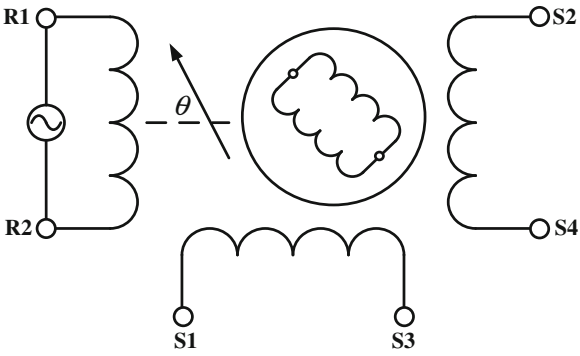

Fig. 52.2 The principle diagram of the variable reluctance resolver

secondary winding coupling occurring sine and cosine wave variation with the variation of the angular position [3]. The principle diagram of the variable reluctance resolver is shown in Fig. 52.2.

In Fig. 52.2, *R*1–*R*2 is the exciting winding or the primary winding, *S*1–*S*3 and *S*2–*S*4 are the secondary windings. When the primary winding inputs the high-frequency sine wave, the pulse magnetic field is rotating with the rotor, thus the winding *S*1–*S*3 and *S*2–*S*4 induce corresponding sine and cosine signal varying with the rotor position [4]. The relationship between the input and output is shown in formula 52.1.

$$\begin{cases} E_{R1-R2} = E_0 \sin\omega t \\ E_{S1-S3} = E_0 \sin\omega t \sin\theta \\ E_{S2-S4} = E_0 \sin\omega t \cos\theta \end{cases} \tag{52.1}$$

E_0 is the amplitude of the exciting signal.
ω is the angular frequency of the exciting signal.
θ is the angle of the rotor position.

52.2.2 Δ-Σ Modulation Principle

Δ-Σ modulation uses the oversampling method to convert the input analog voltage into digital signal. The digital signal is the input of the integrator. The integrator can be seen as a low-pass filter and has −6 dB inhibitory ability for noise. The integrator transmits the output data to the 1-bit A/D converter, the A/D converter outputs the 0 and 1 bit stream, the bit stream transmit back to the differential amplifier through the 1-bit D/A converter [5]. The first-order Δ-Σ modulation principle block diagram is shown in Fig. 52.3.

The first-order Δ-Σ modulator *Z*-domain transfer function is shown in formula 52.2

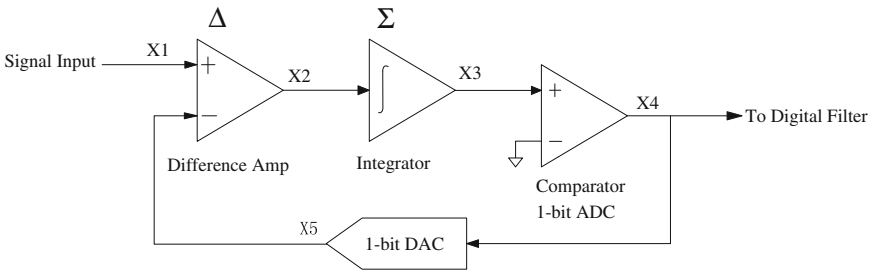

Fig. 52.3 The first-order Δ-Σ modulation principle block diagram

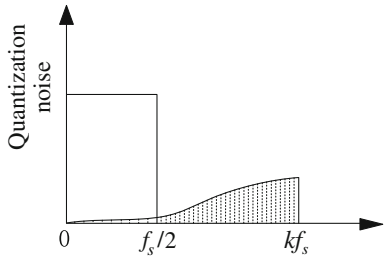

Fig. 52.4 Quantization noise after Δ-Σ modulation

$$Y(Z) = Z^{-1}X(Z) + \left(1 - Z^{-1}\right)E(z) \tag{52.2}$$

In formula 52.2, it is shown that the first-order Δ-Σ modulation has no distortion transmission to the input signal $X(Z)$, while to the quantization noise $E(Z)$, in the view of frequency domain, the noise signal transmits through a high-pass filter. Quantization noise after Δ-Σ modulation is shown in Fig. 52.4. By Δ-Σ modulation, the baseband quantization noise is greatly reduced [6].

Due to increasing orders, the second-order Δ-Σ modulation noise shaping effect is better than the first-order Δ-Σ modulation in the case of the same sample frequency. That is, its output baseband has letter noise signal.

52.2.3 The CIC Filter Principle

CIC extraction filter has two main roles: One is removing high-frequency noise signal, the other is reducing the sample frequency [7]. CIC extraction filter includes two basic parts, the integral part and the comb-shaped part. The block diagram of CIC extraction filter is shown in Fig. 52.5.

Single-stage CIC extraction filter, namely series $N = 1$, integrator of the integral part is a unipolar point of IIR filter, its feedback coefficient is 1, the Z-domain transfer function is shown in formula 52.3.

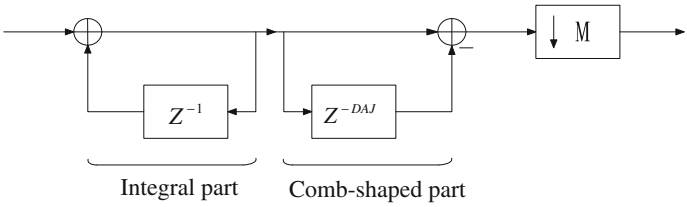

Fig. 52.5 CIC extraction filter block diagram

$$H_1(Z) = \frac{1}{1 - Z^{-1}} \tag{52.3}$$

Comb-shaped part is a symmetrical FIR filter, the Z-domain transfer function is shown in formula 52.4

$$H(Z) = 1 - Z^{-DM} \tag{52.4}$$

M is an integer frequency conversion factor, D is the differential delay factor, which called the differential time delay. According to the above analysis, the transfer function of the CIC extraction filter is shown in formula 52.5.

$$H(Z) = \frac{1}{1 - Z^{-1}}\left(1 - Z^{-DM}\right) \tag{52.5}$$

The amplitude-frequency response of the transfer function is shown in formula 52.6

$$H\left(e^{j\omega}\right) = \left|\frac{\sin\left(\frac{\omega DM}{2}\right)}{\sin\left(\frac{\omega}{2}\right)}\right| \tag{52.6}$$

52.2.4 Hardware Circuits Design of the Resolver Demodulation

The resolver demodulation circuits schematic is shown in Fig. 52.6. The filter chip AMC1210 generates two complementary PWM waves PWM1 and PWM2 to drive the primary side of the resolver. In its two mutually perpendicular secondary sides induced sine waves CHA+ , CHA− and cosine waves CHB+ , CHB−. The second-order Δ-Σ modulator ADS1205 demodulates the receiving sine and cosine wave signal by oversampling and noise shaping technology, moving the noise to the high-frequency band, and then transmits the resulting bit stream data to AMC1210 to do digital filter through interface OUTA and OUTB. The AMC1210 filters out the high-frequency noise signal by CIC filter on the one hand, on the other hand

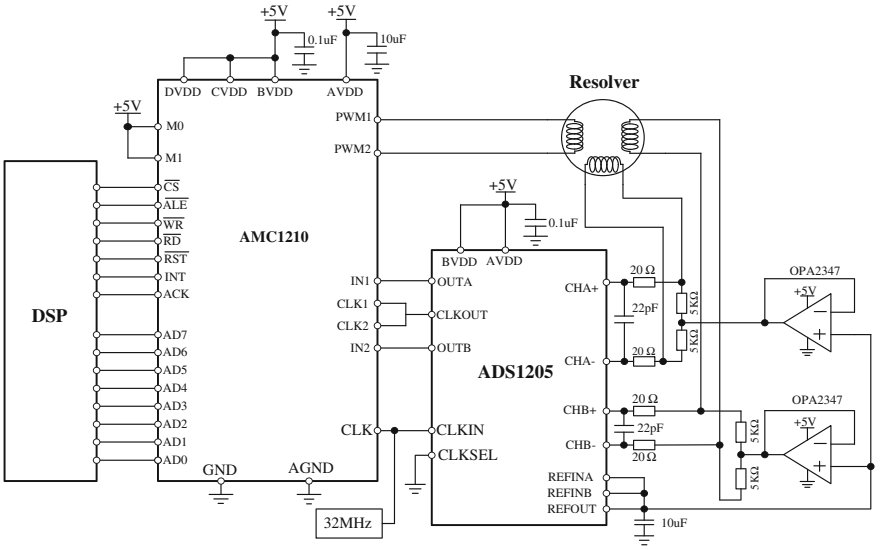

Fig. 52.6 Resolver demodulation circuit schematic

reduces the sample rate [8]. DSP calculates the motor rotor position signal θ according to formula 52.7, and then generates corresponding SPWM signal to control the movement of the motor rotor according to the motor rotor position information.

$$\theta = \text{arc tan}\frac{E_{S1-S3}}{E_{S2-S4}} \tag{52.7}$$

In formula 52.7, θ is the motor rotor position, E_{s1-s3}, E_{s2-s4} are the two secondary winding signal of the resolver, respectively.

52.3 Results and Analysis

The experiment adopts the three-phase and six-pole surface permanent magnet synchronous motor, the main parameters are: rated power P = 2.4 KW, rated voltage U = 280 V, rated phase current I = 3.8 A, rated speed n = 10,000 RPM, torque constant K_T = 0.156 N m A^{-1}, the stator phase inductance L = 2.060 mH, stator phase resistance R = 0.728 Ω.

Through the oscilloscope observation, the signal waveform of the resolver is shown in Fig. 52.7. It can be seen that the signal is very stable and has no distortion, moreover, the signal has high quality and low noise. The amplitude of the signal is 4.4 V. The frequency of the signal is 10 kHz. Proving the demodulation circuits

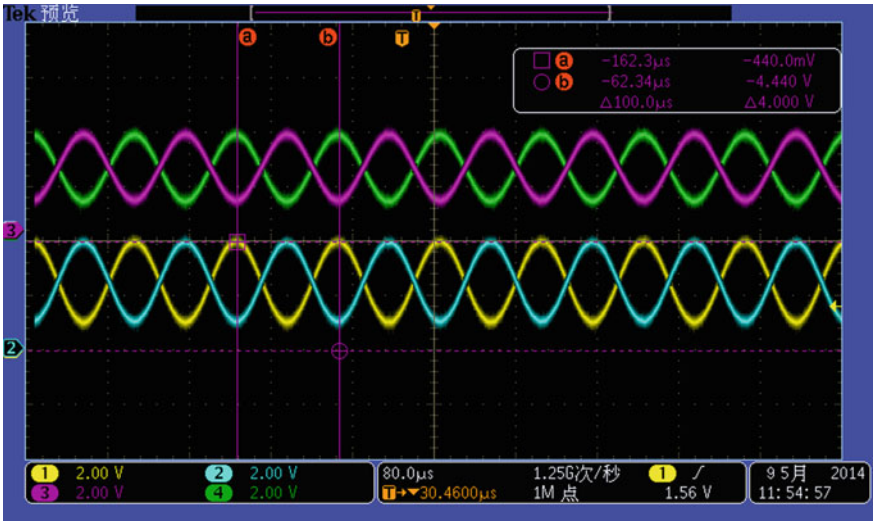

Fig. 52.7 The induction signal in the secondary winding of the resolver

with the combination of ADS1205 and AMC1210 has high-speed, high signal-to-noise ratio, strong anti-interference ability, and stable ability.

The host computer is written by LabVIEW software, Fig. 52.8 shows the actual running state of the motor under the given speed 10,000 RPM. When given the speed command of 10,000 RPM through the host computer, in the left top of the Fig. 52.8, we can see that the motor speed is stabilized at around 10,004 RPM,

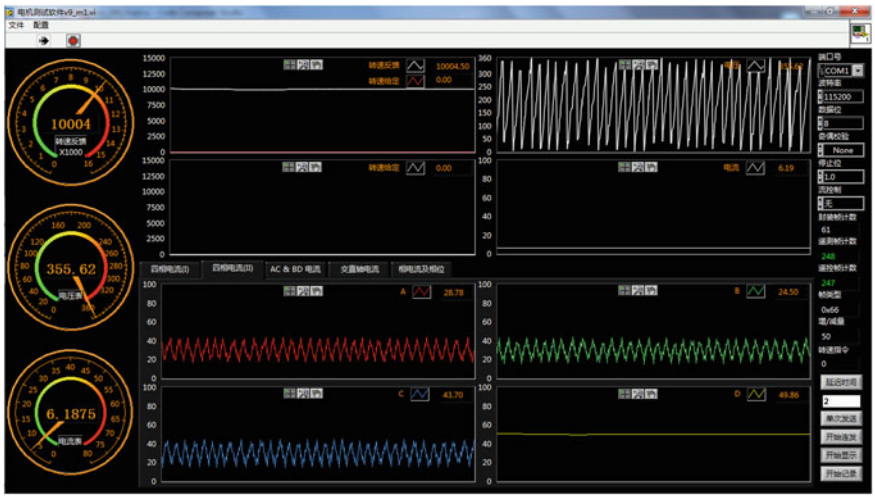

Fig. 52.8 The actual running state of the PMSM with the given speed 10,000 RPM

indicating that the steady-state error of the PMSM is very small. In the lower parts of the Fig. 52.8 shows the three-phase current waveform of the PMSM, indicating that the control effect is perfect. Therefore, the demodulation circuits are very suitable for high-speed and high-precision control of PMSM.

52.4 Conclusion

In this paper, the design of the demodulation circuits of the resolver with the combination of ADS1205 and AMC1200 has good characteristics such as high-speed, high-precision, high signal-to-noise ratio, strong anti-interference ability, stable and reliable performance and cheap price, etc. The experiment shows that the control system is very stable and reliable, and the PMSM can reach the high speed of 10,000 RPM. It also shows that the demodulation circuits satisfy the requirements of high-speed and high-precision control of the PMSM. On whole, the design is feasible.

References

1. Mo H, Min L, Wang J, Ren L (2013) Summarizing commentary on modern high-performance AC servo system-PM servo motor. Micromotors 46(9):1–10 (in Chinese)
2. Wu HX, Ye YG, Ni T, Guo QB (2011) Summary of detecting rotor position technique for brushless DC motor. Micromotors 44(8):75–81 (in Chinese)
3. Chen Y, Chen C, Zhou J (2013) Detection technology of rotor position for permanent magnet synchronous motor. Electr Mach Control Appl 40(7):47–51 (in Chinese)
4. Attaianse C, Tomasso G (2007) Position measurement in industrial drives by means of low-cost resolver-to-digital converter. IEEE Trans Instrum Meas 56(6):2155–2159
5. Hao Z, Yang H, Zhang C, Qisong W, Yin T (2010) An improved digital filter for sigma-delta ADC. J Electron Inf Technol 32(4):1012–1016 (in Chinese)
6. Qianyu W, Zhang Z, Li R, Shi L (2010) Design of decimation filter for sigma-delta A/D converter. Microelectronics 40(2):173–176 (in Chinese)
7. Yan X, Tian K (2013) Design and implementation of CIC filter based on FPGA. Audio Eng 37 (2):66–68 (in Chinese)
8. Sarma S, Agrawal VK, Udupa S (2008) Software-based resolver-to-digital conversion using a DSP. IEEE Trans Ind Electron 55(1):371–379

Chapter 53
Analysis and Design of Disturbance Observer for Piezoelectric Hysteresis Nonlinear System

Hefei Sun and Zhen Zhang

Abstract Disturbance observer (DOB) is widely used in high accurate control of servo systems. But hysteresis nonlinearity of the piezoelectric actuator in the system decreases the performance of the system and even causes oscillation. The focus of this paper is on three areas. First, Hammerstein hysteresis model is proposed to describe the dynamic hysteresis effects of piezoelectric actuator. Then, the influences of the hysteresis in the piezoelectric actuator on the DOB performances are analyzed using describing function method. Finally, a DOB combined with hysteresis compensator is designed for piezoelectric actuator. The simulation and experimental results show that, compared with control case without hysteresis compensation, the hysteresis inverse compensator improves the performance of the system and decreases oscillation in high frequency.

Keywords Disturbance observer · Hysteresis nonlinearity · Hammerstein model · Describing function method · Hysteresis compensator

53.1 Introduction

Recently, there are many applications of DOB in the accurate tracking control system at high speeds such as hard disk drives and manufacturing applications [1–3]. The idea of DOB is to enforce robust input/output behavior by introducing appropriate compensation to modeling error, parameter perturbations, and external disturbances [4]. Piezoelectric actuators with high precision and fast response have been widely used in high-performance tracking control. However, the hysteresis characteristics in piezoelectric actuators decrease the performance. In some published works of DOB design, non-inverse compensation regards the hysteresis nonlinearity as a disturbance modeled by an operator-based hysteresis model [5].

H. Sun (✉) · Z. Zhang
Beijing University of Aeronautics and Astronautics, Beijing 100191, China
e-mail: 18811789604@163.com

Z. Deng and H. Li (eds.), *Proceedings of the 2015 Chinese Intelligent Automation Conference*, Lecture Notes in Electrical Engineering 337,
DOI 10.1007/978-3-662-46463-2_53

Nevertheless, experimental studies show that the hysteresis effects are not "simple" nonlinearities to be considered as disturbances [6, 7]. Thus, to effectively compensate hysteresis effects operating at different excitation frequencies and avoid potential limit cycles resulting from inexact cancellation, it is essential to employ an inverse-based compensation of the hysteresis.

In this paper, Hammerstein nonlinear model is used to describe the dynamic hysteresis effects in the piezoelectric actuator [8]. The hysteresis nonlinear block in the Hammerstein model is based on the Modified Prandtl-Ishlinskii (MPI) hysteresis model [9]. Based on the MPI model, a hysteresis compensator is designed. An LTI block in Hammerstein model is identified by cascading the inverse compensator with the piezoelectric actuator. Then describing function method is used to analyze the hysteresis effects on DOB performances. A novel disturbance observer combined with hysteresis compensation is proposed. Simulation results show that the bandwidth increases effectively by hysteresis compensation. Experimental results show that the designed disturbance observer with inverse compensation effectively eliminates the high-frequency oscillations caused by hysteresis nonlinearity and improves control accuracy.

53.2 Dynamic Hysteresis Modeling of Piezoelectric Actuator

53.2.1 Hammerstein Hysteresis Model for Piezoelectric Actuator

In this subsection, a block-oriented model is proposed for the PZT actuator shown in Fig. 53.1. The model is of Hammerstein model structure, in which H presents a hysteresis nonlinear subsystem and G presents an LTI subsystem. The subsystems in Fig. 53.1 do not correspond to the physical component in the PZT actuator. An identification method of the proposed Hammerstein model is designed. By the identification method the proposed model is equivalent to the physical system of the PZT actuator. The identification method is given as follows:

Step 1: A quasi-static excitation signal u is applied to the PZT actuator, and then the output of the PZT suspension v is measured.
Step 2: From the measured data (u, v), the subsystem H is modeled using MPI [10] hysteresis model. The hysteresis compensator H^{-1} is designed based on the inverse of the subsystem H [9].

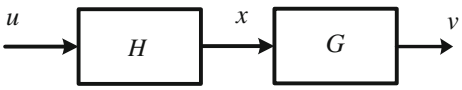

Fig. 53.1 Hammerstein system of the PZT suspension

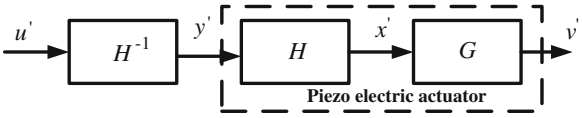

Fig. 53.2 Identification of the LTI subsystem

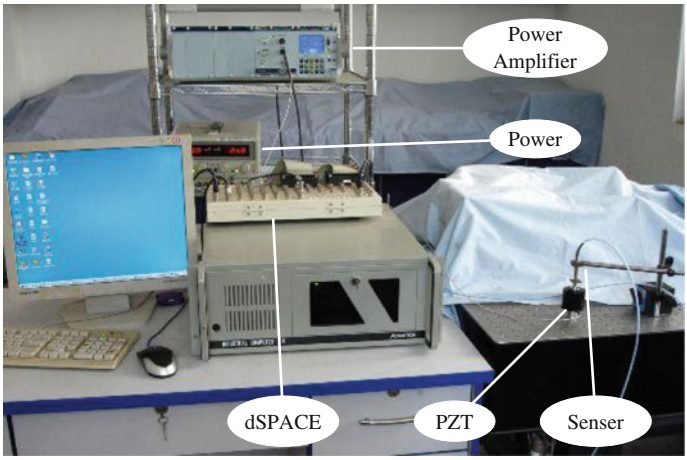

Fig. 53.3 Experimental system

Step 3: By cascading the inverse compensator H^{-1} with the PZT actuator shown in Fig. 53.2, the subsystem G can be measured and identified.

An experimental system is set up to acquire modeling data as shown in Fig. 53.3. The D/A converter transforms the control signal to piezoelectric actuator by the specified power amplifier (0–150 V). The displacement is measured by the eddy current sensor, and the corresponding transfer ratio of displacement to the voltage measured is 8 mV/um. Finally, actuator displacement is transformed via the A/D converter to dSPACE control card and recorded in the PC. The real-time control experiment works with a sampling frequency 10 kHz.

Figure 53.4 gives the static hysteresis subsystem in Hammerstein model and the identified LTI subsystem is expressed as

$$G = \frac{3.114\text{e}04s + 1.8\text{e}07}{s^2 + 3.979\text{e}04s + 1.846\text{e}07} \tag{53.1}$$

Figure 53.5 gives the modeling results under different input frequency and the relative error (RE) and Root Mean Square Error (RMSE) are given in Table 53.1. It is shown that the proposed model agrees well with experimental data.

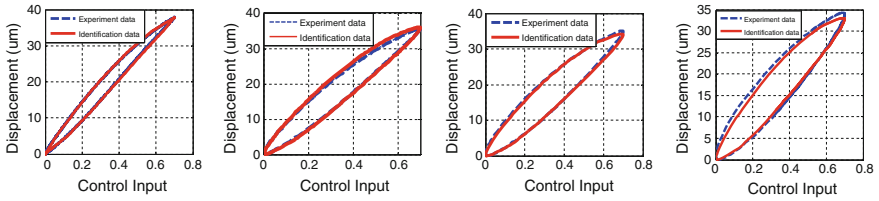

Fig. 53.4 Identification results of hysteresis subsystem

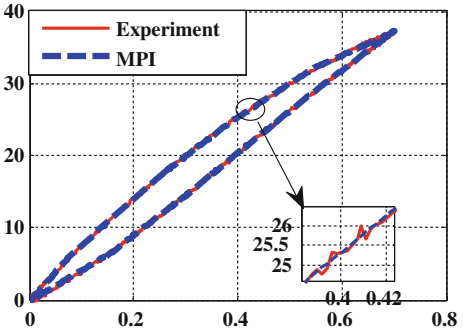

Fig. 53.5 Dynamic hysteresis modeling results

Table 53.1 Dynamic models error under different input frequency

	1 Hz	40 Hz	70 Hz	100 Hz
RE (um)	0.2236	0.4873	0.5712	0.9558
RMSE	0.0110	0.0214	0.264	0.0457

53.2.2 Hysteresis Compensator

From the identified H, the inverse compensator H^{-1} is designed and used to cancel the hysteresis effects in the piezoelectric actuator [9]. The input signal is sinusoidal wave with 1 Hz frequency. The hysteresis loop and its inverse are shown in Fig. 53.6a. The responses of the open loop hysteresis compensation system are given in Fig. 53.6b. It can be seen in Fig. 53.6b that the hysteresis effects are reduced significantly by the hysteresis compensator.

53.3 Disturbance Observer

In this section, the disturbance observer is briefly described first. Then the describing function method is used to analyze the influences of the hysteresis on the DOB performances. Finally a novel DOB combining with hysteresis compensator is designed based on the proposed hysteresis model of piezoelectric actuator.

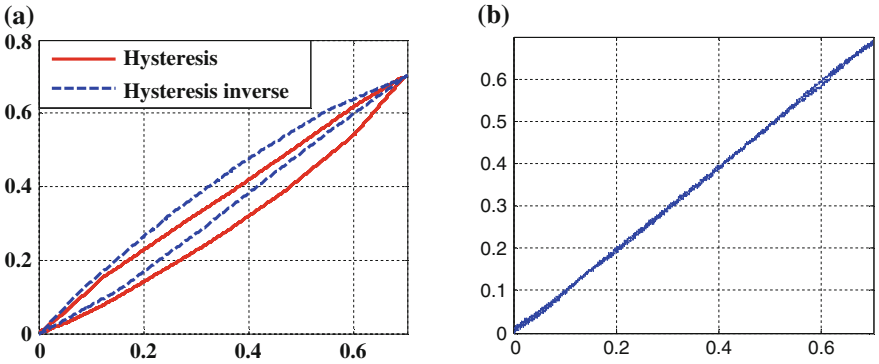

Fig. 53.6 Hysteresis inverse compensation

53.3.1 Disturbance Observer

Figure 53.7 shows the structure of the disturbance observer. In Fig. 53.9, $G_p(s)$ is the plant, $G_n(s)$ is the nominal model of the plant, and $Q(s)$ is a low-pass filter. Signal *u, d, n, y* are the command, disturbance, noise, and output respectively. Signal $\hat{d}$ is the disturbance estimate after filtering by low-pass filtering. The command u is normally provided by an outer loop controller designed based on the nominal plant model $G_n(s)$. An appropriately designed $Q(s)$ can provide a good balance between disturbance rejection performance versus stability robustness and noise sensitivity. There have been some work focusing on the design of it [10].

From Fig. 53.7, the transfer functions of the DOB are given as follows:

$$G_{\mathrm{UY}} = \frac{G_P G_n}{G_n + [G_P - G_n]Q} \tag{53.2}$$

$$G_{\mathrm{DY}} = \frac{G_P G_n[1 - Q]}{G_n + [G_P - G_n]Q} \tag{53.3}$$

$$G_{\mathrm{NY}} = \frac{-G_P Q}{G_n + [G_P - G_n]Q} \tag{53.4}$$

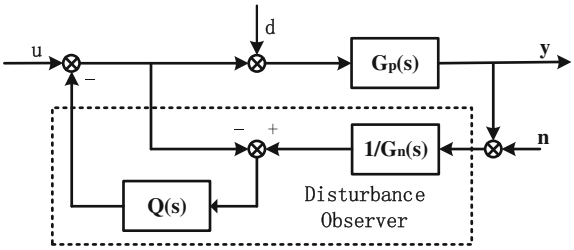

Fig. 53.7 The block diagam of DOB

As $Q \to 1$ at low frequencies, $G_{UY} \to G_n$ and $G_{DY} \to 0$. It illustrates that the plant can be regarded as the nominal model and the low frequency disturbance is suppressed. At high frequencies, $Q \to 0$ and $G_{NY} \to 0$. This means that the high frequency noise can be suppressed by DOB. The allowable bandwidth of Q is limited by the unmodeled dynamics. Usually, these unmodeled dynamics are treated as perturbation of the nominal system as

$$G_p(s) = G_n(s)(1 + \Delta(s)) \tag{53.5}$$

$\Delta(s)$ is unmodeled dynamics. Since the open-loop gain for the disturbance observer system, in the absence of unmodeled dynamics, is

$$G_{\text{ol}}(s) = \frac{Q(s)}{1 - Q(s)} \tag{53.6}$$

The complimentary sensitivity function, $T(s)$, for DOB loop is equal to $Q(s)$. So robust stability of the inner loop formed by the disturbance observer is guaranteed by [8]:

$$\|T(j\omega)\Delta(j\omega)\|_\infty \leq 1 \tag{53.7}$$

Some works focus on the limits of time delay as unmodeled dynamics upon bandwidth of Q [8]. In subsection B, the effects of the hysteresis nonlinearity on the DOB will be discussed.

53.3.2 The Effects of Hysteresis on DOB

In this section, the discrete Prandtl-Ishlinskii (PI) model [9] is used to describe the hysteresis nonlinearity and the describing function method is applied to analyze the disturbance observer system with hysteresis nonlinearity. Disturbance observer for piezoelectric actuator is as shown in Fig. 53.8, in which the proposed Hammerstein model is used to describe the dynamic hysteresis. The subsystem H is represented by PI model.

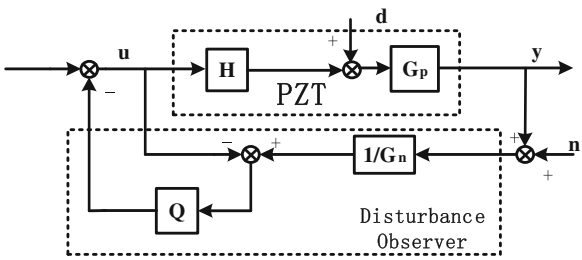

Fig. 53.8 The block diagram of DOB with hysteresis

Let the input be $x = A\sin(wt)$, then the describing function of the play operator is:
when $A/r < 1$, the output is zero;
when $A/r \geq 1$, the output is as follows:

$$\begin{aligned} N(A) &= m + jn \\ &= \frac{K}{\pi}\left[\frac{\pi}{2} + \arcsin\left(1 - \frac{2r}{A}\right) + 2\left(1 - \frac{2r}{A}\right)\sqrt{\frac{r}{A}\left(1 - \frac{r}{A}\right)}\right] + j * \frac{4Kr}{A}\left(\frac{r}{A} - 1\right) \end{aligned} \tag{53.8}$$

where $m = \frac{K}{\pi}\left[\frac{\pi}{2} + \arcsin\left(1 - \frac{2r}{A}\right) + 2\left(1 - \frac{2r}{A}\right)\sqrt{\frac{r}{A}\left(1 - \frac{r}{A}\right)}\right]$, $n = \frac{4Kr}{A}\left(\frac{r}{A} - 1\right)$.

Therefore, the discrete PI model can be expressed as

$$\begin{aligned} N_{PI} &= \sum_{i=1}^{n} (w_{\text{hi}} m_i + j w_{\text{hi}} n_i) \\ &= \sqrt{\left(\sum_{i=1}^{n} w_{\text{hi}} m_i\right)^2 + \left(\sum_{i=1}^{n} w_{\text{hi}} n_i\right)^2} \angle \arctan \frac{\sum_{i=1}^{n} w_{\text{hi}} m_i}{\sum_{i=1}^{n} w_{\text{hi}} n_i} \end{aligned} \tag{53.9}$$

The describing function of H is $N(A)$, then the plant can be expressed as

$$N_{PI} G_p = (1 + \Delta) G_n \tag{53.10}$$

Assume that $G_p = G_n$,

$$\Delta = N_{PI} - 1 \tag{53.11}$$

According to (53.7), to visualize the limit imposed by hysteresis on the robust stability of DOB, consider the Bode plot of the magnitudes of $1/\Delta$ and candidates for Q as shown in Fig. 53.11. The candidate Q-filters are all chosen to be of the form

$$Q(s) = \frac{3\tau s + 1}{\tau^3 s^3 + 3\tau^2 s^2 + 3\tau s + 1} \tag{53.12}$$

53.3.3 DOB Combined with Hysteresis Compensator

As the hysteresis effects in piezoelectric actuator decrease the performances of the system, a novel DOB is designed based on the proposed Hammerstein hysteresis model. In this DOB, the inverse compensator H^{-1} is used to cancel the hysteresis effects of the piezoelectric actuator shown in Fig. 53.9.

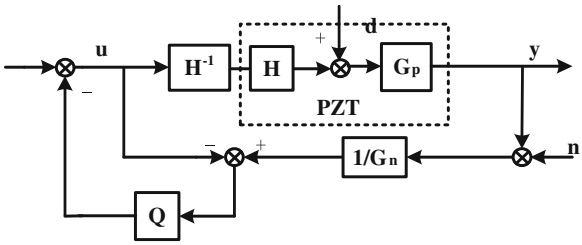

Fig. 53.9 DOB combined with hysteresis compensation

By hysteresis inverse compensation, it can be assumed that the plant is an LTI system because the inverse compensation error is small as shown in Fig. 53.6b.

53.4 Simulation and Experimental Results

In this section, the simulation and experimental results of the designed DOB are given. In order to illustrate the effects of the inverse compensator, three controllers results are given: (1) PID control; (2) PID control with DOB; (3) PID control with DOB combining with hysteresis inverse compensation. In all cases, the parameters of PID controller and DOB are the same.

53.4.1 Simulation Results

For both disturbance observers, the filter with a cutoff frequency is 450 Hz. Choose step signal as input, $d = 20\sin(50t)$ as disturbance. Figure 53.10 gives the block diagrams of PID control with DOB combined with hysteresis compensator. Figure 53.11 compares the output results of three cases. Figure 53.12 compares the

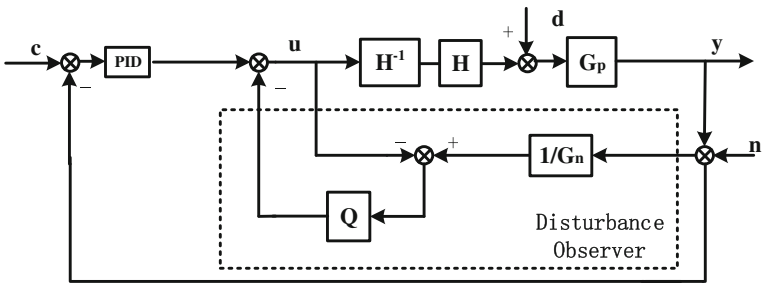

Fig. 53.10 PID control with DOB combined with hysteresis compensator

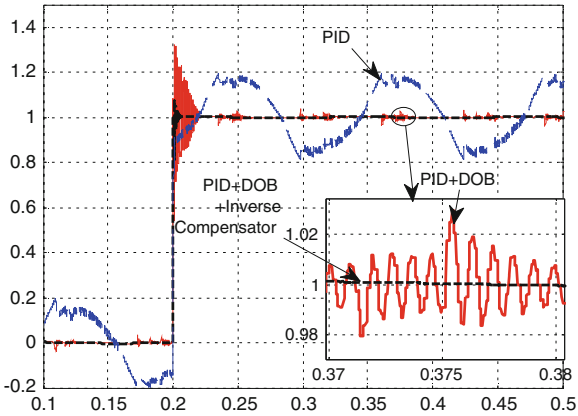

Fig. 53.11 Comparison of the output results

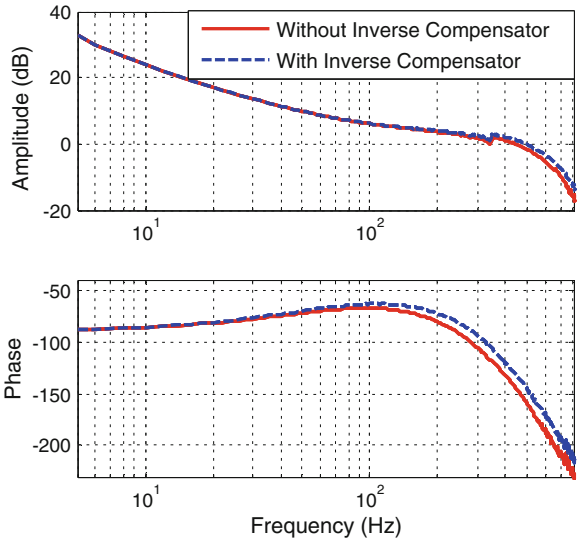

Fig. 53.12 Comparison of bode diagram of DOB with and without hysteresis compensation

bode diagram of DOB with hysteresis compensation and without hysteresis compensation.

In case one, the peak–peak error is about 0.4. In case two, the DOB is used to suppress the disturbance, the peak–peak error is reduced to 0.075. In case one and case two control results, there are high frequency oscillations owing to hysteresis in the piezoelectric actuator. For the third case, from Fig. 53.11, it can be seen that the peak–peak error is reduced to 0.02 and high frequency oscillations are eliminated. Figure 53.12 shows that the DOB with hysteresis compensation has a phase margin of $\phi_m = 40^\circ$ and the DOB without hysteresis compensation has a smaller phase margin of $\phi_m = 30^\circ$.

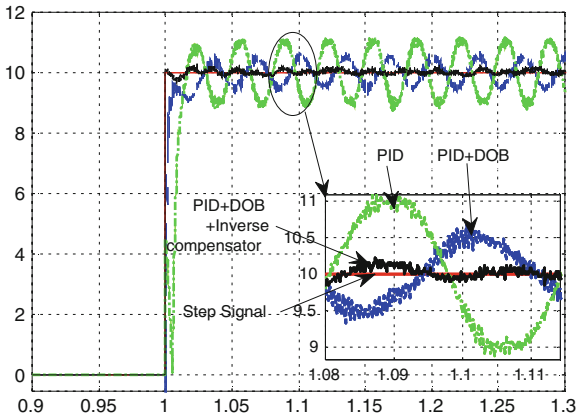

Fig. 53.13 Comparison of the output results

From the simulation results, it can be seen that disturbance observer can effectively suppress the disturbance of hysteresis system, hysteresis compensation can eliminate the oscillations and improve performances of the system.

53.4.2 Experimental Results

Experimental results of three cases are shown in Fig. 53.13. The comparison of three control results is shown in Table 53.1. Figure 53.14 shows the Power Spectrums of the tracking control errors.

It can be seen from Table 53.2 that by using the hysteresis compensation, the control accuracy is improved significantly. From Fig. 53.14, it is shown that the oscillation of the system around 3,700–6,400 Hz owing to hysteresis can be suppressed effectively by hysteresis compensator.

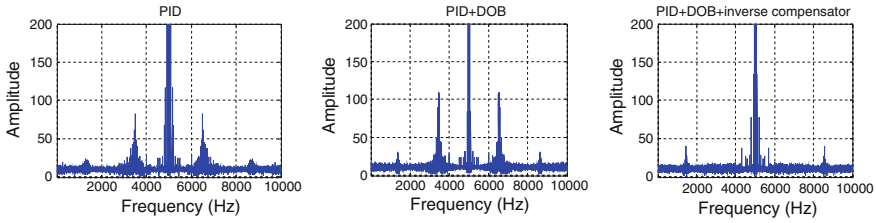

Fig. 53.14 Power spectrum of control results

Table 53.2 Dynamic models error

	PID	PID + DOB	PID + DOB + Compensator
RE	0.5435	0.2545	0.1085
RMSE	0.0766	0.0360	0.0153
Peak–peak error	2.2	1	0.5

53.5 Conclusions

In this paper, Hammerstein hysteresis model is proposed to describe the dynamic hysteresis effects of piezoelectric system. The hysteresis nonlinear block in the Hammerstein model is based on the Modified Prandtl-Ishlinskii (MPI) hysteresis model. Based on the proposed hysteresis model, a hysteresis compensator is designed. Then, the influences of the hysteresis in the piezoelectric actuator on the DOB performances are analyzed using describing function method. Simulation results illustrate that the hysteresis decreases the bandwidth of the system and cause high frequency oscillation. Finally, a DOB combined with hysteresis compensator is designed for piezoelectric actuator. The experimental results show that, compared with control case without hysteresis compensation, the hysteresis inverse compensator improves the performance.

References

1. Ohnishi K (1987) A new servo method in mechatronics. Trans Jpn Soc Elect Eng 107-D: 83–86
2. Umeno T, Hori Y (1991) Robust speed control of dc servomotors using modern two degrees-of-freedom controller design. IEEE Trans Ind Electron 38:363–368
3. White MT, Tomizuka M, Smith C (2000) Improved track following in magnetic disk drives using a disturbance observer. IEEE/ASME Trans Mechatron 5(1):3–11
4. Yang J, Li S, Chen W-H (2011) Non-linear disturbance observer-based robust control for systems with mismatched disturbances/uncertainties. IET Control Theory Appl 5(18): 2053–2062
5. Al Janaideh M, Rakheja S, Su C-Y (2009) Experimental characterization and modeling of rate-dependent hysteresis of a piezoceramic actuator. Mechatronics 19(5):656–670
6. Al Janaideh M, Rakheja S, Su C-Y (2009) Experimental characterization and modeling of rate-dependent hysteresis of a piezoceramic actuator. Mechatronics 19(5):656–670
7. El-Shaer AH, Al Janaideh M, Krejčí P, Tomizuka M (2012) Robust performance enhancement using disturbance observers for hysteresis compensation based on generalized Prandtl-Ishlinskii model. In: American control conference, pp 1664–1669
8. Wang Z, Zhang Z, Zhou K, Mao J (2013) Rate-dependent dynamic modeling and tracking control for piezoelectric hysteresis nonlinear systems. In: Chinese control conference, pp 303–308

9. Kuhnen K (2009) Modeling. Identification and compensation of complex hysteresis nonlinearities: a modified Prandtl-Ishlinskii approach. Eur J Control 9(4):407–418
10. Saito E, Katsura S (2012) A filter design method in disturbance observer for improvement of robustness against disturbance in time delay system. In: Industrial electronics (ISIE), pp 1650–1655

Chapter 54
PID Tuning for LOS Stabilization System Controller Based on BBO Algorithm

Kuifeng Su, Tianqing Chang, Bin Zhu and Bin Han

Abstract This paper is a discussion on a novel controller tuning method for the PID-based BBO method. The proposed approach had superior characteristics, including stable convergence characteristic, easy implementation, and good computational efficiency. From experimental results, the designed PID controllers-based BBO have less overshoot and short response time compared to that of the classical method. Therefore, BBO approach is taken as a better solution to improve the performance of the PID controller.

Keywords PID controller · Biogeography-based optimization · Line-of-sight

54.1 Introduction

Line-of-sight (LOS) stabilization systems are an essential part of modern surveillance and fire control systems, and form the basis of many implementation for acquisition, searching, targeting and navigation. Stabilization systems are used to keep the LOS steady in inertial space to eliminate the shake from carrier and point the LOS to desired direction. The stabilization performance of LOS is the key factor in modern fire control and surveillance systems. Therefore, the controller design is very important progress. Conventionally, these controllers have been designed using classical techniques and implemented in the digital or analog domain. Many control methods such as Robust control, fuzzy logical control, adaptive control, and slide-model control have been studied [1–6]. Among them, the best known is the proportional-integral derivative (PID) controller, which has been widely used for its simplicity and robust performance in a wide range of operating conditions [1]. However, it is difficult to tune the gains of PID controllers properly because the LOS is a multivariate, highly nonlinear system and there is tight coupling between azimuth

K. Su (✉) · T. Chang · B. Zhu · B. Han
Auto-control Engineering Department, Armed Force Engineering Institute, Beijing, China
e-mail: sukuifeng@gmail.com

Z. Deng and H. Li (eds.), *Proceedings of the 2015 Chinese Intelligent Automation Conference*, Lecture Notes in Electrical Engineering 337,
DOI 10.1007/978-3-662-46463-2_54

and elevation axis. Over the past years, many heuristic methods have been proposed for tuning of PID controller parameters. Many artificial intelligence techniques have been employed to improve the controller performance, such as particle swarm optimization, neural-fuzzy logic, and so on.

Previous simulation and application research has shown that Biogeography-based optimization (BBO) works well in noisy environment and has computation efficiency [7–10]. Compared with GA and evolutionary strategy optimization algorithm, it is not related to problems of regeneration and producing next generation; there is also a marked difference between ACO and BBO. ACO will produce a new set of solutions in each iteration, while BBO will maintain its solution set to the next iteration in each iteration and adjust solution space according to the migration probability. BBO has more in common with PSO and DE. Compared with PSO and DE, BBO directly updates by migration of the solution. Therefore, the solutions of BBO algorithm can share properties with each other.

In this paper, the PID controller design is carried out for a two-axis gyro-mirror stabilization system. The LOS is stabilized in azimuth and elevation against the angular disturbances. Two stabilization loops work simultaneously for the overall stabilization of the line-of-sight. This work focuses on the application of BBO to PID controller tuning, and a performance criterion in time domain is proposed for evaluating the performance of a BBO-PID controller that was applied to the complex control system. The gyro-mirror stabilization system experimental results show that the proposed method has better performance.

54.2 Line-of-Sight Stabilization System

The schematic diagram of the LOS stabilization system is shown in Fig. 54.1. It consists of three main components where the first component consists of the flywheel and its motor and controller. The second component consists of two gimbal structure that is responsible for providing two DOF to the flywheel; the inner and outer gambal provides movement along the yaw and the pitch axis, respectively. The third component is a mirror that is geared to the gimbals through a 2:1 reduction drive mechanism. Specifically, the inner gimbal provides movement along the yaw axis while the outer gimbal provides movement along the pitch axis. As can be seen, the controllers in the gyroscope drive the torque motor in the

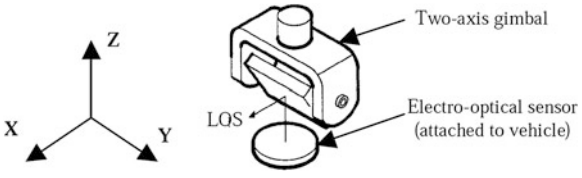

Fig. 54.1 Stabilized mirror and coordinate system

gimbals for tracking applications. The flywheel is driven by a DC torque motor and the angular velocity is kept as constant as possible.

For the convenience of design, installation to realization of target tracking system, steering stabilization is generally used. Target tracking as a pointing control system is implemented via two servo loops, the outer track or pointing loop and an inner stabilization or rate loop. Cameras, FLIR, or other tracking sensors detect the feature to get the target location. The track controller uses this information to generate rate control reference signal, which direct the gimbal of sight to the target LOS. The stabilization rate loop is used to isolate all sensors from platform motion and external disturbances, which perturbs the tracking sight. Typical line-of-sight stabilization control system structure is shown in Fig. 54.2.

Where, M_d is the moment output of torque motor, M_f is the disturbance of moment, ω_f is the disturbance of velocity, θ is the angle after integration of output angular velocity. DC torque motors are used for LOS control systems because of their excellent performance, ease of control, and high efficiency characteristics (Fig. 54.3).

According the above figure, on the condition of continual current, the armature circuit is

$$U_a = E_a + I_a R_a + L_a \frac{\mathrm{d}I_a}{\mathrm{d}t} \tag{54.1}$$

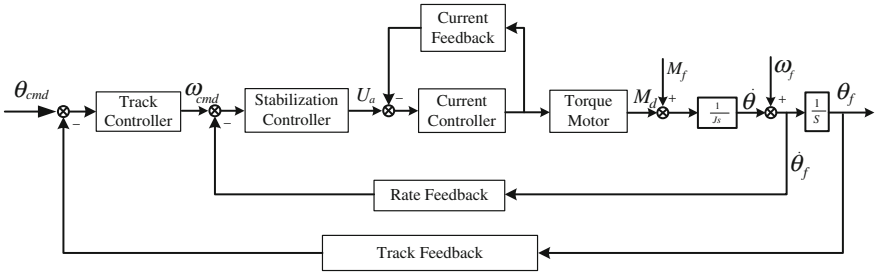

Fig. 54.2 Block diagram of line-of-sight stabilization

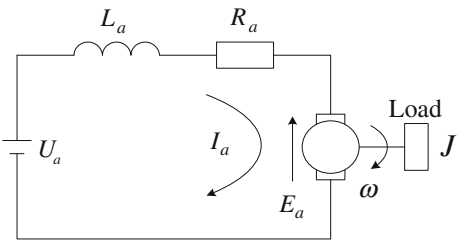

Fig. 54.3 DC motor, equivalent circuit

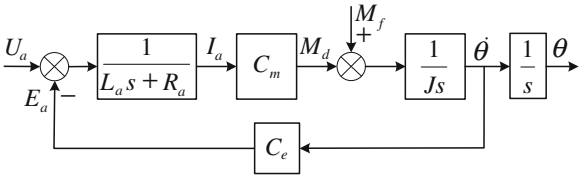

Fig. 54.4 Block diagram of torque motor

where U_a is the control voltage, E_a is the armature back electromotive force, R_a is the armature winding resistance, I_a is armature current, L_a is the whole inductance. The equation of armature back electromotive force is,

$$E_a = C_e \frac{\mathrm{d}\theta}{\mathrm{d}t} \tag{54.2}$$

where, C_e is the back electromotive force constant, θ is the angle of rotor. The moment is as follows:

$$M_d = C_m I_a \tag{54.3}$$

where C_m is the motor moment coefficient. The equation for moment balance is

$$J \frac{\mathrm{d}^2\theta}{\mathrm{d}t^2} = M_d + M_f \tag{54.4}$$

where J is the platform moment of inertia, M_d is the torque output of motor M_f is the torque of friction disturbance. Support the initial condition is zero, making Laplace transformation with Eqs. 54.1. and 54.2, then

$$\begin{cases} U_a(s) = E_a(s) + I_a(s)R_a + L_a s I_a(s) \\ E_a(s) = C_e s\theta(s) \\ M_d(s) = C_m I_a(s) \\ Js^2\theta(s) = M_d(s) + M_f(s) \end{cases} \tag{54.5}$$

According to the above equation, the block diagram of torque motor is as follows (Fig. 54.4).

54.3 BBO Algorithm

According to the island migration model of biogeography, Dan Simon proposed BBO in 2008. In biogeography, the richness of species on the island entirely depends on the two processes, namely the immigration of new species and extinction of

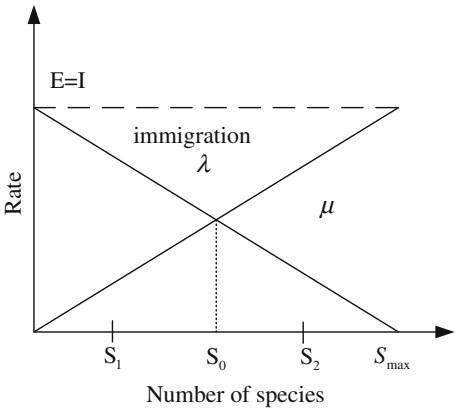

Fig. 54.5 The two solutions of the problem S_1 is relatively poor, while S_2 is relatively good

species that originally occupied the island, as shown in Fig. 54.5. When the immigration rate is equal to the extinction rate, species on the island reaches a dynamic equilibrium, that is, the species counts is relatively stable, and the category of species is S_0 at this time; when the species counts on the islands is 0, the immigration rate of species λ reaches the maximum; when the category of species on the island reaches the maximum $S_{\max}$, the emigration rate or extinction rate of species μ reaches the maximum. However, the composition of species is constantly changing and updating. This is the core of the theory of island biogeography.

54.4 BBO-PID for the Gyro-Mirror Control System

BBO is employed to tune PID parameters (K_p, K_i, K_d) using the model of line-of-sight, the optimization system structure is shown in Fig. 54.6. First, it produces initial habitat of BBO in search space represented by matrix, and HIS is mapped as the number and mobility (λ, μ) of species S for each habitat. Each habitat represents a candidate solution for PID parameters where their values are set in the range of 0–200.

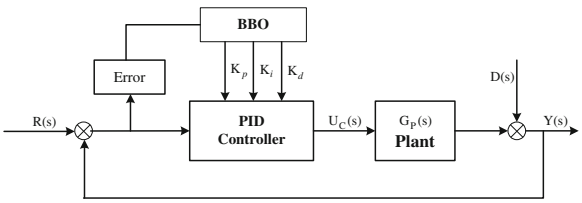

Fig. 54.6 Structure for PID parameters tuned-based BBO

Furthermore, performance index is defined as a quantitative measure to describe the system performance of the designed PID controller, which is the fitness of the optimization problem. Using this BBO optimization technique, PID parameters can be tuned to meet the required specification. For a PID-controlled system, there are often four indices to depict the system performance: ISE, ITAE and ITSE. They are defined as follows:

$$\mathrm{ISE} = \int_0^\infty e^2(t)\mathrm{d}t \tag{54.6}$$

$$\mathrm{ITAE} = \int_0^\infty t|e(t)|\mathrm{d}t \tag{54.7}$$

$$\mathrm{ITSE} = \int_0^\infty te^2(t)\mathrm{d}t \tag{54.8}$$

To improve the instantaneous response and reduce steady error, we take ITSE as fitness of the PID parameters optimization. Utilize the immigration rate and emigration rate to restore the habitat, and then recalculate each HIS. For each habitat, refresh the probability distribution of species, update the species according to

Table 54.1 Optimized PID parameters

Tuning method	K_p	K_i	K_d
Z-N PID	157.5	327.8	38.1
BBO-ISE	102.3	27.9	29.75
BBO-ITSE	98.9	29.3	20.6

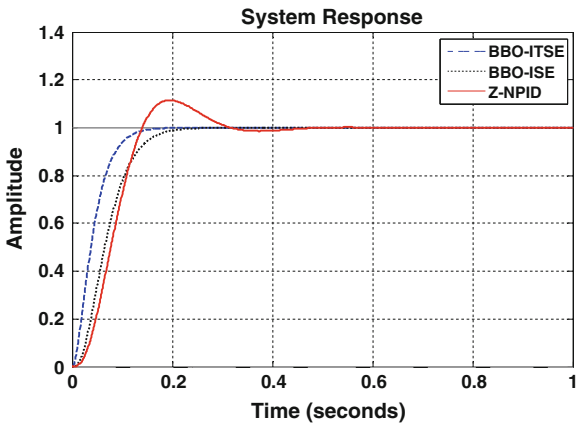

Fig. 54.7 Trajectory of system response for different PID parameter

mutation operator, and then recalculate the fitness. End the algorithm cycle according to the termination condition.

Compared with conventional Z-N tuned PID controller, the system response produces high overshoot, but better performance is obtained with the implementation of BBO-based PID controller tuning. The different fitness for BBO algorithm gives different system performance, as shown in Table 54.1. Furthermore, Fig. 54.7 gives the trajectory of system response for the above PID parameters.

54.5 Conclusion

In this work is proposed a novel controller tuning method for the PID controller parameters optimization-based BBO method. From the results, the designed PID controllers-based BBO have less overshoot compared to that of the classical method (Z-N). The proposed method integrates the BBO algorithm with ITSE performance criterion into a BBO-PID controller, which has short settling time compared with other criteria such as ISE and ITAE. Therefore, the benefit of using a BBO approach is observed as a complement solution to improve the performance of the PID controller designed by conventional method.

References

1. Asuntha A, Srinivasan A (2014) Intelligent PID controller tuning using PSO for linear system. Int J Innovative Sci Eng Technol 1(5):166–174
2. Visioli A (2001) Tuning of PID controllers with fuzzy logic. Proc Inst Elect Eng Contr Theory Appl 148(1):1–8
3. Seng TL, Khalid MB, Yusof R (1999) Tuning of a neuro-fuzzy controller by genetic algorithm. IEEE Trans Syst Man Cybern B 29:226–236
4. Solihin MI, Tack LF Kean ML (2011) Tuning of PID controller using particle swarm optimization (PSO). In: Proceeding of the international conference on advanced science, Malaysia, pp 458–461
5. Krohling RA, Rey JP (2001) Design of optimal disturbance rejection PID controllers using genetic algorithm. IEEE Trans Evol Comput 5:78–82
6. Mitsukura Y, Yamamoto T, Kaneda M (1999) A design of self-tuning PID controllers using a genetic algorithm. In: Proceedings of American control conference, San Diego, CA, pp 1361–1365
7. Simon D (2008) Biogeography-based optimization. IEEE Trans Evol Comput 6(12):702–713
8. Simon D, Ergezer M, Dawei D (2009) Markov analysis of biogeography-based optimization. http://academic.csuohio.edu/simond/bbo
9. Simon D, Ergezer M, Dawei D (2009) Markov models for biogeography-based optimization and genetic algorithms with global uniform recombination. http://academic.csuohio.edu/simond/bbo/markov/MarkovJournal.pdf
10. Simon D (2009) A probabilistic analysis of a simplified biogeography-based optimization algorithm. http://academic.csuohio.edu/simond/bbo/simplified/bbosimplified.pdf

Chapter 55
Low Altitude Photogrammetry Positioning Technology in Evaluation of GNSS Dynamic Positioning Accuracy

Dian-Wei Cong and Qi-Feng Xu

Abstract Positioning accuracy test of GNSS is of great significance. The dynamic positioning evaluation technology is worthy of study. This paper gives a good solution. When the geodetic coordinates of the ground mark points are known, the exterior orientation elements of the high quality nonmetric digital camera can be precisely calculated in low altitude photogrammetry. The simulation results show that the coordinates of the exposure station of the camera can be precisely calculated. Finally, an actual test was held in the actual photogrammetry environment. These works lay the foundation for low altitude photogrammetry evaluation test for the next step.

Keywords Photogrammetry · Space resection · Dynamic positioning · Exterior orientation · Digital camera · Accuracy test · Camera calibration

55.1 Introduction

The positioning accuracy of the GNSS (global navigation satellite system) is an important technical indicator. The positioning accuracy is determined by the comprehensive effect of a series of error sources. Theoretically, it can be calculated according to the formula by the influence of the basis superposition error sources. The method used to estimate the PVT (positioning, velocity and timing) accuracy of GPS can follow the basic equation:

$$\mathrm{Ac} = \mathrm{UERE} \times \mathrm{DOP}$$

where, Ac means PVT accuracy and UERE means the user equivalent range error. Some error source (such as atmospheric propagation delay, the multipath effect,

D.-W. Cong (✉) · Q.-F. Xu
Zhengzhou Institute of Surveying and Mapping, Zhengzhou 450001, China
e-mail: congdianwei@sina.com

Z. Deng and H. Li (eds.), *Proceedings of the 2015 Chinese Intelligent Automation Conference*, Lecture Notes in Electrical Engineering 337,
DOI 10.1007/978-3-662-46463-2_55

etc.) characteristics are hard to be modeled because they are not the same as theoretical characteristics. Then the theoretical positioning accuracy cannot reflect the real performance of the GNSS. Therefore, accuracy test should be carried on in the actual conditions of application when the system is completed.

There are many studies on the static positioning accuracy [1, 2]. The static positioning accuracy can illustrate the accuracy of GNSS measurements in a certain range, but it has limitations as it cannot fully reflect the dynamic positioning accuracy.

The dynamic positioning value varies with time because the carrier is usually in movement. It is instantaneous and unrepeatable. There are a number of differences between dynamic positioning accuracy evaluation and static positioning accuracy evaluation. The dynamic positioning techniques should be synchronous to GNSS positioning. The positioning accuracy should be three times better than the positioning accuracy of GNSS. These factors greatly limit the dynamic evaluation methods. It is much more difficult to implement the evaluation dynamic positioning accuracy than the static positioning.

This paper summarizes the existing evaluation methods of dynamic positioning. Aircraft equipped with CCD takes a photograph of the ground coding markers. The 3D coordinates of the marks are known. The 3D coordinates of the CCD can be solved by one single image space resection method. If the positioning accuracy is high enough, the method can be used as the receiver dynamic evaluation method.

Photography is instantaneous. There are essential differences between photogrammetry positioning technology and GNSS positioning method. These basic concepts of measurement are different. Using photography method can avoid the same work mode, the measurements, and the systematic bias. Photogrammetry accuracy is uncorrelated with movement speed. So the photogrammetry technique is suitable for evaluation of GNSS dynamic positioning. This paper verified the feasibility of the method through simulation experiments. An actual test was held in the actual photogrammetry environment. These works lay the foundation for low altitude photogrammetry evaluation test for the next step.

55.2 The Existing Evaluation Methods of Dynamic Positioning

There are some dynamic positioning technologies, which include system simulation method, trajectory simulation method, photography method, radio ranging method, DGNSS (Differential GNSS) method, double antenna method, and so on.

System simulation method can simulate several parts of GNSS (including the space segment and the test environment of ground segment) [3, 4]. This method is applicable to static, low dynamic, and high dynamic circumstances. But the accuracy is closely related to the system model which has been established.

Trajectory simulation method can generate circular motion or linear motion or sine motion trajectory through setting up the testing equipment [5]. It is limited because the movement of equipment is restrained. The trajectory has a periodic evaluation and hence is not suitable for high dynamic positioning evaluation.

The Information Engineering University established the first domestic high accuracy dynamic positioning standard using photography method [6]. It can take a photograph to the known coordinate marks with two mutually perpendicular CCD digital cameras placed on the vehicle. Using the elevation database information and the angle between the device and the symbol, we can calculate the high accuracy coordinate of the camera. Dynamic positioning accuracy is better than 0.1 m, but due to limited dynamic range of the vehicle, the speed of device should be less than 100 km/h. This method can get 2D location accuracy only.

Radio ranging method sets up a number of special base stations on the ground (3D coordinates are known). It can calculate the three-dimensional position by measuring the distance between the movement carrier and the rangefinder. The dynamic positioning accuracy is on the meter level. This method is applicable to static, low dynamic, and high dynamic circumstances. This method has used in the evaluation of GPS at the early stage of construction. Its disadvantage is using the radio measuring distance as GNSS did and the systematic error cannot be eliminated.

DGNSS method is also a kind of radio measurement method. The dynamic positioning accuracy can reach decimeter level or even centimeter level [7, 8]. But it requires that the receiver cannot lose lock in the process of measurement. Its disadvantage is that it also uses the radio measuring distance as GNSS did.

Double antenna method can obtain the distance between the two receivers fixed on the plane [9]. The true distance can be measured in advance. The reliability of the result is unreliable because the distance error is related to two receivers.

55.3 Low Altitude Photogrammetry Positioning Technology

In photogrammetry, the spatial position and posture of CCD can be calculated by the elements of exterior orientation [10]. One image has six parameters. Three parameters are used to describe the exposure station's coordinate (X, Y, Z) in the camera, the other three parameters are attitude parameters.

Single image space resection is an important photogrammetry positioning technology. Exterior orientation elements can be calculated with the control points and the corresponding image point coordinates. The basic principles of the single image space resection can be viewed from the related literature [11].

55.4 Simulation Test of Low Altitude Photogrammetry Positioning Technology

The paper has set the simulation environment of low altitude photogrammetry. The aircraft equipped with CCD takes a photograph of the ground coding marks. The 3D coordinates of the CCD can be solved by one single image space resection method. If the positioning accuracy is high enough, the method can be used as the receiver dynamic positioning evaluation method.

The following simulation test will be divided into two situations. We will view the positioning accuracy from the different flight height and different focal length. Considering the measurement cameras are too expensive and the nonmetric cameras are developing rapidly, the test chose Hasselblad H4D-60 digital camera which have 60 million pixels. The CCD size is 40.2 mm × 53.7 mm, single pixel size is 6.858×10^{-6} m. Assume that the camera has been strictly calibrated.

The camera pose can be adjusted to near-normal case photography by attitude adjusting platform. The image coordinates measurement error is 1 pixel. The number of each simulation test is 100 times. Four ground code points are distributed on the four corners of the square. The ground code marker coordinates are precisely measured in geodetic coordinates. The accuracy can reach the centimeter level.

55.4.1 Simulation Test with Different Flight Height

Set the camera focal length to 100 mm. The ground points are the same as shown in Fig. 55.1: Code points are distributed on the four corners of the 20 m^2. Point 5 is the

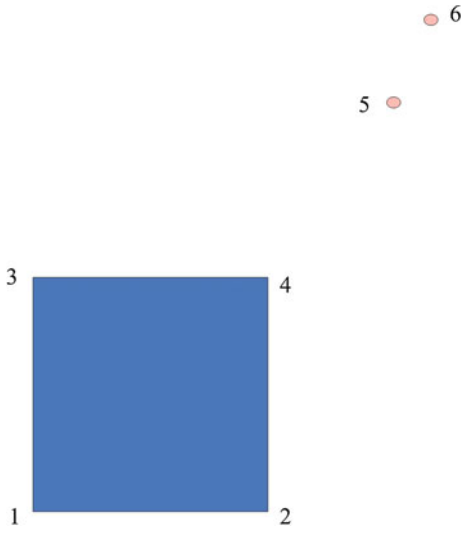

Fig. 55.1 Schematic diagram of different flight height simulation

Table 55.1 The calculation errors of camera's position when the flight height is 200 m (unit: m)

	d*X*s	d*Y*s	dZs
1σ	0.437560613	0.443856312	0.336413988
2σ	0.875121226	0.887712624	0.672827976

Table 55.2 The calculation errors of camera's position when the flight height is 100 m (unit: m)

	d*X*s	d*Y*s	dZs
1σ	0.071163429	0.087174613	0.048225149
2σ	0.142326858	0.174349226	0.096450299

real exposure station of the camera. Point 6 is the iterative position of the camera. The ground field area is 80.4 × 107.4 m when the flight height is 200 m. The ground field area is 40.2 × 53.7 m when the flight height is 100 m. The calculation errors of the exposure station camera's position are shown in Tables 55.1 and 55.2. 'd*X*s', 'd*Y*s', 'dZs 'represents the errors between the calculating position and real exposure station of the camera.

Tables 55.1 and 55.2 show data on the basis of the same focal length, same ground code points, and same image coordinates measurement error. The position accuracy is increased about 6 times when the flight height decreases doubled (from 200 to 100 m). The main reason is that angle is the basic concept of photogrammetry. The flight height reduction can cause the images structure of the ground code points to be more reasonable.

55.4.2 Simulation Test with Different Focal Length

Two groups of experiments were carried out when the camera focal length is 100 and 60 mm. The flight height is 200 m. The ground points shown in Fig. 55.1 adjusted according to the focal length. The ground field area is 80.4 m × 107.4 m when the camera focal length is 100 mm. The ground field area is 134 m × 179 m when the camera focal length is 60 mm. The calculation errors of the exposure station camera's position are shown in Tables 55.3 and 55.4.

Tables 55.3 and 55.4 show data on the basis of the same flight height and same image coordinates measurement error. The position accuracy is increased about 4 times when the focal length decreases 2/5 (from 100 to 60 mm). The main reason is that the angle is the basic concept of photogrammetry. The focal length reduction can cause the images structure of the ground code points to be more reasonable.

Table 55.3 The calculation errors of camera's position when the focal length is 100 mm (unit: m)

	d*X*s	d*Y*s	dZs
1σ	0.119324073	0.149378271	0.151389177
2σ	0.238648146	0.298756541	0.302778355

Table 55.4 The calculation errors of camera's position when the focal length is 60 mm (unit: m)

	d*X*s	d*Y*s	d*Z*s
1σ	0.024345139	0.046510749	0.028954216
2σ	0.048690278	0.093021499	0.057908432

55.5 Accuracy Test of Photogrammetry Positioning Technology

A practical test was held to verify the actual photography positing accuracy. The camera used was Hasselblad H4D-60 (Fig. 55.2). The mark was designed as in Fig. 55.3. We set 21 marks on the teaching building according to the rules in Fig. 55.4. The test area is 33 × 45 m. Then we take photos of marks as shown in Fig. 55.5.

The center coordinates of the marks can be calculated by the software. Because the elements can greatly affect the measuring results, the inner orientation elements, lens distortion, image plane distortion and eccentric distortion have been accurately calibrated (Table 55.5). We can get 6 elements of exterior orientation (real exposure station and attitude parameter) according to the collinearity equation. The real exposure station can compare with the coordinate calculated of exposure station. Then the photogrammetry positioning accuracy can be calculated (Table 55.6).

Some conclusions can be obtained from the actual test. Photogrammetry can get a good positioning accuracy which is better than 5 cm in three directions at a distance of 36 m. We can get a possible deduction according to the relationship between accuracy and distance. The positioning accuracy can be achieved 0.28 m by photography when the distance increases to 200 m. The accuracy can meet the test demand for satellite navigation system testing.

The purpose of this method is used to evaluate the receiver dynamic positioning accuracy. So we should guarantee the photography measurement time and the receiver positioning keeping strictly synchronous. The time delay of camera's electronic shutter is in tens of milliseconds and the number is not fixed. It cannot

Fig. 55.2 Hasselblad camera (H4D-60)

Fig. 55.3 The designed mark

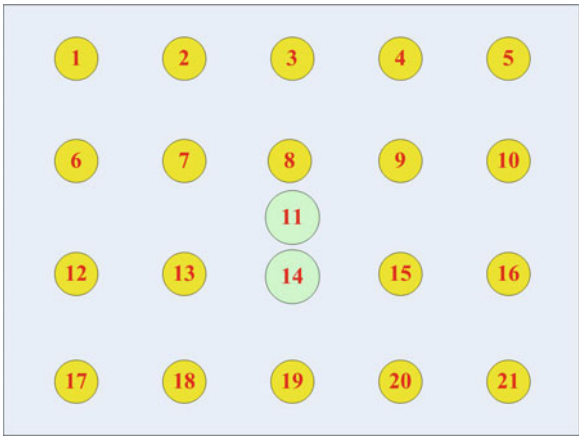

Fig. 55.4 The rules of setting marks

Fig. 55.5 Taken photograph

Table 55.5 Hasselblad H4D-60 camera calibration results

Name	Parameter calibration	Numerical value
Elements of interior orientation (unit: mm)	f	35.16886519
	$x0$	−0.07538115
	$y0$	0.13781071
Radial distortion	$k1$	$-2.04596877 \times 10^{-6}$
	$k2$	$1.44537223 \times 10^{-8}$
	$k3$	$-2.05053145 \times 10^{-11}$
Decentering distortion	$p1$	$8.68344598 \times 10^{-6}$
	$p2$	$-6.63216415 \times 10^{-6}$
Image plane distortion	$b1$	$2.30406854 \times 10^{-4}$
	$b2$	$1.40071523 \times 10^{-4}$

Table 55.6 Photogrammetry positioning accuracy (unit: m)

	X (m)	Y (m)	Z (m)
Real exposure station	0.010	−0.429	−0.069
Coordinate calculated of exposure station	−0.037	−0.395	−0.021
Photogrammetry positioning accuracy	0.047	−0.034	−0.048

meet the demand of time synchronization. We have developed a liquid crystal shutter that can guarantee the synchronizing time better than 1 ms [6].

55.6 Conclusion and Prospect

Photogrammetry positioning technology has essential difference measurements in principle with GNSS positioning method. These basic concepts of measurement are different. So the photography method can avoid using the same work mode, the measurements, and the systematic bias. Photogrammetry accuracy is independent of movement speed. So the Photogrammetry technique is suitable for evaluation of GNSS dynamic positioning accuracy.

This paper summarizes the existing dynamic positioning accuracy evaluation methods and gives another good technology. Two situations of simulation tests (different fight height test and different focal length test) have been developed. Simulation test results show that the three-dimensional coordinates of the camera's exposure station can be precisely calculated. Finally, an actual test was held in the actual photography environment. These works lay the foundation for practical evaluation test for the next step.

References

1. Liu J-C, Sang H-S (2011) Dynamic positioning accuracy test analysis of GNSS carrier-phase receiver. In: CSNC, ShangHai, pp 112–115 (in Chinese)
2. Wang Ke-xiao (2011) Handheld GPS Positioning Accuracy and Error. GNSS World of China. (9):83–86. (in Chinese)
3. Yu B (2010) Summarizing the test range of global satellite navigation system. In: CSNC, BeiJing, pp 152–156 (in Chinese)
4. Zheng JJ (2010) COMPASS ground test system and high precision self-calibration. In: CSNC, BeiJing, pp 80–85 (in Chinese)
5. Qin S-W (2008) Research on accuracytest of RTK-GPS dynamic positioning. J Geodesy Geodyn 28(5):65–68 (in Chinese)
6. Lv Z-W (2008) CCD photogramm etry positioning principle and its static positioning result. J Geomatics Sci Technol 25(4):60–63 (in Chinese)
7. Song MJ (2011) The assessing and analysis of the airborne GPS kinematic-to-kinematic relative positioning. In: CSNC, ShangHai pp 98–100 (in Chinese)
8. Wu F (2010) Velocity determination based on GPS derived pseudoranges. Geomatics Inf Sci Wuhan Univer 35(9):1034–1037 (in Chinese)
9. Liu Y, Song Z-G (2005) The method research of the dynamic positioning accuracy in the GPS measures system. GNSS World Chin 1:36–40 (in Chinese)
10. Feng W-H (2002) Short-distance photogrammetry. Wuhan University Press, WuHan, pp 15–21 (in Chinese)
11. Zhang B-M (2008) Photogrammetry. The Publishing house of Surveying and Mapping, pp 66–74 (in Chinese)

Chapter 56
Discrete-Time Integral Sliding Mode Fault-Tolerant Control with Uncertainties

Duan Wenjie, Wang Dayi and Liu Chengrui

Abstract This paper researches fault-tolerant control for discrete-time multi-input multi-output (MIMO) linear time-invariant (LTI) systems with both matched and unmatched uncertainties. A discrete-time integral sliding mode (DISM) controller and an improved direct method for control allocation are proposed as the reconfigurable control method. Closed-loop stability with matched and unmatched uncertainties for discrete-time MIMO LTI systems with DISM is studied, and the accuracy boundaries for are determined for the final states. A spacecraft model is simulated with multi-faults, efficiency factor inaccuracies, matched uncertainties, and unmatched uncertainties, which exemplifies our FTC scheme.

Keywords Discrete-time · Integral sliding mode · Fault-tolerant · Uncertainties

56.1 Introduction

Fault-tolerant control (FTC) is a hot research topic, especially for aircrafts and spacecrafts with high requirements for reliability, maintainability, and survivability [1–4]. Fault detection and diagnosis (FDD) and reconfigurable control (RC) are two main research fields in FTC [5]. FDD information, the basis of active RC, is always assumed to be precise, whereas inaccuracies may exist. Moreover, external disturbances and model uncertainties also affect the performance of FTC. All uncertainties, which can be divided into the two categories of matched uncertainties and unmatched uncertainties, are a challenge for FTC.

To design FTC schemes factoring in uncertainties, a robust controller is urgently required. ISM is favorable for withstanding uncertainties [6–10]. ISM controller and control allocation are both used in the FTC scheme [11–13], where control allocation is used to redistribute the actuator redundancy based on FDD information. However, uncertainties are not accounted for. As most control strategies are

D. Wenjie (✉) · W. Dayi · L. Chengrui
Beijing Institute of Control Engineering, Beijing 100189, China

Z. Deng and H. Li (eds.), *Proceedings of the 2015 Chinese Intelligent Automation Conference*, Lecture Notes in Electrical Engineering 337,
DOI 10.1007/978-3-662-46463-2_56

implemented in discrete time, we proposed the design of a discrete-time integral sliding mode controller (DISM) [14–17]. Most of the papers on DISM controllers only consider matched uncertainties [14–16]. Reference [17] studies system stability with a DISM controller for single-input linear time-invariant (LTI) systems, using both matched and unmatched uncertainties. However, closed-loop stability for multi-input discrete-time LTI systems with unmatched uncertainties for a DISM controller remains unaddressed, and it is more complicated than that for single-input discrete-time LTI systems.

In this paper, we design an FTC scheme including DISM and control allocation for discrete-time MIMO LTI systems. Multi-faults, the inaccuracy of FDD information, matched uncertainties, and unmatched uncertainties are considered. Closed-loop stability is studied, and the accuracy boundaries of the final states under different cases are determined. For the control allocation problem, different methods are used, such as the direction method [18, 19], pseudo-inverse method [11–13, 20], and optimal method [21]. The solution for the direct method spans the whole attainable moment space (AMS). We improve this method by rearranging the facets of the AMS by an angle indicator in order to decrease the number of calculations required.

The rest of this paper is organized as follows. Section 56.2 briefly states the problem of DISM FTC and establishes the discrete-time model. Section 56.3 constructs the sliding mode, presents the design of the virtual controller and discusses the control allocation process. Section 56.4 applies the FTC scheme to a spacecraft model. Finally, a conclusion is provided in Sect. 56.5.

56.2 DISM FTC Problem

A continuous MIMO LTI system with uncertainties is represented by

$$\begin{cases} \dot{x} = Ax(t) + Bv(t) + \xi(t) \\ v(t) = B_0 W(t) u(t) + \eta(t) \end{cases} \tag{56.1}$$

where $A \in \mathbb{R}^{n\times n}$ is the system matrix, $x(t) \in \mathbb{R}^n$ is the state vector, $u(t) \in \mathbb{R}^p$ is the vector of control inputs of all actuators, $v(t) \in \mathbb{R}^q$ is the virtual control input, $\xi(t) \in \mathbb{R}^n$ denotes uncertainties,

$B_0 \in \mathbb{R}^{n\times p}$ is determined by mounting orientations of all actuators, and $B \in \mathbb{R}^{n\times q}$ is the control effective matrix about the virtual control, which will be discussed later. $\eta(t) \in \mathbb{R}^q$ contains all known matched disturbances, and $\mathrm{W}(t) = \mathrm{diag}\{\omega_1(t), \omega_2(t), \ldots, \omega_p(t)\} \in \mathbb{R}^{p\times p}$ is a diagonal matrix denoting the efficiency factors of all actuators satisfying $0 \le \omega_i(t) \le 1$, where $\omega_i(t) = 1$, $\omega_i(t) = 0$ and $0 < \omega_i(t) < 1$ denote that the *ith* actuator is totally healthy, totally stuck, and partly stuck, respectively. If the input command to the *ith* actuator is τ_{di}, its actual output torque is $\omega_i(t) * \tau_{di}$. For a system with q_0 degrees of freedom (DOFs), we have $q = q_0$, which means that the dimension of the virtual input equals the DOFs.

Assumption 56.1

$$\text{rank}(W) \geq q$$

This assumption guarantees that (56.1) is always controllable, i.e., when faults occur, the over-actuated system always has enough available actuators. In this paper, we do not consider the under-actuated case when $\text{rank}(W) < q$.

In this paper, the efficiency matrix B in (56.1) is required to have the form

$$B = \begin{bmatrix} b_1 \\ b_2 \\ \vdots \\ b_n \end{bmatrix} \tag{56.2}$$

where $b_i \in \mathbb{R}^q$ is a row vector with no more than one non-zero parameter. For instance, $b_i = [0, 1, 0]$ $(q = 3)$. B is of full column rank, i.e., $p < n$, so there exists zero vectors in B. I_n can be described by B and its orthocomplement row space $B^{\perp}$, i.e., $BB^{+} + B^{\perp}B^{\perp +} = I_n$ [10]. Thus, matched uncertainties and unmatched uncertainties can be respectively defined as

$$\begin{aligned} \xi_m(t) &= B^{+}\xi(t) \in \mathbb{R}^q \\ \xi_u &= B^{\perp}B^{\perp +}\xi(t) \in \mathbb{R}^n \end{aligned} \tag{56.3}$$

From (56.3), we have

$$\xi(t) = BB^{+}\xi(t) + B^{\perp}B^{\perp +}\xi(t) = B\xi_m(t) + \xi_u(t) \tag{56.4}$$

Assumption 56.2 ξ_m and ξ_u are bounded and smooth, which satisfy

$$\begin{aligned} 0 \leq \|\xi_m\| \leq \delta_m < \infty \\ 0 \leq \|\xi_u\| \leq \delta_u < \infty \end{aligned} \tag{56.5}$$

The new virtual control: $v_1(t) = v(t) + \eta$, which means that the analytical disturbance η is directly compensated by $v_1(t)$. Then, (56.1) can be rewritten as

$$\dot{x}(t) = \mathrm{A}x(t) + B(v(t) + \xi_m(t)) + \xi_u(t) \tag{56.6}$$

where, for simplicity, we still use $v(t)$ in (56.6) to denote $v_1(t)$ by neglecting the subscript and the new $v(t)$ is the one that has compensated η.

The FTC control allocation strategy is shown in Fig. 56.1, which clearly shows that the control allocation depends on efficiency factors $W(t)$. $W(t)$ can be obtained

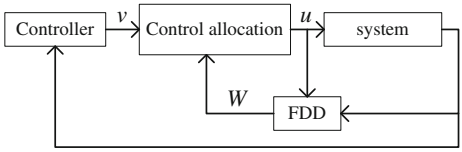

Fig. 56.1 Control allocation strategy

online using a fault reconstruction scheme such as sliding observers [22] through the differences between the measurement of the actual actuator deflection and its desired value. When faults occur, $W(t)$ changes online, and then, the control command will be reallocated among all available actuators so as to obtain the desired virtual control input. The efficiency factors are assumed to have been obtained with whatever method is employed with the FDD, denoted as $\widehat{W}(t)$, however, $\widehat{W}(t)$ may not be exactly accurate. To obtain better FTC performances, we will evaluate all uncertainties in the DISM controller.

For the *ith* actuator, its actual efficiency factor $w_i(t)$ and its estimation $\hat{w}_i(t)$ are proposed to have the following relationship [12, 13]

$$w_i(t) = (1 - \delta_i(t))\hat{w}_i(t) \tag{56.7}$$

where $\delta_i(t)$ describes the inaccuracy level ($\delta_i(t) \in [0, 1]$). According to (56.6), if $\hat{w}_i(t) = 0$, whatever $\delta_i(t)$ is, $w_i(t) = 0$. In a practical case, if $\hat{w}_i(t) = 0$ and $\delta_i(t) = 0.1$, we may have $w_i(t) = 0.1$, in which case, (56.7) is incorrect. In this paper, we propose that

$$W(t) = \hat{W}(t) - \delta(t) \tag{56.8}$$

where $\delta(t) = \mathrm{diag}\left(\left[\delta_1(t), \delta_2(t), \ldots, \quad, \delta_p(t)\right]\right)$, $\delta_i(t)$ is redefined as the residual value, i.e., $\delta_i(t) = \hat{w}_i(t) - w_i(t)$.

Then, (56.6) can be rewritten as

$$\begin{aligned} \dot{x}(t) &= Ax(t) + B\left\{B_0\left[\hat{W}(t) - \delta(t)\right]u(t) + \xi_m(t)\right\} + \xi_u(t) \\ &= Ax(t) + B\left[B_0\hat{W}(t)u(t) + \xi_m(t) - B_0\delta(t)u(t)\right] + \xi_u(t) \\ &= Ax(t) + B\left[v'(t) + \xi'_m(t)\right] + \xi_u(t) \end{aligned} \tag{56.9}$$

where $v'(t) = B_0\hat{W}(t)u(t), \xi'_m(t) = \xi_m(t) - B_0\delta(t)u(t)$. It is obvious that the inaccuracy of W produces matched uncertainties. As (56.9) has the same form as (56.6), the following discussion is based on (56.6).

This paper develops the DISM FTC method for MIMO linear system with matched and unmatched uncertainties.

The discrete-time model can be obtained by discretization of (56.6). High-order Tailor expansions, used in [16, 17], are not appropriate for uncertainties because the derivatives of the uncertainties and high-order derivatives are not known. Our paper

employs an Euler approximation, and the corresponding discrete time description with sample time T is

$$x_{k+1} = \Phi x_k + \Gamma\left(v_k + \xi_{m,k}\right) + T\xi_{u,k} \tag{56.10}$$

where $\Phi = I + AT$, $\Gamma = BT$. Defining $d_{m,k} = \xi_{m,k}T$, $d_{u,k} = \xi_{u,k}T$, then $d_k = Bd_{m,k} + d_{u,k} = \left(B\xi_{m,k} + \xi_{u,k}\right)T$.

In (56.10), (Φ, Γ) is always controllable.

56.3 Controller Design

In this section, the framework of the DISM FTC scheme is constructed. First, the discrete-time integral sliding surface and the DISM controller are designed to maintain a sliding motion and ensure the closed-loop stability considering matched and matched uncertainties. Then, an improved control allocation scheme is introduced.

56.3.1 Controller

A discrete-time integral sliding-surface is defined as the following:

$$\begin{aligned} \sigma_{k+1} &= G(x_{k+1} - x_0) + \varepsilon_{k+1} \\ \varepsilon_{k+1} &= \varepsilon_k + Ex_k \end{aligned} \tag{56.11}$$

where $E = -G(\Phi - I - \Gamma K_0)$, $G \in \mathbb{R}^{q\times n}$ is selected so as to make $G\Gamma$ invertible, K_0 is the gain matrix that distributes all eigenvalues of $(\Phi - \Gamma K_0)$ in the unit circle. $v_k = -K_0 x_k$ can stabilize (56.10) without $\xi_{m,k}$ and $\xi_{u,k}$.

Proposition 56.1 *For system* (56.10), *the sliding mode parameter* σ_k, *in* (56.11), *will have a final accuracy of* $O(T^2)$ *if controller* (56.12) *is accepted.*

$$v_k = -K_0 x_k - \hat{\xi}_{m,k} - (G\Gamma)^{-1} GT\hat{\xi}_{u,k} - (G\Gamma)^{-1}\sigma_k \tag{56.12}$$

where $\hat{\xi}_{m,k}$ *and* $\hat{\xi}_{u,k}$ *are uncertainties estimated by their last values,* $\hat{\xi}_{m,k} = \xi_{m,k-1}$, $\hat{\xi}_{u,k} = \xi_{u,k-1}$, *which are calculated by*

$$\begin{aligned} \hat{d}_k &= d_{k-1} = x_k - \phi x_{k-1} - \Gamma v_{k-1} \\ \xi_{m,k} &= \hat{d}_{m,k}/T = B^{+}\hat{d}_k/T \\ \xi_{u,k} &= \hat{d}_{u,k}/T = B^{\perp}B^{\perp+}\hat{d}_k/T \end{aligned} \tag{56.13}$$

Proof (56.11) can be rewritten as

$$\sigma_{k+1} = G(x_{k+1} - x_0) + \varepsilon_k + Ex_k \tag{56.14}$$

From a backward expression of the first equation of (56.11), we can obtain

$$\varepsilon_k = \sigma_k - G(x_k - x_0) \tag{56.15}$$

Substituting (56.15) into (56.11) leads to

$$\sigma_{k+1} = G(x_{k+1} - x_0) + \sigma_k - G(x_k - x_0) + Ex_k \tag{56.16}$$

Substituting (56.10) into (56.16), we have

$$\sigma_{k+1} = (G\Phi - G + E)x_k + G\Gamma\xi_{m,k} + GT\xi_{u,k} + \sigma_k \tag{56.17}$$

Because $E = -G(\Phi - I - \Gamma K_0)$, we have

$$\sigma_{k+1} = G\Gamma K_0 x_k + G\Gamma v_k + G\Gamma\xi_{m,k} + GT\xi_{u,k} + \sigma_k \tag{56.18}$$

Substitution of (56.12) into (56.18) leads to

$$\sigma_{k+1} = G\Gamma\left(\xi_{m,k} - \hat{\xi}_{m,k}\right) + GT\left(\xi_{u,k} - \hat{\xi}_{u,k}\right) \tag{56.19}$$

According to Assumption 56.2 and Euler discretization, we have

$$\begin{aligned} \xi_{m,k} - \hat{\xi}_{m,k} &= \xi_{m,k} - \xi_{m,k-1} = O(T) \\ \xi_{u,k} - \hat{\xi}_{u,k} &= \xi_{u,k} - \xi_{u,k-1} = O(T) \end{aligned} \tag{56.20}$$

Due to $\Gamma = BT$, we obtain

$$\sigma_{k+1} = O(T^2) \tag{56.21}$$

Thus, we know that our controller can ensure the DISM. Next, we will analyze the closed-loop stability.

Define $\Phi_0 = (\Phi - \Gamma K_0)$. □

Assumption 56.3 All the eigenvalues of Φ_0 are nonzero and distinct.

This assumption can be achieved by the pole assignment method.

Proposition 56.2 *For system* (56.10), *if controller* (56.12) *is adopted, under Assumption* 56.3, *the closed-loop stability is determined by the unmatched uncertainties,*

(1) if $\xi_{u,k} \in L_2 \bigcap L_\infty$, the final state $x_k = O(T^2)$;

(2) if $\xi_{u,k} \in L_\infty$, x_k is within the boundary $\frac{\delta_u T + O(T^2)}{1 - \lambda_1}$.

Proof A backward expression of (56.19) is

$$\sigma_k = G\Gamma(\xi_{m,k-1} - \hat{\xi}_{m,\,k-1}) + GT(\xi_{u,\,k-1} - \hat{\xi}_{u,\,k-1}) \tag{56.22}$$

Substituting (56.22) into (56.12) leads to

$$v_k = -K_0 x_k + Q_{1,\,k} \tag{56.23}$$

where $Q_{1,\,k} = -\widehat{\xi}_{m,\,k} - (G\Gamma)^{-1}GT\widehat{\xi}_{u,k} - \left(\xi_{m,\,k-1} - \widehat{\xi}_{m,\,k-1}\right) - (G\Gamma)^{-1}GT\left(\xi_{u,k-1} - \widehat{\xi}_{u,k-1}\right)$.

Substituting (56.23) into (56.10) leads to the closed-loop system equation,

$$\begin{aligned} x_{k+1} &= (\Phi - \Gamma K_0)x_k + \Gamma\left(\xi_{m,\,k} - \hat{\xi}_{m,\,k}\right) - \Gamma\left(\xi_{m,\,k-1} - \hat{\xi}_{m,\,k-1}\right) \\ &\quad + T\xi_{u,\,k} - \Gamma(G\Gamma)^{-1}GT\hat{\xi}_{u,\,k} - \Gamma(G\Gamma)^{-1}GT\left(\xi_{u,\,k-1} - \hat{\xi}_{u,\,k-1}\right) \\ &= (\Phi - \Gamma K_0)x_k + (I - \Upsilon)T\xi_{u,\,k} + Q_{u,\,k}T + Q_{m,\,k} \end{aligned} \tag{56.24}$$

□

where $\Upsilon = \Gamma(G\Gamma)^{-1}G$, $Q_{u,\,k} = \Upsilon(\xi_{u,\,k} - \widehat{\xi}_{u,\,k}) - \Upsilon(\xi_{u,\,k-1} - \widehat{\xi}_{u,\,k-1})$, $Q_{m,\,k} = \Gamma\left(\xi_{m,\,k} - \hat{\xi}_{m,\,k}\right) - \Gamma\left(\xi_{m,\,k-1} - \hat{\xi}_{m,\,k-1}\right)$.

Similar to (56.20), we can obtain $Q_{m,\,k} = O(T^2)$. From (56.24), the size and nature of the unmatched uncertainties will determine the closed-loop stability, and we analyze the effects of unmatched uncertainties in the closed-loop system.

In this paper, $G = B^{\mathrm{T}}$ is used; then, Υ can be obtained as follows:

$$\Upsilon = \mathrm{diag}(\upsilon_1, \ldots, \upsilon_n) \tag{56.25}$$

where $\upsilon_i = 0$ if b_i is a zero vector, otherwise, $\upsilon_i = 1$.

Then, we obtain

$$\Upsilon * \xi_u = 0 \tag{56.26}$$

which means that $Q_{u,\,k} = \Upsilon(\xi_{u,\,k} - \hat{\xi}_{u,\,k}) - \Upsilon(\xi_{u,\,k-1} - \hat{\xi}_{u,\,k-1}) = 0$. Thus, (56.24) can be rewritten as

$$x_{k+1} = (\Phi - \Gamma K_0)x_k + (I - \Upsilon)T\xi_{u,\,k} + Q_{m,\,k} \tag{56.27}$$

We define $\Phi_0 = (\Phi - \Gamma K_0)$, $\Phi_1 = (I - \Upsilon)$; then, (56.27) can be written in the form of

$$x_{k+1} = \Phi_0 x_k + \Phi_1 T\xi_{u,\,k} + Q_{m,\,k} \tag{56.28}$$

The solution of (56.28) is

$$x_k = \Phi_0^k x_0 + \sum_{i=0}^{k-1} \Phi_0^i \Phi_1 T \xi_{u,\,k} + \sum_{i=0}^{k-1} \Phi_0^i Q_{m,\,k} \tag{56.29}$$

According to Assumption 56.3, Φ_0 can be described as

$$\Phi_0 = PJP^{-1} \tag{56.30}$$

where $J = \mathrm{diag}([\lambda_1 \quad \lambda_2 \quad \cdots \quad \lambda_n])$, $1 > \lambda_1 > \lambda_2 > \cdots > \lambda_n > -1$. P is the transection matrix satisfying $P^{-1}P = I$.

Substituting (56.30) into (56.29) yields

$$x_k = PJ^kP^{-1}x_0 + P\sum_{i=0}^{k-1} J^iP^{-1}\Phi_1 T\xi_{u,\,k} + P\sum_{i=0}^{k-1} J^iP^{-1}Q_{m,\,k} \tag{56.31}$$

According to (56.25), we know that $\Phi_1 = I - \Upsilon = \mathrm{diag}(1-\upsilon_1, \ldots, 1-\upsilon_n)$. Then, we can get

$$\|\Phi_1\| \le 1 \tag{56.32}$$

Then, from (56.31), we have

$$\begin{aligned} \|x_k\| \le T\|P\| \sum_{i=0}^{k-1} \|J\|^i \left\|P^{-1}\right\| \|\Phi_1\| \left\|\xi_{u,k}\right\| \\ + \|P\| \sum_{i=0}^{k-1} \|J\|^i \left\|P^{-1}\right\| \left\|Q_{m,k}\right\| \end{aligned} \tag{56.33}$$

where $\|J\| = \lambda_1$, $\left\|\xi_{u,\,k}\right\| \le \delta_u$.

When k is sufficiently large, we get

$$\|x_k\| \le \left(T\left\|\xi_{u,\,k}\right\| + \left\|Q_{m,\,k}\right\|\right) \sum_{i=0}^{\infty} \lambda_1^i = \frac{\delta_u T + O(T^2)}{1-\lambda_1} \tag{56.34}$$

The ultimate bound of x_k is determined by $\xi_{u,\,k}$. We discuss two cases as in [6] for $\xi_{u,\,k}$:

(1) if $\xi_{u,\,k} \in L_2 \bigcap L_\infty$, $k \to \infty$, $\xi_{u,\,k} \to 0$, from (56.34), $x_k \le O(T^2)$;

(2) if $\xi_{u,\,k} \in L_\infty$, according to (56.34), x_k is within the boundary $\|x_k\| \le \frac{\delta_u T + O(T^2)}{1-\lambda_1}$.

Note that when $\xi_{m,\,k} = 0$, the conclusions of the aforementioned two cases for $\xi_{u,\,k}$ are $x_k = 0$ and $\|x_k\| \le \frac{\delta_u T}{1-\lambda_1}$, respectively.

56.3.2 Control Allocation

We improve the direct method proposed by Durham [18, 19] in this section. Redundancy is very important for FTC, and control allocation is used to treat the redundancy when faults occur, which can redistribute the virtual control to redundant actuators without changing the virtual control law. The control allocation problem in this paper is about finding a solution u of the equation

$$v = B_0 \hat{W} u \tag{56.35}$$

The directed method yields the solution within the maximum attainable moment space (AMS). W define $F = B_0 \hat{W} \in \mathbb{R}^{p \times q}$. Variance in $\hat{W}$ leads to changes in the AMS, and we should update the AMS according to the online FDD information.

There are two main steps in the original method: set up AMS and get all the vertices and then find the intersection facet and determine the controls. The speed of the method is improved by adding a new step to rearrange the search process along a predefined sequence using an angle indicator. The improved method is described below in A, B, and C, where B represents our improvements.

A: Computation of the AMS

F can be subdivided as $F = [F_1, F_2, \ldots, F_q]$. For every pairwise combination of (F_i, F_j), two parallel facets s_{ij} and s_{ji} are located on the boundary of the AMS with the maximum distance between each other. All the boundary facets compose a set, defined as $\partial\Phi_T$, including a total of $q \times (q-1)$ facets.

For s_{ij}, using the following three steps, all the vertices can determined.

First, the normal vector of s_{ij}, n_{ij} is

$$n_{ij} = F_i \times F_j \tag{56.36}$$

where n_{ij} points to the outside of the envelope.

Second, the facet s_{ij} is

$$m_{ij} = \sum_{k=1,\, k \neq i,\, j}^{q} m_{k,\,\max} \tag{56.37}$$

where, $m_{k,\max} = \begin{cases} F_k u_{k,\max} \text{ if } F_k^T n_{ij} > 0 \\ F_k u_{k,\max} \text{ if } F_k^T n_{ij} > 0 \end{cases}$, $u_{k,\,\max}$ and $u_{k,\,\min}$ are the maximum and minimum values, respectively, of the k^{th} control of u.

Third, the vertices of s_{ij} can be obtained by

$$vt_{ij} = m_{ij} + F_i \begin{bmatrix} u_{i,\min} \\ u_{i,\min} \\ u_{i,\max} \\ u_{i,\max} \end{bmatrix} + F_j \begin{bmatrix} u_{j,\min} \\ u_{j,\max} \\ u_{j,\max} \\ u_{j,\min} \end{bmatrix} \tag{56.38}$$

B: Rearrangement of all the facets

It is proposed that the facets of $\partial\Phi_T$ are rearranged in an ascending sequence by the following indicator:

$$\mu_{ij} = \frac{n_{ij}v}{|n_{ij}||v|} \tag{56.39}$$

where μ_{ij} is the cosine of the corner between n_{ij} and v. The smaller the magnitude of μ_{ij} is, the smaller the corner between n_{ij} and v we can obtain. We executed this arrangement using the MATLAB tool for bubble sorting.

C: Computation of the control input

To determine the intersection facet, we evaluate all the facets in $\partial\Phi_T$ one by one using the following:

$$\begin{aligned}\alpha_3 v = {} & \alpha_1 F_i\left(u_{i,\max} - u_{i,\min}\right) \\ & + \alpha_2 F_j\left(u_{j,\max} - u_{j,\min}\right) + vt_{ij,1}\end{aligned} \tag{56.40}$$

where α_1, α_2 and α_3 are three parameters, $vt_{ij,1}$ is the first vertex of s_{ij}.

If $\alpha_3 > 0$, $\alpha_1 \in [0,\ 1]$, $\alpha_2 \in [0,\ 1]$, then s_{ij} is the desired facet.

s_{ij} corresponds to control vector u_{ij}, and we can determine the controls with

$$u_b = u_{ij} + \alpha_1(u_{i,\max} - u_{i,\min}) + \alpha_2(u_{j,\max} - u_{j,\min}) \tag{56.41}$$

If $\alpha_3 \geq 1$, $u = u_b/\alpha_3$; if $\alpha_3 < 1$, the desired moment exceeds the maximum available moment, and we set $u = u_b$. Thus, $\alpha_3 < 1$ represents that the input of the system is saturated.

Note that If the AMS is a regular polygon, the intersection facet can be obtained very quickly by our rearranged sequence. Additionally, the direct method can point out saturation. When a certain direction is saturated, the solution is $u = u_b$, where u_b is located on the edge of AMS, pointing from the origin to the intersection point. The solution u_b represents the maximum output ability of the system.

56.4 Simulation

56.4.1 System Description

The model of a spacecraft with reaction wheels is

$$\begin{aligned}
& I_x\ddot{\phi} + \left[\left(I_y - I_z\right)\omega_0^2 - \omega_0 h_y(t)\right]\phi + \\
& \left[\left(I_y - I_z - I_x\right)\omega_0 - h_y(t)\right]\dot{\phi} = -\dot{h}_x(t) + \omega_0 h_z(t) \\
& I_y\ddot{\theta} + h_x(t)\left(\dot{\phi} + \omega_0\varphi\right) - h_z(t)\left(\dot{\phi} - \omega_0\phi\right) = -\dot{h}_y(t) \\
& I_z\ddot{\phi} + \left[\left(I_y - I_x\right)\omega_0^2 - \omega_0 h_y(t)\right]\phi - \\
& \left[\left(I_y - I_z - I_x\right)\omega_0 - h_y(t)\right]\dot{\phi} = -\dot{h}_z(t) - \omega_0 h_x(t)
\end{aligned} \tag{56.42}$$

where ϕ, θ, and φ are Euler angles; I_x, I_y and I_z are the moments of inertia; $h_x(t)$, $h_y(t)$, and $h_z(t)$ are the total angular momenta in the axis directions; and ω_0 is the orbital angular velocity.

For a spacecraft with reaction wheels, attitude regulation is achieved by angular momentum exchanges between the satellite and wheels. We define $h(t) = \{h_1(t), \ldots, h_{n_u}(t)\}$, where n_u is the number of momentum wheels.

$$h(t) = h_0 + \int_{t_0}^{t} \dot{h}(t)\mathrm{d}\tau \tag{56.43}$$

where $h(t)$ should be calculated at every time-step, which increases the complexity. Equation (56.42) can be written in vector form as

$$\begin{aligned} \dot{x}(t) &= \mathrm{A}_1^{-1}(\mathrm{A}_2 + \Delta A)x(t) + \mathrm{A}_1^{-1}\mathrm{B}_1 v_1(t) + \mathrm{A}_1^{-1}\xi_1(t) \\ &= \mathrm{A}x(t) + \mathrm{B}v_1(t) + \xi_0(t) \end{aligned} \tag{56.44}$$

where $x = \begin{bmatrix} \varphi & \dot{\varphi} & \theta & \dot{\theta} & \psi & \dot{\psi} \end{bmatrix}^T$, $\mathrm{A}_1 = \mathrm{diag}([1 \quad \mathrm{I_x} \quad 1 \quad \mathrm{I_y} \quad 1 \quad \mathrm{I_z}])$, $\mathrm{A} = \mathrm{A}_1^{-1}\mathrm{A}_2$, $B = \mathrm{A}_1^{-1}\mathrm{B}_1$, $\xi_0(t) = \mathrm{A}_1^{-1}\xi_1(t) + \mathrm{A}_1^{-1}\Delta\mathrm{A}x(t)$,

$$\mathrm{A}_2 = \begin{bmatrix} 0, & 1, & 0, & 0, & 0, & 0 \\ -(I_y - I_z\omega_0^2), & 0, & 0, & 0, & 0, & -(I_y - I_z - I_x)\omega_0 \\ 0, & 0, & 0, & 1, & 0, & 0 \\ 0, & 0, & 0, & 0, & 0, & 0 \\ 0, & 0, & 0, & 0, & 0, & 1 \\ 0, & (I_y - I_z - I_x)\omega_0, & 0, & 0, & -(I_y - I_x)\omega_0^2, & 0 \end{bmatrix},$$

$$\Delta A = \begin{bmatrix} 0 & 0 & 0 & 0 & 0 & 0 \\ \omega_0 h_y & 0 & 0 & 0 & 0 & h_y \\ 0 & 0 & 0 & 0 & 0 & 0 \\ -\omega_0 h_x & h_z & 0 & 0 & -h_z\omega_0 & -h_x \\ 0 & 0 & 0 & 0 & 0 & 0 \\ 0 & -h_y & 0 & 0 & \omega_0 h_y & 0 \end{bmatrix},$$

$$\mathrm{B}_1 = \begin{bmatrix} 0 & 1 & 0 & 0 & 0 & 0 \\ 0 & 0 & 0 & 1 & 0 & 0 \\ 0 & 0 & 0 & 0 & 0 & 1 \end{bmatrix}^T,$$

$$\xi_1(t) = [\,0 \quad \omega_0 h_z(t) \quad 0 \quad 0 \quad 0 \quad -\omega_0 h_x(t)\,]^T,$$

$$v(t) = -\begin{bmatrix} \dot{h}_x(t) & \dot{h}_y(t) & \dot{h}_z(t) \end{bmatrix}^T = -B_0\dot{h}(t)$$

Adding uncertainties into (56.44), we obtain

$$\dot{x}(t) = Ax(t) + Bv(t) + \xi(t) \tag{56.45}$$

where $v(t) = v_1(t) + B^+\xi_0 = B_0W(t)u(t) + B^+\xi_0$.

Next, (56.45) should be written in a discrete form as discussed in (56.10). Considering the inaccuracy of the efficiency factors discussed in (56.7) $\sim$ (56.9) and rewriting (56.45) in a discrete form leads to

$$\begin{cases} x_{k+1} = \Phi x_k + \Gamma\left(v_k + \xi_{m,k}\right) + T\xi_{u,k} \\ v_k = B_0\widehat{W}_{u_k} + B^+\xi_0 - B_0\delta_k u_k \end{cases} \tag{56.46}$$

where $\delta_k = \left\{\delta_1, \delta_2, \ldots, \delta_p\right\}$ is the inaccuracy matrix of all efficiency factors, $\Phi = I + AT$ and $\Gamma = TB$.

56.4.2 Simulation Results

The parameters used are $I_x = 200\,\text{kgm}^2$, $I_y = 100\,\text{kgm}^2$, $I_z = 180\,\text{kgm}^2$, $\omega_0 = 2\pi/36000$, $T = 0.01\,\text{s}$, $\beta = 35.26°$. The uncertainties are $\xi_m = [0.05\sin(-2\pi t)\ 0\ 0]^{\mathrm{T}}$, $\xi_{u1} = \begin{bmatrix} 0.05e^{-2\pi t} & 0 & 0 & 0 & 0 & 0 \end{bmatrix}^T$, $\xi_{u2} \in L_\infty = \begin{bmatrix} 0.05\sin(-2\pi t) & 0 & 0 & 0 & 0 & 0 \end{bmatrix}^T$.

Case I: Faults δ, ξ_m and ξ_{u1} exist

In this case, $\hat{W} = \text{diag}(\begin{bmatrix} 0.8 & 1 & 0.6 & 1 & 1 & 1 \end{bmatrix})$, $\delta = \text{diag}(\begin{bmatrix} 0.1 & 0 & 0.2 & 0 & 0 & 0 \end{bmatrix})$. Matched uncertainty ξ_m and unmatched uncertainty ξ_{u1} exist. Faults occur at $t = 3\,\text{s}$, when $t > 3\,\text{s}$, $\hat{W} = \text{diag}(\begin{bmatrix} 1 & 0 & 1 & 0 & 1 & 1 \end{bmatrix})$, i.e., two wheels are totally stuck. The initial values are $x_0 = \begin{bmatrix} 0.1 & 0 & 0 & 0 & 0 & 0 \end{bmatrix}^T$, $u_0 = \begin{bmatrix} 0 & 0 & 0 & 0 & 0 & 0 \end{bmatrix}^T$.

The controller, designed as shown in (56.12), is

$$v_k = -K_0x_k - \hat{\xi}_{m,k} - (G\Gamma)^{-1}GT\hat{\xi}_{u,k} - (G\Gamma)^{-1}\sigma_k \tag{56.47}$$

where K is obtained using the MATLAB function "place" as "K = place(Φ, Γ, ker)" and $\ker = \begin{bmatrix} 0.991 & 0.992 & 0.993 & 0.994 & 0.995 & 0.996 \end{bmatrix}$; $\hat{\xi}_{u,k}$ and $\hat{\xi}_{m,k}$ is obtained by (56.13).

After simulation, the system states are shown in Fig. 56.2. Input commands for all actuators are shown in Fig. 56.3. The outputs of the actuators are Wu. From the simulation, we can see that all faults and uncertainties have been well treated by our

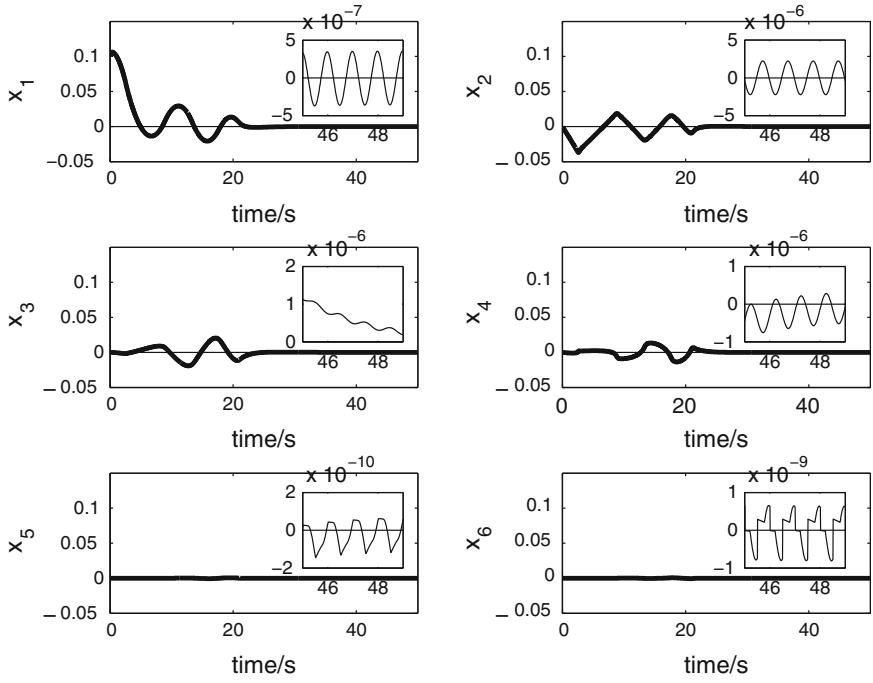

Fig. 56.2 State variable histories for case I

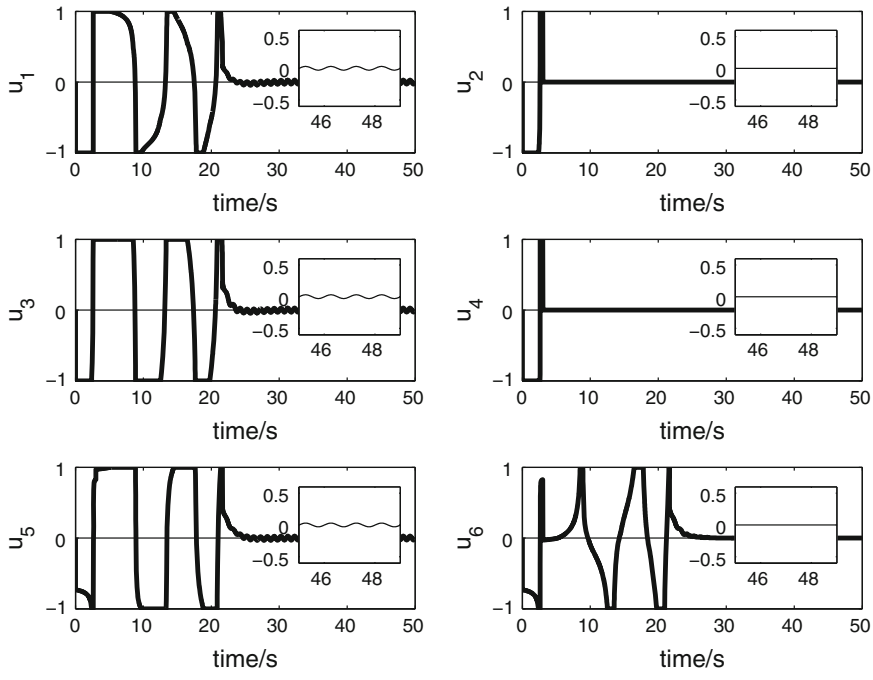

Fig. 56.3 Wheel output histories for case I

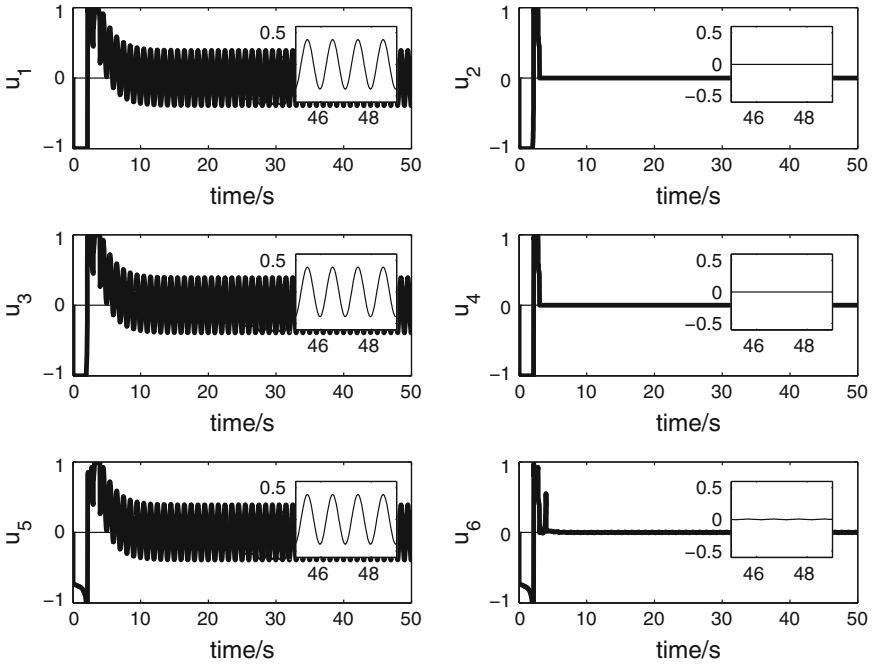

Fig. 56.5 Wheel output histories for case II

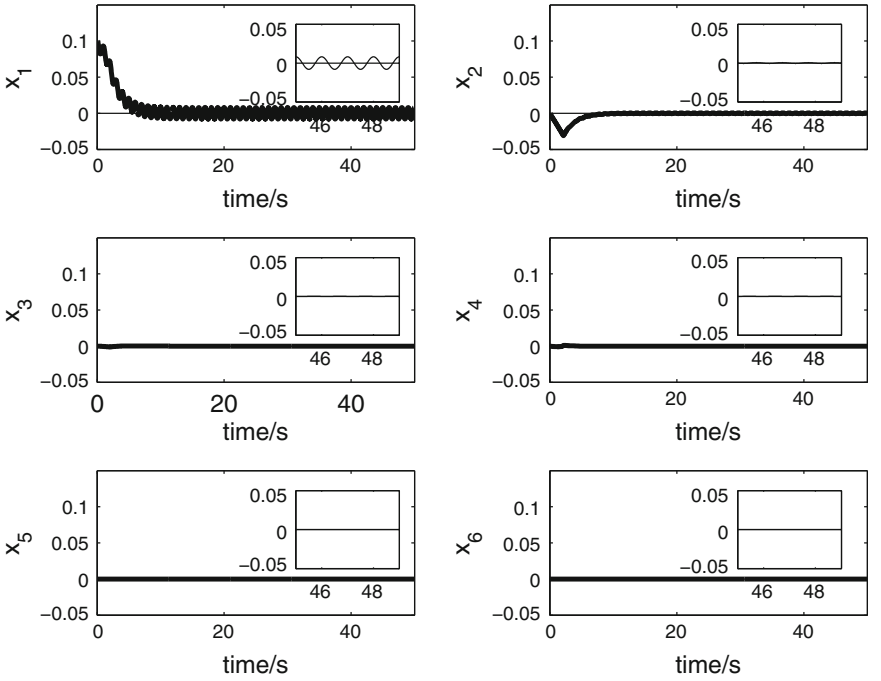

Fig. 56.4 State variable histories for case II

controller and the final accuracy of $x(k)$ is 10^{-6}. Because $x(k) < O(T^2) = 10^{-4}$, Proposition 56.2 is satisfied for all state variables.

Case II: Faults δ, ξ_m and ξ_{u2} exist

In this case, all the initial conditions and parameters are the same as those of case I, but with a different kind of unmatched uncertainties, ξ_{u2}. The controller is also designed as (56.12), which is not repeated here. The simulation results are illustrated in Figs. 56.4 and 56.5. From the figures, it is obvious that the system states is maintained within a certain bound. According to Proposition 56.2, the final boundary is $\|x\| \leq \frac{0.05*0.01+0.0001}{(1-0.996)} = 0.15$, and it is clear that the simulation results meet the analysis requirements.

56.4.3 Simulation Summary

We discuss FTC problems for a spacecraft with multi-faults, efficiency factor inaccuracies, matched uncertainties, and unmatched uncertainties in this section. Simulations show that the efficiency factor inaccuracy problem is addressed satisfactorily using matched uncertainties. Two cases for unmatched uncertainties are discussed and simulated: (1) $\xi_u \in L_2 \bigcap L_\infty$; (2) $\xi_u \in L_\infty$. Figures 56.2 and 56.3 show that if $\xi_u \in L_2 \bigcap L_\infty$, the system is stable, whereas Figs. 56.4 and 56.5 illustrate that if $\xi_u \in L_\infty$, x is bounded. The simulations prove Proposition 56.2.

56.5 Conclusions

This paper is devoted to FTC for discrete-time multi-input multi-output LTI systems with matched/unmatched uncertainties. The discrete-time sliding mode and control allocation are researched. Both matched and unmatched uncertainties are studied for closed-loop stability and final state boundaries with a discrete-time sliding mode controller. The uncertainties caused by the inaccuracy of efficient factors are treated as matched uncertainties (ξ_m). With the controller in this paper, it is concluded that the size and nature of unmatched uncertainties (ξ_u) determine the stability of the final closed-loop system. Two different cases $\xi_u \in L_\infty$ and $\xi_u \in L_2 \bigcap L_\infty$ are explored, with bounded or stable $(O(T^2))$ system final states. Control allocation is important for FTC, and we improve the direct method by rearranging the facets of the AMS with an angle indicator for decreasing the number of calculations required. Our proposed scheme is tested using an spacecraft model in simulations in the presence of multi-faults, inaccurate efficiency factors, matched uncertainties, and two kinds of unmatched uncertainties.

References

1. Lombaerts T, Oort EV, Chu QP, Mulder JA, Joosten D (2010) Online aerodynamic model structure selection and parameter estimation for fault tolerant control. J Guidance Control Dyn 33(3):707–723
2. Alwi H, Edwards C (2010) Evaluation of a sliding mode fault-tolerant controller for the El Al incident. J Guidance Control Dyn 33(3):677–694
3. Cao L, Chen XQ, Sheng T (2013) Fault tolerant small satellite attitude control using adaptive non-singular terminal sliding mode. Adv Space Res 51(12):2374–2393
4. Cai WC, Liao XH, Song DY (2008) Indirect robust adaptive fault-tolerant control for attitude tracking of spacecraft. J Guidance Control Dyn 31(5):1456–1463
5. Zhang YM, Jiang J (2008) Bibliographical review on reconfigurable fault-tolerant control systems. Ann Rev Control 32(2):229–252
6. Xu JX, Pan YJ, Lee TH (2003) Analysis and design of integral sliding mode control based on Lyapunov's direct method. In: Proceedings of the American control conference Denver, pp 192–196, June 2003
7. Rubagotti M, Estrada A, Castanos F, Ferrara A, Fridman L (2011) Integral sliding mode control for nonlinear systems with matched and unmatched perturbations. IEEE Trans Autom Control 56(11):2011–2699
8. Choi HH (2011) On the existence of linear sliding surfaces for a class of uncertain dynamic systems with mismatched uncertainties. Automatica 35:2699–2011
9. Cao WJ, Xu JX (2004) Nonlinear integral-type sliding surface for both matched and unmatched uncertain systems. IEEE Trans Autom Control 49(8):1355–1360
10. Castaños F, Fridman L (2006) Analysis and design of integral sliding manifolds for systems with unmatched perturbations. IEEE Trans Autom Control 51(5):853–858
11. Hamayun MT, Edwards C, Alwi H (2010) Integral sliding mode fault tolerant control incorporating on-line control allocation. In: 2010 11th International Workshop on variable structure systems Mexico City, pp 100–105, 26–28 June 2010
12. Alwi H, Edwards C (2008) Fault tolerant control using sliding modes with on-line control allocation. Automatica 47(7):859–1866
13. Hamayun MT, Edwards C, Alwi H (2012) Design and analysis of an integral sliding mode fault-tolerant control scheme. IEEE Trans Autom Control 57(7):1783–1789
14. Su WC, Drakunov SV, Özgüner Ü (2000) An $O(T^2)$ boundary layer in sliding mode for sampled-data systems. IEEE Trans Autom Control 45(3):482–485
15. Pai MC (2009) Robust tracking and model following of uncertain dynamic systems via discrete-time integral sliding mode control. Int J Control Autom Syst 7(3):374–381
16. Abidi K, Xu JX, Xinghuo Y (2007) On the discrete-time integral sliding-mode control. IEEE Trans Autom Control 52(4):709–715
17. Xi Z, Hesketh T (2010) Brief paper: discrete time integral sliding mode control for systems with matched and unmatched uncertainties. Control Theor Appl 4(5):889–896
18. Durham WC (1994) Attainable moments for the constrained control allocation problem. J Guidance Control Dyn 17(6):1371–1379
19. Durham WC (1994) Constrained control allocation: three-moment problem. J Guidance Control Dyn 17(2):330–336
20. Jin J (2005) Modified pseudoinverse redistribution methods for redundant controls allocation. J Guidance Control Dyn 28(5):1076–1079
21. Tjønnås J, Johansen TA (2008) Adaptive control allocation. Automatica 44(11):2754–2765
22. Edwards C, Spurgeon SK, Patton RJ (2000) Sliding mode observers for fault detection and isolation. Automatica 36:541–553

Chapter 57
Parametric Design of a Descriptor Functional Observer for Standard Linear Systems

Guosheng Wang, Feng Guo and Bing Liang

Abstract A parametric design problem of a descriptor functional observer for standard linear systems is investigated. The design aim of the descriptor functional observer for standard linear systems is to present the parametric form of the descriptor functional observer which can estimate the system state as the time goes into infinity. Based on the parametric solutions for a class of Sylvester matrix equations, the parametric expressions of all the gain matrices for the descriptor functional observer in standard linear systems are proposed. Finally, a numerical example and its simulation results show that the proposed parametric design method of the descriptor functional observer for standard linear systems is effective and simple.

Keywords Standard linear system · Descriptor functional observer · Parametric design

57.1 Introduction

Since state estimation is initially proposed [1, 2], the theory of observers for linear time-invariant systems, which reconstruct the state from measurements of the input and output, is well established [3–6]. An impulsive observer that estimates the exact state of a linear continuous-time system in predetermined finite time is investigated in [3]. Design of finite time state observers in linear time-invariant systems is investigated in [4]. Design of parametric unknown input observers in linear

G. Wang (✉) · F. Guo
Department of Control Engineering, Academy of Armored Force Engineering, Beijing 100072, China
e-mail: gswang@126.com

B. Liang
School of Information Engineering, Jiangxi University of Science and Technology, Ganzhou 341000, China
e-mail: lbwgs@126.com

Z. Deng and H. Li (eds.), *Proceedings of the 2015 Chinese Intelligent Automation Conference*, Lecture Notes in Electrical Engineering 337,
DOI 10.1007/978-3-662-46463-2_57

time-invariant systems is investigated in [5]. The design of a perfect reduced-order unknown-input observer for standard systems is formulated and solved in [6]. By using a parametric solution for a class of Sylvester matrix equations [7–9], the parametric expressions of all the gain matrices for the descriptor functional observer for standard linear systems are proposed in this paper.

57.2 Problem Formulation

Consider a class of standard linear systems in the form of

$$\begin{cases} \dot{x}(t) = Ax(t) + Bu(t) \\ y(t) = Cx(t) \end{cases}, \quad x(t_0) = x_0,\ t \geq t_0, \tag{57.1}$$

where $x \in \Re^n$, $u \in \Re^p$ and $y \in \Re^q$ are the state vector, the input vector, and the output vector, respectively, of system (57.1); $A \in \Re^{n\times n}$, $B \in \Re^{n\times p}$ and $C \in \Re^{q\times n}$ are known matrices satisfying the following two assumptions:

Assumption 57.1 $\text{rank}(B) = p$ and $\text{rank}(C) = q$;

Assumption 57.2 The matrix pair $(A,\ C)$ is observable, that is,

$$\text{rank}\begin{bmatrix} sI - A^T & C^T \end{bmatrix} = n,\ \forall s \in \mathbb{C}$$

Consider a functional observer of form

$$\begin{cases} E\dot{z} = Fz + Gu + Hy \\ \hat{x} = Pz + Qy \end{cases} \tag{57.2}$$

where $z \in \Re^n$ is the state vector of observer (57.2), and $E \in \Re^{n\times n}$ with $\text{rank}(E) = n$, $F \in \Re^{n\times n}$, $G \in \Re^{n\times p}$, $H \in \Re^{n\times q}$, $P \in \Re^{n\times n}$ and $Q \in \Re^{n\times q}$ are the gain matrices of observer (57.2) to be determined.

Definition 57.1 Given the standard linear system (57.2) satisfying Assumptions A1 and A2, if there exist constant matrices $E \in \Re^{n\times n}$, $F \in \Re^{n\times n}$, $G \in \Re^{n\times p}$, $H \in \Re^{n\times q}$, $P \in \Re^{n\times q}$ and $Q \in \Re^{n\times n}$ in (57.2) such that the following two conditions hold simultaneously:

$$\lim_{t\to\infty}[z(t) - Tx(t)] = 0 \ \text{ and } \ \lim_{t\to\infty}[\hat{x}(t) - x(t)] = 0 \tag{57.3}$$

where $T \in \Re^{n\times n}$, the observer (57.2) is called as a descriptor functional observer of system (57.1).

Problem DPDFO (Parametric Design of Descriptor Functional Observer). Given the standard linear system (57.1) satisfying Assumptions A1 and A2, if the

descriptor functional observer exits, determine the parametric expressions of the gain matrices $E \in \Re^{n\times n}$, $F \in \Re^{n\times n}$, $T \in \Re^{n\times n}$, $G \in \Re^{n\times p}$, $H \in \Re^{n\times q}$, $P \in \Re^{n\times q}$ and $Q \in \Re^{n\times n}$ in (57.2) and (57.3) such that the estimation conditions (57.3) hold.

57.3 Solution to Problem DPDFO

57.3.1 Existing Condition for the Descriptor Functional Observer

In the next theorem, we give the necessary and sufficient condition for the descriptor functional observer.

Theorem 57.1 *Given the linear time-invariant system* (57.1) *satisfying Assumption A1 and Assumption A2, the descriptor functional observer* (57.2) *for the standard linear system* (57.1) *exists if and only the following equations hold*

$$FT - ETA + HC = 0 \tag{57.4}$$

$$G - ETB = 0 \tag{57.5}$$

and

$$QC + PT - I = 0 \tag{57.6}$$

Proof Denote the observer error by

$$e_1 = z(t) - Tx(t) \tag{57.7}$$

Multiplying E_1 on both the left sides of (57.7) and differentiating the obtained result with respect to time, we obtain

$$E\dot{e}_1 = E\dot{z}(t) - ET\dot{x}(t) \tag{57.8}$$

Substituting (57.1) and (57.2) into (57.8), we obtain

$$E\dot{e}_1 = E\dot{z}(t) - ET\dot{x}(t) = Fe_1 + (FT - ETA + HC)x + (G - ETB)u \tag{57.9}$$

From (57.9), we can find that

$$E\dot{e}_1 = Fe_1 \tag{57.10}$$

holds, if and only if the following conditions hold:

$$FT - ETA + HC = 0 \tag{57.11}$$

and

$$G - ETB = 0 \tag{57.12}$$

while the following condition holds

$$\lim_{t\to\infty} e_1 = \lim_{t\to\infty} [z(t) - Tx(t)] = 0 \tag{57.13}$$

if and only if the eigenvalues of the matrix pair (E, F) have negative real parts.

In addition, we denote the state estimator as

$$e_2 = \hat{x}(t) - x(t) \tag{57.14}$$

Substituting (57.2) into (57.14), we obtain

$$e_2 = \hat{x}(t) - x(t) = Pe_1 + (QC + PT - I)x \tag{57.15}$$

From (57.14), we can find that

$$e_2 = Pe_1 \tag{57.16}$$

if and only if the following condition holds:

$$QC + PT - I = 0 \tag{57.17}$$

Based on the above reductions, we know that the two conditions in (57.3) hold for the descriptor functional observer of system (57.1) if and only if Eqs. (57.4), (57.5), and (57.6) hold. □

Based on Theorem 57.1, we will put forward the parametric expressions of the gain matrices of the descriptor functional observer in the standard linear system for Problem DPDFO and the corresponding algorithm to design the parametric descriptor functional observer of the standard linear system in the next two subsections.

57.3.2 Parametric Solutions to Matrices E, F, T and H

Because of $\text{rank}(E) = n$, without loss of generality, we select the matrix E as a Vandermonde matrix in the following form:

$$E = \begin{bmatrix} 1 & a_1 & a_1^2 & \cdots & a_1^{n-1} \\ 1 & a_2 & a_2^2 & \cdots & a_2^{n-1} \\ \vdots & \vdots & \vdots & \vdots & \vdots \\ 1 & a_{n-1} & a_{n-1}^2 & \cdots & a_{n-1}^{n-1} \\ 1 & a_n & a_n^2 & \cdots & a_n^{n-1} \end{bmatrix} \tag{57.18}$$

where $a_i, i = 1, 2, \ldots, n$ can be selected from any real scalars.

From (57.4), we can obtain

$$FTE - ETAE + HCE = 0 \tag{57.19}$$

Denote

$$TE = T_1 \tag{57.20}$$

$$AE = A_1 \tag{57.21}$$

and

$$CE = C_1 \tag{57.22}$$

Then Eq. (57.19) can be changed into

$$FT_1 - T_1A_1 + HC_1 = 0 \tag{57.23}$$

Assume that the matrix F is nondefective, thus the matrix can be written as

$$F = W\,\Lambda W^{-1} \tag{57.24}$$

where $\Lambda = \mathrm{diag}(s_1, s_2, \ldots, s_n)$, $s_i, i = 1, 2, \ldots, n$ is a group of distinct complex scalars that are self-conjugate and have negative real parts, and the matrix W is an eigenvector matrix of the matrix F.

Substituting (57.24) into (57.24), we obtain

$$\Lambda W^{-1}T_1 - W^{-1}T_1A_1 + W^{-1}HC_1 = 0 \tag{57.25}$$

Denote

$$T_2 = W^{-1}T_1 \tag{57.26}$$

and

$$H_1 = W^{-1}H \tag{57.27}$$

From (57.24), we can obtain

$$\Lambda T_2 - T_2 A_1 + H_1 C_1 = 0 \tag{57.28}$$

Transposing (57.27), we obtain

$$A_1^T T_2^T - C_1^T H_1^T = T_2^T \Lambda \tag{57.29}$$

Because the matrix pairs $(A,\ C)$ and $(AE,\ CE)$ are controllable, there are two polynomial matrices $N(s) \in \Re^{n\times q}[s]$ and $D(s) \in \Re^{q\times q}[s]$ such that

$$\begin{bmatrix} sI - (AE)^T & (CE)^T \end{bmatrix} \begin{bmatrix} N(s) \\ D(s) \end{bmatrix} = 0, \quad \forall s \in \mathbb{C} \tag{57.30}$$

From the reference [7–9], we can obtain the column vectors of matrices T_2 and H_1, respectively, as

$$\begin{bmatrix} t_{2i} \\ h_{1i} \end{bmatrix} = \begin{bmatrix} g_i^T N^T(s_i) \\ g_i^T D^T(s_i) \end{bmatrix}, \quad i = 1, 2, \cdots, n \tag{57.31}$$

where the parametric vectors $g_i \in \mathbb{C}^q$, $i = 1, 2, \ldots, n$ satisfy the following constraint:

Constraint C1. $s_i = \overline{s_k} \Leftrightarrow g_i = \overline{g_k}$, $i = 1, 2, \ldots, n$.

Thus

$$T_2 = \begin{bmatrix} g_1^T N^T(s_1) & g_2^T N^T(s_2) & \cdots & g_n^T N^T(s_n) \end{bmatrix} \tag{57.32}$$

and

$$H_1 = \begin{bmatrix} g_1^T D^T(s_1) & g_2^T D^T(s_2) & \cdots & g_n^T D^T(s_n) \end{bmatrix} \tag{57.33}$$

From (57.19), (57.25) and (57.31), we can obtain the parametric expression of the matrix T as

$$T = W \begin{bmatrix} g_1^T N^T(s_1) & g_2^T N^T(s_2) & \cdots & g_n^T N^T(s_n) \end{bmatrix} E^{-1} \tag{57.34}$$

From (57.26) and (57.32), we can obtain the parametric expression of the matrix H as

$$H = W \begin{bmatrix} g_1^T D^T(s_1) & g_2^T D^T(s_2) & \cdots & g_n^T D^T(s_n) \end{bmatrix} \tag{57.35}$$

57.3.3 Parametric Solutions to Matrices G, Q, and P

From (57.5), we can obtain

$$G = EW\left[g_1^T N^T(s_1) \quad g_2^T N^T(s_2) \quad \cdots \quad g_n^T N^T(s_n)\right]E^{-1}B \tag{57.36}$$

From (57.6), we can obtain

$$[Q \quad P] = \left[\begin{matrix} C \\ W\left[g_1^T N^T(s_1) \quad g_2^T N^T(s_2) \quad \cdots \quad g_n^T N^T(s_n)\right]E^{-1} \end{matrix}\right]^+ \tag{57.37}$$

where $[.]^+$ stands for the matrix's pseudoinverse.

57.4 A Numerical Example

Consider the standard linear system (57.1) with the parameters

$$A = \begin{bmatrix} -15 & 21 & -8 \\ 4 & -7 & 3 \\ -1.5 & 3 & -1.5 \end{bmatrix},\ B = \begin{bmatrix} 0 \\ 0 \\ 1 \end{bmatrix},\ C = \begin{bmatrix} 6 & -8 & 3 \\ -3.5 & 6 & -2.5 \end{bmatrix}$$

We select the matrix E as

$$E = \begin{bmatrix} 1 & 2 & 4 \\ 1 & 3 & 9 \\ 1 & 4 & 16 \end{bmatrix}$$

It is easy to test that the matrix pairs (A, C) and (AE, CE) are observable. Compute the polynomial matrices $N(s)$ and $D(s)$ satisfying (57.30) as

$$N(s) = \begin{bmatrix} s+3 & -1 \\ 0 & 1 \\ 1 & 0 \end{bmatrix},\ D(s) = \begin{bmatrix} -s^2 - 5s - 6 & s+2 \\ s+3 & -s-2 \end{bmatrix}$$

Without loss of generality, we choose the matrix F as

$$F = \begin{bmatrix} -2 & 0 & 0 \\ 0 & -3 & 0 \\ 0 & 0 & -5 \end{bmatrix}$$

Thus the eigenvalues of the Hurwitz matrix F are by $s_1 = -2$, $s_2 = -3$, $s_3 = -5$ and the eigenvector matrix W of matrix F is $W = I_3$. Denote the free parameter vectors $g_i \in \mathbb{C}^2$, $i = 1, 2, 3$ by

$$g_1 = \begin{bmatrix} a \\ b \end{bmatrix},\ g_2 = \begin{bmatrix} c \\ d \end{bmatrix},\ g_3 = \begin{bmatrix} e \\ f \end{bmatrix}$$

where a, b, c, d, e, and f are real scalars.

Calculate the parametric expressions of the matrices T and H from (57.34) and (57.35) as

$$T = \begin{bmatrix} 6a - 6b + 3.5d - e - 0.5f & 8b - 8a - 6d + 2e + f & 3a - 3b + 2.5d - e - 0.5f \\ 6b - 3.5d + 0.5f & 6d - 8b - f & 3b - 2.5d + 0.5f \\ 6a - 3.5c + 0.5e & 6c - 8a - e & 3a - 2.5c + 0.5e \end{bmatrix}$$

$$H = \begin{bmatrix} 0 & a \\ -d & d \\ -6e - 3f & 3f - 2e \end{bmatrix}$$

From (57.36), we can obtain

$$G = \begin{bmatrix} 197.5a + 39.5b - 107c - 26.75d + 8.5e + 4.25f \\ 395a + 79b - 240.75c - 53.5d + 29.75e + 8.5f \\ 671.5a + 118.5b - 428c - 80.25d + 59.5e + 12.75f \end{bmatrix}$$

From (57.37), we can obtain the parametric expressions of matrices Q and P. Because their expressions are too long, we don't show them in this paper.

Specially, we select the free parametric vector as

$$g_1 = \begin{bmatrix} -1 \\ 1 \end{bmatrix},\ g_2 = \begin{bmatrix} 0 \\ -1 \end{bmatrix},\ g_3 = \begin{bmatrix} -1 \\ 0 \end{bmatrix}$$

And we can obtain

$$T = \begin{bmatrix} -14.5 & 20 & -7.5 \\ 9 & -14 & 5.5 \\ -6.5 & 9 & -3.5 \end{bmatrix},\ H = \begin{bmatrix} 0 & -1 \\ 1 & -1 \\ 6 & 2 \end{bmatrix},\ G = \begin{bmatrix} -139.75 \\ -292.25 \\ -532.25 \end{bmatrix}$$

$$Q = \begin{bmatrix} 2.7188 & 1.1797 \\ 5.3125 & 1.3711 \\ 9.4063 & 1.3574 \end{bmatrix},\ P = \begin{bmatrix} 1.6563 & 0.8281 & -0.75 \\ 3.8594 & 2.2344 & -1.2813 \\ 6.9219 & 4.2734 & -2.1094 \end{bmatrix}$$

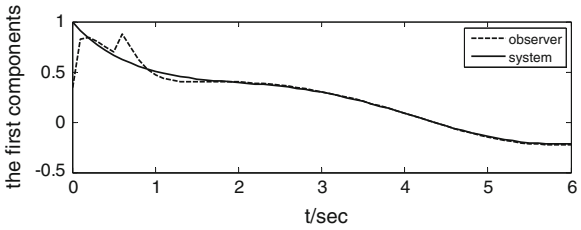

Fig. 57.1 The first state components of the system and the observer

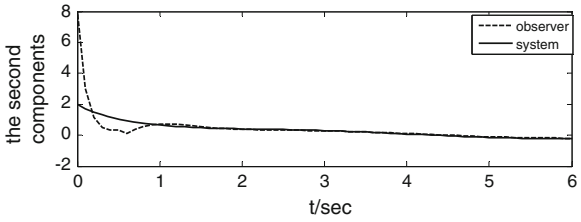

Fig. 57.2 The second state components of the system and the observer

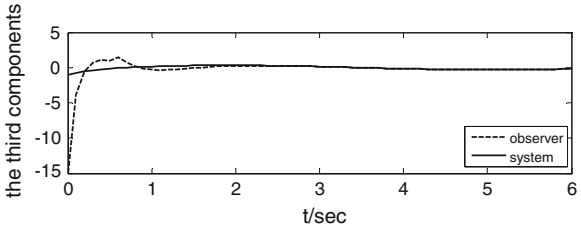

Fig. 57.3 The third state components of the system and the observer

Substituting the above gain matrices into the descriptor functional observer in (57.2), we finish the design of the descriptor functional observer in this standard linear system. Assume that $u(t) = \sin t$ is the input signal of the system (57.1), $x_0 = [1 \quad 2 \quad -1]^T$ is the initial state of the system (57.1) and $z_0 = [5 \quad 7 \quad 8]^T$ is the initial state of the descriptor functional observer. Using the Matlab function ODE45, we give the simulation results to compare the state components of system (57.1) and the descriptor functional observer in Figs. 57.1, 57.2 and 57.3. We can see that the errors between the linear system and the designed descriptor functional observer converge to zero as time goes into infinity.

57.5 Conclusion

In this paper the design problem of a descriptor functional observer for standard linear systems is studied. The parametric expressions of the gain matrices for the descriptor functional observer are proposed by using the parametric solution to a class of the matrix equations. Finally, the simulation results show that this proposed method of designing the descriptor functional observer in standard linear systems is simple and effective.

References

1. Kalman R, Bucy R (1961) Observing the state of a linear system. ASME J Basic Eng 83(3):95
2. Luenberger D (1964) Observing the state of a linear system. IEEE Trans Mil Electron 8(3):74
3. Raff T, Allgower F (2007) An impulsive observer that estimate the exact state of a linear continuous-time system in predetermined finite time. In: Proceedings of the 11th mediterranean conference on control and automation, 1
4. Wang G, Xia F, Liang, B (2014) A parametric design method of finite time state observers in linear time-invariant systems. In: 26th Chinese control and decision conference, p 795
5. Wang G, Li W, Guo F, Xia F (2014) Design of parametric unknown input observers in linear time-invariant systems. In: Proceeding of the 11th world congress on intelligent control and automation, p 4048
6. Krzemi S, Kaczorek S (2004) Perfect reduced-order unknown-input observer for standard systems. Bull Pol Acad Sci Tech Sci 52(2):103
7. Duan G (1993) Solutions to matrix equation AV + BW = VF and their application to eigenstructure assignment in linear systems. IEEE Trans Autom Control 38(2):276
8. Wang G, Lv Q, Duan G (2007) On the parametric solution to the second-order Sylvester matrix equation EVF2 − AVF − CV = BW. Math Probl Eng 4(2):1
9. Wang G, Wang H, Duan G (2009) On the robust solution to a class of perturbed second-order Sylvester equation. Dyn Continuous Discrete Impulsive Syst Ser A Math Anal 16(1):439

Chapter 58
Stability Analysis of FDCM-Based Controller for Hypersonic Vehicles

Xiong Luo and Ruixin Li

Abstract Adaptive control is a fundamental problem in control system design. This paper addresses an important but challenging issue in the design of intelligent adaptive controllers, which is the stability guarantee. The intelligent adaptive control based on fuzzy dynamic characteristic modeling (FDCM) was proposed for nonlinear system design and analysis through the combination of fuzzy dynamic modeling and characteristic modeling approaches. Motivated by our previous research work, we discuss the stability properties of an FDCM-based controller in its application of hypersonic vehicle. Considering the requirement of complex controller design for hypersonic vehicle, an FDCM-based control design structure is first developed. Then, under some conditions in system parameters of FDCM, our controller stability analysis problem is formulated. By defining a Lyapunov function and using the Lyapunov stability construct, we develop a new result of uniformly asymptotic stability for the proposed FDCM-based controller in hypersonic vehicle control application. This result provides a theoretical guarantee to our proposed controller design and implementation.

Keywords Fuzzy dynamic characteristic modeling (FDCM) · Stability analysis · Controller · Nonlinear golden section controller

58.1 Introduction

Adaptive controller design has been a long-term focus in the control system community to provide mechanisms to control complex nonlinear systems. There is considerable enthusiasm for the research and application of adaptive control methods

X. Luo (✉) · R. Li
School of Computer and Communication Engineering, University of Science and Technology Beijing (USTB), 30 Xueyuan Road, Haidian District, Beijing 100083, China
e-mail: xluo@ustb.edu.cn

X. Luo · R. Li
Beijing Key Laboratory of Knowledge Engineering for Materials Science, 30 Xueyuan Road, Haidian District, Beijing 100083, China

Z. Deng and H. Li (eds.), *Proceedings of the 2015 Chinese Intelligent Automation Conference*, Lecture Notes in Electrical Engineering 337,
DOI 10.1007/978-3-662-46463-2_58

for nonlinear systems. Although many approaches have been used for adaptive control purpose for well over the last decade, their application either has been limited to low-dimensional plants or has been limited to high-dimensional systems in which accurate mathematical models are available or fully understood. Therefore, it is obvious that the difficulties of obtaining a tractable yet accurate mathematical model impose a very challenging obstacle to the controller design problem.

To cope with this obstacle, an effective design method, namely all-coefficient adaptive control, was proposed through the use of the characteristic modeling approach and the golden-section control strategy [1]. While designing such a controller, no accurate model is needed, even the approximate model is not very important. Considering the control performance requirements in engineering practice, this characteristic-modeling-based adaptive control can serve as an alternative and complementary technique in nonlinear system control problem. Furthermore, to improve the modeling performance for complex nonlinear systems, this method can be redesigned with the help of fuzzy dynamic modeling strategy which provides an effective framework for modeling by decomposing a nonlinear into a collection of local linear models [2]. Then, motivated by the fuzzy dynamic modeling method and characteristic modeling method, we presented a novel system analysis approach, namely fuzzy dynamic characteristic modeling (FDCM) method [3]. Due to its fuzzy-rule-based scalability of the fuzzy dynamic model worked as a universal approximator and the practice-requirement-oriented simplification of the characteristic model defined as a second-order differential equation, FDCM plays an important role in dealing with the nonlinear tracking control problems. Because of its unique features, FDCM has been applied to some complex control problems, such as hypersonic vehicle control [4–6], networked control [7], and so on. Although the FDCM-based control system framework was implemented in our previous research work [4], the stability analysis results for the control system of nonlinear cases are inadequate. Motivated by it, the purpose of the present paper is to give a new result of uniformly asymptotic stability for the FDCM-based controller under its application for hypersonic vehicle control problem. This result provides a theoretical guarantee to our proposed controller design and implementation for complex applications.

58.2 Preliminaries

58.2.1 Characteristic Model-Based All-Coefficient Adaptive Control

In view of the practical needs of controller, the characteristic modeling is developed to build up a model for target system through the analysis of the dynamic features of that system. While implementing the characteristic modeling, this method has its unique features [8]. Generally speaking, a characteristic model can be written as a second-order differential equation below:

$$y(k+1) = \alpha_1(k)y(k) + \alpha_2(k)y(k-1) + \beta(k)u(k), \tag{58.1}$$

where $y(k)$ denotes the output and $u(k)$ represents the input at time step k. In addition, the coefficients, i.e., α_1, α_2, and β, are slowly time-varying, and they change within a certain range.

When designing a characteristic model, an online adaptive identification algorithm is adopted instead of deducing from the analytical system equation to obtain those slowly time-varying coefficients. Actually, with the help of online data, we could use any recursive regression method to find the coefficients we need. Here a gradient descent algorithm is given below [9]:

$$\theta(k+1) = \theta(k) + \frac{\gamma_1 \varphi(k)}{\gamma_2 + \varphi^T(k)\varphi(k)} \left[y(k+1) - \varphi^T(k)\theta(k) \right], \tag{58.2}$$

where $\theta(k) = [\alpha_1(k), \alpha_2(k), \beta(k)]$ and $\varphi(k) = [y(k), y(k-1), u(k)]$. In addition, γ_1 and γ_2 are two positive constants. After the coefficients of next time step are calculated, they should be restricted to the range set before. Since it is an online adaptive algorithm, characteristic modeling method can be employed without knowing the exact analytic model before. Then, some all-coefficient adaptive controllers can be designed for the characteristic model. Specifically, the golden-section controller is one of adaptive controllers, which is used together with the characteristic model.

58.2.2 *Fuzzy Dynamic Characteristic Model-Based Intelligent Control*

Characteristic modeling method needs to compress all the information of the high order model into several given characteristic parameters. The characteristic modeling therefore is essentially an online adaptive method, and it is very important to restrict the result coefficients in a reasonable range in order to make the identifier precise enough. For some problem especially when the system changes drastically, e.g., hypersonic vehicle system, covering all the possible state of the system with a single range will cause an inevitable large solution space [4].

To solve this problem, we introduce the fuzzy logic to partition the large space into several smaller subspaces. Here, the whole solution space is divided into r subspaces. Then for each space, a characteristic model is established by restricting the coefficients in corresponding sub-solution-spaces. Finally, the r results are summed up by multiplying with fuzzy factors w_i that describes how close the current system is to this subspace.

The fuzzy dynamic characteristic model can be written as follows [3]:

$$\{L^i\}_{i=1}^r = \left\{ \begin{array}{l} \text{IF} \quad \overset{p}{\underset{j=1}{\text{and}}} \ \xi_j(k) \text{ is } M_j^{i_j} \\ \text{THEN} \ \ y^i(k+1) = \alpha_1^i(k)y(k) + \alpha_2^i(k)y(k-1) + \beta^i(k)u(k) \end{array} \right\}. \tag{58.3}$$

Here, the fuzzy factor is defined as

$$w_i(k) = \frac{a^i(k)}{\sum_{i=1}^r a^i(k)}, \tag{58.4}$$

where $a^i(k) = \prod_{j=1}^p M_j^{i_j}\left(\xi_j(k)\right)$.

We can design the controller in each subspace, and the fuzzy adaptive controller is derived in accordance with parallel distributed compensation (PDC) method.

58.3 Main Results

Considering the high speed of the vehicle during re-entry and the tracking characteristic of the piecewise linear drag acceleration versus velocity profile, a nonlinear differential golden-section adaptive control law is designed [10]. Meanwhile, a suitable compensation control law is also introduced [9].

The PDC-based fuzzy adaptive controller is given as follows:

$$\{R^i\}_{i=1}^r = \left\{ \begin{array}{l} \text{IF} \quad \overset{p}{\underset{j=1}{\text{and}}} \ \xi_j(k) \text{ is } M_j^{i_j} \\ \text{THEN} \ \ u^i(k) = u_g^i(k) + u_a^i(k) \end{array} \right\}, \tag{58.5}$$

where

$$u_g^i(k) = -\frac{1}{\hat{\beta}^i(k)}\left[\left(l_1\hat{\alpha}_1^i(k) + l_2\hat{\alpha}_2^i(k)\right)y(k) - X^i(y(k))(y(k) - y(k-1))\right], \tag{58.6}$$

$$u_a^i(k) = -\frac{1}{\hat{\beta}^i(k)}\left[l_2\left(\hat{\alpha}_1^i(k) + \hat{\alpha}_2^i(k) - 1\right)y(k)\right], \tag{58.7}$$

and $l_1 = 0.382$, $l_2 = 0.618$, $l_1 + l_2 = 1$. In addition, $\hat{\alpha}_1^i$, $\hat{\alpha}_2^i$, and $\hat{\beta}^i$ are the identification results of parameters α_1^i, α_2^i, and β^i obtained by using the weighted least squares method. Specifically, $X^i(y(k))$ is a nonlinear function of $y(k)$.

The control input $u_a^i(k)$ is introduced to the stability analysis. As a suitable compensation control law, it can avoid the case that the control performance is deteriorated or that the closed-loop system is even unstable due to the estimation errors. If the sample time is small enough, $u_a^i(k) \to 0$ since $\left((\hat{\alpha}_1^i(k) + \hat{\alpha}_2^i(k)\right) \to 1$.

Substituting (58.6) and (58.7) into (58.5), we obtain:

$$\begin{aligned} u^i(k) &= u_g^i(k) + u_a^i(k) \\ &= -\frac{1}{\hat{\beta}^i(k)}\left\{\left[\hat{\alpha}_1^i(k) + 2l_2\hat{\alpha}_2^i(k) - X^i(y(k)) - l_2\right]y(k) + X^i(y(k))y(k-1)\right\}. \end{aligned} \tag{58.8}$$

By using the fuzzy inference method with a center-average defuzzifier, product inference, and singleton fuzzifier, the overall FDC-based fuzzy adaptive controller in (58.5) can be written as

$$u(k) = -\sum_{i=1}^{r}\frac{w_i(k)}{\hat{\beta}^i(k)}\left\{\left[\hat{\alpha}_1^i(k) + 2l_2\hat{\alpha}_2^i(k) - X^i(y(k)) - l_2\right]y(k) + X^i(y(k))y(k-1)\right\}. \tag{58.9}$$

By substituting (58.9) into (58.3) and using the fuzzy inference method mentioned above, we obtain the equation of the close-loop system as follows:

$$y(k+1) = \sum_{i=1}^{r}\sum_{j=1}^{r} w_i(k)w_j(k)\left[-\bar{h}_1^{ij}(k, y(k))y(k) - \bar{h}_2^{ij}(k, y(k))y(k-1)\right], \tag{58.10}$$

where

$$\bar{h}_1^{ij}(k, y(k)) = -\alpha_1^i(k) + \frac{\beta^i(k)}{\hat{\beta}^j(k)}\left[\hat{\alpha}_1^j(k) + 2l_2\hat{\alpha}_2^j(k) - X^j(y(k)) - l_2\right], \tag{58.11}$$

$$\bar{h}_2^{ij}(k, y(k)) = -\alpha_2^i(k) + \frac{\beta^i(k)}{\hat{\beta}^j(k)}\, X^j(y(k)). \tag{58.12}$$

Then the closed-loop system (58.10) can be transformed into the following form:

$$Y(k+1) = \sum_{i=1}^{r}\sum_{j=1}^{r} w_i(k)w_j(k)\left[\Lambda^{ij}(k, y(k))\, Y(k)\right], \tag{58.13}$$

where

$$\Lambda^{ij}(k, y(k)) = \begin{bmatrix} 0 & 1 \\ -\bar{h}_2^{ij}(k, y(k)) & -\bar{h}_1^{ij}(k, y(k)) \end{bmatrix}, \tag{58.14}$$

$$Y(k) = \begin{bmatrix} y(k) & y(k+1) \end{bmatrix}^{\mathrm{T}}. \tag{58.15}$$

For written convenience, we have the following definitions:

$$\Lambda^{ij}(k) \triangleq \Lambda^{ij}(k, y(k)), \quad \bar{h}_1^{ij}(k) \triangleq \bar{h}_1^{ij}(k, y(k)) \text{ and } \bar{h}_2^{ij}(k) \triangleq \bar{h}_2^{ij}(k, y(k)).$$

We provide the following stability condition for the closed-loop system (58.13).

Theorem 58.1 *Assuming* $0 < \beta^i(k)/\hat{\beta}^i(k) \leq 2$ *and* $|X^i(y(k))| < H$ *where* H *is a constant for all* $i \in \{1,2,\ldots,r\}$, *the closed-loop system* (58.13) *designed by the fuzzy adaptive controller* (58.5) *and parameter estimation algorithm* (58.2), *is uniformly asymptotic stable where its origin is the equilibrium point, if for all* $i, j \in \{1,2,\ldots,r\}$, *let*

$$F_1(k) = \sum_{i=1}^{r} \sum_{j=1}^{r} \bar{h}_1^{ij}(k) \quad \text{and} \quad F_2(k) = \sum_{i=1}^{r} \sum_{j=1}^{r} \bar{h}_2^{ij}(k),$$

the following conditions hold:

(1) *Let* $\Delta F_1(k) = F_1(k+1) - F_1(k) = \sum_{i=1}^{r} \sum_{j=1}^{r} \left(\bar{h}_1^{ij}(k+1) - \bar{h}_1^{ij}(k)\right)$ *be the change rate of* $F_1(k)$, *then it satisfies*:

$$D_{1,\min}(k) < -\varepsilon_1 \Delta F_1(k) < D_{1,\max}(k). \tag{58.16}$$

(2) *Give the following definitions*:

$$\Delta F_1^2(k) = F_1^2(k+1) - F_1^2(k) = \sum_{i=1}^{r} \sum_{j=1}^{r} \left[\left(\bar{h}_1^{ij}(k+1)\right)^2 - \left(\bar{h}_1^{ij}(k)\right)^2 \right], \tag{58.17}$$

$$\Delta F_2^2(k) = F_2^2(k+1) - F_2^2(k) = \sum_{i=1}^{r} \sum_{j=1}^{r} \left[\left(\bar{h}_2^{ij}(k+1)\right)^2 - \left(\bar{h}_2^{ij}(k)\right)^2 \right]. \tag{58.18}$$

Then they satisfy:

$$\Delta F_1^2(k) < N_{1,\max}(k), \quad \Delta F_2^2(k) < N_{2,\max}(k) \tag{58.19}$$

where

$$D_{1,\min}(k) = \frac{S(k)}{2} - \sqrt{q_{11}(k) q_{22}(k) - \bar{\delta}}, \tag{58.20}$$

$$D_{2,\max}(k) = \frac{S(k)}{2} + \sqrt{q_{11}(k) q_{22}(k) - \bar{\delta}}, \tag{58.21}$$

$$N_{1,\max}(k) = -F_2^2(k+1) + (1 + 2\varepsilon_1 - \delta_2)F_1^2(k+1) - F_1^4(k+1) + \delta_2 - \delta_1 - \delta_{22}, \tag{58.22}$$

$$N_{2,\max}(k) = (1 - \delta_2)F_2^2(k+1) - F_1^2(k+1)F_2^2(k+1) + \delta_1 - \delta_{11}, \tag{58.23}$$

where ε_1, $\bar{\delta}$, δ_1, δ_2, δ_{11}, $\delta_{22} \in \mathbb{R}^+$ *and they are all small scalar constants. In addition, they satisfy*:

$$\delta_1 < \delta_2, \ \bar{\delta} < \delta_{11}\ \delta_{22}, \quad \text{and} \quad \varepsilon_1 < \delta_1/(\sqrt{3}H_1),$$

where H_1 *denotes the upper bound of* $|F_1(k)|$, *which means*:

$$|F_1(k)| = \left| \sum_{i=1}^{r} \sum_{j=1}^{r} \bar{h}_1^{ij}(k) \right| < H_1.$$

And

$$S(k) = -2p_{12}(k+1) - 2[p_{12}(k+1)F_2(k+1) - p_{22}(k+1)F_1(k+1)F_2(k+1)],$$

where $P(k) = \begin{bmatrix} p_{11}(k) & p_{12}(k) \\ p_{21}(k) & p_{22}(k) \end{bmatrix}$, $Q(k) = \begin{bmatrix} q_{11}(k) & q_{12}(k) \\ q_{21}(k) & q_{22}(k) \end{bmatrix}$, *and*

$$\begin{cases} p_{11}(k) = F_2^2(k) + \delta_1 \\ p_{12}(k) = p_{21}(k) = \varepsilon_1 F_1(k), \\ p_{22}(k) = F_1^2(k) + \delta_2 \end{cases}$$

and

$$\begin{cases} q_{11}(k) = p_{11}(k) - p_{22}(k+1)F_2^2(k+1) \\ q_{12}(k) = q_{21}(k) = p_{12}(k) + p_{21}(k+1)F_2(k+1) - p_{22}(k+1)F_1(k+1)F_2(k+1). \\ q_{22}(k) = p_{22}(k) - p_{11}(k+1) + 2p_{12}(k+1)F_1(k+1) - p_{22}(k+1)F_1^2(k+1) \end{cases}$$

Proof With the definitions mentioned above, the fuzzy dynamic characteristic model system (58.13) can be transformed into the following form:

$$Y(k+1) = \sum_{i=1}^{r} \sum_{j=1}^{r} w_i(k) w_j(v) \left[\Lambda^{ij}(k) Y(k) \right] = \Lambda(k) Y(k), \tag{58.24}$$

where $\Lambda(k) = \sum_{i=1}^{r} \sum_{j=1}^{r} \Lambda^{ij}(k) = \begin{bmatrix} 0 & 1 \\ -F_2(k) & -F_1(k) \end{bmatrix}$.

Define a Lyapunov function as:

$$V(k) = Y^{\mathrm{T}}(k)\, P(k)\, Y(k). \tag{58.25}$$

Then, $\Delta V(k) = -Y^{\mathrm{T}}(k)\left[P(k) - \Lambda^{T}(k)P(k+1)\Lambda(k+1)\right] Y(k)$.
Therefore, with the definition, we have

$$Q(k) = P(k) - \Lambda^{\mathrm{T}}(k+1)P(v+1)\Lambda(k+1). \tag{58.26}$$

Firstly, by following similar approach used in proving Theorem 58.1 in [10], we can easily conclude that $P(k)$ is uniformly bounded and positive definite. Moreover, we can prove that $Q(k)$ is also uniformly bounded and positive definite through the use of the similar analysis of Theorem 58.1 in [10].

Then, there exists a uniformly bounded and positive definite matrix $P(k)$, such that the matrix $Q(k)$ defined by (58.26) is uniformly bounded and positive definite, from the Lyapunov stability theory, we can conclude that the closed loop system is uniformly asymptotic stable. □

Remark 58.1 Since $\left((\alpha_1^i(k) + \alpha_2^i(k)\right) \to 1$ when the sample time is small enough, the control input $u_a^i(k)$ is set to 0. Then the control output in R^i is only a nonlinear differential golden-section adaptive control. It means $u^i(k) = u_g^i(k)$.

Remark 58.2 In the condition of this theorem, it should be noted that the origin of this closed-loop system is the equilibrium point. This stability theorem is therefore presented when the proposed controller is designed for the case of maintaining the system output at 0. For other output tracking applications, the control law should be rewritten by using $(y(k) - y^*(k))$ and $(y(k-1) - y^*(k-1))$ to replace $y(k)$ and $y(k-1)$ in (58.5), respectively. Here $y^*(k)$ represents the desired system output at step k.

58.4 Conclusion

This paper has investigated the problem of stability for a class of FDCM-based controllers in its application of hypersonic vehicles. Starting from the general formulation of FDCM-based controller, in view of the high speed of the hypersonic vehicle during re-entry and the tracking characteristic of requirements, a special controller has been developed through the combination of a nonlinear differential golden-section adaptive control law and a suitable compensation control law. The stability condition under which the closed-loop system is uniformly asymptotic stable is derived. This result may also be useful for obtaining similar performance guarantee for FDCM-based controller in other complex applications.

Acknowledgments This work was jointly supported by the National Natural Science Foundation of China (Grants Nos. 61174103, 61174069) and the Aerospace Science Foundation of China (Grant No. 2014ZA74001).

References

1. Wu HX, Hu J, Xie YC (2007) Characteristic model-based all-coefficient adaptive control method and its applications. IEEE Trans Syst Man Cybern Pt C Appl Rev 37(2):213–221
2. Cao SG, Rees NW, Feng G (1997) Analysis and design for a class of complex control systems part I: fuzzy modeling and identification. Automatica 33(6):1017–1028
3. Luo X, Sun ZQ, Sun FC (2009) A new approach to fuzzy modeling and control for nonlinear dynamic systems: neuro-fuzzy dynamic characteristic modeling and adaptive control mechanism. Int J Control Autom Syst 7(1):123–132
4. Luo X, Li J (2011) Fuzzy dynamic characteristic model based attitude control of hypersonic vehicle in gliding phase. Sci China Ser F-Inf Sci 54(3):448–459
5. Luo X, Liu F, Sun FC (2014) Attitude tracking control for hypersonic vehicles based on type-2 fuzzy dynamic characteristic modeling method. Fuzzy Systems (FUZZ-IEEE), IEEE International Conference on 6–11 July, 2014, pp 113–120
6. Li HB, Sun ZQ, Min HB, Deng JQ (2011) Fuzzy dynamic characteristic modeling and adaptive control of nonlinear systems and its application to hypersonic vehicles. Sci China Ser F-Inf Sci 54(3):460–468
7. Deng JQ, Li HJ, Hu S et al (2012) Networked control systems based on the adaptive control methods of characteristic modeling and fuzzy dynamic characteristic modeling. J Univ Sci Tech Beijing 34(1):1–5 (in Chinese)
8. Wu HX, Liu YW, Liu ZH et al (2001) Characteristic modeling and the control of flexible structure. Sci China Ser F-Inf Sci 44(4):278–291
9. Lei YJ, Wu HX (2006) Tracking control of robotic manipulators based on the all-coefficient adaptive control method. Int J Control Autom Syst 4(2):139–145
10. Yang JC, Hu J, Ni ML (2008) Adaptive guidance law design based on characteristic model for reentry vehicles. Sci China Ser F-Inf Sci 51(12):2005–2021